UNIVERSIDADE FEDERAL DE PERNAMBUCO

CENTRO DE CIÊNCIAS EXATAS E DA NATUREZA

DEPARTAMENTO DE QUÍMICA FUNDAMENTAL

PROGRAMA DE PÓS-GRADUAÇÃO EM QUÍMICA

ESTUDOS ESPECTROSCÓPICOS DE MATERIAIS

METAL-ORGÂNICOS BASEADOS EM ÍONS

LANTANÍDEOS

Tese de Doutorado em Química

Marcelo Oliveira Rodrigues

UNIVERSIDADE FEDERAL DE PERNAMBUCO

CENTRO DE CIÊNCIAS EXATAS E DA NATUREZA

DEPARTAMENTO DE QUÍMICA FUNDAMENTAL

PROGRAMA DE PÓS-GRADUAÇÃO EM QUÍMICA

Tese apresentada ao Programa de Pós-Graduação em Química como parte dos requisitos para a obtenção de título de Doutor em Química.

Aluno: Marcelo Oliveira Rodrigues

Orientador: Severino Alves Júnior / Gilberto F. de Sá

Agência Financiadora: CNPq

Recife

Outubro, 2010

Tese submetida ao Corpo Docente do Programa de Pós-Graduação em Química do Departamento de Química Fundamental da Universidade Federal de Pernambuco como parte dos requisitos necessários para a obtenção do Grau de Doutor em Química.

Aprovada:

_____
Prof. Severino Alves Junior
(Orientador)
Departamento de Química Fundamental
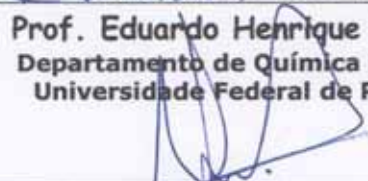Universidade Federal de Pernambuco

_____
Prof. Eduardo Henrique Lago Falcão
Departamento de Química Fundamental
Universidade Federal de Pernambuco
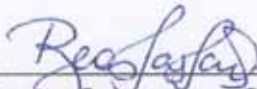
_____
Prof. Jefferson Luiz Princival
Departamento de Química Fundamental
Universidade Federal de Pernambuco

_____
Prof. Ricardo Oliveira Freire
Departamento de Química
Universidade Federal de Sergipe

_____
Profa. Beate Saegesser Santos
Departamento de Ciências Farmacêuticas
Universidade Federal de Pernambuco

"Estudos Espectroscópicos de Materiais Metal-Orgânicos Baseados em Íons Lantanídeos"

por

Marcelo Oliveira Rodrigues

Departamento de Química Fundamental
Centro de Ciências Exatas e da Natureza
Universidade Federal de Pernambuco
Recife-PE-Brasil
05 de novembro de 2010

"Querer o meu não é roubar o seu, pois o que eu quero é só função de eu!"

(Raul Seixas)

AGRADECIMENTOS

Resumo

A presente tese apresenta estudos espectroscópicos de vários Materiais Metal-Orgânicos (MMOs) contendo íons lantanídeos e está dividida em três capítulos. Capítulo 1 intitulado: *"Modelagem e Estudos Espectroscópicos de Materiais Metal-orgânicos contendo íons Lantanídeos"*, em que será apresentada a síntese hidrotermal, caracterização e estudos espectroscópicos teóricos/experimentiais de três LOFs (*Lanthanide-Organic Framework*) usando como centros metálicos os íons Eu^{3+}, Tb^{3+} e Gd^{3+} e o ácido melítico (MELL): $[Ln_2(MELL)(H_2O)_6]$ (onde Ln^{3+}= Eu^{3+}, Tb^{3+} ou Gd^{3+}, então designados como **(1.1)**, **(1.2)** e **(1.3)**, respectivamente. O capítulo 2, intitulado *"Processo de Transferência de Energia Sinérgico em Polímeros de Coordenação Heterobimetálicos contendo Lantanídeos"*, reporta a uma investigação detalhada dos processos de transferência de energia Ligante→Metal e Metal→Metal em dois polímeros de coordenação iso-estruturais, $_\infty[(Tb_{1-x}Eu_x)(DPA)(HDPA)]$, onde H_2DPA é o ácido dipicolínico e x = 0,05 e 0,5 respectivamente. O capítulo 3, intitulado *"Síntese e Estudos Teórico e Experimental das Propriedades Espectroscópicas de Compostos Bifosfonatos com Lantanídeos"*, mostra as sínteses caracterização e estudos espectroscópicos dos materiais $[Ln(Hpmd)(H_2O)]$, onde Ln^{3+} = Eu^{3+} **(3.1)**, Gd^{3+} **(3.2)**, Tb^{3+} **(3.3)** e $(Eu_{0,05}Tb_{0,95})^{3+}$ **(3.4)**; H_4pmda é o ácido 1,4-Fenil-bis(metileno)difosfonico.

Palavras Chaves: Lantanídeos, Luminescência, Compostos de Coordenação

Abstract

The present thesis shows spectroscopic studies of diverse Metal-Organic Materials based on lanthanide ions, being divided in three chapters. The first, entitled as *"Modeling, Structural and Spectroscopic Studies of Lanthanide-Organic Frameworks"* are reported the hydrothermal synthesis, characterization and theoretical/experimental spectroscopic investigations of three lanthanide-organic framework materials using as primary building blocks the metallic centers Eu^{3+}, Tb^{3+} and Gd^{3+} and residues of mellitic acid: $[Ln_2(MELL)(H_2O)_6]$ (where Ln^{3+} = Eu^{3+}, Tb^{3+} + and Gd^3; hereafter designated as **(1.1)**, **(1.2)** and **(1.3)**). Chapter 2, entitled as "*Synergic Energy Transfer Processes in Heterobimetallic Lanthanide Coordination Polymers*" are exhibited a detailed investigation of the Ligand→Metal and Metal→Metal energy transfers in two isostructurals 2D coordination polymers, $_\infty[(Tb_{1-x}Eu_x)(DPA)(HDPA)]$, where H_2DPA is pyridine 2,6-dicarboxylic acid and x = 0.05, and 0.50 respectively. The chapter 3 entitled as "*Synthesis, Theoretical and Experimental Spectroscopic Properties of Layered Lanthanide Bisphosphonates*" are shown the synthesis, characterization and spectroscopic studies of pure-phase of $Ln(Hpmd)(H_2O)]$ materials [where Ln^{3+} = Eu^{3+} **(3.1)**, Gd^{3+} **(3.2)**, Tb^{3+} **(3.3)** and $(Eu_{0.05}Tb_{0.95})^{3+}$ **(3.4)**; H_4pmda = 1,4-phenylenebis(methylene)diphosphonic acid (H_4pmd).

Keywords: Lanthanides, Luminescence, Coordination Compounds

LISTA DE FIGURAS

LISTA DE TABELAS

LISTA DE SIGLAS, SÍMBOLOS E ABREVIATURAS

0-D	Zero dimensional
1D	Uma dimensão
2D	Duas dimensões
3D	Três dimensões
A	Ampére
ASTM	*The Americam Society for Testing and Materials*
AZT	Azidotimidina
BDC	1,4-benzenodicarboxilato
bpy	Bipiridina
BTC	1,3,5-benzenotricarboxilato
C300	Cu_3BTC_2
CNHS	Carbono, nitrogênio, hidrogênio e enxofre
DMCL	Dispositivos Moleculares Conversores de Luz
DMF	Dimetilformamida
DMSO	Dimetilsufóxido
DOEL	Diodos Orgânicos Eletroluminescentes
DPA	Dipicolinato
DTG	Termogravimetria Derivada

EDS	Energy Dispersive X-Ray Spectroscopy
GSR	*Gunshot Residue* (Resíduo de disparo de arma de fogo)
H_2DPA	Ácido dipicolínico
H_2O	Água
IRMOF	*Iso-reticular Metal-organic Framework*
IV	Infravermelho
K	Kelvin
KBr	Brometo de potássio
Ln	Lantanídeo
MELL	Ácido melítico
MEV	Microscopia Eletrônica de Varredura
MIL	Material do Instituto Lavoisier
MMO	Material metal-orgânico
MOF	*Metal-organic Framework*
PC	Polímero de coordenação
pdc	3,5-piridinadicarboxilato
PO	Porfirina
ppm	Partes por milhão
pydc	3,5-piridinadicarboxilato
RMN	Ressonância Magnética Nuclear

TE	Transferência de energia
TG	Termogravimetria
THT	Tetrahidrotiofeno
UV	Ultravioleta
V	Volt
Xe-Hg	Xenônio-mercúrio
Z	Número de moléculas por célula
Zn	Zinco
Zn_4O	*Cluster* de zinco
RMI	*Ressonância Magnética de Imagem*
H_4pmd	Ácido 1,4-Fenil-bis(metileno)difosfônico

SUMÁRIO

Polímeros de Coordenação Heterobimetálicos contendo Lantanídeos

CAPÍTULO 3: Síntese e Estudos Teórico e Experimental das Propriedades

Espectroscópicas de Compostos Bifosfonatos com Lantanídeos

Introdução Geral

I. Materiais Metal-Orgânicos (MMOs) – Aspectos Históricos.

A evolução da sociedade tem evidenciado uma série de problemas que, na maioria dos casos, necessitam de soluções específicas. Conseqüentemente, a exploração de novas tecnologias que atendam essas necessidades constitui um dos setores estratégicos mais importantes da atualidade. Esta crescente demanda tem fomentado o desenvolvimento de novos materiais com elevada especificidade e funcionalidade.

A Química do Estado Sólido consiste em investigações relacionadas à síntese, características estruturais, propriedades (físicas e químicas) e aplicações de materiais sólidos. Este ramo da ciência é de fundamental importância, devido a estes compostos possuírem elevada significância para a sociedade atual. A prova disto advém da vasta utilização de materiais sólidos na confecção de dispositivos tecnologicamente estratégicos como: lasers, supercondutores, magnetos, materiais luminescentes, catalisadores, entre outros.[1]

As propriedades físicas e químicas dos compostos dependem quase que exclusivamente da disposição espacial dos seus átomos, íons ou moléculas e da natureza das ligações químicas entre seus constituintes,[2] no entanto, muitos processos mais tradicionais de preparação de materiais sólidos restringem ao controle estrutural e à reatividade dos materiais. Nesta perspectiva, muitos

grupos de pesquisa têm se esforçado no desenvolvimento de métodos sintéticos, visando, principalmente, controlar e entender as propriedades físicas e químicas dos sólidos produzidos, através da correlação entre as estruturas dos reagentes e o produto final da síntese.[3-6]

Os últimos 20 anos têm sido marcados por intensos avanços na química do estado sólido, principalmente, em relação a compostos de coordenação que apresentam estruturas infinitas.[7] Os polímeros de coordenação (PC) também designados como *metal-organic framework* (MOF) constituem uma extensa classe de materiais cristalinos formados por íons metálicos conectados por ligantes orgânicos multifuncionalizados.[8] As estruturas resultantes pela formação da ligação do par metal-ligante incluem desde discretos complexos moleculares zero-dimensional (0-D) até infinitas redes com uma, duas ou três dimensões (1D, 2D ou 3D),[9-12] Figura 1.
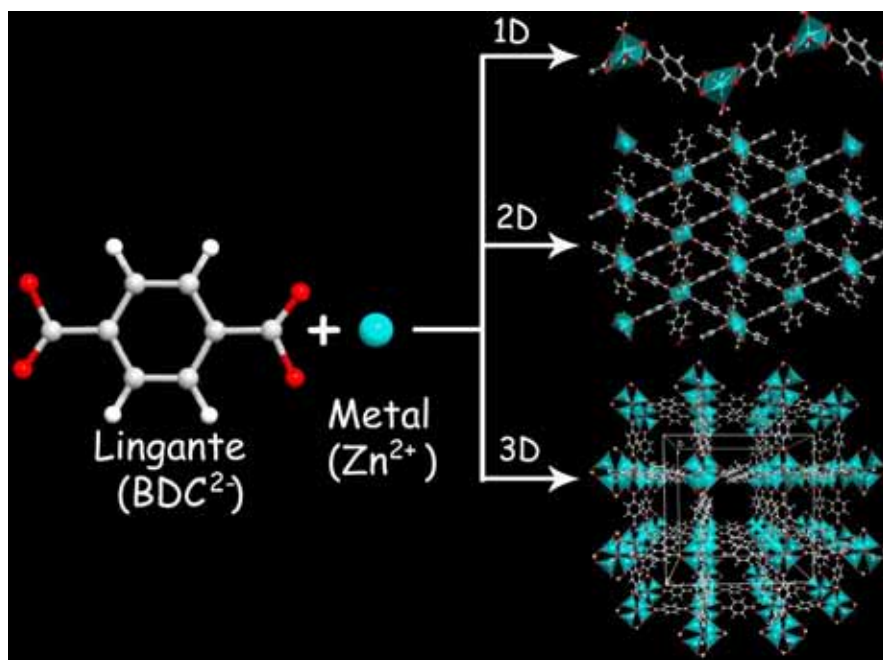
Figura 1: Dimensionalidade estrutural dos Materiais Metal-Orgânicos (1D, 2D e 3D). Ilustrativamente foi utilizado o íon do ligante orgânico 1,4-benzenodicarboxilato (BDC^{2-}) e o cátion Zn^{2+}.

No início do século XVII, o químico alemão chamado Diesbach sintetizou o corante conhecido como Azul da Prússia e somente 372 anos depois sua estrutura pôde ser determinada (Figura 2).[13] De fato, este foi o primeiro relado de um composto sintético que pôde ser considerado como polímero de coordenação. Surpreendentemente, durante muitos anos pouca atenção foi dada a esse material, sendo poucos estudos realizados. Até que na década de

1980, Robinson *et al.* iniciaram uma abordagem acerca do *design* de polímeros de coordenação, cunhando o famoso termo "*node-and-sparcer*".[14]
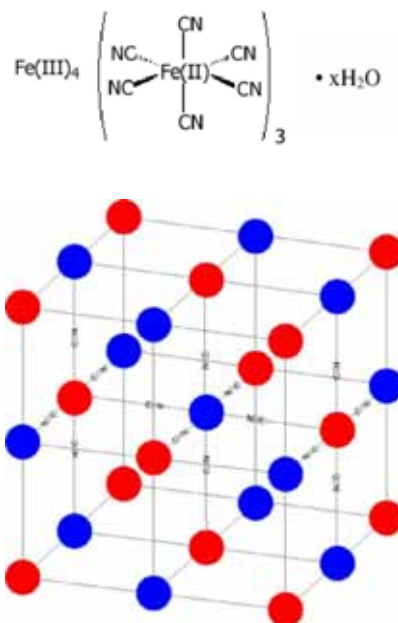
Figura 2: Estrutura cristalográfica do Azul da Prússia. Fe(II): Vermelho; Fe(III): Azul.

Com a introdução da Química Reticular, por alguns considerada como sendo uma vertente da Engenharia de Cristais, tornou-se possível o planejamento estrutural de alguns desses compostos baseado no reconhecimento de padrões sintéticos que favorecessem um determinado modo de coordenação metal-ligante. Com a publicação da MOF-5 em 1999[15] e subseqüentemente das IRMOF[16] (Figura 3), Yaghi provou a hipótese de que em

condições experimentais as quais preservam os aspectos geométricos e direcionais de centros metálicos e ligantes orgânicos é possível a formação de arquiteturas moleculares específicas.[3,17,18] Vale salientar que em seus experimentos para obtenção da MOF-5 e das IRMOF, Yaghi baseou-se na estrutura do *cluster* de zinco (Zn_4O) presente no acetato de zinco anidro,[19] conhecida desde 1953.[20]
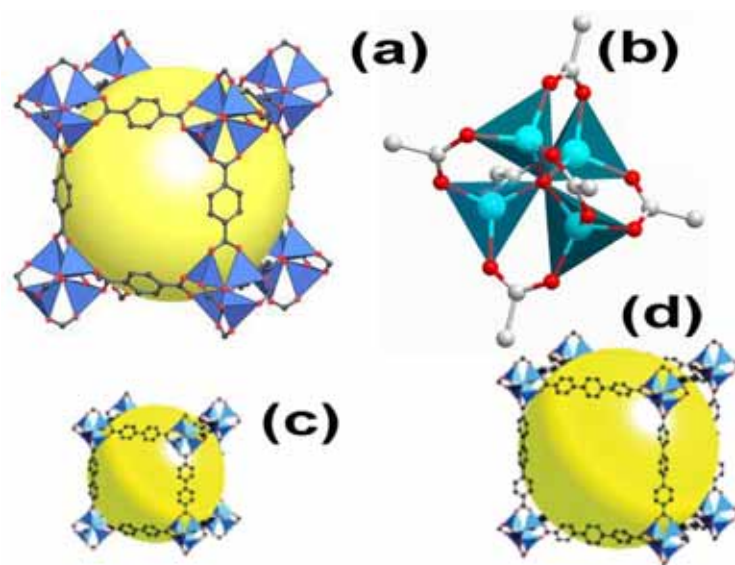
Figura 3: Ilustração das estruturas: (a) MOF-5; (b) *cluster* de Zn_4O; (c) IRMOF-10; (d) IRMOF. Adaptado das ref. 15, 16 e 20.

Subseqüentemente, diversos grupos de pesquisa contribuíram substancialmente para o desenvolvimento de investigações acerca das

estruturas e propriedades desses sólidos. Fato este, indubitavelmente evidenciado pelo elevado número de artigos científicos publicados na literatura desde então (Figura 4).[7,21-24]
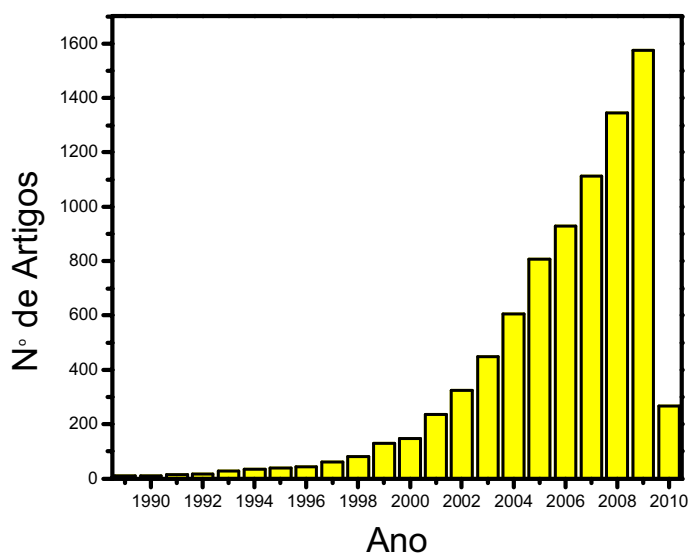
Figura 4: Número de artigos contendo as palavras-chaves "*metal-organic framework*" contidos nos títulos ou *abstracts* dos últimos 20 anos. (Fonte: *Web of Science*, 08/03/2010).

II. *Síntese de Materiais Metal-Orgânicos.*

As metodologias de preparação de MOFs são consideradas processos simples quando comparados com sínteses de moléculas orgânicas como: éteres de coroas, criptatos, dendrímeros e outros. No entanto, esta simplicidade tem seu preço, uma vez que é fundamental obter cristais de MOFs com tamanho e qualidade adequados para determinação estrutural.

Em temperaturas inferiores a 100ºC normalmente são usados métodos sintéticos que envolvem gradientes de concentração,[15,25-27] entretanto para sínteses acima desta temperatura é aplicada a técnica solvotermal.[28] Os métodos de gradientes de concentração para preparação de MOFs envolvem a variação da concentração da amostra ou dos reagentes pela remoção do solvente ou pelo transporte de massa em meios onde os mesmos são pouco solúveis. Para esta metodologia podem ser destacadas a evaporação e as difusões (em gel, líquido-líquido, líquido-vapor).[29] Apesar destas sínteses gerarem cristais com boa qualidade, são limitadas por demandarem tempo, não permitirem maiores controles da cinética de nucleação e das arquiteturas moleculares, pois restringem ajustes às condições de síntese.[30] Na figura 5 são mostrados esquemas das sínteses que envolvem gradientes de concentração.
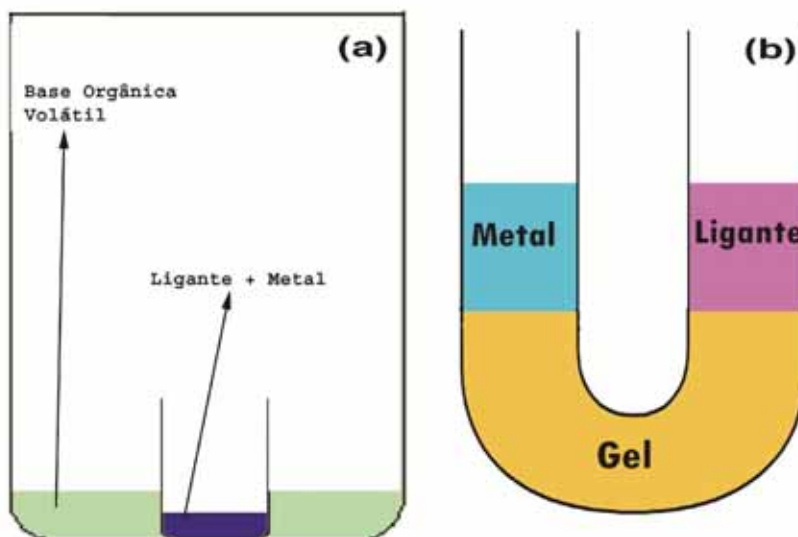
Figura 5: Ilustração de sínteses de MOFs envolvendo gradiente de concentração. (a) Difusão líquido-vapor; (b) Difusão em gel.

O método solvotermal ocupa lugar de destaque no que se refere à síntese de MOFs. Esse tipo de síntese envolve o uso da água ou outro solvente orgânico (alcoóis, dialquilformamidas, piridina, DMSO) em um recipiente hermeticamente fechado (autoclave, Figura 6) submetido a temperaturas normalmente acima do ponto de ebulição do solvente. A maioria dos trabalhos utiliza a água como solvente, pois o processo hidrotermal mimetiza processos geológicos de crescimento de cristais que ocorrem na crosta terrestre.
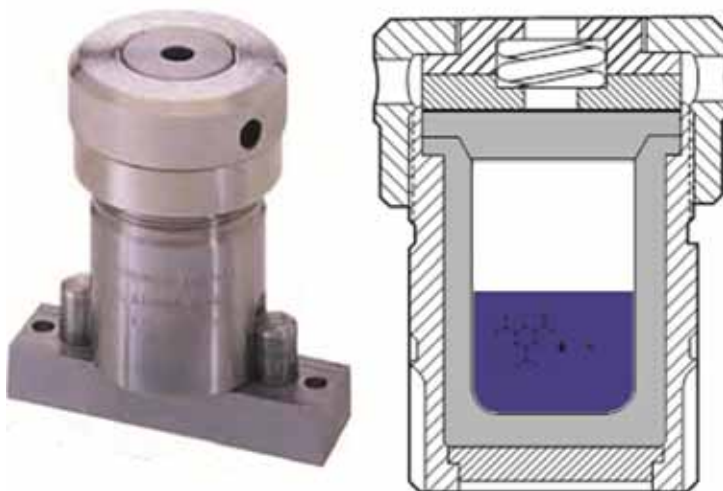
Figura 6: Reatores usados em síntese solvotermal.

Sob condições severas de temperatura e pressão as propriedades físicas do solvente utilizado mudam consideravelmente. Por exemplo, a viscosidade da água diminui com o aumento da temperatura. A 500°C com 10 bar de pressão somente 10% de sua magnitude é preservada. Logo, a mobilidade dos íons e moléculas dissolvidos é consideravelmente aumentada quando comparada a condições normais de temperatura e pressão, isto permite a nucleação e crescimento dos cristais. Similarmente, a constante dielétrica da água é significativamente reduzida em condições extremas. As implicações disto estão associadas ao aumento da solubilidade dos reagentes sólidos nas condições da reação e aumento da constante de dissociação devido à redução da interação

intermolecular. Gerardin *et. al* monitoraram a variação de pH da água em condições hidrotermais usando RMN e constataram que a 180ºC o respectivo valor é 5,5.[31]

Variações da síntese solvotermal têm sido propostas. Cheetham e colaboradores[32] mostraram utilização de dois líquidos imiscíveis (água e 1-pentanol ou ciclohexanol) para preparo de MOFs, no qual cristais com excelente qualidade foram formados na interface dos dois solventes. Outra variante bastante interessante consiste no uso de radiação de microondas. Com este método é possível sintetizar MMOs em tempos curtos, controlar a distribuição de tamanho das partículas,[33] além de facilitar o controle dos parâmetros experimentais.[21] Silva *et al*[34] demonstraram a síntese da $[Ce_2(pydc)_2(Hpydc)(H_2O)_2]Cl \cdot (9+y)H_2O$ com apenas 30 minutos de irradiação contra os 3 dias da síntese solvotermal convencional. Da mesma forma, Chang e colaboradores preparam a MIL-100 por 1 hora de irradiação em 220ºC contra as 96 horas do método hidrotermal.[35]

Em virtude do largo interesse nesses materiais, novas alternativas sintéticas vêm sendo propostas. Em recente trabalho, Yaghi, produziu uma série de MMOs (MOF-5, MOF-74, MOF-177, MOF-199 e IRMOF-0) utilizando precipitação à temperatura ambiente.[36] Basicamente, os materiais são obtidos através da agitação de todos os reagentes por algumas horas em balões

contendo DMF. Alternativamente, Qiu mostrou a versatilidade do uso de ultrasom para a síntese de $[Zn_3(BTC)_2 \cdot 12H_2O]$[37] e pesquisadores da BASF desenvolveram uma rota eletroquímica para preparação da Cu-BTC (Basolite® C300) em escala industrial.[38] No último caso, ânodos sacrificiais de cobre com 5,0 mm de espessura são oxidados em presença do 1,3,5-bezenotricarboxilato dissolvido em metanol durante 150 minutos sob 12-19 V e 3,0 A.[39]

III. Aplicação de Materiais Metal-Orgânicos

Os sólidos inorgânicos porosos são considerados por muitos pesquisadores materiais industrialmente estratégicos,[40] pois cerca de 20-30% do total de materiais de uso doméstico em países industrializados os utilizam de alguma maneira.[41] Aplicações em catálise, petroquímica, separação seletiva, entre outras[42-46] utilizam a elevada estabilidade térmica, área superficial e a porosidade destes compostos, comprovando o quanto estes materiais estão consolidados e são importantes no cenário mundial.[47]

Alguns MMOs combinam o quase ilimitado controle dimensional e a área superficial[48-50] sem o comprometimento das propriedades físicas e químicas,[51] características que os tornam principais concorrentes das zeólitas e outros sólidos inorgânicos relacionados.[51] Embora as vantagens dos MMOs sobre os sólidos inorgânicos clássicos sejam evidentes, somente um limitado número de

aplicações dos MMOs tem sido discutido em escala laboratorial[52] e existe somente um grupo de pesquisa que tem se aventurado em testes a níveis industriais.[38,39]

É importante destacar que devido ao papel crucial em muitos processos químicos industriais, a catálise heterogênea sem dúvida é uma das mais promissoras aplicações dos MMOs.[53-55] Fujita foi o pioneiro a demonstrar essa potencialidade quando reportou a propriedade catalítica específica do [Cd(NO$_3$)(4,4´-bpy)$_2$] para a reação de cianolização de aldeídos.[56] Nugyen *et. al.* mostrou que o material intitulado ZnPO-MOF (derivado de zinco e porfirina) produz um aumento na taxa da reação de transferência do grupo acila entre o *N*-acetilimidazol e o 3-piridilcarbinol (Esquema (**1**)), em 2420 vezes em relação a reação não-catalisada.[57]
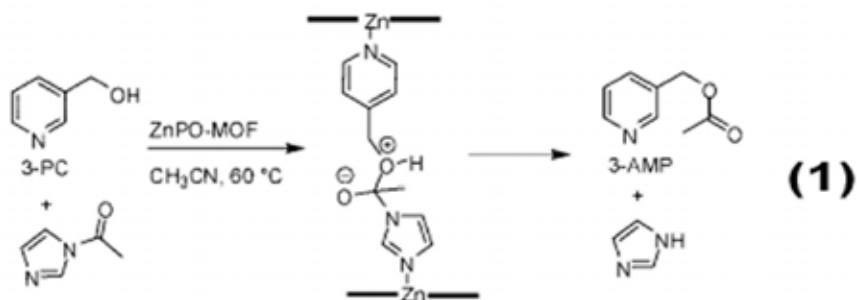
A MOF-5 tem sido usada como suporte catalítico para nanopartículas de óxidos metálicos em diversas reações como: síntese de metanol[58] e

hidrogenação do etil-cinamato[59]. Recentemente, Wolczansk e Visseaux verificaram o potencial de MMOs em reações de Ziegler-Natta para preparação de polímeros dispersos, lineares e atáticos.[60,61] Em reações que envolvem compostos quirais, Kim *et al* reportou o primeiro exemplo de catálise assimétrica como uma MOF homoquiral baseada em um derivado do ácido tartárico[62] e Lin preparou uma série de MMOs homoquirais baseada em lantanídeos e ligantes fosfonatos e examinou as atividades catalíticas desses materiais.[63]

Em virtude da necessidade de desenvolvimento de tecnologias limpas e decréscimo das reservas energéticas de origem fóssil, diversos grupos têm se dedicado a pesquisas envolvendo o desenvolvimento de tecnologias para a estocagem, purificação e separação de gases, baseadas em MMOs.[64-69] O primeiro exemplo foi divulgado por Kitagawa em 1997 quando confinou uma grande quantidade de gás metano em MMOs.[70] Subseqüentemente, outros trabalhos demonstraram a vasta capacidade de adsorção de gases como: metano (CH_4),[71,72] hidrogênio (H_2),[73,74] dióxido de carbono (CO_2)[75-77] e nitrogênio (N_2).[78] A remoção de *tio* derivados (THT, tetrahidrotiofeno) em gás natural foi realizada por pesquisadores da BASF. Neste experimento, representado pela Figura 7, a MOF Cu-BTC foi capaz de remover traços de THT (10-15 ppm) a níveis comparáveis a produtos comercializados para esta

finalidade (Norit-RB4 e Carbo Tech-C38/4).[38] Ainda no âmbito da purificação e

remoção de contaminantes, Moos e colaboradores se valeram da afinidade de

algumas MMOs por derivados de enxofre para utilizarem-nas na desulforização

de combustíveis.[79]
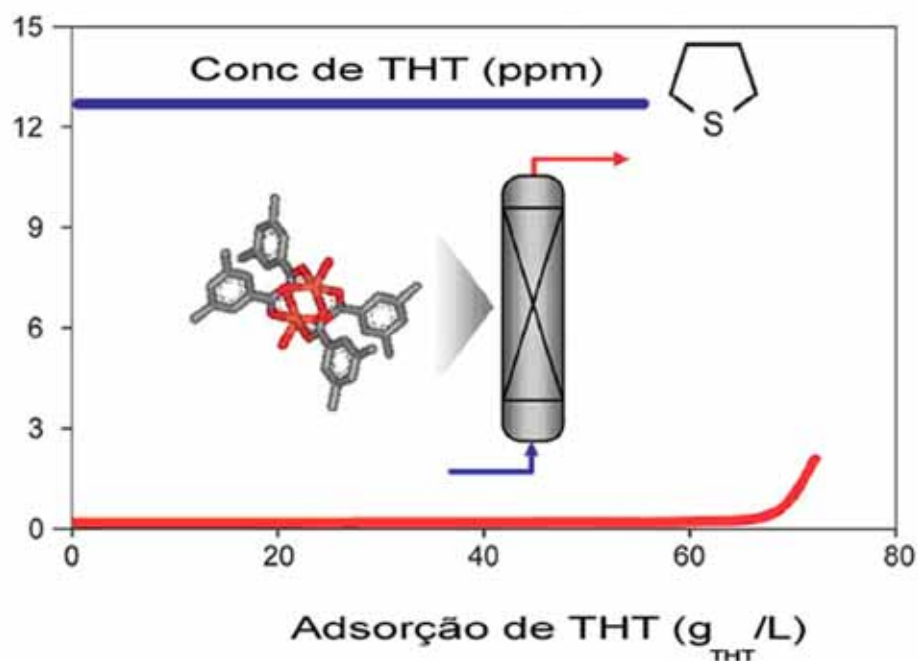
Figura 7: Ilustração do experimento de remoção de THT em gás natural usando

MMOs. Adaptado da ref. 38.

Outras emergentes aplicações consistem nas utilizações dos MMOs como

carreadores de drogas e agentes de contrastes em Ressonância Magnética de

Imagem.[80,81] Nesta perspectiva, Horcajada e colaboradores tem divulgado a drástica adsorção de analgésico Iboprofeno (0,35 a 1,4 g/g) nas MOFs desidratadas, MIL-100 e MIL-101.[82] No seu mais recente trabalho diversos fármacos (AZT, benzofenonas, cafeína, doxoribucina e outros) têm sido adsorvidos em MOFs e seus efeitos testado *in vivo*, adicionalmente ensaios de RMI (Ressonância Magnética de Imagem) foram realizados.[80] Já Boyes e colaboradores propõem o uso de MMOs na Multifuncinal Nanomedicina visando a marcação e tratamento de Câncer.[83]

O desenvolvimento de sensores ópticos baseados nesses materiais também tem sido proposto.[50,84-86] O princípio básico do funcionamento de sistemas consiste na variação do sinal óptico após a interação do analito com a fase sensora (MMOs).[87] Cheng e colaboradores vem reportando uma série de protótipos baseados em MMOS com lantanídeos para o sensoriamento de espécies. O Tb(BTC)·G (BTC = Bezenotricarboxilato, G = moléculas de solventes) foi proposto para o sensoriamento do ânion F^-,[88] enquanto o EuBTC para pequenas moléculas (etanol, DMF, acetona)[89] e o $[Eu(pdc)_{1,5}(DMF)]\cdot(DMF)_{0,5}(H_2O)_{0,5}]$ (pdc = 3,5-piridinedicarboxilato) para a detecção de íons metálicos.[90] Harbuzaru *et. al.* têm apresentado novos MMOs baseado em Ln^{3+} íons e os efeitos de supressão e aumento da luminescência em presença da água ou etanol e em função do pH, respectivamente.[86,91] A

luminescência oriunda dos ligantes orgânicos também tem sido utilizadas para o monitoramento de espécies, o exemplo interessante é o uso do $[Zn_3(BTC)_2 \cdot 12H_2O]$ para a análise de alquilaminas em solução de acetonitrila via titulação espectrofotométrica.[37]

Em trabalhos recentes desenvolvidos pelo grupo de terras raras do Departamento de Química Fundamental da Universidade Federal de Pernambuco, MMOs vêm sendo empregados como novas fases estacionárias para extração em fase sólida de pesticidas.[92,93] O material 2D $_\infty[(Gd)(DPA)(HDPA)]$, mostrou uma potencial adsorção seletiva de três pesticidas (bifentrin, tetradifon e fosalona) dos seis estudados, enquanto o 3D $_\infty[(La_{0,9}Eu_{0,1})_2(DPA)_3(H_2O)_3]$ pode ser usado em análises de pirimicarbe, metil-paration, malation, procimidona, α-endosulfano e β-endosulfano. Já o $[Zn(BDC)(H_2O)_2]_n$ sintetizado por Wanderley apresenta boa perfomance para análise de seis pesticidas dos sete estudados em matriz de planta medicinal.[94] Na vanguarda, Geder e colaboradores desenvolveram MMOs altamente luminescentes que foram aplicados em uma nova metodologia para exame residográfico de arma de fogo (Figura 8).[95]
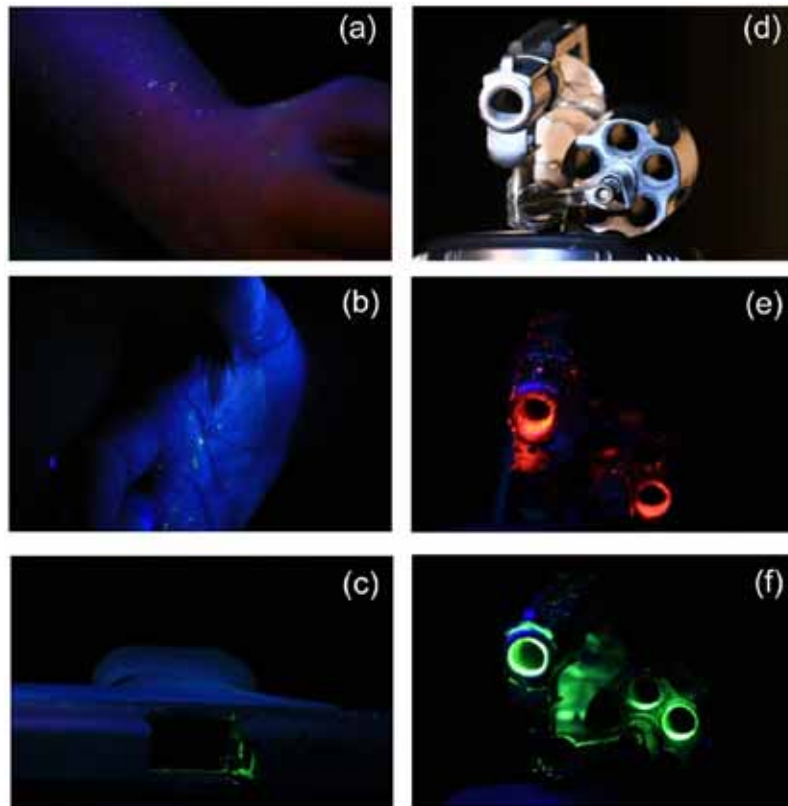
Figura 8: Ilustração do experimento detecção de GSR por MMOs luminescentes. (a) e (b): Membros superiores e mãos do atirador sob luz UV mostrando pontos brilhantes do marcador; (c): Pistola sob luz UV após disparo com munição marcada; (d): Revolver sem irradiação da luz UV; (e) e (f): Revolveres sob luz UV após disparo.

A utilização dos MMOs sob a forma granular, apesar de ser a mais difundida atualmente, restringe às opções de exploração das potencialidades destes compostos.[96] Logo, a incorporação em matrizes e a fixação em

superfícies são alternativas viáveis que facilitam a manipulação e sofisticam a aplicação desses materiais. Recentemente, Alledorf observou que a energia da interação molecular analito-MMOs pode ser convertida em energia mecânica para criação de um sensor reversível e altamente seletivo através do crescimento de uma monocamada de MMOs na superfície de um *microcantilever*.[96]

IV. Referências

(1)   Rao, C. N. R.; Gopalakrishnan, J. *New directions in solid state chemistry : structure, synthesis, properties, reactivity and materials design / C.N.R. Rao and J. Gopalakrishnan*; Cambridge University Press: Cambridge [Cambridgeshire] ; New York :, 1986.

(2)   Miller, G. J. *Complex rare-earth tetrelides, RE5(SixGe(1-x))4: new materials for magnetic refrigeration and a superb playground for solid state chemistry*; *Chem Soc Rev* **2006**, *35*, 799-813.

(3)   Yaghi, O. M.; O'Keeffe, M.; Ockwig, N. W.; Chae, H. K.; Eddaoudi, M.; Kim, J. *Reticular synthesis and the design of new materials*; *Nature* **2003**, *423*, 705-714.

(4)   Ramanan, A.; Whittingham, M. S. *How Molecules Turn into Solids: the Case of Self-Assembled Metal−Organic Frameworks*; *Crystal Growth & Design* **2006**, *6*, 2419-2421.

(5)   Ockwig, N. W.; Delgado-Friedrichs, O.; O'Keeffe, M.; Yaghi, O. M. *Reticular Chemistry: Occurrence and Taxonomy of Nets and Grammar for the Design of Frameworks*; *Accounts of Chemical Research* **2005**, *38*, 176-182.

(6)   Papaefstathiou, G. S.; MacGillivray, L. R. *Inverted metal-organic frameworks: solid-state hosts with modular functionality*; *Coordination Chemistry Reviews* **2003**, *246*, 169-184.

(7)   Long, J. R.; Yaghi, O. M. *The pervasive chemistry of metal-organic frameworks*; *Chem Soc Rev* **2009**, *38*, 1213-1214.

(8)   Rowsell, J. L. C.; Yaghi, O. M. *Metal-organic frameworks: a new class of porous materials*; *Microporous and Mesoporous Materials* **2004**, *73*, 3-14.

(9)   Lu, W.-G.; Jiang, L.; Feng, X.-L.; Lu, T.-B. *Four 3D Porous Metal−Organic Frameworks with Various Layered and Pillared Motifs*; *Crystal Growth & Design* **2008**, *8*, 986-994.

(10)   Zang, S.; Su, Y.; Song, Y.; Li, Y.; Ni, Z.; Zhu, H.; Meng, Q. *Tuning the Framework Formation of Ni(II) Complexes by Controlling the Hydrolysis of 2,2',3,3'-Thiodiphthalic Dianhydride: Syntheses, Crystal Structures, and Physical Properties*; *Crystal Growth & Design* **2006**, *6*, 2369-2375.

(11)   Lu, W.-G.; Jiang, L.; Feng, X.-L.; Lu, T.-B. *Three 3D Coordination Polymers Constructed by Cd(II) and Zn(II) with Imidazole-4,5-Dicarboxylate and 4,4'-Bipyridyl Building Blocks*; *Crystal Growth & Design* **2005**, *6*, 564-571.

(12)   Wu, C.-D.; Ma, L.; Lin, W. *Hierarchically Ordered Homochiral Metal−Organic Frameworks Built from Exceptionally Large Rectangles and Squares*; *Inorganic Chemistry* **2008**, *47*, 11446-11448.

(13)   Stuart R. Batten; Suzanne M. Neville; David R Turner *Coordination Polymers: Design, Analysis and Applications*; RSC Publishing: Cambridge, 2009.

(14)   Robson, R. *A net-based approach to coordination polymers*; *Journal of the Chemical Society-Dalton Transactions* **2000**, 3735-3744.

(15)   Li, H.; Eddaoudi, M.; O'Keeffe, M.; Yaghi, O. M. *Design and synthesis of an exceptionally stable and highly porous metal-organic framework*; *Nature* **1999**, *402*, 276-279.

(16)   Eddaoudi, M.; Kim, J.; Rosi, N.; Vodak, D.; Wachter, J.; O'Keeffe, M.; Yaghi, O. M. *Systematic Design of Pore Size and Functionality in Isoreticular MOFs and Their Application in Methane Storage*; *Science* **2002**, *295*, 469-472.

(17)   Tranchemontagne, D. J. L.; Ni, Z.; O'Keeffe, M.; Yaghi, O. M. *Reticular chemistry of metal-organic polyhedra*; *Angewandte Chemie-International Edition* **2008**, *47*, 5136-5147.

(18)   Tranchemontagne, D. J.; Mendoza-Cortes, J. L.; O'Keeffe, M.; Yaghi, O. M. *Secondary building units, nets and bonding in the chemistry of metal-organic frameworks*; *Chemical Society Reviews* **2009**, *38*, 1257-1283.

(19)   Braga, C. F.; Longo, R. L. *Structure of functionalized porous metal-organic frameworks by molecular orbital methods*; *Journal of Molecular Structure: THEOCHEM* **2005**, *716*, 33-38.

(20)   Vanniekerk, J. N.; Schoening, F. R. L.; Talbot, J. H. *The Crystal Structure of Zinc Acetate Dihidrate, $Zn(CH_3COO)_2.2H_2O$*; *Acta Crystallographica* **1953**, *6*, 720-723.

(21)   Ferey, G. *Hybrid porous solids: past, present, future*; *Chem Soc Rev* **2008**, *37*, 191-214.

(22)   Kitagawa, S.; Kitaura, R.; Noro, S. *Functional porous coordination polymers*; *Angew Chem Int Ed Engl* **2004**, *43*, 2334-2375.

(23)   Champness, N. R. *Coordination frameworks--where next?*; *Dalton Trans* **2006**, 877-880.

(24)   Li, Q. W.; Zhang, W. Y.; Miljanic, O. S.; Knobler, C. B.; Stoddart, J. F.; Yaghi, O. M. *A metal-organic framework replete with ordered donor-acceptor catenanes*; *Chemical Communications* **2010**, *46*, 380-382.

(25)   de Bettencourt-Dias, A. *Isophthalato-based 2D coordination polymers of Eu(III), Gd(III), and Tb(III): Enhancement of the terbium-centered luminescence through thiophene derivatization*; *Inorganic Chemistry* **2005**, *44*, 2734-2741.

(26)   Kim, J.; Chen, B.; Reineke, T. M.; Li, H.; Eddaoudi, M.; Moler, D. B.; O'Keeffe, M.; Yaghi, O. M. *Assembly of Metal−Organic Frameworks from Large Organic and Inorganic Secondary Building Units: New Examples and Simplifying Principles for Complex Structures⊿*; *Journal of the American Chemical Society* **2001**, *123*, 8239-8247.

(27)   Guo, X.; Zhu, G.; Fang, Q.; Xue, M.; Tian, G.; Sun, J.; Li, X.; Qiu, S. *Synthesis, Structure and Luminescent Properties of Rare Earth Coordination Polymers Constructed from Paddle-Wheel Building Blocks*; *Inorganic Chemistry* **2005**, *44*, 3850-3855.

(28)   Kyono, A.; Kimata, M.; Hatta, T. *Hydrothermal synthesis and structural investigation of silver magnesium complex of benzenehexacarboxylic acid (mellitic acid), Ag2Mg2[C-6(COO)6]center dot 8H(2)O with two-dimensional layered structure*; *Inorganica Chimica Acta* **2004**, *357*, 2519-2524.

(29)   Qiu, S.; Zhu, G. *Molecular engineering for synthesizing novel structures of metal-organic frameworks with multifunctional properties*; Coordination Chemistry Reviews **2009**, *253*, 2891-2911.

(30)   Paz, F. A. A.; Rocha, J.; Klinowski, J.; Trindade, T.; Shi, F.-N.; Mafra, L. *Optimised hydrothermal synthesis of multi-dimensional hybrid coordination polymers containing flexible organic ligands*; Progress in Solid State Chemistry **2005**, *33*, 113-125.

(31)   Gerardin, C.; In, M.; Allouche, L.; Haouas, M.; Taulelle, F. *In Situ pH Probing of Hydrothermal Solutions by NMR*; Chemistry of Materials **1999**, *11*, 1285-1292.

(32)   Forster, P. M.; Thomas, P. M.; Cheetham, A. K. *Biphasic Solvothermal Synthesis: A New Approach for Hybrid Inorganic−Organic Materials*; Chemistry of Materials **2001**, *14*, 17-20.

(33)   Taylor, K. M. L.; Jin, A.; Lin, W. B. *Surfactant-assisted synthesis of nanoscale gadolinium metal-organic frameworks for potential multimodal imaging*; Angewandte Chemie-International Edition **2008**, *47*, 7722-7725.

(34)   Silva, P. c.; Valente, A. A.; Rocha, J. o.; Almeida Paz, F. A. *Fast Microwave Synthesis of a Microporous Lanthanide−Organic Framework*; Crystal Growth & Design **2010**, *10*, 2025-2028.

(35)   Jhung, S. H.; Lee, J. H.; Chang, J. S. *Microwave synthesis of a nanoporous hybrid material, chromium trimesate*; Bulletin of the Korean Chemical Society **2005**, *26*, 880-881.

(36)   Tranchemontagne, D. J.; Hunt, J. R.; Yaghi, O. M. *Room temperature synthesis of metal-organic frameworks: MOF-5, MOF-74, MOF-177, MOF-199, and IRMOF-0*; Tetrahedron **2008**, *64*, 8553-8557.

(37)   Qiu, L. G.; Li, Z. Q.; Wu, Y.; Wang, W.; Xu, T.; Jiang, X. *Facile synthesis of nanocrystals of a microporous metal-organic framework by an ultrasonic method and selective sensing of organoamines*; *Chemical Communications* **2008**, 3642-3644.

(38)   Czaja, A. U.; Trukhan, N.; Muller, U. *Industrial applications of metal-organic frameworks*; *Chemical Society Reviews* **2009**, *38*, 1284-1293.

(39)   Mueller, U.; Schubert, M.; Teich, F.; Puetter, H.; Schierle-Arndt, K.; Pastre, J. *Metal-organic frameworks - prospective industrial applications*; *Journal of Materials Chemistry* **2006**, *16*, 626-636.

(40)   Navrotsky, A.; Trofymluk, O.; Levchenko, A. A. *Thermochemistry of Microporous and Mesoporous Materials*; *Chemical Reviews* **2009**, *109*, 3885-3902.

(41)   Davis, M. E.; Maxwell, I. E. *Solid catalysts and porous solids*; *Current Opinion in Solid State and Materials Science* **1996**, *1*, 55-56.

(42)   Tsai, S.-T.; Chao, P.-Y.; Chuang, Y.-Y.; Ho, G. H.; Chuang, S.-H.; Tsai, T.-C.; Lee, C.-Y.; Huang, J.-F. *Study of Molecular-Shape Selectivity of Zeolites by Gas Chromatography*; *Journal of Chemical Education* **2008**, *85*, 1558.

(43)   Larsen, S. C. *Nanocrystalline Zeolites and Zeolite Structures: Synthesis, Characterization, and Applications*; *The Journal of Physical Chemistry C* **2007**, *111*, 18464-18474.

(44)   Egeblad, K.; Christensen, C. H.; Kustova, M.; Christensen, C. H. *Templating Mesoporous Zeolites†*; *Chemistry of Materials* **2007**, *20*, 946-960.

(45)   Smit, B.; Maesen, T. L. M. *Molecular Simulations of Zeolites: Adsorption, Diffusion, and Shape Selectivity*; *Chemical Reviews* **2008**, *108*, 4125-4184.

(46)   Costa, E.; De Lucas, A.; Uguina, M. A.; Ruiz, J. C. *Synthesis of 4A zeolite from calcined kaolins for use in detergents*; *Industrial & Engineering Chemistry Research* **1988**, *27*, 1291-1296.

(47)   Davis, M. E. *Ordered porous materials for emerging applications*; *Nature* **2002**, *417*, 813-821.

(48)   Chae, H. K.; Siberio-Perez, D. Y.; Kim, J.; Go, Y.; Eddaoudi, M.; Matzger, A. J.; O'Keeffe, M.; Yaghi, O. M. *A route to high surface area, porosity and inclusion of large molecules in crystals*; *Nature* **2004**, *427*, 523-527.

(49)   Tsai, C.-C.; Luo, T.-T.; Yin, J.-F.; Lin, H.-C.; Lu, K.-L. *An Unprecedentedly Huge Square-Grid Copper(II)−Organic Framework Material Built from a Bulky Pyrene-Derived Elongated Cross-Shaped Scaffold*; *Inorganic Chemistry* **2009**, *48*, 8650-8652.

(50)   Chen, B.; Xiang, S.; Qian, G. *Metal−Organic Frameworks with Functional Pores for Recognition of Small Molecules*; *Accounts of Chemical Research* **2010**.

(51)   Saha, D.; Deng, S. *Structural Stability of Metal Organic Framework MOF-177*; *The Journal of Physical Chemistry Letters* **2009**, *1*, 73-78.

(52)   Kuppler, R. J.; Timmons, D. J.; Fang, Q.-R.; Li, J.-R.; Makal, T. A.; Young, M. D.; Yuan, D.; Zhao, D.; Zhuang, W.; Zhou, H.-C. *Potential applications of metal-organic frameworks*; *Coordination Chemistry Reviews* **2009**, *253*, 3042-3066.

(53)   Corma, A.; García, H.; Llabrés i Xamena, F. X. *Engineering Metal Organic Frameworks for Heterogeneous Catalysis*; *Chemical Reviews* **2010**.

(54)   Kesanli, B.; Lin, W. *Chiral porous coordination networks: rational design and applications in enantioselective processes*; *Coordination Chemistry Reviews* **2003**, *246*, 305-326.

(55)   Zhang, X.; Llabrés i Xamena, F. X.; Corma, A. *Gold(III) - metal organic framework bridges the gap between homogeneous and heterogeneous gold catalysts*; *Journal of Catalysis* **2009**, *265*, 155-160.

(56)   Fujita, M.; Kwon, Y. J.; Washizu, S.; Ogura, K. *Preparation, Clathration Ability, and Catalysis of a Two-Dimensional Square Network Material Composed of Cadmium(II) and 4,4'-Bipyridine*; *Journal of the American Chemical Society* **1994**, *116*, 1151-1152.

(57)   Shultz, A. M.; Farha, O. K.; Hupp, J. T.; Nguyen, S. T. *A Catalytically Active, Permanently Microporous MOF with Metalloporphyrin Struts*; *Journal of the American Chemical Society* **2009**, *131*, 4204-4205.

(58)   Müller, M.; Hermes, S.; Kähler, K.; van den Berg, M. W. E.; Muhler, M.; Fischer, R. A. *Loading of MOF-5 with Cu and ZnO Nanoparticles by Gas-Phase Infiltration with Organometallic Precursors: Properties of Cu/ZnO@MOF-5 as Catalyst for Methanol Synthesis*; *Chemistry of Materials* **2008**, *20*, 4576-4587.

(59)   Opelt, S.; Türk, S.; Dietzsch, E.; Henschel, A.; Kaskel, S.; Klemm, E. *Preparation of palladium supported on MOF-5 and its use as hydrogenation catalyst*; *Catalysis Communications* **2008**, *9*, 1286-1290.

(60)   Tanski, J. M.; Wolczanski, P. T. *Covalent Titanium Aryldioxy One-, Two-, and Three-Dimensional Networks and Their Examination as Ziegler−Natta Catalysts*; *Inorganic Chemistry* **2001**, *40*, 2026-2033.

(61)   Vitorino, M. J.; Devic, T.; Tromp, M.; Ferey, G.; Visseaux, M. *Lanthanide Metal-Organic Frameworks as Ziegler-Natta Catalysts for the Selective Polymerization of Isoprene*; *Macromolecular Chemistry and Physics* **2009**, *210*, 1923-1932.

(62)   Seo, J. S.; Whang, D.; Lee, H.; Jun, S. I.; Oh, J.; Jeon, Y. J.; Kim, K. *A homochiral metal-organic porous material for enantioselective separation and catalysis*; *Nature* **2000**, *404*, 982-986.

(63)   Evans, O. R.; Ngo, H. L.; Lin, W. *Chiral Porous Solids Based on Lamellar Lanthanide Phosphonates*; *Journal of the American Chemical Society* **2001**, *123*, 10395-10396.

(64)   Couck, S.; Denayer, J. F. M.; Baron, G. V.; Rémy, T.; Gascon, J.; Kapteijn, F. *An Amine-Functionalized MIL-53 Metal−Organic Framework with Large Separation Power for CO2 and CH4*; *Journal of the American Chemical Society* **2009**, *131*, 6326-6327.

(65)   Cavenati, S.; Grande, C. A.; Rodrigues, A. r. E.; Kiener, C.; Müller, U. *Metal Organic Framework Adsorbent for Biogas Upgrading*; *Industrial & Engineering Chemistry Research* **2008**, *47*, 6333-6335.

(66)   Liu, J.; Culp, J. T.; Natesakhawat, S.; Bockrath, B. C.; Zande, B.; Sankar, S. G.; Garberoglio, G.; Johnson, J. K. *Experimental and Theoretical Studies of Gas Adsorption in Cu3(BTC)2: An Effective Activation Procedure*; *The Journal of Physical Chemistry C* **2007**, *111*, 9305-9313.

(67)   Hartmann, M.; Kunz, S.; Himsl, D.; Tangermann, O.; Ernst, S.; Wagener, A. *Adsorptive Separation of Isobutene and Isobutane on Cu3(BTC)2*; *Langmuir* **2008**, *24*, 8634-8642.

(68)   Karra, J. R.; Walton, K. S. *Effect of Open Metal Sites on Adsorption of Polar and Nonpolar Molecules in Metal−Organic Framework Cu-BTC*; *Langmuir* **2008**, *24*, 8620-8626.

(69)   Rowsell, J. L. C.; Spencer, E. C.; Eckert, J.; Howard, J. A. K.; Yaghi, O. M. *Gas Adsorption Sites in a Large-Pore Metal-Organic Framework*; *Science* **2005**, *309*, 1350-1354.

(70)   Kondo, M.; Yoshitomi, T.; Matsuzaka, H.; Kitagawa, S.; Seki, K. *Three-Dimensional Framework with Channeling Cavities for Small Molecules: {[M2(4, 4prime-bpy)$_3$(NO$_3$)$_4$]·xH$_2$O}$_n$ (M= Co, Ni, Zn) Angewandte Chemie International Edition in English* **1997**, *36*, 1725-1727.

(71)   Thornton, A. W.; Nairn, K. M.; Hill, J. M.; Hill, A. J.; Hill, M. R. *Metal−Organic Frameworks Impregnated with Magnesium-Decorated Fullerenes for Methane and Hydrogen Storage*; *Journal of the American Chemical Society* **2009**, *131*, 10662-10669.

(72)   Wu, H.; Zhou, W.; Yildirim, T. *High-Capacity Methane Storage in Metal−Organic Frameworks M2(dhtp): The Important Role of Open Metal Sites*; *Journal of the American Chemical Society* **2009**, *131*, 4995-5000.

(73)   Furukawa, H.; Miller, M. A.; Yaghi, O. M. *Independent verification of the saturation hydrogen uptake in MOF-177 and establishment of a benchmark for hydrogen adsorption in metal-organic frameworks*; *Journal of Materials Chemistry* **2007**, *17*, 3197-3204.

(74)   Kaye, S. S.; Dailly, A.; Yaghi, O. M.; Long, J. R. *Impact of preparation and handling on the hydrogen storage properties of Zn4O(1,4-benzenedicarboxylate)(3) (MOF-5)*; *Journal of the American Chemical Society* **2007**, *129*, 14176-+.

(75)   Wang, B.; Cote, A. P.; Furukawa, H.; O/'Keeffe, M.; Yaghi, O. M. *Colossal cages in zeolitic imidazolate frameworks as selective carbon dioxide reservoirs*; *Nature* **2008**, *453*, 207-211.

(76)   Walton, K. S.; Millward, A. R.; Dubbeldam, D.; Frost, H.; Low, J. J.; Yaghi, O. M.; Snurr, R. Q. *Understanding inflections and steps in carbon dioxide adsorption isotherms in metal-organic frameworks*; *Journal of the American Chemical Society* **2008**, *130*, 406-+.

(77)   Zhao, Z.; Li, Z.; Lin, Y. S. *Adsorption and Diffusion of Carbon Dioxide on Metal−Organic Framework (MOF-5)*; *Industrial & Engineering Chemistry Research* **2009**, *48*, 10015-10020.

(78)   Ma, S.; Sun, D.; Ambrogio, M.; Fillinger, J. A.; Parkin, S.; Zhou, H.-C. *Framework-Catenation Isomerism in Metal−Organic Frameworks and Its Impact on Hydrogen Uptake*; *Journal of the American Chemical Society* **2007**, *129*, 1858-1859.

(79)   Achmann, S.; Hagen, G.; Hämmerle, M.; Malkowsky, I. M.; Kiener, C.; Moos, R. *Sulfur Removal from Low-Sulfur Gasoline and Diesel Fuel by Metal-Organic Frameworks*; *Chemical Engineering & Technology* **2010**, *33*, 275-280.

(80)   Horcajada, P.; Chalati, T.; Serre, C.; Gillet, B.; Sebrie, C.; Baati, T.; Eubank, J. F.; Heurtaux, D.; Clayette, P.; Kreuz, C.; Chang, J. S.; Hwang, Y. K.; Marsaud, V.; Bories, P. N.; Cynober, L.; Gil, S.; Ferey, G.; Couvreur, P.; Gref, R. *Porous metal-organic-framework nanoscale carriers as a potential platform for drug delivery and imaging*; *Nature Materials* **2010**, *9*, 172-178.

(81)   Rowe, M. D.; Chang, C.-C.; Thamm, D. H.; Kraft, S. L.; Harmon, J. F.; Vogt, A. P.; Sumerlin, B. S.; Boyes, S. G. *Tuning the Magnetic Resonance Imaging Properties of Positive Contrast Agent Nanoparticles by Surface Modification with RAFT Polymers*; *Langmuir* **2009**, *25*, 9487-9499.

(82)   Horcajada, P.; Serre, C.; Vallet-Regí, M.; Sebban, M.; Taulelle, F.; Férey, G. *Metal-Organic Frameworks as Efficient Materials for Drug Delivery13*; *Angewandte Chemie International Edition* **2006**, *45*, 5974-5978.

(83)   Rowe, M. D.; Thamm, D. H.; Kraft, S. L.; Boyes, S. G. *Polymer-Modified Gadolinium Metal-Organic Framework Nanoparticles Used as Multifunctional Nanomedicines for the Targeted Imaging and Treatment of Cancer*; *Biomacromolecules* **2009**, *10*, 983-993.

(84)   Zhao, B.; Chen, X. Y.; Cheng, P.; Liao, D. Z.; Yan, S. P.; Jiang, Z. H. *Coordination polymers containing 1D channels as selective luminescent probes*; *Journal of the American Chemical Society* **2004**, *126*, 15394-15395.

(85)   Chen, B. L.; Yang, Y.; Zapata, F.; Lin, G. N.; Qian, G. D.; Lobkovsky, E. B. *Luminescent open metal sites within a metal-organic framework for sensing small molecules*; *Advanced Materials* **2007**, *19*, 1693-1696.

(86)   Harbuzaru, Bogdan V.; Corma, A.; Rey, F.; Atienzar, P.; Jordá, Jose L.; García, H.; Ananias, D.; Carlos, Luis D.; Rocha, J. *Metal-Organic Nanoporous Structures with Anisotropic Photoluminescence and Magnetic Properties and Their Use as Sensors13*; *Angewandte Chemie International Edition* **2008**, *47*, 1080-1083.

(87)   Suh, M. P.; Cheon, Y. E.; Lee, E. Y. *Syntheses and functions of porous metallosupramolecular networks*; *Coordination Chemistry Reviews* **2008**, *252*, 1007-1026.

(88)   Chen, B.; Wang, L.; Zapata, F.; Qian, G.; Lobkovsky, E. B. *A Luminescent Microporous Metal−Organic Framework for the Recognition and Sensing of Anions*; *Journal of the American Chemical Society* **2008**, *130*, 6718-6719.

(89)   Chen, B.; Yang, Y.; Zapata, F.; Lin, G.; Qian, G.; Lobkovsky, E. B. *Luminescent Open Metal Sites within a Metal-Organic Framework for Sensing Small Molecules*; *Advanced Materials* **2007**, *19*, 1693-1696.

(90)   Chen, B.; Wang, L.; Xiao, Y.; Fronczek, Frank R.; Xue, M.; Cui, Y.; Qian, G. *A Luminescent Metal-Organic Framework with Lewis Basic Pyridyl Sites for the Sensing of Metal Ions13*; *Angewandte Chemie International Edition* **2009**, *48*, 500-503.

(91)   Harbuzaru, Bogdan V.; Corma, A.; Rey, F.; Jordá, Jose L.; Ananias, D.; Carlos, Luis D.; Rocha, J. *A Miniaturized Linear pH Sensor Based on a Highly Photoluminescent Self-Assembled Europium(III) Metal-Organic Framework13*; *Angewandte Chemie International Edition* **2009**, *48*, 6476-6479.

(92)   de Carvalho, P. H.; Barreto, A. S.; Rodrigues, M. O.; Prata Vde, M.; Alves, P. B.; de Mesquita, M. E.; Alves, S., Jr.; Navickiene, S. *Two-dimensional coordination polymer matrix for solid-phase extraction of pesticide residues from plant Cordia salicifolia*; *Journal of Separation Science* **2009**, *32*, 2132-2138.

(93)   Barreto, A. S.; da Silva, R. L.; dos Santos, S. C. G.; Rodrigues, M. O.; de Simone, C. A.; de Sa, G. F.; Alves, S.; Navickiene, S.; Mesquita, M. E. *Potential of metal-organic framework as a new material for solid-phase extraction of pesticides from lettuce (Lactuca sativa) by gas chromatography-mass spectrometry*; *Analytica Chimica Acta* **2010**, *Submetido*.

(94)   Aquino, A.; Wanderley, K. A.; O., P.-S. C.; de Sa, G. F.; Souza, M. R. R.; Maciel, S. T. A.; Alexandre, M. R.; Alves, S.; Navickiene, S. *Coordination polymer as new adsorbent material for matrix solid-phase dispersion extraction method for the analysis of pesticides in dehydrated medicinal plant Hyptis pectinata*; *Journal of Chromatographic A* **2010**, *Submetido*.

(95)   Weber, I. T.; Melo, A. J. G.; Junior, S. A.; Lucena, M. A. M.; Rodrigues, M. O. In *INPI*; UNIVERSIDADE FEDERAL DE PERNAMBUCO, Ed. Brasil, 2009; Vol. PI 0901063-7.

(96)   Hermes, S.; Schröder, F.; Chelmowski, R.; Wöll, C.; Fischer, R. A. *Selective Nucleation and Growth of Metal−Organic Open Framework Thin Films on Patterned COOH/CF3-Terminated Self-Assembled Monolayers on Au(111)*; *Journal of the American Chemical Society* **2005**, *127*, 13744-13745.

Capítulo 1:

Modelagem e Estudos Espectroscópicos de Materiais Metal-orgânicos contendo íons Lantanídeos
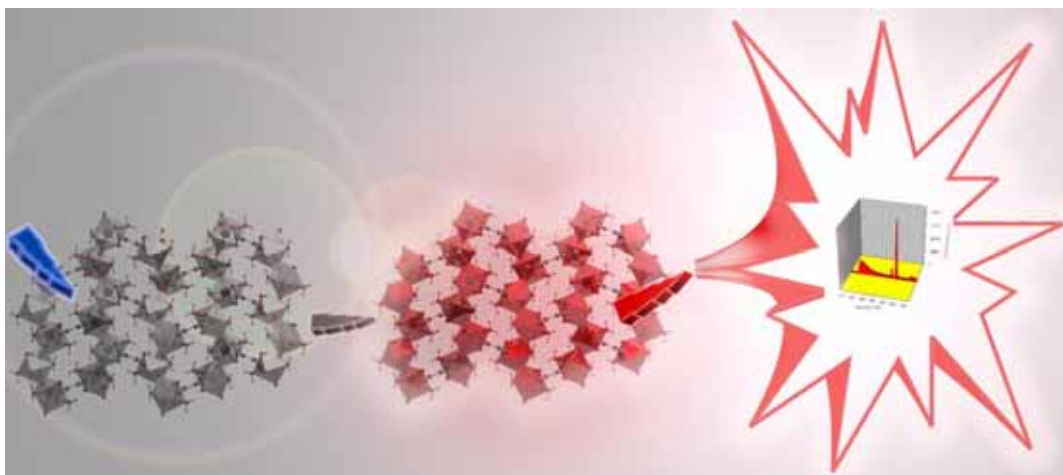
"É dando no burro que a carroça anda!"

(Zé Buneco)

1.1   Introdução

Embora todo avanço conceitual a respeito dos Materiais Metal-orgânicos (MMOs), estes compostos ainda são considerados como paradigmas para Engenharia de Cristais em virtude das limitações associadas à modelagem de novos sólidos funcionais. Toda essa problemática advém do ainda restrito grau de manipulação das interações intermoleculares, ligações de hidrogênio e das ligações coordenadas, que por sua vez repercutem consideravelmente na previsibilidade estrutural e nas propriedades físicas e químicas desses materiais.[1-4]

As diversas metodologias de sínteses que dão origem a estes MMOs são baseadas, unicamente, em processos de autorganização.[5,6] Ou seja, a obtenção desses materiais é alicerçada por um complexo algoritmo em que as informações químicas e estruturais do ligante são reconhecidas pelos íons metálicos através de sua geometria de coordenação ou *vise-versa*.[7] Além disso, o pH, temperatura, solvente, pressão, tempo de reação são agentes químicos e físicos externos que alteram severamente a dinâmica dos processos de autorganização.[8,9] Evidentemente, este amplo conjunto de variáveis conduziria a resultados incertos, no entanto, muitos grupos de pesquisa têm buscado minimizar este complexo problema através do desenvolvimento de condições sintéticas que preservam a integridade e a orientação geométrica dos ligantes e metais. Esses conceitos designados como *"building-blocks"* ou *"node-and-spacers"* foram pioneiramente delineados

por Robson, Hoskins e colaboradores, os quais são considerados fundamentais para o *design* de MMOs. [10]

Os metais de transição são freqüentemente utilizados na construção de materiais. Isto é atribuído aos baixos números de coordenação inerentes a esta classe de metais, entre 2 a 7 dependendo do estado de oxidação, que originam um número limitado de geometrias de coordenação, obviamente esta característica facilita o controle topológico dos sólidos.[11] Já os altos números de coordenação entre 6 e 12 e a geometrias de coordenação dos íons lantanídeos tornam-nos interessantes para a construção de polímeros de coordenação, pois devido a rica e variada estereoquímica causam dissimetria nos centros metálicos gerando topologias pouco comuns.[12-14]

Em virtude das propriedades espectroscópicas inerente aos íons lantanídeos (tempos de vidas longos e bandas de emissão finas e bem definidas),[15] tem crescido o interesse na utilização desses íons para confecção de novas redes de coordenação, visando a obter Dispositivos Moleculares Conversores de Luz (DMCL)[16,17] proporcionando a estes compostos quase que uma instantânea funcionalidade.[18] Isto é enfatizado pelas diversificadas áreas que estes sistemas são aplicados, nas quais se pode destacar: dispositivos eletroluminescentes, integrantes de circuitos elétricos e displays, Diodos Orgânicos Eletroluminescentes (DOELs),[19] sensores ópticos,[18,20,21] entre outros.

Várias classes de ligantes orgânicos têm sido empregadas nas sínteses de MOFs contendo lantanídeos, dentre os quais os policarboxilatos aromáticos são de especial interesse devido à estabilidade química e a capacidade de potencializar a emissão dos íons devido ao efeito antena.[22,23] A hegemonia dos policarboxilatos aromáticos é limitada pela presença de dois átomos de oxigênios carboxílicos que por sua vez possibilitam diversos modos de coordenação aos metais, ocasionando na redução do grau de previsibilidade estrutural dos compostos.

A utilização de cálculos computacionais baseados em modelos teóricos especificamente projetados para a determinação das geometrias de coordenação de complexos de lantanídeos é uma das formas encontradas para solucionar o problema causado pela ausência de previsão estrutural.[24-27] Adicionalmente, estes cálculos auxiliam na determinação dos estados excitados dos ligantes[28,29] que são informações indispensáveis para que evidentemente se possa, com bastante segurança e precisão, projetar redes de coordenação contendo lantanídeos mais luminescentes do que àquelas em destaque na literatura.

O ácido melítico (Figura 1.1) possui seis grupos carboxilatos que possibilitam a ligação com vários centros metálicos, adotar diversos modos de coordenação e conseqüentemente gerar redes multidimensionais.[30-33] É importante salientar que prévios trabalhos destacam a utilização deste ligante na preparação de materiais metalorgânicos, no entanto, investigações

detalhadas das propriedades fotofísicas destes compostos até a publicação deste trabalho eram inexistentes.[34]

Nosso grupo de pesquisa tem sido pioneiro no desenvolvimento de ferramentas teóricas para predição e simulação das propriedades espectroscópicas de compostos de lantanídeos dentre as quais podem ser destacadas: energia dos estados singleto e tripleto dos ligantes,[35,36] espectros eletrônicos de complexos de lantanídeos,[37-39] parâmetros de intensidades, Ω_λ (λ = 2, 4 e 6),[40-42] taxas de transferência de energia entre o ligante e os íons e rendimento quântico. [26,41,43]
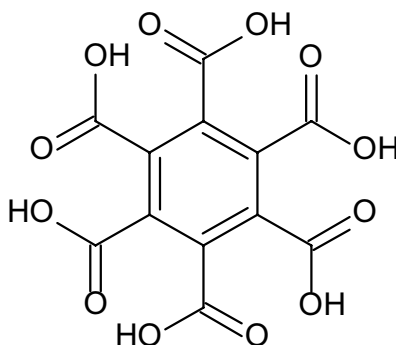
Figura 1.1: Ilustração da estrutura do ácido melítico.

Diante deste prognóstico, este capítulo está dedicado a reportar um detalhado estudo das propriedades espectroscópicas do material [Ln_2(MELL)(H_2O)$_6$] (Ln= Eu^{3+}, Tb^{3+} e Gd^{3+}; designados respectivamente como **(1.1), (12) e (1.3)**). É importante destacar que a os materiais são iso-estruturais ao material de Lantânio previamente reportado por Willians e colaboradores e que recentemente Lin *et al.* reportou as potencialidades do uso do

[Gd$_2$(MELL)(H$_2$O)$_6$] como agente de contraste em RMN.[44] No presente estudo estão em destaque uma completa abordagem a respeito da caracterização dos compostos e propriedades espectroscópicas: parâmetros de intensidade, taxas de transferência (W_{ET}) e retrotransferência (W_{BT}) de energia, taxas de decaimento radiativo (A_{rad}) e não-radiativos (A_{nrad}), eficiência quântica (η) e rendimento quântico (q) baseadas na estrutura otimizada usando o modelo Sparkle/AM1.

1.2 Materiais e Métodos

1.2.1 Reagentes

Os óxidos dos lantanídeos (Eu$_2$O$_3$, Gd$_2$O$_3$ e Tb$_4$O$_7$) 99,9% são de procedência Aldrich e foram calcinados a 900 ºC por 6 horas. Ácido melítico, obtido também da Aldrich, foi usado sem purificação prévia. O ácido nítrico concentrado e os padrões usados nas medidas de rendimento quântico, óxido de magnésio (MgO) e salicilato de sódio (NaSal) são todos oriundos da Merck.

1.2.2 Preparação dos Nitratos de Lantanídeos

Os nitratos de Eu^{3+} e Gd^{3+} foram obtidos pela reação do respectivo óxido, previamente calcinado, com ácido nítrico concentrado e 15 mL de água deionizada conforme a reação de precipitação mostrada a seguir (Equação 1.1). O fim da reação foi determinado com a estabilização do pH em 5, após

sucessivas evaporações do solvente. Finalmente o sólido formado foi transferido para um recipiente, lacrado e mantido sob vácuo em dessecador a pressão reduzida usando sílica-gel como agente secante.

$$Ln_2O_3 + 6\,HNO_3 \xrightarrow[\Delta]{H_2O} 2\,Ln(NO_3).6H_2O \qquad (1.1)$$
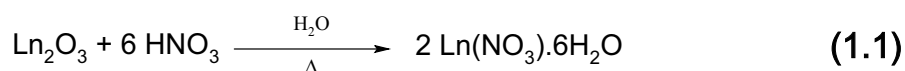
A obtenção do nitrato de térbio foi conduzida de maneira similar ao método aplicado ao európio e gadolínio, porém com a ressalva de que o óxido de térbio usado consiste em uma mistura de Tb^{3+} e Tb^{4+}, logo foi imprescindível a redução do térbio (IV) por adição de pequenas alíquotas de 0,5 mL de peróxido de hidrogênio. A adição de H_2O_2 foi interrompida quando a solução resultante tornou-se límpida. Da mesma maneira nitrato de térbio sólido formado foi devidamente acondicionado como descrito anteriormente. Esse procedimento pode ser visualizado através das semi-reações mostradas nas Equações 1.2, 1.3 e 1.4 respectivamente:

$$Tb_2O_3 + 6\,H^+ \longrightarrow 2\,Tb^{3+} + 3\,H_2O \qquad (1.2)$$

$$2\,TbO_2 + H_2O_2 + 6\,H^+ \longrightarrow 2\,Tb^{3+} + O_2 + 4\,H_2O \qquad (1.3)$$

$$\overline{Tb_4O_7 + H_2O_2 + 12\,H^+ \longrightarrow 4\,Tb^{3+} + O_2 + 7H_2O} \qquad (1.4)$$
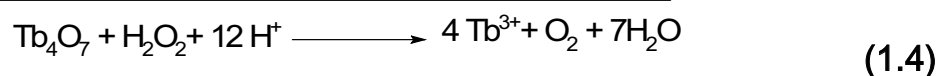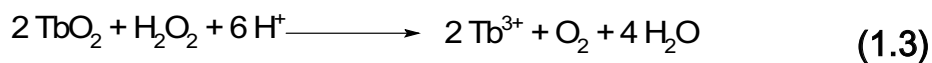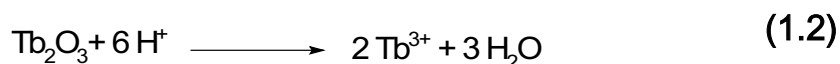
1.2.3 Sínteses

Uma mistura equimolar (0,85 mmol) de ácido melítico e $Ln(NO_3)_3 \cdot 6H_2O$ em 4,0 mL de água deionizada foi adicionada em um reator de inóx revestido com teflon (8,0 mL). A reação foi mantida a 433 K por 72 horas em uma estufa com circulação forçada de ar. A reação apresentou rendimento de aproximadamente 75% após o produto ser lavado com acetona e seco ao ar. Todos os materiais são insolúveis em água e em solventes orgânicos.

Dados de IV (em cm^{-1}):

(**1.1** 3468-3213 (forte), 1609 (forte), 1568 (forte), 1449 (forte), 1344 (forte), 918 (fraca), 676 (fraca), 590 (fraca), 505 (fraca);

(**1.2**) 3468-3213 (forte), 1611 (forte), 1555 (forte), 1443 (forte), 1338 (forte), 918 (fraca), 719 (fraca), 676 (fraca), 590 (fraca), 548 (fraca), 492 (fraca);

(**1.3**) 3486-3000 (forte), 1609 (forte), (forte), 1454 (forte), 1344 (forte), 918 (fraca), 673 (fraca), 587 (fraca), (fraca).

Faixas de temperaturas de decomposição (K):

(**1.1**) 383-458 K (-5,25 %), 458-533 K (-8,40%), 700-1200 K (-37,4%);

(**1.2**) 376-458 K (-4,92%), 453-549 (-8,43%), 750-1210 (-37,31%);

(**1.3**): 387-454 K (-4,93%), 454-550 K (-8,42%), 780-1165 K (-37,1%).

1.2.4 Instrumentação

1.2.4.1   Análise Elementar

As análises elementares de C, H, e N das redes de coordenação foram realizadas em um equipamento CHNS-O Analyzer Flash (112 Series EA Thermo Finningan).

1.2.4.2   Espectroscopia de Absorção na Região do Infravermelho

Os espectros de infravermelho foram obtidos em pastilhas de KBr com resolução de 4 cm^{-1} em um espectrofotômetro Brucker, modelo IF66.

1.2.4.3   Termogravimetria e Termogravimetria Derivada

As curvas TG/DTG foram obtidas na faixa de temperatura entre 298 e 1473K, utilizando uma termobalança modelo TGA 50 da marca Shimadzu, sob atmosfera dinâmica de nitrogênio (50 mL.min^{-1}), razão de aquecimento de 10K.min^{-1}, utilizando cadinho de platina contendo massa de amostra em torno de 3,0 mg. A calibração do instrumento foi verificada antes dos ensaios e empregando-se um padrão de oxalato de cálcio monohidratado, conforme norma ASTM (The Americam Society for Testing and Materials, 1993).

1.2.4.4   Espectroscopia de Luminescência

Os espectros de emissão e excitação à temperatura ambiente e 77 K foram realizados em um ISS PC1 Spectrofluorometer. O monocromador de

excitação é equipado com uma lâmpada de Xenônio com 300 W. A emissão é coletada em um monocromador com resolução de 0,1 nm equipado com uma fotomultiplicadora. As fendas de emissão e excitação usadas na aquisição dos dados foram de 0,5 nm.

1.2.4.5   Tempos de Decaimento dos Estados Excitados

Os decaimentos dos estados excitados $^5D_0$ e $^5D_4$ dos íons Eu^{3+} e Tb^{3+} respectivamente, foram adquiridos utilizando um laser de nitrogênio pulsado (λ=337 nm) modelo VSL 337ND com largura temporal de 10 ns e taxa de repetição em 20 Hz. A fotomultiplicadora usada para estas medidas foi o modelo 1P 285 Hamamatsu acoplado a um monocromador modelo 10 da Jobin Yvon. O sinal da fotomultiplicadora foi analisado por um box-car modelo 115 da Eg&G com resolução temporal de 50 ns.

1.2.4.6   Rendimentos Quânticos de Emissão

Os rendimentos quânticos (q_x) foram obtidos através de medidas relativas utilizando fósforos padrões como referência, cujos respectivos rendimentos foram previamente mensurados através de métodos absolutos. Esta metodologia foi desenvolvida por Brill e colaboradores nos laboratórios de pesquisas de Phillips (Philips Research Laboratories) e apresenta desvio na ordem de 10%.[45]

Neste trabalho o rendimento quântico foi obtido à temperatura ambiente e de acordo com as seguintes ressalvas:

- ➤ Todos os padrões e amostras apresentassem o mesmo alinhamento óptico durante a aquisição dos espectros;

- ➤ As amostras fossem excitadas no mesmo comprimento de onda;

- ➤ Todos os compostos envolvidos estivessem com a mesma granulometria. Esta última precaução minimiza as interferências causadas pelo tamanho dos grãos nas intensidades das curvas de reflectâncias difusa [92], evitando assim, a sub ou superestimativa dos valores de rendimentos quânticos atribuídos às amostras.

Os valores de rendimento quântico são determinados de acordo com a relação representada na equação (1.5):

$$q = \left[\left(\frac{1-r_p}{1-r_x}\right)\left(\frac{\Delta\phi_x}{\Delta\phi_p}\right)\right] \times \Phi_p \qquad \textbf{(1.5)}$$

onde r_p é a reflectividade, ou seja a quantidade de radiação incidente refletida, r_x é a reflectividade da amostra, $\Delta\Phi_r$ e $\Delta\Phi_x$ correspondem as áreas sob a curvas de emissão do padrão e da amostra respectivamente, e q_p é o rendimento quântico absoluto do padrão.

As reflectividades, r_p e r_x, são obtidas em relação a um padrão de reflectância, neste caso foi usado o MgO, cuja reflectividade r_{MgO} = 0,91. O padrão de rendimento quântico usado nas medidas foi o salicilato de sódio (q_p

= 55%), pois apresenta rendimento quântico constante na região de comprimento de onda de 250 a 370 nm.[46]

O procedimento de aquisição dos resultados consiste em duas etapas:

➢ Medidas de reflectância difusa das amostras, dos padrões de rendimento quântico e reflectividade. Fixa-se o monocromador de excitação no comprimento de onda desejado e faz-se a varredura de emissão na região do espectro que compreenda a excitação da amostra.

➢ Medidas de emissão das amostras e do padrão de rendimento quântico.

1.2.4.7   Difração de Raios-X de Monocristal

Os monocristais de $[Ln_2(MELL)(H_2O)_6]$ foram manualmente montados sobre um Hampton Research CryoLoops usando o óleo FOMBLIN Y perfluoropolyether (Aldrich)[47] sob o auxílio de estereomicroscópio Stemi 2000 equipado com lentes Carl Zeiss. Os dados foram coletados em um Bruker X8 Kappa com detector de área (CCD) APEX II (Mo K_α monocromada com $\lambda = 0,71073$ Å) controlado pelo pacote de *software* APEX-2 e equipado com criostato Oxford Cryosystems Series 70. As imagens foram processadas usando o SAINT+ e os dados foram corrigidos para absorção pelo método semi-empírico implementado no SADABS. As estruturas foram resolvidas usando Patterson implementado no SHELXS-97[48] que possibilitou identificar os centros metálicos. Todos outros átomos (excetos os hidrogênio) foram

localizados via mapas de Fourier-diferença através de sucessivos ciclos do Método de Mínimos Quadrados (F^2) usando o SHELXL-97[49] e refinados usando parâmetros anisotrópicos. Os átomos de hidrogênio ligados as moléculas de água coordenadas aos íons Ln^{3+} foram identificados pelos mapas Fourier-diferenças e adicionados ao modelo estrutural com as distâncias O—H e H---H fixadas em 0,95(1) e 1,55(1), além disso os U_{iso} foram fixados em $1,5 \times U_{eq}$ em relação aos dos átomos de oxigênio em que estão conectados para garantir uma geometria razoável.

1.2.4.8   *Parâmetros de Intensidade*

Os valores dos parâmetros Ω_2 e Ω_4 são em função das transições $^5D_0 \rightarrow {}^7F_2$ e $^5D_0 \rightarrow {}^7F_4$ respectivamente e[i], por sua vez, são presumidos usando a transição $^5D_0 \rightarrow {}^7F_1$ como referência. Esta consideração é feita devido à transição $^5D_0 \rightarrow {}^7F_1$ ser controlada pelo mecanismo de dipolo magnético e em decorrência não sofre influência do campo ligante. As equações usadas nos cálculos são mostradas nas equações abaixo [50]:

$$A_{01} = 0,31 \times 10^{-11} \times \eta^3 \times (\sigma_1)^3 \qquad \textbf{(1.6)}$$

---

[i] As transições induzidas por dipolo elétrico podem ser caracterizadas por três fenomenológicos parâmetros de intensidade Ω_λ ($\lambda = 2$, 4 e 6). Estes parâmetros são originados da teoria de Judd-Ofelt e representam o quadrado do deslocamento de carga devido à transição induzida por dipolo elétrico. É importante destacar que estes parâmetros podem ser utilizados para relacionar propriedades espectroscópicas e estruturais de materiais. O parâmetro Ω_2 dá informação acerca da transição hipersensitiva, ou seja sonda as pequenas variações do ambiente químico do metal, como por exemplo: simetria do sítio de coordenação e influência da natureza do ligante. Os valores de Ω_2 aumentam em função do número de coordenação, grau de basicidade do ligante e nível de interação da ligação metal-ligante. Os parâmetros Ω_4 e Ω_6 dependem de outras transições e estão associados a efeitos de longa distância. A rigidez da matriz tem forte efeito sobre esses dois últimos parâmetros. Para maiores informações consulte o capítulo 167 do livro *Handbook on the Physical and Chemistry of Rare Earth, vol. 25* e as referências 68 e 69.

Onde:

$A_{01} \to$ probabilidade da transição $^5D_0 \to {^7F_1}$;

$\eta \to$ índice de refração do composto (1,5);

$\sigma \to$ energia media da transição[ii];

$0,31 \cdot 10^{-11} \to$ constante característica ao íon Eu^{3+};

$$\frac{A_{02} \times \sigma_2}{A_{01} \times \sigma_1} = \frac{S_{02}}{S_{01}} \qquad (1.7)$$

Onde:

$A_{02} \to$ probabilidade da transição $^5D_0 \to {^7F_2}$;

$\sigma_1 \to$ energia da transição $^5D_0 \to {^7F_1}$;

$\sigma_2 \to$ energia da transição $^5D_0 \to {^7F_2}$;

$S_{01} \to$ área sob a curva da transição $^5D_0 \to {^7F_1}$;

$S_{02} \to$ área sob a curva da transição $^5D_0 \to {^7F_2}$;

$$A_{02} = 2,33 \cdot 10^8 \times (\sigma_2)^3 \times \frac{\eta(\eta^2 + 2)^2}{9} \times \Omega_2 \qquad (1.8)$$

Onde:

[ii] A energia da transição está associada ao baricentro da transição. Estes valores foram obtidos através da média da largura de banda a meia altura. Isto é feito da seguinte maneira: integra-se a transição; divide-se a área por 2 e retira-se a média da energias neste ponto.

$\Omega_2 \rightarrow$ parâmetro de intensidade;

$A_{02} \rightarrow$ Probabilidade da transição $^5D_0 \rightarrow {}^7F_2$;

$\sigma_2 \rightarrow$ energia da transição $^5D_0 \rightarrow {}^7F_2$;

$\eta \rightarrow$ índice de refração do composto (1,5);

$2,33.10^8 \rightarrow \left\langle {}^5D_0 \left\| U^{(2)} \right\| {}^7F_2 \right\rangle^2$ da tabela de Carnall;[51]

$$\frac{A_{04} \times \sigma_4}{A_{01} \times \sigma_1} = \frac{S_{04}}{S_{01}} \qquad (1.9)$$

Onde:

$A_{04} \rightarrow$ probabilidade da transição $^5D_0 \rightarrow {}^7F_4$;

$\sigma_1 \rightarrow$ energia da transição $^5D_0 \rightarrow {}^7F_1$;

$\sigma_4 \rightarrow$ energia da transição $^5D_0 \rightarrow {}^7F_4$;

$S_{01} \rightarrow$ área sob a curva da transição $^5D_0 \rightarrow {}^7F_1$;

$S_{04} \rightarrow$ área sob a curva da transição $^5D_0 \rightarrow {}^7F_4$;

$$A_{04} = 2,4.10^8 \times (\sigma_4)^3 \times \frac{\eta(\eta^2 + 2)^2}{9} \times \Omega_4 \qquad (1.10)$$

Onde:

$\Omega_4 \rightarrow$ parâmetro de intensidade;

$A_{04} \rightarrow$ Probabilidade da transição $^5D_0 \rightarrow {}^7F_4$;

$\sigma_4 \rightarrow$ energia da transição $^5D_0 \rightarrow {}^7F_4$;

$\eta \rightarrow$ índice de refração do composto (1,5);

$2,4.10^8 \rightarrow \left\langle {}^5D_0 \left\| U^{(2)} \right\| {}^7F_2 \right\rangle^2$ da tabela de Carnall.[51]

1.2.4.9   Modelagem

A geometria otimizada do composto contento o íon Eu^{3+} foi calculada usando o Modelo Sparkle/AM1[24] implementado no MOPAC 2007.[52] A geometria calculada foi usada para o previsão dos estados excitados singleto e tripleto do ligante.[28,29] Os parâmetros de intensidade teóricos, Ω_λ (λ = 2, 4 e 6) e as taxas de transferência ligante-lantanídeo foram calculados baseados nos modelos criados por Malta e colaboradores.[53-55]

1.3   Resultados e Discussão

1.3.1 Estrutura Cristalográfica e Otimização via Sparkle/AM1

Os estudos cristalográficos revelaram que os compostos (1.1), (1.2) e (1.3) são isoestruturais aos materiais baseados em lantânio e gadolínio previamente publicado por Willians[56] e Li.[44] Todos os dados cristalográficos, intensidade das medidas, solução da estrutura e refinamentos estão resumidos na Tabela 1.1.

Tabela 1.1. Dados cristalográficos e detalhes de refinamento para $[Ln_2(MELL)(H_2O)_6]$

	(1.1)	(1.2)	(1.3)
Formula	$C_6 H_6 O_9 Eu$	$C_6 H_6 O_9 Tb$	$C_6 H_6 O_9 Gd$
Peso Molecular	374,07	381,03	379,36
Sistema Cristalino	Ortorrômbico	Ortorrômbico	Ortorrômbico
Grupo Espacial	*P n n m*	*P n n m*	*P n n m*
Temperatura /K	296(2) K	150(2) K	150(2) K
Cela Unitária /Å	a = 13,4361(5) Å	a = 13,3410(3) Å	a = 13,3662(6)
	b = 6,6250(2) Å	b = 6,57180(10) Å	b = 6,5897(3) Å
	c = 10,1416(4) Å	c = 10,0912(2) Å	c = 10,1045(4) Å
	α = β = γ =90°.	α = β = γ =90°.	α = β = γ =90°.
Volume/Å³	902,75(6) Å3	884,74(3)	890,00(7) Å3
Z	4	4	4
D_d/g cm⁻³	2,752	2,861	2,831
μ(Mo-Kα)/mm⁻¹	6,985	7,032	7,4908
Tamanho do Cristal/mm	0,35 x 0,35 x 0,30	0,20 x 0,19 x 0,17	0,20 x 0,19 x 0,17
Faixa de θ	3,67 a 25,35°	3,70 a 25,33°	3,69 a 25,33°
Index ranges	-16<=h<=15 7<=k<=7	16<=h<=16	-15<=h<=16
	2<=l<=11	7<=k<=6	7<=k<=7
		12<=l<=12	12<=l<=12
Reflexões coletadas	7990	9245	12523
Reflexões Independentes	848 (R_{int} = 0.0232)	855 (R_{int} = 0.0182)	860 (R_{int} = 0.0193)
Completância para theta = 25.35°	96,5 %	99,5 %	99,7 %
R indices Final [I>2σ(I)][a,b]	*R1 = 0,0193, wR2 = 0,0506*	*R1 = 0,0119 wR2 = 0,0274*	*R1 = 0,0118 wR2 = 0,0289*
R indices Final (todos os dados)[a,b]	*R1 = 0,0205 wR2 = 0,0510*	*R1 = 0,0126 wR2 = 0,0277*	*R1 = 0,0119 wR2 = 0,0289*
CCDC Number	721858	721859	721857

$$^a R1 = \sum \left\| F_o \right| - \left| F_c \right\| / \sum \left| F_o \right|; \quad ^b wR2 = \sqrt{\sum \left[w \left(F_o^2 - F_c^2 \right)^2 \right] / \sum \left[w \left(F_o^2 \right)^2 \right]}$$

O ânion melitato é coordenado a oito íons Ln^{3+} através de seus seis grupos carboxilatos: dois grupos estão coordenados a quatro cátions através do modo de coordenação *syn-syn* em ponte, enquanto os quatro

remanescentes coordenam-se aos lantanídeos como *syn-syn* quelatos[iii].[57]

Cada íon Ln^{3+} está coordenado a seis átomos de oxigênio provenientes de seis melitatos simetricamente relacionados e três moléculas de água completam a esfera de coordenação do metal, logo o poliedro de coordenação formado pode ser descrito como um prisma distorcido tri-encapuzado, como pode ser observado na Figura 1.2.
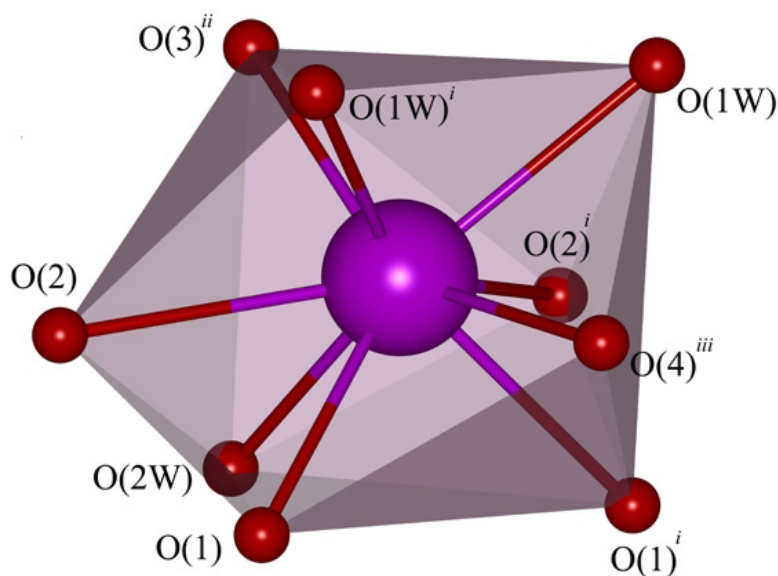
Figura 1.2: Poliedro de coordenação do íon lantanídeo em $[Ln_2(MELL)(H_2O)_6]$, descrito como prisma distorcido tri-encapuzado. Operações de simetria usadas para gerar átomos equivalentes: [i]x, y, 1-z; [ii]3/2-x, y+1/2, 3/2-z; [iii]3/2-x, y-1/2, 3/2-z.

[iii] Denominação dos modos de coordenação típico de carboxilatos:
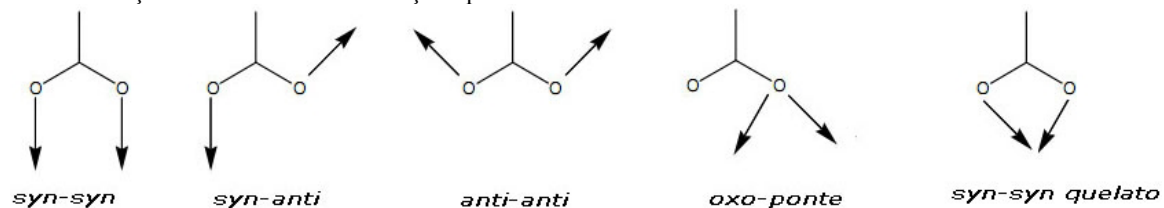
Os grupos carboxilatos estão distorcidos em relação ao plano dos anéis aromáticos. É importante destacar que este comportamento já foi observado em compostos similares e é devido aos modos de coordenação metal-ligante adotados. Os comprimentos de ligação Ln—O e os ângulos O—Ln—O do poliedro de coordenação são mostrados na Tabela 1.2.

Tabela 1.2. Distâncias interatômicas (Å) e ângulos (°) em $[Ln_2(MELL)(H_2O)_6]$

	(1.1)	(1.2)	(1.3)
Ln(1)−O(3)^i	2,320(4)	2,296(3)	2,309(3)
Ln(1)−O(4)^{ii}	2,369(4)	2,344(3)	2,356(2)
Ln(1)−O(1W)^{iii}	2,424(3)	2,3904(18)	2,4067(18)
Ln(1)−O(1W)	2,424(3)	2,3904(18)	2,4067(18)
Ln(1)−O(1)^{iii}	2,502(3)	2,4664(17)	2,4792(16)
Ln(1) −O(1)	2,502(3)	2,4664(17)	2,4792(16)
Ln(1)−O(2W)	2,503(4)	2,482(3)	2,494(3)
Ln(1)−O(2)^{iii}	2,575(3)	2,5563(18)	2,5636(18)
Ln(1)−O(2)	2,575(3)	2,5563(18)	2,5636(18)
O(3)^i—Ln(1)—O(4)^{ii}	145,44(14)	145,32(9)	145,07(9)
O(3)^i—Ln(1) —O(1W)^{iii}	83,92(10)	84,33(7)	84,29(6)
O(4)^{ii}—Ln(1) —O(1W)^{iii}	70,24(10)	69,84(7)	69,73(6)
O(3)^i—Ln(1) —O(1W)	83,92(10)	84,33(7)	84,29(6)
O(4)^{ii}—Ln(1) —O(1W)	70,24(10)	69,84(7)	69,73(6)
O(1W)^{iii}—Ln(1) —O(1W)	81,60(17)	81,96(10)	82,06(10)

O(3)^{i}—Ln(1) —O(1)^{iii}	128,59(8)	129,06(5)	129,03(5)
O(4)^{ii}—Ln(1) —O(1)^{iii}	72,25(9)	71,96(6)	72,13(6)
O(1W)^{iii}—Ln(1) —O(1)^{iii}	142,42(10)	141,76(6)	141,82(6)
O(1W) —Ln(1) —O(1)^{iii}	83,76(10)	83,54(6)	83,49(6)
O(3)^{i}—Ln(1) —O(1)	128,59(8)	129,06(5)	129,03(5)
O(4)^{ii}—Ln(1) —O(1)	72,25(9)	71,96(6)	72,13(6)
O(1W)^{iii}—Ln(1) —O(1)	83,76(10)	83,54(6)	83,49(6)
O(1W) —Ln(1) —O(1)	142,42(10)	141,76(6)	141,82(6)
O(1)^{iii}—Ln(1) —O(1)	87,19(12)	86,40(8)	86,50(8)
O(3)^{i}—Ln(1) —O(2W)	79,85(14)	79,64(9)	79,95(9)
O(4)^{ii}—Ln(1) —O(2W)	134,72(14)	135,04(9)	134,98(9)

Operações de simetria para gerar átomos equivalentes:

^{i} -x+3/2,y+1/2,-z+3/2 ^{ii} -x+3/2,y-1/2,-z+3/2

^{iii} x,y,-z+1 ^{iv} -x+1,-y,z ^{v} x,y,-z+2

Os anéis aromáticos e os íons Ln^{3+} são empilhados sobre plano *bc* formando uma rede em duas dimensões. Desta forma, a estrutura resultante tem canais hexagonais distorcidos em 1-D[iv] com tamanho de cavidade de 8,3 x 6,6 Å e que se propagam ao longo do eixo cristalográfico *c* (Figura 3). Todos *aqua* ligantes estão envolvidos em ligações de hidrogênio com os átomos de oxigênio oriundos dos grupos carboxilatos, atuando como doadores bifurcados com *graph set* representação *S(3)*. Todos os detalhes geométricos das ligações de hidrogênio são mostrados na Tabela 1.3.

[iv] Os canais são 1D por se propagarem apenas na direção cristalográfica *c*.
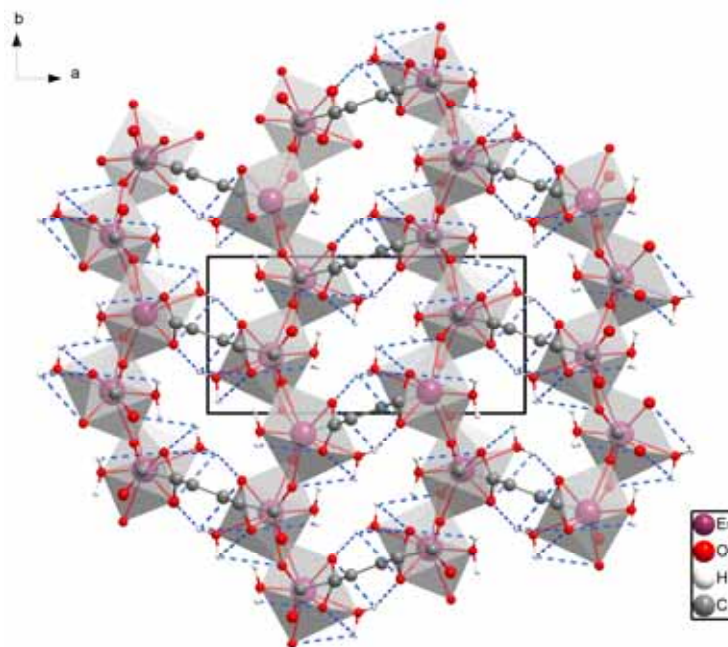
Figura 1.3: Vista ao longo do eixo cristalográfico *c* da estrutura [Ln$_2$(MELL)(H$_2$O)$_6$], evidenciando os canais hexagonais ocupados pelos *aqua*-ligantes. As ligações de hidrogênio são representadas pelas linhas pontilhadas azuis.

Tabela 1.3. Ligações de hidrogênio em [Ln$_2$(MELL)(H$_2$O)$_6$], (Å e °)

D-H...A	d(D-H)	d(H...A)	d(D...A)	<(DHA)
(1.1)				
O(1W)-H(1A)...O(1)^{vi}	0,95(3)	1,95(2)	2,847(4)	158(5)
O(1W)-H(1B)...O(2)^{vii}	0,94(3)	1,826(18)	2,745(4)	164(4)
O(2W)-H(2A)...O(1)^{viii}	0,947(10)	1,96(2)	2,859(4)	158(5)
O(2W)-H(2B)...O(2W)^{ix}	0,947(10)	2,16(4)	3,028(9)	151(7)
(1.2)				
O(1W)-H(1A)...O(1)^{vi}	0,941(10)	1,923(13)	2,836(2)	163(3)
O(1W)-H(1B)...O(2)^{vii}	0,941(10)	1,822(13)	2,739(2)	164(3)
O(2W)-H(2A)...O(1)^{viii}	0,945(10)	1,931(12)	2,861(3)	167(3)
O(2W)-H(2B)...O(2W)^{ix}	0,946(10)	2,01(2)	2,938(5)	165(5)

	(1.3)			
O(1W)-H(1A)...O(1)^{vi}	0,939(10)	1,916(11)	2,840(3)	167(3)
O(1W)-H(1B)...O(2)^{vii}	0,940(10)	1,823(14)	2,736(3)	163(3)
O(2W)-H(2A)...O(1)^{viii}	0,939(10)	1,960(15)	2,863(3)	160(3)

Um fragmento da cela unitária contendo 382 átomos, sendo 12 cátions de Eu^{3+}, foi otimizado usando o modelo Sparkle/AM1. É importante salientar que inicialmente foram removidos 20 íons de Eu^{3+} e os átomos de oxigênio provenientes de fragmentos incompletos dos melitatos, visando minimizar o efeito de desordem causado pelos fragmentos incompletos. Um dos 12 poliedros foi escolhido para ser utilizado nos cálculos das propriedades espectroscópicas e suas coordenadas atômicas, polarizabilidades e fatores de carga estão dispostos na Tabela 1.4. Na Figura 1.4 é mostrada uma comparação entre a cela unitária obtida experimentalmente e a otimizada usando o Sparkle/AM1.

Tabela 1.4. Coordenadas atômicas e os fatores de carga e polazabilidade obtidos para (1.1).

Atoms	X (Å)	Y (Å)	Z (Å)	g	α
Eu	0,000 (0,000)	0,000 (0,000)	0,000 (0.000)	–	–
O	2,276 (1,931)	-0,763 (-0,908)	-0,671 (-0.927)	0,018	2,21
O	1,188 (0,872)	-2,186 (-2,065)	0,053 (0.624)	0,018	2,21
O	1,273 (1,311)	2,138 (1,800)	0,143 (0.672)	0,018	2,21
O	-0,286 (-0,860)	2,108 (1,862)	1,289 (1.093)	0,018	2,21
O	-1,360 (-1,849)	-0,985 (-1,202)	1,751 (0.843)	0,018	2,21
O	0,698 (0,281)	0,890 (0,591)	-2,256 (-2.300)	1,231	6,48
O	-0,656 (-0,727)	-1,516 (-1,719)	-1,898 (-1.495)	1,231	6,48
O	1,770 (0,745)	0,105 (-0,009)	1,783 (2.278)	1,231	6,48
O	-1,807 (-1,854)	1,461 (1,141)	-0,966 (-1.083)	1,231	6,48

Figura 1.4: Estrutura molecular de **(1.1)** obtidas via: (a) Cristalografia de mono-cristais e (b) Otimizada usando o modelo Sparkle/AM1. As setas vermelhas indicam os locais onde foram removidos os íon Eu^{3+}.

1.3.2 Propriedades Espectroscópicas

Nas investigações sobre transferência de energia intramolecular em complexos de lantanídeos, a determinação dos níveis excitados do ligante

fazem parte do protocolo de rotina.[58] Nos espectros de emissão dos complexos com o íon gadolínio (Gd^{3+}) são mostradas apenas as bandas características da emissão do ligante ao invés das linhas características da transição do íon. Este comportamento é esperado, pois o mais baixo nível excitado ($^6P_{7/2}$) designado ao Gd^{3+} é localizado em 32150 cm^{-1},[59] além disso, a possibilidade da excitação direta do metal usando radiação ultravioleta pode ser desprezada, devido à força do oscilador do ligante ser bastante elevada e está situada na mesma região espectral de absorção do Gd^{3+}.[58] Na figura 1.5 está mostrado o espectro de emissão de (1.3) coletado a 77K após excitação em 320 nm. A posição do tripleto foi estimada a partir da transição zero-fónon,[v] que foi considerada como transição 0-0 situada em 415,2 nm (24085 cm^{-1}).[58,60,61]

---

[v] A transição zero-fonon foi estimada como o início da banda de fosforescência de acordo com o digrama de harmônicos esféricos do princípio de Frank-Condon mostrado abaixo.
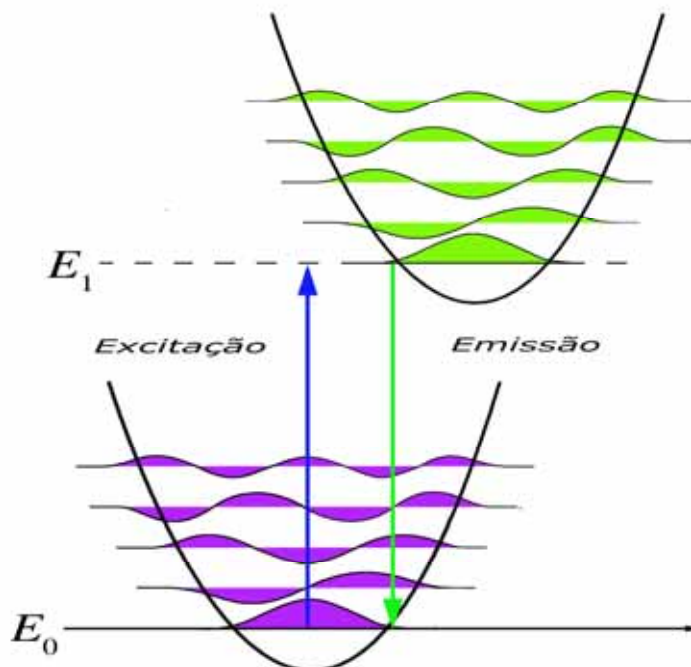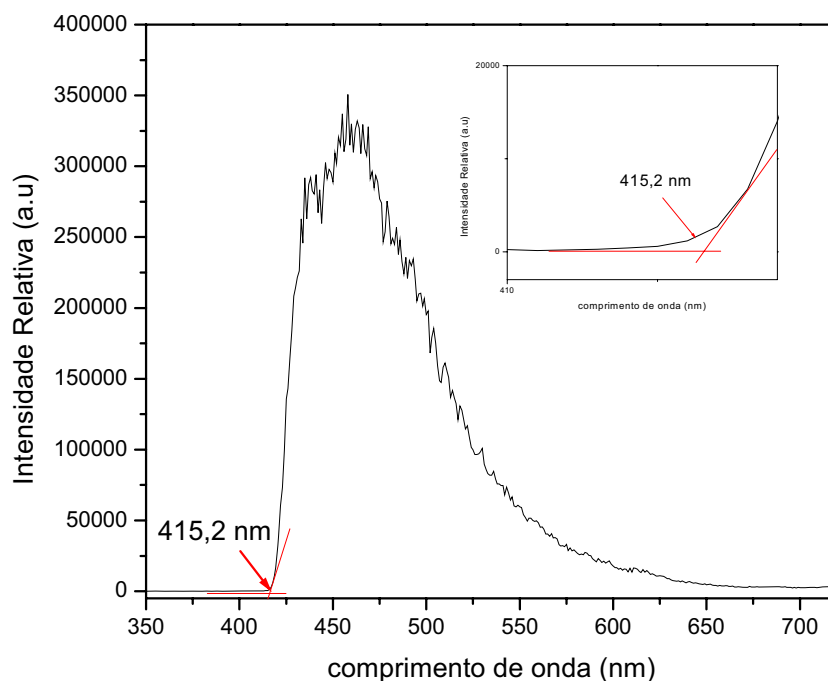
Figura 1.5: Espectro de emissão à 77K de **(1.3)**.

Na figura 1.6 são mostrados os espetros de excitação de **(1.1)** e **(1.2)** adquiridos à temperatura ambiente monitorando as emissões dos íons Eu^{3+} e Tb^{3+} em 614 e 545 nm nas regiões de 200-600 nm e 200-500 nm, respectivamente. O espectro de excitação de **(1.1)** mostra uma banda larga situada entre 220 e 350 nm (λ_{max} = 312 nm) que pode ser designada à transição π–π* inerentes ao ligante orgânico. As intensas linhas observadas na região de 350-580 nm são atribuídas às transições $f-f$ do Eu^{3+} e indicam que o processo de sensitização do íon através do ligante não é muito eficiente. No caso de **(1.2)** foi observado uma banda com absorção máxima em 320 nm

típica das transições do ligante e linhas muito fracas devidas às transições $f - f$ do Tb^{3+}, caracterizando o processo eficiente de transferência de energia.
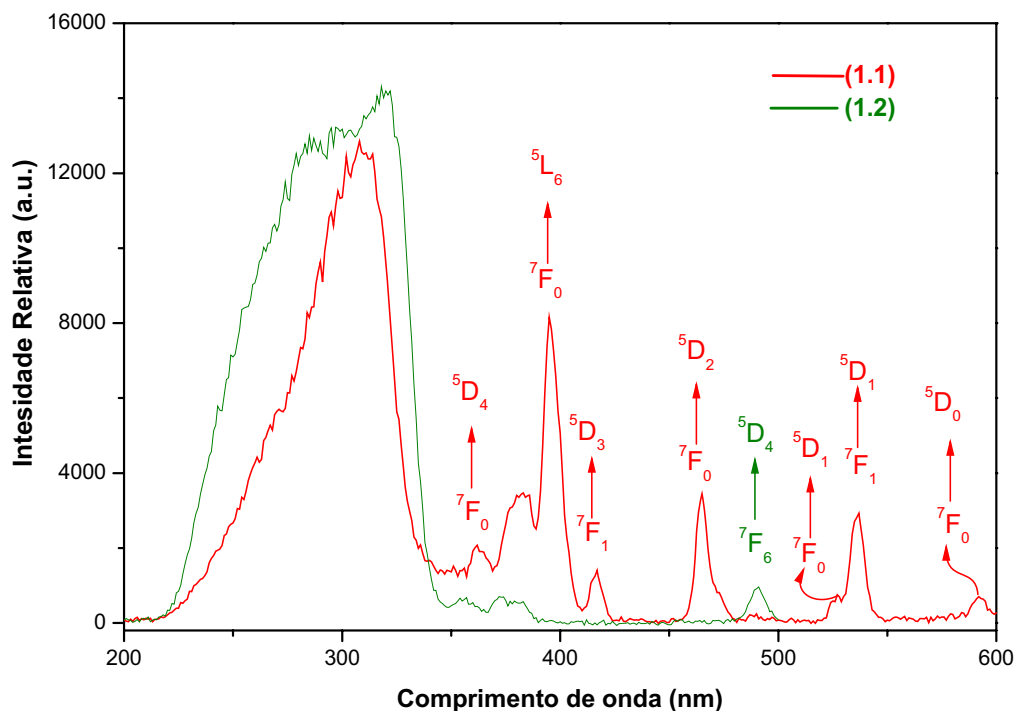
Figura 1.6: Espectro de excitação de **(1.1)** e **(1.2)**.

O espectro de emissão de **(1.2)** (Figura 1.7) adquirido à temperatura ambiente após excitação em 320 nm mostra intensas linhas associadas às transições $^5D_4 \rightarrow ^7F_J$ do Tb^{3+}. A transição $^5D_4 \rightarrow ^7F_5$ centrada em 545nm é a mais forte e corresponde a 66% do espectro integrado. No caso do Tb^{3+}, o principal canal responsável pela supressão da luminescência é a retrotransferência,[62] no entanto, de acordo com Latva[63] esse mecanismo de supressão somente é

observado quando a diferença de energia entre o nível tripleto do ligante e $^5D_4$ do Tb^{3+} (20400 cm^{-1}) é inferior a cerca de 1850 cm^{-1}. Evidentemente, no presente caso o mecanismo supressor não desempenha papel importante, visto que o eficiente processo de transferência de energia é confirmado através dos consideráveis valores de rendimento quântico e tempos de vida[vi] (37% e 0,74 ms, respectivamente).
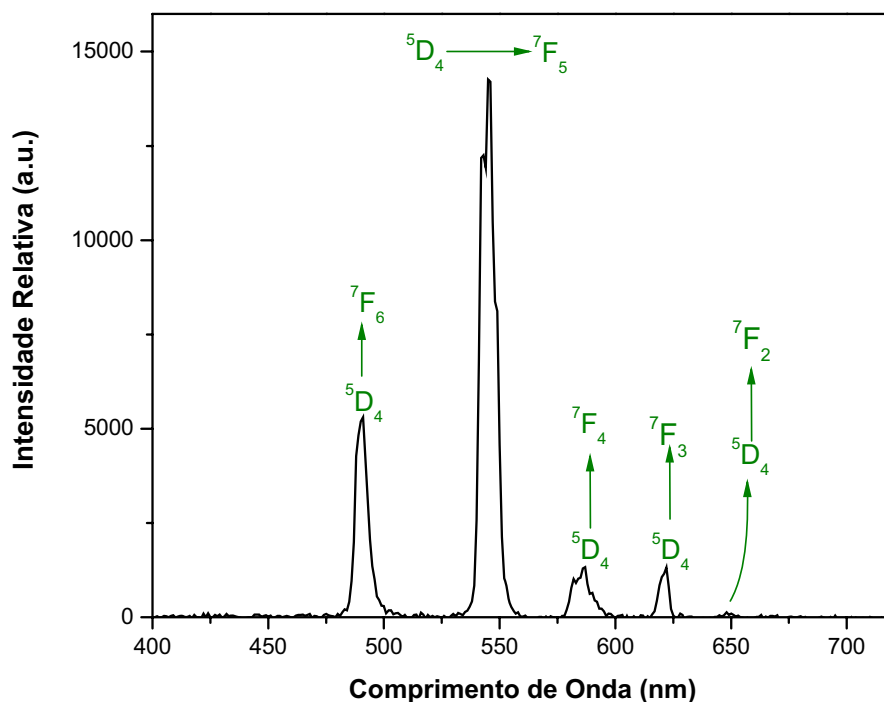
Figura 1.7: Espectro de emissão de **(1.2)**.

[vi] Tempo de vida de um material luminescente é definido como o tempo para a intensidade da luminescência decair até 1/e ou 0,368 de sua intensidade original.

O espectro de emissão de (1.1) (Figura 1.8) coletado a 77 K após excitação em 312 e 394 nm, mostra linhas características das transições $^5D_0 \rightarrow {}^7F_J$, sendo a $^5D_0 \rightarrow {}^7F_2$ (614 nm) responsável pela coloração vermelha do material. A banda entre 410 e 580 nm pode ser atribuída às emissões originadas do ligante e confirma que o processo de transferência de energia ligante-metal é ineficiente como previamente constatado no espectro de excitação do material (Figura 1.6).

As relativas intensidades e os desdobramentos das bandas de emissão são dependentes do grau da remoção da degenerescência $(2J + 1)$ devido à influência da simetria do ambiente de coordenação no metal.[64] Os estudos cristalográficos revelaram que o ambiente de coordenação do Eu^{3+} é levemente desviado da geometria de um prisma trigonal tri-encapuzado, implicando que o grupo pontual da esfera de coordenação do Eu^{3+} é reduzido da simetria D_{3h} para D_3. De acordo com a regra de seleção para transições regidas por dipolo elétrico sob o efeito do grupo pontual D_3, a transição $^5D_0 \rightarrow {}^7F_0$ é ausente e a $^5D_0 \rightarrow {}^7F_2$ apresenta uma pequena banda lateral em região de menor energia.[65] Esses resultados demonstram que a análise do ambiente de coordenação baseado no espectro de emissão está em excelente concordância com dados obtidos da difração de raios-x.
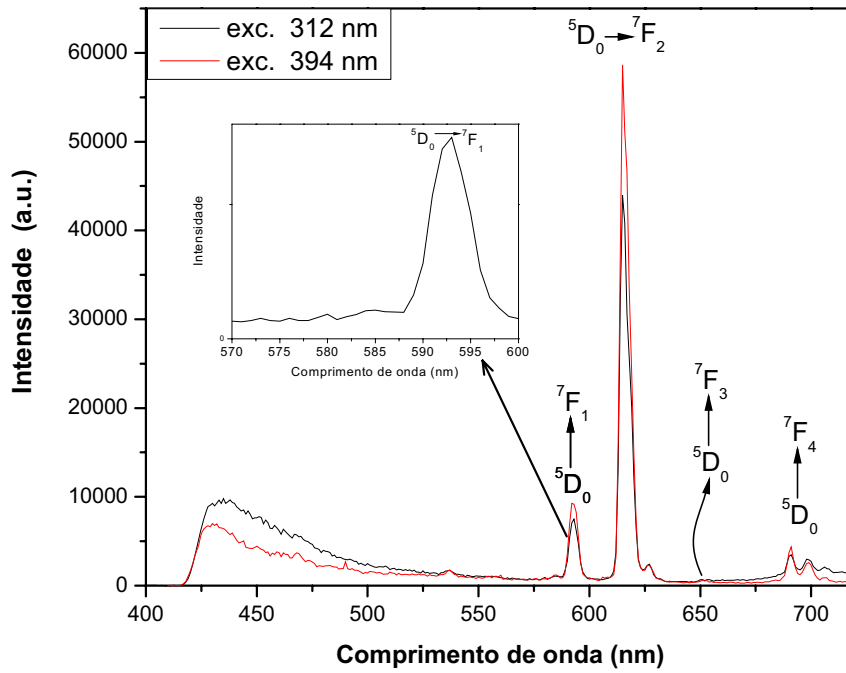
Figura 1.8: Espectro de emissão de **(1.1)**.

Na Tabela 1.5 são dispostos os valores teóricos e experimentais dos parâmetros de intensidade (Ω_2, Ω_4), taxas radiativas e não-radiativas (A_{rad} e A_{nrad}, respectivamente), eficiência (η), rendimento quântico (q) e tempo de vida da emissão (τ) de **(1.1)**.

Tabela 1.5. Parâmetros de intensidade, taxas radiativas e não-radiativas, eficiência quântica e rendimento quântico experimentais e calculados a partir das estruturas otimizada pelo modelo Sparkle/AM1. O tempo de vida de **(1.1)** foi obtido experimentalmente.

| | Ω_2 | Ω_4 | A_{rad} | A_{nrad} | τ | η | q |
	$(10^{-20}cm^2)$	$(10^{-20}cm^2)$	(s^{-1})	(s^{-1})	(ms)	$(\%)$	$(\%)$
Experimental	11,82	2,72	441,70	2336,08	0,36	15,9	8,0
Sparkle/AM1	10,22	6,84	459,16	2318,62	–	16,5	16,3

Os valores calculados estão em boa concordância com os obtidos experimentalmente, o que caracteriza a eficiência da metodologia empregada. Os elevados valores da A_{nrad} e os baixos valores de A_{rad} e tempos de vida indicam que canais não-radiativos provenientes das moléculas de água coordenadas ao Ln^{3+} são eficientes no processo de relaxação. Portanto, a associação de um ineficiente processo de transferência de energia com canais não-radiativos eficientes fornecem uma plausível explicação para o baixo rendimento quântico experimental obtido para **(1.1)**. O rendimento quântico teórico foi calculado usando o valor de A_{nrad} experimental e apresenta valor na mesma ordem de magnitude do experimental (ver Tabela 1.5). Isto é devido aos cálculos não levarem em conta o acoplamento com os osciladores O—H das moléculas de água coordenadas ao Eu^{3+}.

Os valores obtidos para Ω_2 são relativamente baixos em comparação as sistemas baseados em β-dicetonas,[37,38,66] podendo ser atribuído a diferencias entre os poliedros de coordenação e ao reduzido grau de polarização do ácido

melítico em comparação as β-dicetonas, que por sua vez reflete na intensidade da transição hipersensível $^5D_0 \rightarrow {}^7F_2$.[67] O parâmetro Ω_4 é menos sensível a alterações na esfera de coordenação que o Ω_2, porém seus valores refletem a rigidez do ambiente químico ao redor do íon Ln^{3+}.[68,69] Os baixos valores de (1.1) indicam considerável rigidez estrutural associada ao material.

Para elucidar com mais detalhes o processo de TE entre o MELL e o Eu^{3+} foi aplicado o método para resolução das equações de taxas desenvolvido por Malta e colaboradores.[70] Na figura 1.9 está ilustrado o diagrama de transferência de energia proposto para (1.1).
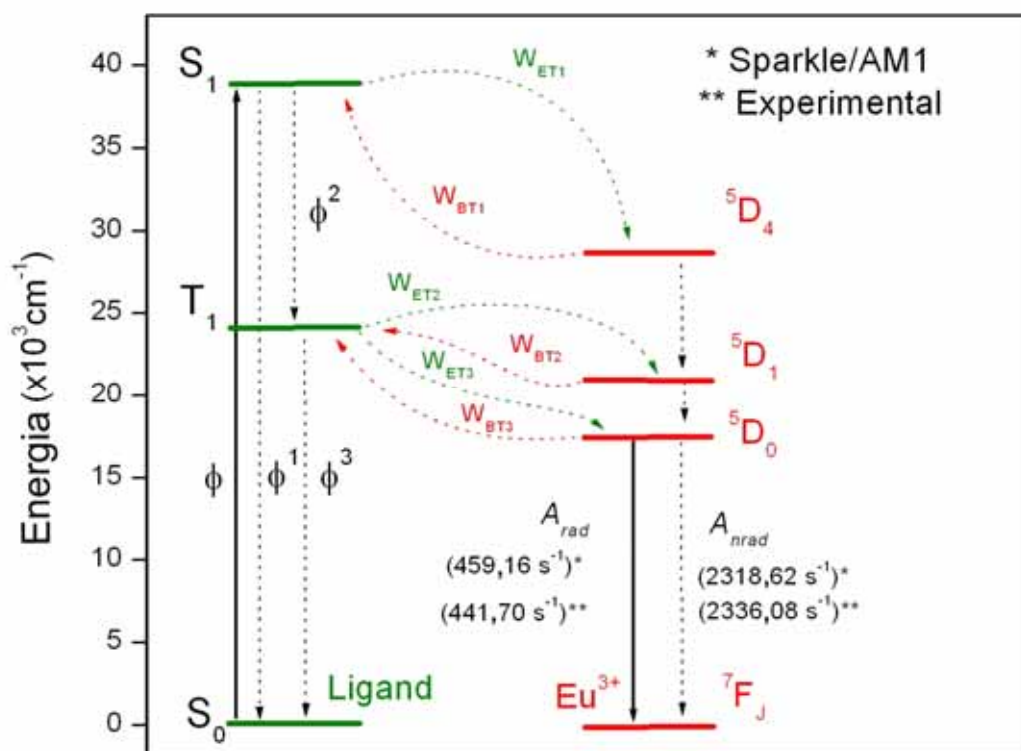
Figura 1.9: Diagrama de transferência de energia proposto para (1.1).

Como pode ser observado, a transferência de energia ligante-metal pode ocorrer pelos estados excitados singleto e tripleto. Porém devido ao curto tempo de vida do nível singleto e a posição não ressonante com os níveis do Eu^{3+} esse canal não deve ser eficiente.[15] Os valores teóricos para o singleto e tripleto calculados para geometria otimizada pelo modelo Sparkle/AM1 são 39075 cm^{-1} e 24635 cm^{-1}, respectivamente. O tripleto calculado está em boa concordância com o estimado experimentalmente (24213 cm^{-1}).

As taxas de transferência e retrotransferência de energia são sumarizadas na Tabela 1.6. Devido à posição não ressonante do nível singleto do ligante com os níveis emissores do Eu^{3+}, foi considerado nos cálculos das taxas o canal Singleto $\rightarrow$ $^5D_4$.

Tabela 1.6. Taxas de transferência e retrotransferência de energia calculados para (**1.1**).

Geometria	Singleto $\rightarrow$ $^5D_4$		Tripleto $\rightarrow$ $^5D_1$		Tripleto $\rightarrow$ $^5D_0$	
	W_{ET1} (s^{-1})[a]	W_{BT1} (s^{-1})[b]	W_{ET2} (s^{-1})[a]	W_{BT2} (s^{-1})[b]	W_{ET3} (s^{-1})[a]	W_{BT3} (s^{-1})[b]
Raio-X	$4{,}15 \times 10^5$	$1{,}72 \times 10^{-12}$	$2{,}30 \times 10^9$	$4{,}84 \times 10^4$	$1{,}08 \times 10^9$	4,96
Sparkle/AM1	$8{,}45 \times 10^4$	$1{,}08 \times 10^9$	$2{,}36 * 10^8$	0	$3{,}20 \times 10^{-3}$	$1{,}53 \times 10^{-7}$

[a] W_{ET} – Taxa de transferência

[b] W_{BT} – Taxa de retrotransferência

Esses resultados demonstram que a transferência de energia ocorre predominantemente via tripleto $\rightarrow {}^5D_1$.

1.4 Conclusão

Três MMOs foram preparados pela reação hidrotermal dos íons Eu^{3+}, Tb^{3+} e Gd^{3+} e ácido melítico como ligante orgânico. Os compostos são iso-estruturais e cristalizam em sistema ortorrômbico com grupo espacial *Pnnm*. Os materiais formam estruturas tridimensionais com canais hexagonais que se propagam ao logo do eixo cristalográfico *c* (Figura 1.3). O composto **(1.2)** é um material bastante luminescente, justificado pelo eficiente processo de transferência de energia entre os ligantes orgânicos e o Tb^{3+}. Isto é confirmado com os valores de rendimento quântico e tempo de vida, (37% e 0,74 ms, respectivamente).

A geometria otimizada de **(1.1)** foi obtida através do modelo Sparkle/AM1 e mostra boa concordância com a estrutura cristalográfica. A geometria calculada do ambiente de coordenação foi utilizada para simular os parâmetros de intensidade, taxa radiativa, eficiência quântica e rendimento quântico do material. Os resultados demonstram a robustez da metodologia utilizada, a qual fornece uma nova perspectiva para investigação de materiais metalorgânicos baseados em Eu^{3+}.

1.5   Referências

(1)   Robson, R., A net-based approach to coordination polymers, *Journal of the Chemical Society-Dalton Transactions* **2000**, 3735-3744.

(2)   Rowsell, J. L. C.; Yaghi, O. M., Metal-organic frameworks: a new class of porous materials, *Microporous and Mesoporous Materials* **2004**, *73*, 3-14.

(3)   Yaghi, O. M.; O'Keeffe, M.; Ockwig, N. W.; Chae, H. K.; Eddaoudi, M.; Kim, J., Reticular synthesis and the design of new materials, *Nature* **2003**, *423*, 705-714.

(4)   Janiak, C., Engineering coordination polymers towards applications, *Dalton Transactions* **2003**, 2781-2804.

(5)   Shimizu, G. K. H., Assembly of metal ions and ligands with adaptable coordinative tendencies as a route to functional metal-organic solids, *Journal of Solid State Chemistry* **2005**, *178*, 2519-2526.

(6)   Wu, J. Y.; Yang, S. L.; Luo, T. T.; Liu, Y. H.; Cheng, Y. W.; Chen, Y. F.; Wen, Y. S.; Lin, L. G.; Lu, K. L., Time-evolving self-organization and autonomous structural adaptation of cobalt(II)-organic framework materials with scu and pts nets, *Chemistry-a European Journal* **2008**, *14*, 7136-7139.

(7)   Lehn, J. M., Perspectives in Supramolecular Chemistry - from Molecular Recognition Towards Self-Organization, *Pure and Applied Chemistry* **1994**, *66*, 1961-1966.

(8)   Long, La-Sheng, pH effect on the assembly of metal organic architectures, *CrystEngComm* **2010**, in press.

(9)   Lu, Y. L.; Wu, J. Y.; Chan, M. C.; Huang, S. M.; Lin, C. S.; Chiu, T. W.; Liu, Y. H.; Wen, Y. S.; Ueng, C. H.; Chin, T. M.; Hung, C. H.; Lu, K. L., Influence of

water content on the self-assembly of metal-organic frameworks based on pyridine-3,5-dicarboxylate, *Inorganic Chemistry* **2006**, *45*, 2430-2437.

(10)   Stuart R. Batten; Suzanne M. Neville; David R Turner *Coordination Polymers: Design, Analysis and Applications*; RSC Publishing: Cambridge, 2009.

(11)   Kitagawa, S.; Kitaura, R.; Noro, S., Functional porous coordination polymers, *Angew Chem Int Ed Engl* **2004**, *43*, 2334-75.

(12)   Broker, G. A.; Klingshirn, M. A.; Rogers, R. D., Green chemistry and lanthanide-based crystal engineering, *Journal of Alloys and Compounds* **2002**, *344*, 123-127.

(13)   Pan, L.; Huang, X. Y.; Li, J.; Wu, Y. G.; Zheng, N. W., Novel single- and double-layer and three-dimensional structures of rare-earth metal coordination polymers: The effect of lanthanide contraction and acidity control in crystal structure formation, *Angewandte Chemie-International Edition* **2000**, *39*, 527-530.

(14)   Wu, J. Y.; Yeh, T. T.; Wen, Y. S.; Twu, J.; Lu, K. L., Unusual robust luminescent porous frameworks self-assembled from lanthanide ions and 2,2 '-bipyridine-4,4 '-dicarboxylate, *Crystal Growth & Design* **2006**, *6*, 467-473.

(15)   Bunzli, J. C. G.; Piguet, C., Taking advantage of luminescent lanthanide ions, *Chemical Society Reviews* **2005**, *34*, 1048-1077.

(16)   Pavithran, R.; Kumar, N. S. S.; Biju, S.; Reddy, M. L. P.; Junior, S. A.; Freire, R. O., 3-phenyl-4-benzoyl-5-isoxazolonate complex of Eu3+ with tri-n-octylphosphine oxide as a promising light-conversion molecular device, *Inorganic Chemistry* **2006**, *45*, 2184-2192.

(17)   Pavithran, R.; Reddy, M. L. P.; Junior, S. A.; Freire, R. O.; Rocha, G. B.; Lima, P. P., Synthesis and luminescent properties of novel europium(III) heterocyclic

beta-diketone complexes with Lewis bases: Structural analysis using the Sparkle/AM1 model, *European Journal of Inorganic Chemistry* **2005**, 4129-4137.

(18)   Zhao, B.; Chen, X. Y.; Cheng, P.; Liao, D. Z.; Yan, S. P.; Jiang, Z. H., Coordination polymers containing 1D channels as selective luminescent probes, *Journal of the American Chemical Society* **2004**, *126*, 15394-15395.

(19)   de Bettencourt-Dias, A., Isophthalato-based 2D coordination polymers of Eu(III), Gd(III), and Tb(III): Enhancement of the terbium-centered luminescence through thiophene derivatization, *Inorganic Chemistry* **2005**, *44*, 2734-2741.

(20)   Harbuzaru, Bogdan V.; Corma, Avelino; Rey, Fernando; Jordá, Jose L.; Ananias, Duarte; Carlos, Luis D.; Rocha, João, A Miniaturized Linear pH Sensor Based on a Highly Photoluminescent Self-Assembled Europium(III) Metal-Organic Framework13, *Angewandte Chemie International Edition* **2009**, *48*, 6476-6479.

(21)   Harbuzaru, Bogdan V.; Corma, Avelino; Rey, Fernando; Atienzar, Pedro; Jordá, Jose L.; García, Hermenegildo; Ananias, Duarte; Carlos, Luis D.; Rocha, João, Metal-Organic Nanoporous Structures with Anisotropic Photoluminescence and Magnetic Properties and Their Use as Sensors13, *Angewandte Chemie International Edition* **2008**, *47*, 1080-1083.

(22)   Daiguebonne, C.; Kerbellec, N.; Guillou, O.; Bunzli, J. C.; Gumy, F.; Catala, L.; Mallah, T.; Audebrand, N.; Gerault, Y.; Bernot, K.; Calvez, G., Structural and luminescent properties of micro- and nanosized particles of lanthanide terephthalate coordination polymers, *Inorganic Chemistry* **2008**, *47*, 3700-3708.

(23)   de Lill, D. T.; de Bettencourt-Dias, A.; Cahill, C. L., Exploring lanthanide luminescence in metal-organic frameworks: Synthesis, structure, and guest-sensitized luminescence of a mixed europium/terbium-adipate framework and a terbium-adipate framework, *Inorganic Chemistry* **2007**, *46*, 3960-3965.

(24)   Freire, R. O.; Rocha, G. B.; Simas, A. M., Sparkle model for the calculation of lanthanide complexes: AM1 parameters for Eu(III), Gd(III), and Tb(III), *Inorganic Chemistry* **2005**, *44*, 3299-3310.

(25)   Freire, R. O.; Vila-Nova, S. P.; Brunet, E.; Juanes, O.; Rodriguez-Ubis, J. C.; Alves, S., Structure elucidation of lanthanide complexes by theoretical tools Novel pyrazole-pyridine Tb(111) tripod, *Chemical Physics Letters* **2007**, *443*, 378-382.

(26)   Freire, R. O.; Silva, F. R. G. E.; Rodrigues, M. O.; de Mesquita, M. E.; Junior, N. B. D., Design of europium(III) complexes with high quantum yield, *Journal of Molecular Modeling* **2005**, *12*, 16-23.

(27)   Freire, R. O.; Rocha, G. B.; Simas, A. M., Lanthanide complex coordination polyhedron geometry prediction accuracies of ab initio effective core potential calculations, *Journal of Molecular Modeling* **2006**, *12*, 373-389.

(28)   Zerner, M. C. *ZINDO manual, QTP*; University of Florida: Gainesville, FL. 32611, 1990.

(29)   Zerner, M. C.; Loew, G. H.; Kirchner, R. F.; Muellerwesterhoff, U. T., Intermediate Neglect of Differential-Overlap Technique for Spectroscopy of Transition-Metal Complexes - Ferrocene, *Journal of the American Chemical Society* **1980**, *102*, 589-599.

(30)   Yang, E.; Zhang, J.; Li, Z. J.; Gao, S.; Kang, Y.; Chen, Y. B.; Wen, Y. H.; Yao, Y. G., Interweaving 3D network with double helical tubes filled by 1D coordination polymer chains, *Inorganic Chemistry* **2004**, *43*, 6525-6527.

(31)   Kyono, A.; Kimata, M.; Hatta, T., Hydrothermal synthesis and structural investigation of silver magnesium complex of benzenehexacarboxylic acid (mellitic acid), $Ag_2Mg_2[C_{-6}(COO)_6]$ $8H_2O$ with two-dimensional layered structure, *Inorganica Chimica Acta* **2004**, *357*, 2519-2524.

(32)   Kumagai, H.; Kawata, S.; Kitagawa, S., Fabrication of infinite two-dimensional sheets of tetragonal metal(II) lattices - X-ray crystal structures and magnetic properties of [M(CA)(pyz)](n) (M2+ = Mn^{2+} and Co2+; H(2)CA = chloranilic acid; pyz = pyrazine), *Inorganica Chimica Acta* **2002**, *337*, 387-392.

(33)   Harnisch, J. A.; Thomas, L. M.; Guzei, I. A.; Angelici, R. J., Syntheses and structures of Group 1 mellitate compounds, K-6[C-6(COO)(6)]center dot 8H(2)O and Cs-5[C-6(COO)(6)H]center dot 7H(2)O, *Inorganica Chimica Acta* **1999**, *286*, 207-214.

(34)   Rodrigues, M. O.; Paz, F. A.; Freire, R. O.; de Sa, G. F.; Galembeck, A.; Montenegro, M. C.; Araujo, A. N.; Alves, S., Modeling, structural, and spectroscopic studies of lanthanide-organic frameworks, *Journal of Physical Chemistry B* **2009**, *113*, 12181-12188.

(35)   de Mesquita, M. E.; Junior, S. A.; Oliveira, F. C.; Freire, R. O.; Junior, N. B. C.; de Sa, G. F., Synthesis, spectroscopic studies and structure prediction of the new Tb(3-NH2PIC)(3)center dot 3H(2)O complex, *Inorganic Chemistry Communications* **2002**, *5*, 292-295.

(36)   Biju, S.; Reddy, M. L. P.; Freire, R. O., 3-phenyl-4-aroyl-5-isoxazolonate complexes of Tb3+ as promising light-conversion molecular devices, *Inorganic Chemistry Communications* **2007**, *10*, 393-396.

(37)   Lima, P. P.; Ferreira, R. A. S.; Freire, R. O.; Paz, F. A. A.; Fu, L. S.; Alves, S.; Carlos, L. D.; Malta, O. L., Spectroscopic study of a UV-photostable organic-inorganic hybrids incorporating an Eu3+ beta-diketonate complex, *Chemphyschem* **2006**, *7*, 735-746.

(38)   dos Santos, E. R.; dos Santos, M. A. C.; Freire, R. O.; Junior, S. A.; Barreto, L. S.; de Mesquita, M. E., On the use of theoretical tools in the study of photophysical properties of the new Eu(fod)(3) complex with diphenbipy, *Chemical Physics Letters* **2006**, *418*, 337-341.

(39)   Freire, R. O.; Albuquerque, R. Q.; Junior, S. A.; Rocha, G. B.; de Mesquita, M. E., On the use of combinatory chemistry to the design of new luminescent EU3+ complexes, *Chemical Physics Letters* **2005**, *405*, 123-126.

(40)   de Mesquita, M. E.; Silva, F. R. G. E.; Albuquerque, R. Q.; Freire, R. O.; da Conceicao, E. C.; da Silva, J. E. C.; Junior, N. B. C.; de Sa, G. F., Eu(III) and Gd(III) complexes with pirazyne-2-carboxylic acid: luminescence and modelling of the structure and energy transfer process, *Journal of Alloys and Compounds* **2004**, *366*, 124-131.

(41)   Souza, A. P.; Paz, F. A. A.; Freire, R. O.; Carlos, L. D.; Malta, O. L.; Alves, S.; de Sa, G. F., Synthesis, crystal structure, and modelling of a new tetramer complex of europium, *Journal of Physical Chemistry B* **2007**, *111*, 9228-9238.

(42)   Beltrao, M. A.; Santos, M. L.; Mesquita, M. E.; Barreto, L. S.; da Costa, N. B.; Freire, R. O.; dos Santos, M. A. C., Spectroscopic properties of the Eu(fod)(3)Phen-NO incorporated carboxylate glass, *Journal of Luminescence* **2006**, *116*, 132-138.

(43)   Rodrigues, M. O.; da Costa, N. B.; de Simone, C. A.; Araujo, A. A. S.; Brito-Silva, A. M.; Paz, F. A. A.; de Mesquita, M. E.; Junior, S. A.; Freire, R. O., Theoretical and experimental studies of the photoluminescent properties of the coordination polymer [Eu(DPA)(HDPA)(H2O)(2)]center dot 4H(2)O, *Journal of Physical Chemistry B* **2008**, *112*, 4204-4212.

(44)   Taylor, K. M. L.; Jin, A.; Lin, W. B., Surfactant-assisted synthesis of nanoscale gadolinium metal-organic frameworks for potential multimodal imaging, *Angewandte Chemie-International Edition* **2008**, *47*, 7722-7725.

(45)   Bril, A.; Jagerveenis, A. W. D., Some Methods of Luminescence Efficiency Measurements, *Journal of Research of the National Bureau of Standards Section a-Physics and Chemistry* **1976**, *80*, 401-407.

(46)   Malta, O. L.; Brito, H. F.; Menezes, J. F. S.; Silva, F. R. G. E.; Donega, C. D.; Alves, S., Experimental and theoretical emission quantum yield in the compound Eu(thenoyltrifluoroacetonate)(3).2(dibenzyl sulfoxide), *Chemical Physics Letters* **1998**, *282*, 233-238.

(47)   Kottke, T.; Stalke, D., Crystal Handling at Low-Temperatures, *Journal of Applied Crystallography* **1993**, *26*, 615-619.

(48)   Sheldrick, G. M., *SHELXS-97, Program for Crystal Structure Solution, University of Göttingen* **1997**.

(49)   Sheldrick, G. M., *SHELXL-97, Program for Crystal Structure Refinement, University of Göttingen* **1997**.

(50)   Gonçalves, Rogéria. Rocha. , Síntese e caracterização espectroscópica de complexos esquaratos de lantanideos (III). Dissertação de Mestrado, UNESP, 1996.

(51)   Carnall, W. T.; Crosswhite, H.; Crosswhite, H. M. *Energy Structure and Transition Probabilities of the Trivalent Lanthanides in LaF₃*; Argonne National Laboratory Report, 1977.

(52)   Stewart, J. J. P.; Version 7.058 ed.; Chemistry, S. C., Ed.; Colorado Springs, USA: 2008.

(53)   Malta, O. L.; Brito, H. F.; Menezes, J. F. S.; Silva, F. R. G. E.; Alves, S.; Farias, F. S.; de Andrade, A. V. M., Spectroscopic properties of a new light-converting device Eu(thenoyltrifluoroacetonate)(3) 2(dibenzyl sulfoxide). A theoretical analysis based on structural data obtained from a sparkle model, *Journal of Luminescence* **1997**, *75*, 255-268.

(54)   Malta, O. L.; Legendziewicz, J.; Huskowska, E.; Turowska-Tyrk, I.; Albuquerque, R. Q.; Donega, C. D.; Silva, F. R. G. E., Experimental and theoretical

study of ligand field, 4f-4f intensities and emission quantum yield in the compound Eu(bpyO(2))(4)(ClO4)(3), *Journal of Alloys and Compounds* **2001**, *323*, 654-660.

(55)   Malta, O. L.; dos Santos, M. A. C.; Thompson, L. C.; Ito, N. K., Intensity parameters of 4f-4f transitions in the Eu(dipivaloylmethanate)(3) 1,10-phenanthroline complex, *Journal of Luminescence* **1996**, *69*, 77-84.

(56)   Chui, S. S. Y.; Siu, A.; Feng, X.; Zhang, Z. Y.; Mak, T. C. W.; Williams, I. D., Hydrothermal synthesis of three new 3-D framework rare-earth mellitates, *Inorganic Chemistry Communications* **2001**, *4*, 467-470.

(57)   Cao, R.; Sun, D. F.; Liang, Y. C.; Hong, M. C.; Tatsumi, K.; Shi, Q., Syntheses and characterizations of three-dimensional channel-like polymeric lanthanide complexes constructed by 1,2,4,5-benzenetetracarboxylic acid, *Inorganic Chemistry* **2002**, *41*, 2087-2094.

(58)   Júnior, Severino Alves, Estudos espectroscópicos de complexos mistos de β-dicetona com íons lantanídeos (III), UFPE, 1998.

(59)   Shi, Mei; Li, Fuyou; Yi, Tao; Zhang, Dengqing; Hu, Huaiming; Huang, Chunhui, Tuning the Triplet Energy Levels of Pyrazolone Ligands to Match the 5D0 Level of Europium(III), *Inorganic Chemistry* **2005**, *44*, 8929-8936.

(60)   Alves, S.; deAlmeida, F. V.; deSa, G. F.; Donega, C. D., Luminescence and quantum yields of Eu3+ mixed complexes with 1-phenyl-1,3-butanedione and 1,10-phenanthroline or 1,10-phenanthroline-N-oxide, *Journal of Luminescence* **1997**, *72-4*, 478-480.

(61)   Rodrigues, M. O.; Brito-Silva, A. M.; Alves, S.; De Simone, C. A.; Araujo, A. A. S.; de Carvalho, P. H. V.; Santos, S. C. G.; Aragao, K. A. S.; Freire, R. O.; Mesquita, M. E., Structural and Spectroscopic Studies of the 2d Coordination Polymers (Infinity)[Tb(Dpa)(Hdpa)] and (Infinity)[Gd(Dpa)(Hdpa)], *Quimica Nova* **2009**, *32*, 286-291.

(62)   Tedeschi, C.; Azema, J.; Gornitzka, H.; Tisnes, P.; Picard, C., A solid-state study of eight-coordinate lanthanide(III) complexes (Ln = Eu, Gd, Tb, Dy) with 1-hydroxy-2-pyridinone, *Dalton Transactions* **2003**, 1738-1745.

(63)   Latva, M.; Takalo, H.; Mukkala, V. M.; Matachescu, C.; RodriguezUbis, J. C.; Kankare, J., Correlation between the lowest triplet state energy level of the ligand and lanthanide(III) luminescence quantum yield, *Journal of Luminescence* **1997**, *75*, 149-169.

(64)   Kang, J. G.; Kim, T. J., Luminescence and crystal-field analysis of europium and terbium complexes with oxydiacetate and 1,10-phenanthroline, *Bulletin of the Korean Chemical Society* **2005**, *26*, 1057-1064.

(65)   Binnemans, K.; VanHerck, K.; GorllerWalrand, C., Influence of dipicolinate ligands on the spectroscopic properties of europium(III) in solution, *Chemical Physics Letters* **1997**, *266*, 297-302.

(66)   de Mesquita, M. E.; Junior, S. A.; Junior, N. B. C.; Freire, R. O.; Silva, F. R. G. E.; de Sa, G. F., Synthesis, sparkle model, intensity parameters and spectroscopic studies of the new Eu(fod)(3)phen-NO complex, *Journal of Solid State Chemistry* **2003**, *171*, 183-188.

(67)   Ewa Huskowska; Ilona Turowska-Tyrk; Janina Legendziewicz; Riehl, James P., The structure and spectroscopy of lanthanide(III) complexes with 2,2-bipyridine-1,1-dioxide in solution and in the solid state: effects of ionic size and solvent on photophysics, ligand structure and coordination, *New Journal of Chemitry* **2002**, *26*, 7.

(68)   K. Driesen; S. Fourier; C. Görller-Walrand; Binnemans, K., Judd–Ofelt analysis of lanthanide doped silica–PEG hybrid sol–gels, *Physical Chemistry Chemical Physics* **2003**, *5*, 5.

(69)   Huskowska, E.; Turowska-Tyrk, I.; Legendziewicz, J.; Riehl, J. P., The structure and spectroscopy of lanthanide(III) complexes with 2,2 '-bipyridine-1,1 '-dioxide in solution and in the solid state: effects of ionic size and solvent on photophysics, ligand structure and coordination, *New Journal of Chemistry* **2002**, *26*, 1461-1467.

(70)   Malta, O. L.; Silva, F. R. G. E., A theoretical approach to intramolecular energy transfer and emission quantum yields in coordination compounds of rare earth ions, *Spectrochimica Acta Part a-Molecular and Biomolecular Spectroscopy* **1998**, *54*, 1593-1599.

Anexo 1
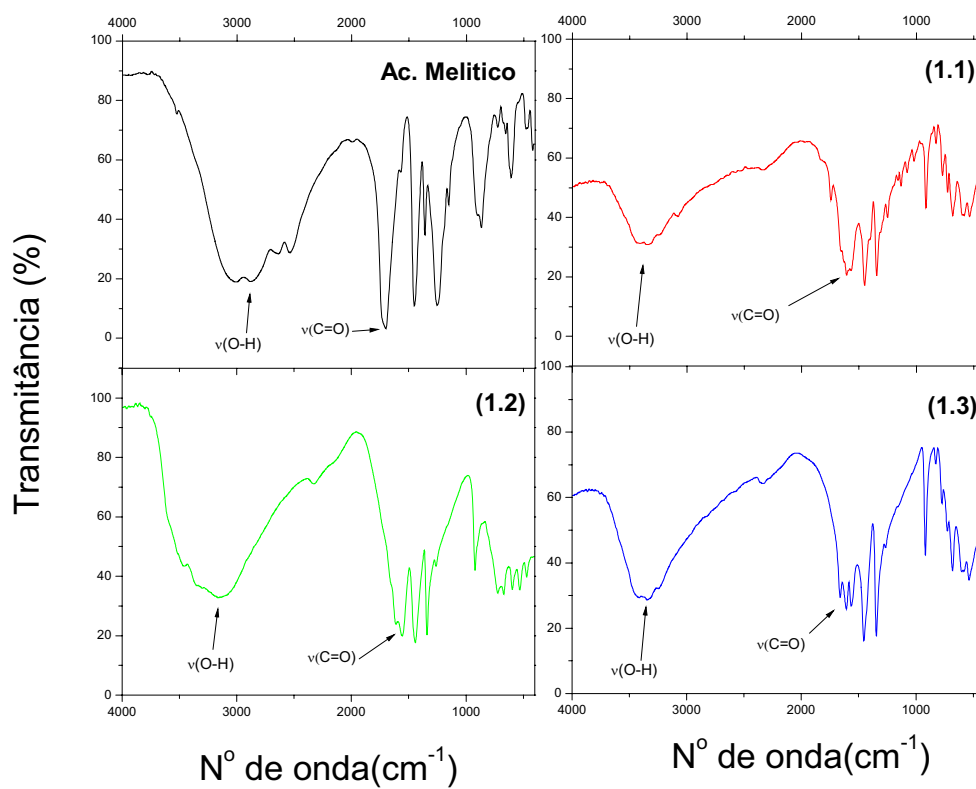
Figura 1.1A: Espectros de Infravermelho do ácido melítico, **(1.1)** e **(1.2)** e **(1.3).**
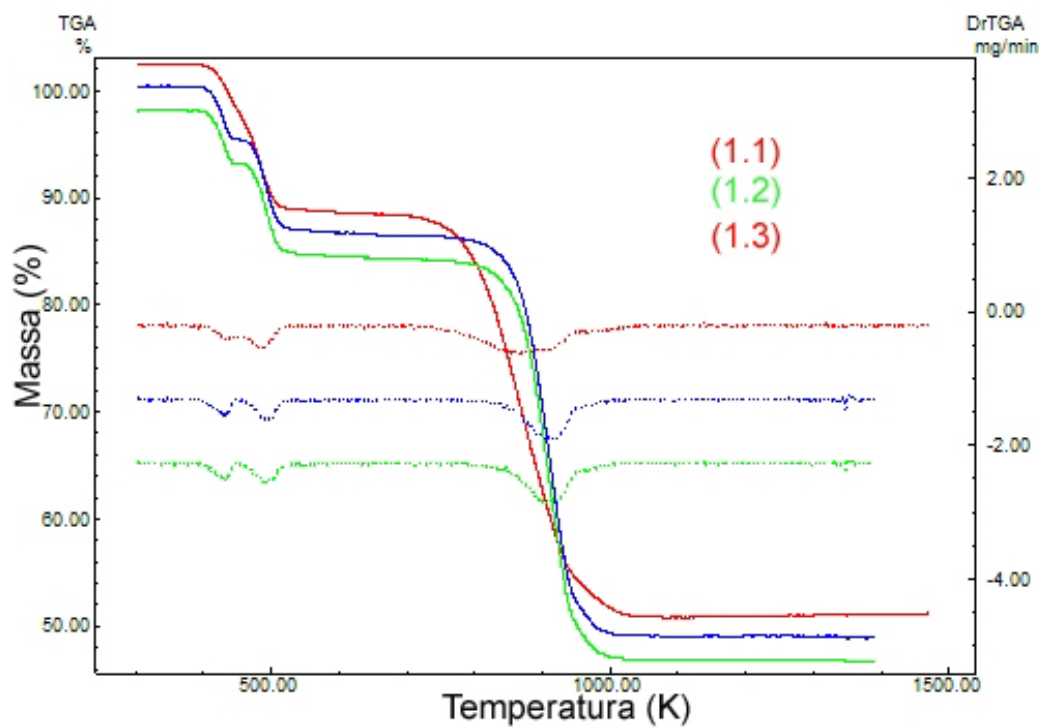
Figura 1.2A: Curvas Termogravimétricas (TGA) e Termogravimetria Derivada (DTG) para **(1.1)**, **(1.2)** e **(1.3)**.
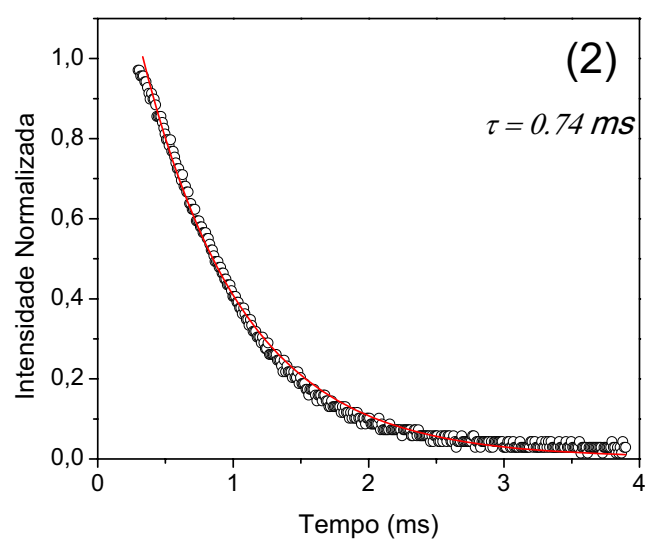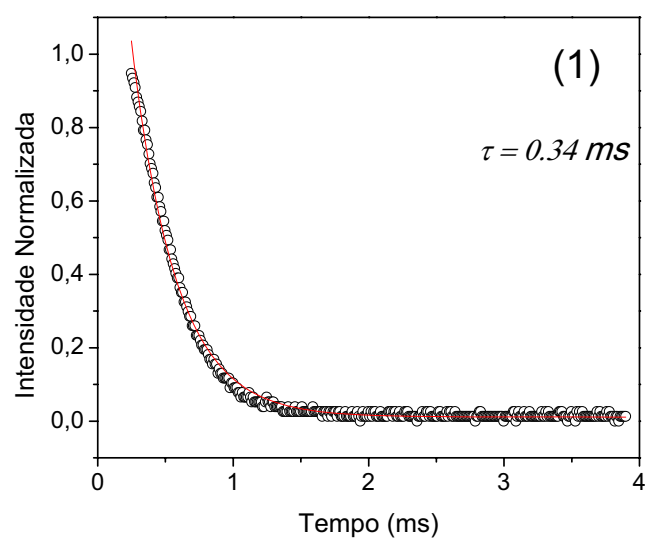
Figura 1.3A: Curvas normalizadas de decaimento dos estados $^5D_0$ e $^5D_4$ para

(1.1) e (1.2) obtidos à temperatura ambiente.

Capítulo 2

Processo de Transferência de Energia Sinérgico em Polímeros de Coordenação Heterobimetálicos contendo Lantanídeos
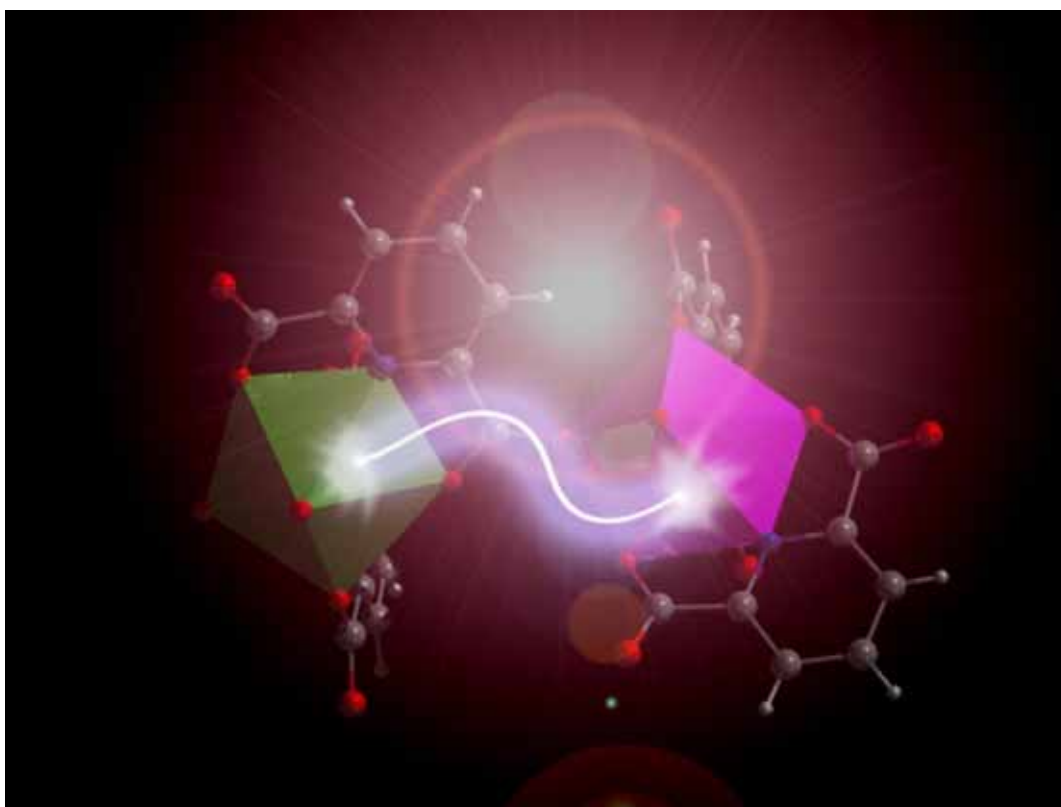
"Os verdadeiros detentores do conhecimento são os seres mais humildes que

conheço..."

(Mané de Nínguem de Zé Boneco)

2.1 Introdução

As pesquisas baseadas em compostos de lantanídeos vêm crescendo consideravelmente nas últimas décadas, desde que Lenh propôs o uso destes compostos como Dispositivos Moleculares Conversores de Luz — DMCL.[1] Historicamente, muitos grupos de pesquisa consideram este momento como uma marco na química dos lantanídeos,[2] porque a proposta de Lenh veio seguida de uma série de novas propostas tecnológicas para utilização da luminescência típica de alguns íons lantanídeos, dentre as quais podem ser destacadas: sondas ópticas em ensaios imunológicos,[3,4] materiais eletroluminescentes,[5-7] sensores,[8-12] entre outros.

A obtenção de eficientes DMCLs não é uma simples tarefa, pois para o planejamento de compostos de lantanídeos altamente luminescentes é necessário o entendimento de cada etapa envolvida no processo de transferência de energia (TE).[13] Nestas perspectivas, alguns grupos têm se dedicado ao planejamento e síntese de polímeros de coordenação fotoluminescentes, visando aproveitar as características destes materiais para aplicações tecnológicas.[14-16] Uma das formas mais difundidas para o melhoramento das propriedades luminescentes de compostos com lantanídeos consiste na síntese e/ou na modificação de compostos orgânicos. Este tipo de metodologia tem como objetivo ajustar os níveis tripleto dos ligantes com os estados emissores dos íons Ln^{3+} para aperfeiçoar o efeito antena,[5,7,17,18] no entanto, em muitos casos essas estratégias são muito dispendiosas e não

79

garantem que os estados tripletos dos ligantes estejam em condições ideais para uma boa transferência de energia.[19,20]

O desenvolvimento de materiais contendo, simultaneamente, mais que um tipo de íon lantanídeo possibilita a modulação da intensidade de emissão, obtenção de luminescência em diversas regiões do espectro eletromagnético, além de permitir a investigação dos processos de TE entre os diferentes centros ópticos.[21,22] Embora existam alguns relatos na literatura destacando materiais baseados em misturas de Eu^{3+}/Tb^{3+}, os processos de transferência de energia entre Tb^{3+} e Eu^{3+} nesses materiais não têm sido investigados em detalhes.[23-26] Quando o Eu^{3+} é usado como receptor de energia do Tb^{3+} é comum observar que a emissão do Eu^{3+} é consideravelmente intensificada.[27,28] Recentes trabalhos têm demonstrado as conseqüências dos efeitos dos processos e TE entre Tb^{3+} e Eu^{3+} em materiais destinados para aplicação em sensores químicos, físicos e biológicos baseados em chaveamento óptico entre esses íons.[29-33]

Neste capítulo será reportado uma abordagem nos processos de TE em dois polímeros de coordenação iso-estruturais, $_\infty[(Tb_{1-x}Eu_x)(DPA)(HDPA)]$ onde HDPA = ácido dipicolínico e x = 0,05 e 0,5. Serão abordados os efeitos da concentração e da temperatura sobre as emissões, tempos de vida e taxas de transferência de energia e rendimento quântico.

2.2 Materiais e Métodos

2.2.1 Reagentes

Os nitratos dos lantanídeos foram preparados de acordo com a metodologia descrita no Capítulo 1. Ácido dipicolínico (Figura 2.1) foi obtido da Aldrich e usado sem purificação prévia.
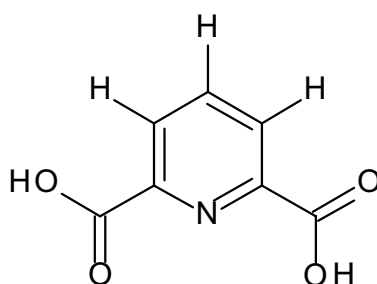
Figura 2.1: Ilustração da estrutura do ácido dipicolínico.

2.2.2 Sínteses

Os compostos foram preparados a partir das misturas contendo 0,35 mmol de $Ln(NO_3)_3 \cdot 6H_2O$ (Ln= Tb^{3+} e Eu^{3+} nas respectivas proporções 0,3325/0,0175 e 0,175/0,175 mmol), 0,75 mmol de H_2DPA em 4,0 mL de água deionizada foram adicionadas em um reatores de inóx revestido com teflon (8,0 mL). A reação foi mantida a 433 K por 72 horas em uma estufa com circulação forçada de ar. O material contendo somente íon Tb^{3+} no retículo foi preparado seguindo o mesmo procedimento. As reações apresentaram rendimentos de

aproximadamente 60% após os produtos serem lavados com acetona e secos ao ar. Todos os materiais são pouco solúveis em água e insolúveis em solventes orgânicos. As curvas termogravimétricas e termogravimétricas diferenciais, análise elementar, espectros de infravermelho, EDS e padrões de raios-x de pós estão disponíveis no Anexo 2.

2.2.3 Instrumentação

2.2.3.1   Análise Elementar

As análises elementares de C, H, e N das redes de coordenação foram realizadas em um equipamento CHNS-O Analyzer Flash (112 Series EA Thermo Finningan).

2.2.3.2   Espectroscopia de Absorção na Região do Infravermelho

Os espectros de infravermelho foram obtidos em pastilhas de KBr com resolução de 4 cm^{-1} em um espectrofotômetro Brucker, modelo IF66.

2.2.3.3   Termogravimetria e Termogravimetria Derivada

As curvas TG/DTG foram obtidas na faixa de temperatura entre 25 e 1200°C utilizando uma termobalança modelo TGA 50 da marca Shimadzu, sob atmosfera dinâmica de nitrogênio (50 mL.min^{-1}), razão de aquecimento de

10°C.min^{-1}, utilizando cadinho de platina contendo massa de amostra em torno de 3 mg. A calibração do instrumento foi verificada antes dos ensaios, empregando-se um padrão de oxalato de cálcio monohidratado, conforme norma ASTM (The Americam Society for Testing and Materials, 1993).

2.2.3.4   Espectroscopia de Luminescência

Os espectros de emissão foram obtidos à temperatura ambiente usando como fonte de excitação um Laser HeCd, λ_{exc} = 320 nm, o sinal foi filtrado em um monocromador duplo com 600 linhas e coletado em uma fotomultiplicadora. Os espectros de emissão resolvidos no tempo foram adquiridos à temperatura ambiente usando um espectrofluorímetro SPEX-Fluorlog 2 acoplado a um fosforímetro SPEX 1934-D.

2.2.3.5   Tempos de Decaimento dos Estados Excitados

Os decaimentos dos estados excitados $^5D_0$ e $^5D_4$ dos íons Eu^{3+} e Tb^{3+}, respectivamente, foram adquiridos em temperatura variada (6 a 300K) utilizando um laser de Nd:YAG (λ_{exc} = 355 nm) modelo com largura temporal de 5 ns e taxa de repetição em 20 Hz, filtrado em monocromador duplo, coletado em uma fotomultiplicadora e analisado por um osciloscópio Hewlett Packard 54501A 100 MHZ .

2.2.3.6 Rendimentos Quânticos de Emissão

Os rendimentos quânticos (q_x) foram obtidos através de medidas absolutas usando uma esfera de integração modelo C9920-02 da Hamamatsu com uma lâmpada de Xenônio de 150 W acoplada ao monocromador. As medidas foram realizadas em triplicata. O método apresenta erro de 10%.

2.2.3.7 Difração de Raios-X por Pó e Monocristal

A difração de raios-X de pó, as medidas foram realizadas à temperatura ambiente em um difratômetro Rigaku RINT2000 com ânodo rotatório de cobre ($\lambda_{k\alpha1}$ = 1,5404 Å, $\lambda_{k\alpha2}$ = 1,5444 Å, $I_{\alpha2}/I_{\alpha1}$ = 0,5). As intensidade foram coletadas através do método passo a passo (step by step) num intervalo de 2θ entre 5 e 50°, com $\Delta_{2\theta}$ de 0,02°, fenda Soller de 2,5° de divergência, fenda de espalhamento de 0,5° e fenda de recepção de 0,3 mm.

O monocristal de $_\infty$[(Tb$_{1-x}$Eu$_x$)(DPA)(HDPA)] foi manualmente montado sobre um Hampton Research CryoLoops usando o óleo FOMBLIN Y perfluoropolyether (Aldrich) sob o auxílio de estereomicroscópio Stemi 2000 equipado com lentes Carl Zeiss. A cela unitária foi indexada a partir dos dados coletados num Bruker X8 Kappa com detector de área (CCD) APEX II (Mo K$_\alpha$ monocromada com λ = 0,71073 Å) controlado pelo pacote de software APEX-2 e equipado com criostato Oxford Cryosystems Series 70.

2.2.3.8   Microscopia Eletrônica de Varredura e Mapa de EDS

As imagens de microscopia eletrônica das amostras foram coletadas em suportes de alumínio revestido com fita de carbono, usando um microscópio eletrônico de varredura SU-70 trabalhando a 15 kV.

2.5   Resultados e Discussão

Como os raios de Eu^{3+} e do Tb^{3+} são muito próximos, é de se esperar que não tenha segregação dos íons nas amostras e que haja apenas pequenas variações nos parâmetros de cela dos materiais. As análises por difração de raios-x de monocristal para o composto $_\infty[(Tb_{0,5}Eu_{0,5})(DPA)(HDPA)]$ mostraram que o material cristaliza em sistema monoclínico com grupo espacial *P2$_1$/c* e parâmetros de cela muito próximos (iso-estrutural) aos do composto de Európio e Térbio reportados anteriormente.[34,35] A estrutura supramolecular dos materiais consiste de lamelas em duas dimensões interconectadas via interações π–π.   Na Figura 2.2 está ilustrada a estrutura do $_\infty[(Tb_{1-x}Eu_x)(DPA)(HDPA)]$ destacando as distâncias mais curtas dos pares Ln^{3+}–Ln^{3+}. Para cada íon lantanídeo existem outros 14 íons vizinhos mais próximos na mesma lamela, cujas distâncias estão entre 6,3 e 11,0 Å.   Já nas lamelas adjacentes, existem quatro íons mais próximos com distância média de 10 Å.
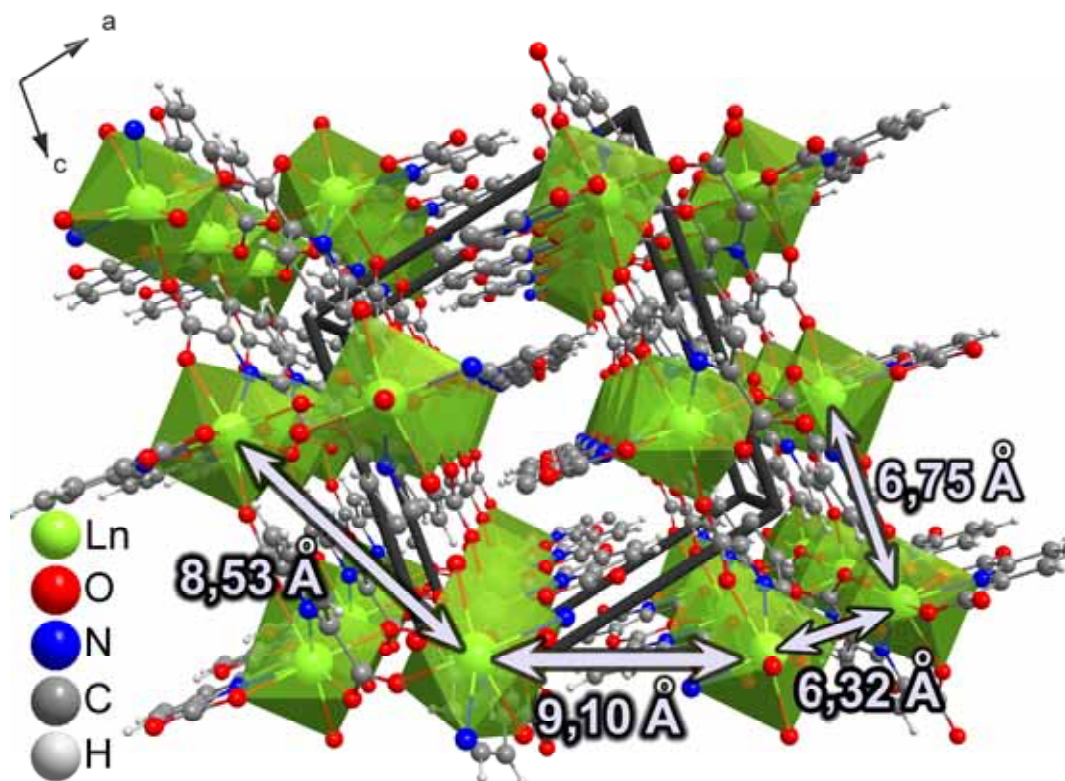
Figura 2.2: Ilustração da projeção central de estruturas do $_\infty$[Ln(DPA)(HDPA)] ao longo do eixo cristalográfico *b*, evidenciando as distâncias intermetálicas mais próximas.

O refinamento de Rietiveld[36] foi realizado usando o programa GSAS[37] usando como premissa o modelo de posições atômicas descrita por Fernandes *et al.*[34] O perfil das reflexões foram ajustados usando a função Thompson-Cox-Hastings[38] modificado por Young & Desai,[39] a orientação preferencial foi corrigida usando o modelo de harmônicos esféricos proposto por Jarvinen.[40] O padrão de difração de pós e o refinamento de Rietveld para o composto $_\infty$[(Tb$_{0,95}$Eu$_{0,05}$)(DPA)(HDPA)] é mostrado na Figura 2.3. Os parâmetros de rede e os detalhes do refinamento são mostrados na Tabela 2.1.
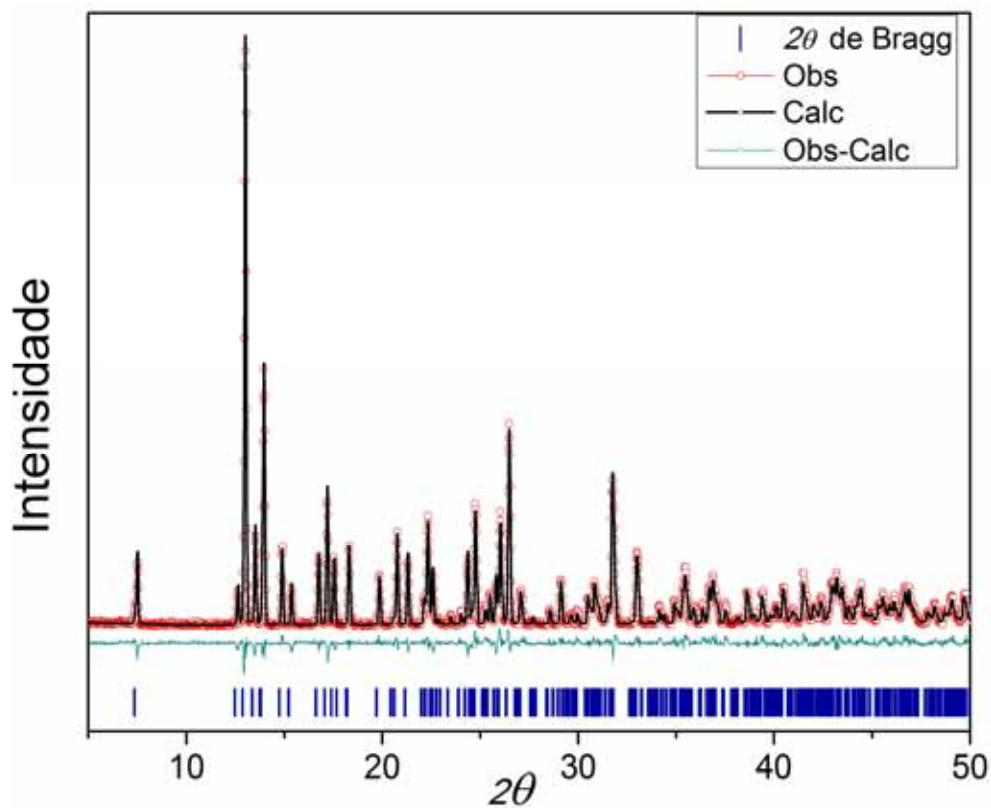
Figura 2.3: Padrões de difração de raios-x de resultado final do Refinamento de Rietveld para $_\infty$[(Tb$_{0,95}$Eu$_{0,05}$)(DPA)(HDPA)].

Tabela 2.1: Pârametros de rede e dados do refinamento de Rietveld.

Composto	$_\infty$[(Tb$_{0.95}$Eu$_{0.05}$)(DPA)(HDPA)]	$_\infty$[(Tb$_{0.5}$Eu$_{0.5}$)(DPA)(HDPA)]
Cela Unitária		
Fórmula	C$_{14}$H$_6$N$_2$O$_8$(Tb$_{0,95}$Eu$_{0,05}$)	C$_{14}$H$_6$N$_2$O$_8$(Tb$_{0,5}$Eu$_{0,5}$)
Peso molecular	489,60	486,44
Sistema Cristalino	Monoclínico	Monoclínico
Grupo Espacial	P21/c	P21/c
a/Å	12,3182(3)	12,3190(4)
b/Å	8,4030(2)	8,4034(3)
c/Å	13,5742(3)	13,5748(4)

$\alpha/^o$	90,00	90,00
$\beta/^o$	102,399(2)	102,400(3)
$\gamma/^o$	90,00	90,00
Volume/$\AA^3$	1372,305(5)	1372,52(9)
Z	4	4
D_c/g cm^{-3}	2,401	2,401
Função de Perfil	pV-TCHZ	pV-TCHZ
Parâmetros de Caglioti	U = 0,00(4) V = 54,45(2) W = 5,47(1)	U = 0,000(13) V = 64,56(3) W = 5,858(4)
No. de parâmetros refinados	49	46
Fatores de confiabilidade do refinamento		
Rp	9,35	10,72
Rwp	12,84	14,59
RF^2	5,04	9,38
$\chi 2$	2,003	2,584

As distribuições dos íons Eu^{3+} e Tb^{3+} nos polímeros de coordenação foram avaliadas através do EDS *mapping*. As Figuras 2.4 e 2.5 mostram as correspondentes imagens de MEV e EDS mapping para os elementos Eu^{3+} e Tb^{3+} nos materiais $_\infty[(Tb_{0,95}Eu_{0,05})(DPA)(HDPA)]$ e $_\infty[(Tb_{0,5}Eu_{0,5})(DPA)(HDPA)]$, respectivamente. Os resultados confirmam a presença de ambos os íons e indicam uma distribuição aleatória no retículo cristalino.
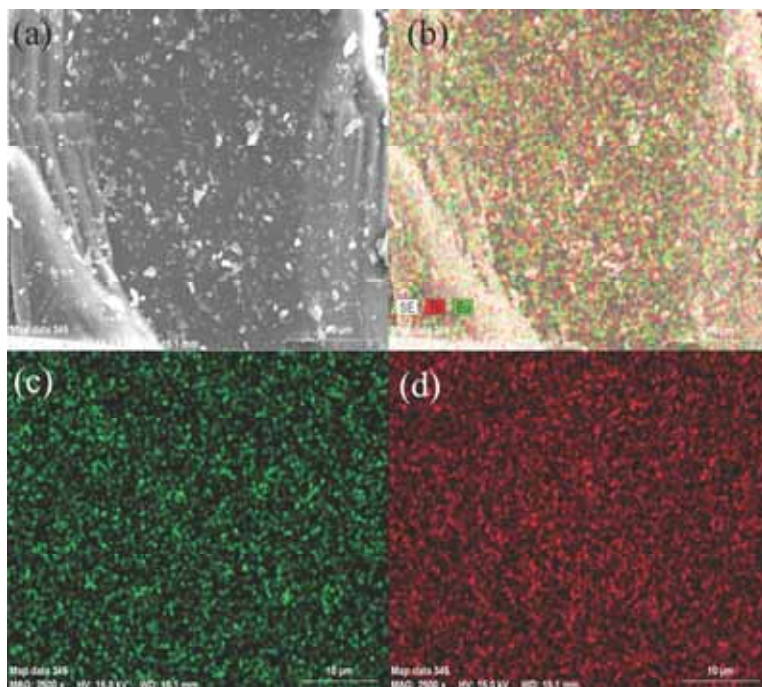
Figura 2.4: (a) Imagens de microscopia eletrônica e mapeamento por EDS obtidas para $\infty[(Tb_{0,95}Eu_{0,05})(DPA)(HDPA)]$, (b) Tb^{3+}/Eu^{3+}, (c) Eu^{3+} e (d) Tb^{3+}.
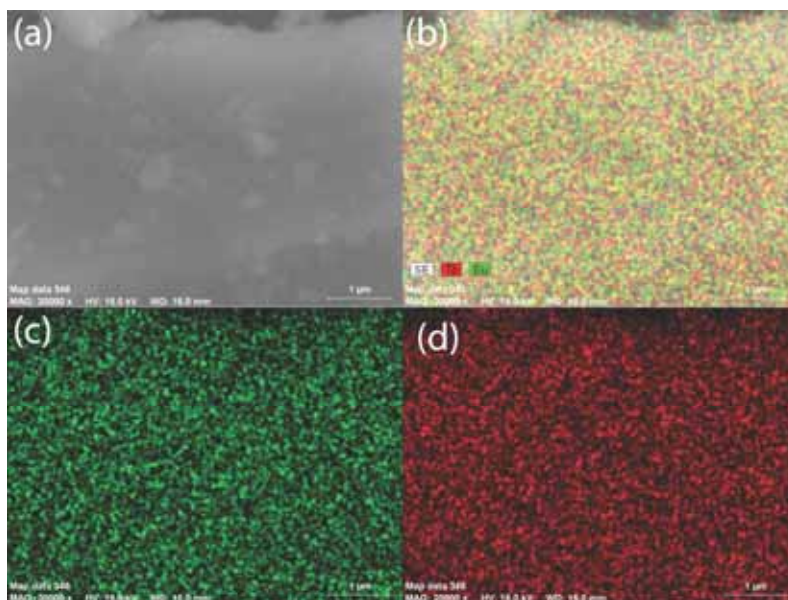
Figura 2.5: (a) Imagens de microscopia eletrônica e mapeamento por EDS obtidas para $\infty[(Tb_{0,5}Eu_{0,5})(DPA)(HDPA)]$, (b) Tb^{3+}/Eu^{3+}, (c) Eu^{3+} e (d) Tb^{3+}.

Na Figura 2.6 pode ser observado os espectros de emissão de $_\infty$[(Tb$_{0,95}$Eu$_{0,05}$)(DPA)(HDPA)] e $_\infty$[(Tb$_{0,5}$Eu$_{0,5}$)(DPA)(HDPA)] obtidos à temperatura ambiente após excitação em 320 nm.
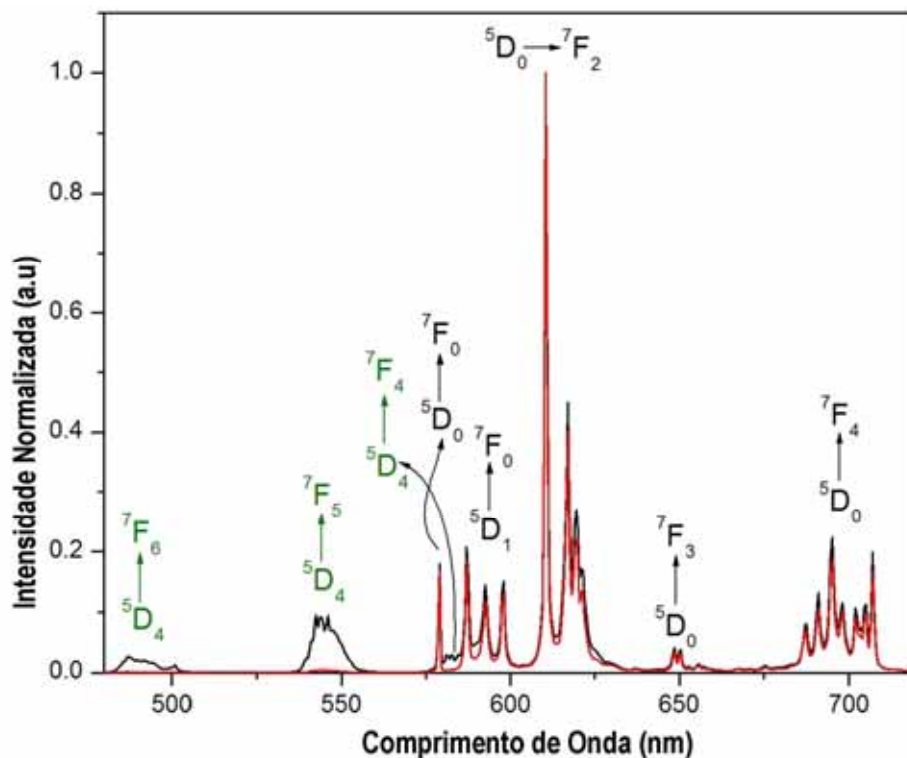
Figura 2.6: Espectros de emissão de $_\infty$[(Tb$_{0,95}$Eu$_{0,05}$)(DPA)(HDPA)] (preto) e $_\infty$[(Tb$_{0,5}$Eu$_{0,5}$)(DPA)(HDPA)] (vermelho).

Os espectros mostram que as transições $^5D_4 \rightarrow {}^7F_J$ do íon Tb^{3+} são significativamente suprimidas mesmo em baixa concentração, indicando um processo eficiente de TE Tb$^{3+}\rightarrow$Eu^{3+}. As bandas de emissão do Eu^{3+} são consideravelmente influenciadas pelo ambiente de coordenação, portanto as

intensidades relativas e os desdobramentos das linhas podem ser usados como sondas do sítio de simetria.[33] Os espectros de $_\infty$[(Tb$_{0,95}$Eu$_{0,05}$)(DPA)(HDPA)] e $_\infty$[(Tb$_{0,5}$Eu$_{0,5}$)(DPA)(HDPA)] mostram três componentes *Starks* bem definidas atribuídas à transição $^5D_0 \rightarrow {}^7F_1$ do Eu^{3+}, indicando que a primeira esfera de coordenação do metal possui grupo pontual de baixa simetria, além disso, as linhas centradas em 581 nm podem ser atribuídas às transições $^5D_0 \rightarrow {}^7F_0$. A regra de seleção para as transições controladas por dipolo elétrico indica que a $^5D_0 \rightarrow {}^7F_0$ somente é observada se a simetria do grupo pontual ao redor do Eu^{3+} for C$_{nv}$, C$_n$ ou C$_s$.[41] De acordo com os resultados de cristalografia as substituições do Tb^{3+} por Eu^{3+} não causam alterações estruturais, portanto os íon lantanídeos estão localizados em ambiente de coordenação com grupo pontual C_1.[34]

De acordo com a teoria de Förster-Dexter, a condição fundamental para ocorrer transferência de energia entre duas espécies é a sobreposição dos espectros de absorção do receptor com o de emissão do doador.[42] Esta condição é satisfeita entre 540 e 590 nm para ambos os materiais, onde as transições de emissão $^5D_4 \rightarrow {}^7F_5$ e $^5D_4 \rightarrow {}^7F_4$ do Tb^{3+} sobrepõem respectivamente as linhas de excitação $^7F_{0,1} \rightarrow {}^5D_1$ e $^7F_{0,1} \rightarrow {}^5D_0$ do Eu^{3+} (Figura 2.7).
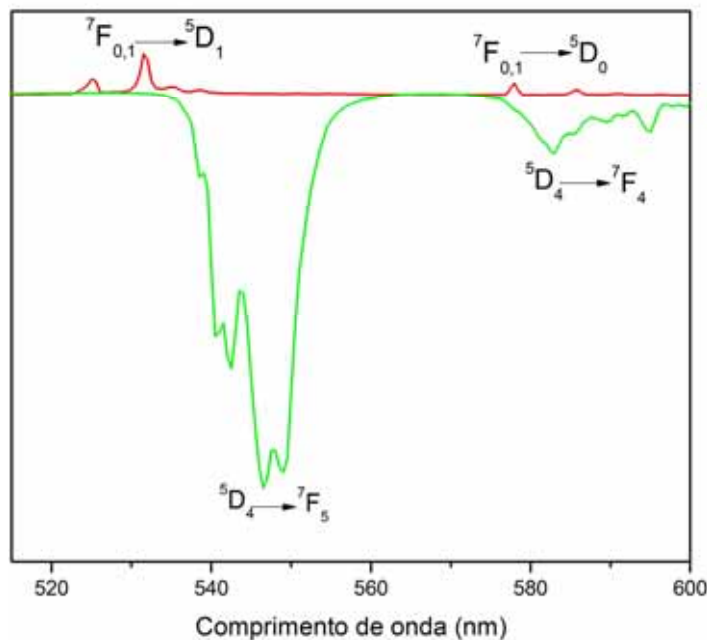
Figura 2.7: Sobreposição dos espectros de excitação (x10) do íon Eu^{3+} em $_\infty[(Tb_{0,95}Eu_{0,05})(DPA)(HDPA)]$, vermelho, com o espectro de emissão do $_\infty[(Tb)(DPA)(HDPA)]$, verde, retirado da ref. 38.

De acordo com Oczko[43] e Taboada[44], em temperaturas baixas (T<100K) o multipleto $^7F_1$ é pobremente populado, enquanto as populações do $^7F_2$ podem ser ignoradas. Partindo desta premissa podemos considerar que a TE $Tb^{3+} \rightarrow Eu^{3+}$ ocorre preferencialmente através dos canais $^7F_0 \rightarrow {}^5D_1$ e $^7F_0 \rightarrow {}^5D_0$ do Eu^{3+}. Obviamente, em temperaturas acima de 100K, os canais de TE são aumentados pelos multipletos $^7F_1$ e $^7F_2$ termicamente populados, o que pode contribuir para o aumento das taxas de transferência.

A Figura 2.8 apresenta os respectivos espectros de emissão resolvidos no tempo normalizados para $_\infty[(Tb_{0,95}Eu_{0,05})(DPA)(HDPA)]$ e

$_\infty$[(Tb$_{0,5}$Eu$_{0,5}$)(DPA)(HDPA)] obtidos à temperatura ambiente após excitação em 320 nm e seguindo a respectiva seqüência de atrasos: 0,01, 0,025, 0.05, 0,5, 1,0 e 2,0 ms.
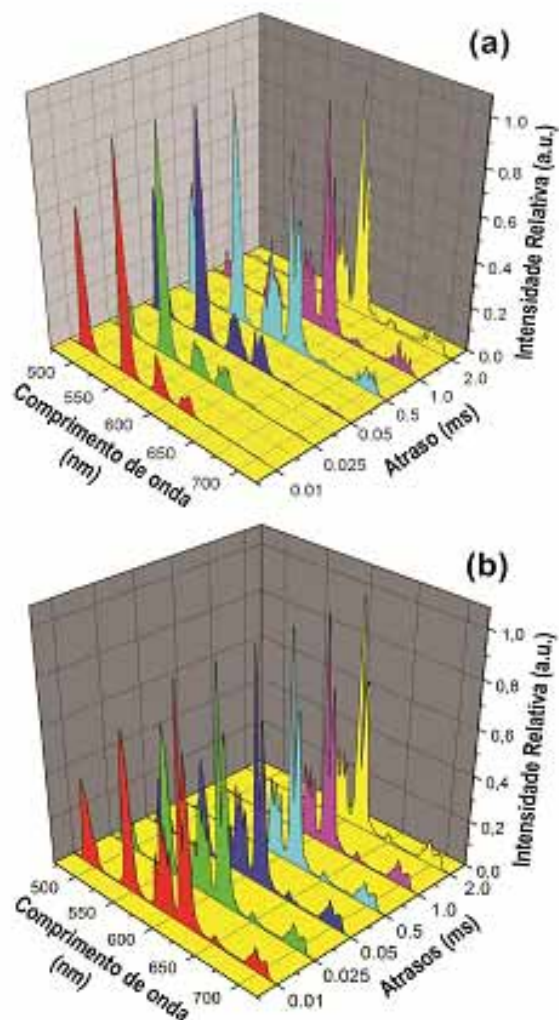
Figura 2.8: Espectros normalizados de emissão resolvidos no tempo. (a) $_\infty$[(Tb$_{0,95}$Eu$_{0,05}$)(DPA)(HDPA)]. (b) $_\infty$[(Tb$_{0,5}$Eu$_{0,5}$)(DPA)(HDPA)].

Em ambos os casos, pode ser observado que a emissão do íon Tb^{3+} é mais proeminente em domínios temporais curtos, porém com a evolução temporal dos experimentos as transições $^5D_4 \rightarrow {}^7F_J$ são extremamente suprimidas. Esse comportamento espectral é atribuído a uma eficiente migração de energia do Tb^{3+} para o Eu^{3+}. Os espectros de emissão resolvido no tempo de $_\infty[(Tb_{0,5}Eu_{0,5})(DPA)(HDPA)]$ (Figura 2.8 (b)) são simultaneamente compostos das componentes de emissão do Eu^{3+} e Tb^{3+} mesmo em curtos tempos de atrasos, isto claramente evidencia que além da transferência de energia oriunda do íon Tb^{3+}, existem contribuições importantes das energias originárias do tripleto do ligante para excitar os íons Eu^{3+}. Já no caso do $_\infty[(Tb_{0,95}Eu_{0,05})(DPA)(HDPA)]$, as linhas de emissão do Eu^{3+} não são observados em atrasos de 0,01 ms, no entanto, com a gradual evolução temporal dos atrasos a emissão do Eu^{3+} surge, indicando que a excitação do nível $^5D_0$ do cátion Eu^{3+} deve ocorrer preferencialmente via migração de energia proveniente do estado $^5D_4$ do Tb^{3+}. Prévios trabalhos demonstraram que o ligante H_2DPA não possui condição adequada de ressonância entre os níveis tripleto e o $^5D_0$ do Eu^{3+},[45-48] porém a energia transferida do nível tripleto do ligante não pode ser negligenciada, pois de acordo com Klink e colaboradores, as taxas de transferência de energia Ligante→Metal em complexos de lantanídeos são da ordem de 10^7 s^{-1}.[49] É fundamental deixar claro desde já, que em virtude dos resultados abordados acima deliberadamente foi decidido investigar com maior rigor o material com menor

concentração de Eu^{3+} na rede, pois o efeito da transferência de energia oriunda do ligante parece não ser um fator complicador.

Nas Figuras 2.9 e 2.10 são mostradas as respectivas curvas normalizadas de decaimento e tempos de vida (τ_d) em função da temperatura para $_\infty[(Tb_{0,95}Eu_{0,05})(DPA)(HDPA)]$ e $_\infty[(Tb_{0,5}Eu_{0,5})(DPA)(HDPA)]$ obtidos após excitação em 355 nm e monitorando as emissões dos níveis $^5D_4$ (545 nm) e $^5D_0$ (612 nm) do Tb^{3+} e Eu^{3+}, respectivamente. Os perfis das curvas de excitação do íon Eu^{3+} em $_\infty[(Tb_{0,95}Eu_{0,05})(DPA)(HDPA)]$ e $_\infty[(Tb_{0,5}Eu_{0,5})(DPA)(HDPA)]$ e os respectivos tempos de excitação em função da temperatura em $_\infty[(Tb_{0.95}Eu_{0.05})(DPA)(HDPA)]$ (Figura 2.11) indicam que processos relativamente lentos são responsáveis pela excitação do nível emissor $^5D_0$. Os tempos de excitação foram estimados de acordo com a Equação 2.1 proposta por Ranson:[50]

$$ n = n_0 + n_1 \left[1 - \exp\left(-(t - t_0) \Big/ \tau_r \right) \right] \qquad (2.1) $$

onde, n, n_0, n_1, t_0 e τ_1 são: populações totais do nível emissor $^5D_0$, populações do nível emissor $^5D_0$ oriundas da excitação direta do íon pelo nível tripleto, populações que alimentam o nível emissor $^5D_0$ originárias do nível excitado

com energia maior ($^5D_1$), tempo de atraso do osciloscópio e tempo de excitação, respectivamente. Como a intensidade de luminescência é proporcional ao número de fótons, consideram-se as amplitudes inicias no tempo t = 0 ms do osciloscópio como sendo os valores iniciais para $n_0 \approx 0,1$ e os valores de n_1 e t_0 são tratados como parâmetros livre durante o fit. Este tipo de critério foi adotado visando sondar as populações do estado $^5D_0$ em função da temperatura e, conseqüentemente, obter informações mais precisas a respeito do mecanismo de transferência de energia. As curvas de decaimento em função da temperatura dos íons Tb^{3+} e Eu^{3+} em $_\infty[(Tb_{0,95}Eu_{0,05})(DPA)(HDPA)]$ e $_\infty[(Tb_{0,5}Eu_{0,5})(DPA)(HDPA)]$ obedecem ao perfil de decaimento mono-exponencial.
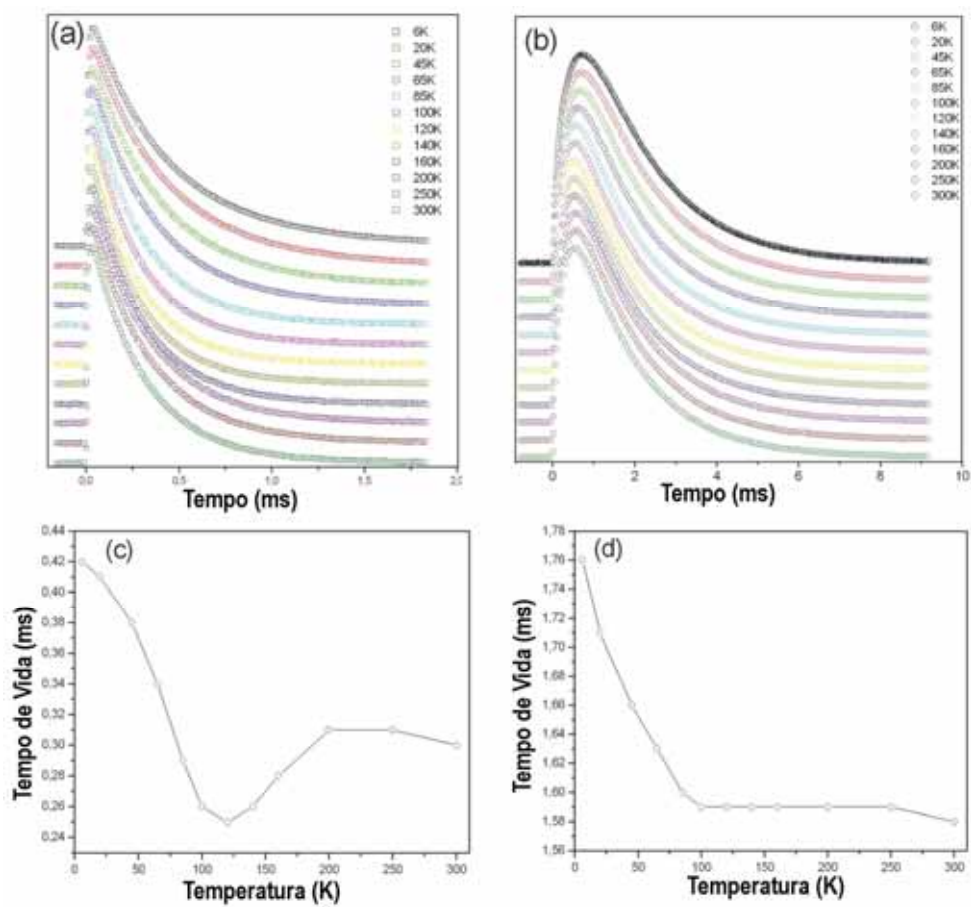
Figura 2.9: Curvas normalizadas de decaimento dos estados: (a) $^5D_4$ do Tb^{3+};

(b) $^5D_0$ do Eu^{3+}. Tempos de vida em função da temperatura: (c) Tb^{3+}; (d) Eu^{3+}.

Resultados referentes ao material $_\infty$[(Tb$_{0,95}$Eu$_{0,05}$)(DPA)(HDPA)].
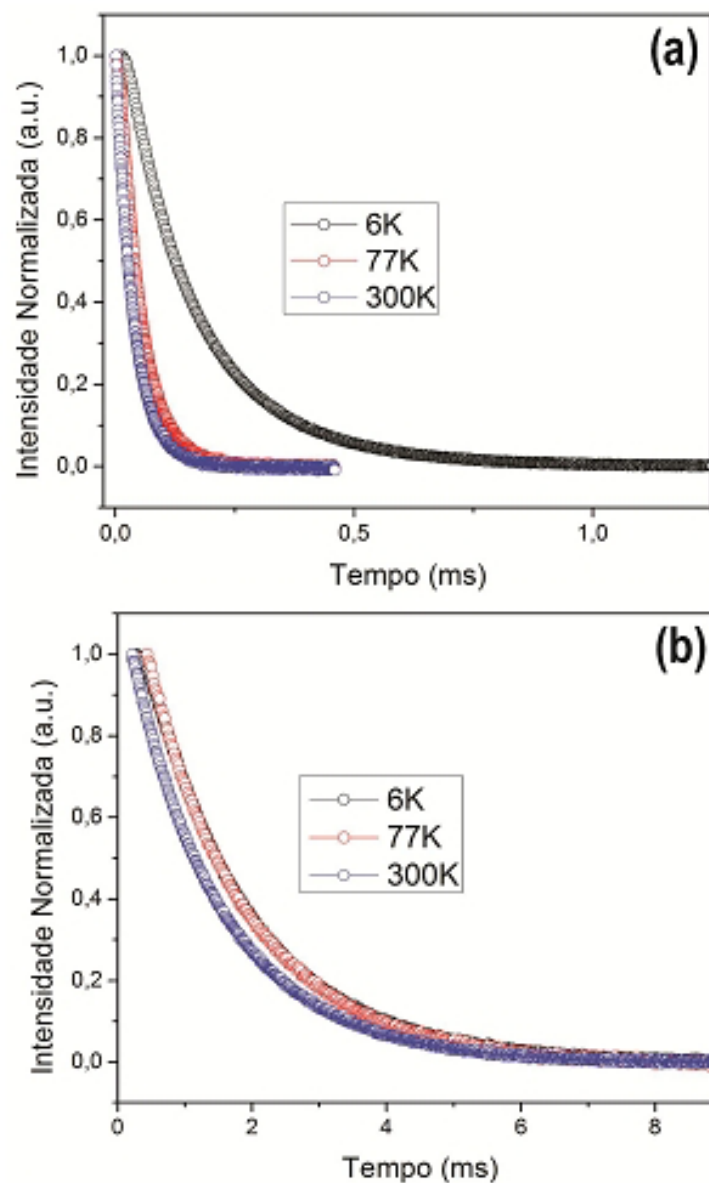
Figura 2.10: Curvas normalizadas de decaimento em função da temperatura do

$_\infty$[(Tb$_{0,5}$Eu$_{0,05}$)(DPA)(HDPA)]: (a) $^5D_4$ do Tb^{3+}; (b) $^5D_0$ do Eu^{3+}.
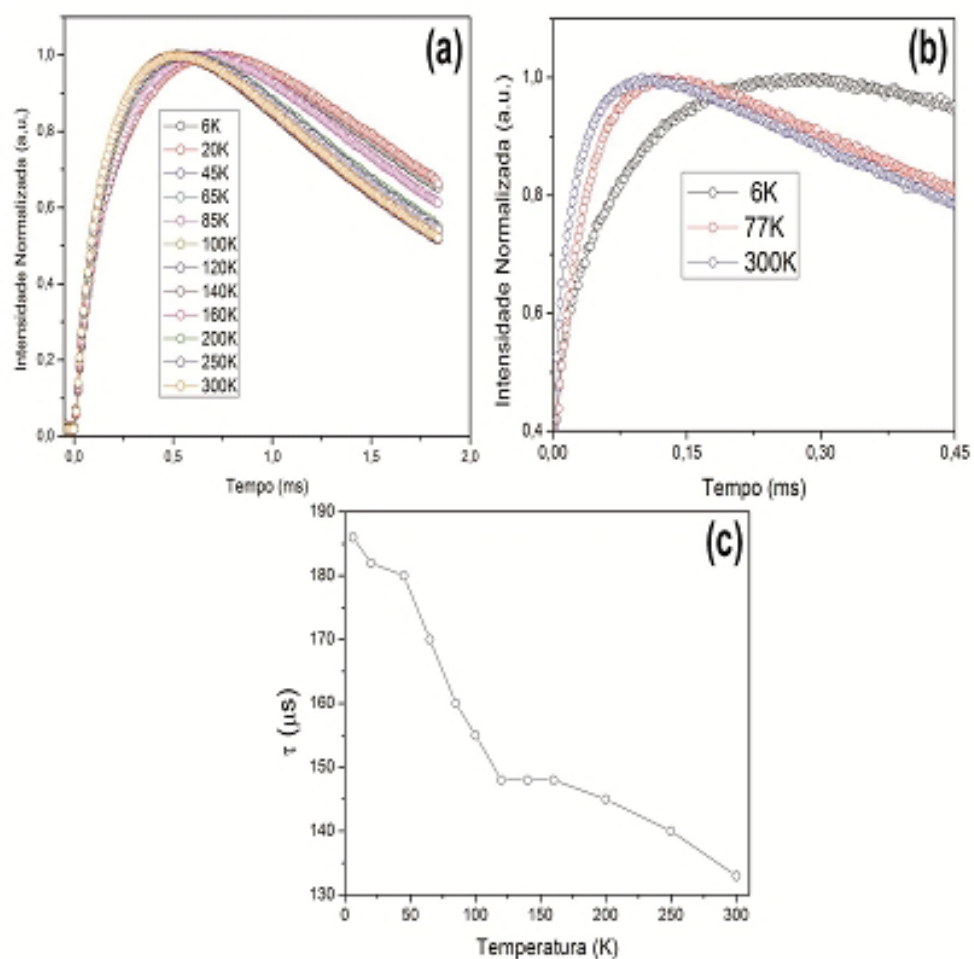
Figura 2.11: Perfil das curvas de excitação do nível $^5D_0$ do Eu^{3+}. (a) $_\infty[(Tb_{0,95}Eu_{0,05})(DPA)(HDPA)]$; (b) $_\infty[(Tb_{0,5}Eu_{0,5})(DPA)(HDPA)]$; (c) tempos de excitação em função da temperatura para $_\infty[(Tb_{0,95}Eu_{0,05})(DPA)(HDPA)]$.

Na Tabela 2.2 são sumarizados os tempos de vida monitorando as emissões do Tb^{3+} e Eu^{3+} e os tempos de excitação para o nível $^5D_0$ obtido em diferentes temperaturas nos materiais $_\infty[(Tb_{0,95}Eu_{0,05})(DPA)(HDPA)]$ e $_\infty[(Tb_{0.5}Eu_{0.5})(DPA)(HDPA)]$.

Tabela 2.2. Tempos de vida (τ_d) em função da temperatura para $_\infty[(Tb_{0,95}Eu_{0,05})(DPA)(HDPA)]$ e $_\infty[(Tb_{0,5}Eu_{0,5})(DPA)(HDPA)]$ monitorando as emissões do Tb^{3+} e Eu^{3+} em 542 e 616 nm e tempos de excitação (τ_r) para o nível $^5D_0$ do Eu^{3+} em $_\infty[(Tb_{0,95}Eu_{0,05})(DPA)(HDPA)]$.

$_\infty[(Tb_{0,95}Eu_{0,05})(DPA)(HDPA)]$			
	542 nm	*616 nm*	
Temperatura	τ_d	τ_d	τ_r
(K)	*(ms)*	*(ms)*	*(µs)*
6	0,42	1,76	186
20	0,41	1,71	182
45	0,38	1,65	180
65	0,34	1,63	170
85	0,30	1,60	160
100	0,26	1,60	155
120	0,25	1,59	148
140	0,26	1,59	148
160	0,28	1,59	148
200	0,32	1,59	145
250	0,32	1,59	140
300	0,30	1,58	133
$_\infty[(Tb_{0,5}Eu_{0,5})(DPA)(HDPA)]$			
	542 nm	*616 nm*	
6	0,16	71,0	
77	0,05	31,0	
300	0,04	25,0	

Os tempos de vida dos lantanídeos em $_\infty[(Tb_{0,95}Eu_{0,05})(DPA)(HDPA)]$ e $_\infty[(Tb_{0,95}Eu_{0,05})(DPA)(HDPA)]$ diminuem em função da temperatura devido a

processos de relaxação por fônons. É importante destacar em temperaturas acima de 120 K (ver Figura 2.9 (c) e Tabela 2.2) os tempos de vida do íon Tb^{3+} na amostra $_{\infty}[(Tb_{0,95}Eu_{0,05})(DPA)(HDPA)]$ apresentam pequeno aumento que pode ser atribuído a processos termicamente ativados de retrotransferência de energia oriunda do Eu^{3+}. Estes resultados são a mais clara demonstração que o mecanismo de TE entre os centros metálicos não podem ser consideradas simplesmente como $Tb^{3+} \rightarrow Eu^{3+}$ como proposto por prévios relatos.[51-54]

Enquanto os tempos de vida nos dão informações a respeito dos decaimentos radiativos e não-radiativos e das taxas de eficiências do processo de TE $Tb^{3+} \rightarrow Eu^{3+}$ nas curvas de excitação, estão implícitos detalhes do mecanismo de transferência de energia, simplesmente, porque é possível sondar a distribuição e saturação das populações dos estados excitados durante a migração de energia entre os centros opticamente ativos.[55] Em termos de tempos de vida do Eu^{3+} medidos a 300 K, foi observado que para o material $_{\infty}[(Tb_{0,95}Eu_{0,05})(DPA)(HDPA)]$ há um considerável aumento para $\tau_d =$ 1,58 ms em comparação ao material contento apenas o íon Eu^{3+} reportado anteriormente,[34] enquanto para $_{\infty}[(Tb_{0,5}Eu_{0,5})(DPA)(HDPA)]$ não foi constatado significativas mudanças (τ_d = 1,40 ms) provavelmente devido ao efeito de concentração[i].

---

[i] O aumento da concentração causa a auto-supressão da emissão dos íons Eu^{3+} devido a processos relacionados a transferência de energia do tipo $Eu^{3+} \rightarrow Eu^{3+}$.

A TE Tb$^{3+}\rightarrow$ Eu^{3+} nos compostos $_\infty$[(Tb$_{0,95}$Eu$_{0,05}$)(DPA)(HDPA)] e $_\infty$[(Tb$_{0,95}$Eu$_{0,05}$)(DPA)(HDPA)] reduz drasticamente os tempos de decaimento do Tb^{3+} quando comparados com o material $_\infty$[Tb(DPA)(HDPA)] (consultar Anexo 1), porém as curvas de decaimento continuam sendo exponencial simples mesmo com a presença de íons receptores. Em conjunção com a curta distância entre os centros metálicos e o fato destes ocuparem o domínio cristalino, a difusão de energia Tb$^{3+}\rightarrow$Tb^{3+} é bastante rápida.[56,57] Conseqüentemente, as taxas de TE para os pares Tb$^{3+}\rightarrow$Eu^{3+} são uma média, justificando os decaimentos mono-exponenciais dos íons Tb^{3+} nos materiais estudados.[58] Em casos em que ocorre difusão lenta de energia entre o par doador—doador as respectivas curvas de decaimento apresentam perfis não-exponenciais em curtos domínios temporais, devido à transferência direta de energia entre o par doador—aceptor mais próximo e uma componente exponencial em escala temporal mais longa devido à difusão de energia entre as espécies doadoras.[59,60]

As taxas e as eficiências de TE (k_{TE} e η_{TE}) referentes ao processo Tb$^{3+}\rightarrow$ Eu^{3+} foram estimadas de acordo com as Equações (2.2) e (2.3):[61,62]

$$k_{TE} = \tau_1^{-1} - \tau_0^{-1} \qquad\qquad (2.2)$$

$$\eta_{TE} = \frac{\tau_1^{-1} - \tau_0^{-1}}{\tau_1^{-1}}$$ (2.3)

onde, τ_0 e τ_1 são os tempos de vida do íon Tb^{3+} $^5D_4$ em 545 nm nos compostos $_\infty[Tb(DPA)(HDPA)]$ e $_\infty[(Tb_{1-x}Eu_x)(DPA)(HDPA)]$, respectivamente.

Admitindo que a interação entre os pares Tb^{3+} e Eu^{3+} seja por dipolo elétrico–dipolo elétrico e que o efeito da contração dos íons lantanídeos seja desprezado, portanto as distâncias críticas de transferência de energia (raio de Förster) podem ser estimadas pela Equação (4):

$$k_{TE} = \frac{3}{2} K^2 \tau_0^{-1} \left(\frac{R_0}{R} \right)^6$$ (4)

onde R é a distância Ln^{3+}–Ln^{3+} (6,32 Å), K^2 é o fator de orientação (K^2 = 2/3 para orientação aleatória) e R_0 é a distância crítica. Na Figura 2.12 estão mostrados a comparação entre os dados em função da temperatura referentes à k_{TE} do processo $Tb^{3+} \rightarrow Eu^{3+}$, as taxas de decaimento do Tb^{3+} (k_d) no composto $_\infty[(Tb_{0,95}Eu_{0,05})(DPA)(HDPA)]$ e a k_d para o composto contento apenas Tb^{3+} no retículo cristalino.
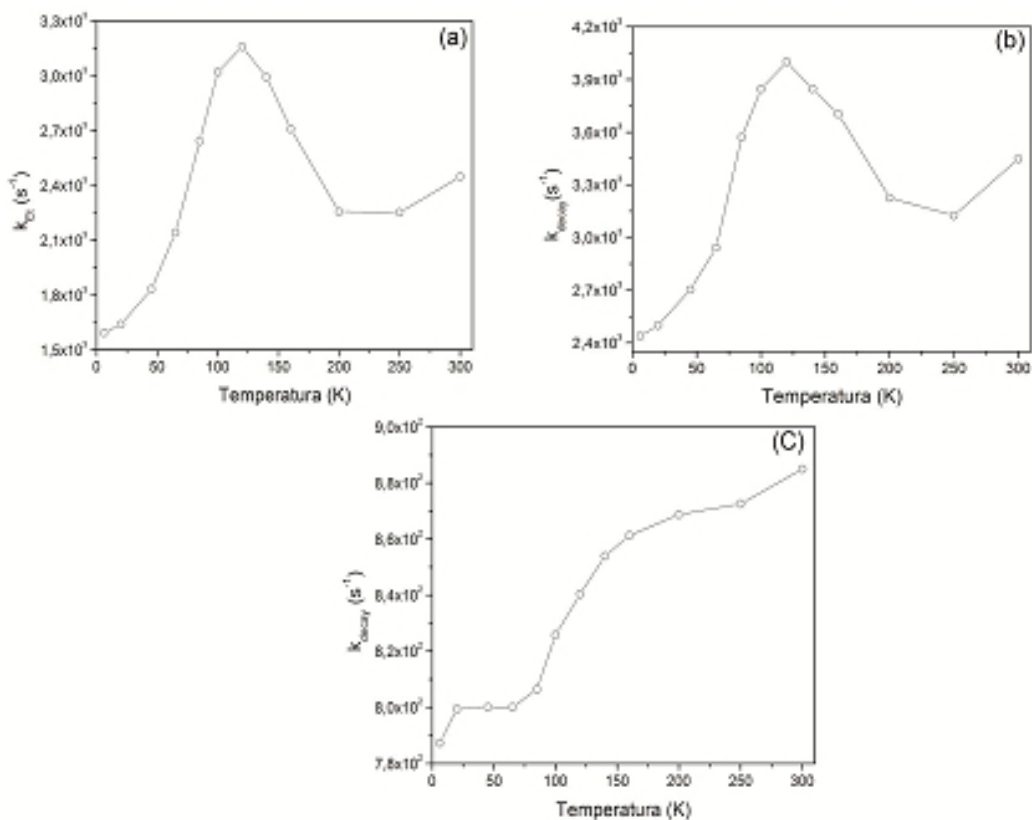
Figura 2.12: Perfil das taxas transferência de energia e decaimento em função da temperatura. (a) k_{TE} do processo Tb^{3+}→Eu^{3+} em $_\infty$[(Tb$_{0,95}$Eu$_{0,05}$)(DPA)(HDPA)]; (b) k_d do Tb^{3+} $^5D_4$ em $_\infty$[(Tb$_{0,95}$Eu$_{0,05}$)(DPA)(HDPA)]; (c) k_d do Tb^{3+} $^5D_4$ em $_\infty$[Tb(DPA)(HDPA)].

Os valores de taxas de TE obtidos usando a Equação (2.2) mostram a grande dependência das taxas de relaxação do Tb^{3+} na amostra $_\infty$[(Tb$_{0,95}$Eu$_{0,05}$)(DPA)(HDPA)], fato este que justifica o mesmo perfil dos dados apresentados na Figura 2.12 (a) e (b). Como pode ser observado na Figura 2.12 (a), na faixa de 6 a 120 K as k_{TE} são aumentadas devido ao crescimento da assistência dos fônons para o processo de TE Tb^{3+} → Eu^{3+}. Acima de 120 K

era esperado que as k_{TE} seguissem a mesma tendência da faixa de temperatura anterior, no entanto, o comportamento foi completamente oposto, pois as taxas de transferência são gradualmente reduzidas na região de 120 a 300 K. Isto pode ser explicado pela diferença de energia entre os níveis $^5D_4$ e $^5D_1$ do Tb^{3+} e Eu^{3+} ser cerca de 1300 cm^{-1}, logo, pequena o suficiente para permitir processos de retrotransferência de energia termicamente ativados típicos dessa faixa de temperatura. Esse efeito de retrotransferência fica bem evidente ao ser constatado a tendência quase que linear das taxas de decaimento do Tb^{3+} em função da temperatura no material $_\infty$[Tb(DPA)(HDPA)] (Figura 2.12 (c)).

Os valores de R_0 e η_{TE} variam nas faixas de 7,15–7,93 Å e 67–79%, respectivamente, com os dados acompanhando a mesma tendência daqueles apresentados pelas k_{TE} e k_d para o composto $_\infty$[(Tb$_{0,95}$Eu$_{0,05}$)(DPA)(HDPA)] com o aumento da temperatura. Esses resultados indicam que o íon Tb^{3+} está apto a transferir energia eficientemente para íons Eu^{3+} que ocupam os sítios com 6,32 e 6,75 Å de distância. Já para o composto $_\infty$[(Tb$_{0,5}$Eu$_{0,5}$)(DPA)(HDPA)], os valores médios para R_0 e $\eta_{TE,}$ 31 Å e 97% respectivamente, indicam que o Tb^{3+} pode transferir energia para íons Eu^{3+} localizados em diferentes lamelas.

Claramente, a transferência de energia em $_\infty$[(Tb$_{0,95}$Eu$_{0,05}$)(DPA)(HDPA)] não ocorre aleatoriamente, ou seja, nem todo íon Tb^{3+} pode excitar diretamente o Eu^{3+}. Considerando que em baixas concentrações os íons Eu^{3+} estão

distribuídos no polímero de coordenação em pequenos aglomerados (*clusters*) ou isolados, logo a TE $Tb^{3+} \rightarrow Eu^{3+}$ ocorre somente entre centros metálicos mais próximos.[23] No caso de elevadas concentrações os íons Eu^{3+} estão arranjados predominantemente como *clusters*, desta forma, somente os íons localizados nas fronteiras do *cluster* podem ser excitados pelos íons Tb^{3+}, enquanto os íons Eu^{3+} no centro do *cluster* são exclusivamente excitados via difusão de energia $Eu^{3+} \rightarrow Eu^{3+}$ e através da antena.[63] Nesse contexto a amostra $_\infty[(Tb_{0,95}Eu_{0,05})(DPA)(HDPA)]$ é mais adequada que $_\infty[(Tb_{0,5}Eu_{0,5})(DPA)(HDPA)]$ para avaliar o impacto da energia transferida do Tb^{3+} sobre a luminescência do Eu^{3+}, visto que em baixas concentrações o efeito de excitação proveniente do processo de difusão de energia entres os íons Eu^{3+} é minimizado.

Na Figura 2.13 está mostrado as taxas de excitação do Eu^{3+}, k_r, e a distribuição relativa das populações dos níveis $^5D_0$ e $^5D_1$ em função da temperatura.
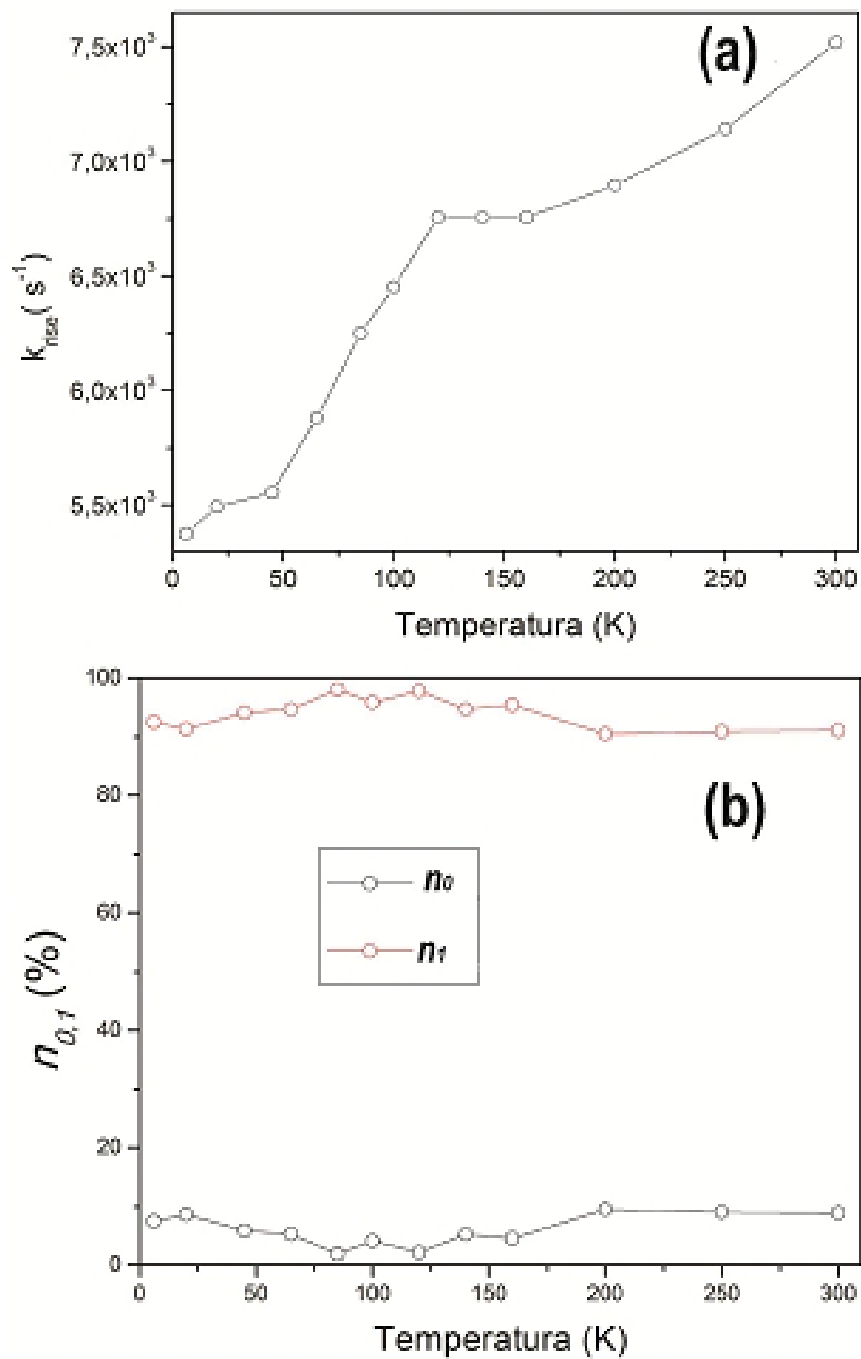
Figura 2.13: Taxas de excitação e valores relativos de n_0 e n_1 do Eu^{3+} em função da temperatura na amostra $_\infty$[(Tb$_{0,95}$Eu$_{0,05}$)(DPA)(HDPA)].

Como esperado, a dependência com a temperatura das taxas de excitação do Eu^{3+} é resultado da variação nas eficiências do processo de TE, sugerindo que o processo é controlado por interações multipolares como descrito pela Teoria de Förster.[42,64] As taxas de excitação do Eu^{3+} mostram que parte da energia é oriunda da TE proveniente do nível $^5D_4$ do Tb^{3+}, pois as constantes de excitação estão na mesma ordem de magnitude e exibem tendência semelhante às taxas de transferência de energia do processo $Tb^{3+} \rightarrow Eu^{3+}$ em função da temperatura. A cinética das populações do nível emissor $^5D_0$ do Eu^{3+} nos materiais $_\infty[(Tb_{0,95}Eu_{0,05})(DPA)(HDPA)]$ e $_\infty[(Tb_{0,5}Eu_{0,5})(DPA)(HDPA)]$ é resultado de processos complexos que envolvem diversos canais como: excitação direta via tripleto — $^5D_0$; TE via $^5D_4 \rightarrow {}^5D_0$; interação entre os níveis $^5D_0 \rightarrow {}^5D_0$ (difusão de energia); conversão interna dos estados excitados, $^5D_{1,2,3} \rightarrow {}^5D_0$. Diante disto, seria de extrema pretensão determinar com exatidão o mecanismo de transferência de energia nos sistemas estudados, no entanto, pode-se fazer uma estimativa baseada nos n_0 e n_1 extraídos das curvas de excitação (Figura 2.9 (b)). Os valores de n_0 e n_1, mostrados na Figura 2.13(b), indicam que o caminho provável para excitação do estado $^5D_0$ ocorre através da conversão interno do nível $^5D_1$, haja vista, que os valores de n_1 alcançam cerca de 90%.

Na Figura 2.14 são mostradas as curvas de excitação do íon Tb^{3+} obtidas a 6K dos compostos $_\infty[(Tb_{0,95}Eu_{0,05})(DPA)(HDPA)]$, $_\infty[(Tb_{0,5}Eu_{0,5})(DPA)(HDPA)]$ e $_\infty[Tb(DPA)(HDPA)]$.
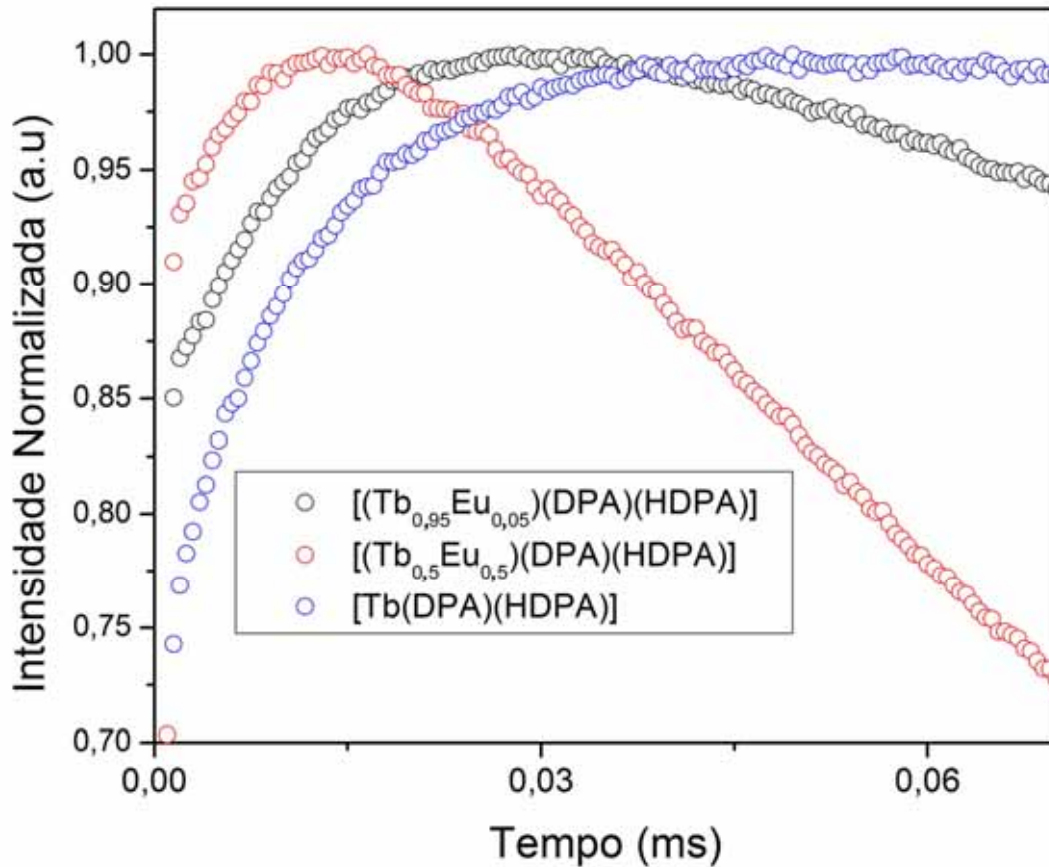
Figura 2.14: Curvas de excitação do íon Tb³⁺ adquiridos a 6 K.

Os respectivos tempos de subida de 8,7 μs, 4,25 μs e 10,5 μs para $_{\infty}$[(Tb$_{0,95}$Eu$_{0,05}$)(DPA)(HDPA)], $_{\infty}$[(Tb$_{0,5}$Eu$_{0,5}$)(DPA)(HDPA)] e $_{\infty}$[Tb(DPA)(HDPA)] foram obtidos usando a Equação (1). Evidentemente, as populações do estado $^5D_4$ do Tb³⁺ no material $_{\infty}$[Tb(DPA)(HDPA)] são resultados de processos associados à direta excitação do íon no nível $^5D_2$ (355 nm ≈ 28170 cm⁻¹), difusão de energia entre os íons Tb³⁺ e energia transferida do ligante. Baseados em todas as observações foi proposto um digrama de energia para

os materiais (Figura 2.15) evidenciando os mais prováveis canais e as respectivas constantes de transferência de energia.
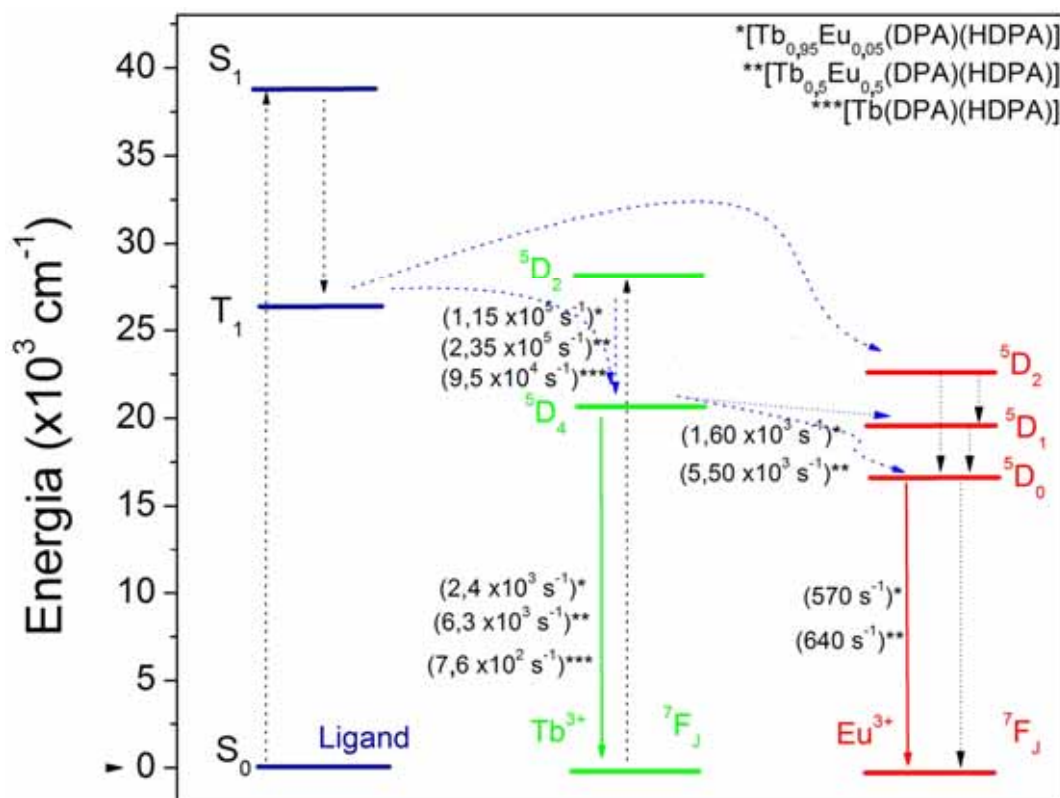
Figura 2.15: Ilustração do diagrama de energia mostrando os possíveis canais de transferência e as respectivas constantes a 6 K.

Como esses materiais não apresentarem moléculas de água coordenadas ao íon Ln^{3+}, algo bastante incomum levando em consideração que a síntese é realizada em água, e devido às melhorais associadas aos mecanismos de conversão de energia, pode ser observado um considerável incremento das intensidades de emissão dos compostos. A prova irrefutável

disto são os valores de rendimento quântico de 90% e 57% adquiridos para $_\infty[(Tb_{0,95}Eu_{0,05})(DPA)(HDPA)]$ e $_\infty[(Tb_{0,5}Eu_{0,5})(DPA)(HDPA)]$, respectivamente.[ii]

2.4   *Conclusão*

Dois polímeros de coordenação, $_\infty[(Tb_{0,95}Eu_{0,05})(DPA)(HDPA)]$ e $_\infty[(Tb_{0,5}Eu_{0,5})(DPA)(HDPA)]$, foram sintetizados e o processo de transferência de energia entre os centros metálicos foi estudado em detalhes. A difração de raios-x demonstrou que os materiais são isomorfos ao $_\infty[Tb(DPA)(HDPA)]$, previamente reportado na literatura.

Os espectros de emissão resolvidos no tempo de $_\infty[(Tb_{0,95}Eu_{0,05})(DPA)(HDPA)]$ indicaram que a sensitização do D_0 do Eu^{3+} ocorre preferencialmente através do $^5D_4$ do Tb^{3+}. No entanto, para o $_\infty[(Tb_{0,5}Eu_{0,5})(DPA)(HDPA)]$ foi observado que além da energia transferida do Tb^{3+} existe uma intensa contribuição do tripleto do ligante para excitação dos íons Eu^{3+}. As taxas de transferência de energia do processo $Tb^{3+} \rightarrow Eu^{3+}$ (k_{TE}) e as taxas de excitação (k_r) do Eu^{3+} são dependentes da temperatura indicando processo de interação multipolar como descrito por Förster. Além disso, essas taxas estão na mesma ordem de grandeza no $_\infty[(Tb_{0,95}Eu_{0,05})(DPA)(HDPA)]$ reforçando que a excitação do Eu^{3+} ocorre via Tb^{3+}.

As taxas de excitação do Tb^{3+} mostram significativas diferenças quando comparadas à apresentada pelo material puro ($_\infty[Tb(DPA)(HDPA)]$) indicando

---

[ii] O rendimento quântico relativo do $_\infty[Tb(DPA)(HDPA)]$ é 50%. Todos os procedimentos para realização da medida estão descritos na ref. 38.

que há existência de canais paralelos de excitação do Tb^{3+} associados ao íon Eu^{3+}. Estes resultados são fortes evidências que a energia flui sinergicamente entre os centros metálicos. Os valores de rendimento quântico de 90% e 57% adquiridos para $_{\infty}[(Tb_{0,95}Eu_{0,05})(DPA)(HDPA)]$ e $_{\infty}[(Tb_{0,5}Eu_{0,5})(DPA)(HDPA)]$, respectivamente, são a prova irrefutável da modulação dos processo de TE nos materiais.

2.5   Referências

(1)   Lehn, J. M., Perspectives in Supramolecular Chemistry - from Molecular Recognition Towards Molecular Information-Processing and Self-Organization, *Angewandte Chemie-International Edition* **1990**, *29*, 1304-1319.

(2)   de Sa, G. F.; Malta, O. L.; Donega, C. D.; Simas, A. M.; Longo, R. L.; Santa-Cruz, P. A.; da Silva, E. F., Spectroscopic properties and design of highly luminescent lanthanide coordination complexes, *Coordination Chemistry Reviews* **2000**, *196*, 165-195.

(3)   Nishiyabu, R.; Hashimoto, N.; Cho, T.; Watanabe, K.; Yasunaga, T.; Endo, A.; Kaneko, K.; Niidome, T.; Murata, M.; Adachi, C.; Katayama, Y.; Hashizume, M.; Kimizuka, N., Nanoparticles of Adaptive Supramolecular Networks Self-Assembled from Nucleotides and Lanthanide Ions, *Journal of the American Chemical Society* **2009**, *131*, 2151-2158.

(4)   Gassner, A. L.; Duhot, C.; Bunzli, J. C. G.; Chauvin, A. S., Remarkable tuning of the photophysical properties of bifunctional lanthanide tris(dipicolinates) and its consequence on the design of bioprobes, *Inorganic Chemistry* **2008**, *47*, 7802-7812.

(5)   Bunzli, J. C. G.; Piguet, C., Taking advantage of luminescent lanthanide ions, *Chemical Society Reviews* **2005**, *34*, 1048-1077.

(6)   Kim, H. J.; Eichinger, A.; Skerra, A., High-affinity recognition of lanthanide(III) chelate complexes by a reprogrammed human lipocalin 2, *Journal of the American Chemical Society* **2009**, *131*, 3565-3576.

(7)   de Bettencourt-Dias, A.; Viswanathan, S., Nitro-functionalization and luminescence quantum yield of Eu(III) and Tb(III) benzoic acid complexes, *Dalton Transactions* **2006**, 4093-4103.

(8)   Zhao, B.; Chen, X. Y.; Cheng, P.; Liao, D. Z.; Yan, S. P.; Jiang, Z. H., Coordination polymers containing 1D channels as selective luminescent probes, *Journal of the American Chemical Society* **2004**, *126*, 15394-15395.

(9)   Li, Huanrong; Cheng, Wenjing; Wang, Yu; Liu, Binyuan; Zhang, Wenjun; Zhang, Hongjie, Surface modification and munctionalization of microporous hybrid material for luminescence sensing, *Chemistry - A European Journal* **2010**, *16*, 2125-2130.

(10)   Manzoori, Jamshid L.; Jouyban, Abolghasem; Amjadi, Mohammad; Soleymani, Jafar, Spectrofluorimetric determination of folic acid in tablets and urine samples using 1,10-phenanthroline-terbium probe, *Luminescence* **2010**, *9999*, *in press*.

(11)   Harbuzaru, Bogdan V.; Corma, Avelino; Rey, Fernando; Jordá, Jose L.; Ananias, Duarte; Carlos, Luis D.; Rocha, João, A miniaturized linear pH sensor based on a highly photoluminescent self-assembled europium(III) metal-organic framework, *Angewandte Chemie International Edition* **2009**, *48*, 6476-6479.

(12)   Harbuzaru, Bogdan V.; Corma, Avelino; Rey, Fernando; Atienzar, Pedro; Jordá, Jose L.; García, Hermenegildo; Ananias, Duarte; Carlos, Luis D.; Rocha, João, Metal-Organic nanoporous structures with anisotropic photoluminescence and magnetic properties and their Use as Sensors, *Angewandte Chemie International Edition* **2008**, *47*, 1080-1083.

(13)   de Mesquita, M. E.; Silva, F. R. G. E.; Albuquerque, R. Q.; Freire, R. O.; da Conceicao, E. C.; da Silva, J. E. C.; Junior, N. B. C.; de Sa, G. F., Eu(III) and Gd(III) complexes with pirazyne-2-carboxylic acid: luminescence and modelling of the structure and energy transfer process, *Journal of Alloys and Compounds* **2004**, *366*, 124-131.

(14)   Ghosh, S. K.; Bharadwaj, P. K., Self-assembly of lanthanide helicate coordination polymers into 3D metal-organic framework structures, *Inorganic Chemistry* **2004**, *43*, 2293-2298.

(15)   Shi, F. N.; Cunha-Silva, L.; Ferreira, R. A. S.; Mafra, L.; Trindade, T.; Carlos, L. D.; Paz, F. A. A.; Rocha, J., Interconvertable modular framework and layered lanthanide(III)-etidronic acid coordination polymers, *Journal of the American Chemical Society* **2008**, *130*, 150-167.

(16)   de Bettencourt-Dias, A., Lanthanide-based emitting materials in light-emitting diodes, *Dalton Transactions* **2007**, 2229-2241.

(17)   D'Aléo, Anthony; Picot, Alexandre; Baldeck, Patrice L.; Andraud, Chantal; Maury, Olivier, Design of dipicolinic acid ligands for the two-photon sensitized luminescence of europium complexes with optimized cross-sections, *Inorganic Chemistry* **2008**, *47*, 10269-10279.

(18)   Souza, Ana Paula; Paz, Filipe A. Almeida; Freire, Ricardo O.; Carlos, Luís D.; Malta, Oscar L.; Alves, S.; de Sá, Gilberto F., Synthesis, crystal ctructure, and modelling of a new tetramer complex of europium, *The Journal of Physical Chemistry B* **2007**, *111*, 9228-9238.

(19)   Freire, R. O.; Silva, F. R. G. E.; Rodrigues, M. O.; de Mesquita, M. E.; Junior, N. B. D., Design of europium(III) complexes with high quantum yield, *Journal of Molecular Modeling* **2005**, *12*, 16-23.

(20)   Freire, R. O.; Albuquerque, R. Q.; Junior, S. A.; Rocha, G. B.; de Mesquita, M. E., On the use of combinatory chemistry to the design of new luminescent Eu^{3+} complexes, *Chemical Physics Letters* **2005**, *405*, 123-126.

(21)   Sun, H. Y.; Huang, C. H.; Jin, X. L.; Xu, G. X., The Synthesis, Crystal-Structure and Synergistic Fluorescence Effect of a Heteronuclear Lanthanide Complex (HLC) (Na$_3$TbLa$_2$(C$_7$H$_3$SO$_6$)$_4$26H$_2$O, *Polyhedron* **1995**, *14*, 1201-1206.

(22)   Kahwa, I. A.; Parkes, C. C.; Mcpherson, G. L., Energy-Transport in Photoexcited Crystals of K$_3$[Tb(C$_2$O$_4$)$_3$(H$_2$O)] 2H$_2$O - Transfer from Tb^{3+} to Nd^{3+} and Eu^{3+}, *Physical Review B* **1995**, *52*, 11777-11783.

(23)   de Lill, D. T.; de Bettencourt-Dias, A.; Cahill, C. L., Exploring lanthanide luminescence in metal-organic frameworks: Synthesis, structure, and guest-sensitized luminescence of a mixed europium/terbium-adipate framework and a terbium-adipate framework, *Inorganic Chemistry* **2007**, *46*, 3960-3965.

(24)   Zhang, T.; Xu, Z.; Qian, L.; Teng, F.; Xu, X. R.; Tao, D. L., Improved emission of Eu^{3+} by energy transfer via Tb3+ in coprecipitates Tb$_x$Eu$_{(1-x)}$(aspirin)$_3$(phen), *Journal of Applied Physics* **2005**, *98*, 0653031-0653034.

(25)   Comby, S.; Scopelliti, R.; Imbert, D.; Charbonniere, L.; Ziessel, R.; Bunzli, J. C. G., Dual emission from luminescent nonalanthanide clusters, *Inorganic Chemistry* **2006**, *45*, 3158-3160.

(26)   Armelao, L.; Bottaro, G.; Quici, S.; Cavazzini, M.; Raffo, M. C.; Barigelletti, F.; Accorsi, G., Photophysical properties and tunable colour changes of silica single layers doped with lanthanide(III) complexes, *Chemical Communications* **2007**, 2911-2913.

(27)   Ishizaka, T.; Nozaki, R.; Kurokawa, Y., Luminescence properties of Tb3+ and Eu^{3+}-doped alumina films prepared by sol-gel method under various

conditions and sensitized luminescence, *Journal of Physics and Chemistry of Solids* **2002**, *63*, 613-617.

(28)   Lv, Y. G.; Zhang, J. C.; Cao, W. L.; Fu, Y. L.; Han, Z. Y., Luminescence properties of complex $Tb_{0.25}Eu_{0.75}(TTA)_2$(N-HPA)Phen, *Journal of Alloys and Compounds* **2009**, *468*, 406-409.

(29)   Tremblay, M. S.; Sames, D., Synthesis of luminescent heterometallic bis-lanthanide complexes via selective, sequential metallation, *Chemical Communications* **2006**, 4116-4118.

(30)   Piguet, C.; Bunzli, J. C. G., Mono- and polymetallic lanthanide-containing functional assemblies: a field between tradition and novelty, *Chemical Society Reviews* **1999**, *28*, 347-358.

(31)   Liu, Y.; Qian, G. D.; Wang, Z. Y.; Wang, M. Q., Temperature-dependent luminescent properties of Eu-Tb complexes synthesized in situ in gel glass, *Applied Physics Letters* **2005**, *86*.

(32)   Tremblay, M. S.; Halim, M.; Sames, D., Cocktails of Tb^{3+} and Eu^{3+} complexes: A general platform for the design of ratiometric optical probes, *Journal of the American Chemical Society* **2007**, *129*, 7570-7577.

(33)   Reisfeld, R.; Zigansky, E.; Gaft, M., Europium probe for estimation of site symmetry in glass films, glasses and crystals, *Molecular Physics* **2004**, *102*, 1319-1330.

(34)   Fernandes, A.; Jaud, J.; Dexpert-Ghys, J.; Brouca-Cabarrecq, C., Study of new lanthanide complexes of 2,6-pyridinedicarboxylate: synthesis, crystal structure of Ln(Hdipic)(dipic) with Ln = Eu, Gd, Tb, Dy, Ho, Er, Yb, luminescence properties of Eu(Hdipic)(dipic), *Polyhedron* **2001**, *20*, 2385-2391.

(35)   Rodrigues, M. O.; Brito-Silva, A. M.; Alves, S.; De Simone, C. A.; Araujo, A. A. S.; de Carvalho, P. H. V.; Santos, S. C. G.; Aragao, K. A. S.; Freire, R. O.; Mesquita, M. E., Structural and Spectroscopic Studies of the 2d Coordination Polymers $_\infty$[Tb(DPA)(HDPA)] and $_\infty$[Gd(DPA)(HDPA)], *Quimica Nova* **2009**, *32*, 286-291.

(36)   Rietveld, H. M., A Profile Refinement Method for Nuclear and Magnetic Structures, *Journal of Applied Crystallography* **1969**, *2*, 65-71.

(37)   Larson, Allen.C., Von Dreele, R.B. *General Structure Analysis System (GSAS)*, Los Alamos ational Laboratory, 2004.

(38)   Thompson, P.; Cox, D. E.; Hastings, J. B., Rietveld Refinement of Debye-Scherrer Synchrotron X-Ray Data from Al_2O_3, *Journal of Applied Crystallography* **1987**, *20*, 79-83.

(39)   Young, R. A. ; Desai, P. In *Archiwun Nauki o Materialach* 1989; Vol. 10, p 71-90.

(40)   Jarvinen, M., Application of symmetrized harmonics expansion to correction of the preferred orientation effect, *Journal of Applied Crystallography* **1993**, *26*, 525-531.

(41)   Binnemans, K.; GorllerWalrand, C., Application of the Eu^{3+} ion for site symmetry determination, *Journal of Rare Earths* **1996**, *14*, 173-180.

(42)   Speiser, S., Photophysics and mechanisms of intramolecular electronic energy transfer in bichromophoric molecular systems: Solution and supersonic jet studies, *Chemical Reviews* **1996**, *96*, 1953-1976.

(43)   Oczko, G.; Legendziewicz, J.; Mrozinski, J.; Meyer, G., Comparative spectroscopic and magnetic studies of two types of Ln and Ln : Cu trichloroacetates, *Journal of Alloys and Compounds* **1998**, *277*, 219-224.

(44)   Taboada, S.; de Andres, A.; Saez-Puche, R., Excitation and desexcitation processes of Eu^{3+} luminescence in Eu_2BaZnO_5, *Journal of Alloys and Compounds* **1998**, *277*, 279-283.

(45)   Rodrigues, M. O.; da Costa, N. B.; de Simone, C. A.; Araujo, A. A. S.; Brito-Silva, A. M.; Paz, F. A. A.; de Mesquita, M. E.; Junior, S. A.; Freire, R. O., Theoretical and experimental studies of the photoluminescent properties of the coordination polymer $[Eu(DPA)(HDPA)(H_2O)_2]$ $4H_2O$, *Journal of Physical Chemistry B* **2008**, *112*, 4204-4212.

(46)   Reinhard, C.; Gudel, H. U., High-resolution optical spectroscopy of Na-3[Ln(DPA)_3] $13H_2O$ with Ln = Er^{3+}, Tm^{3+}, Yb^{3+}, *Inorganic Chemistry* **2002**, *41*, 1048-1055.

(47)   George, M. R.; Golden, C. A.; Grossel, M. C.; Curry, R. J., Modified dipicolinic acid ligands for sensitization of europium(III) luminescence, *Inorganic Chemistry* **2006**, *45*, 1739-1744.

(48)   Lamture, J. B.; Zhou, Z. H.; Kumar, A. S.; Wensel, T. G., Luminescence Properties of Terbium(III) Complexes with 4-Substituted Dipicolinic Acid Analogs, *Inorganic Chemistry* **1995**, *34*, 864-869.

(49)   Klink, S. I.; Grave, L.; Reinhoudt, D. N.; van Veggel, F. C. J. M.; Werts, M. H. V.; Geurts, F. A. J.; Hofstraat, J. W., A systematic study of the photophysical processes in polydentate triphenylene-functionalized Eu^{3+}, Tb^{3+}, Nd^{3+}, Yb^{3+}, and Er^{3+} complexes, *Journal of Physical Chemistry A* **2000**, *104*, 5457-5468.

(50)   Ranson, R. M.; Evangelou, E.; Thomas, C. B., Modeling the fluorescent lifetime of Y2O3 : Eu, *Applied Physics Letters* **1998**, *72*, 2663-2664.

(51)   Li, Q.; Li, T.; Wu, J. G., Luminescence of europium(III) and terbium(III) complexes incorporated in poly(vinyl pyrrolidone) matrix, *Journal of Physical Chemistry B* **2001**, *105*, 12293-12296.

(52)   Sendor, D.; Hilder, M.; Juestel, T.; Junk, P. C.; Kynast, U. H., One dimensional energy transfer in lanthanoid picolinates. Correlation of structure and spectroscopy, *New Journal of Chemistry* **2003**, *27*, 1070-1077.

(53)   Joshi, B. C., Enhanced Eu3+ Emission by Nonradiative Energy-Transfer from Tb^{3+} in Zinc Phosphate-Glass, *Journal of Non-Crystalline Solids* **1995**, *180*, 217-220.

(54)   Kerbellec, N.; Kustaryono, D.; Haquin, V.; Etienne, M.; Daiguebonne, C.; Guillou, O., An Unprecedented Family of Lanthanide-Containing Coordination Polymers with Highly Tunable Emission Properties, *Inorganic Chemistry* **2009**, *48*, 2837-2843.

(55)   Kenyon, A. J.; Wojdak, M.; Ahmad, I.; Loh, W. H.; Oton, C. J., Generalized rate-equation analysis of excitation exchange between silicon nanoclusters and erbium ions, *Physical Review B* **2008**, *77*, 035318- 035326.

(56)   Gandrud, W. B.; Moos, H. W., Rare-Earth Infrared Lifetimes and Exciton Migration Rates in Trichloride Crystals, *Journal of Chemical Physics* **1968**, *49*, 2170.

(57)   Gfeller, N.; Calzaferri, G., Energy migration in dye-loaded hexagonal microporous crystals, *Journal of Physical Chemistry B* **1997**, *101*, 1396-1408.

(58)   Zych, E.; Hreniak, D.; Strek, W., Spectroscopic properties of Lu$_2$O$_3$/Eu^{3+} nanocrystalline powders and sintered ceramics, *Journal of Physical Chemistry B* **2002**, *106*, 3805-3812.

(59)   Misra, V.; Mishra, H., Role of diffusion in excitation energy transfer and migration, *Journal of Chemical Physics* **2007**, *127*.

(60)   Weber, M. J., Luminescence Decay by Energy Migration and Transfer - Observation of Diffusion-Limited Relaxation, *Physical Review B* **1971**, *4*, 2932.

(61)   Ke, H. Y. D.; Birnbaum, E. R., Many-Body Nonradiative Energy-Transfer in a Crystalline Europium (III) Edta Complex, *Journal of Luminescence* **1995**, *63*, 9-17.

(62)   Liu, Y.; Yang, Y.; Qian, G. D.; Wang, Z. Y.; Wang, M. Q., Energy transfer processes from $Tb3^+$, to Eu^{3+}, in ternary chelate doped in gel glasses via in situ technique, *Materials Science and Engineering B-Solid State Materials for Advanced Technology* **2007**, *137*, 74-79.

(63)   Toda, K.; Honma, T.; Sato, M., Unusual concentration quenching of europium luminescence in new layered perovskite compound, $RbLa_{1-x}Eu_xTa_2O_7$ (0<=x<=1), *Journal of Luminescence* **1997**, *71*, 71-75.

(64)   Forster, T., 10th Spiers Memorial Lecture - Transfer Mechanisms of Electronic Excitation, *Discussions of the Faraday Society* **1959**, 7-17.

Anexo 2

Análise Elementar de CHN.

Fórmula (Calculado/Experimental):

$C_{14}H_7N_2O_8Tb_{0,95}Eu_{0,05}$: C: 34,53/34,6%; H: 1,44/1,40%; N: 5,75/5,80%;

$C_{14}H_7N_2O_8Tb_{0,5}Eu_{0,5}$; C: 34,31/34,34%; H: 1,30/1,28%; N: 5,72/5,70%.
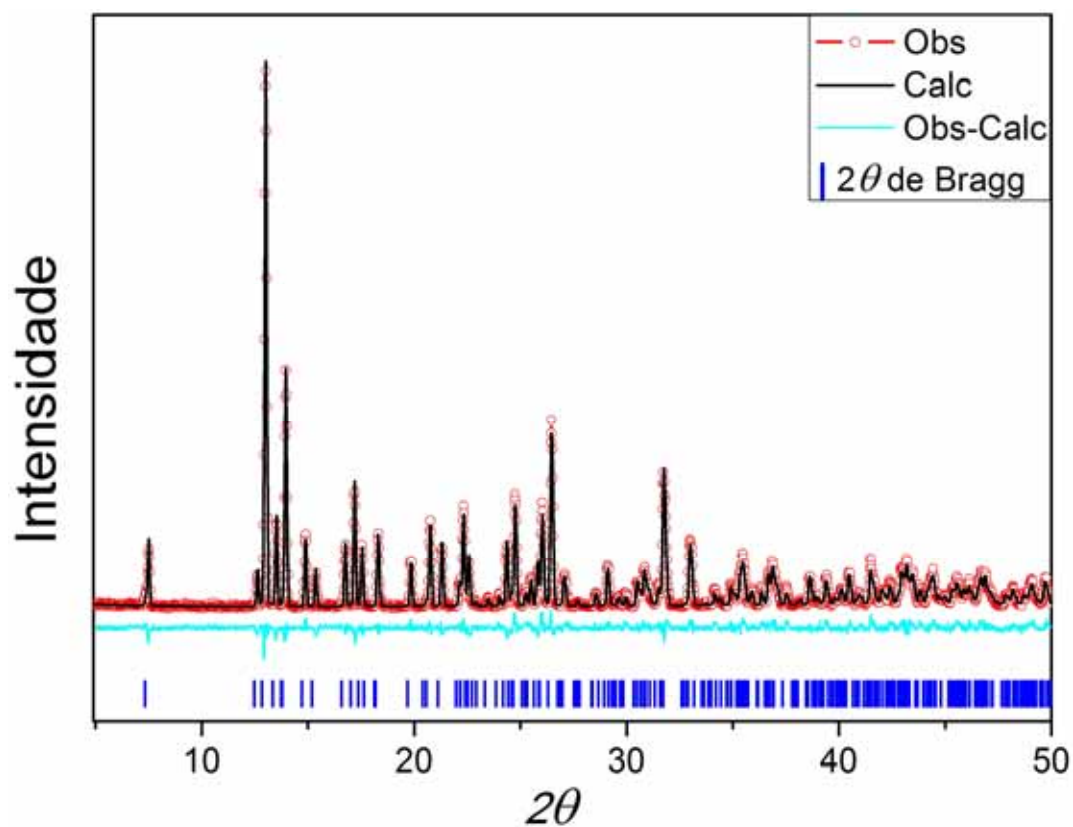
Figura 2.1A: Padrões de difração de raios-x de resultado final do Refinamento de Rietveld para $_\infty[(Tb_{0,5}Eu_{0,5})(DPA)(HDPA)]$.
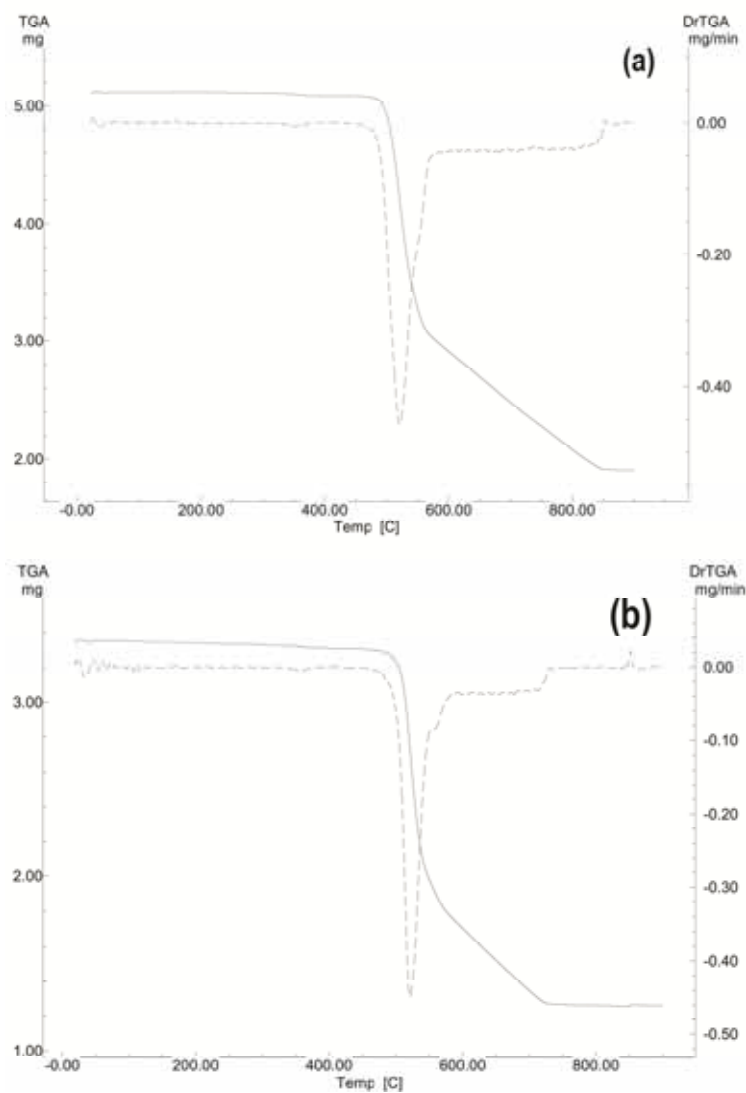
Figura 2.2A: Curvas termogravimétricas (TGA) e termogravimetria derivada (DTG): (a) ∞[(Tb$_{0,95}$Eu$_{0,05}$)(DPA)(HDPA)]; (b) ∞[(Tb$_{0,5}$Eu$_{0,5}$)(DPA)(HDPA)].
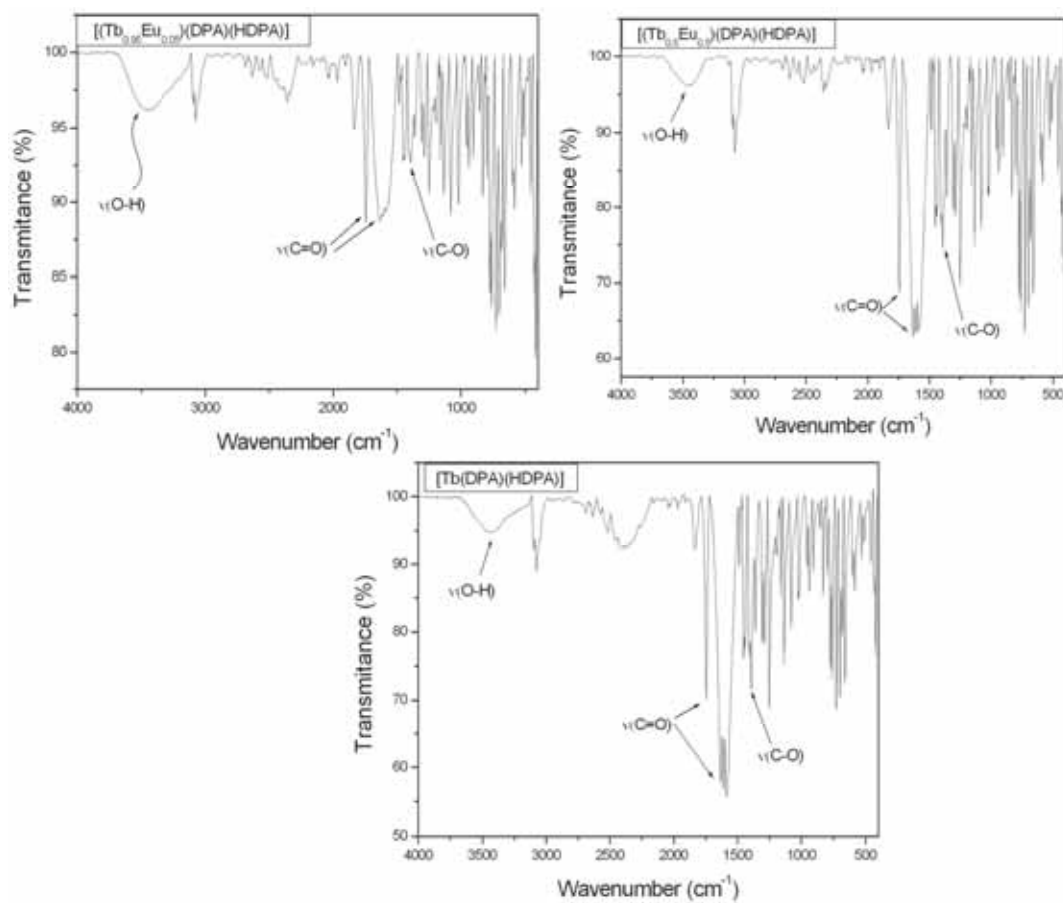
Figura 2.3A: Espectros de Infravermelho de $_\infty[(Tb_{0,95}Eu_{0,05})(DPA)(HDPA)]$, $_\infty[(Tb_{0,5}Eu_{0,5})(DPA)(HDPA)]$ e $_\infty[Tb(DPA)(HDPA)]$.

Tabela 2.1A. Tempos de vida em função da temperatura de $_\infty$[Tb(DPA)(HDPA)].

	542 nm
Temperatura (K)	τ_{decay} (ms)
6	1,31
20	1,28
45	1,27
65	1,24
85	1,23
100	1,21
120	1,19
140	1,19
160	1,17
200	1,16
250	1,11
300	1,08
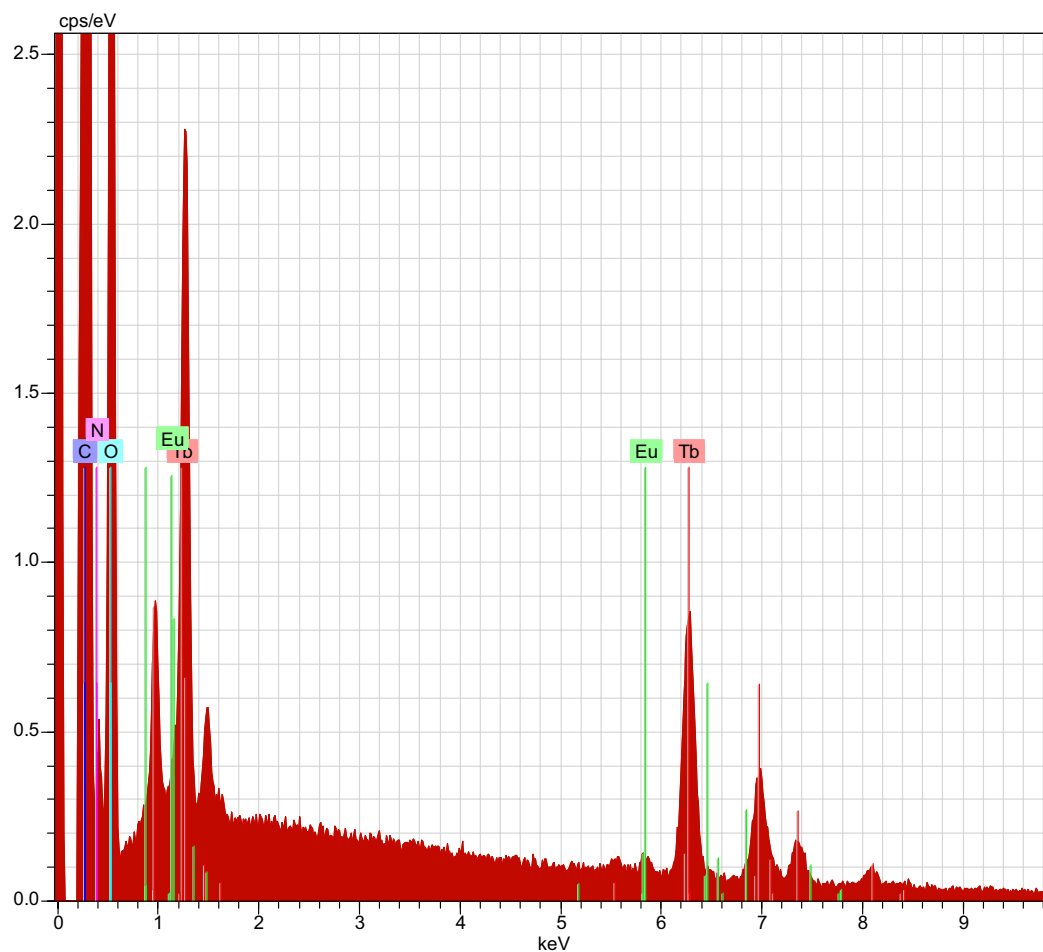
Spectrum: ∞[(Tb$_{0,95}$Eu$_{0,05}$)(DPA)(HDPA)]

```
Element     Series     Net   unn. C norm. C Atom. C Error
                             [wt.-%]  [wt.-%]  [at.-%]    [%]
----------------------------------------------------------
Terbium   L-series 22014    72,65    90,50    90,11    2,2
Europium  L-series  2879     7,62     9,50     9,89    0,3
----------------------------------------------------------
                    Total:  80,27   100,00   100,00
```

Figura 2.3A: EDS do ∞[(Tb$_{0,95}$Eu$_{0,05}$)(DPA)(HDPA)].
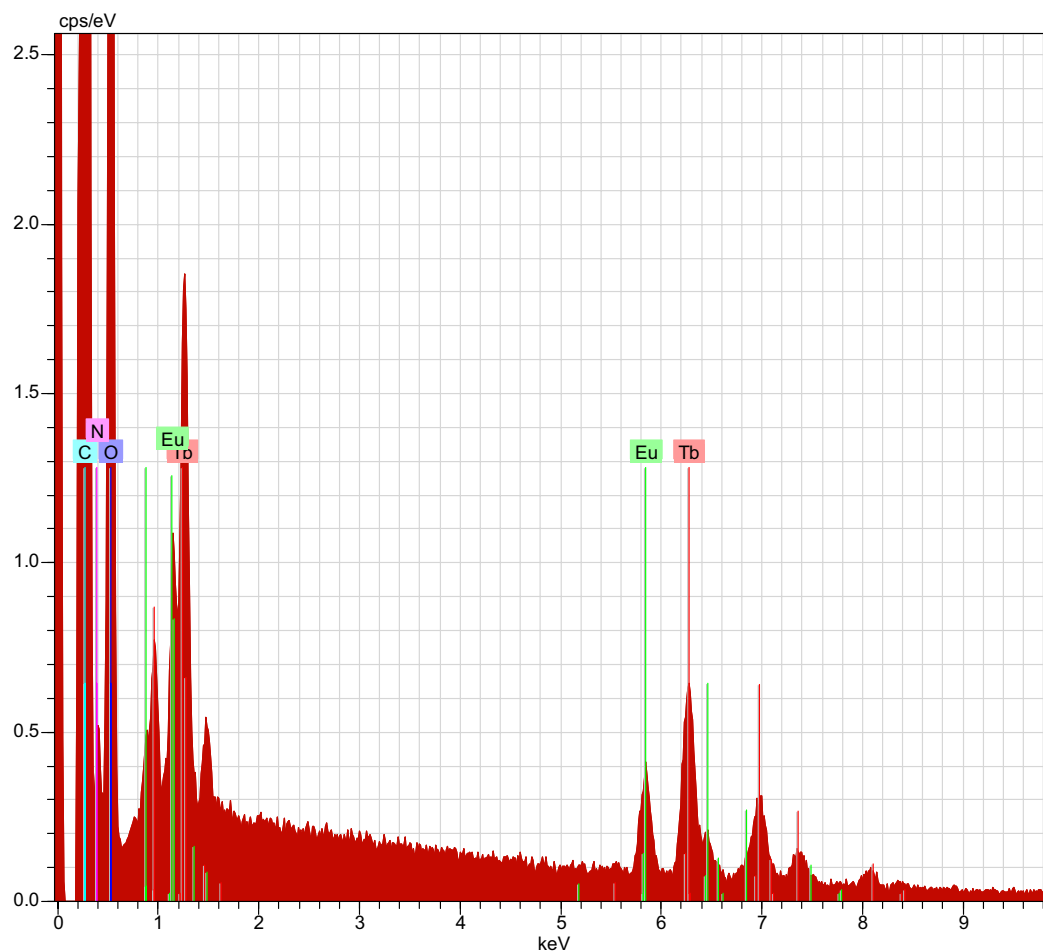
```
Spectrum: ∞[(Tb0,5Eu0,5)(DPA)(HDPA)]
Element     Series    Net   unn. C norm. C Atom. C Error
                            [wt.-%] [wt.-%] [at.-%]   [%]
--------------------------------------------------------
Terbium   L-series 15501    55,37   69,73   68,77   1,7
Europium  L-series  8246    24,04   30,27   31,23   0,8
--------------------------------------------------------
                    Total:  79,40  100,00  100,00
```

Figura 2.4A: EDS do ∞[(Tb$_{0,5}$Eu$_{0,5}$)(DPA)(HDPA)].

126

Capítulo 3

Síntese e Estudos Teórico e Experimental das Propriedades Espectroscópicas de Compostos Bifosfonatos com Lantanídeos
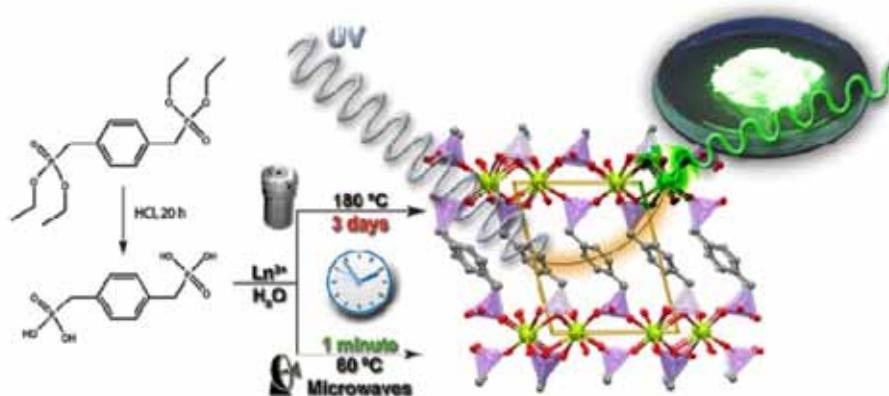
"Quem não pode com a macumba, não carregue o patuá"

3.1   Introdução

A construção de Materiais Metal-Orgânicos (MMOS) tem utilizado quase que hegemonicamente os ligantes policarboxilatos,[1-6] porém os derivados fosfonatos são bastante interessantes, pois os três átomos de oxigênio posicionados tetraédricos imitam os "*building blocks*" das zeólitas e possibilitam "ancorar" diversos metais (metais de transição e lantanídeos).[7-15] Recentes trabalhos desenvolvidos por Plasbt *et al*. relatam aspectos estruturais, sintéticos e a excepcional propriedades de troca iônica de sistemas baseados no ligante ácido 1,4-Fenileno-bis(metilidino)tetrakis-fosfônico com íons lantanídeos.[15-17]

O ácido 1,4-Fenil-bis(metileno)difosfônico (H_4pmd) tem sido utilizado na construção de MOMs com vários metais dos blocos *p* e *d* da tabela periódica– Cd^{2+},[18] Co^{2+},[19] Ni^{2+},[18] Ga^{3+},[20] Mn^{2+},[18] Pb^{2+} [21] e Zn^{2+}.[22] Surpreendentemente, os materiais $[Ce(Hpmd)(H_2O)]$ e $[Pr(Hpmd)(H_2O)]$ são os únicos exemplares de MOMs que utilização do H_4pmd como ligante.[23] Seguindo a filosofia de estudos espectroscópicos nos âmbitos teórico-experimental e na modulação das propriedades luminescentes de MMOs demonstrado anteriormente,[24-26] este capítulo é dedicado a investigações dos materiais $[Ln(Hpmd)(H_2O)]$ (Ln^{3+} = Eu^{3+} **(3.1)**, Gd^{3+} **(3.2)**, Tb^{3+} **(3.3)** e $(Eu_{0,05}Tb_{0,95})^{3+}$ **(3.4)**). Vale salientar que para o estudo teórico de transferência de energia, TE, envolvendo o par isolado de íons Tb^{3+}:Eu^{3+} na amostra **(3.4)**   foi utilizado a metodologia recentemente

desenvolvida por Malta[27] e os respectivos resultados foram confrontados com os experimentais.

3.2 Materiais e Métodos

3.2.1 Reagentes

Os cloretos dos lantanídeos foram obtidos da Aldrich. O ácido 1,4-Fenil-bis(metileno)difosfônico foi obtido da hidrólise ácida do derivado éster etílico como ilustrado na Esquema 3.1.
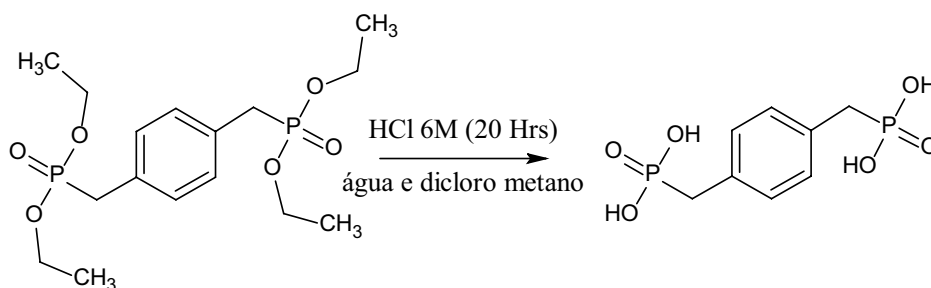
Figura 3.1: Ilustração do processo de obtenção do ácido 1,4-Fenil-bis(metileno)difosfonico a partir do derivado Tetraetil-*p*-xilenodifosfonato.

3.2.2 Sínteses

Os materiais foram preparados a partir da mistura contendo equimolar (1:1) dos cloretos de lantanídeos com o ácido 1,4-Fenil-bis(metileno)difosfonico em 12,00 mL de água destilada. As suspensões foram mantidas sob agitação magnética por 30 minutos e em seguida foram transferidas para reatores revestidos de teflon da Parr (23,00 mL) e aquecidos por 180 ºC por 72 horas.

130

As reações apresentaram rendimentos de aproximadamente 80% após os produtos serem lavados com acetona e secos ao ar. Todos os compostos são insolúveis em água e em solventes orgânicos. As curvas termogravimétricas e termogravimétricas diferenciais, análise elementar, espectros de infravermelho, EDS e padrões de raios-x de pós estão disponíveis no Anexo 3.

3.2.3 Instrumentação

3.2.3.1   Análise Elementar

As análises elementares de C, H, e N das redes de coordenação foram realizadas em um equipamento CHNS-O Analyzer Flash (112 Series EA Thermo Finningan).

3.2.3.2   Espectroscopia de Absorção na Região do Infravermelho

Os espectros de infravermelho foram obtidos em pastilhas de KBr com resolução de 4 cm^{-1} em um espectrofotômetro Brucker, modelo IF66.

3.2.3.3   Termogravimetria e Termogravimetria Derivada

As curvas TG/DTG foram obtidas na faixa de temperatura entre 25 e 1200°C, utilizando uma termobalança modelo TGA 50 da marca Shimadzu, sob atmosfera dinâmica de nitrogênio (50 mL.min^{-1}), razão de aquecimento de

$10^oC.min^{-1}$, utilizando cadinho de platina contendo massa de amostra em torno de 3 mg. A calibração do instrumento foi verificada antes dos ensaios, empregando-se um padrão de oxalato de cálcio monohidratado, conforme norma ASTM (The Americam Society for Testing and Materials, 1993).

3.2.3.4   *Espectroscopia de Luminescência*

Os espectros de excitação e emissão foram adquiridos à temperatura ambiente em um *Fluorolog-3 Spectrometer*, modelo FL3-2T com dupla excitação e emissão única   (TRIAX 320), acoplado a uma fotomultiplicadora R928P *Hamamatsu*. A fonte de excitação era de uma lâmpada de xenônio de 450 W. As fendas de excitação e emissão foram de 0,3 e 0,3 nm, respectivamente, e o passo de 0,1 nm.

Os espectros de emissão à temperatura variada (6 – 300K) foram obtidos em um Criostato *JANIS* RESEARCH ST 100, usando como fonte de excitação um Laser Nd:YAG, λ_{exc} =266 nm, o sinal foi filtrado em um monocromador duplo com 600 linhas e coletado em uma fotomultiplicadora.

3.2.3.5   *Tempos de Decaimento e Excitação dos Estados Excitados*

Os decaimentos dos estados excitados $^5D_0$ e $^5D_4$ dos íons Eu^{3+} e Tb^{3+}, respectivamente, foram adquiridos em temperatura variada (6 a 300K em um Criostato *JANIS* RESEARCH ST 100) utilizando um laser de Nd:YAG (λ_{exc} =

266 nm) com largura temporal de 5 ns e taxa de repetição em 20 Hz, filtrado em monocromador duplo, coletado em uma fotomultiplicadora e analisado por um osciloscópio Hewlett Packard 54501A 100 MHZ.

3.2.3.6   *Rendimentos Quânticos de Emissão*

Os rendimentos quânticos (q_x) foram obtidos através de medidas absolutas usando uma esfera de integração modelo C9920-02 da Hamamatsu com uma lâmpada de Xenônio de 150 W acoplada ao monocromador. As medidas foram realizadas em triplicata. O método apresenta erro de 10%.

3.2.3.7   *Difração de Raios-X por Pós e Refinamento das Estruturas*

A difração de raios-X de pó, as medidas foram realizadas à temperatura ambiente em um difratômetro X'Pert MPD Philips com ânodo rotatório de cobre ($\lambda_{k\alpha1}$ = 1,5404 Å, $\lambda_{k\alpha2}$ = 1,5444 Å, $I_{\alpha2}/I_{\alpha1}$ = 0,5), equipado com um detector X'Celerator. As intensidade foram coletadas através do método passo contínuo (passo 0,02º) num intervalo de 2θ entre 4 e 110º.

3.2.3.8 Microscopia Eletrônica de Varredura e Mapa de EDS

As imagens de microscopia eletrônica das amostras foram coletadas em suportes de alumínio revestido com fita de carbono, usando um microscópio eletrônico de varredura Hitachi S-4100 trabalhando a 25 kV. As amostras foram submetidas a deposição de carbono usando um Polaron Carbon Coater CC765,

3.2.3.9 Cálculo Teórico das Taxas de Transferência de entre Íons.

O procedimento teórico adotado para descrever os processos de transferência de energia (TE) entre os íons lantanídeos foi desenvolvido por Malta.[27] Estas equações são baseadas em expressões derivadas por Kushida,[28-30] entretanto sem incluir a influência da blindagem, para os mecanismos de transferência de energia por dipolo-dipolo (W_{d-d}), dipolo-quadrupolo (W_{d-q}), e quadrupolo-quadrupolo $[(W]_{q-q})$. As Equações (3.1), (3.2) e (3.3) utilizadas no método são mostradas a seguir:

$$W_{d-d} = \frac{(1-\sigma_1^D)^2(1-\sigma_1^A)^2}{[U_D][U_A]}\frac{4\pi e^4}{3\hbar R^6}\left(\sum_K \Omega_K^D \langle\psi_D J_D \| U^{(k)}\|\psi_D' J_D'\rangle^2\right)$$
$$\times\left(\sum_K \Omega_K^A \langle\psi_A' J_A' \| U^{(k)}\|\psi_A J_A\rangle^2\right)F \tag{3.1}$$

$$W_{d-q} = \frac{\left(1 - \sigma_1^D\right)^2 \left(1 - \sigma_2^A\right)^2}{[J_D^*][J_A]} \frac{2\pi}{\hbar} \frac{e^4}{R^8} \left(\sum_K \Omega_K^D \langle \psi_D J_D \| U^{(k)} \| \psi_D^* J_D^* \rangle^2 \right) \times \langle r^2 \rangle_A^2 \langle f \| C^{(2)} \quad (3.2)$$

$$\times \langle \psi_A^* J_A^* \| U^{(2)} \| \psi_A J_A \rangle^2 F$$

$$W_{q-q} = \frac{\left(1 - \sigma_2^D\right)^2 \left(1 - \sigma_2^A\right)^2}{[J_D^*][J_A]} \frac{28\pi}{5\hbar} \frac{e^4}{R^{10}}$$

$$\times \langle r^2 \rangle_D^2 \langle r^2 \rangle_A^2 \langle f \| C^{(2)} \| f \rangle^4 \langle \psi_D J_D \| U^{(2)} \| \psi_D^* J_D^* \rangle^2 \qquad (3.3)$$

$$\times \langle \psi_A^* J_A^* \| U^{(2)} \| \psi_A J_A \rangle^2 F$$

O índice A é utilizado para enfatizar a espécie aceitadora de energia, à medida que o índice D é utilizado para enfatizar a espécie doadora de energia. Nas equações acima [J] = 2(J) + 1. O R equivale a distância entre o íon doador e o aceitador de energia. A quantidade $\langle r^2 \rangle$ equivale a integral radial que expressa a distância entre o dado lantanídeo e os elétrons dos orbitais 4 f.[31] As quantidades (1 - σ_λ) são os fatores de blindagem (também conhecidos como fatores de Sternheimer) devidos os subníveis 5s e 5p preenchidos dos íons terra raras. As quantidades $\langle \psi^* J^* \| U^{(2)} \| \psi J \rangle$ são os elementos reduzidos de matriz, no esquema de aclopamento intermediário, dos operadores tensionais $U^{(l)}$, já $\langle l \| C^{(2)} \| l \rangle$ para lantanídeos $l = 3$ é o elemento de matriz reduzido dos operadores tensionais de Racah.[32] Os Ω_k são os parâmetros de Judd-Ofelt do dipolo elétrico forçado.

Os valores de σ_2, σ_4 e σ_6 utilizados foram os calculados por Edvardsson e Klintenberg.[33] Como estes pesquisadores não determinaram os valores de σ_1, foi

utilizada uma equação proposta por Malta[27] que relaciona os fatores de blindagem com as integrais de recobrimento radial, ρ, entre os subníveis 4f e os orbitais de valência do átomo ligante, para fazer tal previsão. Para o cálculo do σ_1 foi utilizada a Equação (3.4):

$$(1 - \sigma_k) = \rho(2\beta)^{k+1} \tag{3.4}$$

onde β é um número muito próximo de 1 e um valor típico do recobrimento ρ em compostos de lantanídeos é 0,05. Então fazendo $k = 1$ pode-se determinar o valor do σ_1.

A quantidade F presente nas equações anteriores são em geral obtidos a partir de informações do recobrimento espectral das bandas de absorção do aceitador e as bandas de emissão do doador, de acordo com a Equação (3.5):

$$F = \frac{ln2}{\sqrt{\pi}} \frac{1}{\hbar^2 \gamma_D \gamma_A} \left\{\left[\left(\frac{1}{\hbar\gamma_D}\right)^2 + \left(\frac{1}{\hbar\gamma_A}\right)^2\right] ln2\right\}^{-\frac{1}{2}} \times \exp\left[\frac{1}{4}\frac{\left(\frac{2\Delta}{(\hbar\gamma_D)^2}ln2\right)^2}{\left[\left(\frac{1}{\hbar\gamma_D}\right)^2 + \left(\frac{1}{\hbar\gamma_A}\right)^2\right]ln2} - \left(\frac{\Delta}{\hbar\gamma_D}\right)^2 ln2\right] \tag{3.5}$$

onde $\hbar\gamma$ representa a largura de banda à meia altura e o Δ a diferença de energia entre as transições de energia do doador e do aceitador envolvidos no processo de TE. Os valores típicos de F para um par de íons lantanídeos estão na faixa de 10^{-12} e 10^{-13} erg^{-1}. Os valores para as estimativas numéricas do processo de transferência de energia entre os dois íons lantanídeos encontram-se disponíveis na Tabela 3.1.

Tabela 3.1. Valores para as estimativas numéricas do processo de transferência de energia.

	$\lambda = 2$	$\lambda = 4$	$\lambda = 6$
$<1 \| C^{(\lambda)} \| 1>$	-1,366	1,128	-1,27
$< r^{(\lambda)} >$ (Európio)	0,9175	2,0200	9,0390
$< r^{(\lambda)} >$ (Térbio)	0,8220	1,6510	6,8520
σ_λ (Európio)	0,502	0,0190	-0,0308
σ_λ (Térbio)	0,486	0.0193	-0,0300

σ_1 (Térbio) = σ_1 (Európio) = 0,900

$J_D(^5D_4$ do Térbio) = 4; $J_A(^5D_0$ do Európio) = 0

$< ^5D_4 \| U^{(2)} \| ^7F_4 >^2$ Térbio = 0,0009; $< ^5D_0 \| U^{(2)} \| ^7F_j >^2$ Európio = 0,0032

$$\sum \Omega_k \langle \psi^* J^* \| U^{(2)} \| \psi J \rangle \approx 1 \times 10^{-20} cm^2$$

3.3   Resultados e Discussão

3.3.1 Estrutura Cristalográfica e Geometria Spakle/PM3

Os compostos [Ln(Hpmd)(H$_2$O)] (Ln^{3+} = Eu^{3+} **(3.1)**, Gd^{3+} **(3.2)**, Tb^{3+} **(3.3)** e (Eu$_{0,05}$Tb$_{0,95}$)$^{3+}$ **(3.4)**) possuem estruturas idênticas aos compostos [Ce(Hpmd)(H$_2$O)] e [Pr(Hpmd)(H$_2$O)] previamente descritos por Paz e colaboradores (Figura 3.2).[23]
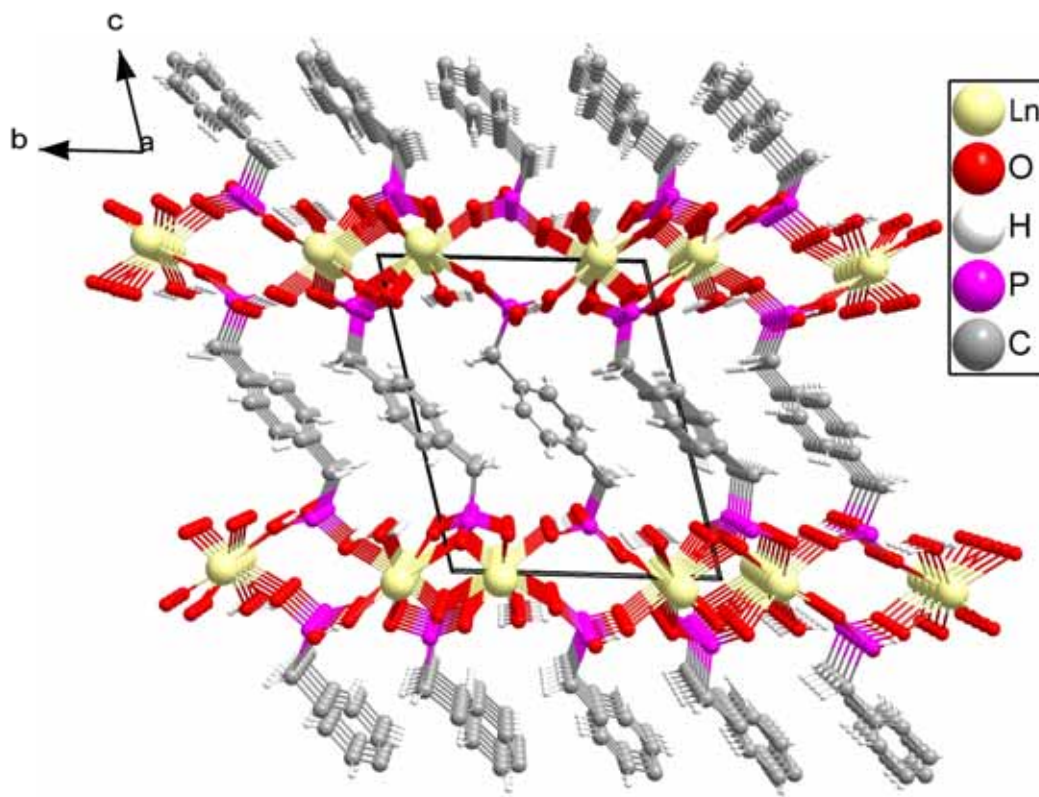
Figura 3.2: Ilustração da estrutura do [Ln(Hpmd)(H$_2$O)] vista ao longo do eixo cristalográfico *a*.

Os materiais possuem cristalograficamente apenas um íon Ln[3+] coordenado a sete átomos de oxigênio provenientes de uma molécula de água e cinco grupos fosfonatos. O poliedro {LnO$_7$} pode ser melhor descrito como prisma trigonal monoencapuzado distorcido, como pode ser observado na Figura 3.3.
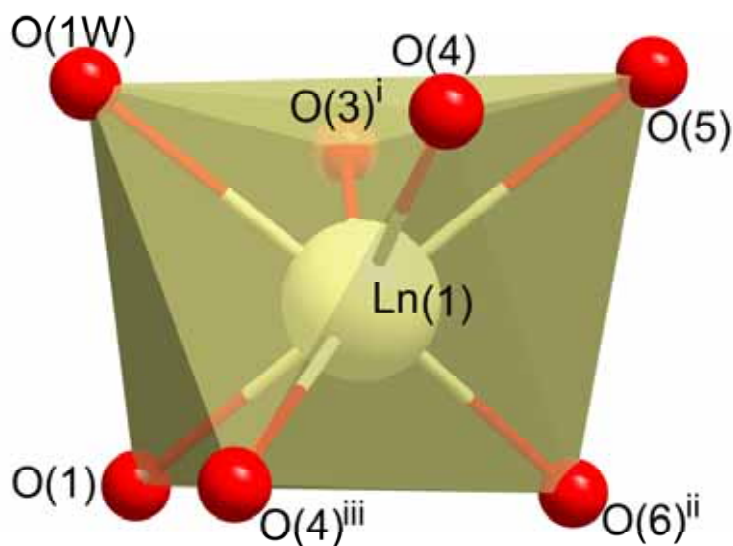
Figura 3.3: Poliedro de coordenação {LnO$_7$} dos materiais [Ln(Hpmd)(H$_2$O)]. Operações de simetria usadas para gerar átomos equivalentes: *2-x, 1-y, -z,* (ii) *3-x, -y, -z,* (iii) *2-x, -y, -z.*

Os padrões de pós foram facilmente indexados utilizando o DICVOL04 e o refinamento de Rietveld foi realizado usando como premissa o modelo de posições atômicas do [Ce(Hpmd)(H$_2$O)] utilizando o FullProf.2k. As estruturas abordadas neste capítulo foram depositadas ao banco de dados CCDC (Cambridge Crystallographic Data Centre) com as seguintes numerações CCDC-775633 e 775636 para **(3.1)** e **(3.4),** respectivamente. O padrão de difração de pós, o refinamento de Rietveld e a imagem de MEV para o composto **(3.1)** é mostrado na Figura 3.4. Os parâmetros de rede e as distâncias e ângulos selecionados estão dispostos nas Tabelas 3.2 e 3.3.
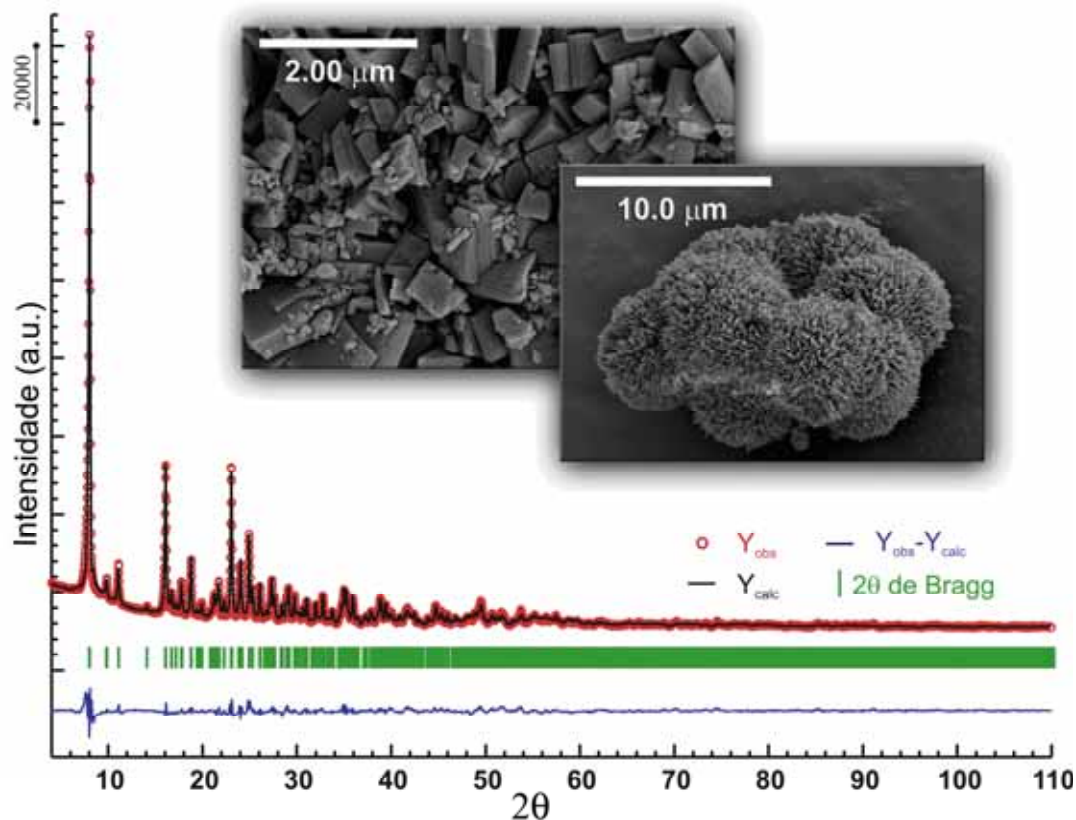
Figura 3.4: Padrão de difração de raios-x, resultado final do refinamento de

Rietveld e imagem de MEV para **(3.1)**.

Tabela 3.2. Dados cristalográficos e detalhes do refinamento de Rietveld para
[Ln(Hpmd)(H$_2$O)], onde Ln^{3+} = Eu^{3+} **(3.1)**, Gd^{3+} **(3.2)**, Tb^{3+} **(3.3)** e (Eu$_{0,05}$Tb$_{0,95}$)$^{3+}$ **(3.4)**

	Eu^{3+} **(3.1)**	Gd^{3+} **(3.2)**
Cela unitária		
Fórmula	C$_8$H$_{11}$EuO$_7$P$_2$[a]	C$_8$H$_{11}$GdO$_7$P$_2$[a]
Peso Molecular	433,07 [a]	438,36 [a]
Sistema Critalino	Triclinic	Triclinic
Grupo Espacial	P$\bar{1}$	P$\bar{1}$
a/Å	5,6110(4)	5,6010(4)
b/Å	9,3974(6)	9,3849(7)
c/Å	11,4933(8)	11,4837(8)
α/°	75,069(3)	75,205(4)

140

$\beta/°$	81,651(3)	81,625(4)
$\gamma/°$	80,964(4)	81,120(4)
Volume/Å³	574,80(7)	573,06(7)
Z	2	2
D_c/g cm⁻³	2,502 [a]	2,502 [a]
Função de Perfil	Cauchy	Cauchy
Parâmetros de Caglioti	U = 0,28(2)	U = 0,36(2)
	V = -0,188(7)	V = -0,230(8)
	W = 0,0442(7)	W = 0,0483(8)
Deslocamento do Zero [2θ°]	0,021(1)	0,020(2)
Fatores de Confiabilidade do Refinamento		
R_p	2,09	1,80
R_{wp}	2,91	2,56
R_{exp}	0,84	0,76
χ^2	12,2	11,5
Fatores de Confiabilidade Estrutural		
R_{Bragg}	11,7	12,1
R_F	16,4	19,3
Figuras de Mérito da Indexação		
M(n)	60,8 (n = 20)	66,7 (n = 15)
F(n)	115,6 (n = 20)	114,6 (n = 15)
	Tb^{3+} (3.3)	$(Eu_{0.05}Tb_{0.95})^{3+}$ (3.4)
Cela Unitária		
Fórmula	$C_8H_{11}TbO_7P_2$[a]	$C_8H_{11}Eu_{0,05}Tb_{0,95}O_7P_2$[a]
Peso Molecular	440,03 [a]	439,68 [a]
Sistema Cristalino	Triclínico	Triclínico
Grupo Espacial	$P\bar{1}$	$P\bar{1}$
a/Å	5,5882(5)	5,5886(5)
b/Å	9,3484(8)	9,3490(8)
c/Å	11,4594(10)	11,4605(10)
$\alpha/°$	75,325(4)	75,316(5)
$\beta/°$	81,698(4)	81,704(4)
$\gamma/°$	81,177(5)	81,175(5)
Volume/Å³	568,76(8)	568,88(9)
Z	2	2

D_d/g cm^{-3}	2,569 [a]	2,567 [a]
Parâmetros de Perfil		
Função de Perfil	Cauchy	Cauchy
Caglioti law parameters	U = 0,49(9)	U = 0,43(3)
	V = -0,33(1)	V = -0,30(1)
	W = 0,070(1)	W = 0,068(1)
Deslocamento do Zero [2θº]	-0,004(2)	-0,011(2)
Fatores de Confiabilidade do Refinamento		
R_p	2,22	2,38
R_{wp}	2,96	3,22
R_{exp}	0,74	0,78
χ^2	16,1	17,2
Fatores de Confiabilidade Estrutural		
R_{Bragg}	12,8	13,0
R_F	20,4	22,7
Figuras de Mérito da Indexação		
M(n)	106,3 (n = 11)	45,3 (n = 15)
F(n)	174,2 (n = 11)	80,3 (n = 15)

[a] Os átomos de hidrogênio foram adicionados empiricamente

Tabela 3.3. Distâncias interatômicas (Å) e ângulos (graus) selecionados para o ambiente de coordenação do Eu^{3+} em **(3.1)**.[a]

Eu(1)–O(1W)	2,4010(17)	Eu(1)–O(4)[iii]	2,4698(15)
Eu(1)–O(1)	2,1986(16)	Eu(1)–O(5)	2,5598(16)
Eu(1)–O(3)[i]	2,2356(15)	Eu(1)–O(6)[ii]	2,2448(17)
Eu(1)–O(4)	2,6100(16)		
O(1W)–Eu(1)–O(4)[iii]	90,32(5)	O(3)[i]–Eu(1)–O(4)[iii]	156,82(6)
O(1W)–Eu(1)–O(4)	79,07(5)	O(3)[i]–Eu(1)–O(5)	75,17(5)
O(1W)–Eu(1)–O(5)	102,32(5)	O(3)[i]–Eu(1)–O(6)[ii]	95,36(6)
O(1)–Eu(1)–O(1W)	83,59(6)	O(4)[iii]–Eu(1)–O(4)	74,47(6)

O(1)–Eu(1)–O(3)[i]	83,54(6)	O(4)[iii] –Eu(1)–O(5)	125,21(5)
O(1)–Eu(1)–O(4)	147,67(5)	O(5)–Eu(1)–O(4)	56,76(5)
O(1)–Eu(1)–O(4)[iii]	78,60(6)	O(6)[ii] –Eu(1)–O(1W)	167,72(6)
O(1)–Eu(1)–O(5)	154,90(5)	O(6)[ii] –Eu(1)–O(4)	110,37(5)
O(1)–Eu(1)–O(6)[ii]	91,37(6)	O(6)[ii] –Eu(1)–O(4)[iii]	99,68(6)
O(3)[i] –Eu(1)–O(1W)	72,99(6)	O(6)[ii] –Eu(1)–O(5)	77,77(6)
O(3)[i] –Eu(1)–O(4)	116,44(5)		

[a] Operações de simetria para gerar átomos equivalentes: (i) *2-x, 1-y, -z*, (ii) *3-x, -y, -z*; (iii) *2-x, -y, -z*.

Um fragmento contendo 244 átomos dentre os quais seis são íons Eu^{3+} foi submetido à otimização utilizando o modelo Sparkle/PM3.[34] Com objetivo de minimizar efeitos de desordem os fragmentos incompletos foram modificados similarmente ao processo realizado no fragmento do $[Eu_2(MELL)(H_2O)_6]$, **(1.1)** descrito no Capítulo 1. É importante salientar que um dos seis poliedros de coordenação foi escolhido como base de cálculo das propriedades espectroscópicas do material e suas coordenadas atômicas, polarizabilidade e fator de carga estão dispostos na Tabela 3.4. As distâncias médias Eu---Eu e Eu—O são 4,06 e 2,43 Å respectivamente, estando bem próximas com os valores obtidos da estrutura cristalográfica. Na Figura 3.5 estão evidenciados o fragmento calculado e a sobreposição dos poliedros de coordenação experimental e otimizado pelo Sparkle/PM3.

Tabela 3.4. Coordenadas atômicas para estrutura cristalográfica e otimizada pelo modelo Sparkle/PM3 (entre parênteses) e os fatores de carga (g) e polazabilidade (α) obtidos para **(3.1)**.

Atoms	X (Å)	Y (Å)	Z (Å)	g	α
Eu	0,000 (0,000)	0,000 (0,000)	0,000 (0,000)	–	–
O	-1,889 (-2,161)	0,650 (0,602)	1,514 (1,058)	0,356	3,261
O	-0,569 (-0,192)	-2,078 (-2,097)	1,396 (1,257)	1,793	3,524
O	1,668 (1,588)	-1,153 (-0,892)	1,651 (1,663)	1,164	5,895
O	1,936 (1,991)	0,215 (-0,129)	-1,433 (-1,380)	1,164	5,895
O	-1,750 (-1,681)	-1,339 (-1,373)	-1,156 (-1,066)	1,793	3,524
O	0,928 (0,601)	1,871 (1,823)	1,009 (1,430)	1,164	5,895
O	-0,896 (-0,876)	1,663 (1,664)	-1,418 (-1,473)	1,164	5,895
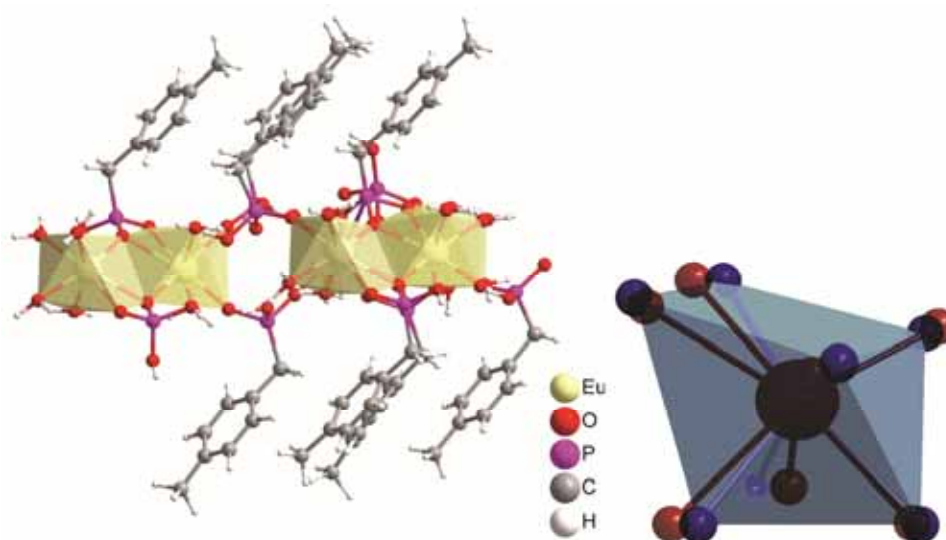
Figura 3.5: Fragmento da estrutura **(3.1)** otimizado pelo modelo Sparkle/PM3 e a comparação entre os poliedros de coordenação (Azul: Experimental; Vermelho: Calculado).

3.3.2 Propriedades Espectroscópicas

3.3.2.1 Propriedades Espectroscópicas dos Compostos (3.1), (3.2) e (3.3)

Na Figura 3.6 é mostrado o espectro de emissão de composto **(3.2)** entre 340-700 nm obtido a 77 K após excitação em 320 nm. O espectro mostra uma larga banda de fosforescência do ligante H_4pmd situada na região espectral dentre 350e 680 nm. A posição do tripleto (T_1) foi estimada a partir da transição 0-0 situada em 355 nm (28170 cm^{-1}).[35] Este resultado indica que a energia de excitação transferida do ligante para os níveis respectivos emissores $^5D_4$ (20400 cm-1) e $^5D_0$ (17300 cm^{-1}) do Tb^{3+} e Eu^{3+} não ocorre diretamente.
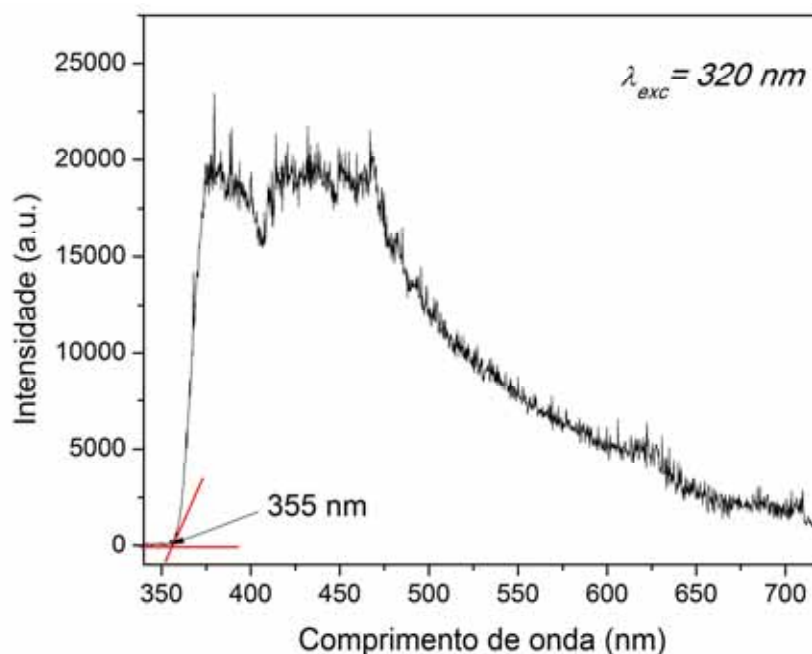
Figura 3.6: Espectro de emissão de **(3.2)** a 77 K.

A Figura 3.7 mostra os espetros de excitação de **(3.1)** e **(3.3)** adquiridos à temperatura ambiente monitorando as emissões dos íons Eu^{3+} e Tb^{3+} em 614 e 545 nm nas regiões de 200-600 nm e 200-520 nm, respectivamente.
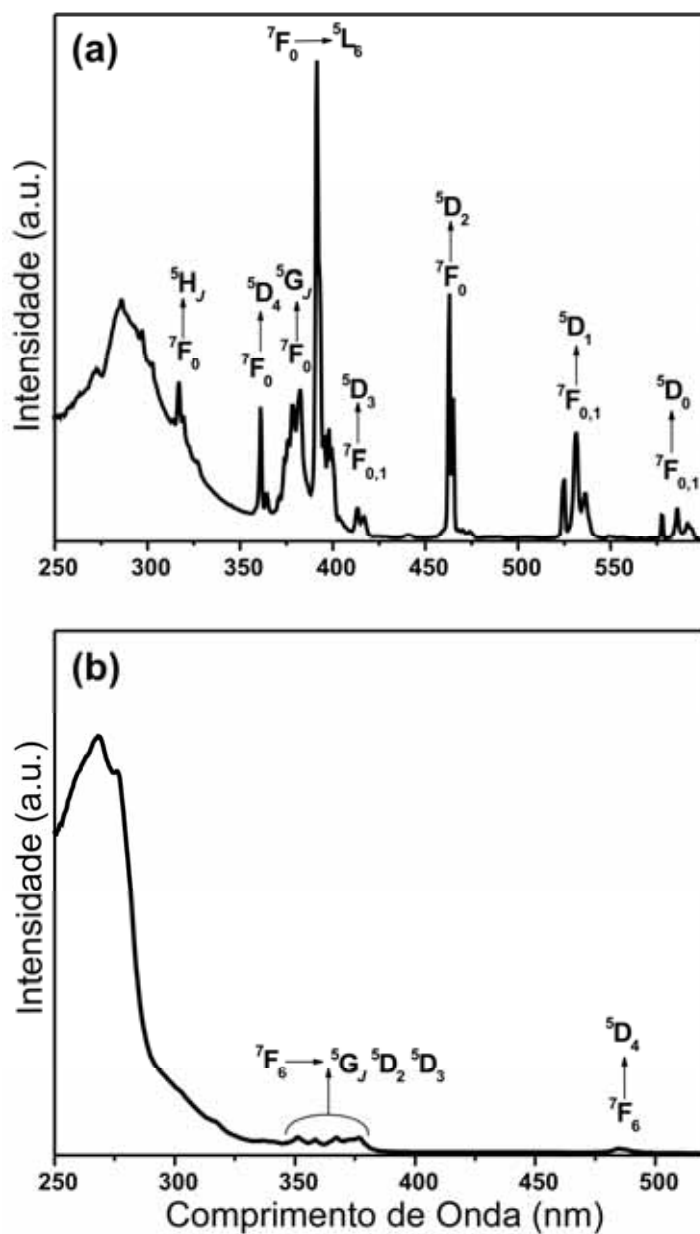
Figura 3.7: Espectro de excitação coletados a 300 K: (a): **(3.1)**; (b): **(3.3)**.

O espectro de excitação de (**3.1**), Figuras 3.7 (a), mostra uma banda larga entre 250-350 nm (λ_{max} = 286 nm),atribuída as transições $\pi \rightarrow \pi^{*}$ do ligante H4pmd, e linhas finas típicas das transições $^{7}F_{1,0} \rightarrow {}^{5}D_{4-0}$, $^{5}L_{6}$, $^{5}G_{2-6}$, $^{5}H_{3-7}$ e $^{5}F_{1-5}$ intra-$4f^{6}$ do íon Eu^{3+}. O perfil do espectro de excitação indica que a excitação indireta do íon (via ligante) não é o processo mais eficiente. No caso do espectro de excitação de (**3.3**) a banda centrada em 270 nm associada às transições do ligante e linhas muito fracas devidas às transições $f - f$ do Tb^{3+}, caracterizando a maior eficiência do processo indireto de excitação do íon Ln^{3+}.

A Figura 3.8 exibe os espetros de emissão do composto (**3.3**) adquiridos à 300 K na região espectral de 450-720 nm sob excitação em 266 nm e a imagem do material sob irradiação de luz UV (λ_{max} = 255 nm).
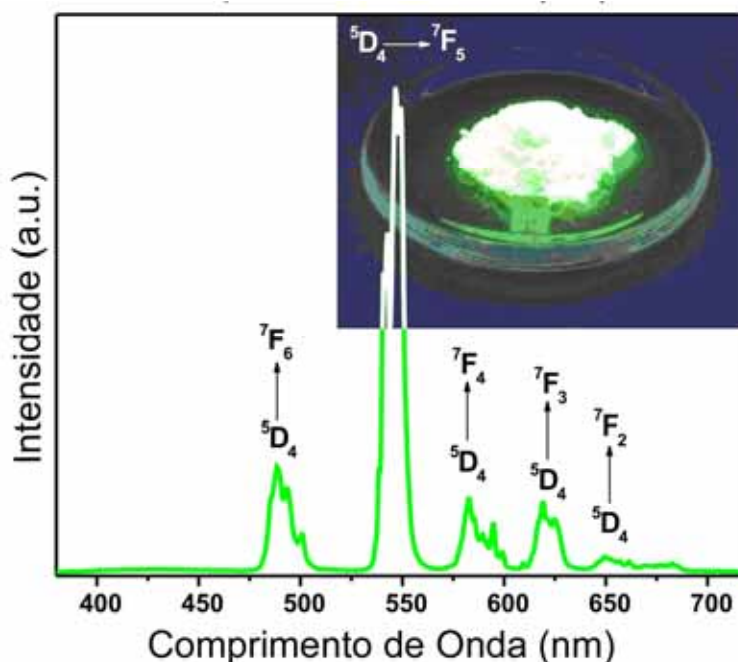
Figura 3.8: Espectros de emissão de (**3.3**) a 300 K e a imagem do comportamento do material sob irradiação de luz UV.

O espectro de emissão de (3.3) mostra as transições $^5D_4 \rightarrow {}^7F_J$ do Tb^{3+} responsáveis pela coloração verde (Figura 3.7). A transição $^5D_4 \rightarrow {}^7F_5$ (545 nm) é a mais intensa correspondendo a 58% do espectro integrado. A transição $^5D_3 \rightarrow {}^7F_4$ normalmente observada em 473 nm é ausente, sugerindo que existe processos eficientes de relaxação do $^5D_3$ para o $^5D_4$ que pode ser induzido pelas freqüências vibrônicas oriundas do ligante orgânico[36] ou por de desativação do estado excitado $^5D_3$ via transferência de energia ressonante com os íons Tb^{3+} adjacentes. [37-39]

Os tempos de vida em função da temperatura são sumarizados na Figura 3.9. As respectivas curvas e tempos de vida estão dispostos no Anexo 3 (Figura 3.4A e Tabela 3.1A.)
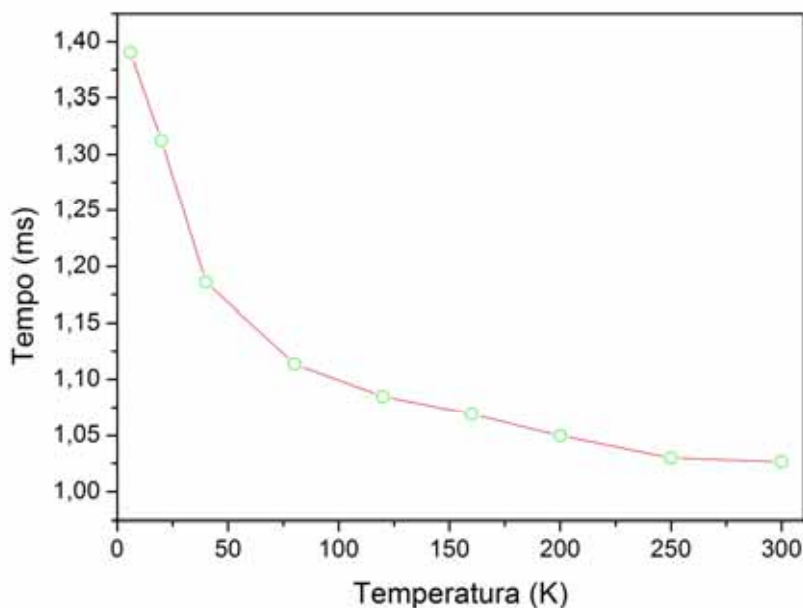
Figura 3.9: Tempos de vidas em função da temperatura de (3.3) a 300 K monitorando a emissão da transição $^5D_4 \rightarrow {}^7F_5$ (545 nm) e excitação em 266 nm.

Em todas as temperaturas as curvas de decaimento são de 1ª ordem em concordância com as evidências cristalográficas de apenas um único ambiente químico para o íon Ln^{3+}, além disso, o perfil mono-exponencial indica que a migração de energia entre os centros metálicos, $Tb^{3+} \leftrightarrow Tb^{3+}$, é bastante rápida devido a curta distância intermetálica ou completamente desprezível. Como pode ser observado na Tabela 3.4, os tempos de vida diminuem em função da temperatura em virtude do aumento da contribuição não-radiativa durante o processo de relaxação. O material **(3.3)** apresenta rendimento quântico absoluto relativamente baixo (14%) quando comparado ao dos materiais apresentados no Capítulo 2, isso pode ser justificado pelo forte interação do par $Tb^{3+} \leftrightarrow Tb^{3+}$ devido a curta distância cristalográfica (4,13Å) associado ao acoplamento com os modos vibracionais da molécula de água coordenada ao metal e pela posição do tripleto não estar em condição ideal de ressonância com o nível emissor.

Na Figura 3.10 está exposto o espectro de emissão do composto **(3.1)** adquiridos a 6 K na região espectral de 560-720nm sob excitação em 266 nm e a imagen do material sob irradiação de luz UV (λ_{max} = 255 nm).
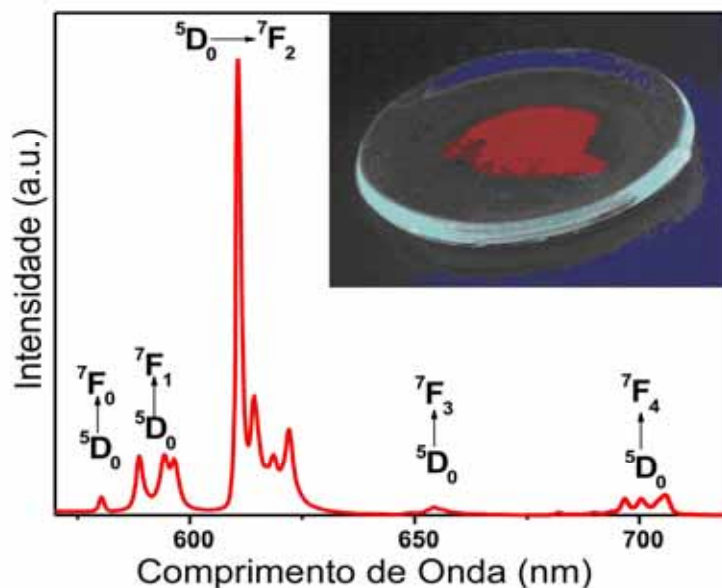
Figura 3.10: Espectros de emissão de **(3.1)** a 6 K e a imagem do comportamento do material sob irradiação de luz UV.

O espectro de emissão de **(3.1)** exibe linhas características das transições $^5D_0 \rightarrow {}^7F_J$ do íon Eu^{3+}. Vale salientar que as relativas intensidades e os desdobramentos das linhas de emissão dependem do grau da remoção da degenerescência ($2J + 1$) devido ao efeito da simetria do ambiente de coordenação no metal.[40] O espectro obtido a 6 K apresenta três componentes *Starks* bem definidas designadas à transição $^5D_0 \rightarrow {}^7F_1$ do Eu^{3+}, que indicam baixa simetria do grupo pontual que representa a primeira esfera de coordenação do íon. A presença de um única transição $^5D_0 \rightarrow {}^7F_0$ centrada em 580 nm a 6 K confirma a presença de apenas centro emissor inserido em ambiente químico com as possíveis simetria pontuais C_{nv}, C_n ou C_s.[41] De acordo com os resultados de cristalografia o poliedro de coordenação $\{EuO_7\}$

descrito como prisma trigonal monoencapuzado distorcido possui simetria pontual C_s em plena concordância com as informações derivadas do espectro de emissão.

Os parâmetros de intensidade experimentais e teóricos e Ω_2 e Ω_4 foram obtidos utilizando a mesma metodologia descrita no Capítulo 1 para o composto **(1.1)**, $[Eu_2(MELL)(H_2O)_6]$. A Tabela 3.5 disponibiliza os valores experimentais e teóricos dos parâmetros de intensidade, taxas radiativa e não-radiativas, (A_{rad} e A_{nrad}, respectivamente) eficiência quântica (η) e rendimento quântico para **(3.1)**.

Tabela 3.5. Parâmetros de intensidade Ω_2, Ω_4 e Ω_6, taxa radiativa (A_{rad}) e não-radiativa (A_{nrad}), eficiência quântica (η) e rendimento quântico (q). Valores teóricos derivados da geometria otimizada pelo modelo Sparkle/PM3. Os dados experimentais incluem o tempo de vida de emissão (τ_d) do íon Eu^{3+}.

Compound	Ω_2 (10^{-20} cm^2)	Ω_4 (10^{-20} cm^2)	Ω_6 (10^{-20} cm^2)	A_{rad} (s^{-1})	A_{nrad} (s^{-1})	τ_d (ms)	η (%)	q (%)
$[Eu(Hpmd)(H_2O)]$(*experimental*)	6,21	3,52	—	351	1961	0,51	16,0	1,0[a] 4,0[b]
$[Eu(Hpmd)(H_2O)]$(*Sparkle/PM3*)	6,39	3,28	1,54	291,7	1669,3	—	14,9	1,6

[a] λ_{exc} = 270 nm; [b] λ_{exc} = 394 nm

Os valores teóricos apresentados na Tabela 3.5 mostram boa concordância com os experimentais. O parâmetro Ω_2 é sensível a variações do ambiente químico e apresenta valores para **(3.1)** próximos ao relatados para

compostos baseado em carboxilatos que por sua vez são muito inferiores aos comumente encontrado em derivados β-dicetonatos. Isto pode ser interpretado como resultado de similaridades e discrepâncias nas geometrias de coordenação e polarizabilidade do ambiente químico do composto **(3.1)** em relação complexos derivados de carboxilatos e β-dicetonatos respectivamente.[42] O parâmetro Ω_4 é sensível a efeitos de longa distância pois seus valores refletem a rigidez da matriz.[43] Materiais mais rígidos apresentam valores baixos para Ω_4.[44] O valor de 3,52 10^{-20} cm² para **(3.1)** é maior que aqueles encontrados para sistemas rígidos (vidros, óxidos mistos cristalinos e sólidos estendidos)[45,46] e indica que embora haja rígidas camadas de fosfonatos coordenadas ao íon no material, também existe um relativo grau de flexibilidade atribuída ao ligante orgânico. Os baixos valores de tempos de vida (0,51 ms a 300 K) e taxa radiativa (A_{rad} = 315 s⁻¹), elevada contribuição das taxas não radiativas (A_{nrad} = 1961 s⁻¹), tripleto do ligante totalmente discrepante com os níveis $^5D_1$ e $^5D_0$ fornecem uma boa justificativa para os rendimentos quântico irrisório apresentado por **(3.1)**.

Os τ_d em função e as taxas de decaimento da temperatura são mostrados na Figura 3.11. As curvas de decaimento e os tempos de vida do material **(3.1)** podem ser acessados no Anexo 3 (Figura 3.5A e Tabela 3.2A).
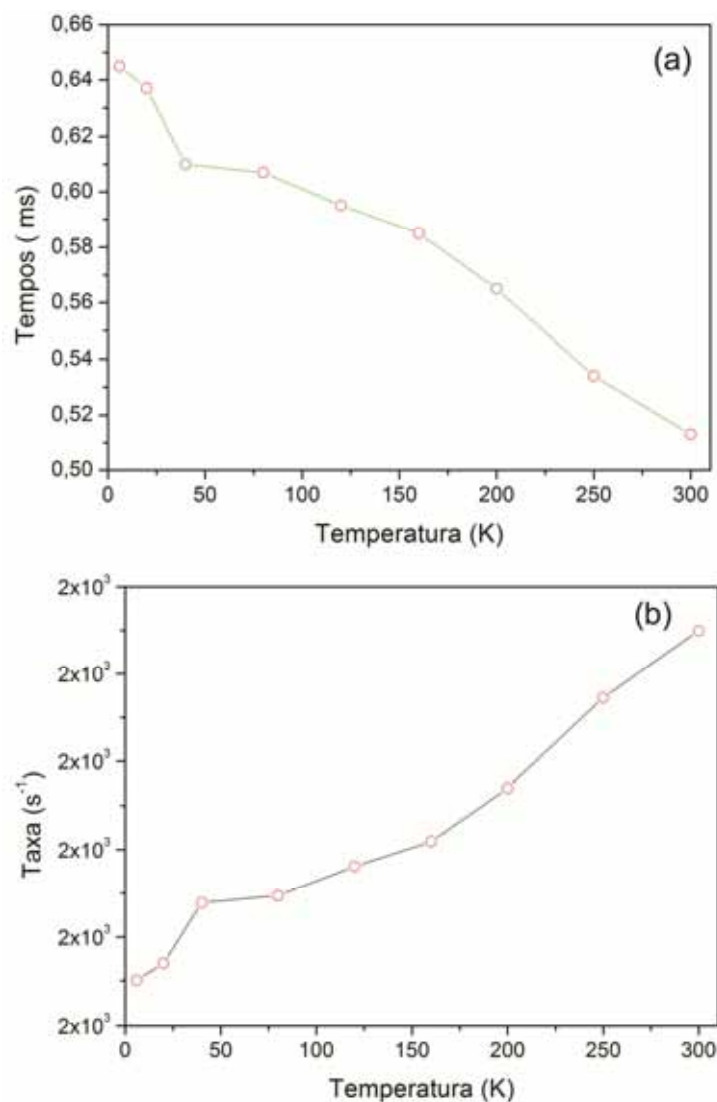
Figura 3.11: Tempos de vida (a) e Taxas de Decaimento (b) do composto **(3.1)** em função da temperatura obtidas pelo monitoramento da emissão da transição $^5D_0 \rightarrow {^7}F_2$ (610 nm) e excitação em 266 nm.

Os tempos de vida (τ_d) do **(3.1)** foram obtidos através de ajuste exponencial de 1ª ordem e são coerentes com apenas um ambiente de coordenação onde centro emissor está inserido. Similarmente ao composto **(3.3)** os tempos de decaimento são sensíveis a temperatura devido ao

acoplamento com fônons da matriz. A Figura 3.12 mostra as curvas normalizadas de excitação, os tempos de excitação (τ_r) e taxas (k_r). Na Figura 3.13 são exibidas as populações relativas (%) dos estados excitados $^5D_0$ e $^5D_1$ de acordo com os critérios de ajuste das curvas abordados no Capítulo 2.

Os valores da taxas de excitação, k_r, são dependentes da temperatura e estão em boa concordância com relatos na literatura.[47] Os valores das populações relativas extraídos do ajustes das curvas de excitação evidenciam que a TE $T_1 \rightarrow {}^5D_0$ é o caminho menos provável para explicar a emissão vermelha de (3.1). Claramente a excitação do $^5D_0$ é proveniente das relaxações dos estados de mais alta energia do Eu^{3+}, visto que a posição estimada do T_1 do ligante (28170 cm^{-1}) é mais ressonante com o nível $^5D_4$ (27586 cm^{-1}). É importante salientar que o modelo adotado simplifica esse mecanismo, pois admite que somente o nível $^5D_1$ é o principal canal de excitação do $^5D_0$, porém demonstra ser uma ferramenta útil para qualitativamente desvendar o caminho mais provável para excitação do principal nível emissor em sistemas em que a posição do tripleto seja ressonante aos níveis $^5D_1$ e $^5D_0$.
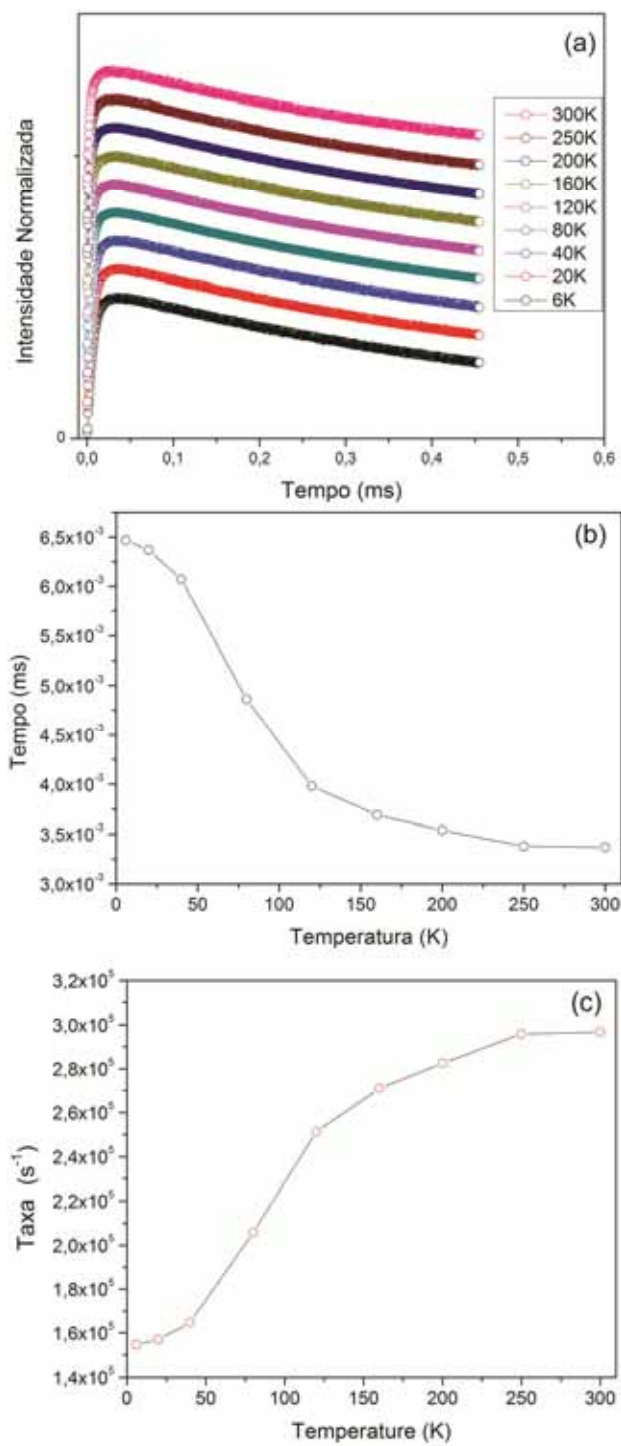
Figura 3.12: (a) Curvas de Excitação; (b) Tempos de excitação — (τ_r); (c) Taxas de excitação — (k_r) como funções da função da temperatura para o composto (3.1).
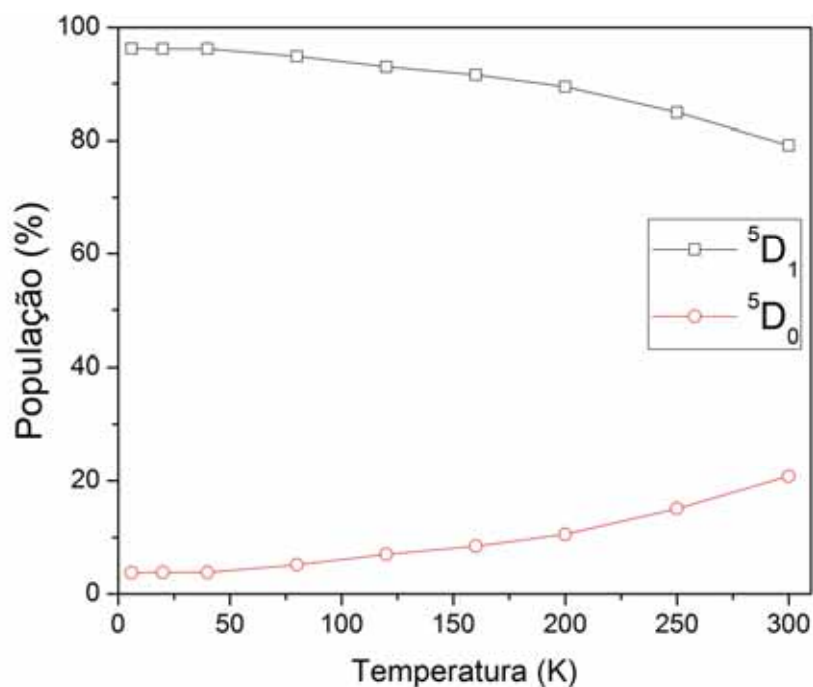
Figura 3.13: Populações relativas dos estados excitados $^5D_1$ e $^5D_0$ em função da temperatura.

Com o objetivo de elucidar com mais detalhes o processo de TE entre o Hpmd e o Eu^{3+} foi necessário modificar a metodologia para resolução das equações de taxas desenvolvido por Malta[48,49] aplicada ao composto $[Eu_2(MELL)(H_2O)_6]$ através da inserção de novos canais de transferência de energia ($T_1 \rightarrow {}^5D_4$), fato esse justificado pela posição estimada do tripleto do Hpmd estar mais ressonante com o estado $^5D_4$ do Eu^{3+} íon. Na Tabela 3.6 estão dispostos os valores da taxas de transferência e retrotransfêrencia para

(3.1) entre o estado tripleto (T_1) para os níveis $^5D_4$, $^5D_1$ e $^5D_0$ do Eu^{3+} e do nível singleto (S_1) para o $^5D_4$.

Tabela 3.6. Valores calculados das taxas de transferência de energia (W_{ET}) e retrotrasnferência (W_{BT}) para [Eu(Hpmd)(H_2O)] **(3.1)**.

Níveis do Ligante (cm^{-1})	Estados 4f (cm^{-1})	RL (Å)	Taxas de Transferência (s^{-1})	Taxas de Retrotrasnferência (s^{-1})
S_1 (39575 cm^{-1})	$\rightarrow$ $^5D_4$ (27600)	6,24381	W_{ET1} = 1,049×10^3	W_{BT1} = 0,000
T_1 (29085 cm^{-1})	$\rightarrow$ $^5D_4$ (27600)	8,66435	W_{ET2} = 1,063×10^7	W_{BT2} = 0,887
T_1 (29085 cm^{-1})	$\rightarrow$ $^5D_1$ (19070)	8,66435	W_{ET3} = 2,427×10^5	W_{BT3} = 0,000
T_1 (29085 cm^{-1})	$\rightarrow$ $^5D_0$ (17300)	8,66435	W_{ET4} = 1,902×10^4	W_{BT4} = 0,000

Os valores estimados teóricos para as energias do singleto (S_1) e tripleto (T_1) do ligante Hpmd são 39575 e 29085 cm^{-1} respectivamente, sendo o último em boa concordância com o valor experimental (28170 cm^{-1}). Os cálculos mostram que o canal de TE S_1→$^5D_4$ não é eficiente , fato esse justificado pelo curto tempo de vida do estado singleto e energia não ressonante com os níveis do Eu^{3+} considerados no cálculo. Os valores das taxas indicam que o principal canal de transferência de energia é o T_1→$^5D_4$, enquanto os canais T_1→$^5D_1$ e T_1→$^5D_0$ é menos favorecidos devido à larga diferença de energia entres os respectivos níveis. O proposto mecanismo está representado pelo diagrama de energia ilustrado na Figura 3.14.
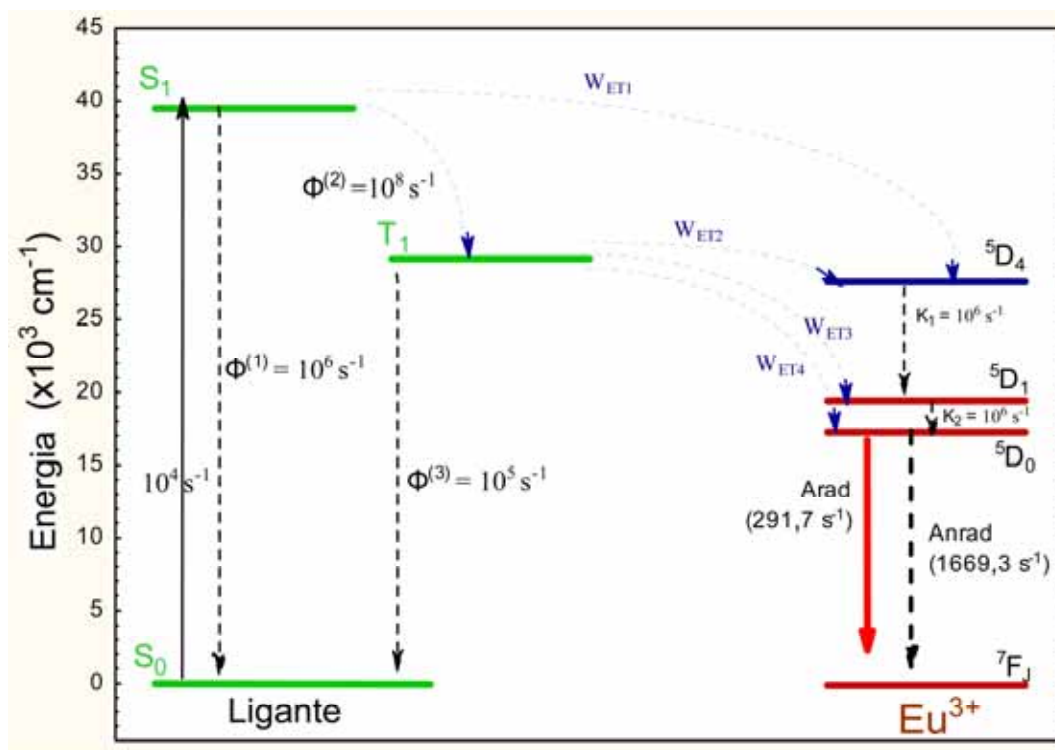
Figura 3.14: Diagrama de transferência de energia para a estrutura calculada pelo modelo Sparkle/PM3 para o composto **(3.1)**

3.3.2.2 Propriedades Espectroscópicas do Composto (3.4)

Os espectros de excitação normalizados de **(3.4)** obtidos a temperatura ambiente via monitoramento da emissão do Tb^{3+} em 545 nm e do Eu^{3+} em 610 são mostrados na Figura 3.15 (a) e (b) respectivamente.
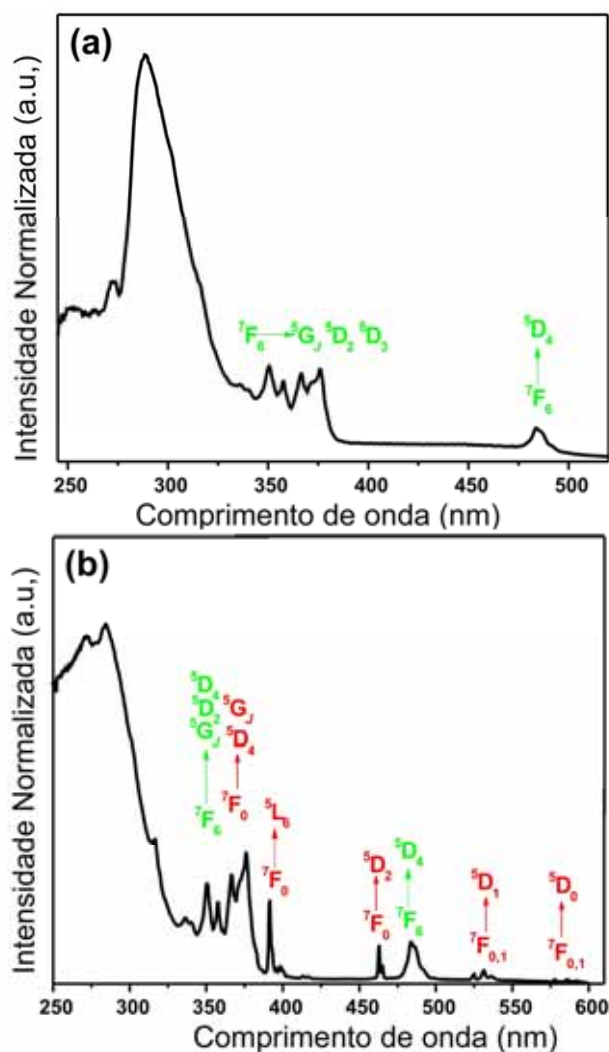
Figura 3.15: Espectros de excitação de **(3.4)** obtidos via monitoramento das transições (a) $^5D_4 \rightarrow ^7F_5$ em 545nm do Tb^{3+} e (b) $^5D_0 \rightarrow ^7F_2$ em 610 do íon Eu^{3+}.

O espectro monitorando a emissão do Tb^{3+} mostra aspecto similar ao do composto **(3.3)** onde pode ser observada a banda em 290 nm designada as transições π-π^* do ligante Hpmd e linhas absorção características das transições $4f^8$ do íon Tb^{3+}. O espectro de excitação monitorando a emissão do Eu^{3+} (Figura 3.14(b)) apresenta evidencias interessantes associadas a TE do

Tb^{3+} para o Eu^{3+}, pois exibe simultaneamente uma série de linhas típicas de ambos os centros metálicos.

A Figura 3.16 mostra espectros de emissão normalizados de (3.3) obtido à temperatura ambiente através de excitações em 290, 391 e 483 nm e a imagem do composto sob irradiação de luz UV em 255 nm.
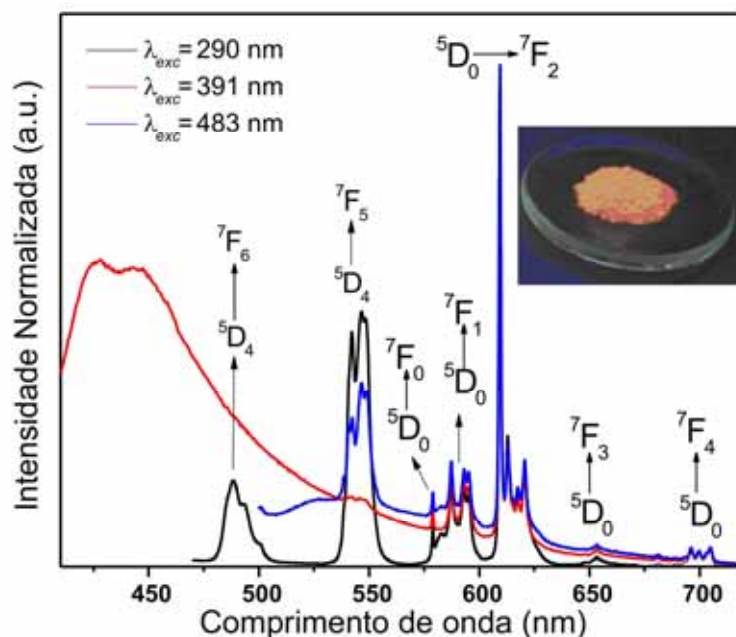
Figura 3.16: Espectros de emissão de (3.4) obtidos via monitoramento das transições (a) $^5D_4{\rightarrow}^7F_5$ em 545nm do Tb^{3+} e (b) $^5D_0{\rightarrow}^7F_2$ em 610 do íon Eu^{3+}.

É interessante observar a tonalidade rósea do material (3.4) mesmo embora a amostra contenha 95% de íons Tb^{3+} em seus centros metálicos. Os espectros mostram linhas características das transições $^5D_4{\rightarrow}^7F_J$ e $^5D_0{\rightarrow}^7F_J$ dos íons Tb^{3+} e Eu^{3+} respectivamente, além disso é possível observar a significativa supressão da luminescência do íon Tb^{3+} em presença de apenas 5% do Eu^{3+},

justificando a cor rosa do material e indicando a presença de canais eficientes de transferência de energia entre os íons. Estes resultados corroboram com o indício de TE entre os metais conforme observado nos espectros de excitação monitorando a emissão do Eu^{3+} (Figura 3.14 (b)). Nos espectros de **(3.4)** as transições $^5D_0 \rightarrow {}^7F_J$ do Eu^{3+} apresentam intensidades relativas e componentes *Starks* similares as encontradas no composto com 100% Eu^{3+}, **(3.1)**. Vale destacar que estes resultados estão consistentes com as investigações cristalográficas (Tabela 3.2 e Figura 3.1A) e mostraram que substituições dos íons não causam significativas alterações estruturais no material.

De maneira geral, as teorias de TE entre espécies doadoras e receptoras seguem a premissa da sobreposição dos espectros de absorção do receptor com o de emissão do doador (Figura 3.17).
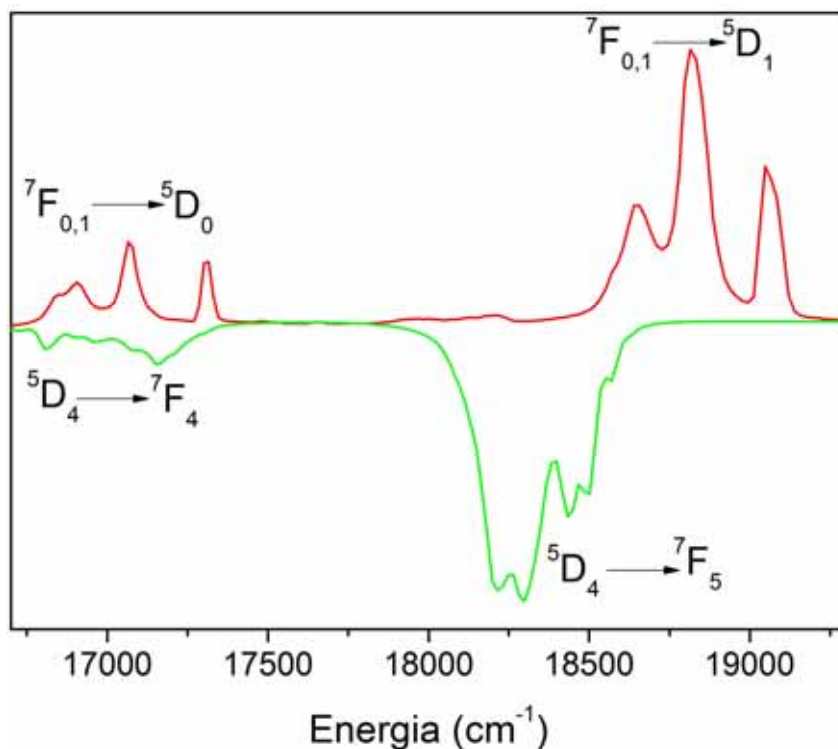
Figura 3.17: Ilustração da sobreposição dos espectros de absorção do Eu^{3+} (vermelho) e emissão do Tb^{3+} (verde) obtida dos espectros dos materiais que contém 100% dos íons **(3.1)** e **(3.3)**, respectivamente.

Como pode ser observado na Figura 3.16 para o composto **(3.4)** esta condição é satisfeita na região espectral entre 530 e 600 nm onde as transições $^5D_4 \rightarrow {}^7F_5$ e $^5D_4 \rightarrow {}^7F_4$ do Tb^{3+} sobrepõem respectivamente as linhas de excitação $^7F_{0,1} \rightarrow {}^5D_1$ e $^7F_{0,1} \rightarrow {}^5D_0$ do Eu^{3+}. A sobreposição entre as transições $^5D_4 \rightarrow {}^7F_4$ do Tb^{3+} predominante governada pelo mecanismo de dipolo elétrico (DE), e a $^7F_1 \rightarrow {}^5D_0$ do Eu^{3+} regida pelo mecanismo de dipolo magnético (DM) não deve contribuir significantemente para taxas de transferência de energia, visto que apenas a pequena parcela da componente de dipolo magnético da $^5D_4 \rightarrow {}^7F_4$ do Tb^{3+} deve participar do processo de TE,

logo a interação DE-DM não seria significativa. No entanto a participação de mecanismos controlados por dipolo elétrico gerados pelo acoplamento eletron-fônon ligante-lantanídeos designados como transições vibrônicas [50] podem favorecer os processo de TE entre o íons.[51] As componentes vibrônicas das transições $^7F_1 \rightarrow {}^5D_0$ e $^7F_0 \rightarrow {}^5D_0$ do Eu^{3+} [52,53] são sobrepostas pela $^5D_4 \rightarrow {}^7F_4$ do Tb^{3+}, gerando interações entre as transições do tipo DE-DE que por sua vez podem ser consideradas como canais eficientes de TE do Tb^{3+} para o Eu^{3+}.

A Figura 3.18 mostra os tempos de vida (τ_d) em função da temperatura monitorando a emissão do Tb^{3+} e do Eu^{3+} em 545 e 610 nm e excitação em 266 nm para o composto (3.4). As curvas de tempos de vida em função da temperatura para os íons Tb^{3+} e Eu^{3+} estão disponibilizados nas Figuras 3.7A e 3.8A e Tabelas 3.3A e 3.4A no Anexo 3, respectivamente.

Os τ_d para os respectivos íons foram obtidos em todas as temperaturas via ajustes monos-exponenciais das curvas. Como pode ser constado na Figura 3.18 (a) e (b), os tempos são reduzidos em função da temperatura devido ao aumento de contribuições não-radiativas associadas aos fônons da rede, vale destacar que esse comportamento é similar aos tempos de vida dos compostos (3.1) e (3.3) previamente abordados. Comparativamente, os τ_d do Tb^{3+} na amostra (3.4) são consideravelmente menores que aqueles apresentados pelo material (3.3). Isso pode ser explicado pela presença de eficientes canais transferência de energia $Tb^{3+} \rightarrow Eu^{3+}$. Em contrapartida, os τ_d

versus temperatura do Eu^{3+} em **(3.4)** são aumentados em média de 33% em comparação aos do composto **(3.1)** justificado pela redução do efeito de interação do par $Eu^{3+}\leftrightarrow Eu^{3+}$ (supressão por concentração) e pela contribuição do estado $^5D_4$ do Tb^{3+} na no processo de excitação do nível $^5D_0$ do Eu^{3+}.
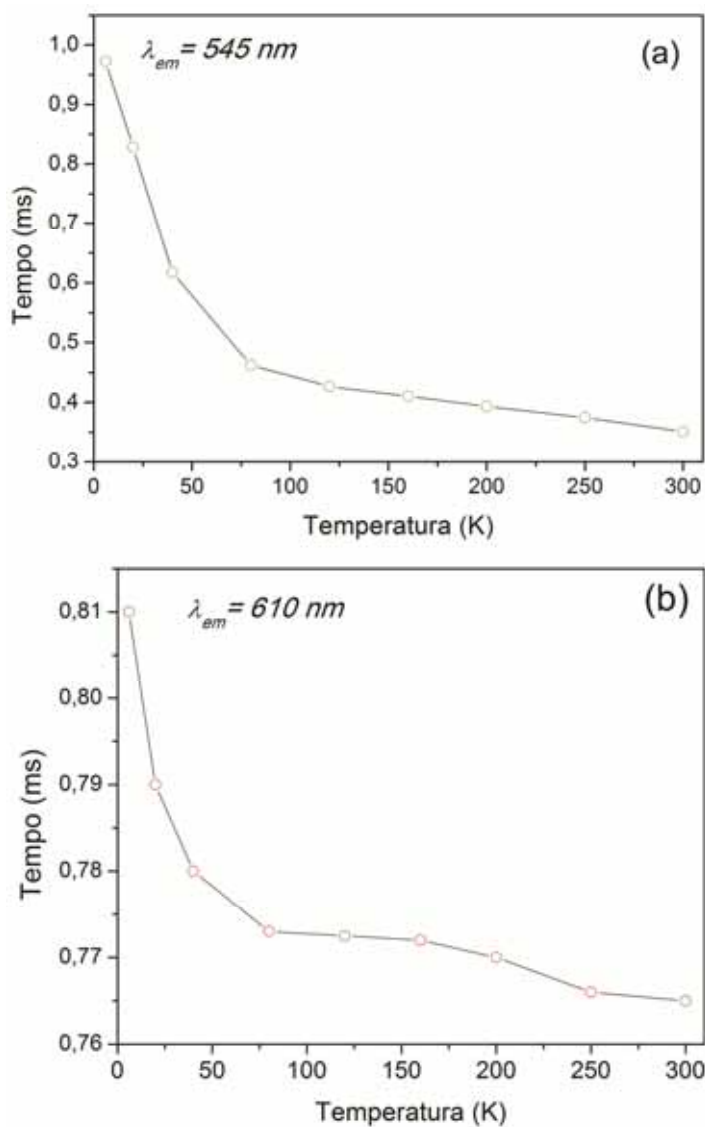
Figura 3.18: Tempos de vida em função da temperatura sob excitação em 266 nm: (a) Tb^{3+} λ_{em}= 545 nm; (b) Eu^{3+} λ_{em}= 610 nm.

As parcelas de excitação nas curvas do Eu^{3+} em **(3.4)** foram ajustadas de acordo com os critérios abordados no Capítulo 2. Na Figura 3.19 são exibidas as populações relativas dos níveis $^5D_1$ e $^5D_0$ em função da temperatura.
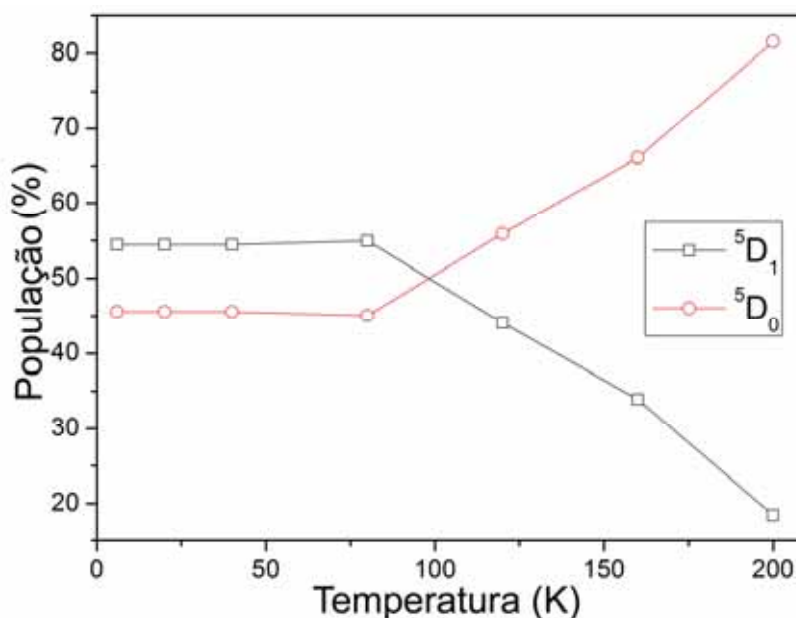
Figura 3.19: Populações relativas dos níveis $^5D_1$ (Vermelho) e $^5D_0$ (Azul) em função da temperatura.

Os dados mostrados na Figura 3.19 denotam o efeito da transferência de energia do nível $^5D_4$ do Tb^{3+} sobre os níveis $^5D_1$ e $^5D_0$. Fica evidente que a privilegiada condição de ressonância entre estes estados favorecem os canais de transferência $^5D_4{\rightarrow}^5D_1$ e $^5D_4{\rightarrow}^5D_0$. Em comparação com as populações relativas encontradas para o composto **(3.1)** (Figura 3.13) é possível perceber o aumento substancial das populações do nível emissor $^5D_0$ oriundas da excitação do íon pelo nível $^5D_4$ do Tb^{3+}, além disso, acima de 80 K ocorre inversão entre as mesmas. Isto pode ser facilmente explicado pelo aumento

165

das populações termicamente ativadas do multipleto $^7F_1$ facilitando a TE $Tb^{3+} \rightarrow$ Eu^{3+}.[51]

As taxas e as eficiências de TE (k_{TE} e η_{TE}) referentes ao processo $Tb^{3+} \rightarrow$ Eu^{3+} em **(3.4)** foram estimadas de acordo com as Equações (2.2) e (2.3) discutidas previamente no Capítulo 2. A Figura 3.20 mostra k_{TE} e η_{TE} em função da temperatura.
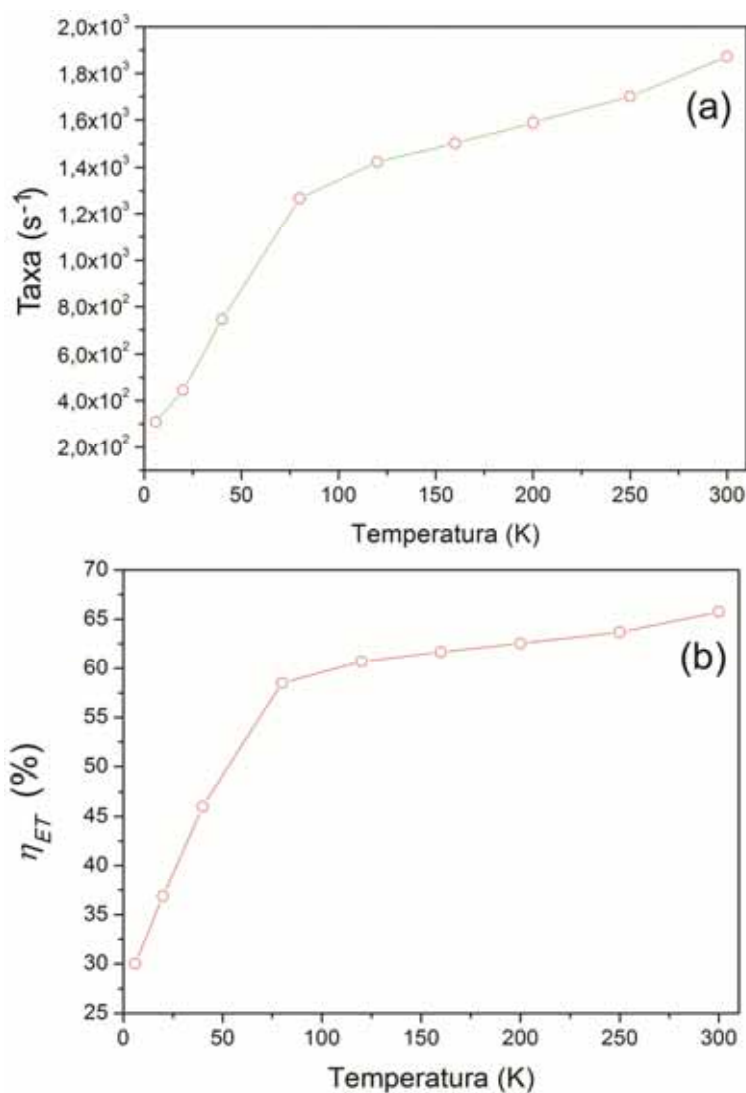
Figura 3.20: (a) Taxa e (b) eficiência de transferência de energia do processo $Tb^{3+} \rightarrow Eu^{3+}$ em função da temperatura.

A taxa e a eficiência do processo de transferência $Tb^{3+} \rightarrow Eu^{3+}$ aumentam em função da temperatura, variando entre $3,08 \times 10^2$ e $1,872 \times 10^3$ s^{-1} e 30—66 % respectivamente, em conseqüência à compensação da diferença de energia por fônons e pelo aumento das populações termicamente ativadas do multipleto $^7F_1$ do Eu^{3+}.

Neste estágio de discussão é fundamental deixar claro que essas taxas de transferência de energia obtidas pelas diferenças entre os recíprocos dos tempos de vida da amostra com e sem a espécie receptora induzem a uma interpretação equivocada do processo de TE, pois estes tempos e taxas são valores médios de todos os sítios que emitem na amostra. O modelo representado pela amostra **(3.4)** possui apenas uma pequena parcela, ≈5,0%, de seus sítios ocupados por espécies receptoras (íons Eu^{3+}) e distribuições aleatórias e distintas de subpopulações de espécies doadoras (íons Tb^{3+}) no retículo cristalino, em que cada subpopulação pode ser definida em termos de número e de localizações de aceptores ao redor do íon doador. Portanto, mensurar a magnitude de um único e microscópico processo de TE $Tb^{3+} \rightarrow Eu^{3+}$ na amostra em questão é impossível, pois cada subpopulação de espécie doadoras, em geral, serão caracterizas por processos de TE locais e evidentemente as taxas obtidas pela Equação (2.2) refletem essa média. Outro ponto importante e bastante controverso é avaliar as contribuições dos mecanismos Dipolo–Dipolo (D-D), Dipolo–Quadripolo (D-Q), Quadripolo–Quadripolo (Q-Q) e Troca, em processos de TE. A fim de contornar

esse dois problemas foi aplicado o procedimento teórico desenvolvido por Malta[27] para descrever processos de TE entre íons lantanídeos. Na Tabela 3.7 estão sumarizados os valores das taxas de transferência de energia por mecanismos considerando os canais $Tb^{3+}/^5D_4 \rightarrow Eu^{3+}/^5D_1$ e $Tb^{3+}/^5D_4 \rightarrow Eu^{3+}/^5D_0$. As distâncias R equivalentes ao par doador–receptor foram utilizadas os valores de distâncias mais curtos obtidos por cristalografia (4,13 Å) e calculados via modelo Sparkle/PM3 (3,87 Å).

Tabela 3.7 Valores calculados das taxas de transferência para os tipos de mecanismos no processo $Tb^{3+} \rightarrow Eu^{3+}$ em **(3.4)**.

	Taxas para R_{exp} (4,13 Å)	Taxas para R_{teor} (3,87 Å)
Tb $^5D_4 \rightarrow$ Eu $^5D_1$		
W_{D-D}	$1,558 \times 10^2$ (s^{-1})	$2,232 \times 10^2$ (s^{-1})
W_{D-Q}	$3,972 \times 10^2$ (s^{-1})	$6,412 \times 10^2$ (s^{-1})
W_{Q-Q}	$3,827 \times 10^2$ (s^{-1})	$6,963 \times 10^2$ (s^{-1})
W_{troca}	0,47 (s^{-1})	20,79 (s^{-1})
Tb $^5D_4 \rightarrow$ Eu $^5D_0$		
W_{D-D}	$2,7260 \times 10^2$ (s^{-1})	$3,904 \times 10^2$ (s^{-1})
W_{D-Q}	$5,851 \times 10^2$ (s^{-1})	$9,445 \times 10^2$ (s^{-1})
W_{Q-Q}	$5,637 \times 10^2$ (s^{-1})	$1,026 \times 10^3$ (s^{-1})
W_{troca}	0,27 (s^{-1})	12,12 (s^{-1})

Os valores das taxas para um único processo $Tb^{3+} \rightarrow Eu^{3+}$ calculadas pelo modelo do Malta estão na mesma ordem de magnitude daqueles obtidos experimentalmente por meio da Equação (2.2). Estes resultados são fortes indícios de que a transferência de energia experimental ocorre

predominantemente entre os doadores e receptores mais próximos, além disso, ficou evidenciado que para os canais investigados os mecanismos D-Q e Q-Q são dominantes.

Embora tenha sido constado que o processo de TE $Tb^{3+} \rightarrow Eu^{3+}$ alcance eficiência na ordem de ≈70% e tenha aumentado os tempos de emissão do Eu^{3+}, de fato isso pouco impactou no rendimento quântico absoluto (q = 2,0%) apresentado pela amostra **(3.4).**

3.4   Conclusão

Os MMOs $[Ln(Hpmd)(H_2O)]$ (Ln^{3+} = Eu^{3+} **(3.1)**, Gd^{3+} **(3.2)**, Tb^{3+} **(3.3)** e $(Eu_{0,05}Tb_{0,95})^{3+}$ **(3.4)**) foram obtidos via síntese hidrotermal. Os compostos são iso-estruturais ao $[Ce(Hpmd)(H_2O)]$ e cristalizam   em sistema triclínico com grupo espacial $P\bar{1}$. Os materiais possuem cristalograficamente apenas um íon Ln^{3+} coordenado sete átomos de oxigênio provenientes de uma molécula de água e cinco grupos fosfonatos. O poliedro $\{LnO_7\}$ pode ser melhor descrito como prisma trigonal monoencapuzado distorcido. Um fragmento de **(3.1)** otimizado pelo modelo Sparkle/PM3 apresenta boa concordância com a estrutura cristalográfica. A geometria otimizada do poliedro de coordenação foi utilizada   como   premissa   para   simular   propriedades   espectroscópicas (parâmetros de intensidade, taxa radiativa, eficiência quântica e rendimento quântico)   de   **(3.1)**   e   os   resultados   são   similares   aos   obtidos experimentalmente. O composto **(3.3)** apresenta coloração verde quando

submetido à radiação UV, porém baixo rendimento quântico devido a processos eficientes de supressão da luminescência. O espectro de emissão, curvas de tempos de vida do material **(3.4)** mostram a existência de processo eficiente de TE (η=70%) oriundo do Tb^{3+} para o Eu^{3+}. As taxas calculadas a partir do modelo desenvolvido pelo Malta estão em boa concordância com aas obtidas experimentalmente e ainda indicam que os mecanismos de Dipolo-Qdripolo e Quadripolo-Quadripolo são dominantes.

3.5   Referências

(1)   Ferey, G., Hybrid porous solids: past, present, future, *Chemical Society Reviews* **2008**, *37*, 191-214.

(2)   Ötvös, Sándor B.; Berkesi, Ottó; Körtvélyesi, Tamás; Pálinkó, István, Synthesis and Spectroscopic and Computational Characterization of Zn4O(Alicyclic or Aromatic Carboxylate)6 Complexes as Potential MOF Precursors, *Inorganic Chemistry* **2010**, *49*, 4620-4625.

(3)   Zhao, Xiaoliang; He, Haiyan; Hu, Tuoping; Dai, Fangna; Sun, Daofeng, Interpenetrating Polyhedral MOF with a Primitive Cubic Network Based on Supermolecular Building Blocks Constructed of a Semirigid C3-Symmetric Carboxylate Ligand, *Inorganic Chemistry* **2009**, *48*, 8057-8059.

(4)   Davies, Robert P.; Less, Rob; Lickiss, Paul D.; Robertson, Karen; White, Andrew J. P., Structural Diversity in Metal−Organic Frameworks Built from Rigid Tetrahedral [Si(p-$C_6H_4CO_2$)$_4$]$_4$− Struts, *Crystal Growth & Design* **2010**, *in press*.

(5)   Eddaoudi, Mohamed; Li, Hailian; Yaghi, O. M., Highly Porous and Stable Metal−Organic Frameworks: Structure Design and Sorption Properties, *Journal of the American Chemical Society* **2000**, *122*, 1391-1397.

(6)   Yaghi, O. M.; O'Keeffe, M.; Ockwig, N. W.; Chae, H. K.; Eddaoudi, M.; Kim, J., Reticular synthesis and the design of new materials, *Nature* **2003**, *423*, 705-714.

(7)   Shimizu, George K. H.; Vaidhyanathan, Ramanathan; Taylor, Jared M., Phosphonate and sulfonate metal organic frameworks, *Chemical Society Reviews* **2009**, *38*, 1430-1449.

(8)   Evans, Owen R.; Ngo, Helen L.; Lin, Wenbin, Chiral Porous Solids Based on Lamellar Lanthanide Phosphonates, *Journal of the American Chemical Society* **2001**, *123*, 10395-10396.

(9)   Taylor, Jared M.; Mah, Roger K.; Moudrakovski, Igor L.; Ratcliffe, Christopher I.; Vaidhyanathan, Ramanathan; Shimizu, George K. H., Facile Proton Conduction via Ordered Water Molecules in a Phosphonate Metal−Organic Framework, *Journal of the American Chemical Society* **2010**, *in press*.

(10)   Liang, Junmei; Shimizu, George K. H., Crystalline Zinc Diphosphonate Metal−Organic Framework with Three-Dimensional Microporosity, *Inorganic Chemistry* **2007**, *46*, 10449-10451.

(11)   Murugavel, R.; Walawalkar, M. G.; Dan, Meenakshi; Roesky, H. W.; Rao, C. N. R., Transformations of Molecules and Secondary Building Units to Materials: A Bottom-Up Approach, *Accounts of Chemical Research* **2004**, *37*, 763-774.

(12)   Samanamu, Christian R.; Zamora, Elena Nicole; Montchamp, Jean-Luc; Richards, Anne F., Synthesis of homo and hetero metal-phosphonate frameworks from bi-functional aminomethylphosphonic acid, *Journal of Solid State Chemistry* **2008**, *181*, 1462-1471.

(13)   Zhang, Xiang-Dong; Ge, Chun-Hua; Zhang, Xiao-Yan; Shi, Chun-Yue; He, Cui; Yin, Jing, Two-dimensional square grid of neutral phosphonate ligands and eight-coordinated metal ions, *Inorganic Chemistry Communications* **2008**, *11*, 1224-1226.

(14)   Li, Xinfa; Cao, Rong; Li, Yafeng, Three dimensional lanthanide-organic frameworks containing tetranuclear Ln (Ln = La, Nd) cluster secondary building blocks, *Inorganic Chemistry Communications* **2009**, *12*, 667-671.

(15)   Plabst, Monika; Stock, Norbert; Bein, Thomas, Hydrogen-Bonded Networks of Ammonium Bis- and Tetrakisphosphonates—Synthesis, High-Throughput Screening and Structural Trends, *Crystal Growth & Design* **2009**, *9*, 5049-5060.

(16)   Plabst, Monika; Bein, Thomas, 1,4-Phenylenebis(methylidyne)tetrakis(phosphonic acid): A New Building Block in Metal Organic Framework Synthesis, *Inorganic Chemistry* **2009**, *48*, 4331-4341.

(17)   Plabst, Monika; McCusker, Lynne B.; Bein, Thomas, Exceptional Ion-Exchange Selectivity in a Flexible Open Framework Lanthanum(III)tetrakisphosphonate, *Journal of the American Chemical Society* **2009**, *131*, 18112-18118.

(18)   Stock, N.; Bein, T., Inorganic-Organic Hybrid Materials: Hydrothermal Synthesis and Characterization of the Metal Diphosphonates $M_2(O_3PCH_2C_6H_4CH_2PO_3)\cdot 2H_2O$ (M=Mn, Ni, Cd), *Journal of Solid State Chemistry* **2002**, *167*, 330-336.

(19)   Konar, Sanjit; Zoń, Jerzy; Prosvirin, Andrey V.; Dunbar, Kim R.; Clearfield, Abraham, Synthesis and Characterization of Four Metal−Organophosphonates with One-, Two-, and Three-Dimensional Structures, *Inorganic Chemistry* **2007**, *46*, 5229-5236.

(20)   Harvey, Howard G.; Herve, Anne C.; Hailes, Helen C.; Attfield, Martin P., Synthesis, Crystal Structures, and Modifications of Novel Framework Gallium Diphosphonates, *Chemistry of Materials* **2004**, *16*, 3756-3766.

(21)   Irran, Elisabeth; Bein, Thomas; Stock, Norbert, Inorganic-organic hybrid materials: synthesis and crystal structure determination from powder diffraction data of $Pb_2(O_3PCH_2C_6H_4CH_2PO_3)$, *Journal of Solid State Chemistry* **2003**, *173*, 293-298.

(22)   Xu, Xianzhu; Wang, Peng; Hao, Rong; Gan, Meina; Sun, Fuxing; Zhu, Guang-shan, Synthesis and characterization of a novel three-dimensional open-framework: Metal diphosphonate, $Zn[HO_3PCH_2(C_6H_4)CH_2PO_3H]$, *Solid State Sciences* **2009**, *11*, 68-71.

(23)   Goto, Y.; Sato, H.; Shinkai, S.; Sada, K., "Clickable" Metal-Organic Framework, *Journal of the American Chemical Society* **2008**, *130*, 14354.

(24)   Rodrigues, M. O.; da Costa, N. B.; de Simone, C. A.; Araujo, A. A. S.; Brito-Silva, A. M.; Paz, F. A. A.; de Mesquita, M. E.; Junior, S. A.; Freire, R. O., Theoretical and experimental studies of the photoluminescent properties of the coordination polymer $[Eu(DPA)(HDPA)(H_2O)_2]$ $4H_2O$, *Journal of Physical Chemistry B* **2008**, *112*, 4204-4212.

(25)   Rodrigues, M. O.; Paz, F. A.; Freire, R. O.; de Sa, G. F.; Galembeck, A.; Montenegro, M. C.; Araujo, A. N.; Alves, S., Modeling, structural, and spectroscopic studies of lanthanide-organic frameworks, *Journal of Physical Chemistry B* **2009**, *113*, 12181-12188.

(26)   Rodrigues, M. O.; Brito-Silva, A. M.; Alves, S.; De Simone, C. A.; Araujo, A. A. S.; de Carvalho, P. H. V.; Santos, S. C. G.; Aragao, K. A. S.; Freire, R. O.; Mesquita, M. E., Structural and Spectroscopic Studies of the 2D Coordination Polymers $_\infty[Tb(Dpa)(Hdpa)]$ and $_\infty[Gd(Dpa)(Hdpa)]$, *Quimica Nova* **2009**, *32*, 286-291.

(27)	Malta, O. L., Mechanisms of non-radiative energy transfer involving lanthanide ions revisited, *Journal of Non-Crystalline Solids* **2008**, *354*, 4770-4776.

(28)	Kushida, T., Energy-transfer and cooperative optical transitions in rare-earth doped inorganic materials .1. Transition probability calculation, *Journal of the Physical Society of Japan* **1973**, *34*, 1318-1326.

(29)	Kushida, T., Energy-transfer and cooperative optical transitions in rare-earth doped inorganic materials .2. Comparison with experiments, *Journal of the Physical Society of Japan* **1973**, *34*, 1327-1333.

(30)	Kushida, T., energy-transfer and cooperative optical transitions in rare-earth doped inorganic materials .3. Dominant transfer mechanism, *Journal of the Physical Society of Japan* **1973**, *34*, 1334-1337.

(31)	Freeman, A. J.; Desclaux, J. P., Dirac-Fock studies of some electronic properties of rare-earth ions, *Journal of Magnetism and Magnetic Materials* **1979**, *12*, 11-21.

(32)	Carnall, W. T.; Crosswhite, H.; Crosswhite, H. M. *Energy Structure and Transition Probabilities of the Trivalent Lanthanides in LaF$_3$*; Argonne National Laboratory Report, 1977.

(33)	Edvardsson, S.; Klintenberg, M., Role of the electrostatic model in calculating rare-earth crystal-field parameters, *Journal of Alloys and Compounds* **1998**, *275*, 230-233.

(34)	Freire, R. O.; Rocha, G. B.; Simas, A. M., Sparkle/PM3 for the Modeling of Europium(III), Gadolinium(III) and Terbium(III) Complexes, *Journal Of the Brazilian Chemical Society* **2009**, *20*, 1638-1645.

(35)   Alves, S.; deAlmeida, F. V.; deSa, G. F.; Donega, C. D., Luminescence and quantum yields of Eu^{3+} mixed complexes with 1-phenyl-1,3-butanedione and 1,10-phenanthroline or 1,10-phenanthroline-N-oxide, *Journal of Luminescence* **1997**, *72-4*, 478-480.

(36)   de Mesquita, M. E.; Junior, S. A.; Oliveira, F. C.; Freire, R. O.; Junior, N. B. C.; de Sa, G. F., Synthesis, spectroscopic studies and structure prediction of the new $[Tb(3-NH_2PIC)_3]$ $3H_2O$ complex, *Inorganic Chemistry Communications* **2002**, *5*, 292-295.

(37)   Annapurna, K.; Dwivedi, R. N.; Kundu, P.; Buddhudu, S., Emission spectra of Tb^{3+}: $Bi_2O_3-B_2O_3-R_2O$ (R = Li, Na & K) glasses, *Journal of Materials Science* **2005**, *40*, 1051-1053.

(38)   Wakefield, G.; Keron, H. A.; Dobson, P. J.; Hutchison, J. L., Structural and optical properties of terbium oxide nanoparticles, *Journal of Physics and Chemistry of Solids* **1999**, *60*, 503-508.

(39)   Nakazawa, E.; Shionoya, S, Relaxation between Excited Levels of Tb^{3+} Ion Due to Resonance Energy Transfer, *Journal of the Physical Society of Japan* **1970**, *28*, 1260-1265.

(40)   Kang, J. G.; Kim, T. J., Luminescence and crystal-field analysis of europium and terbium complexes with oxydiacetate and 1,10-phenanthroline, *Bulletin of the Korean Chemical Society* **2005**, *26*, 1057-1064.

(41)   Binnemans, K.; Gorller-Walrand, C., Application of the Eu^{3+} ion for site symmetry determination,, *Journal of Rare Earth* **1996**, *14*, 173-180.

(42)   Souza, A. P.; Rodrigues, L. C. V.; Brito, H. F.; Alves Jr, S.; Malta, O. L., Photoluminescence study of new lanthanide complexes with benzeneseleninic acids, *Journal of Luminescence* **2010**, *130*, 181-189.

(43)   Huskowska, E.; Turowska-Tyrk, I.; Legendziewicz, J.; Riehl, J. P., The structure and spectroscopy of lanthanide(III) complexes with 2,2 '-bipyridine-1,1 '-dioxide in solution and in the solid state: effects of ionic size and solvent on photophysics, ligand structure and coordination, *New Journal of Chemistry* **2002**, *26*, 1461-1467.

(44)   Driesen, K.; Fourier, S.; Gorller-Walrand, C.; Binnemans, K., Judd-Ofelt analysis of lanthanide doped silica-PEG hybrid sol-gels, *Physical Chemistry Chemical Physics* **2003**, *5*, 198-202.

(45)   Ananias, D.; Kostova, M.; Paz, F. A.; Neto, A. N.; De Moura, R. T., Jr.; Malta, O. L.; Carlos, L. D.; Rocha, J., Molecule-like Eu^{3+}-dimers embedded in an extended system exhibit unique photoluminescence properties, *Journal of the American Chemical Society* **2009**, *131*, 8620-6.

(46)   Liu, Chunxu; Liu, Junye; Dou, Kai, Judd−Ofelt Intensity Parameters and Spectral Properties of Gd$_2$O$_3$:Eu^{3+} Nanocrystals, *The Journal of Physical Chemistry B* **2006**, *110*, 20277-20281.

(47)   Osawa, Masahisa; Hoshino, Mikio; Wada, Tatsuo; Hayashi, Fumi; Osanai, Shuichi, Intra-Complex Energy Transfer of Europium(III) Complexes Containing Anthracene and Phenanthrene Moieties, *The Journal of Physical Chemistry A* **2009**, *113*, 10895-10902.

(48)   Malta, O. L.; Silva, F. R. G. E., A theoretical approach to intramolecular energy transfer and emission quantum yields in coordination compounds of rare earth ions, *Spectrochimica Acta Part A-Molecular and Biomolecular Spectroscopy* **1998**, *54*, 1593-1599.

(49)   de Sá, G. F.; Malta, O. L.; Donega, C. D.; Simas, A. M.; Longo, R. L.; Santa-Cruz, P. A.; da Silva, E. F., Spectroscopic properties and design of highly luminescent lanthanide coordination complexes, *Coordination Chemistry Reviews* **2000**, *196*, 165-195.

(50)   Stavola, M.; Isganitis, L.; Sceats, M. G., Cooperative vibronic spectra involving rare-earth ions and water-molecules in hydrated salts and dilute aqueous-solutions, *Journal of Chemical Physics* **1981**, *74*, 4228-4241.

(51)   Berry, M. T.; May, P. S.; Hu, Q., Calculated and observed $Tb^{3+}(^5D_4) \rightarrow Eu^{3+}$ electronic energy transfer rates in $Na_3[Tb_{0.01}Eu_{0.99}(oxydiacetate)_3]\ 2NaClO_4\ 6H_2O$, *Journal of Luminescence* **1997**, *71*, 269-283.

(52)   Tanaka, Masanori; Nishimura, Goro; Kushida, Takashi, Contribution of J mixing to the $^5D_0 \rightarrow ^7F_0$ transition of Eu^{3+} ions in several host matrices, *Physical Review B* **1994**, *49*, 16917.

(53)   Morley, J. P.; Faulkner, T. R.; Richardson, F. S., Optical-emission spectra and crystal-field analysis of Eu^{3+} in the cubic Cs_2NaYCl_6 host, *Journal of Chemical Physics* **1982**, *77*, 1710-1733.

Anexo 3

Análise Elementar de CNHS.

Fórmula (Calculado/Experimental):

1. C: 22,20/23,37 (%); H: 2,56/2,62 (%).

2. C: 21,90/22,37 (%); H: 2,53/2,66 (%).

3. C: 21,80/22,08 (%); H: 2,52/2,59 (%).

4. C: 21,90/23,00 (%); H: 2,52/2,58 (%).
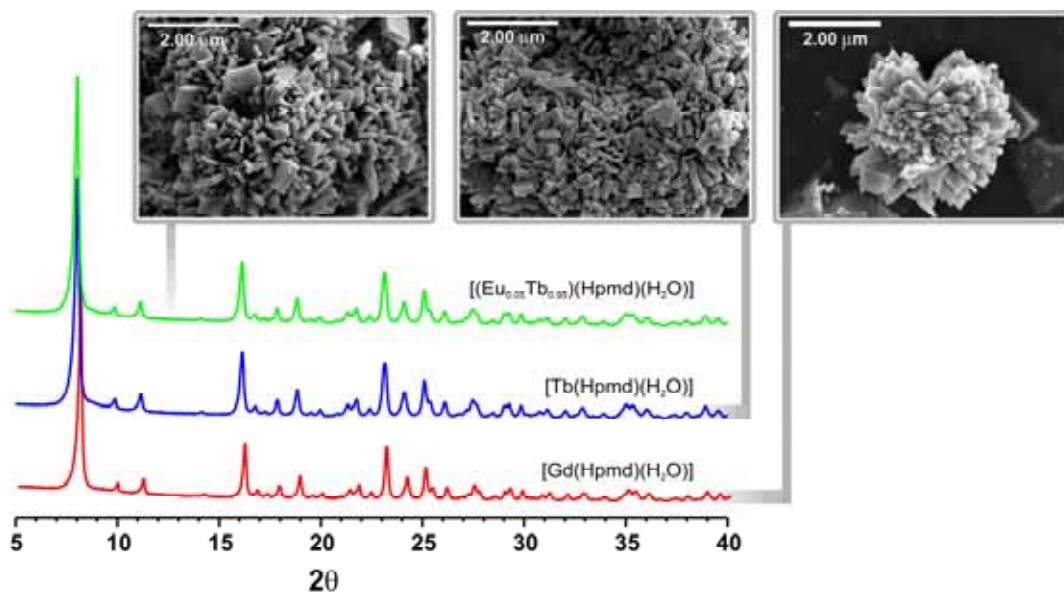
Figura 3.1A: Padrão de difração de raios-x dos materiais **(3.4)**, **(3.3)** e **(3.2)** imagens de MEV.
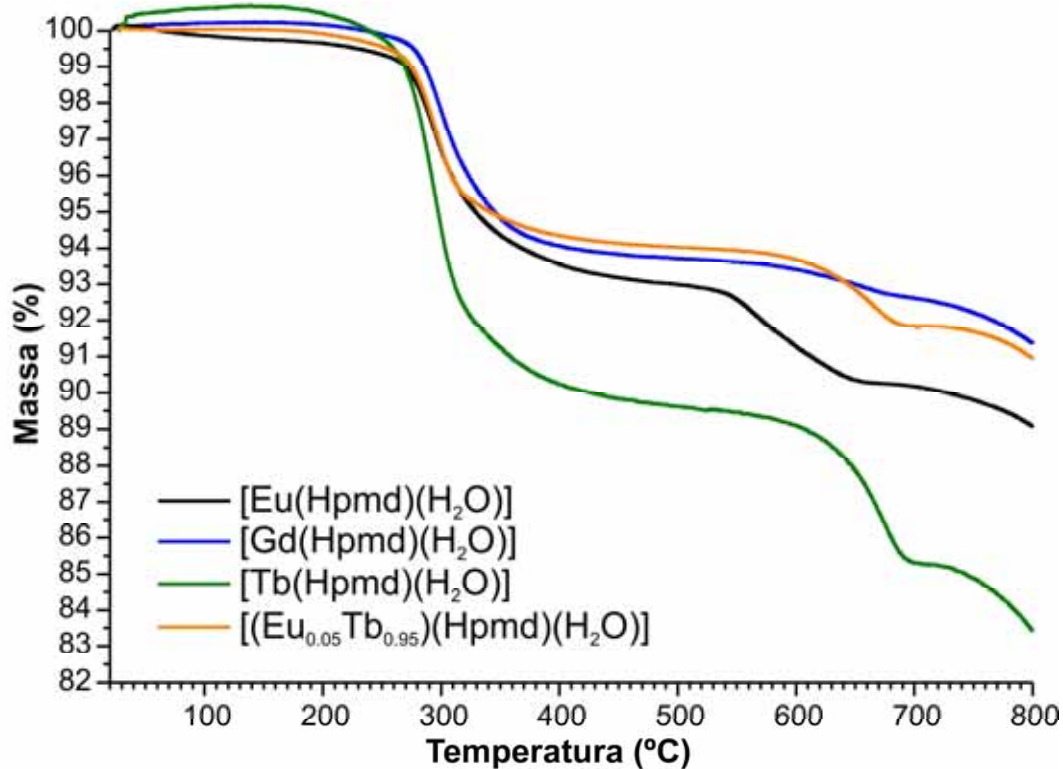
Figura 3.2A: Curvas termogravimétricas (TGA)

Eventos de perdas de massa para as amostras (Pico da DTG entre os parênteses):

1. 150-450 °C: -6,5% (*290 °C*); 450-700 °C: -3,1% (*564 °C*).

2. 195-515 °C: -6,5 (*300 °C*); 515-700 °C: -1,1% (*645 °C*).

3. 180-490 °C: -10,9% (*295 °C*); 490-725 °C: -4,5% (*675 °C*).

4. 180-490 °C: -6,0% (*295 °C*); 490-735 °C: -2,2 % (*670 °C*).
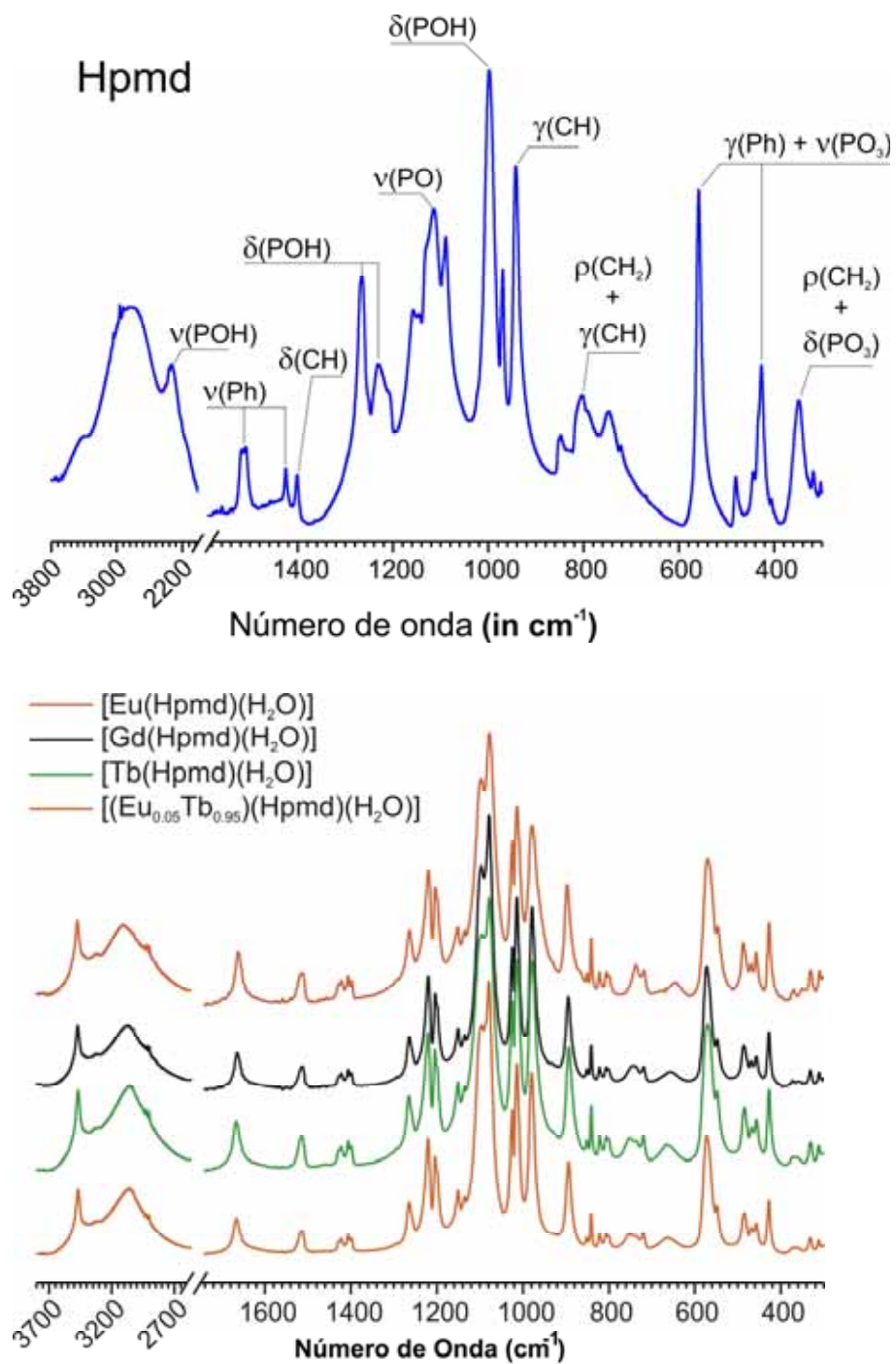
Figura 3.3A: Espectros de Infravermelho do ligante (acima) e dos materiais [Ln(Hpmd)(H₂O)].
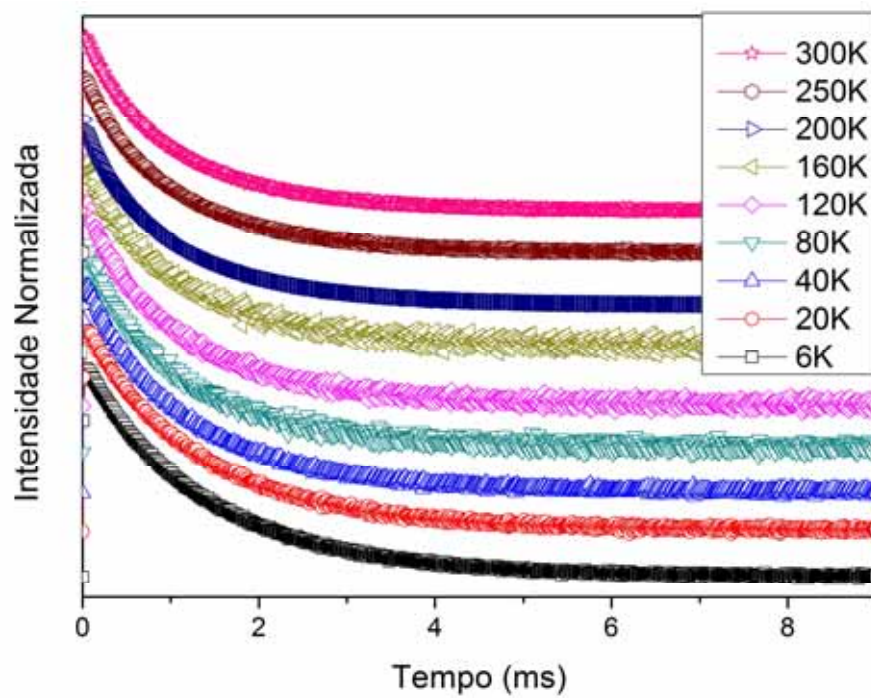
Figura 3.4A: Curvas normalizadas de tempos de vida de **(3.3)** em função da temperatura monitorando o nível $^5D_4$ (545 nm) do Tb^{3+}.

Tabela 3.1A. Tempos de Vida e subida monitorando o nível $^5D_4$ (545 nm) do Tb^{3+} em **(3.3)**.

Temperatura (K)	τ_d (ms)
6	1,40
20	1,30
40	1,20
80	1,11
120	1,08
160	1,07
200	1,05
250	1,03
300	1,02
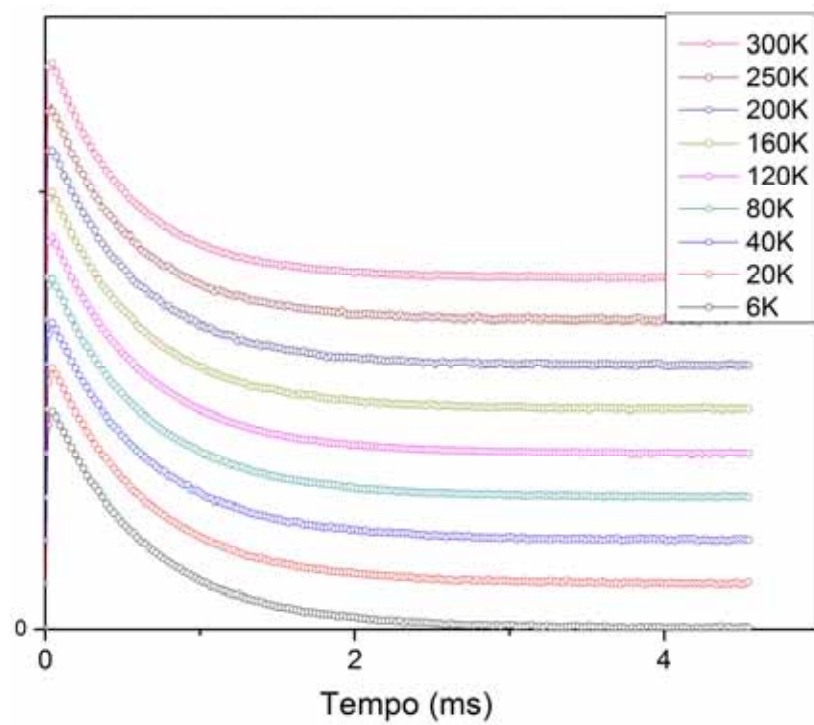
Figura 3.5A: Curvas normalizadas de tempos de vida de **(3.1)** em função da temperatura monitorando o nível $^5D_0$ (610nm) do Eu^{3+}.

Tabela 3.2A. Tempos de Vida e subida monitorando o nível $^5D_0$ (610nm) do Eu^{3+} em **(3.1)**.

Temperatura (K)	τ_d (ms)
6	0,63
20	0,62
40	0,62
80	0,61
120	0,60
160	0,58
200	0,56
250	0,53
300	0,51

Figura 3.6A: Mapas de EDS da distribuição de Eu^{3+} (Azul), Tb^{3+}(Verde) e P (vermelho) no material **(3.4)**.
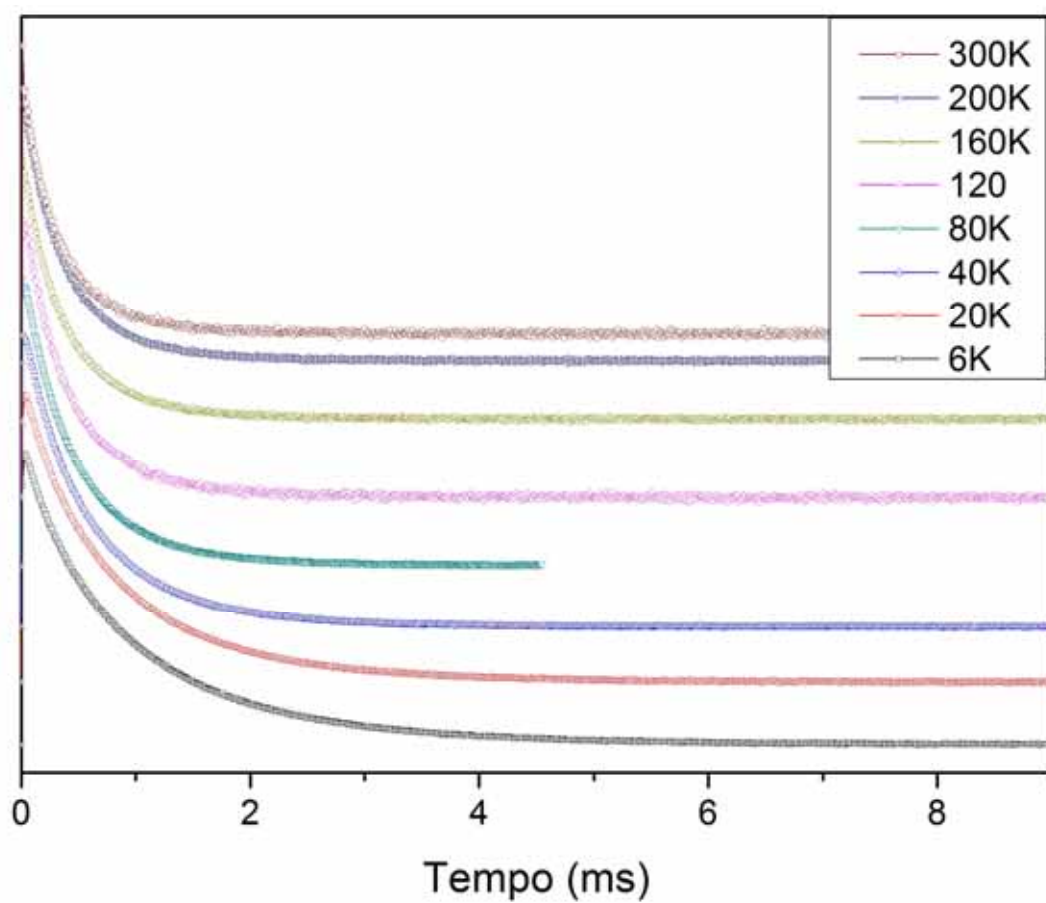
Figura 3.7A: Curvas de tempos de vida do **(3.4)** em função da temperatura monitorando o nível $^5D_4$ (545 nm) do Tb^{3+}.

Tabela 3.3A. Tempos de Vida e subida monitorando o nível $^5D_4$ (545 nm) do Tb^{3+} em **(3.4)**.

Temperatura (K)	τ_d (ms)
6	0,97
20	0,83
40	0,62
80	0,46
120	0,43
160	0,41
200	0,39
250	0,37
300	0,35
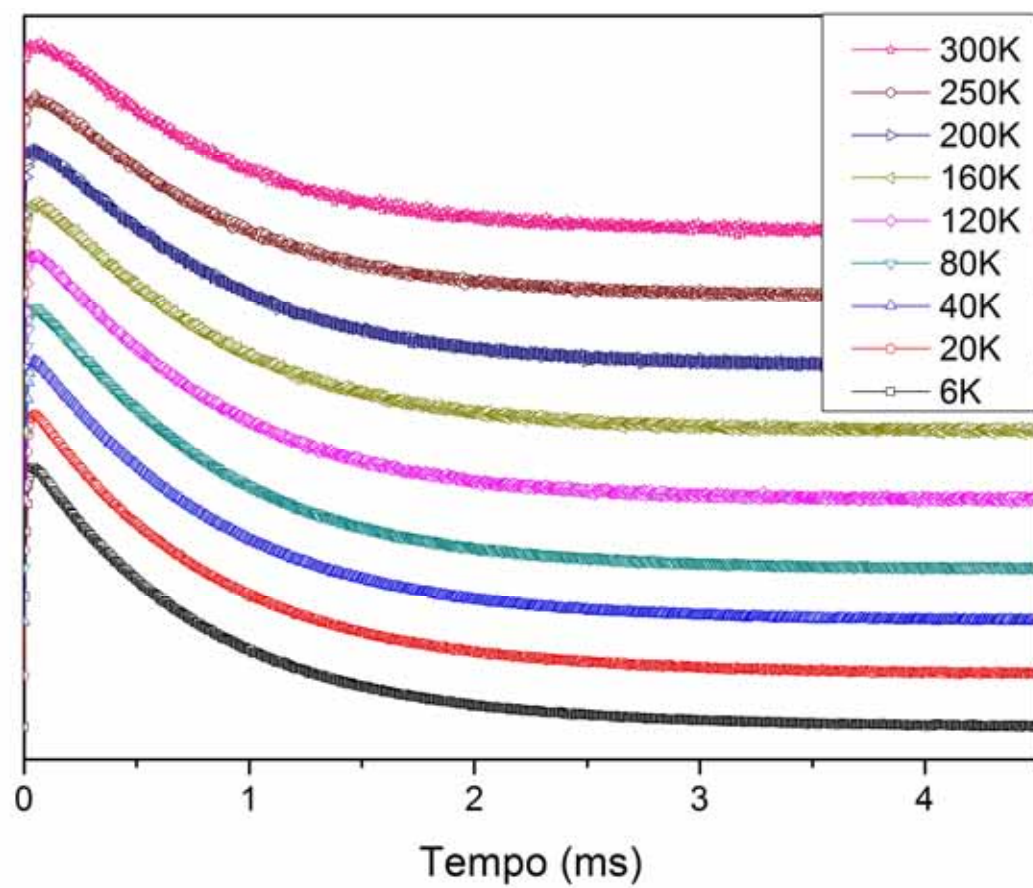
Figura 3.8A: Curvas de tempos de vida do **(3.4)** em função da temperatura monitorando o nível $^5D_0$ (610 nm) do Eu^{3+}.

Tabela 3.4A. Tempos de Vida monitorando o nível $^5D_0$ (610nm) do Eu^{3+} em **(3.4)**.

Temperatura (K)	τ_d (ms)
6	0,63
20	0,62
40	0,62
80	0,61
120	0,60
160	0,58
200	0,56
250	0,53
300	0,51

Figura 3.9A: Curvas de excitação do **(3.4)** em função da temperatura monitorando o nível $^5D_0$ (610 nm) do Eu^{3+} e os respectivos resultados dos ajustes das curvas

Perspectivas Gerais
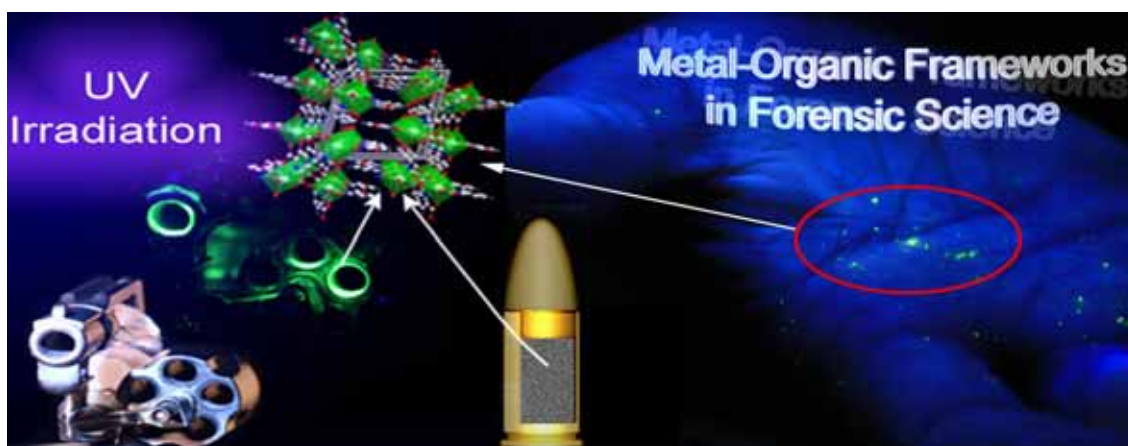
4.0   Perspectivas Gerais

➢ Aprofundar as investigações espectroscópicas (teórico/experimental) focado em transferência de energia entre espécies opticamente ativas;

➢ Otimizar a luminescência de MMOs através da modulação da concentração de espécies emissoras;

➢ Realizar experimentos de conversão ascendente de energia em MMOs;

➢ Realizar dopagem com metais de transição (rutênio, zinco, cádmio, prata, alumínio) nos sistemas estudados e avaliar as características estruturais e as propriedades espectroscópicas dos respectivos compostos;

➢ Avaliar a viabilidade desses MMOs na adsorção e sensoriamento de espécies (pesticidas, corantes, metais pesados);

➢ Testar os MMOs descritos no cap 1 e 2 em exames residográficos de GSR.

Anexo 4:

Artigos publicados e Patentes

Theoretical and Experimental Spectroscopic Approach of Fluorinated Ln³⁺−β-Diketonate Complexes

Edjane R. dos Santos,[†] Ricardo O. Freire,[‡] Nivan B. da Costa, Jr.,[‡] Filipe A. Almeida Paz,[§] Carlos A. de Simone,[||] Severino A. Júnior,[‡] Adriano A. S. Araújo,[†] Luiz Antônio O. Nunes,[||] Maria E. de Mesquita,[†] and Marcelo O. Rodrigues*[‡,§]

Department of Chemistry, UFS, 49100-000 São Cristóvão, SE, Brazil, Department of Chemistry Fundamental, UFPE, 50590-470 Recife, PE, Brazil, Department of Chemistry, CICECO, University of Aveiro, Campus Universitário de Santiago, 3810-193 Aveiro, Portugal, Department of Chemistry, UFAL, 57072-970 Maceió, AL, Brazil, and Physics Institute of São Carlos, IFSC/USP, 13560-970 São Carlos, SP, Brazil

Received: September 18, 2009

In this paper we report the synthesis of two new complexes, [Eu(fod)₃(phen)] and [Tb(fod)₃(phen)] (fod = 6,6,7,7,8,8,8-heptafluoro-2,2-dimethyl-3,5-octadionate and phen = 1,10-phenanthroline), and their complete characterization, including single-crystal X-ray diffraction, UV−vis spectroscopy, IR spectroscopy, and TGA. The complexes were studied in detail via both theoretical and experimental approaches to the photophysical properties. The [Eu(fod)₃(phen)] complex crystallizes in the monoclinic space group $P2_1/c$. The crystal structure of [Eu(fod)₃(phen)] exhibits an offset π−π stacking interaction between the phenanthroline ligands of adjacent lanthanide complexes. The Eu³⁺ cation is coordinated to three fod anionic ligands and to one phen. The symmetry around Eu³⁺ is best described as a highly distorted square antiprism. The molar absorption coefficients of [Eu(fod)₃(phen)] and [Tb(fod)₃(phen)] revealed an improved ability to absorb light in comparison with the stand-alone phen and fod molecules. [Tb(fod)₃(phen)] emits weak UV excitation, with this feature being explained by the triplet-⁵D₄ resonance, which contributes significantly to the nonradiative deactivation of Tb³⁺, causing a short lifetime and low quantum yield. The intensity parameters (Ω_2, Ω_4, and Ω_6) of [Eu(fod)₃(phen)] were calculated for the X-ray and Sparkle/AM1 structures and compared with values obtained for [Eu(fod)₃(H₂O)₂] and [Eu(fod)₃(phen-*N*-O)] (phen-*N*-O = 1,10-phenanthroline *N*-oxide) samples. Intensity parameters were used to predict the radiative decay rate. The theoretical quantum efficiencies from the X-ray and Sparkle/AM1 structures are in good agreement with the experimental values, clearly attesting to the efficacy of the theoretical models.

Introduction

The electronic configuration of lanthanide ions, Ln³⁺, leads to photoluminescent properties due to the 4f−4f transitions.[1−3] Because these transitions are forbidden by spin and parity selection rules, and the absorption coefficients of Ln³⁺ are very small, the f states are trivially populated indirectly through coordinated organic ligands (antenna effect), which act as metal sensitizers. In these systems, UV light is absorbed by the ligands directly coordinated to Ln³⁺.[4] The energy is afterward transferred to one or several excited states of the Ln³⁺ ion, and at last, the metal ion emits light, normally in the visible and near-infrared range.[5−7]

Lanthanide-based complexes are important in the development of light-conversion molecular devices (LCMDs),[8,9] because they exhibit long lifetimes and large quantum efficiencies and, consequently, are highly luminescent. These properties have been widely explored in many applications, such as luminescent probes in biomedical assays,[2,10,11] organic light-emitting diodes (OLEDs),[12,13] and luminescent sensors for chemical species.[14−18]

The development of highly efficient LCMDs has been the object of intensive research from groups around the world.[19−23] This is not a simple task because the design of highly luminescent lanthanide complexes embodies the understanding of each of the stages involved in the energy transfer process.[24] As the indirect excitation of the lanthanide ions is the typical pathway to obtain materials with a good quantum yield, a diversity of ligands have been developed and used in the synthesis of new Eu³⁺ and Tb³⁺ complexes, among which the β-diketonates deserve to be singled out.[8,25−30] The success of Eu³⁺ and Tb³⁺ complexes with β-diketonates as promising LCMDs is based on the respective very intense ⁵D₄ → ⁷F₅ and ⁵D₀ → ⁷F₂ transitions and high radiative rate decays.[31] Structurally, the bidentate mode typical of β-diketonates allows the synthesis of tris complexes, with the coordination sphere being usually completed by two or three water molecules. In fact, the presence of directly coordinated water molecules provokes the detriment of the luminescent properties by the vibronic coupling with the O−H oscillators. Notwithstanding, this drawback can be easily eliminated via replacement of water by chromophores, leading to more luminescent complexes.[32−36]

The complex [Ln(fod)₃(H₂O)₂] (where fod = 6,6,7,7,8,8,8-heptafluoro-2,2-dimethyl-3,5-octadionate) has been widely applied as an NMR shift agent,[37−41] a catalyst in organic reactions,[42,43] and the subject of a handful of spectroscopic properties.[44−49] In previous studies, we have demonstrated that

* To whom correspondence should be addressed. E-mail: marcelorodrigues@ua.pt. Phone at UFPE: +55 81 2126-7459. Fax at UFPE: +55 81 2126-8442. Phone at the University of Aveiro: +351 234 370200 (ext 24918).
† UFS.
‡ UFPE.
§ University of Aveiro and UFAL.
|| IFSC/USP.

Fluorinated Ln^{3+}−β-Diketonate Complexes

J. Phys. Chem. A, Vol. 114, No. 30, 2010 **7929**

the replacement of the coordinated water molecules in the [Eu(fod)$_3$(H$_2$O)$_2$] by phen-*N*-O (1,10-phenanthroline *N*-oxide) or diphenyldipyridyl (4,4′-diphenyl-2,2′-dipyridyl) can cause significant improvements in the photoluminescent properties.[50,51] In addition, we have also investigated the effect on these properties of the inclusion of the complexes in glass and polymeric matrixes.[52−54]

In the field of coordination compounds, the semiempirical Sparkle/AM1 model has proven its effectiveness in lanthanide chemistry because it allows the prediction of the coordination geometry for both small lanthanide complexes and more sophisticated structures (e.g., lanthanide−organic frameworks) in relatively short time and with a low computational demand.[55,56] In this paper we report the synthesis, characterization, and photoluminescence properties of the [Eu(fod)$_3$(phen)] and [Tb(fod)$_3$(phen)] complexes (phen = 1,10-phenanthroline). Spectroscopic properties, such as Ω_λ intensity parameters ($\lambda = 2, 4,$ and 6), energy transfer (W_{ET}) and back-transfer (W_{BT}) rates, radiative (A_{rad}) and nonradiative (A_{nrad}) decay rates, quantum efficiency (η), and quantum yield (q), of [Eu(fod)$_3$(phen)] were theoretically modeled using the electronic and spectroscopic semiempirical models and compared with those of [Eu(fod)$_3$(H$_2$O)$_2$] and [Eu(fod)$_3$(phen-*N*-O)].

Experimental Details

Synthesis of [Eu(fod)$_3$(phen)]. The [Eu(fod)$_3$(H$_2$O)$_2$] complex and phen were purchased from Aldrich and used as received. [Eu(fod)$_3$(phen)] was obtained by reacting 0.1 mmol of phen with 0.1 mmol of [Eu(fod)$_3$(H$_2$O)$_2$] in 40.0 mL of dry ethanol. The reaction was maintained under vigorous magnetic stirring and refluxed for a period of 24 h. The pure product was recrystallized from ethanol and dried under low pressure over P$_2$O$_5$. A large amount of large single crystals were grown by slow evaporation of the [Eu(fod)$_3$(phen)] ethanolic solution at ambient conditions. Anal. Calcd for C$_{42}$H$_{38}$F$_{21}$N$_2$O$_6$Eu: C, 41.26; H, 3.54; N, 2.29. Found: C, 41.41; H, 3.57; N, 2.18. TGA: 305−341 K ($\Delta m = 4.52\%$), 343−378 K ($\Delta m = 1.48\%$), 378−446 K ($\Delta m = 1.80\%$), 446−604 ($\Delta m = 75.34\%$), 604−692 K ($\Delta m = 7.08\%$), and 692−903 K ($\Delta m = 2.11\%$). Selected FT-IR data (cm^{-1}): 3690−3100 (w), 2973 (s), 1621 (vs), 1512 (vs), 1347 (s), 1227 (vs).

[Tb(fod)$_3$(H$_2$O)$_2$] was prepared by reacting 0.2 mmol of TbCl$_3$(H$_2$O)$_6$ with 0.6 mmol of fod in 40 mL of dry ethanol. The pH of the reaction was adjusted to 6−7 with the slow addition of a diluted NaOH ethanolic solution. The reaction was maintained under vigorous magnetic stirring for 24 h. The pure product was isolated by recrystallization. [Tb(fod)$_3$(phen)] was prepared by a procedure analogous to that described for [Eu(fod)$_3$(phen)]. Anal. Calcd for C$_{42}$H$_{43}$F$_{21}$N$_2$O$_6$Tb: C, 41.90; H, 3.16; N, 2.33. Found: C, 41.85; H, 3.14; N, 2.33. TGA: 278−342 K ($\Delta m = 3.52\%$), 358−378 K ($\Delta m = 0.71\%$), 446−604 K ($\Delta m = 76.51\%$), 604−695 K ($\Delta m = 1.08\%$), and 695−903 K ($\Delta m = 0.34\%$). Selected FT-IR data (cm^{-1}): 3684−3130 (w), 2970 (s), 1631 (vs), 1511 (vs), 1348 (s), 1230 (vs).

General Instrumentation. Elemental analysis was performed on a Flash 1112 series EA Thermo Finnigan CHNS-O analyzer. FT-IR spectra were recorded on 99.999% KBr pellets (spectral range 4000−400 cm^{-1}) using a Bruker IFS 66$^+$ instrument. Absorption spectra were obtained on a Perkin-Elmer Lambda 6 model 2688-002 UV−vis spectrometer.

Photoluminescence spectra at room temperature and 77 K were collected using an ISS PC1 spectrofluorometer. The excitation device was equipped with a 300 W xenon lamp and a photographic grating. Emission spectra were collected with a 25 cm monochromator (resolution 0.1 nm) connected to a photomultiplier. The excitation and emission slit widths were fixed at 1.0 mm. All monochromators had 1200 grooves/mm. Lifetime measurements were made at 298 K by monitoring the maximum emission at 611 nm using a Fluorolog 3 ISA/Jobin-Yvon spectrofluorometer equipped with a Hamamatsu R928P photomultiplier, a Spex 1934 D phosphorimeter, and a xenon pulsed lamp with 150 W of power.

Experimental intensity parameters, Ω_λ, for [Eu(fod)$_3$(phen)] were determined from the emission spectrum using the following equation:

$$\Omega_\lambda = \frac{4e^2\omega^3 A_{0J}}{3\hbar\chi\langle^7 F||U^{(\lambda)}||^5 D_0\rangle^2} \quad (1)$$

Details of the physical values in eq 1 are widely discussed in the literature.[55]

The experimental quantum yield (q) was determined by employing the method developed by Bril et al.,[52] for which the q value for a given sample can be calculated by a direct comparison with standard phosphors whose q values were previously determined by absolute measurements. q can thus be determined by

$$q = \left(\frac{1 - r_{ST}}{1 - r_x}\right)\left(\frac{\Delta\Phi_x}{\Delta\Phi_{ST}}\right)q_{ST} \quad (2)$$

where r_{ST} and r_x correspond to the amount of exciting radiation reflected by the standard and the sample, respectively, and q_{ST} is the quantum yield of the standard phosphor. The terms $\Delta\Phi_x$ and $\Delta\Phi_{ST}$ correspond to the respective integrated photon flux (photon·s^{-1}) for the sample and standard phosphors. BaSO$_4$ (Aldrich, $r = 100\%$), Y$_2$O$_3$/3% Eu^{3+} (YOX-U719 Philips, $\Phi = 99\%$), and GdMgB$_5$O$_{10}$/Tb^{3+},Ce^{3+} (CBT-U734 Philips, $\Phi = 95\%$) were used as the reflectance standard and standard phosphors for Eu^{3+} and Tb^{3+}, respectively.[32]

Termogravimetric (TG) data were collected with an SDT model 2960 thermobalance, TA Instruments, in the 294−1063 K temperature range, using an alumina crucible with ca. 10.0 mg of sample, under a dynamic nitrogen atmosphere (50 mL·min^{-1}) and with a heating rate of 10 K·min^{-1}.

Single-Crystal X-ray Diffraction Studies. A suitable single crystal of [Eu(fod)$_3$(phen)] was mounted on a glass fiber using Fomblin Y perfluoropolyether vacuum oil (LVAC 25/6) purchased from Aldrich.[57] Data were collected at ambient temperature on an Enraf Nonius FR590 charge-coupled device (CCD) area-detector diffractometer (Mo Kα graphite-monochromated radiation, $\lambda = 0.71073$ Å) controlled by the COLLECT software package.[58] Images were processed using the software packages of Denzo and Scalepack,[59] and the data were corrected for absorption by the empirical method employed in Sortav.[60,61] The structure was solved by the direct methods of SHELXS-97[62,63] and refined by full-matrix least-squares on F^2 using SHELXL-97.[63,64] All non-hydrogen atoms were successfully refined using anisotropic displacement parameters.

Hydrogen atoms bound to carbon were located at their idealized positions using appropriate HFIX instructions in SHELXL (43 for the aromatic and 33 for the terminal −CH$_3$ methyl groups) and included in subsequent refinement cycles in riding-motion approximation with isotropic thermal displacement parameters (U_{iso}) fixed, respectively, at 1.2 or 1.5 times

the U_{eq} of the carbon atom to which they are attached. The last difference Fourier map synthesis showed the highest peak (2.357 e·Å^{-3}) and deepest hole (-1.277 e·Å^{-3}) located 0.82 and 0.76 Å from Eu(1), respectively.

Crystallographic data (excluding structure factors) for the structure reported in this paper have been deposited with the Cambridge Crystallographic Data Centre as supplementary publication no. CCDC-747008. Copies of the data can be obtained free of charge on application to CCDC, 12 Union Rd., Cambridge CB2 2EZ, U.K. (fax (+44) 1223 336033, e-mail deposit@ccdc.cam.ac.uk).

Theoretical Studies

The ground-state geometries of [Tb(fod)$_3$(phen)], [Eu(fod)$_3$(phen)], [Eu(fod)$_3$(H$_2$O)$_2$], and [Eu(fod)$_3$(phen-*N*-O)] were obtained with the Sparkle/AM1 model,[65] implemented in the MOPAC2007 software[66] package. Previous studies showed that the Sparkle/AM1 calculations are highly accurate in calculations of geometries and competitive with other ab initio/ ECP methods with the advantage of being hundreds of times faster.[65,67,68] For this reason, the Sparkle model has been applied in calculations of the ground-state geometries of lanthanide complexes.[65] Calculated geometries have been successfully applied in the prediction of spectroscopic properties such as singlet and triplet energy levels,[69−71] UV absorption spectra and 4f−4f intensity parameters,[33,71] and energy transfer rates and quantum efficiencies.[21] We used the following MOPAC keywords: PRECISE, GNORM = 0.25, SCFCRT = 1.D-10 (to increase the SCF convergence criterion), and XYZ (for Cartesian coordinates).

All geometries and crystallographic and Sparkle/AM1 models were used to calculate the singlet and triplet excited states using the configuration interaction single (CIS) based on the inter- mediate neglect of differential overlap/spectroscopic (INDO/ S) method,[72,73] implemented in the ZINDO program.[74] The theoretical values of the intensity parameters, Ω_λ, were calcu- lated using the Judd−Ofelt theory.[75,76] The procedure we have employed is identical to that described in ref 53.

The energy transfer processes between the ligands and the lanthanide cation were described using the theoretical procedure developed by Malta and collaborators.[77,78] According to their model, the energy transfer rates, W_{ET}, can be inferred from the sum of two terms:

$$W_{ET} = W_{ET}^{mm} + W_{ET}^{em} \tag{3}$$

where W_{ET}^{mm} corresponds to the energy transfer rate obtained from the multipolar mechanism and is given by

$$W_{ET}^{mm} = \frac{2\pi}{\hbar} \frac{e^2 S_L}{(2J+1)G} F \sum_\lambda \gamma_\lambda \langle \alpha' J' || U^{(\lambda)} || \alpha J \rangle^2 +$$
$$\frac{2\pi}{\hbar} \frac{e^2 S_L}{(2J+1)G R_L^6} F \sum_\lambda \Omega_\lambda^{ed} \langle \alpha' J' || U^{(\lambda)} || \alpha J \rangle^2 \tag{4}$$

W_{ET}^{mp} corresponds to the dipole-2$^\lambda$ pole mechanism ($\lambda = 2, 4,$ and 6) and W_{ET}^{dd} to the dipole−dipole mechanism. The R_L parameter has been calculated by

$$R_L = \frac{\sum_i c_i^2 R_{L,i}}{\sum_i c_i^2} \tag{5}$$

with c_i being the molecular orbital coefficient of atom i contributing to the ligand state (triplet or singlet) involved in the energy transfer and $R_{L,i}$ corresponding to the distance from atom i to Eu^{3+}. The second term of eq 3, W_{ET}^{em}, corresponds to the energy transfer rate obtained from the exchange mechanism. This term is calculated by

$$W_{ET}^{em} =$$
$$\frac{8\pi}{3\hbar} \frac{e^2(1-\sigma_0)^2}{(2J+1)R_L^4} F \langle \alpha' J' || S || \alpha J \rangle^2 \sum_m | \langle \phi | \sum_k \mu_z(k) s_m(k) | \phi' \rangle |^2 \tag{6}$$

where J is the total angular momentum quantum number of the lanthanide cation. G is the degeneracy of the ligand initial state, and α specifies a given 4f spectroscopic term. The quantity F is given by

$$F = \frac{1}{\hbar \gamma_L} \sqrt{\frac{\ln 2}{\pi}} \exp\left[-\left(\frac{\Delta}{\hbar \gamma_L}\right)^2 \ln 2 \right] \tag{7}$$

where γ_L is the ligand-state bandwidth at half-maximum and Δ is the transition energy difference between the donor and acceptor involved in the transfer process. The quantity γ_λ is given by

$$\gamma_\lambda = (\lambda + 1) \frac{\langle r^\lambda \rangle^2}{(R_L^{\lambda+2})^2} \langle 3 || C^{(\lambda)} || 3 \rangle^2 (1 - \sigma_\lambda)^2 \tag{8}$$

The $\langle r^\lambda \rangle$ quantity is the expected radial value of r^λ for 4f electrons (eq 8), $\langle 3 || C^{(\lambda)} || 3 \rangle$ is a reduced matrix element of the Racah tensor operator $\mathbf{C}^{(\lambda)}$,[79] and σ_λ are the screening factors due to the 5s and 5p filled subshells of the lanthanide cation. The quantities given by $\langle ... || ... || ... \rangle$ are the reduced matrix elements of the unit tensor operators $\mathbf{U}^{(\lambda)}$,[80] R_L is the distance from the lanthanide cation to the region of the coordinated molecule where the donor (or acceptor) state is localized, S is the total spin operator of the lanthanide cation, μ_z is the z component of the electric dipole operator and s_m ($m = 0, \pm 1$) is a spherical component of the spin operator (both for the ligand electrons), and σ_0 is a distance-dependent screening factor.[81]

The theoretical fluorescence branching ratio is similar to the spontaneous emission probability (*A*) of the transition and can be obtained from the Einstein coefficient to express the rate of relaxation from an excited state, $^5D_0$, to a final state, ^7F_J, with $J = 0−6$. The spontaneous emission probability taking into account the magnetic dipole mechanisms and the forced electric dipole is then given by

$$A(^5D_0 - {}^7F_J) = \frac{64\pi^4 \nu^3}{3h(2J+1)} \left[\frac{n(n^2+2)^2}{9} S_{ed} + n^3 S_{md} \right] \tag{9}$$

Fluorinated $Ln^{3+}-\beta$-Diketonate Complexes

J. Phys. Chem. A, Vol. 114, No. 30, 2010 **7931**

TABLE 1: Crystal and Structure Refinement Data for [Eu(fod)₃(phen)]

empirical formula	$C_{42}H_{38}EuF_{21}N_2O_6$
fw	1217.70
temp	295(2) K
wavelength	0.71073 Å
cryst syst	monoclinic
space group	$P2_1/c$
unit cell dimensions	$a = 14.2130(3)$ Å, $\alpha = 90°$
	$b = 19.9060(5)$ Å, $\beta = 102.148(2)°$
	$c = 17.5720(5)$ Å, $\gamma = 90°$
vol	4860.2(2) Å³
Z	4
density(calcd)	1.664 Mg/m³
abs coeff	1.417 mm⁻¹
F(000)	2416
cryst size	$0.20 \times 0.19 \times 0.19$ mm³
θ range for data collection	3.51−25.09°
index ranges	$-15 \leq h \leq +16$, $-23 \leq k \leq +23$,
	$-20 \leq l \leq +18$
no. of reflns collected	49613
no. of independent reflns	8249 ($R_{int} = 0.0611$)
completeness to $\theta = 25.09°$	95.5%
refinement method	full-matrix least-squares on F^2
no. of data/restraints/params	8249/0/649
final R indices [$I > 2\sigma(I)$][a,b]	R1 = 0.0729, wR2 = 0.2098
R indices (all data)	R1 = 0.0916, wR2 = 0.2298
largest diff peak and hole	2.357 and −1.277 e·Å⁻³

[a] R1 = $\sum||F_o| - |F_c||/\sum|F_o|$. [b] wR2 = $\{\sum[w(F_o^2 - F_c^2)^2]/\sum[w(F_o^2)^2]\}^{1/2}$.

where ν is the energy gap between the $^5D_0$ and ^7F_J states (cm⁻¹), h is Planck's constant, $2J + 1$ is the degeneracy of the initial state, and n is the refractive index of the medium. S_{ed} and S_{md} are the electric and magnetic dipole strengths, respectively. S_{ed} is given by

$$S_{ed} = e^2 \sum_{\lambda=2,4,6} \Omega_\lambda |\langle ^5D_0||U^{(\lambda)}||^7F_J\rangle|^2 \qquad (10)$$

where Ω_λ (with $\lambda = 2, 4, 6$) are the Judd−Ofelt intensity parameters and $|\langle ^5D_0||U^{(\lambda)}||^7F_J\rangle|^2$ are the squared reduced matrix

elements whose values are 0.0032, 0.0023, and 0.0002 for $J = 2, 4,$ and 6, respectively.[82,83]

The $^5D_0 \rightarrow {}^7F_J$ transitions ($J = 0, 3,$ and 5) are forbidden in the magnetic and induced electric dipole schemes; i.e., their strengths are taken as zero. $^5D_0 \rightarrow {}^7F_1$ is the only transition which does not have an electric dipole contribution and can be theoretically determined: $S_{md} = 9.6 \times 10^{-42}$ esu²/cm².[84] Therefore, the theoretical radiative decay rate (A_{rad}) of the following equation is ultimately calculated as the sum of all individual spontaneous emission coefficients for the $^5D_0 \rightarrow {}^7F_{0,1,2,4}$ transitions:

$$A_{rad} = \sum_{J=1}^{6} A(^5D_0 - {}^7F_J) \qquad (11)$$

The emission quantum efficiency η can be expressed as

$$\eta = \frac{A_{rad}}{A_{rad} + A_{nrad}} \qquad (12)$$

Results and Discussion

[Eu(fod)₃(phen)] was directly isolated as large single crystals from the slow evaporation in ethanol. Details of the crystal data, intensity measurements, and structure solution refinements are summarized in Table 1.

The asymmetric unit contains a single Eu³⁺ ion coordinated to three fod anionic ligands and to one *N,N'*-bidentate ligand, phen, in a typical eight-coordination fashion as represented in Figure 1. The symmetry around the Eu³⁺ cation is best described as a distorted square antiprism, with the two "square" planes being defined by O(1)···O(2)···O(4)···O(5) and by O(3)···O(6)···N(1)···N(2), respectively. The anionic fod residues appear as typical *O,O*-chelates via the ketone functional groups, forming six-membered rings with an average bite angle of 72.4°, which is in good agreement with those found in related Eu³⁺−β-diketonate complexes.[27,33,85−88]

As illustrated in Figure 2, the crystal structure of [Eu(fod)₃(phen)] exhibits an offset $\pi-\pi$ interaction between the
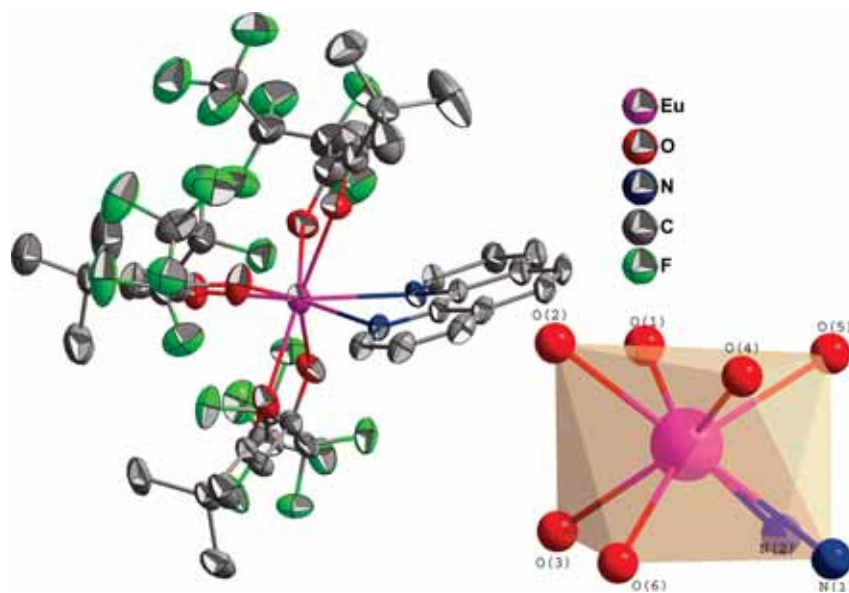
Figure 1. Asymmetric unit of [Eu(fod)₃(phen)] emphasizing the slightly distorted square antiprismatic coordination environment of Eu³⁺. Hydrogen atoms were omitted for clarity, and the ellipsoids were drawn at the 30% probability level.

7932 *J. Phys. Chem. A, Vol. 114, No. 30, 2010*

Santos et al.
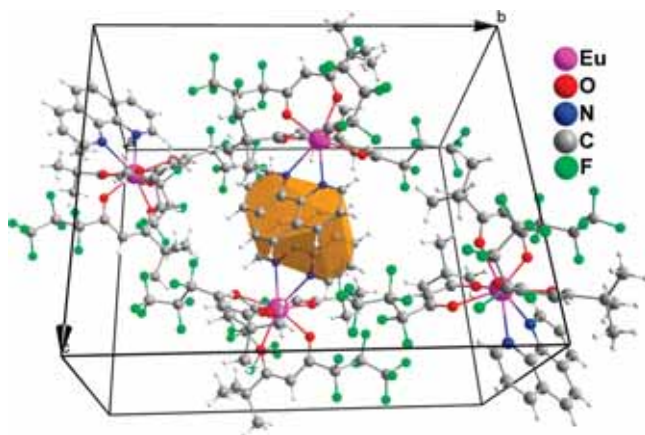
Figure 2. Schematic representation of the offset $\pi-\pi$ stacking interactions between adjacent [Eu(fod)₃(phen)] complexes.

TABLE 2: Selected Bond Lengths (Å) and Angles (deg) for [Eu(fod)₃(phen)][a]

Eu(1)−O(1)	2.335(6) (2.382)
Eu(1)−O(2)	2.346(5) (2.387)
Eu(1)−O(4)	2.346(6) (2.387)
Eu(1)−O(5)	2.355(6) (2.359)
Eu(1)−O(3)	2.360(5) (2.387)
Eu(1)−O(6)	2.407(6) (2.388)
Eu(1)−N(1)	2.591(6) (2.513)
Eu(1)−N(2)	2.600(7) (2.515)
O(1)−Eu(1)−O(5)	72.9(2) (62.27)
O(2)−Eu(1)−O(4)	73.0(2) (62.51)
O(3)−Eu(1)−O(6)	71.31(19) (62.16)
N(1)−Eu(1)−N(2)	63.1(2) (66.41)

[a] The values in parentheses are from Sparkle/AM1.
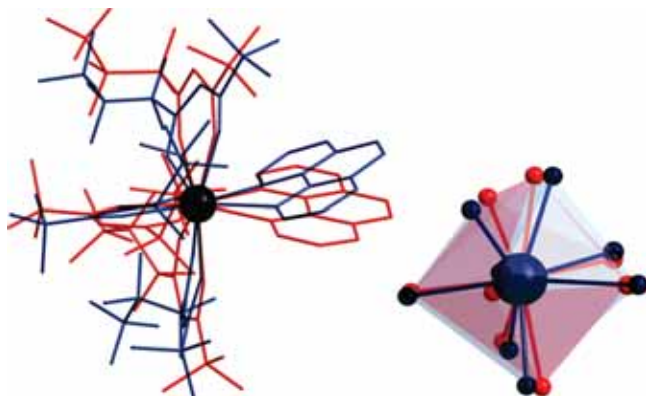
Figure 3. Superimposition of [Eu(fod)₃(phen)] complexes and coordination environments: crystallographic structures are represented in blue, while the Sparkle/AM1-optimized geometries are in red. Sparkle/AM1 geometries are slightly dislocated to facilitate the comprehension of the schemes.

phen ligands of adjacent lanthanide complexes, with a centroid-to-centroid distance of ca. 3.6 Å.[89] Table 2 shows selected metric values of the bond distances and angles of the Eu³⁺ coordination environment for [Eu(fod)₃(phen)] arising from the single-crystal X-ray and Sparkle/AM1 models. The crystallographic Eu−O and Eu−N average bond distances are ca. 2.38 and 2.56 Å, respectively. These values are within the expected range for Eu−O and Eu−N distances in Eu³⁺−β-diketonates complexes.[85] The average Eu−O and Eu−N predicted values obtained from Sparkle/AM1 are ca. 2.38 and 2.51, respectively (Table 2), agreeing well with those obtained from the crystallographic studies.
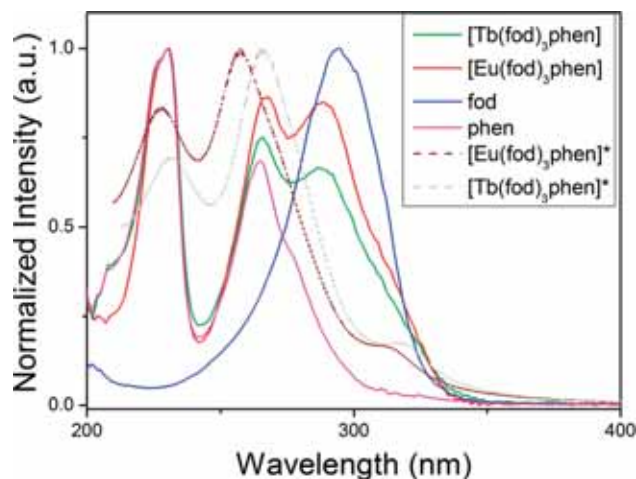
Figure 4. Normalized absorption spectra of [Eu(fod)₃(phen)], [Tb(fod)₃(phen)], fod, and phen. Experimental spectra were collected from an ethanolic solution at 300 K. The asterisks denote the theoretical spectra, which were calculated using INDO/CIS.

TABLE 3: Molar Absorption Coefficients (ε) and Maximum Absorption Intensities (λ) of fod, phen, [Eu(fod)₃(phen)], and [Tb(fod)₃(phen)]

sample	ε (10^3 mol⁻¹ cm⁻¹ L)	λ (nm)
fod	1.082	295
phen	3.312	230
[Eu(fod)₃(phen)]	8.252	230
[Tb(fod)₃(phen)]	7.578	230

Figure 3 shows a superimposition between the asymmetric unit and the Sparkle/AM1-optimized structure. One can observe that the C₃F₇ and C₃H₉ groups of fod ligands and the aromatic rings of phen show different spatial arrangements in comparison with the crystallographic model. We attribute this fact to the higher degree of freedom associated with these groups because the geometry optimizations are performed for the molecules in a vacuum. The [Tb(fod)₃(phen)] Sparkle/AM1-optimized structure is given in Figure S3 in the Supporting Information.

Figure 4 shows the normalized absorption spectra of [Eu(fod)₃(phen)] and [Tb(fod)₃(phen)] and normalized absorption spectra of fod and phen registered in ethanolic solutions (10^{-4} mol L⁻¹), at 300 K, and the theoretically predicted spectra obtained via the INDO/CIS method. Table 3 lists the molar absorption coefficients (ε). The electronic absorption spectra of [Eu(fod)₃(phen)] and [Tb(fod)₃(phen)] show the same spectral profile: three bands (λ_{max} = 230 nm) arising from the sum of the corresponding precursors. [Eu(fod)₃(phen)] and [Tb(fod)₃(phen)] display average calculated ε values 2.4 and 7.3 times those of phen and fod, respectively, revealing the ability of the materials to absorb light. The theoretical spectra exhibit similarities to the experimental data, despite the fact that they also display a small blue shift, which can be justified by the fact that all calculations were performed by considering the molecular units of the materials as being in a vacuum.

Figure 5 shows the excitation spectra of [Eu(fod)₃(phen)] and [Tb(fod)₃(phen)] registered at 300 K in the 200−550 and 200−450 nm ranges by monitoring the Eu³⁺ and Tb³⁺ emissions at ca. 611 and 545 nm, respectively. The spectra exhibit broad bands characteristic of the electronic transitions $\pi \rightarrow \pi^*$ of the ligands, with the maximum peaking at ca. 348 nm. The weaker signals observed in the 450−550 nm region arise from the f–f absorption of the Eu³⁺ cation, unequivocally proving the indirect excitation of the lanthanide centers via a typical antenna effect involving the organic ligands. Comparatively, the integrated

Fluorinated Ln$^{3+}-\beta$-Diketonate Complexes

J. Phys. Chem. A, Vol. 114, No. 30, 2010 **7933**
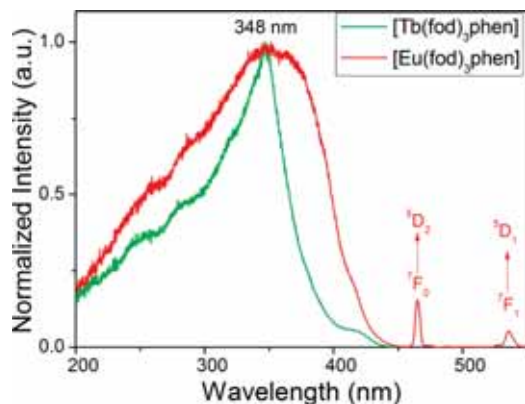
Figure 5. Excitation spectrum of [Eu(fod)$_3$(phen)] recorded at ca. 300 K by monitoring the emission of Eu^{3+} at ca. 611 nm.

excitation band of [Tb(fod)$_3$(phen)] is 40% narrower than that of the analogous Eu^{3+} complex, indicating that the antenna effect for the Tb^{3+} compound is less efficient.

Figure 6 depicts the solid-state emission spectra of [Eu(fod)$_3$(phen)] and [Tb(fod)$_3$(phen)] recorded at 300 K upon excitation at 348 nm. The [Tb(fod)$_3$(phen)] complex shows a weak green color upon UV excitation even though its emission spectrum exhibits well-defined $^5D_4 \rightarrow \, ^7F_J$ transitions. The $^5D_4 \rightarrow \, ^7F_5$ transition (545 nm) is the strongest corresponding to ca. 62% of the integrated spectrum. Indeed, the triplet position calculated for [Ln(fod)$_3$(phen)] (Ln^{3+} = Eu^{3+} or Tb^{3+}) is 19838.3 cm^{-1}, being slightly below the Tb^{3+} $^5D_4$ level ($\Delta E = 562$ cm^{-1}). Nevertheless, the profiles observed in the excitation and emission spectra of [Tb(fod)$_3$(phen)] indicate that the triplet calculated for the compounds is underestimated. This can be explained by the error of ± 1000 cm^{-1} associated with the theoretical method. Noteworthy, this short discrepancy does not disqualify the methodology.[4,55,90,91] When the lowest triplets of the organic ligands are below the emitter levels of the Ln^{3+} ions, fluorescence or phosphorescence arising from the ligand or no emission is normally observed.[24,92,93] Indeed the experimental observations demonstrate that the triplet-$^5D_4$ resonance contributes significantly to nonradiative deactivation of the Tb^{3+} ion and provides a plausible way to justify the short lifetime, 0.23 ms, and quantum yield, $q = 28.0\%$, obtained for [Tb(fod)$_3$(phen)].

The spectrum of [Eu(fod)$_3$(phen)] displays the typical narrow bands corresponding to the centered Eu^{3+} $^5D_0 \rightarrow \, ^7F_J$ transitions, whose main emission, centered at ca. 611 nm, corresponds to the hypersensitive $^5D_0 \rightarrow \, ^7F_2$ transition. The relative intensities and splitting of the emissions bands are particularly influenced by the symmetry of the first coordination sphere.[3] The emission spectrum has a single peak at ca. 580 nm attributed to the $^5D_0 \rightarrow \, ^7F_0$ transition. Even at low temperature, the $^5D_0 \rightarrow \, ^7F_0$ transition remains unaltered, clearly indicating that the Eu^{3+} chemical environment has a low symmetry without an inversion center.[86] The selection rules for the electric dipole transition indicate that $^5D_0 \rightarrow \, ^7F_0$ is only observed if the point symmetry of Eu^{3+} is C_{nv}, C_n, or C_s.[94] In addition, because Eu^{3+} $^7F_0$ is nondegenerate and the ligand field can not split it, the single peak at 580 nm indicates that there is only one emitter Eu^{3+} center in the material.[95] This is confirmed by the fact that the lifetime (τ) of the excited state $^5D_0$ was determined from a single-exponential fitting of the decay curve, also being consistent with the presence of a single crystallographically independent Eu^{3+} center. This spectroscopic information is in excellent agreement with the crystallographic and Sparkle/AM1 models.
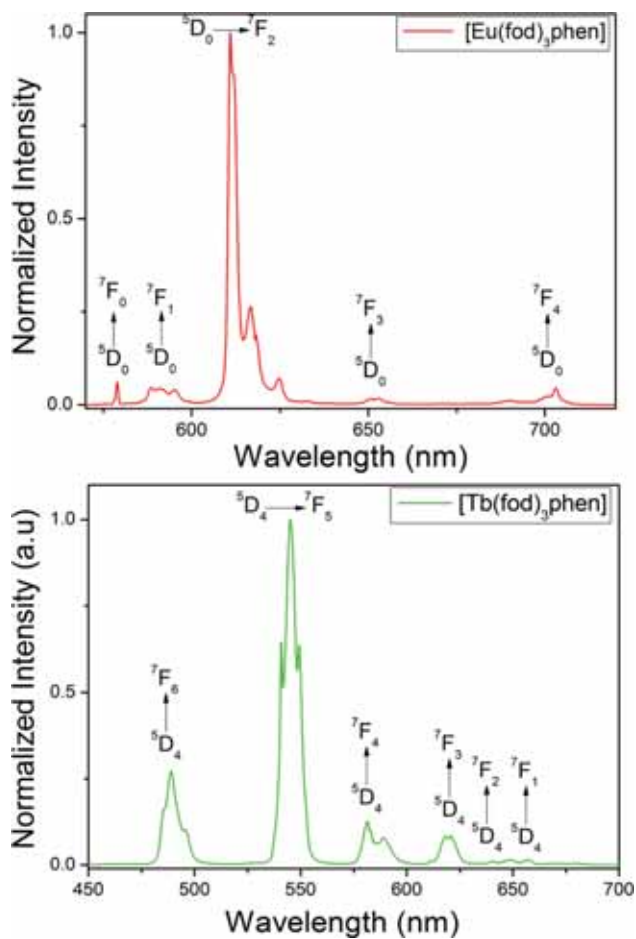
Figure 6. Normalized emission spectra of [Eu(fod)$_3$(phen)] and [Tb(fod)$_3$(phen)] at 300 K upon excitation at 348 nm.

The $^5D_0 \rightarrow \, ^7F_1$ transition is ruled by a magnetic dipole mechanism, and its intensity is largely independent of the ligand field effects. Nevertheless, the respective transition reflects the site symmetry of Eu^{3+} in the number of the lines.[96] This transition appears in the 588−600 nm range and exhibits three well-defined Stark components, thus supporting the presence of a single low-symmetry site for Eu^{3+}. Moreover, the $^5D_0 \rightarrow \, ^7F_2/^5D_0 \rightarrow \, ^7F_1$ ratio for [Eu(fod)$_3$(phen)] is ca. 11, which is well within the expected range (ca. 8−12) typical of europium centers exhibiting a highly asymmetric coordination environment.[51]

The theoretical intensity parameters were calculated from the structural data given in Tables S1−S3 (Supporting Information) using the procedure described in ref 53. The charge factors (g) and the ligand ion polarizability (α) were restricted to physically acceptable values and were treated as freely varying parameters using a nonlinear minimization of a four-dimension response surface.[51,55,56] The charge factors and the α values adjusted for [Eu(fod)$_3$(phen)], [Eu(fod)$_3$(H$_2$O)$_2$], and [Eu(fod)$_3$(phen-N-O)] are given in Tables 4 and Tables S1 and S2, respectively.

Table 4 summarizes the theoretical and experimental values for the intensity parameters (Ω_2, Ω_4, and Ω_6), radiative and nonradiative rates of spontaneous emission (A_{rad} and A_{nrad}, respectively), quantum efficiency (η), and quantum yield (q) for three Eu$^{3+}-\beta$-diketonate complexes studied in this paper. The analysis of the intensity parameters Ω_λ leads to the conclusion that these results reflect good agreement between the theoretical and experimental data. Considering the results collected in Table 4, one can observe an extraordinary increase of the Ω_2 values for [Eu(fod)$_3$(phen)] and [Eu(fod)$_3$(phen-N-

TABLE 4: Theoretical Intensity Parameters Ω_2, Ω_4, and Ω_6, Radiative (A_{rad}) and Nonradiative (A_{nrad}) Decay Rates, and Quantum Efficiency (η) and Quantum Yield (q) Values Derived from the Single-Crystal X-ray Diffraction and Optimized Sparkle/PM3 Models[a]

compd	Ω_2 (10^{-20} cm^2)	Ω_4 (10^{-20} cm^2)	Ω_6 (10^{-20} cm^2)	A_{rad} (s^{-1})	A_{nrad} (s^{-1})	τ (ms)	η (%)	q (%)
[Eu(fod)$_3$(phen)][b]	19.00	2.60		601.0	575.5	0.85	51.0	40.0
[Eu(fod)$_3$(phen)], X-ray structure	13.36	2.06	27.44	503.5	673.0		43.0	42.0
[Eu(fod)$_3$(phen)], Sparkle/AM1 structure	16.49	2.62	39.47	615.7	560.8		52.3	51.0
[Eu(fod)$_3$(H$_2$O)$_2$][b]	10.90	2.10		426.5	1186.4	0.62	26.5	
[Eu(fod)$_3$(H$_2$O)$_2$], Sparkle/AM1 structure	9.86	2.24	34.34	406.9	1206.0		25.0	25.0
[Eu(fod)$_3$(phen-*N*-O)][b]	24.50	13.40		876.0	1797.8	0.37	33.0	
[Eu(fod)$_3$(phen-*N*-O)], Sparkle/AM1 structure	19.35	15.92	23.05	889.4	1775.4		33.5	33.0

[a] Related experimental data, including the lifetime (τ) of the Eu^{3+} center, were obtained at ambient temperature for the as-synthesized [Eu(fod)$_3$(phen)], [Eu(fod)$_3$(H$_2$O)$_2$], and [Eu(fod)$_3$(phen-*N*-O)] samples. [b] Experimental values.
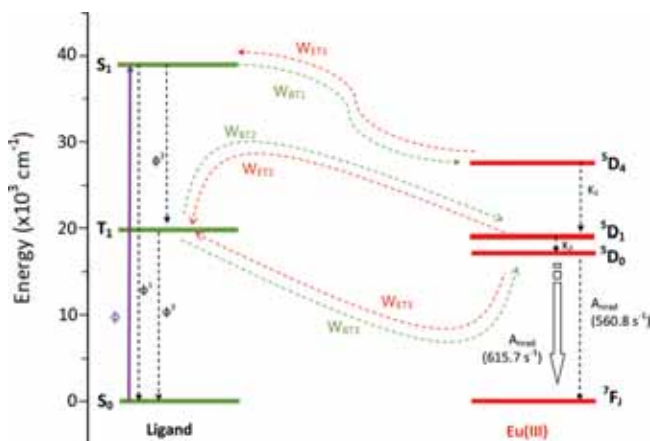
Figure 7. Energy level diagram for [Eu(fod)$_3$(phen)] showing the most probable channels for the intramolecular energy transfer process.

O)] in comparison with that of [Eu(fod)$_3$(H$_2$O)$_2$], caused by the high sensitivity of Ω_2 to the small change of the coordination environment.[97] Comparatively, the reason for the differences in Ω_2 values between [Eu(fod)$_3$(phen)] and [Eu(fod)$_3$(phen-*N*-O)] has its origin in the variations of the basicity degrees of the ligands (phen and phen-*N*-O) and anisotropic features of the metal–ligand bonds. In addition, the theoretical calculations show that the effects of the dynamic coupling associated with the ligand ion polarizability (α) are more prominent for [Eu(fod)$_3$(phen-*N*-O)], corroborating its high Ω_2 value.

Table 4 also includes the experimental values of the lifetimes for the three compounds. The increase of the lifetimes from 0.62 to 0.85 ms and radiative rates (from 426.5 to 601 s^{-1}) and the sensible reduction of the nonradiative rates from 1186.40 to 575.5 s^{-1} of [Eu(fod)$_3$(H$_2$O)$_2$][51] and [Eu(fod)$_3$(phen)], respectively, are a consequence of the substitution of the two coordinated water molecules by phenanthroline. These aspects are directly associated with the reduction of nonradiative decay

channels from vibronic coupling with harmonics of the O–H oscillator and corroborate the high values of the quantum yield ($q = 40.0\%$) and lifetime ($\tau = 0.85$ ms) obtained for [Eu(fod)$_3$(phen)]. While a substantial influence of the ligand phen-*N*-O on the relative intensities of the $^5D_0 \rightarrow {}^7F_J$ transitions was observed, the high contribution of the nonradiative rate, 1797.8 s^{-1}, justifies the lower values of η and τ of [Eu(fod)$_3$(phen-*N*-O)] when compared with those of [Eu(fod)$_3$(phen)]. It is important to note that the theoretical methodology shows similar results for the energy transfer mechanisms of [Eu(fod)$_3$(phen)] and [Eu(fod)$_3$(phen-*N*-O)] molecules in a vacuum. Unfortunately, the absence of crystallographic information for [Eu(fod)$_3$-(phen-*N*-O)][50] is a cumber to estimation of the energy mechanism in the crystalline domain and to indentification of the nonradiative channels responsible for the anomalous values of A_{nrad}, η, and τ in comparison with those of [Eu(fod)$_3$(phen)]. In addition, the results summarized in Table 4 further show excellent agreement between the theoretical and the experimental values for the A_{rad}, A_{nrad}, quantum efficiency (η), and quantum yields (q) of the three compounds.

The energy transfer and back-transfer rates and quantum yield for the Eu^{3+} compounds were calculated on the basis of some constraints: The values of the Eu^{3+} electronic levels arise from the free ion at intermediate coupling,[98] and the singlet level of the complex is resonant with Eu^{3+} $^5D_4$ (27600 cm^{-1}), while $^5D_1$ and $^5D_0$ are resonant with the lowest triplet. Additionally, the oscillator strength of the singlet states must be larger than 0.2, the singlet state must have an energy below 40000 cm^{-1}, and only the triplet state of the lowest energy was considered, which is related to the singlet state previously chosen. According to the selection rules, the energy transfer between the triplet and the $^5D_1$ level occurs via the exchange mechanism, and the energy transfer between the singlet and the $^5D_4$ level occurs via the multipolar mechanism. The energy transfer between the triplet and $^5D_0$ is forbidden for both mechanisms, but this selection rule can be relaxed due to the thermal population of the $^7F_1$

TABLE 5: Calculated Values of Intramolecular Energy Transfer and Back-Transfer Rates for Eu^{3+}–β-Diketonate Compounds

compd	level (cm^{-1})	Δ (cm^{-1})	RL (Å)	transfer rate (s^{-1})	back-transfer rate (s^{-1})
[Eu(fod)$_3$(phen)] (X-ray)	S (37569.3) $\rightarrow$ $^5D_4$ (27600)	9969.3	3.218	8.29×10^5	1.99×10^{-15}
	T (19654.1) $\rightarrow$ $^5D_1$ (19070)	584.1	3.372	2.08×10^{11}	1.31×10^{10}
	T (19654.1) $\rightarrow$ $^5D_0$ (17300)	2354.1	3.372	1.45×10^{11}	$1.99 \times x10^6$
[Eu(fod)$_3$(phen)] (Sparkle/AM1)	S (39032.4) $\rightarrow$ $^5D_4$ (27600)	11432.4	3.369	9.35×10^4	0.00
	T (19838.3) $\rightarrow$ $^5D_1$ (19070)	768.3	3.991	7.54×10^{10}	1.92×10^9
	T (19838.3) $\rightarrow$ $^5D_0$ (17300)	2538.3	3.991	5.01×10^{10}	2.78×10^5
[Eu(fod)$_3$(H$_2$O)$_2$] (Sparkle/AM1)	S (38285.5) $\rightarrow$ $^5D_4$ (27600)	10685.5	3.354	2.47×10^5	0.00
	T (21313.0) $\rightarrow$ $^5D_1$ (19070)	2243.0	3.465	1.03×10^{11}	2.37×10^6
	T (21313.0) $\rightarrow$ $^5D_0$ (17300)	4013.0	3.465	4.85×10^{10}	2.44×10^2
[Eu(fod)$_3$(phen-*N*-O)] (Sparkle/AM1)	S (39250.2) $\rightarrow$ $^5D_4$ (27600)	11650.2	3.923	1.38×10^5	0.00
	T (20233.8) $\rightarrow$ $^5D_1$ (19070)	1163.8	4.284	1.84×10^{10}	7.32×10^7
	T (20233.8) $\rightarrow$ $^5D_0$ (17300)	2933.8	4.284	1.12×10^{10}	9.67×10^3

Fluorinated $Ln^{3+}-\beta$-Diketonate Complexes

J. Phys. Chem. A, Vol. 114, No. 30, 2010 **7935**

level at room temperature and via the mixing of the *J* states due to the interaction with the ligand field. On the basis of this information, we have calculated both the transfer and back-transfer rates between the ligand and the Eu^{3+} levels. Typical values of the remaining transfer rates were assumed to be identical to those found for coordination compounds, namely, $\Phi = 10^4 \text{ s}^{-1}$, $\Phi^{(1)} = 10^6 \text{ s}^{-1}$, $\Phi^{(2)} = 10^8 \text{ s}^{-1}$, and $\Phi^{(3)} = 10^5 \text{ s}^{-1}$.

In Figure 7 an energy diagram for the two ligands and Eu^{3+} in [Eu(fod)$_3$(phen)] is proposed. Full lines concern the radiative transitions, whereas the dashed lines concern those associated with nonradiative paths. The curved lines are related to the ligand → lanthanide energy transfer or back-transfer. The energy transfer rates from the ligand triplet state (T1) to the $^5D_1$ and $^5D_0$ levels, energy transfer rates from the singlet state (S1), and singlet and triplet values are summarized in Table 5.

The three compounds show high T1 → $^5D_1$ back-transfer rate values, which can be explained by a short energy difference between the excited states. Clearly, the values of the energy transfer rate indicate that the process is predominant from the triplet state of the ligand to the $^5D_1$ and $^5D_0$ levels of Eu^{3+}.

Conclusions

The complexes [Eu(fod)$_3$(phen)] and [Tb(fod)$_3$(phen)] were synthesized and characterized, and their photophysical properties were submitted to a detailed scrutiny. The [Tb(fod)$_3$(phen)] complex shows a faint green color upon UV excitation, with this fact being explained by the triplet-$^5D_4$ resonance, which contributes significantly to the nonradiative deactivation of Tb^{3+}, ultimately being the cause of a short lifetime and low quantum yield. The properties of the [Eu(fod)$_3$(phen)] material were studied under a theoretical (using the Sparkle/AM1 model) and an experimental perspective and compared with those of [Eu(fod)$_3$(H$_2$O)$_2$] and [Eu(fod)$_3$(phen-*N*-O)]. The asymmetric unit has a single Eu^{3+} ion coordinated to three fod anionic ligands and to one *N,N'*-bidentate ligand, phen, in a typical eight-coordination mode. The optimized molecular geometry of [Eu(fod)$_3$(phen)] was obtained by employing the Sparkle/AM1 model and agrees well with the crystallographic model. Theoretical intensity parameters, calculated from the crystallographic and Sparkle models, are also in agreement with those acquired experimentally. Values of intermolecular energy transfer rates calculated for [Eu(fod)$_3$(phen)], [Eu(fod)$_3$(H$_2$O)$_2$], and [Eu(fod)$_3$(phen-*N*-O)] indicate that the energy transfer process occurs predominantly from the triplet state of the ligand to the $^5D_1$ and $^5D_0$ levels of Eu^{3+}. These results, associated with the excellent predictions of the intensity parameters, radiative rates, and quantum efficiencies certify the efficacy of the theoretical models used in all calculations.

References and Notes

(1) de Bettencourt-Dias, A. *Inorg. Chem.* **2005**, *44*, 2734–2741.

(2) Bunzli, J. C. G.; Piguet, C. *Chem. Soc. Rev.* **2005**, *34*, 1048–1077.

(3) Bunzli, J. C. G. In *Lanthanide Probes in Life, Chemical and Earth Sciences: Theory and Practice*; Choppin, G. R. B., Ed.; Elsevier: Amsterdam, 1989.

(4) Rodrigues, M. O.; Brito-Silva, A. M.; Alves, S.; De Simone, C. A.; Araújo, A. A. S.; de Carvalho, P. H. V.; Santos, S. C. G.; Aragão, K. A. S.; Freire, R. O.; Mesquita, M. E. *Quim. Nova* **2009**, *32*, 286–291.

(5) Freire, R. O.; Silva, F. R. G. E.; Rodrigues, M. O.; de Mesquita, M. E.; Junior, N. B. D. *J. Mol. Model.* **2005**, *12*, 16–23.

(6) de Sá, G. F.; Malta, O. L.; Donega, C. D.; Simas, A. M.; Longo, R. L.; Santa-Cruz, P. A.; da Silva, E. F. *Coord. Chem. Rev.* **2000**, *196*, 165–195.

(7) de Bettencourt-Dias, A.; Viswanathan, S. *Dalton Trans.* **2006**, 4093–4103.

(8) Pavithran, R.; Kumar, N. S. S.; Biju, S.; Reddy, M. L. P.; Júnior, S. A.; Freire, R. O. *Inorg. Chem.* **2006**, *45*, 2184–2192.

(9) Mesquita, M. E.; Nobre, S. S.; Fernandes, M.; Ferreira, R. A. S.; Santos, S. C. G.; Rodrigues, M. O.; Carlos, L. D.; Bermudez, V. D. *J. Photochem. Photobiol., A* **2009**, *205*, 156–160.

(10) Poupart, S.; Boudou, C.; Peixoto, P.; Massonneau, M.; Renard, P. Y.; Romieu, A. *Org. Biomol. Chem.* **2006**, *4*, 4165–4177.

(11) Nishioka, T.; Yuan, J. L.; Yamamoto, Y.; Sumitomo, K.; Wang, Z.; Hashino, K.; Hosoya, C.; Ikawa, K.; Wang, G. L.; Matsumoto, K. *Inorg. Chem.* **2006**, *45*, 4088–4096.

(12) Kido, J.; Okamoto, Y. *Chem. Rev.* **2002**, *102*, 2357–2368.

(13) Dias, A. D.; Viswanathan, S. *Chem. Commun.* **2004**, 1024–1025.

(14) Zhao, B.; Chen, X. Y.; Cheng, P.; Liao, D. Z.; Yan, S. P.; Jiang, Z. H. *J. Am. Chem. Soc.* **2004**, *126*, 15394–15395.

(15) Hanaoka, K.; Kikuchi, K.; Kojima, H.; Urano, Y.; Nagano, T. *J. Am. Chem. Soc.* **2004**, *126*, 12470–12476.

(16) Viguier, R. F. H.; Hulme, A. N. *J. Am. Chem. Soc.* **2006**, *128*, 11370–11371.

(17) Hovinen, J. *Bioconjugate Chem.* **2007**, *18*, 597–600.

(18) dos Santos, C. M. G.; Fernandez, P. B.; Plush, S. E.; Leonard, J. P.; Gunnlaugsson, T. *Chem. Commun.* **2007**, 3389–3391.

(19) Yang, C.; Fu, L. M.; Wang, Y.; Zhang, J. P.; Wong, W. T.; Ai, X. C.; Qiao, Y. F.; Zou, B. S.; Gui, L. L. *Angew. Chem., Int. Ed.* **2004**, *43*, 5010–5013.

(20) Dong, Y. B.; Wang, P.; Ma, J. P.; Zhao, X. X.; Wang, H. Y.; Tang, B.; Huang, R. Q. *J. Am. Chem. Soc.* **2007**, *129*, 4872–4873.

(21) Freire, R. O.; Albuquerque, R. Q.; Júnior, S. A.; Rocha, G. B.; de Mesquita, M. E. *Chem. Phys. Lett.* **2005**, *405*, 123–126.

(22) Parkesh, R.; Lee, T. C.; Gunnlaugsson, T. *Org. Biomol. Chem.* **2007**, *5*, 310–317.

(23) Li, S. F.; Zhong, G.; Zhu, W. H.; Li, F. Y.; Pan, J. F.; Huang, W.; Tian, H. *J. Mater. Chem.* **2005**, *15*, 3221–3228.

(24) Binnemans, K. *Chem. Rev.* **2009**, *109*, 4283–4374.

(25) Leonard, J. P.; dos Santos, C. M. G.; Plush, S. E.; McCabe, T.; Gunnlaugsson, T. *Chem. Commun.* **2007**, 129–131.

(26) Bellusci, A.; Barberio, G.; Crispini, A.; Ghedini, M.; La Deda, M.; Pucci, D. *Inorg. Chem.* **2005**, *44*, 1818–1825.

(27) Bruno, S. M.; Ferreira, R. A. S.; Paz, F. A. A.; Carlos, L. D.; Pillinger, M.; Ribeiro-Claro, P.; Goncalves, I. S. *Inorg. Chem.* **2009**, *48*, 4882–4895.

(28) De Silva, C. R.; Li, J.; Zheng, Z.; Corrales, L. R. *J. Phys. Chem. A* **2008**, *112*, 4527–4530.

(29) Wang, J.; Wang, R.; Yang, J.; Zheng, Z.; Carducci, M. D.; Cayou, T.; Peyghambarian, N.; Jabbour, G. E. *J. Am. Chem. Soc.* **2001**, *123*, 6179–6180.

(30) Irfanullah, M.; Iftikhar, K. *Inorg. Chem. Commun.*, in press.

(31) Melby, L. R.; Abramson, E.; Caris, J. C.; Rose, N. J. *J. Am. Chem. Soc.* **1964**, *86*, 5117-&.

(32) Malta, O. L.; Brito, H. F.; Menezes, J. F. S.; Silva, F. R. G. E.; Donega, C. D.; Alves, S. *Chem. Phys. Lett.* **1998**, *282*, 233–238.

(33) Lima, P. P.; Ferreira, R. A. S.; Freire, R. O.; Paz, F. A. A.; Fu, L. S.; Alves, S.; Carlos, L. D.; Malta, O. L. *ChemPhysChem* **2006**, *7*, 735–746.

(34) Pavithran, R.; Reddy, M. L. P.; Júnior, S. A.; Freire, R. O.; Rocha, G. B.; Lima, P. P. *Eur. J. Inorg. Chem.* **2005**, 4129–4137.

(35) de Mesquita, M. E.; Silva, F. R. G. E.; Albuquerque, R. Q.; Freire, R. O.; da Conceição, E. C.; da Silva, J. E. C.; Júnior, N. B. C.; de Sá, G. F. *J. Alloys Compd.* **2004**, *366*, 124–131.

(36) Donegá, C. D.; Júnior, S. A.; de Sá, G. F. *J. Alloys Compd.* **1997**, *250*, 422–426.

(37) Shoffner, J. P. *Anal. Chem.* **1975**, *47*, 341–343.

(38) Atkins, R. L.; Moore, D. W.; Henry, R. A. *J. Org. Chem.* **1973**, *38*, 400–402.

(39) Lamar, G. N.; Faller, J. W. *J. Am. Chem. Soc.* **1973**, *95*, 3817–3818.

(40) Roberts, R. L.; Blackmer, G. L. *J. Agric. Food Chem.* **1974**, *22*, 542–545.

(41) Iftikhar, K. *Polyhedron* **1996**, *15*, 1113–1120.

(42) Uemura, T.; Suzuki, T.; Onodera, N.; Hagiwara, H.; Hoshi, T. *Tetrahedron Lett.* **2007**, *48*, 715–719.

(43) Tamura, O.; Mita, N.; Imai, Y.; Nishimura, T.; Kiyotani, T.; Yamasaki, M.; Shiro, M.; Morita, N.; Okamoto, I.; Takeya, T.; Ishibashi, H.; Sakamoto, M. *Tetrahedron* **2006**, *62*, 12227–12236.

(44) Iftikhar, K.; Sayeed, M.; Ahmad, N. *Inorg. Chem.* **1982**, *21*, 80–84.

(45) Werts, M. H. V.; Duin, M. A.; Hofstraat, J. W.; Verhoeven, J. W. *Chem. Commun.* **1999**, 799–800.

(46) Villata, L. S.; Wolcan, E.; Feliz, M. R.; Capparelli, A. L. *J. Photochem. Photobiol., A* **1998**, *115*, 185–189.

(47) Villata, L. S.; Wolcan, E.; Feliz, M. R.; Capparelli, A. L. *J. Phys. Chem. A* **1999**, *103*, 5661–5666.

(48) Wolcan, E.; Villata, L.; Capparelli, A. L.; Feliz, M. R. *Photochem. Photobiol. Sci.* **2004**, *3*, 322–327.

(49) Richardson, F. S.; Brittain, H. G. *J. Am. Chem. Soc.* **1981**, *103*, 18–24.

(50) de Mesquita, M. E.; Júnior, S. A.; Júnior, N. B. C.; Freire, R. O.; Silva, F. R. G. E.; de Sá, G. F. *J. Solid State Chem.* **2003**, *171*, 183–188.

(51) dos Santos, E. R.; dos Santos, M. A. C.; Freire, R. O.; Junior, S. A.; Barreto, L. S.; de Mesquita, M. E. *Chem. Phys. Lett.* **2006**, *418*, 337–341.

(52) de Farias, R. F.; Alves, S.; Belian, M. F.; de Sá, G. F. *J. Colloid Interface Sci.* **2001**, *243*, 523–524.

(53) Beltrão, M. A.; Santos, M. L.; Mesquita, M. E.; Barreto, L. S.; da Costa, N. B.; Freire, R. O.; dos Santos, M. A. C. *J. Lumin.* **2006**, *116*, 132–138.

(54) de Farias, R. F.; Alves, S.; Belian, M. F.; de Sá, G. F. *Opt. Mater.* **2002**, *18*, 431–434.

(55) Rodrigues, M. O.; da Costa, N. B.; de Simone, C. A.; Araújo, A. A. S.; Brito-Silva, A. M.; Paz, F. A. A.; de Mesquita, M. E.; Júnior, S. A.; Freire, R. O. *J. Phys. Chem. B* **2008**, *112*, 4204–4212.

(56) Rodrigues, M. O.; Paz, F. A.; Freire, R. O.; de Sa, G. F.; Galembeck, A.; Montenegro, M. C.; Araujo, A. N.; Alves, S. *J. Phys. Chem. B* **2009**, *113*, 12181–12188.

(57) Kottke, T.; Stalke, D. *J. Appl. Crystallogr.* **1993**, *26*, 615–619.

(58) Hooft, R. *COLLECT: Data Collection Software*; Nonius B.V.: Delft, The Netherlands, 1998.

(59) Otwinowski, Z.; Minor, W. In *Methods in Enzymology*; Carter, C. W., Jr., Sweet, R. M., Eds.; Academic Press: New York, 1997; Vol. 276, p 307.

(60) Blessing, R. H. *Acta Crystallogr., A* **1995**, *51*, 33–38.

(61) Blessing, R. H. *J. Appl. Crystallogr.* **1997**, *30*, 421.

(62) Sheldrick, G. M. *SHELXS-97, Program for Crystal Structure Solution*; University of Göttingen: Göttingen, Germany, 1997.

(63) Sheldrick, G. M. *Acta Crystallogr., A* **2008**, *64*, 112–122.

(64) Sheldrick, G. M. *SHELXS-97, Program for Crystal Structure Solution*; University of Göttingen: Göttingen, Germany, 1997.

(65) Freire, R. O.; Rocha, G. B.; Simas, A. M. *Inorg. Chem.* **2005**, *44*, 3299–310.

(66) Stewart, J. J. P. *MOPAC2007*, version 7.058; Stewart Computational Chemistry: Colorado Springs, CO, 2007.

(67) Freire, R. O.; Rocha, G. B.; Albuquerque, R. Q.; Simas, A. M. *J. Lumin.* **2005**, *111*, 81–87.

(68) Freire, R. O.; Rocha, G. B.; Simas, A. M. *J. Mol. Model.* **2006**, *12*, 373–389.

(69) Lima, P. P.; Nobre, S. S.; Freire, R. O.; Júnior, S. A.; Sá Ferreira, R. A.; Pischel, U.; Malta, O. L.; Carlos, L. D. *J. Phys. Chem. C* **2007**, *111*, 17627–17634.

(70) de Mesquita, M. E.; Júnior, S. A.; Oliveira, F. C.; Freire, R. O.; Júnior, N. B. C.; de Sá, G. F. *Inorg. Chem. Commun.* **2002**, *5*, 292–295.

(71) da Costa, N. B.; Freire, R. O.; dos Santos, M. A. C.; Mesquita, M. E. *J. Mol. Struct.: THEOCHEM* **2001**, *545*, 131–135.

(72) Zerner, M. C.; Loew, G. H.; Kirchner, R. F.; Muellerwesterhoff, U. T. *J. Am. Chem. Soc.* **1980**, *102*, 589–599.

(73) Ridley, J. E.; Zerner, M. C. *Theor. Chim. Acta* **1976**, *42*, 223–236.

(74) Zerner, M. C. *ZINDO Manual*; QTP, University of Florida: Gainesville, FL, 1990.

(75) Judd, B. R. *Phys. Rev.* **1962**, *127*, 750–761.

(76) Ofelt, G. S. *J. Chem. Phys.* **1962**, *37*, 511–520.

(77) Malta, O. L.; Silva, F. R. G. E. *Spectrochim. Acta, Part A* **1998**, *54*, 1593–1599.

(78) Malta, O. L.; Silva, F. R. G. E.; Longo, R. *Chem. Phys. Lett.* **1999**, *307*, 518–526.

(79) Judd, B. R. *Operator Techniques in Atomic Spectroscopy*, 2nd ed.; Princeton University Press: Princeton, NJ, 1998.

(80) Carnall, W. T. C., H.; Crosswhite, H. M. *Energy Structure and Transition Probabilities of the Trivalent Lanthanides in LaF₃*; Argonne National Laboratory Report; Argonne National Laboratory: Argonne, IL, 1977.

(81) Malta, O. L.; Brito, H. F.; Menezes, J. F. S.; Silva, F. R. G. E.; Alves, S.; Farias, F. S.; de Andrade, A. V. M. *J. Lumin.* **1997**, *75*, 255–268.

(82) Malta, O. L.; dos Santos, M. A. C.; Thompson, L. C.; Ito, N. K. *J. Lumin.* **1996**, *69*, 77–84.

(83) Van Deun, R.; Binnemans, K.; Gorller-Walrand, C.; Adam, J. L. *J. Phys.: Condens. Matter* **1998**, *10*, 7231–7241.

(84) Weber, M. J.; Varitimo, Te.; Matsinge, Bh. *Phys. Rev. B* **1973**, *8*, 47–53.

(85) Batista, H. J.; de Andrade, A. V. M.; Longo, R. L.; Simas, A. M.; de Sá, G. F.; Ito, N. K.; Thompson, L. C. *Inorg. Chem.* **1998**, *37*, 3542–3547.

(86) Fernandes, J. A.; Braga, S. S.; Pillinger, M.; Ferreira, R. A. S.; Carlos, L. D.; Hazell, A.; Ribeiro-Claro, P.; Gonçalves, I. S. *Polyhedron* **2006**, *25*, 1471–1476.

(87) Yang, Y. T.; Driesen, K.; Nockemann, P.; Van Hecke, K.; Van Meervelt, L.; Binnemans, K. *Chem. Mater.* **2006**, *18*, 3698–3704.

(88) De Silva, C. R.; Maeyer, J. R.; Dawson, A.; Zheng, Z. P. *Polyhedron* **2007**, *26*, 1229–1238.

(89) Janiak, C. *J. Chem. Soc., Dalton Trans.* **2000**, 3885–3896.

(90) Schmidt, K.; Brovelli, S.; Coropceanu, V.; Beljonne, D.; Cornil, J.; Bazzini, C.; Caronna, T.; Tubino, R.; Meinardi, F.; Shuai, Z.; Brédas, J.-L. *J. Phys. Chem. A* **2007**, *111*, 10490–10499.

(91) Albert, I. D. L.; Marks, T. J.; Ratner, M. A.; Rauh, R. D. *J. Phys. Chem. A* **2000**, *104*, 837–844.

(92) Latva, M.; Takalo, H.; Mukkala, V. M.; Matachescu, C.; RodriguezUbis, J. C.; Kankare, J. *J. Lumin.* **1997**, *75*, 149–169.

(93) Tedeschi, C.; Azema, J.; Gornitzka, H.; Tisnes, P.; Picard, C. *Dalton Trans.* **2003**, 1738–1745.

(94) Binnemans, K.; VanHerck, K.; GorllerWalrand, C. *Chem. Phys. Lett.* **1997**, *266*, 297–302.

(95) Klink, S. I.; Grave, L.; Reinhoudt, D. N.; van Veggel, F. C. J. M.; Werts, M. H. V.; Geurts, F. A. J.; Hofstraat, J. W. *J. Phys. Chem. A* **2000**, *104*, 5457–5468.

(96) Kang, J. G.; Kim, T. J. *Bull. Korean Chem. Soc.* **2005**, *26*, 1057–1064.

(97) Driesen, K.; Fourier, S.; Gorller-Walrand, C.; Binnemans, K. *Phys. Chem. Chem. Phys.* **2003**, *5*, 198–202.

(98) Porcher, P. Doctorate Thesis, Université Pierre et Marie Curie−Paris VI, Paris, 1977.

Theoretical and Experimental Spectroscopic Approach of Fluorinated Ln^{3+} β-Diketonate Complexes

Edjane R. dos Santos[1], Ricardo O. Freire[2], Nivan B. da Costa Jr.[2], Filipe A. Almeida Paz[3], Carlos A. de Simone[4], Severino A. Júnior[2], Adriano A. S. Araújo[1], Luiz Antônio O. Nunes,[4] Maria E. de Mesquita[1] and Marcelo O. Rodrigues[2,3].

[1] Department of Chemistry, UFS, 49100-000, São Cristóvão - SE, Brazil.
[2] Department of Chemistry Fundamental, UFPE, 50590-470, Recife - PE, Brazil.
[3] Department of Chemistry, CICECO, University of Aveiro, Campus Universitário de Santiago, 3810-193, Aveiro, Portugal.
[3] Department of Chemistry, UFAL, 57072-970, Maceió – AL, Brazil
[4] Physics Institute of São Carlos, IFSC/USP, 13560-970, São Carlos-SP, Brazil

Author email address: marcelorodrigues@ua.pt (Marcelo O. Rodrigues)

Supporting Information

.

Table S1 - Spherical atomic coordinates for the single-crystal X-ray and Sparkle/AM1 (inside the parentheses) [Eu(fod)$_3$phen] complex, unsigned deviation obtained for the lanthanide-coordinated-atom distances, charge factors (g) and the polarizability (α) of the coordinated atom.

Atom	R(Å)	θ(°)	φ(°)	Unsigned deviation	g[a]	α[a]
Eu (III)	0.000 (0.000)	0.000 (0.000)	0.000 (0.000)	**0.000**	—	—
O (fod)	2.337 (2.383)	90.000 (88.997)	0.000 (-9.149)	0.045	1.176	0.011
O (fod)	2.368 (2.389)	90.000 (88.134)	85.224 (78.684)	0.020	1.176	0.011
O (fod)	2.342 (2.389)	58.726 (57.188)	289.918 (293.402)	0.048	1.176	0.011
O (fod)	2.402 (2.388)	19.612 (26.369)	67.020 (89.146)	0.014	1.176	0.011
O (fod)	2.348 (2.387)	119.844 (126.723)	243.877 (250.378)	0.039	1.176	0.011
O (fod)	2.328 (2.388)	164.527 (170.634)	25.414 (51.006)	0.060	1.176	0.011
N (phen)	2.599 (2.514)	114.415 (108.022)	157.751 (151.105)	0.084	2.516	0.061
N (phen)	2.591 (2.515)	64.073 (63.380)	196.970 (201.800)	0.077	2.516	0.061

[a] Obtained using a non-linear minimization approach

Table S2 - Spherical atomic coordinates for Sparkle/AM1 [Eu(fod)$_3$(H$_2$O)$_2$] complex, charge factors (g) and the polarizability (α) of the coordinated atom.

Atom	R(Å)	θ(°)	φ(°)	g[a]	α[a]
Eu (III)	0.000	0.000	0.000	—	—
O (fod)	2.378	94.378	351.000	0.936	2.875
O (fod)	2.383	84.925	82.252	0.936	2.875
O (fod)	2.382	53.561	300.521	0.936	2.875
O (fod)	2.382	24.019	101.170	0.936	2.875
O (fod)	2.382	126.060	244.453	0.936	2.875
O (fod)	2.381	168.515	109.253	0.936	2.875
O (H$_2$O)	2.395	51.782	217.622	1.905	1.394
O (H$_2$O)	2.395	106.566	143.703	1.905	1.394

[a] Obtained using a non-linear minimization approach

Table S3 - Spherical atomic coordinates for Sparkle/AM1 [Eu(fod)$_3$.phen*N*-O] complex, charge factors (g) and the polarizability (α) of the coordinated atom.

Atom	R(Å)	θ(°)	φ(°)	g[a]	α[a]
Eu (III)	0.000	0.000	0.000	—	—
O (fod)	2.386	88.593	0.793	0.010	0.020
O (fod)	2.390	92.827	62.954	0.010	0.020
O (fod)	2.387	65.496	276.079	0.010	0.020
O (fod)	2.390	84.492	213.986	0.010	0.020
O (fod)	2.388	145.630	142.437	0.010	0.020
O (fod)	2.387	149.212	292.016	0.010	0.020
N (phen*N*-O)	2.546	70.178	141.297	0.989	0.022
O (phen*N*-O)	2.390	15.975	68.467	1.998	1.738

[a] Obtained using a non-linear minimization technique

Table S4 - Spherical atomic coordinates for the Sparkle/AM1 model of the [Tb(fod)$_3$phen] complex.

Atoms	R (Å)	θ (°)	φ(°)
Tb(III)	0.00	0.00	0.00
O (fod)	2.39	90.00	0.00
O (fod)	2.39	90.00	61.99
O (fod)	2.39	73.88	277.87
O (fod)	2.39	79.79	213.85
O (fod)	2.39	140.62	139.17
O (fod)	2.38	153.93	288.71
N (phen)	2.51	57.50	134.98
N (phen)	2.51	13.56	8.60
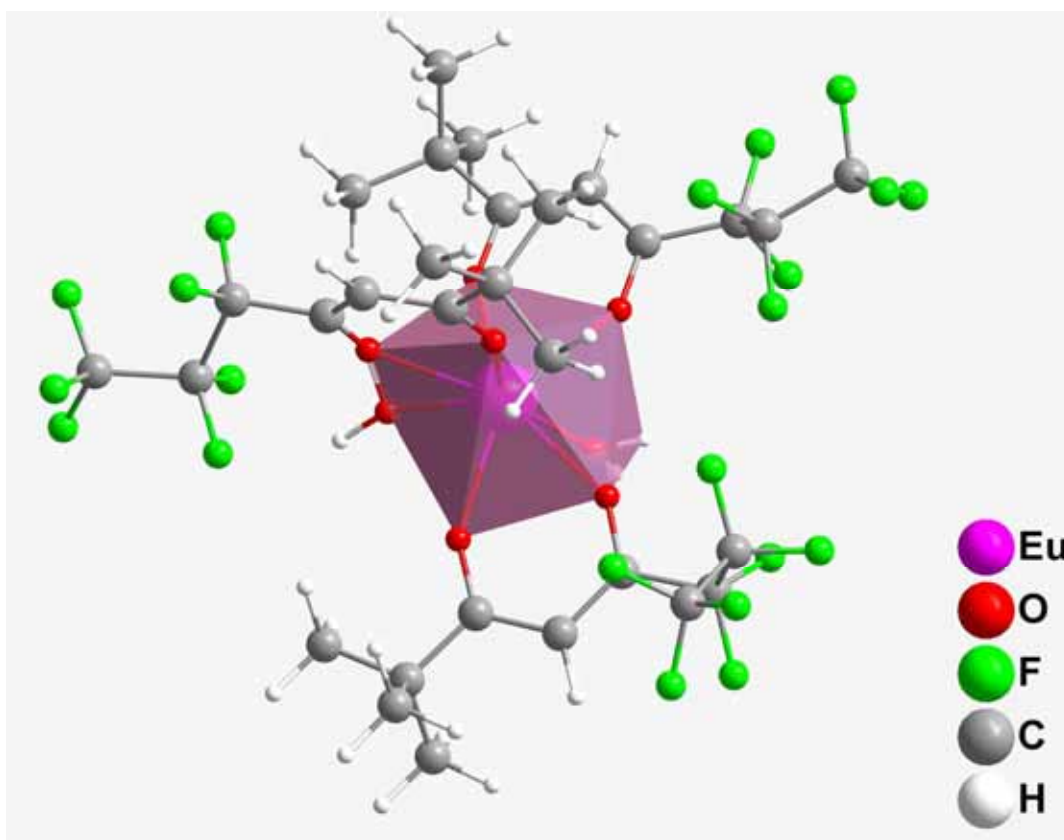
Figure S1 - Optimized molecular structure of [Eu(fod)$_3$(H$_2$O)$_2$] obtained from the Sparkle/AM1 model.
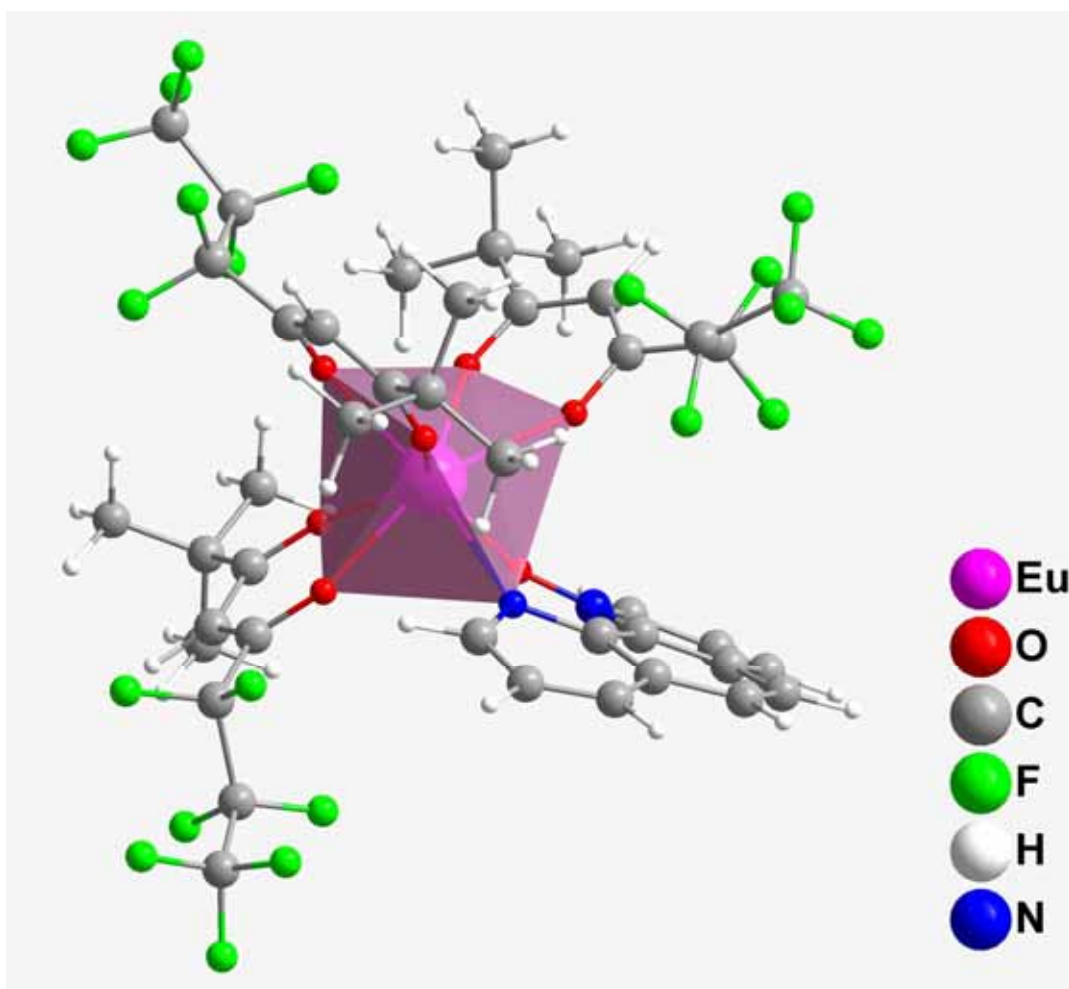
Figure S2 - Optimized molecular structure of [Eu(fod)₃phen*N*-O] obtained from the Sparkle/AM1 model.
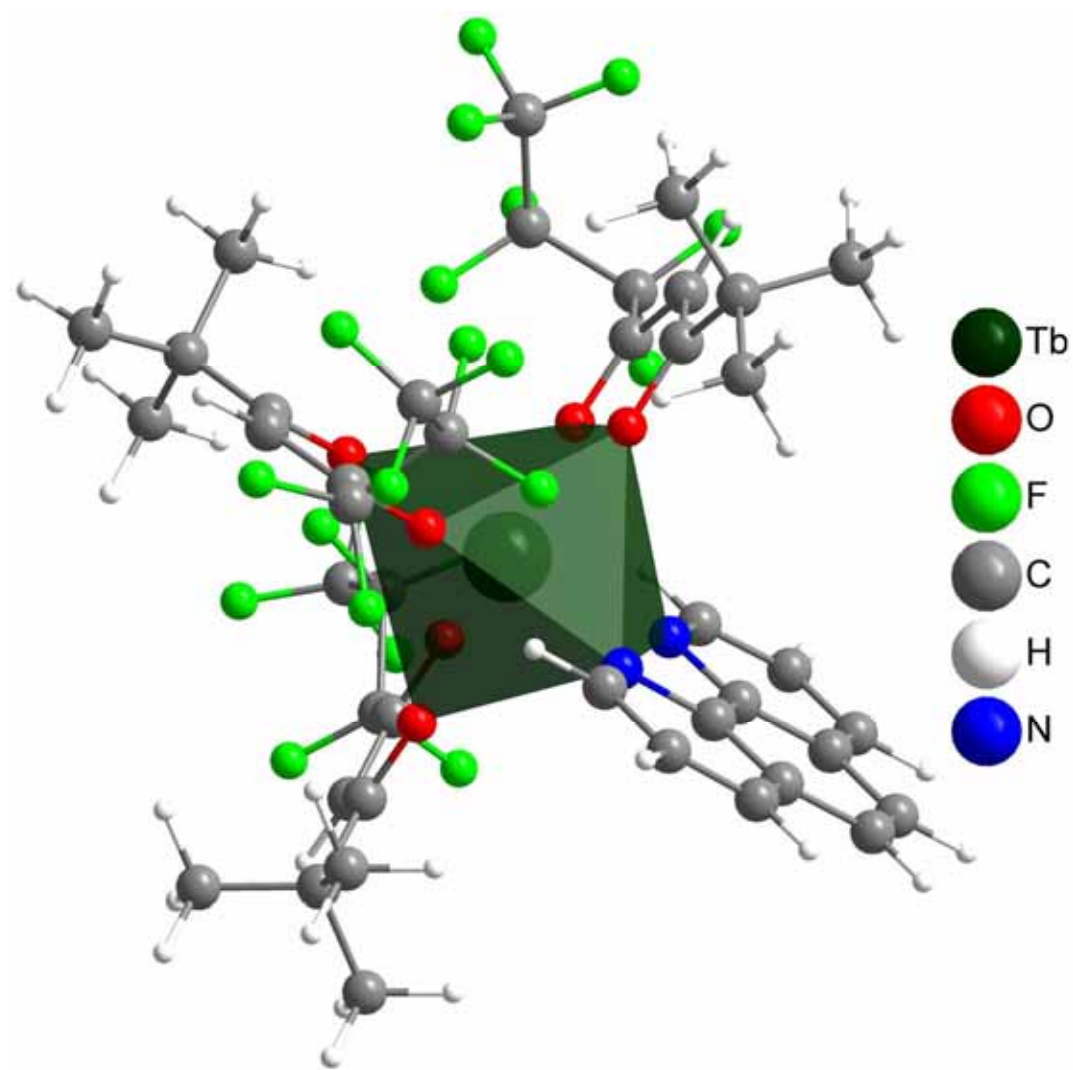
Figure S3 - Optimized molecular structure of [Tb(fod)₃phen] obtained from the Sparkle/AM1 model.
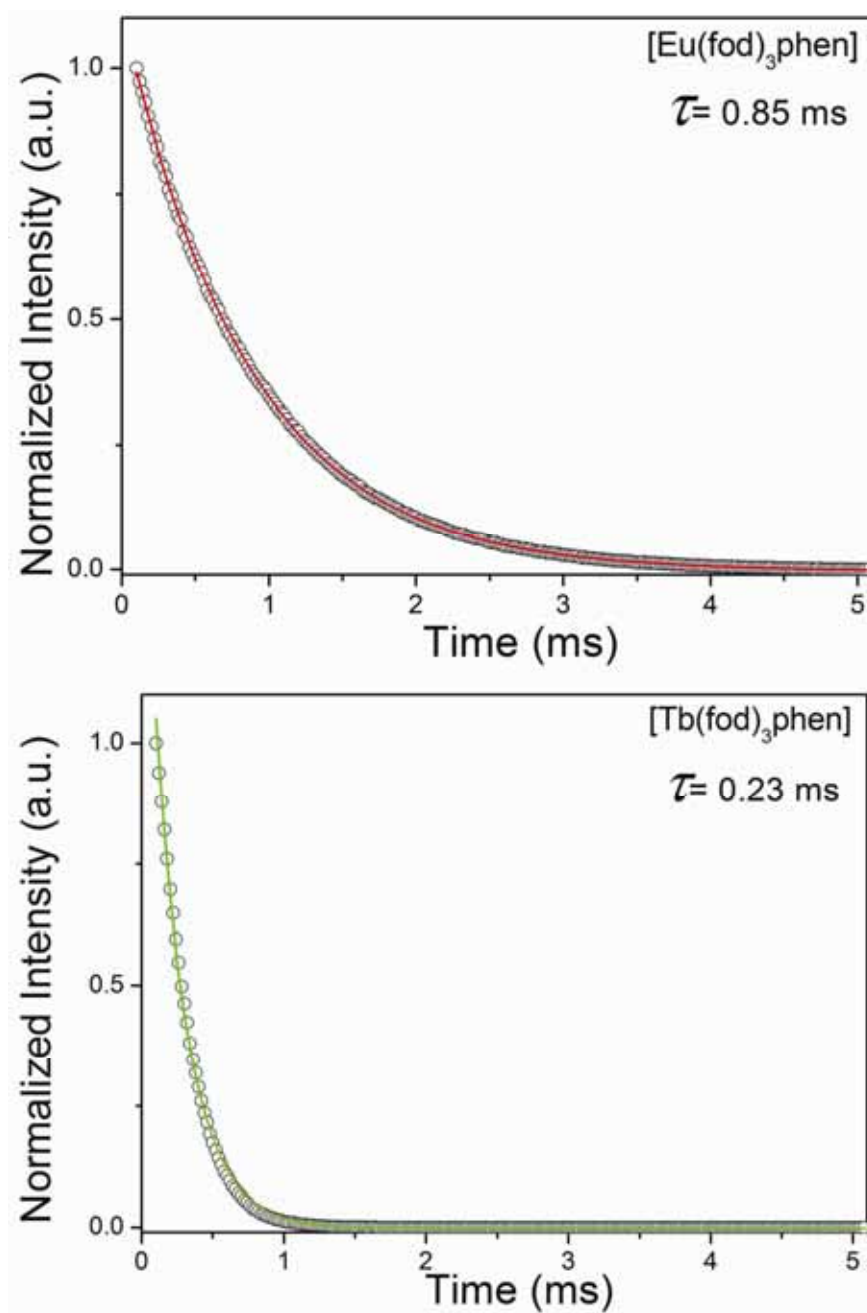
Figure S4 –Normalized decay curves of [Eu(fod)$_3$phen] and [Tb(fod)$_3$phen] at 300K, upon excitation at 348 nm and by monitoring the respective $^5D_0\rightarrow^7F_2$ and $^5D_4\rightarrow^7F_5$ transitions at 611 and 545 nm. Red and green solid lines correspond to the best fit (R> 0.999).

Alysson S. Barreto[1]
Rogério Luiz da Silva[1]
Silvia Caroline G. dos Santos Silva[1]
Marcelo O. Rodrigues[2]
Carlos A. de Simone[3]
Gilberto F. de Sá[2]
Severino A. Júnior[2]
Sandro Navickiene[1]
Maria Eliane de Mesquita[1]

[1]Departamento de Química, Universidade Federal de Sergipe, São Cristóvão-SE, Brazil
[2]Departamento de Química Fundamental, Universidade Federal de Pernambuco, Recife-PE, Brazil
[3]Departamento de Química, Universidade Federal de Alagoas, Maceió-AL, Brazil

Short Communication

Potential of a metal–organic framework as a new material for solid-phase extraction of pesticides from lettuce (*Lactuca sativa*), with analysis by gas chromatography-mass spectrometry

The metal–organic framework $_{\infty}[(La_{0.9}Eu_{0.1})_2(DPA)_3(H_2O)_3]$ was tested for extraction of pyrimicarb, procymidone, malathion, methyl parathion and α- and β-endosulfan from lettuce, with analysis using GC/MS in SIM mode. Experiments were carried out in triplicate at two fortification levels (0.1 and 0.5 mg/kg), and resulted in recoveries in the range of 78–107%, with RSD values between 1.6 and 8.0% for $_{\infty}[(La_{0.9}Eu_{0.1})_2(DPA)_3(H_2O)_3]$ sorbent. Detection and quantification limits ranged from 0.02 to 0.05 mg/kg and from 0.05 to 0.10 mg/kg, respectively, for the different pesticides studied. The method developed was linear over the range tested (0.05–10.0 µg/mL), with correlation coefficients ranging from 0.9990 to 0.9997. Comparison between $_{\infty}[(La_{0.9}Eu_{0.1})_2(DPA)_3(H_2O)_3]$ and conventional sorbent (silica gel) showed better performance of the $_{\infty}[(La_{0.9}Eu_{0.1})_2(DPA)_3(H_2O)_3]$ polymeric sorbent for all pesticides tested.

1 Introduction

Metal–organic frameworks (MOFs), commonly designated as coordination polymers, are a class of porous organic–inorganic hybrid materials that form an interesting interface between materials science and synthetic chemistry [1, 2]. In recent years, these compounds have received special attention due to the unique structural architecture obtained from self-assembly among metal ions and multifunctional organic ligands, and their promising applications in strategic scientific and industrial fields [3–5].

Most of the reports concerning applications of MOFs have focused on catalysis [5, 6] or gas adsorption [7], while the exploration of these materials as pre-concentrators for SPE has been sparsely reported [8]. The scope of this work is to use MOFs as stationary phases, since they can be tailored to provide selective sorption profiles based on control of structural aspects, such as shape and pore size, as well as

hydrophobic and hydrophilic properties. It is important to stress that the materials conventionally used as pre-concentrators have limited sorption capacity or have low selectivity for specific analytes. Moreover, they can present incomplete or slow desorption of analytes. Therefore, MOFs can be regarded as interesting alternative sorbent materials for use in detection of environmental pollutants.

Pesticides are a broad class of persistent organic pollutants that are commonly found in the environment, since they are widely used to protect fruit and vegetables against a range of pests and fungi and provide quality preservation [9]. There has been considerable interest in developing new selective and sensitive extraction methods based on selective sorptive extraction procedures. The ideal sample preparation method should be fast, accurate, precise and should employ small volumes of organic solvents. Moreover, the sample preparation should make use of less expensive materials [10]. Alternative solid-phase materials have been developed to address these issues. The interest of compounds isolated from environmental, food or biological matrices is always key to the development of an analytical method, and prior disruption of the general sample architecture is often needed [11]. The selectivity of the sorbent is an important parameter to be taken into account [12]. The matrix solid-phase dispersion (MSPD) method has been proven to be a good alternative to classical methods, such as liquid–liquid extraction and SPE, in which the analytes are partitioned between a solid sorbent and a semisolid sample matrix, and

Correspondence: Professor Maria Eliane de Mesquita, Departamento de Química, Universidade Federal de Sergipe, Av. Marechal Rondon, s/n., Jardim Rosa Elze, CEP 49100-000 São Cristóvão, SE, Brazil
E-mail: mariaelianemesquita3@gmail.com
Fax: +55-79-2105-6651.

Abbreviations: 3D, three-dimensional; **MOF,** metal–organic framework; **MSPD,** matrix solid-phase dispersion

the analytes are required to have a greater affinity for the sorbent than for the sample matrix [13]. The target compounds are retained on the solid phase and then removed by eluting with a solvent of greater affinity [14, 15].

The aim of the present study was to evaluate the performance of the three-dimensional (3D) MOF $_\infty[(La_{0.9}Eu_{0.1})_2(DPA)_3(H_2O)_3]$ as a new adsorbent material for the determination of pesticides belonging to four chemical classes, namely organochlorine (endosulfan), organophosphate (malathion and methyl parathion), dicarboximide (procymidone) and carbamate (pirimicarb) in fresh lettuce (*Lactuca sativa*) by MSPD and GC/MS.

2 Materials and methods

2.1 Chemicals and reagents

Acetonitrile and acetone were pesticide grade from Tedia (Fairfield, OH, USA). Certified standards of pirimicarb, methyl parathion, malathion, procymidone, α-endosulfan and β-endosulfan were purchased from Dr. Ehrenstorfer (Augsburg, Germany). All standards were at least 98% pure. Analytical grade anhydrous $MgSO_4$ was supplied from Mallinckrodt Baker (Paris, KY, USA). Powdered activated carbon was supplied from Vetec (Rio de Janeiro, Brazil). Lanthanum (III) oxide (La_2O_3), europium (III) oxide (Eu_2O_3) and pyridine-2,6-dicarboxylic acid (H_2DPA) were supplied from Sigma-Aldrich (St. Louis, MO, USA).

2.2 Synthesis of the coordination polymer

The crystals were obtained from the reaction mixture of La_2O_3 (1.8 mmol, 0.5865 g), Eu_2O_3 (0.2 mmol, 0.0704 g), H_2DPA (8 mmol, 1.3360 g) and water (40.0 mL) in a 100-mL Teflon reactor, maintained under autogenous pressure at 180°C for 3 days and then cooled to room temperature. The solid products were recovered by filtration, washed with acetone and air-dried. Anal. Calc. for the $C_{21}H_{15}N_3O_{15}Ln_2$ (%): C-30.38; H-1.80; N-5.06. Found (%): C-29.37; H-2.01; N-5.36.

2.3 Characterization of the coordination polymer

Infrared spectra were recorded with a Perkin Elmer Spectrum BX FTIR spectrophotometer, in the range 4000–400 cm^{-1}, with averaging of 120 and resolution of 4 cm^{-1}, using the conventional KBr technique (Fig. 1). Thermogravimetric analysis employed a SDT 2960 differential scanning calorimeter (Fig. 2). The purge gas used was high-purity nitrogen (N_2), supplied at a flow rate of 50 mL/min. A TA Instruments Q50 thermobalance was used, at a heating rate of 10°C/min and with high purity N_2 as purge gas (20 mL/min). Data were collected on a Nonius Kappa CCD area-detector diffractometer (Mo-Ka graphite-monochromated radiation, $k = 0.7107$ Å) controlled by the Collect
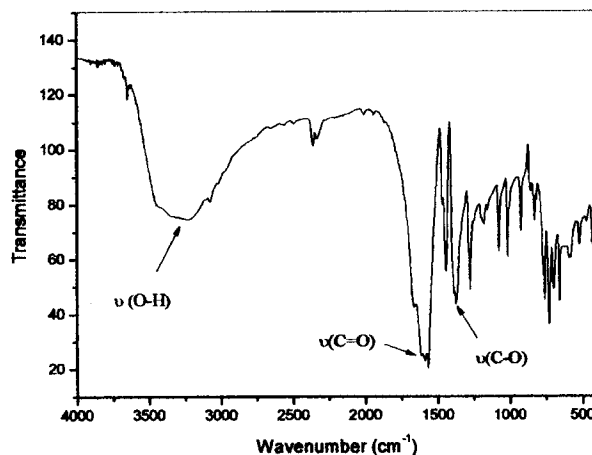
Figure 1. Infrared spectrum of $_\infty[(La_{0.9}Eu_{0.1})_2(DPA)_3(H_2O)_3]$.
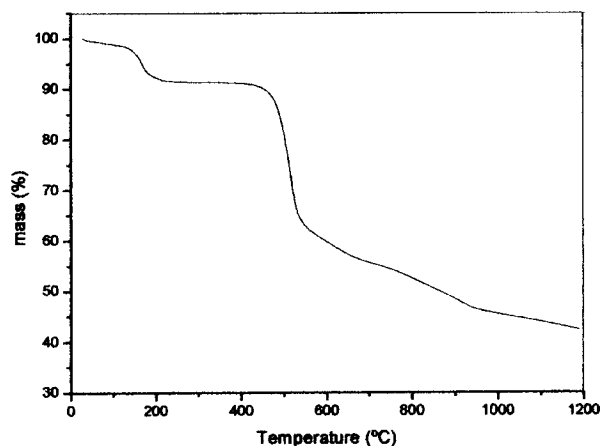
Figure 2. Thermogravimetric curve of $_\infty[(La_{0.9}Eu_{0.1})_2(DPA)_3(H_2O)_3]$.

software package, at room temperature. Images were processed using the Denzo and Scalepack software package, and data were corrected for absorption by the empirical method implemented in SADABS. The structure was solved using the direct methods implemented in SHELXS-97, which allowed the immediate location of the majority of the heavy atoms [16]. All the remaining non-hydrogen atoms were directly located from difference Fourier maps calculated from successive full-matrix least squares refinement cycles on F2 using SHELXL-97 [17].

2.4 Pesticide standard solutions

Stock standard solutions of the pesticides were prepared by precisely weighing out and then dissolving the compounds in acetonitrile to a concentration of 500 μg/mL. These standard solutions were stored at −18°C and were stable for a period of at least 1 month. Working standard solutions were prepared by diluting the stock solutions in acetonitrile as required. Matrix-

matched standards were prepared at the same concentration as those of calibration solutions by adding appropriate amounts of standards to the control matrix extract.

2.5 GC/MS system and operating conditions

A Shimadzu (Kyoto, Japan) system consisting of a QP-2010plus mass spectrometer coupled to a GC-2010 gas chromatograph with a Shimadzu AOC 20i autosampler and a split/splitless injector was used for the identification and quantification of the pesticides. A fused-silica DB-5MS column (5% phenyl–95% polydimethylsiloxane; 30 m × 0.25 mm id, 0.25 μm), supplied by J&W Scientific (Folsom, CA, USA), was employed with helium (purity 99.995%) as carrier gas at a flow rate of 1.6 mL/min. The column temperature was programmed as follows: 60°C for 1 min, then directly to 290°C at 10°C/min, with a hold time of 3 min. The solvent delay was 5 min. The injector port was maintained at 250°C and a 1-μL sample volume was injected in splitless mode (0.7 min). The data were acquired and processed on a personal computer, using Shimadzu GC Solution software. The total analysis time was 27 min, and the equilibrium time was 2 min. The eluent from the GC column was transferred, *via* an interface line heated to 280°C, into the 70 eV electron ionization source, also maintained at 280°C. The analysis was performed in the SIM mode. For the first acquisition window (8.00 to 18.50 min), the ions monitored were m/z 166 and **238** (pirimicarb), m/z 109 and **246** (methyl parathion) and m/z 127 and **173** (malathion). For the second acquisition window (18.50 to 27.00 min), m/z 124 and **283** (procymidone), m/z 195 and **241** (α-endosulfan) and m/z 195 and **241** (β-endosulfan) were monitored. Values of m/z in bold type correspond to the quantification ion for each pesticide.

2.6 Sample preparation and fortification

The lettuce samples used for method development were obtained from an organic farm (pesticide free) located in the municipality of Itabaiana, State of Sergipe, Brazil. A representative portion of sample was diced with a stainless steel knife. Fortified samples were prepared by adding 500 μL of different multicomponent standard solutions to 2 g of sample, resulting in levels of 0.1 and 0.5 mg/kg on a fresh weight basis. The fortified lettuce was left to stand for 30 min at room temperature, to allow the solvent to evaporate, before extraction. Replicates were analyzed at each fortification level. The extraction procedure was as described below.

2.7 Extraction procedure

An aliquot of lettuce (2.0 g) was placed into a glass mortar (*ca.* 50 mL) and 0.5 g of coordination polymer was added. The lettuce was then gently blended into the polymer material with

a glass pestle, until a homogeneous mixture was obtained (*ca.* 3 min). The homogenized mixture was introduced into a 100 × 20 mm id polypropylene column, filled with 0.1 g of silanized glass wool at the base followed by 1.0 g of anhydrous magnesium sulfate and 0.1 g of activated carbon, respectively. A 30-mL portion of acetonitrile was added to the column and the sample was allowed to elute dropwise. The eluent was collected in a graduated conical tube and concentrated to a volume of 1 mL, using first a rotary vacuum evaporator (45°C), followed by a gentle flow of nitrogen. A 1-μL portion of the extract was then directly analyzed by GC/MS.

3 Results and discussion

3.1 Characterization of $_\infty[(La_{0.9}Eu_{0.1})_2(DPA)_3(H_2O)_3]$

A large amount of a single-crystalline phase of the MOF was successfully obtained by hydrothermal reaction. Based on single-crystal X-ray diffraction, the compound was formulated as $_\infty[(La_{0.9}Eu_{0.1})_2(DPA)_3(H_2O)_3]$. All crystallographic data are summarized in Table 1.

It is important to mention that the $_\infty[(La_{0.9}Eu_{0.1})_2(DPA)_3(H_2O)_3]$ is isostructural to a pure La^{3+} compound previously reported. According to the X-ray analyses, the substitution of La^{3+} sites with Eu^{3+} ions does not cause structural changes, and consequently La^{3+} ions are located in the coordination environment. The compounds crystallize in the monoclinic space group $P2_1/c$, with cell parameters very close to the lanthanum compound reported by

Table 1. Crystal data and structure refinement parameters for $_\infty[(La_{0.9}Eu_{0.1})_2(DPA)_3(H_2O)_3]$

Empirical formula	$C_{21} H_{15} La_2 N_3 O_{15}$
Formula weight	829.42
Temperature	295(2) K
Wavelength	0.71073
Crystal system, space group	Monoclinic, $P2_1/c$
Unit cell dimensions	$a = 11.0120(2)$ Å $\alpha = 90$
	$b = 17.5730(3)$ Å $\beta = 100.3090(10)$
	$c = 13.5990(2)$ Å $\gamma = 90$
Volume	2589.11(7) Å^3
Z, Calculated density	4, 1.825 Mg/m^3
Absorption coefficient	3.297 mm^{-1}
F (000)	1352
Crystal size	0.298 × 0.278 × 0.211 mm
Theta range for data collection	2.87–27.31
Limiting indices	−11 < = h < = 13,
	−22 < = k < = 22,
	−16 < = l < = 16
Reflections collected/unique	25 500/5268 [R(int) = 0.1606]
Completeness to theta = 27.31	90.2%
Refinement method	Full-matrix least-squares on F^2
Data/restraints/parameters	5268/0/371
Goodness-of-fit on F^2	1.11
Final R indices [$I > 2$sigma(I)]	R1 = 0.0434, wR2 = 0.0972
R indices (all data)	R1 = 0.0796, wR2 = 0.1057
Largest diff. peak and hole	2.508 and −2.590 e.Å^{-3}
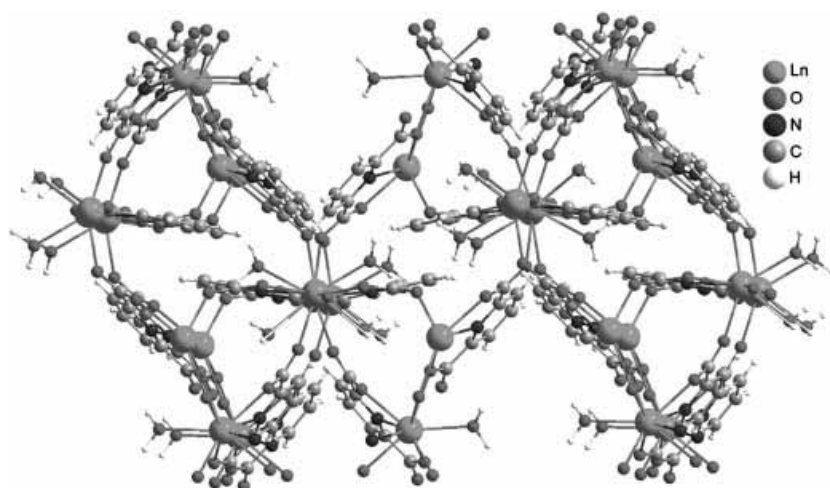
Figure 3. View along the c-axis of the extended structure of $_{\infty}[(La_{0.9}Eu_{0.1})_2(DPA)_3(H_2O)_3]$ showing the channels.

Costes and co-workers [18]. Each DPA ligand is coordinated with three La^{3+} ions *via* nitrogen atoms from pyridine rings and two carboxylate groups, forming a 3D structure. Figure 3 shows the 3D supramolecular structure of $_{\infty}[(La_{0.9}Eu_{0.1})_2(DPA)_3(H_2O)_3]$, with hexagonal and octagonal channels running parallel to the *c*-axis.

Elemental analysis, infrared spectroscopy and thermal decomposition data are in good agreement with the crystallographic structure of $_{\infty}[(La_{0.9}Eu_{0.1})_2(DPA)_3(H_2O)_3]$. The complete dehydration of hydrated lanthanide dipicolinate is a single-step procedure that takes place in a temperature range from 100 to 250°C. Dehydration corresponds to an endothermic process. The dipicolinate ligand decomposition first presents a steep slope and then a slight slope until constant weight loss is observed. This process begins rapidly; then, as the temperature increases, a slow decomposition takes place. Weight losses indicate that the formation of oxycarbonate, $La_2O_2(CO_3)$, occurs at a higher temperature (near 640°C). The oxycarbonate phases are not stable. A major exothermic peak was observed when the decomposition of the dipicolinate takes place, but satellite peaks were observed. A stable oxide was the final product.

3.2 MSPD procedure

The type of sorbent and the polarity of the elution solvent are known to be key factors in MSPD, since they determine both the efficacy of the extraction and the purity of the final extracts [19]. Here, the performance of $_{\infty}[(La_{0.9}Eu_{0.1})_2(DPA)_3(H_2O)_3]$, as a new sorbent material for MSPD, was compared with silica gel, which was previously used as the extracting phase in multiclass analysis of the same pesticides in lettuce in our earlier validated MSPD procedure [20]. Fortification concentrations were selected to achieve the maximum residue levels for pesticides in lettuce, according to Brazilian legislation, which range from 1.0 to 8.0 mg/kg. Recovery experiments were carried out in triplicate, at two fortification levels (0.1 and 0.5 mg/kg). Analyses were performed by GC/MS (SIM), with external calibration using matrix-matched standards. Average recoveries ranged from 78 to 107%, with RSD values of 1.6–8.0%, using $_{\infty}[(La_{0.9}Eu_{0.1})_2(DPA)_3(H_2O)_3]$ as sorbent. Average recoveries using silica gel were in the range from 60 to 103%, with RSD values of 1.6–8.0%. The values obtained were generally satisfactory, considering the recovery range normally considered acceptable (70–130%). Comparison of the $_{\infty}[(La_{0.9}Eu_{0.1})_2(DPA)_3(H_2O)_3]$ polymer with the commercially available silica gel showed that $_{\infty}[(La_{0.9}Eu_{0.1})_2(DPA)_3(H_2O)_3]$ was a better extracting phase for all pesticides investigated. Recoveries of α-endosulfan were lower for silica gel, compared to $_{\infty}[(La_{0.9}Eu_{0.1})_2(DPA)_3(H_2O)_3]$. Table 2 presents recoveries of the six pesticides at two concentration levels in lettuce.

Robustness may be defined as the measure of the ability of an analytical method to remain unaffected by small but deliberate variations in method parameters, and provides an indication of its reliability during normal usage. Robustness testing is a systematic process of varying a parameter and measuring the effect on the method by monitoring system suitability and/or the analysis of samples [21]. In none of the lettuce samples tested was there any excessive interference of matrix peaks in detection of the pesticides. Nearly 90 recovery tests of the six pesticides were conducted with the developed method using different lettuce samples. The functioning of the instrument was unaffected by the large number of different samples of varying origins that were analyzed, with routine clean-up of the insert and/or ion source box sufficient to maintain analytical performance. Furthermore, comparison of the extraction efficiency of the proposed MSPD procedure with that of Wang *et al.* [22], for different lettuce, demonstrates that the average recovery value for the level of 0.5 mg/kg (105%, $n = 3$) for procymidone was better than that reported previously (77%), using the same extraction procedure, but at a concentration level of 1.0 mg/kg ($n = 3$) and with C_{18}-bonded silica (0.5 g) as dispersant material.

Table 2. Average % recoveries (%RSD) of fortified pesticides in lettuce using the MSPD method with GC/MS analysis

Pesticide	Fortification level (mg/kg)	Mean % recovery (%RSD)	
		Silica gel[a)]	$_\infty[(La_{0.9}Eu_{0.1})_2 (DPA)_3(H_2O)_3]^{b)}$
Pirimicarb	0.1	77; 2.7	88; 2.2
	0.25	103; 3.0	–
	0.5	103; 4.6	95; 3.2
Methyl parathion	0.1	89; 1.6	95; 8.0
	0.25	100; 2.9	–
	0.5	72; 3.1	105; 3.0
Malathion	0.1	67; 2.2	79; 3.5
	0.25	120; 2.4	–
	0.5	90; 5.0	98; 6.3
Procymidone	0.1	62; 1.6	82; 4.2
	0.25	80; 6.9	–
	0.5	70; 2.5	105; 5.5
α-Endosulfan	0.1	50; 8.6	78; 5.2
	0.25	60; 7.6	–
	0.5	62; 3.2	97; 6.2
β-Endosulfan	0.1	60; 2.6	81; 1.6
	0.25	50; 8.0	–
	0.5	60; 2.9	107; 2.4

a) $n = 7$.
b) $n = 3$.

The linearity of a method is a measure of the range within which detector response is directly proportional to the concentration of analyte in standard solutions or samples. The linearity for all compounds was determined using blank lettuce samples fortified at concentration levels ranging from 0.05 to 10.0 µg/mL. The slope and intercept values, together with their standard deviations, were determined using regression analyses. Linear regression coefficients for the different pesticides ranged from 0.9990 to 0.9997. The LODs were calculated considering the standard deviation of the analytical noise (a value of seven times the standard deviation of the blank) and the slope of the regression line, and ranged from 0.02 to 0.05 mg/kg. The LOQ were determined as the lowest concentrations giving a response of ten times the average of the baseline noise, calculated using seven unfortified samples. The LOQ values for these compounds ranged from 0.05 to 0.1 mg/kg. The repeatability of the method was assessed using six successive analyses of 5.0 µg/mL pesticide standard solution, and resultant RSDs were in the range of 2.8–3.6%.

3.3 Application of the method to real samples

The MSPD procedure developed was applied to the determination of pesticides in commercial lettuce samples. Four different samples of lettuce, obtained in local markets in the city of Itabaiana, State of Sergipe (Brazil), and originating from conventional agriculture, were analyzed using this method. One of the four samples analyzed, contained pirimicarb insecticide at 0.18 mg/kg, which is lower than the maximum residue level established by Brazilian legislation (1.0 mg/kg).

4 Concluding remarks

A new material for MSPD, $_\infty[(La_{0.9}Eu_{0.1})_2(DPA)_3(H_2O)_3]$, was developed, characterized and tested for the multiclass determination of pesticides in lettuce. Results showed that $_\infty[(La_{0.9}Eu_{0.1})_2(DPA)_3(H_2O)_3]$ can be successfully used in analysis of pirimicarb, methyl parathion, malathion, procymidone, α-endosulfan and β-endosulfan in lettuce. In the case of the insecticide α-endosulfan, the performance of $_\infty[(La_{0.9}Eu_{0.1})_2(DPA)_3(H_2O)_3]$ was better than that observed for silica gel. The new solid phase may be useful in screening protocols used by official regulatory laboratories to identify pesticides in lettuce.

The authors have declared no conflict of interest.

5 References

[1] Yaghi, O. M., O'Keeffe, M., Ockwig, N. W., Chae, H. K., Eddaoudi, M., Kim, J., *Nature* 2003, *423*, 705–714.

[2] Champness, N. R., *Dalton Trans.* 2006, 877–880.

[3] Kitagawa, S., Kitaura, R., Noro, S., *Angew. Chem. Int. Ed.* 2004, *43*, 2334–2375.

[4] Gu, Z. Y., Wang, G., Yan, X. P., *Anal. Chem.* 2010, *82*, 1365–1370.

[5] Mueller, U., Schubert, M., Teich, F., Puetter, H., Schierle-Arndt, K., Pastré, J., *J. Mater. Chem.* 2006, *16*, 626–636.

[6] Shultz, A. M., Farha, O. K., J Hupp, T., Nguyen, S. T., *J. Am. Chem. Soc.* 2009, *131*, 4204–4205.

[7] Nijem, N., Veyan, J. -F. O., Kong, L., Li, K., Pramanik, S., Zhao, Y., Li, J., Langreth, D., Chabal, Y. J., *J. Am. Chem. Soc.* 2010, *132*, 1654–1664.

[8] Zhou, Y. Y., Yan, X. P., Kim, K. N., Wang, S. W., Liu, M. G., *J. Chromatogr. A* 2006, *1116*, 172–178.

[9] Gilbert-Lopez, B., Garcia-Reyes, J. F., Mezcua, M., Molina-Diaz, A., Fernandez-Alba, A. R., *J. Agric. Food Chem.* 2007, *55*, 10548–10556.

[10] Grujic, S., Vasiljevic, T., Radisic, M., Lausevic, M., *Handbook of Pesticides-Methods of Pesticide Residues Analysis*, CRC Press, Boca Raton 2010.

[11] Capriotti, A. L., Cavaliere, C., Giansanti, P., Gubbiotti, R., Samperi, R., Laganá, A., *J. Chromatogr. A* 2010, *1217*, 2521–2532.

[12] Barker, S. A., *J. Chromatogr. A* 2000, *885*, 115–127.

[13] Barker, S. A., *J. Chromatogr. A* 2000, *880*, 63–68.

[14] Barker, S. A., *J. Biochem. Biophys. Meth.* 2007, *70*, 151–162.

[15] Carvalho, P. H., Barreto, A. S., Rodrigues, M. O., Prata, V. M., Alves, P. B., Mesquita, M. E., AlvesJr, S., Navickiene, S., *J. Sep. Sci.* 2009, *32*, 2132–2138.

[16] Sheldrick, G. M., *SHELXS-97-Program for Crystal Structure Solution*, University of Göttingen, 1997.

[17] Sheldrick, G. M., *SHELXL-97-Program for Crystal Structure Refinement*, University of Göttingen, 1997.

[18] Brouca-Cabarrecq, C., Fernandes, A., Jaud, J., Costes, J. P., *Inorg. Chim. Acta* 2002, *332*, 54–60.

[19] Gilbert-López, B., García-Reyes, J. F., Molina-Díaz, A., *Talanta* 2009, *79*, 109–128.

[20] Silva, R. L., Silva, C. P., Navickiene, S., *J. Environ. Sci. Health B* 2010, *45*, 589–594.

[21] Bliesner, D. M., *Validating Chromatographic Methods-A Practical Guide*, Wiley, New Jersey, 2006.

[22] Wang, S., Xu, Y., Pan, C., Jiang, S., Liu, F., *Anal. Biochem.* 2007, *387*, 673–678.

Thermal characterization of usnic acid/collagen-based films

Paula Santos Nunes · Marília Santos Bezerra · L. P. Costa ·
Juliana Cordeiro Cardoso · R. L. C. Albuquerque Jr. · M. O. Rodrigues ·
Gabriela Borin Barin · Francilene Amaral da Silva · A. A. S. Araújo

Abstract The purpose of this study was to evaluate the physical–chemical properties of collagen (CL) and usnic acid/collagen-based (UAC) films, using differential thermal analysis (DTA), thermogravimetry (TG/DTG), infrared spectroscopy (FTIR), and scanning electron microscopy (SEM). Both films were prepared by casting process using polyethylene glycol 1500 (PEG 1500) as plasticizer. In the spectrum of UAC, similar bands of the usnic acid are observed, indicating that the polymerization (film formation) did not affect the stability of the drug. Distinctly, DTA curve of UAC did not show an endothermic peak at 201 °C, indicative that the drug was incorporated into the polymeric system. These results were corroborated by the scanning electron microscopy (SEM). The TG/DTG curves of UAC presented a different thermal decomposition profile compared to the individual compounds and CL. These findings suggest the occurrence of molecular dispersion or solubilization of the drug in the collagen film.

Keywords Casting · Biodegradable films · Usnic acid · Collagen · Thermal characterization

P. S. Nunes · M. S. Bezerra · F. A. da Silva ·
A. A. S. Araújo (✉)
Departamento de Fisiologia, Universidade Federal de Sergipe,
Av. Marechal Rondon, s/n, Cidade Universitária,
CEP 49100-000 São Cristóvão, Sergipe, Brazil
e-mail: adriasa2001@yahoo.com.br

L. P. Costa · M. O. Rodrigues · G. B. Barin
Departamento de Química, Universidade Federal de Sergipe, Av.
Marechal Rondon, s/n, Cidade Universitária, CEP 49100-000
São Cristóvão, Sergipe, Brazil

J. C. Cardoso · R. L. C. Albuquerque Jr.
Instituto de Tecnologia e Pesquisa-ITP, Av. Murilo Dantas, 300,
CEP 49032-490 Aracaju, Sergipe, Brazil

Introduction

Natural polymers have been increasingly studied for controlled-release applications due to their biocompatibility and biodegradability. Materials such as hyaluronic acid [1], fibrin [2], fibrinogen [3], and collagen [4] have been tested as carries for drug delivery systems [5]. Collagen is a potentially useful biomaterial since it is a major constituent of connective tissue. The main applications of collagen as drug delivery systems are collagen-shields in ophthalmology, sponges for burns/wounds, and liposomes–collagen associations for transdermal and sustained drug delivery [6–8].

Formulations such as ointments and wound dressings have been developed for the treatment of severe skin wounds or ulcers including bedsores and burn wounds [9, 10]. These studies generally involved the development and/or the physical characterization of the materials [11, 12]. In this regard, a better understanding of the physical properties of films is of great importance for subsequent applications of these materials. Physical properties are strongly affected by the state of the material: for example, in the glass state the material will be hard and rigid, but in the rubbery state it will be flexible and extendible. Besides, some studies have been carried out in order to incorporate bioactive compounds into collagen-based films, so that such films could work as drug controlled release within the target tissues [13, 14].

As previously reported, usnic acid is one of the most common and abundant lichen metabolites with interesting antibiotic [15], anti-inflammatory [16], antiprotozoal [17], antitumoral [18], larvicidal [19], antipyretic and analgesic [20] activities. The aim of this study was to prepare a collagen-based film constituted of usnic acid-loaded liposomes and to evaluate its physico-chemical properties using differential thermal analysis (DTA), thermogravimetry/derivative thermogravimetry (TG/DTG) and infrared spectroscopy

(FTIR). Films were also characterized regarding microstructure using scanning electron microscopy (SEM).

Experimental

Materials

Usnic acid, 2,6-diacetyl-7,9-dihydroxy-8,9b-dimetyl-1,3 (2H,9bH)-dibenzeno-furandione, was isolated from *Cladonia substellata* Vainio collected in March, 2006, in the Itabaiana county, Sergipe-SE, Brazil. Lichen sample was identified by M. P. Marcelli (Botanical Institute of São Paulo-SP, Brazil), where a voucher specimen was deposited (Deposit #SP393249). All chemicals were of reagent grade. The collagen was prepared according to the method proposed by 21o, 2005 [21].

Extraction and purification of usnic acid

Air-dried lichen (300 g) was extracted with diethyl ether in a Soxhlet apparatus and the precipitate formed on cooling collected, recrystallised from ethanol, yielding 330-mg usnic acid [22].

Films preparation

Collagen-based (CL) films were prepared by casting method using collagen dispersion (2%) in 0.5 M acetic acid with 20% of plasticizer (polyethylene glycol-PEG 1500 Isofar Lot. 021423) in relation to the polymer dry weight. This dispersion was casted onto a clean rimmed perspex plate and allowed to dry at room temperature in order to obtain the films.

Usnic acid-loaded liposomes were prepared by conventional rotary evaporation method. Briefly, phosphatidylcholine (Lipoid GMBH 75% Lot 776095-1) was dissolved in an appropriate volume of chloroform according to the ratio phosphatidilcoline/usnic acid 18:1 w/w. The mixture was dried to a thin lipid film using a rotary evaporator. This film was kept in desiccator for at least 24 h until the organic solvent was totally eliminated. Then, the lipid film was hydrated and dispersed in water, under vigorous magnetic agitation, promoting the formation of the multilamellar vesicles (MLV). Small unilamellar vesicles (SUV) were prepared by probe sonication of the MLV dispersion. After this procedure, the usnic acid-loaded liposomes were mixed with collagen dispersion (2% in 0.5 M acetic acid with 20% of collagen:PEG1500 w:w) in the ratio 1:4 (v/v) in order to obtain the usnic acid/collagen-based films (UAC).

Particle size distribution and ζ-potential measurement

The particle size and surface change potential of usnic acid-loaded liposomes were determined using Zetasizer® (Nano-ZS90, Malvern Instruments, United Kingdom), at 25 °C. Samples of liposomes were diluted in water (1:10) for an effective particle count. The distribution and the mean diameter of particles, as well as their standard deviation and poliydispersity index (PDI) were assessed. The surface change of usnic acid-loaded liposomes was determined by the measurement of the zeta potencial (ζ) by electrophoresis after dilution of liposomes in water, using the same apparatus.

Thermal analysis

TG/DTA curves were obtained in a TA instruments model SDT 2960 Simultaneous using platinum crucibles with about 5 mg of samples, under dynamic nitrogen atmosphere (100 mL min^{-1}) and heating rate of 10 °C.min^{-1} in the temperature range from 25 to 900 °C. The DTA cell was calibrated with indium (m.p. 156.6 °C; $\Delta H_{fus.} = 28.54$ J g^{-1}) and zinc (m.p. 419.6 °C). TG/DTG was calibrated using a $CaC_2O_4 \cdot H_2O$ standard in conformity to ASTM.

Infrared spectroscopy

The infrared absorption data was obtained in the range 4,000–400 cm^{-1} in KBr pellets using a FTIR-Bomen spectrophotometer model MB-120 at room temperature.

Scanning electron microscopy

The dried films were mounted on aluminum stubs, coated with a thin layer of gold and visualized with a JEOL Model JSM-6360-LV scanning electron microscope, at an accelerated voltage of 20 kV.

Results and discussion

Collagen and UA-loaded liposome showed to be a very interesting material for the development of films. The mean of the vesicles was 70 nm and the surface charge 11.8 ± 7.19 mV. The process developed here, produced films slightly yellowish with moderate opacity and good flexibility. The presence of phosphatidylcholine and collagen of its formulation provide it with better properties if compared with other films.

DTA curve of usnic acid showed an endothermic event between 192 and 230 °C with a well-defined peak at 201 °C corresponding to the melting point of the drug (Fig. 1a). Furthermore, the DTA curve showed an
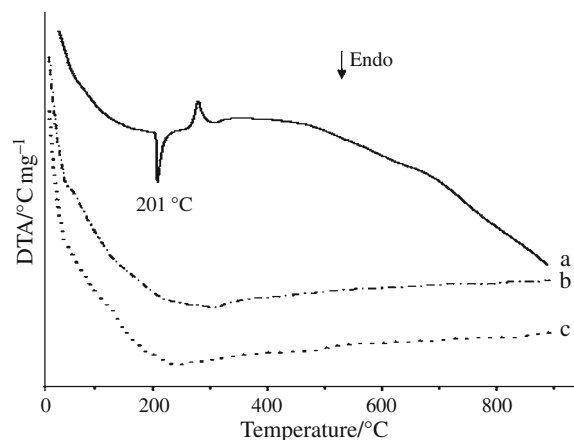
Fig. 1 DTA curves of *a* usnic acid, *b* collagen film and *c* usnic acid–collagen film obtained in heating rate of 10 °C min^{-1} under dynamic nitrogen atmosphere (50 mL min^{-1})

exothermic event caused by thermal decomposition of the examined sample. This second event had a peak at 273.3 °C. TG curves showed an event of fast mass loss occurring in the range of 230 to 350 °C (Fig. 2a), as well as further slow mass loss in the range of 350 to 900 °C, which is usually attributed to the elimination of carbonaceous material.

As seen in Fig. 1b, the CL sample showed a major endothermic transition in the DTA curve between 30 and 80 °C corresponding to its dehydration (unbound water). However, this event was also seen in the TG curve (Fig. 2b) where a humidity loss of about 10.24% was detected. This film showed a thermal stability region between 80 and 175 °C, and an endothermic event indicated by a broad peak at 303 °C, corresponding to the thermal decomposition of this material. This result was confirmed by TG curve.

TG/DTG curve of UAC showed four weight loss events at the following temperature ranges and weight loss
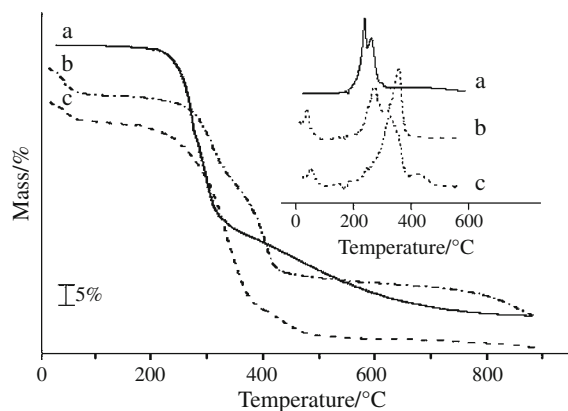
percentages: 25–96, 150–381, 381–516, and 516–880 °C (Fig. 2c). The first event is related to the superficial water releasing. The second and third events correspond to the thermal decomposition process followed by carbonization. The last event is related to the carbon material elimination. DTA curve showed an endothermic peak between 147 and 371 °C, corresponding to the first step of thermal degradation of usnic acid–collagen (Fig. 1c). In addition, the melting peak of usnic acid at 201 °C was not observed, indicating absence of free usnic acid. It was noted that UAC has a different thermal decomposition profile compared to the CL indicating that usnic acid was effectively loaded into the membrane.

The FTIR spectra of free usnic acid, CL and UAC are shown in Fig. 3a–c, respectively. The usnic acid spectrum (Fig. 3a) showed a 1,690 cm^{-1} band corresponding to a conjugated cyclic ketone group. Weak bands at 1,715 and 1,678 cm^{-1} in the infrared spectrum are assigned to the v(C=O) non-conjugated cyclic ketone and the non-aromatic methyl ketone, respectively. Conjugation, electron donating ring substituents and possible intra-molecular hydrogen-bonding, all contribute to the lower wavenumber position of the aromatic methyl ketone to 1,628 cm^{-1}. It is also possible to assign the antisymmetric and symmetric v(COC) aryl alkyl ether modes to bands at approximately 1,283 and 1,072 cm^{-1}, respectively. In the spectrum of UAC (Fig. 3c), similar bands of the usnic acid are observed, indicating that the film formation did not affect the stability of the drug.

The microstructures of CL and UAC analyzed by SEM are presented in Fig. 4. Both films presented a dense structure, typical of protein films, as has been previously reported for films prepared with amaranth proteins [23]. The microstructure of the cross-sectional area of the films revealed that CL structure was dense, with a fibrous formation parallel arranged in relation to the film surface. Notwithstanding, some porous formation was also detected (Fig. 4 and 5), although these cavities seem to be closed

Fig. 2 TG curves of *a* usnic acid, *b* collagen film and *c* usnic acid–collagen film obtained in heating rate of 10 °C min^{-1} under dynamic nitrogen atmosphere (50 mL min^{-1})
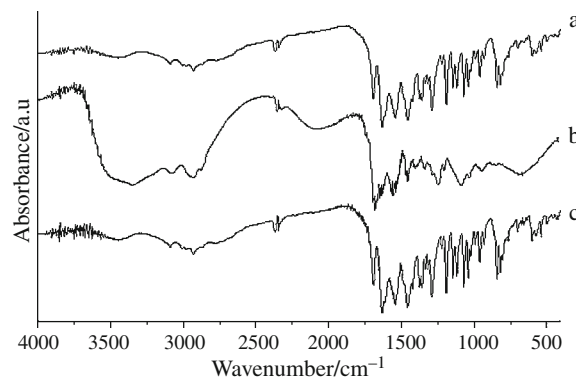
Fig. 3 IR spectra of *a* usnic acid, *b* collagen film, and *c* usnic acid–collagen film
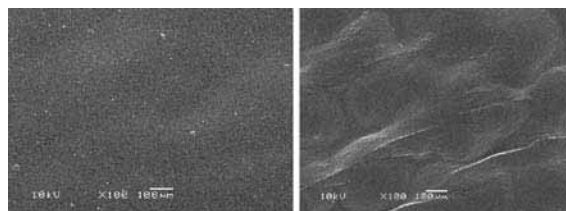
Fig. 4 SEM photographs of surface of **a** collagen membrane and **b** usnic acid–collagen
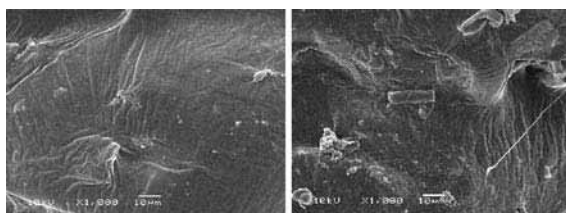
Fig. 5 SEM micrographs of cross-sections of of **a** collagen membrane and **b** usnic acid–collagen films

porous. The surface and cross-sections of UAC film shows non-homogeneities when to compare with CL.

Conclusions

According to the data presented in this study, it was possible to assert that the usnic acid molecules were encapsulated by liposomes and incorporated into the polymeric system as demonstrated in the analysis of the DTA and TG/DTG curves. Furthermore, similar bands of the usnic acid were observed in the IR spectrum of UAC, indicating the presence of the drug in the system. Nevertheless, further studies are required in order to evaluate whether these in vitro models can be used to characterize usnic acid release from collagen-based films.

References

1. Sung KC, Topp EM. Effect of drug hydrophilicity and membrane hydration on diffusion in hyaluronic acid ester membranes. J Control Release. 1995;37:95–104.
2. Lee KY, Yuk SH. Polymeric protein delivery systems. Prog Polym Sci. 2007;32:669–97.
3. Biondi M, Ungaro F, Quaglia F, Netti PA. Controlled drug delivery in tissue engineering. Adv Drug Delivery Rev. 2008;60:229–42.
4. Wallacea DG, Rosenblatt J. Collagen gel systems for sustained delivery and tissue engineering. Adv Drug Delivery Rev. 2003;55:1631–49.
5. Stamatialis DF, Papenburg BJ, Gironés M, Saiful S, Bettahalli SNM, Schmitmeier S, et al. Medical applications of membranes: drug delivery, artificial organs and tissue engineering. J Membr Sci. 2008;308:1–34.
6. Friess W. Collagen—biomaterial for drug delivery. Eur J Pharm Biopharm. 1998;45:113–36.
7. Wachol-Drewek Z, Pfeiffer M, Scholl E. Comparative investigation of drug delivery of collagen implants saturated in antibiotic solutions and a sponge containing gentamicin. Biomaterials. 1996;17:1733–8.
8. Vasantha V, Sehgal PK, Rao KP. Collagen ophthalmic inserts for pilocarpine drug delivery system. Int J Pharm. 1988;47(1–3):95–102.
9. Aoyagi S, Onishi H, Machida Y. Novel chitosan wound dressing loaded with minocycline for the treatment of severe burn wounds. Int J Pharm. 2007;330:138–45.
10. Ulkur E, Oncul O, Karagoz H, Yeniz E, Celikoz B. Comparison of silver-coated dressing (ActicoatTM), chlorhexidine acetate 0.5% (Bactigrass), and fusidic acid 2% (Fucidin) for topical antibacterial effect in methicillin-resistant Staphylococci-contaminated, full-skin thickness rat burn wounds. Burns. 2005;31:874–7.
11. Lira AM, Araújo AAS, Basílio IDJ, Santos BLL, Santana DP, Macedo RO. Compatibility studies of lapachol with pharmaceutical excipients for the development of topical formulations. Therm Acta. 2007;457:1–6.
12. Brito MB, Barin GB, Araújo AAS, Sousa DP, Cavalcanti SCH, Lira AAM, et al. The action modes of Lippia sidoides (Cham) essential oil as penetration enhancers on snake skin. J Therm Anal Calorim. 2009;97(1):323–7.
13. Lee CH, Singla A, Lee Y. Biomedical application of collagen. Int J Pharm. 2001;221:21–2.
14. Thacharodi D, Rao KP. Collagen membrane controlled transdermal delivery of propranolol hydrochloride. Int J Pharm. 1996;131:97–9.
15. Ingólfsdóttir K, Chung GAC, Skúlason VG, Gissurarson SR, Vilhelmsdóttir M. Antimycobacterial activity of lichen metabolites in vitro. Eur J Pharm Sci. 1998;6:141–4.
16. Vijayakumara CS, Viswanathana S, Kannappa UM, Reddya S, Parvathavarthinia AB, Sukumarb E. Anti-inflamatory activity of (+)-usnic acid. Fitoterapia. 2000;71:564–6.
17. Fournet A, Ferreira ME, Arias AR, Ortiz ST, Inchausti A, Yaluff G, et al. Activity of compounds isolated from Chilean lichens against experimental cutaneous leishmaniasis. Comp Biochem Physiol. 1997;116:51–4.
18. Santos NPS, Nascimento SC, Wanderley MSO, Pontes-Filho NT, Silva JF, Castro CMMB, et al. Nanoencapsulation of usnic acid: an attempt to improve antitumour activity and reduce hepatotoxicity. Eur J Pharm Biopharm. 2006;64:154–60.
19. Bomfim RR, Araújo AAS, Cuadros-Orellana S, Melo MGD, Quintans-Júnior LJ, Cavalcanti SCH. Larvicidal activity of Cladonia substellata extract and usnic acid against Aedes aegypti and Artemia salina. Lat Am J Pharm. 2009;28(4):580–4.
20. Ingolfsdottir K. Usnic acid. Phytochemistry. 2002;61:729–36.
21. Ho HO, Lin LH, Sheu MT. Characterization of collagen isolation and application of collagen gel as a drug carrier. J Contr Release. 1997;44:103–12.
22. Kupchan SM, Kopperman HI. L-usnic acid: tumor inhibitor isolated from lichens. Experientia. 1975;31:625–6.
23. Tapia-Blácido D, Sobral PJ, Menegalli FC. Development and characterization of biofilms based on Amaranth flour (Amaranthus caudatus). J Food Eng. 2005;67:215–23.

ARTICLES

Modeling, Structural, and Spectroscopic Studies of Lanthanide-Organic Frameworks

Marcelo O. Rodrigues,[†,‡] **Filipe A. Almeida Paz,**[‡] **Ricardo O. Freire,**[§] **Gilberto F. de Sá,**[†]
André Galembeck,[†] **Maria C. B. S. M. Montenegro,**[||] **Alberto N. Araújo,**[||] **and S. Alves, Jr.*,**[†,||]

*Departamento de Química Fundamental, UFPE, 50590-470 Recife - PE, Brazil, Departamento de Química,
Universidade de Aveiro, CICECO, 3810-193 Aveiro, Portugal, Departamento de Química, UFS,
49100-000 São Cristóvão - SE, Brazil, and Faculdade de Farmácia, Laboratório de Química Física,
UP, 3810-193 Porto, Portugal*

In this paper, we report the hydrothermal synthesis of three lanthanide-organic framework materials using as primary building blocks the metallic centers Eu^{3+}, Tb^{3+}, and Gd^{3+} and residues of mellitic acid: $[Ln_2(MELL)(H_2O)_6]$ (where $Ln^{3+} = Eu^{3+}$, Tb^{3+}, and Gd^3; hereafter designated as (**1**), (**2**) and (**3**)). Structural characterization encompasses single-crystal X-ray diffraction studies, thermal analysis, and vibrational spectroscopy, plus detailed investigations on the experimental and predicted (using the Sparkle/AM1 model) photophysical luminescent properties. Crystallographic investigations showed that the compounds are all isostructural, crystallizing in the orthorhombic space group P*nnm* and structurally identical to the lanthanum 3D material reported by the group of Williams. (**2**) is highly photoluminescent, as confirmed by the measured quantum yield and lifetime (37% and 0.74 ms, respectively). The intensity parameters (Ω_2, Ω_4, and Ω_6) of (**1**) were first calculated using the Sparkle/AM1 structures and then employed in the calculation of the rates of energy transfer (W_{ET}) and back-transfer (W_{BT}). Intensity parameters were used to predict the radiative decay rate. The calculated quantum yield derived from the Sparkle/AM1 structures was approximately 16%, and the experimental value was 8%. We attribute the registered differences to the fact that the theoretical model does not consider the vibronic coupling with O−H oscillators from coordinated water molecules. These results clearly attest for the efficacy of the theoretical models employed in all calculations and open a new window of interesting possibilities for the design in silico of novel and highly efficient lanthanide-organic frameworks.

Introduction

Crystal engineering of inorganic−organic hybrid networks has, without a doubt, emerged as a research field which lies in the interface between synthetic chemistry and materials science. Numerous synthetic and conceptual developments have been reported, in particular concerning the development of protocols for the structural control of an extensive class of crystalline materials with tunable structure, porosity, stability, and functionality.[1,2] Worldwide interest in this new class of compounds arises from their intriguing topological features, ultimately constructed by the self-assembly of metallic ions with multifunctional organic ligands[3] and, on the other, from their promising applications in catalysis,[4] solid-phase extraction,[5] gas storage,[6] magnetic, and as optics materials.[7,8]

The design and assembly of metal-organic frameworks (MOFs) can be envisaged as a complex algorithm in which the chemical and structural information stored in the ligands is recognized by metallic ions through their coordination abilities.[9] Hence, the selection of suitable ligands and metal ions consti-

tutes the aspects for a successful construction of these molecular architectures. In particular, the use of lanthanide ions has received special attention in recent years from several research groups.[10,11] However, most of them have explored the low stereochemical preference inherent to lanthanide ions to introduce dissymmetry at the metal centers thus leading mainly to interesting structures.[12,13] These lanthanide-containing MOFs have great potential to be efficiently used as light-conversion molecular devices (LCMDs)[14] in which the coordinated ligands absorb the incident radiation and transfer energy to the emitting metal ion, thus increasing the overall photoluminescent (PL) properties.[15] These photophysical features have been extensively explored in materials science, in particular in the development of IR-emitters,[16] organic light-emitting diodes (OLEDs),[17] and optic sensors,[18,19] but remain somehow underexplored for MOFs.

Lanthanide-containing MOFs have been assembled from a multitude of organic ligands,[20,21] among which the aromatics polycarboxylates are of particular interest due to their chemical stability and photophysical properties.[22−24] Mellitic acid (benzenehexacarboxylic acid), for instance, is a high connectivity ligand which can establish bridges between several metal centers,[25] adopt several coordination modes,[26,27] and produce multidimensional networks, including 2D and 3D structures.[28] It is important to emphasize that previous reports of MOFs with this ligand detach the synthesis from the structural investiga-

* Corresponding author. E-mail: salvesjr@ufpe.br. Tel.: +55 81 2126-7475. Fax: +55 81 2126-8442.
† UFPE.
‡ CICECO.
§ UFS.
|| UP.

tions.[29] Hence, to date, a detailed study of the photoluminescent properties of functional compounds with mellitic acid residues is inexistent in the literature.

Our research group has been developing over the past few years a number of theoretical approaches which predict very well several spectroscopic properties such as singlet and triplet energy positions,[30−32] electronic spectra of lanthanide complexes,[30−32] ligand field parameters, B_q^k,[33−35] $4f$–$4f$ intensity parameters, Ω_λ ($\lambda = 2, 4,$ and 6),[36−39] energy transfer rates, W_{ET}, between the lanthanide trivalent ions and the ligand, quantum yields, and luminescence efficiencies for these complexes.[40−43] Following our interest in the synthesis and characterization of MOF-type materials containing lanthanide centers,[44−50] in this paper we wish to report a detailed photophysical investigation of the properties of the 3D $[Ln_2(MELL)(H_2O)_6]$ materials (where Ln^{3+} = Eu^{3+}, Tb^{3+}, and Gd^{3+}; hereafter designated as (**1**), (**2**), and (**3**)). The structure of the La-based material has been described by Williams[29] and collaborators, and recently Lin reported the surfactant-assisted synthesis of the nanoscale $[Gd_2(MELL)(H_2O)_6]$ and demonstrated the potential utility in magnetic resonance imaging (MRI).[51] In this report we follow that previous paper by preparing and fully characterizing in the solid state the structures of the Eu^{3+}, Tb^{3+}, and Gd^{3+} based materials. Spectroscopic properties such as intensity parameters Ω_λ ($\lambda = 2, 4$ and 6), rates of energy transfer (W_{ET}), and back-transfer (W_{BT}), radiative (A_{rad}) and nonradiative (A_{nrad}) decay rates, quantum efficiency (η), and quantum yields (q) of these functional materials were theoretically predicted using the optimized Sparkle/AM1 structure. This study attests to the efficacy of the former approach. The semiempirical Sparkle model has also been employed as an important tool in the design of new light-converting molecular devices (LCMDs).[52,53] Because this model permits the treatment of large structures with a great number of atoms in a relatively short period of time, we decided to use it for the first time in the prediction of the complete geometry of a lanthanide-containing MOF material.

Experimental Section

Chemicals. Mellitic acid and lanthanide oxides (99.99%) were purchased from Aldrich and used without further purification. $Ln(NO_3)_3 \cdot 6H_2O$ (where Ln^{3+} = Eu^{3+}, Tb^{3+}, and Gd^{3+}) was obtained by reaction of nitric acid with the corresponding lanthanide oxide.

Syntheses. An equimolar mixture (0.85 mmol) of mellitic acid and $Ln(NO_3)_3 \cdot 6H_2O$ and H_2O (4.0 mL) was placed inside a 8.0 mL Teflon-lined stainless steel autoclave. The reaction took place at 433 K in static conditions and under autogenous pressure over a period of 72 h, after which the vessel was allowed to cool to room temperature (RT). Products were washed with water and acetone and dried in open air. The yield, based on Ln^{3+}, was about 75% for all samples. The hydrothermal synthetic approach afforded high-quality single crystals suitable for X-ray crystallographic analysis, with the empirical formulas determined as $[Ln_2(MELL)(H_2O)_6]$ (where Ln^{3+} = Eu^{3+}, Tb^{3+}, and Gd^{3+}; designated as (**1**), (**2**), and (**3**), respectively). All materials were found to be insoluble in water and in common organic solvents.

Selected FT−IR data (in cm^{-1}). (**1**): 3468−3213 (s), 1609 (s), 1568 (s), 1449 (s), 1344 (s), 918 (w), 676 (w), 590 (w), 505 (w). (**2**): 3468−3213 (s), 1611 (s), 1555 (s), 1443 (s), 1338 (s), 918 (w), 719 (w), 676 (w), 590(w), 548 (w), 492 (w). (**3**): 3486−3000 (s), 1609 (s), 1563 (s), 1454 (s), 1344 (s), 918 (w), 673 (w), 587 (w), 511 (w).

Temperature ranges (K) and observed weight losses. (**1**): 383−458 K (−5.25%), 458−533 K (−8.40%), 700−1200 K (−37.4%). (**2**): 376−458 K (−4.92%), 453−549 K (−8.43%), 750−1210 K (−37.31%). (**3**): 387−454 K (−4.93%), 454−550 K (−8.42%), 780−1165 K (−37.1%).

General Instrumentation. FT-IR spectra were recorded from KBr pellets (in the 400−4000 cm^{-1} spectral range) using a BRUKER IFS 66. Raman spectra were acquired in a Renishaw Raman Image Spectrophotometer, coupled to an optical microscope which focuses the incident radiation inside a 1 μm spot, and equipped with a 632.8 nm laser as the excitation source (4 mW power). Spectra were collected from 28 scans over the 2000−100 cm^{-1} spectral region.

Photoluminescence spectra were acquired using an ISS PC1 spectrofluorimeter at RT and at 77 K. The excitation device was equipped with a 300 W Xe lamp and a pholographic grating. Emission spectra were collected with a 25 cm monochromator (0.1 nm resolution) connected to a photomultiplier. The excitation and emission slit widths were fixed at 1.0 mm. All monochromators are equipped with 1200 grooves/mm. The experimental quantum yield (q) was determined by employing the method developed by Bril et al.,[54] for which q of a given material can be calculated by a direct comparison with standard phosphors with known q values. The quantum yield can, thus, be calculated from

$$q = \left(\frac{1 - r_{ST}}{1 - r_x}\right)\left(\frac{\Delta\Phi_x}{\Delta\Phi_{ST}}\right)q_{ST} \tag{1}$$

where r_{ST} and r_x apply for the exciting radiation reflected by the standard and the sample, respectively, and q_{ST} is the quantum yield of the standard phosphor. The $\Delta\Phi_x$ and $\Delta\Phi_{ST}$ terms correspond to the integrated photon flux (photon·s^{-1}) for the sample and standard phosphors. Sodium salicylate (Merck, PA), whose q_{ST} is 55% at RT as reported by Malta,[55] was used as tandard.

Termogravimetric data (TG) were obtained from ca. 3.0 mg of each sample with a thermobalance model TGA 50 (Shimadzu), in the 298−1473 K temperature range, using a platinum crucible, under dynamic nitrogen atmosphere (50 mL·min^{-1}), and with a heating rate of 10 K·min^{-1}.

Single-Crystal X-Ray Diffraction Studies. Single crystals of $[Ln_2(MELL)(H_2O)_6]$ materials were manually harvested from the crystallization vials and mounted on Hampton Research CryoLoops using FOMBLIN Y perfluoropolyether vacuum oil (LVAC 25/6) purchased from Aldrich[56] with the help of a Stemi 2000 stereomicroscope equipped with Carl Zeiss lenses. Data were collected on a Bruker X8 Kappa APEX II charge-coupled device (CCD) area-detector diffractometer (Mo Kα graphite-monochromated radiation, λ = 0.71073 Å) controlled by the APEX-2 software package[57] and equipped with an Oxford Cryosystems Series 700 cryostream monitored remotely using the software interface Cryopad.[58] Images were processed using the software package SAINT+,[59] and data were corrected for absorption by the multiscan semiempirical method implemented in SADABS.[60] Structures were solved using the Patterson synthesis algorithm implemented in SHELXS-97,[61,62] which allowed the immediate location of the crystallographically independent Ln^{3+} metallic centers. All remaining non-hydrogen atoms were directly located from difference Fourier maps calculated from successive full-matrix least-squares refinement cycles on F^2 using SHELXL-97.[62,63] Non-hydrogen atoms were successfully refined using anisotropic displacement parameters.

Studies of Lanthanide-Organic Frameworks

J. Phys. Chem. B, Vol. 113, No. 36, 2009 **12183**

Hydrogen atoms associated with the coordinated water molecules were markedly visible in difference Fourier maps and were included in the final structural models with the O−H and H···H distances restrained to 0.95(1) Å and 1.55(1) Å, plus U_{iso} fixed at $1.5 \times U_{eq}$ of the attached oxygen atom, to ensure a chemically reasonable geometry for these chemical moieties.

The last difference Fourier map synthesis showed: for **(1)**, the highest peak (0.366 eÅ^{-3}) and deepest hole (−1.697 eÅ^{-3}) located at 0.65 Å from C(3) and at 0.91 Å from O(3), respectively; for **(3)**, the highest peak (0.390 eÅ^{-3}) and deepest hole (−0.852 eÅ^{-3}) located at 0.70 Å from C(2) and at 1.87 Å from O(1W), respectively; for **(2)**, the highest peak (0.417 eÅ^{-3}) and deepest hole (−0.519 eÅ^{-3}) located at 0.75 Å from C(3) and at 0.89 Å from Tb(1), respectively.

Crystallographic data (excluding structure factors) for the structures reported in this paper have been deposited with the Cambridge Crystallographic Data Centre as supplementary publication data (deposition numbers are given in Table S1, Supporting Information). Copies of the data can be obtained free of charge on application to CCDC, 12 Union Road, Cambridge CB2 2EZ, U.K. (fax: (+44) 1223 336033; e-mail: deposit@ccdc.cam.ac.uk).

Theoretical Calculations

Geometry Optimization and Transition Energies. The ground state geometry for the Eu^{3+}-containing material was calculated using the Sparkle/AM1 model.[64] In this report, and for the first time, it was possible to employ a quantum chemical methodology to predict the complete geometry of a lanthanide inorganic−organic hybrid network. The unit cell, composed by a total of 382 atoms including 12 Eu^{3+} ions, was properly optimized. We note that the use of another quantum chemical methodology such as Hartree−Fock (HF) or density functional theory (DFT) using an effective core potential (ECP) to treat the Eu^{3+} ions is unfeasible owing to the high computational effort needed.

In a recent report,[65] we described the complete geometry calculation of a dieuropium complex composed by 134 atoms using HF/6-31G*/ECP methodology. In that paper, we employed the quasi-relativistic ECP of Dolg et al.[66] This calculation was performed on a Pentium IV-3 GHz with 2 GB of RAM in 2880 h. This clearly attests how the use of ab initio or DFT methodologies is unfeasible to investigate lanthanide inorganic−organic hybrid networks.

The Sparkle/AM1 model is implemented in the Mopac2007 software package.[67] The keywords used in the calculation reported in this manuscript were: PRECISE, GNORM = 0.25, SCFCRT = 1.D-10 (to increase the SCF convergence criterion), and XYZ (for Cartesian coordinates).

The single-crystal X-ray structure and Sparkle/AM1 optimized geometry were both used to calculate the singlet and triplet excited states using a configuration interaction single (CIS) approach based on the intermediate neglecting of a differential overlap/spectroscopic (INDO/S) method[68,69] implemented in the ZINDO software program.[70]

Judd−Ofelt Intensity Parameters Calculation. The experimental intensity parameters, Ω_λ, for the Eu^{3+}-containing material were determined from

$$\Omega_\lambda = \frac{4e^2\omega^3 A_{0J}}{3\hbar\chi\langle^7F\|U^\lambda\|^5D_0\rangle^2} \quad (2)$$

where A_{0J} is the coefficient of spontaneous emission for the $^5D_0 \rightarrow {}^7F_J$ transitions; χ is the Lorentz local-field correction term given by $\chi = n(n^2 + 2)^2/9$; n is the refractive index of the medium (in this case $n = 1.5$); and $|\langle^5D_0\|U^{(\lambda)}\|^7F_J\rangle|^2$ are the square reduced matrix element whose values are 0.0032, 0.0023, and 0.0002 for $\lambda = 2$, 4, and 6, respectively.[71,72] The transition $^5D_0 \rightarrow {}^7F_6$ was not observed experimentally; consequently, the experimental Ω_6 parameter could not be estimated.

The coordinative interaction between a lanthanide cation and the bonding atoms of an organic ligand can be described by the Judd−Ofelt theory,[73,74] after which the intensity parameters Ω_λ ($\lambda = 2$, 4, and 6) are defined by

$$\Omega_\lambda = (2\lambda + 1) \sum_{t,p} \frac{|B_{\lambda tp}|^2}{(2t + 1)} \quad (3)$$

with

$$B_{\lambda tp} = \frac{2}{\Delta E}\langle r^{t+1}\rangle\theta(t,p)\gamma_p^t - \left[\frac{(\lambda + 1)(2\lambda + 3)}{2\lambda + 1}\right]\langle r^t\rangle(1 - \sigma_\lambda)\langle f\|C^{(\lambda)}\|f\rangle\Gamma_p^t\delta_{t,\lambda+1} \quad (4)$$

Details on the parameters of eqs 3 and 4 are discussed in detail elsewhere.[75−77]

The values of charge factors (g) and the cation polarizability (α) are given in Table S5 (see Supporting Information). These values, used for the calculation of the γ_p^t and Γ_p^t, respectively, were adjusted using a nonlinear minimization of a four-dimensional surface response. The generate simulating annealing (GSA) method aimed at finding one of its local minima, which ideally should be the global minimum and be chemically consistent. In the minimization procedure, we considered both the Sparkle/AM1 and the crystallographic structural models. The response function, $F_{respectively}$, was defined as

$$F_{resp} = \sum_{i=1}^2 |\Omega_2^{calc} - \Omega_2^{exp}| + |\Omega_4^{calc} - \Omega_4^{exp}| \quad (5)$$

where i runs over Sparkle/AM1 and crystallographic geometries; Ω_2^{Calc} and Ω_4^{Calc} are the intensity parameters calculated for each structure; and Ω_2^{Exp} and Ω_4^{Exp} are the intensity parameters obtained from the experimental emission spectrum. The Ω_6 parameter was not observed, hence it was not considered in the minimization procedure. The values are in the range of those physically acceptable.

Energy Transfer Rates and Quantum Yields. Models used to calculate the energy transfer rates between the ligands and the lanthanide trivalent ion, plus the numerical solution of the rate equations and the emission quantum yields, are described in detail by Malta and collaborators.[78]

Results and Discussion

We have modified the synthetic procedure reported by Williams and collaborators[29] for [La$_2$(MELL)(H$_2$O)$_6$] with the purpose of increasing overall crystallinity and obtaining phase-pure materials with other lanthanide centers. Indeed, we found that by using the primary building blocks in a 1:1 ratio in the initial reactive gel and using longer reaction times at slightly lower temperatures, the compounds could be isolated as large
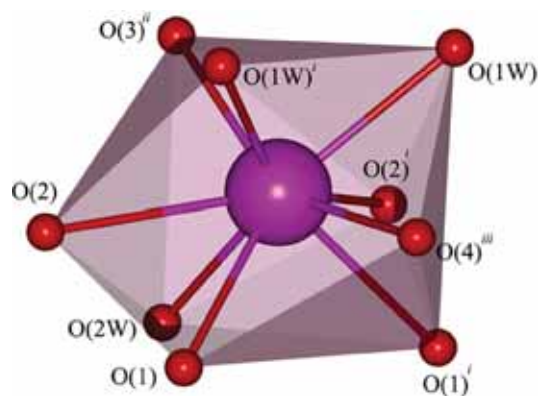
Figure 1. Schematic representation of the tricapped trigonal prismatic coordination polyhedron of the Ln³⁺ ion. Symmetry transformation used to generate equivalent atoms: ^{i}x, y, 1 − z; ^{ii}3/2 − x, y + 1/2, 3/2 − z; ^{iii}3/2 − x, y − 1/2, 3/2 − z.

and very well-formed single crystals (crystal size in the ca. 10−50 μm range).

Single-crystal X-ray diffraction analysis revealed that compounds (**1**), (**2**), and (**3**) are isostructural crystallizing in the orthorhombic space group *Pnnm*, structurally identical to the lanthanum and gadolinium materials reported by Willians[29] and Li[51] (Table S1, Supporting Information).

Each mellitate anion is coordinated to eight Ln³⁺ cations via two coordination modes typical of carboxylate groups:[79] two −COO⁻ groups are bridging four distinct Ln³⁺ via *syn,syn*-bridges, while the remaining four display a *syn,syn*-chelate coordination mode. The crystallographically independent Ln³⁺ ion is thus coordinated to six oxygen atoms arising from six symmetry-equivalent mellitate anions. The coordination sphere is completed by three water molecules. Therefore, the chemical environment is best described as a distorted tricapped trigonal prism as shown in Figure 1.

All carboxylate groups are highly twisted out of the plane of the benzene ring. Noteworthy, these deviations are related to the coordination mode, with this behavior being already reported in similar compounds.[80,81] The Ln−O bond lengths and internal polyhedral O−Ln−O angles for (**1**), (**2**), and (**3**) are typical (see Table S2 in the Supporting Information).[80,82]

The aromatic rings and the Ln³⁺ cations are stacked on the *bc* plane of the unit cell forming a two-dimensional plane net.[83] The resulting framework has a one-dimensional channel system running parallel to the *c*-axis formed by distorted hexagonal pores with average cavity size of ca. 8.3 × 6.6 Å (see Figure 2). All coordinated water molecules, pointing toward the channels, are involved in hydrogen bonding interactions with oxygen atoms of the neighboring carboxylate groups, acting as bifurcated donors, with a graph set motif of S(3):[84] O(1W)−H(1A)···O(1), O(1W)−H(1B)···O(2), O(2W)−H(2A)···O(1), and O(2W)−H(2B)···O(2W). Hydrogen bonding geometric details are given in Table S3 (Supporting Information).

Figure 3 shows a comparison between the crystallographic unit cell and the Sparkle/AM1 optimized geometry for (**1**). It is important to emphasize that the crystallographic unit cell was modified before being optimized using the Sparkle/AM1 method. This was performed to minimize the disorder effect caused by uncompleted fragments. Therefore, 20 symmetry-related Eu³⁺ cations were removed, and the oxygen atoms arising from uncompleted mellitate residues were substituted by water ligands. One of the 12 polyhedra was selected to predict the photoluminescent properties which will be discussed later in this paper. The optimized atomic coordinates for the
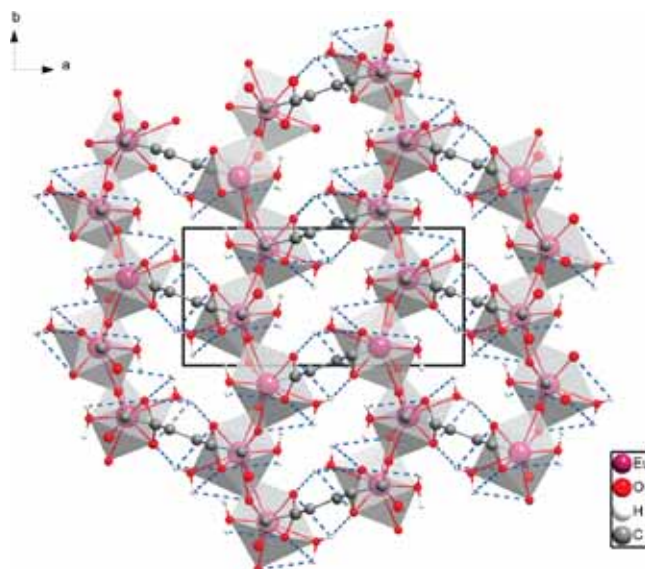
Figure 2. View along the *c*-axis of the extended structure of [Ln₂(MELL)(H₂O)₆], showing the distorted hexagonal channels occupied by aqua ligands. The hydrogen bonds are represented as light-blue dashed lines. For geometrical details on the hydrogen bonds, see Table S3 (Supporting Information).
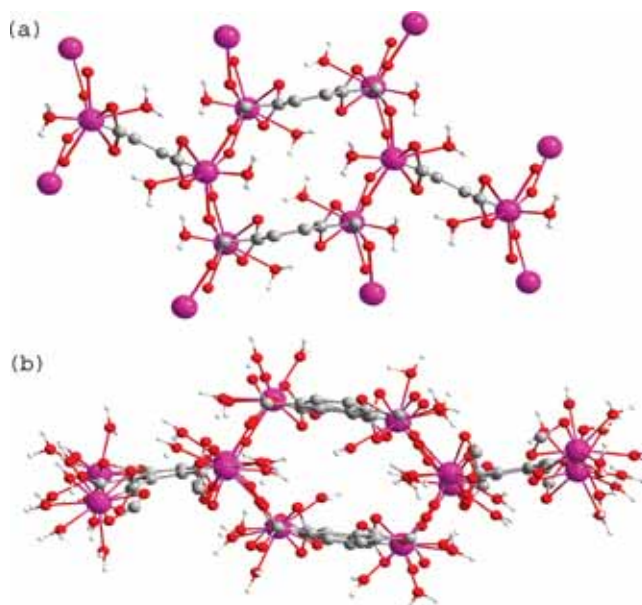
Figure 3. Molecular structure of (**1**): (a) obtained from single-crystal crystallography; (b) optimized by Sparkle/AM1 model.

coordination polyhedron, as determined by the Sparkle/AM1 model, are supplied in Table S5 (see Supporting Information).

The photoluminescence of (**3**) was collected at 77 K (λ_{exc} = 320 nm). Since the emitting level of the Gd³⁺ ion is around 32 000 cm⁻¹, the first excited triplet state of the mellitate ligand is unable to effectively sensitize the metal ion. The triplet state energy level was estimated from the zero phonon, which was considered to be the 0−0 transition[85] centered at 413 nm (24 213 cm⁻¹).

Figure 4 shows the excitation spectra of (**1**) and (**2**) acquired at RT while monitoring the Eu³⁺ and Tb³⁺ emissions at 614 and 545 nm in the 200−600 and 200−500 nm ranges, respectively. The (**1**) excitation exhibits a broadband between 220 and 350 nm (λ_{max} = 312 nm) from the $\pi \rightarrow \pi^*$ electronic transition associated with the organic moiety. The peaks observed in the 350−580 nm range result from the intra *f−f*
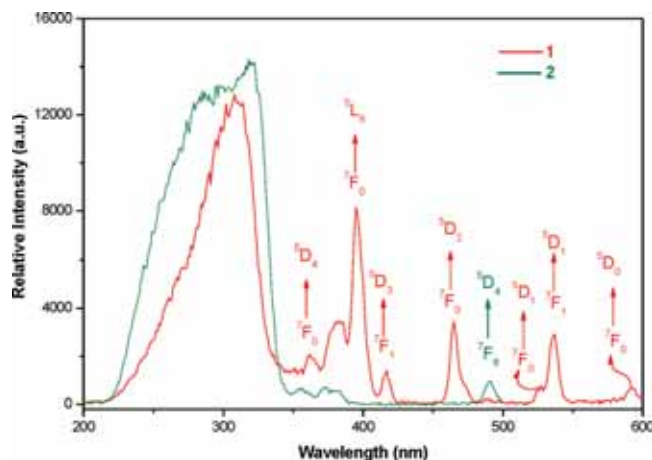
Figure 4. Excitation spectra of (**1**) and (**2**) collected at RT.
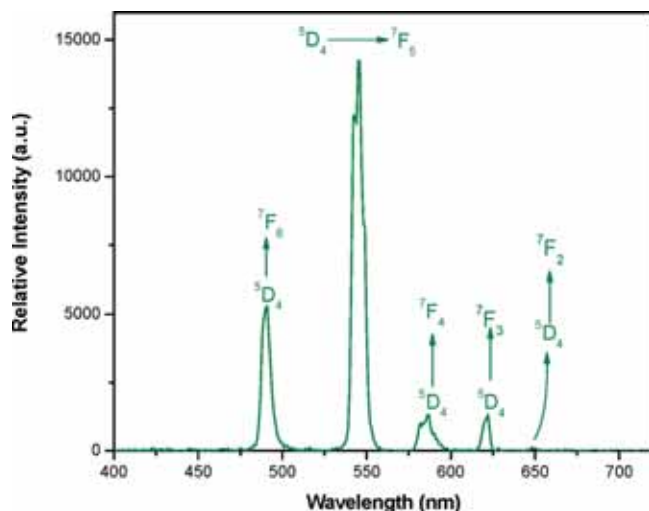
Figure 5. Emission spectra of (**2**) collected at RT in the 400−720 nm spectral range.

transitions of the Eu^{3+} ion. The (**2**) excitation spectrum displays an intense broadband centered at about 320 nm. The transitions corresponding to the Tb^{3+} ion absorption levels are very weak in comparison to those of the ligand, thus indicating that an indirect process of energy transfer is the only photophysical pathway responsible for the high luminescence of the sample.

The emission spectrum of (**2**) (Figure 5) acquired at room temperature markedly shows the typical green Tb^{3+} emission associated with the $^5D_4{\rightarrow}^7F_J$ transitions. The $^5D_4{\rightarrow}^7F_5$ transition centered at ca. 545 nm is the strongest corresponding to ca. 66% of the integrated emission spectrum. The main channel responsible by the photoluminescence quenching is a thermal back transference.[86] According to Latva and co-workers,[87] this quenching mechanism is only observable when the energy difference between the lowest triplet state of the ligand and the $^5D_4$ level of Tb^{3+} (20 400 cm^{-1}) is lower than about 1850 cm^{-1}. In this case, the energy back transference does not seem to play an important role. Efficient energy transference from the antenna ligand to the emitting $^5D_4$ ion level is confirmed with a measured quantum yield of 37% and a long lifetime (τ) of 0.74 ms.

The emission spectra of (**1**) depicted in Figure 6 were collected at 77 K in the 350−720 nm spectral range, by a direct excitation of the Eu^{3+} ion at 394 nm and by the singlet state of the ligand ($\lambda = 310$ nm). The spectra display narrow bands characteristic of the Eu^{3+} $^5D_0{\rightarrow}^7F_J$ transitions. Those
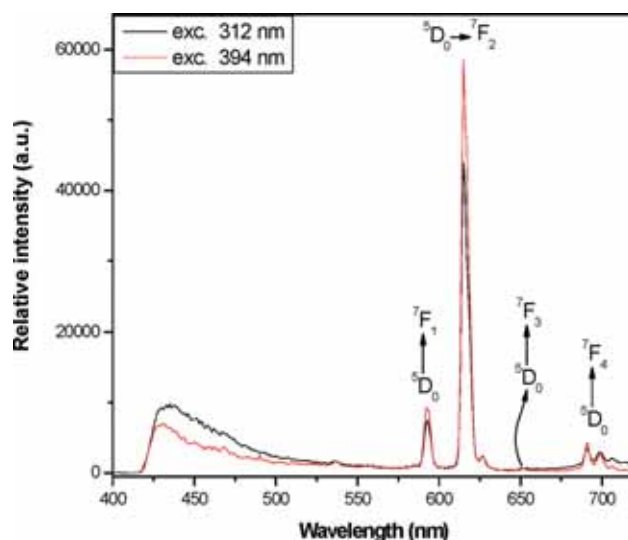
Figure 6. Low temperature (77 K) emission spectra of (**1**) registered in the 400−720 nm spectral range.

attributed to the $^5D_0{\rightarrow}^7F_2$ transition (centered at ca. 614 nm) give the major contribution to the red photoluminescence of the material. A broadband between 410 and 520 nm is attributed to the emission arising from the ligand which provides an inefficient energy transfer from the ligand excited state to the emitting $^5D_0$ level of the Eu^{3+} ion as previously evidenced by the excitation spectrum.

The relative intensities and splitting of the emission bands are dependent upon the extent in which the $(2J + 1)$ degeneracy is removed by the symmetry of the first coordination sphere.[88] As mentioned above and determined from the single-crystal X-ray measurements, the geometry of the nine-coordinated coordination environment around the Ln^{3+} ions is slightly distorted from that of a tricapped trigonal prism. This implies that the point group of the Eu^{3+} coordination sphere is reduced from D_{3h} to D_3 symmetry. In accordance to the selection rules for the electric dipole transition, under D_3 point symmetry the $^5D_0{\rightarrow}^7F_0$ transition is absent and the $^5D_0{\rightarrow}^7F_2$ transition shows a small sideband at the lower energy side.[89] Hence, the analysis of the local lanthanide ion chemical environment provided by emission spectroscopy is in good agreement with the X-ray diffraction data.

Table 1 collects the theoretical and experimental values for the intensity parameters (Ω_2, Ω_4), radiative and nonradiative rates of spontaneous emission (A_{rad} and A_{nrad}, respectively), quantum efficiency (η) and yield (q), and experimental lifetime (τ) for (**1**). The experimental radiative rate ($A_{rad} = 441.70$ s^{-1}), the high value for experimental nonradiative rate ($A_{nrad} = 23\,336.08$ s^{-1}), and the short lifetime τ of 0.34 ms can be associated to the nonradiative decay channels controlling the relaxation process and arising from the vibronic coupling of the O−H oscillators from the water molecules coordinated to the Ln^{3+} cations. Indeed, the inefficient energy transference and the high contribution of the nonradiative relaxation process provide a plausible explanation for the observed low experimental quantum yields ($q = 8\%$).

The theoretical values of the intensity parameters Ω_λ ($\lambda = 2$ and 4) calculated using the crystallographic and Sparkle/ AM1 geometries are in good agreement with those obtained experimentally (Table 1). The value of Ω_2 is relatively low when compared directly to those for Eu−β-diketonates,[14,36,41,42] thus ultimately indicating, on the one hand, a reduced degree

TABLE 1: Theoretical Intensity Parameters Ω_2 and Ω_4, Radiative (A_{rad}) and Nonradiative (A_{nrad}) Decay Rates, Quantum Efficiency (η), and Quantum Yield (q) Values Derived from the Experimental Data and Optimized Sparkle/AM1 Structural Models[a]

| | Ω_2 | Ω_4 | A_{rad} | A_{nrad} | τ | η | q |
	(10^{-20} cm^2)	(10^{-20} cm^2)	(s^{-1})	(s^{-1})	(ms)	(%)	(%)
experimental data	11.82	2.72	441.70	2336.08	0.36	15.9	8.0
Sparkle/AM1 model	10.22	6.84	459.16	2318.62	–	16.5	16.3

[a] Related experimental data, including the lifetime (τ) of the Eu^{3+} center, were obtained at RT for the as-synthesized **(1)** material.
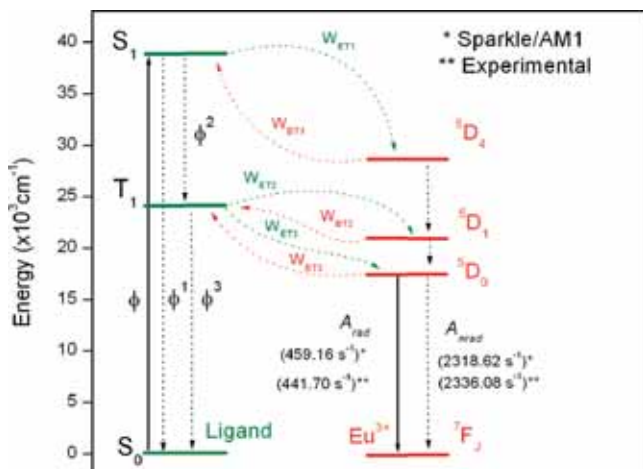
Figure 7. Energy level diagram for the **(1)** material showing the most probable channels for the intramolecular energy transfer processes.

of covalence involving the metal-to-ligand coordination bond and, on the other, a slightly polarized chemical environment in the vicinity of the lanthanide ion. The Ω_4 parameter is less sensitive to the coordination sphere than Ω_2. However, its value reflects the chemical environment rigidity surrounding the Ln^{3+} cation. **(1)** shows a low Ω_4 value (see Table 1) indicating a considerable rigidity associated with the MOFs.[90]

As shown in Figure 7, the ligand-to-metal energy transfer may occur through either the singlet or triplet ligand states. The theoretical singlet and triplet values calculated using the INDO/S-CIS method for the **(1)** Sparkle/AM1 geometry are 39 075 and 24 635 cm^{-1}. The calculated triplet values are in good agreement with the experimental one (24 213 cm^{-1}).

As depicted in the energy level diagram for **(1)** (Figure 7), the singlet state does not have appropriate resonance conditions with the excited states of Eu^{3+}. Nevertheless, we considered the singlet→$^5D_4$ channel in all our calculations. The radiative and nonradiative decay rates calculated from crystallographic and Sparkle/AM1 geometries are given in both Figure 7 and Table 1. The calculated values of A_{rad} and A_{nrad} are in accordance with the experimental data.

The energy transfer rates are larger for those levels dominated by the exchange mechanism, $^5D_0$ and $^5D_1$, than for those dominated by the dipole–dipole interaction. Typical values of the remaining transfer rates were assumed to be identical to those found for coordination compounds, namely, $\Phi = 10^4$, $\Phi^{(1)} = 10^6$, $\Phi^{(2)} = 10^8$, and $\Phi^{(3)} = 10^5$ s^{-1}.[91] The energy transfer

and back-transfer rates from the ligand triplet state (T1) to the $^5D_1$ and $^5D_0$ levels and energy transfer rates from the singlet state (S1) to the $^5D_4$ level are summarized in Table 2. These results clearly indicate that energy transference is predominant from the triplet state of the ligand to the $^5D_1$ and $^5D_0$ levels of the Eu^{3+} ion.

The radiative (A_{rad}) and nonradiative (A_{nrad}) rates and the lifetime value (τ) of the $^5D_0$ level were used in the quantum yield calculations. Obtained results (derived from the Sparkle/AM1 and crystallographic structures) are summarized in Table 1. The theoretical quantum yields are of the same order of magnitude of the experimental one. We attribute the registered differences to the fact that the theoretical model does not consider the vibronic coupling with O–H oscillators from coordinated water molecules.

Conclusion

Three MOF materials constructed from lanthanide ions and mellitic acid residues have been synthesized via a hydrothermal approach, and their structural and spectroscopic properties were investigated. Compounds are isostructural, crystallizing in the orthorhombic space group *Pnnm*. Each mellitate anion is coordinated to eight Ln^{3+}, and due to this high connectivity, remarkable 3D frameworks topologically identical to the rutile structure are formed. The structure contains hexagonal channels running along the [001] crystallographic direction, having a cross-section of about 8.3 × 6.6 Å.

The **(2)** material is highly photoluminescent, a property justified by efficient energy transference from the antenna ligand to the emitting $^5D_4$ Tb^{3+} level. This feature was further confirmed by the measurement of the quantum yield and lifetime (37% and 0.74 ms, respectively).

The optimized molecular geometry for **(1)** was obtained by employing the Sparkle/AM1 approach showing a good agreement with the crystallographic structural model. This theoretical methodology was proven to be a versatile alternative over the more traditional protocols used in MOF research based on lanthanides ions. When compared with Eu–β-diketonates complexes, the value of Ω_2 indicates reduced degree of covalence involving the metal–ligand coordination bond and also a slightly polarizable chemical environment for the lanthanide center. The low value of the Ω_4 parameter reflects the chemical environment rigidity of the Ln^{3+} ions. The small discrepancies registered for the theoretical and experimental values of quantum yields can be rationalized

TABLE 2: Calculated Values of Intramolecular Energy Transfer and Back-Transfer Rates for the (1) Material

| | Singlet → $^5D_4$ | | Triplet → $^5D_1$ | | Triplet → $^5D_0$ | |
geometry	W_{ET1} (s^{-1})[a]	W_{BT1} (s^{-1})[b]	W_{ET2} (s^{-1})[a]	W_{BT2} (s^{-1})[b]	W_{ET3} (s^{-1})[a]	W_{BT3} (s^{-1})[b]
X-ray model	4.15×10^5	1.72×10^{-12}	2.30×10^9	4.84×10^4	1.08×10^9	4.96
Sparkle/AM1 model	8.45×10^4	1.08×10^9	2.36×10^8	0	3.20×10^{-3}	1.53×10^{-7}

[a] W_{ET}, Transfer rate. [b] W_{BT}, Back-transfer rate.

Studies of Lanthanide-Organic Frameworks

J. Phys. Chem. B, Vol. 113, No. 36, 2009 **12187**

taking into account the fact that the model does not account for the vibronic coupling with the water molecules. Nevertheless, an excellent agreement was observed for the theoretical and experimental values of quantum efficiency. These results clearly attest for the efficacy of the theoretical models employed in all calculations and, therefore, a new window of interesting possibilities for the design of novel and highly efficient lanthanide-organic frameworks.

Supporting Information Available: Crystallographic information (in particular crystal solution and refinement, crystallographic distances and hydrogen bonding geometrical parameters) as tabulated data and CIF files. Sparkle/AM1 optimized atomic coordinates for the coordination polyhedron of the Eu^{3+} center in the **(1)** structure. This material is available free of charge via the Internet at http://pubs.acs.org.

References and Notes

(1) Yaghi, O. M.; O'Keeffe, M.; Ockwig, N. W.; Chae, H. K.; Eddaoudi, M.; Kim, J. *Nature* **2003**, *423*, 705–714.

(2) Rowsell, J. L. C.; Yaghi, O. M. *Microporous Mesoporous Mater.* **2004**, *73*, 3–14.

(3) Rosi, N. L.; Kim, J.; Eddaoudi, M.; Chen, B. L.; O'Keeffe, M.; Yaghi, O. M. *J. Am. Chem. Soc.* **2005**, *127*, 1504–1518.

(4) Szeto, K. C.; Prestipino, C.; Lamberti, C.; Zecchina, A.; Bordiga, S.; Bjorgen, M.; Tilset, M.; Lillerud, K. P. *Chem. Mater.* **2007**, *19*, 211–220.

(5) de Carvalho, P. H. V.; Barreto, A. S.; Rodrigues, M. O.; Prata, V. d. M.; Alves, P. B.; de Mesquita, M. E.; Júnior, S. A.; Navickiene, S. *J. Sep. Sci.* **2009**, *32*, 2132–2138.

(6) Dinca, M.; Yu, A. F.; Long, J. R. *J. Am. Chem. Soc.* **2006**, *128*, 17153–17153.

(7) Hifumi, H.; Yamaoka, S.; Tanimoto, A.; Citterio, D.; Suzuki, K. *J. Am. Chem. Soc.* **2006**, *128*, 15090–15091.

(8) de Bettencourt-Dias, A. *Dalton Trans.* **2007**, 2229–2241.

(9) Lehn, J. M. *Pure Appl. Chem.* **1994**, *66*, 1961–1966.

(10) Xu, N.; Shi, W.; Liao, D. Z.; Yan, S. P.; Cheng, P. *Inorg. Chem.* **2008**, *47*, 8748–8756.

(11) Chen, B. L.; Yang, Y.; Zapata, F.; Lin, G. N.; Qian, G. D.; Lobkovsky, E. B. *Adv. Mater.* **2007**, *19*, 1693.

(12) Wang, F. Q.; Zheng, X. J.; Wan, Y. H.; Sun, C. Y.; Wang, Z. M.; Wang, K. Z.; Jin, L. P. *Inorg. Chem.* **2007**, *46*, 2956–2958.

(13) Pan, L.; Huang, X. Y.; Li, J.; Wu, Y. G.; Zheng, N. W. *Angew. Chem., Int. Ed.* **2000**, *39*, 527–530.

(14) Pavithran, R.; Kumar, N. S. S.; Biju, S.; Reddy, M. L. P.; Junior, S. A.; Freire, R. O. *Inorg. Chem.* **2006**, *45*, 2184–2192.

(15) Bunzli, J. C. G.; Piguet, C. *Chem. Soc. Rev.* **2005**, *34*, 1048–1077.

(16) Sun, L. N.; Zhang, H. J.; Yu, J. B.; Yu, S. Y.; Peng, C. Y.; Dang, S.; Guo, X. M.; Feng, J. *Langmuir* **2008**, *24*, 5500–5507.

(17) de Bettencourt-Dias, A. *Inorg. Chem.* **2005**, *44*, 2734–2741.

(18) Zhao, B.; Chen, X. Y.; Cheng, P.; Liao, D. Z.; Yan, S. P.; Jiang, Z. H. *J. Am. Chem. Soc.* **2004**, *126*, 15394–15395.

(19) Park, S. S.; An, B.; Ha, C. S. *Microporous Mesoporous Mater.* **2008**, *111*, 367–378.

(20) Sun, Y. Q.; Zhang, J.; Chen, Y. M.; Yang, G. Y. *Angew. Chem., Int. Ed.* **2005**, *44*, 5814–5817.

(21) Broker, G. A.; Klingshirn, M. A.; Rogers, R. D. *J. Alloys Compd.* **2002**, *344*, 123–127.

(22) Daiguebonne, C.; Kerbellec, N.; Guillou, O.; Bunzli, J. C.; Gumy, F.; Catala, L.; Mallah, T.; Audebrand, N.; Gerault, Y.; Bernot, K.; Calvez, G. *Inorg. Chem.* **2008**, *47*, 3700–3708.

(23) de Lill, D. T.; de Bettencourt-Dias, A.; Cahill, C. L. *Inorg. Chem.* **2007**, *46*, 3960–3965.

(24) Rodrigues, M. O.; Brito-Silva, A. M.; Alves, S.; De Simone, C. A.; Araujo, A. A. S.; de Carvalho, P. H. V.; Santos, S. C. G.; Aragao, K. A. S.; Freire, R. O.; Mesquita, M. E. *Quim. Nova* **2009**, *32*, 286–U28.

(25) Yang, E.; Zhang, J.; Li, Z. J.; Gao, S.; Kang, Y.; Chen, Y. B.; Wen, Y. H.; Yao, Y. G. *Inorg. Chem.* **2004**, *43*, 6525–6527.

(26) Kyono, A.; Kimata, M.; Hatta, T. *Inorg. Chim. Acta* **2004**, *357*, 2519–2524.

(27) Kumagai, H.; Kawata, S.; Kitagawa, S. *Inorg. Chim. Acta* **2002**, *337*, 387–392.

(28) Harnisch, J. A.; Thomas, L. M.; Guzei, I. A.; Angelici, R. J. *Inorg. Chim. Acta* **1999**, *286*, 207–214.

(29) Chui, S. S. Y.; Siu, A.; Feng, X.; Zhang, Z. Y.; Mak, T. C. W.; Williams, I. D. *Inorg. Chem. Commun.* **2001**, *4*, 467–470.

(30) de Mesquita, M. E.; Junior, S. A.; Oliveira, F. C.; Freire, R. O.; Junior, N. B. C.; de Sa, G. F. *Inorg. Chem. Commun.* **2002**, *5*, 292–295.

(31) Biju, S.; Reddy, M. L. P.; Freire, R. O. *Inorg. Chem. Commun.* **2007**, *10*, 393–396.

(32) Freire, R. O.; Vila-Nova, S. P.; Brunet, E.; Juanes, O.; Rodriguez-Ubis, J. C.; Alves, S. *Chem. Phys. Lett.* **2007**, *443*, 378–382.

(33) Albuquerque, R. Q.; Freire, R. O.; Malta, O. L. *J. Phys. Chem. A* **2005**, *109*, 4607–4610.

(34) Freire, R. O.; Rocha, G. B.; Albuquerque, R. Q.; Simas, A. M. *J. Lumin.* **2005**, *111*, 81–87.

(35) Beltrao, M. A.; Santos, M. L.; Mesquita, M. E.; Barreto, L. S.; da Costa, N. B.; Freire, R. O.; dos Santos, M. A. C. *J. Lumin.* **2006**, *116*, 132–138.

(36) dos Santos, E. R.; dos Santos, M. A. C.; Freire, R. O.; Junior, S. A.; Barreto, L. S.; de Mesquita, M. E. *Chem. Phys. Lett.* **2006**, *418*, 337–341.

(37) de Mesquita, M. E.; Junior, S. A.; Silva, F. R. G.; dos Santos, M. A. C.; Freire, R. O.; Junior, N. B. C.; de Sa, G. F. *J. Alloys Compd.* **2004**, *374*, 320–324.

(38) de Mesquita, M. E.; Junior, S. A.; Junior, N. B. C.; Freire, R. O.; Silva, F. R. G. E.; de Sa, G. F. *J. Solid State Chem.* **2003**, *171*, 183–188.

(39) da Costa, N. B.; Freire, R. O.; dos Santos, M. A. C.; Mesquita, M. E. *J. Mol. Struct.-Theochem* **2001**, *545*, 131–135.

(40) Souza, A. P.; Paz, F. A. A.; Freire, R. O.; Carlos, L. D.; Malta, O. L.; Alves, S.; de Sa, G. F. *J. Phys. Chem. B* **2007**, *111*, 9228–9238.

(41) Lima, P. P.; Ferreira, R. A. S.; Freire, R. O.; Paz, F. A. A.; Fu, L. S.; Alves, S.; Carlos, L. D.; Malta, O. L. *ChemPhysChem* **2006**, *7*, 735–746.

(42) de Mesquita, M. E.; Silva, F. R. G. E.; Albuquerque, R. Q.; Freire, R. O.; da Conceicao, E. C.; da Silva, J. E. C.; Junior, N. B. C.; de Sa, G. F. *J. Alloys Compd.* **2004**, *366*, 124–131.

(43) Pavithran, R.; Reddy, M. L. P.; Junior, S. A.; Freire, R. O.; Rocha, G. B.; Lima, P. P. *Eur. J. Inorg. Chem.* **2005**, 412–94137.

(44) Shi, F. N.; Cunha-Silva, L.; Ferreira, R. A. S.; Mafra, L.; Trindade, T.; Carlos, L. D.; Paz, F. A. A.; Rocha, J. *J. Am. Chem. Soc.* **2008**, *130*, 150–167.

(45) Shi, F. N.; Trindade, T.; Rocha, J.; Paz, F. A. A. *Cryst. Growth Des.* **2008**, *8*, 3917–3920.

(46) Soares-Santos, P. C. R.; Cunha-Silva, L.; Paz, F. A. A.; Ferreira, R. A. S.; Rocha, J.; Trindade, T.; Carlos, L. D.; Nogueira, H. I. S. *Cryst. Growth Des.* **2008**, *8*, 2505–2516.

(47) Rodrigues, M. O.; da Costa, N. B.; de Simone, C. A.; Araujo, A. A. S.; Brito-Silva, A. M.; Paz, F. A. A.; de Mesquita, M. E.; Junior, S. A.; Freire, R. O. *J. Phys. Chem. B* **2008**, *112*, 4204–4212.

(48) Chelebaeva, E.; Larionova, J.; Guari, Y.; Ferreira, R. A. S.; Carlos, L. D.; Paz, F. A. A.; Trifonov, A.; Guerin, C. *Inorg. Chem.* **2008**, *47*, 775–777.

(49) Girginova, P. I.; Paz, F. A. A.; Soares-Santos, P. C. R.; Ferreira, R. A. S.; Carlos, L. D.; Amaral, V. S.; Klinowski, J.; Nogueira, H. I. S.; Trindade, T. *Eur. J. Inorg. Chem.* **2007**, *423*, 8–4246.

(50) Cunha-Silva, L.; Mafra, L.; Ananias, D.; Carlos, L. D.; Rocha, J.; Paz, F. A. A. *Chem. Mater.* **2007**, *19*, 3527–3538.

(51) Taylor, K. M. L.; Jin, A.; Lin, W. B. *Angew. Chem., Int. Ed.* **2008**, *47*, 7722–7725.

(52) Freire, R. O.; Albuquerque, R. Q.; Junior, S. A.; Rocha, G. B.; de Mesquita, M. E. *Chem. Phys. Lett.* **2005**, *405*, 123–126.

(53) Freire, R. O.; Silva, F. R. G. E.; Rodrigues, M. O.; de Mesquita, M. E.; Junior, N. B. D. *J. Mol. Model* **2005**, *12*, 16–23.

(54) Bril, A.; Jagerveenis, A. W. D. *J. Res. Natl. Bur. Stand. Sect. A-Phys. Chem.* **1976**, *80*, 401–407.

(55) Malta, O. L.; Brito, H. F.; Menezes, J. F. S.; Silva, F. R. G. E.; Donega, C. D.; Alves, S. *Chem. Phys. Lett.* **1998**, *282*, 233–238.

(56) Kottke, T.; Stalke, D. *J. Appl. Crystallogr.* **1993**, *26*, 615–619.

(57) *APEX-2 Data Collection Software*, Version 2.1-RC13; Bruker AXS, Delft: The Netherlands, 2006.

(58) *Cryopad Remote monitoring and control*, Version 1.451; Oxford Cryosystems: Oxford, United Kingdom, 2006.

(59) *SAINT+ Data Integration Engine*, v. 7.23a; Bruker AXS: Madison, Wisconsin, USA, 1997−2005.

(60) Sheldrick, G. M. *SADABS v.2.01, Bruker/Siemens Area Detector Absorption Correction Program*; Bruker AXS: Madison, Wisconsin, USA, 1998.

(61) Sheldrick, G. M. *SHELXS-97, Program for Crystal Structure Solution*; University of Göttingen, 1997.

(62) Sheldrick, G. M. *Acta Cryst. A* **2008**, *64*, 112–122.

(63) Sheldrick, G. M. *SHELXL-97, Program for Crystal Structure Refinement*; University of Göttingen, 1997.

(64) Freire, R. O.; Rocha, G. B.; Simas, A. M. *Inorg. Chem.* **2005**, *44*, 3299–3310.

(65) Freire, R. O.; Rocha, G. B.; Simas, A. M. *J. Mol. Model* **2006**, *12*, 373–389.

(66) Dolg, M.; Stoll, H.; Savin, A.; Preuss, H. *Theor. Chim. Acta* **1989**, *75*, 173–194.

(67) Stewart, J. J. P. *Version 7.058 ed.*; Chemistry, S. C., Ed.; Colorado Springs, USA: 2008.

(68) Ridley, J. E.; Zerner, M. C. *Theor. Chim. Acta* **1976**, *42*, 223−236.

(69) Zerner, M. C.; Loew, G. H.; Kirchner, R. F.; Muellerwesterhoff, U. T. *J. Am. Chem. Soc.* **1980**, *102*, 589–599.

(70) Zerner, M. C. *ZINDO manual, QTP*; University of Florida: Gainesville, FL, 1990.

(71) Judd, B. R. *Operator Techniques in Atomic Spectroscopy*; McGraw-Hill Book Company: USA, 1998.

(72) Guan, J. B.; Chen, B.; Sun, Y. Y.; Liang, H.; Zhang, Q. J. *J. Non-Cryst. Solids* **2005**, *351*, 849–855.

(73) Judd, B. R. *Phys. Rev.* **1962**, *127*, 750–761.

(74) Ofelt, G. S. *J. Chem. Phys.* **1962**, *37*, 511–&.

(75) Malta, O. L.; Brito, H. F.; Menezes, J. F. S.; Silva, F. R. G. E.; Alves, S.; Farias, F. S.; deAndrade, A. V. M. *J. Lumin.* **1997**, *75*, 255–268.

(76) Malta, O. L.; Ribeiro, S. J. L.; Faucher, M.; Porcher, P. *J. Phys. Chem. Solids* **1991**, *52*, 587–593.

(77) Malta, O. L.; dosSantos, M. A. C.; Thompson, L. C.; Ito, N. K. *J. Lumin.* **1996**, *69*, 77–84.

(78) Malta, O. L.; Legendziewicz, J.; Huskowska, E.; Turowska-Tyrk, I.; Albuquerque, R. Q.; Donega, C. D.; Silva, F. R. G. E. *J. Alloys Compd.* **2001**, *323*, 654–660.

(79) Cao, R.; Sun, D. F.; Liang, Y. C.; Hong, M. C.; Tatsumi, K.; Shi, Q. *Inorg. Chem.* **2002**, *41*, 2087–2094.

(80) Li, Z. F.; Wang, C. X.; Wang, P.; Zhang, Q. H. *Acta Crystallogr., Sect. E: Struct. Rep. Online* **2006**, *62*, M914–M915.

(81) Deluzet, A.; Guillou, O. *Acta Crystallogr., Sect. C: Cryst. Struct. Commun.* **2003**, *59*, M277–M279.

(82) Inabe, T. *J. Mater. Chem.* **2005**, *15*, 1317–1328.

(83) Wu, L. P.; Munakata, M.; KurodaSowa, T.; Maekawa, M.; Suenaga, Y. *Inorg. Chim. Acta* **1996**, *249*, 183–189.

(84) Bernstein, J.; Davis, R. E.; Shimoni, L.; Chang, N. L. *Angew. Chem., Int. Ed.* **1995**, *34*, 1555–1573.

(85) Alves, S.; deAlmeida, F. V.; deSa, G. F.; Donega, C. D. *J. Lumin.* **1997**, *72−4*, 478–480.

(86) Tedeschi, C.; Azema, J.; Gornitzka, H.; Tisnes, P.; Picard, C. *Dalton Trans.* **2003**, 1738–1745.

(87) Latva, M.; Takalo, H.; Mukkala, V. M.; Matachescu, C.; RodriguezUbis, J. C.; Kankare, J. *J. Lumin.* **1997**, *75*, 149–169.

(88) Kang, J. G.; Kim, T. J. *Bull. Korean Chem. Soc.* **2005**, *26*, 1057–1064.

(89) Binnemans, K.; VanHerck, K.; GorllerWalrand, C. *Chem. Phys. Lett.* **1997**, *266*, 297–302.

(90) Driesen, K.; Fourier, S.; Gorller-Walrand, C.; Binnemans, K. *Phys. Chem. Chem. Phys.* **2003**, *5*, 198–202.

(91) Malta, O. L.; Silva, F. R. G. E.; Longo, R. *Chem. Phys. Lett.* **1999**, *307*, 518–526.

Modeling, Structural and Spectroscopic Studies of Lanthanide-Organic Frameworks.

Electronic Supporting Information

Marcelo O. Rodrigues [a,b], Filipe A. Almeida Paz [b], Ricardo O. Freire [c],
Gilberto F. de Sá [a], André Galembeck [a], Maria C. B. S. M. Montenegro[d], Alberto N. Araújo[d], and S.
Alves Jr *[a,d].

[a]*Departamento de Química Fundamental, UFPE, 50590-470, Recife - PE, Brazil.*
[b]*Departamento de Química, Universidade de Aveiro, CICECO, 3810-193 Aveiro, Portugal.*
[c]*Departamento de Química, UFS, 49100-000, São Cristóvão - SE, Brazil.*
[d]*Faculdade de Farmácia, Laboratório de Química Física, UP, 3810-193, Porto, Portugall.*

Corresponding author footnote: Prof° Dr° Severino Alves Júnior (salvesjr@ufpe.br) Departamento de Química Fundamental, UFPE, 50670-901, Recife, PE, Brazil. Tel. +55 81 2126-7475; Fax: +55 81 2126-8442.

Table S1. Crystal and structure refinement data for [Ln_2(MELL)(H_2O)$_6$]

	(1)	(2)
Formula	$C_6 H_6 Eu O_9$	$C_6 H_6 O_9 Tb$
Formula weight	374.07	381.03
Crystal system	Orthorhombic	Orthorhombic
Space group	*P n n m*	*P n n m*
Temperature/K	296(2) K	150(2) K
Unit cell dimensions /Å	a = 13.4361(5) Å	a = 13.3410(3) Å
	α = 90°.	α = 90°.
	b = 6.6250(2) Å	b = 6.57180(10) Å
	β= 90°.	β = 90°.
	c = 10.1416(4) Å	c = 10.0912(2) Å
	γ = 90°.	γ =90°.
Volume/Å^3	902.75(6) Å3	884.74(3)
Z	4	4
D_c/g cm^{-3}	2.752	2.861
μ(Mo-Kα)/mm^{-1}	6.985	.032
Crystal size/mm	0.35 x 0.35 x 0.30	0.20 x 0.19 x 0.17
θ range	3.67 to 25.35°	3.70 to 25.33°
Index ranges	-16<=h<=15	16<=h<=16
	7<=k<=7	7<=k<=6
	2<=l<=11	12<=l<=12
Reflections collected	7990	9245
Independent reflections	848 (R_{int} = 0.0232)	855 (R_{int} = 0.0182)
Completeness to theta = 25.35°	96.5 %	99.5 %
Final *R* indices [I>2σ(I)]^{a,b}	*R1 = 0.0193, wR2 = 0.0506*	*R1 = 0.0119 wR2 = 0.0274*
Final *R* indices (all data)^{a,b}	*R1 = 0.0205 wR2 = 0.0510*	*R1 = 0.0126 wR2 = 0.0277*
Largest diff. peak and hole	0.366 and -1.697 e.Å-3	0.417 and -0.519 e.Å-3
CCDC Number	721858	721859

$$^a R1 = \sum \left\| F_o \right| - \left| F_c \right\| / \sum \left| F_o \right|; \;\; ^b wR2 = \sqrt{ \sum \left[w \left(F_o^2 - F_c^2 \right)^2 \right] / \sum \left[w \left(F_o^2 \right)^2 \right] }$$

Table S2. Selected bond lengths [Å] and angles [°] for **(1)**, **(2)** and **(3)**.

	(1)	**(2)**	**(3)**
Ln(1)─O(3)^{i}	2.320(4)	2.296(3)	2.309(3)
Ln(1)─O(4)^{ii}	2.369(4)	2.344(3)	2.356(2)
Ln(1)─O(1W)^{iii}	2.424(3)	2.3904(18)	2.4067(18)
Ln(1)─O(1W)	2.424(3)	2.3904(18)	2.4067(18)
Ln(1)─O(1)^{iii}	2.502(3)	2.4664(17)	2.4792(16)
Ln(1) ─O(1)	2.502(3)	2.4664(17)	2.4792(16)
Ln(1)─O(2W)	2.503(4)	2.482(3)	2.494(3)
Ln(1)─O(2)^{iii}	2.575(3)	2.5563(18)	2.5636(18)
Ln(1)─O(2)	2.575(3)	2.5563(18)	2.5636(18)
O(3)^{i}—Ln(1)—O(4)^{ii}	145.44(14)	145.32(9)	145.07(9)
O(3)^{i}—Ln(1) —O(1W)^{iii}	83.92(10)	84.33(7)	84.29(6)
O(4)^{ii}—Ln(1) —O(1W)^{iii}	70.24(10)	69.84(7)	69.73(6)
O(3)^{i}—Ln(1) —O(1W)	83.92(10)	84.33(7)	84.29(6)
O(4)^{ii}—Ln(1) —O(1W)	70.24(10)	69.84(7)	69.73(6)
O(1W)^{iii}—Ln(1) —O(1W)	81.60(17)	81.96(10)	82.06(10)
O(3)^{i}—Ln(1) —O(1)^{iii}	128.59(8)	129.06(5)	129.03(5)
O(4)^{ii}—Ln(1) —O(1)^{iii}	72.25(9)	71.96(6)	72.13(6)
O(1W)^{iii}—Ln(1) —O(1)^{iii}	142.42(10)	141.76(6)	141.82(6)
O(1W) —Ln(1) —O(1)^{iii}	83.76(10)	83.54(6)	83.49(6)
O(3)^{i}—Ln(1) —O(1)	128.59(8)	129.06(5)	129.03(5)
O(4)^{ii}—Ln(1) —O(1)	72.25(9)	71.96(6)	72.13(6)
O(1W)^{iii}—Ln(1) —O(1)	83.76(10)	83.54(6)	83.49(6)
O(1W) —Ln(1) —O(1)	142.42(10)	141.76(6)	141.82(6)
O(1)^{iii}—Ln(1) —O(1)	87.19(12)	86.40(8)	86.50(8)
O(3)^{i}—Ln(1) —O(2W)	79.85(14)	79.64(9)	79.95(9)
O(4)^{ii}—Ln(1) —O(2W)	134.72(14)	135.04(9)	134.98(9)

Table S2. (cont.).

O(1W)^{iii}—Ln(1)—O(2W)	135.99(9)	135.93(5)	135.97(5)
O(1W)—Ln(1)—O(2W)	135.99(9)	135.93(5)	135.97(5)
O(1)^{iii}—Ln(1)—O(2W)	75.38(10)	75.69(6)	75.50(6)
O(1)—Ln(1)—O(2W)	75.38(10)	75.69(6)	75.50(6)
O(3)^{i}—Ln(1)—O(2)^{iii}	77.84(7)	77.68(5)	77.90(5)
O(4)^{ii}—Ln(1)—O(2)^{iii}	112.65(7)	112.70(5)	112.63(4)
O(1W)^{iii}—Ln(1)—O(2)^{iii}	147.97(11)	148.07(6)	148.31(6)
O(1W)—Ln(1)—O(2)^{iii}	70.54(11)	70.29(7)	70.35(7)
O(1)^{iii}—Ln(1)—O(2)^{iii}	51.02(9)	51.67(6)	51.41(6)
O(1)—Ln(1)—O(2)^{iii}	128.11(9)	128.17(6)	127.98(6)
O(2W)—Ln(1)—O(2)^{iii}	66.15(7)	66.29(5)	66.24(5)
O(3)^{i}—Ln(1)—O(2)	77.84(7)	77.68(5)	77.90(5)
O(4)^{ii}—Ln(1)—O(2)	112.65(7)	112.70(5)	112.63(4)
O(1W)^{iii}—Ln(1)—O(2)	70.54(11)	70.29(7)	70.35(7)
O(1W)—Ln(1)—O(2)	147.97(11)	148.07(6)	148.31(6)
O(1)^{iii}—Ln(1)—O(2)	128.11(9)	128.17(6)	127.98(6)
O(1)—Ln(1)—O(2)	51.02(9)	51.67(6)	51.41(6)
O(2W)—Ln(1)—O(2)	66.15(7)	66.29(5)	66.24(5)
O(2)^{iii}—Ln(1)—O(2)	129.27(15)	129.45(10)	129.45(9)

Symmetry transformations used to generate equivalent atoms:
^{i} -x+3/2,y+1/2,-z+3/2 ^{ii} -x+3/2,y-1/2,-z+3/2
^{iii} x,y,-z+1 ^{iv} -x+1,-y,z ^{v} x,y,-z+2

Table S3. Hydrogen bonds for **(1)**, **(2)** and **(3)** [Å and °].

D-H...A	d(D-H)	d(H...A)	d(D...A)	<(DHA)
	(1)			
O(1W)-H(1A)...O(1)^{vi}	0.95(3)	1.95(2)	2.847(4)	158(5)
O(1W)-H(1B)...O(2)^{vii}	0.94(3)	1.826(18)	2.745(4)	164(4)
O(2W)-H(2A)...O(1)^{viii}	0.947(10)	1.96(2)	2.859(4)	158(5)
O(2W)-H(2B)...O(2W)^{ix}	0.947(10)	2.16(4)	3.028(9)	151(7)
	(2)			
O(1W)-H(1A)...O(1)^{vi}	0.941(10)	1.923(13)	2.836(2)	163(3)
O(1W)-H(1B)...O(2)^{vii}	0.941(10)	1.822(13)	2.739(2)	164(3)
O(2W)-H(2A)...O(1)^{viii}	0.945(10)	1.931(12)	2.861(3)	167(3)
O(2W)-H(2B)...O(2W)^{ix}	0.946(10)	2.01(2)	2.938(5)	165(5)
	(3)			
O(1W)-H(1A)...O(1)^{vi}	0.939(10)	1.916(11)	2.840(3)	167(3)
O(1W)-H(1B)...O(2)^{vii}	0.940(10)	1.823(14)	2.736(3)	163(3)
O(2W)-H(2A)...O(1)^{viii}	0.939(10)	1.960(15)	2.863(3)	160(3)

Symmetry transformations used to generate equivalent atoms:
^{vi} -x+3/2,y+1/2,z+1/2 ^{vii} -x+3/2,y-1/2,z-3/2
^{viii} -x+1,-y,-z+1 ^{ix} -x+1,-y+1,z.

Table S4. Optimized cartesians coordinates for the crystallographic and Sparkle/AM1 coordination polyhedron (inside parentheses) of the **(1)** structure, plus the values of charge factors (g) and the cation polarizability(α) adjusted using a non-linear minimization of a four-dimensional surface response.

Atoms	X (Å)	Y (Å)	Z (Å)	g	α
Eu	0.000 (0.000)	0.000 (0.000)	0.000 (0.000)	–	–
O	2.276 (1.931)	-0.763 (-0.908)	-0.671 (-0.927)	0.018	2.21
O	1.188 (0.872)	-2.186 (-2.065)	0.053 (0.624)	0.018	2.21
O	1.273 (1.311)	2.138 (1.800)	0.143 (0.672)	0.018	2.21
O	-0.286 (-0.860)	2.108 (1.862)	1.289 (1.093)	0.018	2.21
O	-1.360 (-1.849)	-0.985 (-1.202)	1.751 (0.843)	0.018	2.21
O	0.698 (0.281)	0.890 (0.591)	-2.256 (-2.300)	1.231	6.48
O	-0.656 (-0.727)	-1.516 (-1.719)	-1.898 (-1.495)	1.231	6.48
O	1.770 (0.745)	0.105 (-0.009)	1.783 (2.278)	1.231	6.48
O	-1.807 (-1.854)	1.461 (1.141)	-0.966 (-1.083)	1.231	6.48

Figure S1 - Emission spectrum of **(3)** collected at 77K.

ESTUDOS ESPECTROSCÓPICOS E ESTRUTURAIS DOS POLÍMEROS DE COORDENAÇÃO 2D, ∞[Tb(DPA)(HDPA)] E ∞[Gd(DPA)(HDPA)]

Artigo

Marcelo O. Rodrigues, Antonio M. Brito-Silva e Severino Alves Júnior*
Departamento de Química Fundamental, Universidade Federal de Pernambuco, 50590-470 Recife - PE, Brasil
Carlos A. De Simone
Instituto de Química e Biotecnologia, Universidade Federal de Alagoas, 57072-970 Maceió – AL, Brasil
Adriano Antunes S. Araújo, Pedro Henrique V. de Carvalho, Sílvia Caroline G. Santos, Kennedy Alexandre S. Aragão, Ricardo O. Freire e Maria Eliane Mesquita
Departamento de Química, Universidade Federal de Sergipe, 49100-000 São Cristóvão - SE, Brasil

STRUCTURAL AND SPECTROSCOPIC STUDIES OF THE 2D COORDINATION POLYMERS, ∞[Tb(DPA)(HDPA)] AND ∞[Gd(DPA)(HDPA)]. This paper presents the synthesis of the coordination polymers ∞[Ln(DPA)(HDPA)] (DPA=2,6-pyridinedicarboxylate; Ln= Tb and Gd), their structural and spectroscopic properties. The structural study reveals that the ∞[Ln(DPA)(HDPA)] has a single Ln^{+3} ion coordinated with two H_2DPA ligands in tridentade coordination mode, while two others H_2DPA establish a *syn*-bridge with a symmetry-related Ln^{3+}, forming a two-dimensional structure. The spectroscopic studies show that ∞[Tb(DPA)(HDPA)] compound has high quantum yield ($q_x \approx 50.0\%$), due to the large contribution of radiative decay rate. Moreover triplet level is localized sufficiently over the emitter level $^5D_4$ of the Tb^{3+} ion, avoiding a retrotransference process between these states.

Keywords: lanthanides; coordination polymers; luminescence.

INTRODUÇÃO

Nos últimos anos um aumento significativo nas pesquisas relacionadas aos polímeros de coordenação, como uma interface entre a química sintética e a ciência de materiais, tem desempenhado papel importante na amplificação de parâmetros para predição, controle estrutural e funcional dos sólidos cristalinos.[1] Estudos nesta área promovem um amplo campo interdisciplinar em rápida e constante ascensão, com vasta abrangência para o desenvolvimento de pesquisas. Além disso, estes compostos apresentam promissoras aplicações em diversos setores industriais estratégicos, nas quais se incluem catálise,[2,3] nanotecnologia,[4] armazenamento de gases,[5,6] sistemas óptico-eletrônicos,[7] adsorção[8,9] dentre outros.

A maioria dos trabalhos recém publicados é referente ao emprego de metais de transição na construção de redes de coordenação,[10-12] enquanto os sistemas com lantanídeos são muito menos estudados.[12-14] Os lantanídeos possuem propriedades espectroscópicas peculiares, como tempo de vida longo e bandas de emissão finas e bem definidas.[15] Esses referidos aspectos tornam os compostos com íons lantanídeos excelentes para o uso como dispositivos moleculares conversores de luz (DMLC),[16] com possíveis aplicações em diversificadas áreas,[17] tais como dispositivos eletroluminescentes (DOELs),[18] marcadores na determinação direta de analitos orgânicos[19] e ácidos nucléicos,[20] como sondas luminescentes em imuno-diagnóstico[21] e incorporadas em matrizes sólidas para aplicações ópticas.[22]

Uma série de ligantes tem sido utilizada na síntese de novos polímeros de coordenação, dentre os quais os policarboxilatos aromáticos são particularmente interessantes devido à robustez química e propriedades fotofísicas.[23] Por exemplo, o ácido 2,6-dipicolínico (H₂DPA) tem sido amplamente empregado na síntese de compostos com lantanídeos com potenciais aplicações em imuno-ensaios.[24]

Além disso, o H₂DPA desempenha papel interessante na construção de polímeros de coordenação, pois pode funcionar como ponte entre os centros metálicos e adotar diversos modos de coordenação.[25,26] É importante enfatizar que, apesar de existirem vários relatos de polímeros de coordenação com íons lantanídeos e o H₂DPA, investigações detalhadas das propriedades luminescentes desses compostos são escassas.[27] Nessa perspectiva, este trabalho apresenta um estudo dos aspectos estruturais e espectroscópicos dos polímeros de coordenação 2D ∞[Tb(DPA)(HDPA)] e ∞[Gd(DPA)(HDPA)].

PARTE EXPERIMENTAL

Reagentes

Os óxidos de lantanídeos 99,99% e o ácido 2,6-dipicolínico (H₂DPA) foram obtidos da Aldrich e utilizados sem prévio tratamento. Os nitratos de térbio e gadolínio foram preparados através da reação dos respectivos óxidos com ácido nítrico, como descrito na literatura.[28]

Síntese das redes de coordenação ∞[Tb(DPA)(HDPA)] e ∞[Gd(DPA)(HDPA)]

Os polímeros de coordenação foram preparados a partir da mistura de 0,70 mmol do ligante H₂DPA, 0,35 mmol do $Ln(NO_3)_3 6H_2O$ (Ln= Gd^{3+} e Tb^{3+}) e 4,0 mL de água deionizada. Essa mistura foi selada em um reator de aço inox revestido de Teflon com 8,0 mL de capacidade e submetida a uma temperatura de 145 °C por 72 h sendo, em seguida, resfriada à temperatura ambiente com taxa de 1 ºC/min. Os cristais incolores resultantes foram lavados com água deionizada e acetona e apresentaram rendimentos de aproximadamente 60% em relação ao lantanídeo.

*e-mail: salvesjr@ufpe.br

Difração de raios-X de monocristal

As medidas de raios–X foram realizadas em um difratômetro Enraf-Nonius KappaCCD com detector de área. Os programas usados no estudo cristalográfico foram: determinação da célula unitária e coleta de dados-KappaCCD-Enraf-Nonius;[29] redução de dados-HKL Denzo e Scalepack;[30] coleta de dados-Colecione;[31] solução de estrutura-SHELXS-86;[32] refinamento-SHELXL-97.[33]

Análise elementar

As análises elementares de C, H, e N foram realizadas em um equipamento CHNS-O Analyzer Flash (112 Series EA Thermo Finningan).

Espectroscopia de absorção na região do infravermelho

Os espectros de absorção na região do infravermelho foram obtidos em pastilhas de KBr entre 4000 e 400 cm^{-1} em um espectrofotômetro com transformada de Fourier, da Brucker, modelo IF66.

Termogravimetria/termogravimetria derivada (TG/DTG)

As curvas TG/DTG foram obtidas na faixa de temperatura entre 25 e 1200 °C, utilizando uma termo-balança modelo TGA 50 da marca Shimadzu, sob atmosfera dinâmica de nitrogênio (50 mL min^{-1}), razão de aquecimento de 10 °C min^{-1}, utilizando cadinho de platina contendo massa de amostra em torno de 3 mg. A calibração do instrumento foi verificada conforme norma ASTM (*The Americam Society for Testing and Materials*, 1993).

Espectroscopia de luminescência

Os espectros de emissão e excitação à temperatura ambiente e à 77 K foram realizados em um ISS PC1 Spectrofluorometer. O monocromador de excitação é equipado com uma lâmpada de xenônio com 300 W, a emissão é coletada em um monocromador com resolução de 0,1 nm equipado com uma fotomultiplicadora e as fendas de emissão e excitação usadas na aquisição dos dados foram de 0,5 nm. O rendimento quântico para a rede de coordenação $_\infty$[Tb(DPA)(HDPA)] foi determinado como previamente descrito na literatura.[27,34]

Tempo de vida dos estados excitados

O tempo de vida dos estados excitados foi realizado utilizando como fonte de excitação um laser de Nd:YAG (λ= 355 nm) com largura temporal de 7 ns e freqüência de 5 Hz, um osciloscópio 1012 modelo Tectronix TDS e um detector ET 2000.

RESULTADOS E DISCUSSÃO

A síntese hidrotermal proporcionou a formação de cristais das redes de coordenação $_\infty$[Tb(DPA)(HDPA)] e $_\infty$[Gd(DPA)(HDPA)] adequados para investigações cristalográficas. Os dados de análise elementar apresentaram os seguintes valores (calculado/experimental): $C_{14}H_7N_2O_8$Tb, C: 34,38/33,90%; H: 1,24/1,23%; N: 5,73/5,60%; C_{14} H_7 N_2 O_8 Gd, C: 34,42/34,25%; H: 1,44/1,32%; N: 5,73/5,65%. É importante salientar que os polímeros sintetizados são isomorfos ao [Ho(dipc)(Hdipc)],[35] entretanto, os respectivos parâmetros estruturais não foram determinados. A unidade assimétrica do $_\infty$[Ln(DPA)(HDPA)] e todos os dados cristalográficos, medidas de intensidade, refinamentos e solução da estrutura são mostradas na Figura 1 e na Tabela 1, respectivamente.
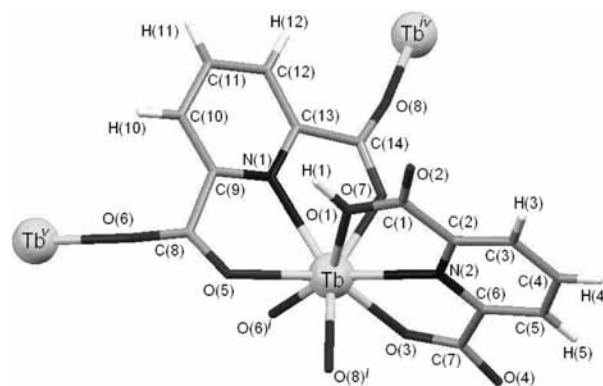
Figura 1. *Unidade assimétrica do $_\infty$[Tb(DPA)(HDPA)]. Operações de simetria usadas para gerar átomos equivalentes: ^{i}: 1- x, -½ + y, ½ -z; ^{ii}: 1 - x, ½ + y , ½ - z; ^{iii}: x, ½ - y , ½ + z; ^{iv}: x, ½ - y, -½ + z; ^{v}: 1-x, -½ + y, ½ - z*

Como os compostos são isomorfos, somente a estrutura do $_\infty$[Tb(DPA)(HDPA)] será descrita em detalhes. Neste polímero de coordenação, o íon Tb^{3+} está coordenado a moléculas do ligante DPA formadas pelos seguintes átomos: DPA1= N(1)-C(1)-C(2)-C(3)-C(4)-C(5)-C(6)-C(7)-O(1)-O(2)-O(3)-O(4) e DPA2= N(2)-C(8)-C(9)-C(10)-C(11)-C(12)-C(13)-C(14)-O(5)-O(6)-O(7)-O(8). Ambos os ligantes atuam como espécies tridentadas através dos átomos de nitrogênio dos anéis heterocíclicos e por dois átomos de oxigênio dos grupos carboxilatos, (N(1), O(1), O(3) e N(2), O(5), O(7)), respectivamente. A natureza polimérica deste composto compete às múltiplas ligações realizadas pela molécula do DPA2 que, por sua vez, também atua como um ligante bis-monodentado por meio dos átomos O(6) e O(8). Desta maneira, o ligante DPA2 funciona como ponte entre três centros metálicos distintos (Tb: x, y, z; Tb^{iv}: x, ½ - y, -½ + z; Tb^v: 1-x, -½ + y, ½ - z), gerando uma cadeia polimérica infinita em 2D ao longo do plano [100], Figura 2. Na Tabela 2 estão mostrado os comprimentos de ligação e os ângulos da primeira esfera de coordenação pertencente ao composto $_\infty$[Tb(DPA)(HDPA)].
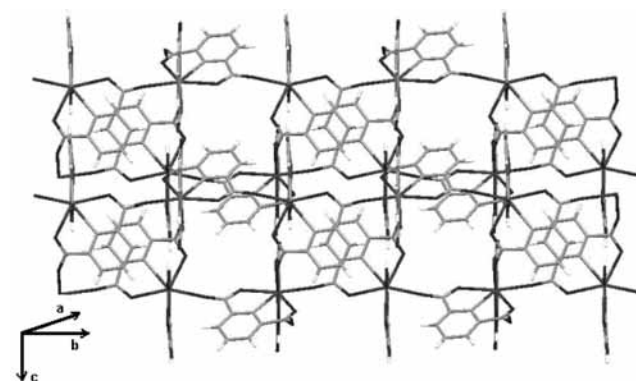
Figura 2. *Rede polimérica do $_\infty$[Tb(DPA)(HDPA)] ao longo do plano [100]*

A esfera de coordenação apresentada pelo Tb^{3+} (Tabela 2) possui número de coordenação 8 e pode ser descrita como antiprisma quadrado distorcido, além disso, a maioria dos compostos formados por lantanídeos e o H$_2$DPA apresentam número de coordenação 9.[27,35] Outro aspecto interessante é que a condição da síntese do referido composto impõe a um dos ligantes a permanência sob a forma monoprotonada, HDPA^{-1}, a fim de manter a eletroneutralidade da rede de coordenação. O respectivo átomo de hidrogênio, H(1), foi localizado ligado ao oxigênio O(1) pela síntese de Fourier. Como conseqüência da ligação H(1)—O(1), a distância interatômica de C(1)—O(1), 1,345 Å, apresenta significativa diferença quando comparada às outras ligações C—O, cuja a média equivale a 1,244 Å.

Tabela 1. Dados cristalográficos e refinamento estrutural dos polímeros de coordenação $_\infty$[Ln(DPA)(HDPA)]

Fórmula empírica	$C_{14} H_7 N_2 O_8$ Tb	$C_{14} H_6$ Gd $N_2 O_8$
Peso molecular	490,13	487,46
Temperatura	293(2) K	293(2) K
Comprimento de onda dos raios-x (K_α Mo)	0,71073 Å	0,71073 Å
Sistema cristalino e grupo espacial	monoclínico, $P2_1/c$	monoclínico, $P2_1/c$
Dimensões da cela unitária	a = 12,2466(4); b = 8,3800(3); c = 13,4939(3) Å ; β= 102.36(2)°	a = 12,2790(4) ; b = 8,3880(3); c = 13,5380 (3) Å ; β= 102,41(2)°
Z (número de moléculas por cela)	4	4
Volume	1352,70(7) Å^3	1361,78(7) Å^3
Densidade calculada	2,402 mg/m^3	2,378 mg/m^3
Coeficiente de absorção	5,282 mm^{-1}	4,924 mm^{-1}
F(000)	932	928
Dimensão do cristal	0,373 x 0,281 x 0,234 mm	0,224 x 0,189 x 0,18 mm
Intervalo de θ para a coleta de dados	2,88 a 24,99°	2,88 a 27,49°
Limites dos índices de Miller	-14≤h≤12, -9≤k≤9, -15≤l≤15	-15≤h≤12, -9≤k≤10, -17≤l≤17
Reflexões coletadas/únicas	5241 / 2017 [R(int) = 0,0363]	8847 / 2841 [R(int) = 0,0284]
Completância para θ = 24,99	84,9%	91,2%
Correção da absorção	Gaussian	Gaussian
Min. e max. Transmissão	0,199 e 0,321	0,214 e 0,432
Método de refinamento	Matriz de mínimos quadrados completa em F^2	Matriz de mínimos quadrados completa em F^2
Dados / restrições / parâmetros	2017 / 0 / 226	2841 / 0 / 226
Concordância sobre F^2	1,105	1,123
Índices R para os dados [I>2σ(I)]	R_1 = 0,0255, wR_2 = 0,0655	R_1 = 0,0210, wR_2 = 0,0526
Índices R para todos os dados	R_1=0,0260, wR_2=0,0660	R_1 = 0,0220, wR_2 = 0,0528
Alturas de picos residuais	0.904 e -0.828 e.Å^{-3}	0.644 e -0.981 e.Å^{-3}

Tabela 2. Distâncias interatômicas (Å) e ângulos (°) referentes à primeira esfera de coordenação do $_\infty$[Tb(DPA)(HDPA)]

Tb-O(1)	2,526(2)	O(6)^{ii}-Tb-N(2)	84,31(9)
Tb-O(3)	2,341(3)	O(8)^{iii}-Tb-N(2)	141,34(9)
Tb-O(5)	2,412(2)	O(3)-Tb-N(2)	136,55(8)
Tb-O(6)^{ii}	2,281(2)	O(7)-Tb-N(2)	63,78(9)
Tb-O(7)	2,388(3)	O(6)^{ii}-Tb-N(1)	144,09(12)
Tb-O(8)^{iii}	2,323(3)	O(8)^{iii}-Tb-N(1)	79,79(10)
Tb-N(1)	2,510(3)	O(3)-Tb-N(1)	65,55(9)
Tb-N(2)	2,484(3)	O(7)-Tb-N(1)	77,94(10)
O(6)^{ii}-Tb-O(8)^{iii}	95,00(9)	O(5)-Tb-N(1)	132,06(9)
O(6)^{ii}-Tb-O(3)	78,54(9)	N(2)-Tb-N(1)	121,55(9)
O(8)^{iii}-Tb-O(3)	80,23(9)	O(6)^{ii}-Tb-O(1)	153,64(9)
O(6)^{ii}-Tb-O(7)	95,05(10)	O(8)^{iii}-Tb-O(1)	92,29(9)
O(8)^{iii}-Tb-O(7)	153,88(11)	O(3)-Tb-O(1)	127,72(8)
O(3)-Tb-O(7)	78,26(8)	O(7)-Tb-O(1)	89,29(9)
O(6)^{ii}-Tb-O(5)	79,61(9)	O(5)-Tb-O(1)	77,43(8)
O(8)^{iii}-Tb-O(5)	76,97(9)	N(2)-Tb-O(1)	74,34(8)
O(3)-Tb-O(5)	146,69(8)	N(1)-Tb-O(1)	62,21(9)
O(7)-Tb-O(5)	128,63(8)		

Operações de simetria usadas para gerar átomos equivalentes: ^{i}: 1- x, -½ + y, ½ -z ; ^{ii}: 1 - x, ½ + y , ½ - z; ^{iii}: x, ½ - y , ½ + z; ^{iv}: x, ½ - y, -½ + z; ^{v}: 1-x, -½ + y, ½ - z.

Pela resolução estrutural foi observado que não existe interação direta entre os diferentes íons Tb³⁺, pois o correspondente valor médio das distâncias Tb---Tb equivale a 6,55 Å. Os comprimentos das ligações Tb—O estão na faixa de 2,341(3) a 2,526(2) Å, já as ligações Tb—N estão na faixa de 2,484(3) a 2,510(3) Å. Usualmente, os comprimentos das ligações Ln—N são mais longos que as Ln—O em compostos com o mesmo ligante.[35-39] Contudo, a ligação Tb—O (1) apresenta um valor superior a todas as outras, devido à peculiar situação causada pela ligação entre os átomos H(1) e o O(1).

Os espectros de absorção na região do infravermelho do ligante livre e dos polímeros de coordenação estão disponíveis no Material Suplementar. O espectro de infravermelho do H_2DPA mostra absorções na região entre 3100 e 2500 cm⁻¹, devido aos estiramentos da ligação H—O dos grupos carboxílicos. Este conjunto de sinais é característico das ligações de hidrogênio formadas pelas interações destes grupos (—COOH) e, por sua vez, estão sobrepondo às bandas dos estiramentos das ligações C—H.[40] Nos espectros de ∞[Tb(DPA)(HDPA)] e ∞[Gd(DPA)(HDPA)] as respectivas bandas atribuídas às vibrações das ligações O—H presentes em um dos ligantes protonado estão situadas em 3440 e 3443 cm⁻¹. As bandas associadas aos estiramentos assimétricos dos grupos carboxilatos estão presentes nos espectros das redes com Tb³⁺ e Gd³⁺ em 1637, 1611 e 1638 e 1607 cm⁻¹, respectivamente. Da mesma forma, as bandas atribuídas aos estiramentos simétricos dos respectivos compostos estão situadas em 1411, 1392 e 1408 e 1392 cm⁻¹. Em comparação com o ligante livre foi constatado que os estiramentos assimétricos foram deslocados de 1700 cm⁻¹, enquanto os simétricos de 1331 e 1302 cm⁻¹ no ligante livre.[40] No espectro de IV da amostra ∞[Tb(DPA)(HDPA)] e ∞[Gd(DPA)(HDPA)] foram observadas bandas intensas localizadas em 1746 e 1742 cm⁻¹. Estes estiramentos são característicos da dupla ligação do grupo carbonila (C=O) e são atribuídos às ligações C(1)—O(2) das respectivas amostras. Conforme observado nos dados cristalográficos, o menor comprimento destas ligações contribui para o deslocamento das respectivas bandas para regiões de maiores energias. A coordenação através dos átomos de nitrogênio pode ser evidenciada através da mudança na intensidade das vibrações em 1574 cm⁻¹ atribuídas ao anel aromático.[35]

As curvas de TG/DTG (Figura 3) das redes de coordenação ∞[Tb(DPA)(HDPA)] e ∞[Gd(DPA)(HDPA)] mostram similaridades quanto ao perfil termo-analítico das curvas. O primeiro evento de decomposição térmica associado aos compostos ∞[Tb(DPA)(HDPA)] e ∞[Gd(DPA)(HDPA)] acontece nas faixas de 285 a 690 °C e de 280 a 685 °C, com perdas de massa equivalentes a 52,3 e 49,7%, respectivamente. Esta etapa é característica da degradação dos ligantes orgânicos. Os estágios de eliminação de material carbonáceo em ambas as redes de coordenação com Tb³⁺ e Gd³⁺ são iniciados próximo

a 680 °C e terminam em aproximadamente 970 °C. Os resíduos das decomposições apresentam massas relativas de 40,8% (Calculado: 39,8%) e 38,9% (Calculado: 37,2%) e são referentes às espécies químicas ¼ Tb_4O_7 e ½ Gd_2O_3, respectivamente.

O espectro de emissão da rede de coordenação ∞[Gd(DPA)(HDPA)] à 77 K, após excitação em 280 nm está mostrado na Figura 4. O nível tripleto foi estimado a partir da zero-fonon, localizado no inicio da banda de emissão, 362 nm (27548 cm⁻¹).[41]
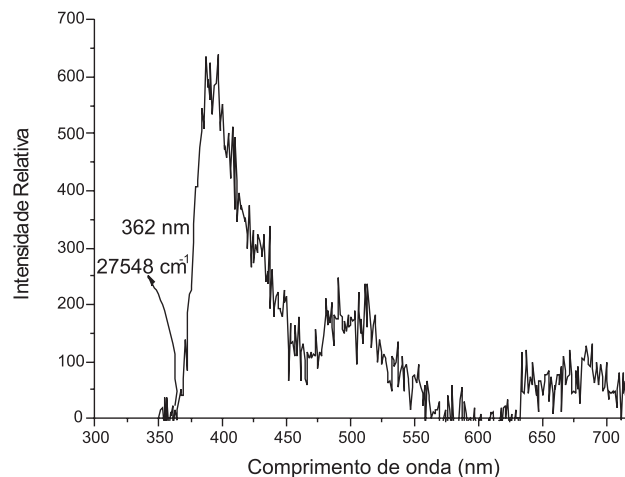
Figura 4. *Espectro de emissão do polímero de coordenação ∞[Gd(DPA)(HDPA)] à 77 K, após a excitação em 280 nm*

O espectro de excitação do composto ∞[Tb(DPA)(HDPA)], adquirido a temperatura ambiente, monitorando a transição mais intensa $^5D_4 \rightarrow {}^7F_5$ (545 nm) apresenta uma larga banda centrada em 280 nm referente à transição $\pi \rightarrow \pi^*$ do ligante. Esta banda evidencia que a fotossensibilização através do processo indireto (via ligante) é responsável pela luminescência do material. O espectro de emissão da rede de coordenação mostra a seqüência típica das transições $^5D_4 \rightarrow {}^7F_J$ (J= 6–2) inerente ao íon Tb³⁺, sendo a transição $^5D_4 \rightarrow {}^7F_5$, com 55,6% do total, a responsável pela intensa coloração verde apresentada pelo composto. Também pôde ser observada a ausência da transição $^5D_3 \rightarrow {}^7F_4$ normalmente monitorada em 437 nm. Este tipo de comportamento indica que o rápido processo de relaxação referente à transição $^5D_3 \rightarrow {}^5D_4$ é induzido pelas elevadas freqüências vibracionais características do ligante.[42,43] Os espectros de excitação e emissão do ∞[Tb(DPA)(HDPA)] são mostrados na Figura 5.

Figura 3. *Curvas TG e DTG dos polímeros de coordenação. ∞[Tb(DPA)(HDPA] e ∞[Gd(DPA)(HDPA]*
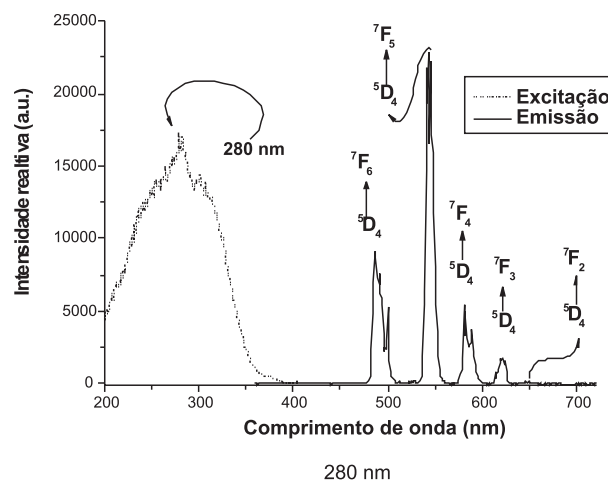
Figura 5. *Espectro de excitação do ∞[Tb(DPA)(HDPA)] monitorando a transição $^5D_4 \rightarrow {}^7F_5$ em 545 nm e espectro de emissão do ∞[Tb(DPA)(HDPA)] excitado à 280 nm, ambos obtidos à 300 K*

A curva de decaimento do estado excitado $^5D_4$, obtida à temperatura ambiente pelo monitoramento da transição $^5D_4 \rightarrow {}^7F_5$, está mostrada na Figura 6. O elevado valor de tempo de vida, $\tau=1,1$ ms, encontrado para a rede de coordenação $_\infty$[Tb(DPA)(HDPA)] pode ser justificado pela ausência de moléculas de água na esfera de coordenação e do arranjo estrutural rígido que restringe os modos vibracionais do ligante.[44] Como conseqüência, o rendimento quântico encontrado para a rede de coordenação $_\infty$[Tb(DPA)(HDPA)] é de 49,8%.
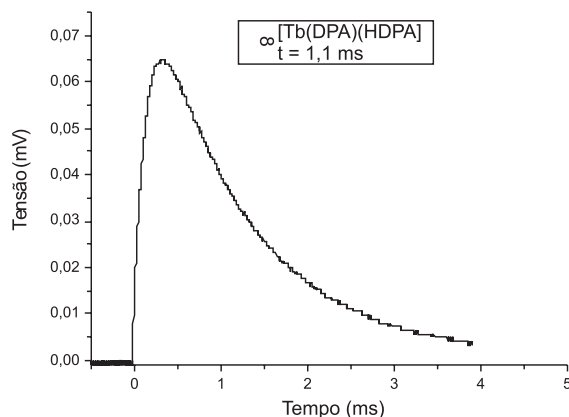
Figura 6. *Curva de decaimento do estado excitado $^5D_4$ do íon Tb^{3+} no polímero de coordenação $_\infty$[Tb(DPA)(HDPA)] à 300 K*

O processo de retro-transferência de energia é um dos principais mecanismos de supressão da luminescência de complexos de Tb^{3+}.[45] Verificando a energia dos níveis tripleto em diversos ligantes, Lavta *et al.*[44] concluíram que a retro-transferência de energia poderia ser observada quando a diferença entre o estado $^5D_4$ do Tb^{3+} (20400 cm^{-1}) e o mais baixo nível de energia tripleto intrínseco aos ligantes é inferior a 1850 cm^{-1}. A respectiva diferença energética, ΔE, entre o nível tripleto do ligante (27548 cm^{-1}) e o estado emissor $^5D_4$ do Tb^{3+} é de 7148 cm^{-1}. Dentro desta perspectiva, ficaria caracterizado que o processo de retro-transferência não possui significativa importância em relação ao composto $_\infty$[Tb(DPA)(HDPA)], visto que o nível de energia sugerido ao nível tripleto do ligante está localizado muito acima do nível emissor do Tb^{3+}. Na Figura 7 apresenta-se o diagrama de energia proposto para a rede de coordenação $_\infty$[Tb(DPA)(HDPA)].
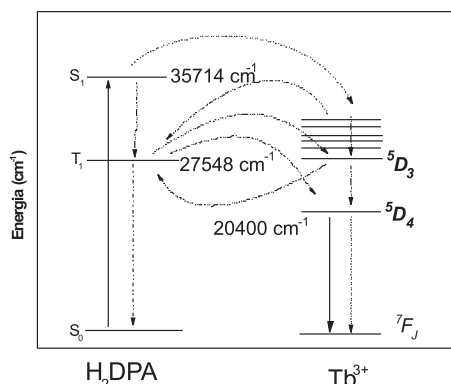
Figura 7. *Diagrama de energia para o $_\infty$[Tb(DPA)(HDPA)], mostrando os mais prováveis canais de transferência de energia intramolecular*

CONCLUSÃO

Das peculiaridades associadas à estrutura do polímero de coordenação $_\infty$[Tb(DPA)(HDPA)], pode-se destacar que a formação da rede de coordenação sem a presença de moléculas de água ligadas diretamente ao metal favorece as propriedades luminescentes do composto.

O elevado rendimento quântico observado para o $_\infty$[Tb(DPA)(HDPA)] poderia ser justificado por fatores estruturais associados à ausência de moléculas supressoras (H_2O) coordenadas ao metal e pela rígida estrutura que reduz os efeitos vibracionais do ligante. Além disso, o nível tripleto estimado para o ligante tende a favorecer o processo de transferência de energia, pois a posição privilegiada em relação ao nível emissor $^5D_4$ do íon Tb^{3+} inibiria o processo de retro-transferência entre esses estados.

MATERIAL SUPLEMENTAR

Os espectros de absorção na região do infravermelho e os dados cristalográficos dos $_\infty$[Gd(DPA)(HDPA)] estão disponíveis em http://quimicanova.sbq.org.br, na forma de arquivo PDF, com acesso livre.

REFERÊNCIAS

1. Grant, A. B.; Marc, A. K.; Robin, D. R. ; *J. Alloys Compd.* **2002**, *344*, 123.
2. Jung, S. S.; Dongmok, W.; Hyoyoung, L.; Sung, I. M. J.; Jinho, O.; Young, J. J.; Kimoon, K.; *Nature* **2000**, *404*, 982.
3. Lin, W.; *J. Solid State Chem.* **2005**, *178*, 2486.
4. Ward, D. M.; *Science* **2003**, *300*, 1104.
5. Garberoglio, G.; Skoulidas, A. I.; Johnson, K. J.; *J. Phys. Chem. B* **2005**, *109*, 13094.
6. Sudik, A. C.; Millward, A. R.; Ockwig, N. W.; Côté, A. P.; Kim, J.; Yaghi, O. M.; *J. Am. Chem. Soc.* **2005**, *127*, 7110.
7. Bettencourt-Dias, A.; *Inorg. Chem.* **2005**, *44*, 2734.
8. Eddaoudi, M.; Kim, J.; Rosi, N.; Vodak, D.; Wachter, J.; O'keeffe, M.; Yaghi, O. M.; *Science* **2002**, 469.
9. Lee, J.Y.; Li, J.; Jagiell, J.; *J. Solid State Chem.* **2005**, *178,* 2527.
10. Kuc, A.; Enyashin, A.; Seifert, G.; *J. Phys. Chem. B* **2007**, *111*, 8179.
11. Hermes, S.; Schröchrter, M. K.; Schimid, R.; Khodeir, L.; Muhler, M.; Tissler A.; Fischer R. W.; Fischer R. A.; *Angew. Chem., Int. Ed.* **2005**, *44*, 6237.
12. Zang, S.; Su, Y.; Li, Y.; Ni, Z.; Meng, Q.; *Inorg. Chem.* **2006**, *45*, 174.
13. Li, Z.; Zhu, G.; Guo, X.; Zhao, X.; Jin, Z.; Qiu, S.; *Inorg. Chem.* **2007**, *46*, 5174.
14. Cao, R.; Sun, D.; Liang, Y.; Hong, M.; Tatsumi, K.; Shi, Q.; *Inorg. Chem.* **2002**, *41*, 2087.
15. de Sá, G. F.; Malta, O. L.; de Mello Donegá, C.; Simas, A. M.; Longo, R. L.; Santa-Cruz, P. A.; da Silva Jr., E. F.; *Coord. Chem. Rev.* **2000**, *196*, 165.
16. Lenh, J. M.; *Angew. Chem., Int. Ed.* **1990**, *29*, 1304.
17. Zhao, B.; Chen, X. Y.; Cheng, P.; Liao, D. Z.; Yan, S. P.; Jiang, Z. H.; *J. Am. Chem Soc.* **2004**, *126*, 15394.
18. Bettencourt-Dias, A.; *Dalton Trans.* **2007**, *9*, 2229.
19. Ocaña J. A.; Barragán, F. J.; Callejón M.; *Talanta* **2004**, *63*, 691.
20. Yegorova, A.; Karasyov, A.; Duerkop, A.; Ukrainets, I.; Antonovich, V.; *Spectrochim. Acta, Part A* **2005**, *61*, 109.
21. Soukka, T.; Antonen, K.; Härmä, H.; Pelkkikangas, A. M.; Huhtinen, P.; Lövgren, T.; *Clin. Chim. Acta* **2003**, *328*, 45.
22. Soares-Santos, P. C. R.; Nogueira, H. I. S.; Paz, F. A. A.; Ferreira, R. A. S.; Carlos, L. D.; Klinowski, J., Trindade, T.; *J. Alloys Compd.* **2004**, *374*, 344.
23. Wang, F. Q.; Zheng, X. J.; Wan, Y. H.; Sun, C. Y.; Wang, Z. S.; Wang, K. Z.; Jin, L. P.; *Inorg. Chem.* **2007**, *46*, 2956.
24. Richardson, F. S.; *Chem. Rev.* **1982**, *83*, 541.

25. Zhao, B.; Yi, L.; Dai, Y.; Chen, X. Y.; Cheng, P.; Liao, D. Z.; Yan, S. P.; Jiang, Z. H.; *Inorg. Chem.* **2005**, *44*, 911.

26. Brayshaw, P. A.; Hall, A. K.; Harrison, W. T. A.; Harrowfield, J. M.; Pearce, D.; Shand, T. M.; Skelton, B. W.; Whitaker, C. R.; White, A. H.; *J. Eur. Inorg. Chem.* **2005**, 1127.

27. Rodrigues, M. O.; da Costa Junior, N. B.; de Simone, C. A.; Araújo, A. A. S.; Brito-Silva, A. M.; Paz, F. A. A.; de Mesquita, M. E.; Júnior, S. A.; Freire, R. O.; *J. Phys. Chem. B* **2008**, *112*, 4204.

28. Choppin, G. R.; Bünzli, J. C. G.; *Lanthanides Probes in Life, Chemical and Earth Sciences—Theory and Practice,* Elsevier: Amsterdan, 1989.

29. *Enraf-Nonius – Difractometer Kappa,* CCD – Nonius BV; Delft: The Netherlands, 1999.

30. Otwinowski, Z.; Minor, W. Em *Methods in Enzymology;* Carter Jr. C. W.; Sweet, R. M., eds.; Academic Press: New York, 1997, vol. 276, p. 307.

31. Enraf-Nonius; *Collect,* Nonius BV, Delft: The Netherlands, 1997-2000.

32. Sheldrick, G. M.; *SHELXS-97 Program for Crystal Structure Resolution,* Universidade de Göttingen, Alemanha, 1997.

33. Sheldrick, G. M.; *SHELXL-97 Program for Crystal Structure Resolution,* Universidade de Göttingen, Alemanha, 1997.

34. Malta, O. L.; Brito, H. F.; Menezes, J. F. S.; Gonçalves e Silva, F. R.; de Mello Donegá, C.; Alves Jr, S.; *Chem. Phys. Lett.* **1998**, *282*, 233.

35. Fernandes, A.; Jaud, J.; Dexpert-Ghys, J.; Brouca-Cabarrecq, C.; *Polyhedron* **2001**, *20*, 2385.

36. Tedeschi, C.; Picard, C.; Azéma, J.; Donnadieu, B.; Tisnès, P.; *New. J. Chem.* **2000***, 24,* 735.

37. Gosh, S. K.; Bharadwaj, P. K.; *Inorg. Chem.* **2005**, *44*, 3156.

38. Gosh, S. K.; Bharadwaj, P. K.; *Inorg. Chem.* **2003**, *42*, 8250.

39. Prasad, T. K.; Rajasekharan, M. V.; *Cryst. Growth Des.* **2006**, *6*, 488.

40. Gonzalez-Baró, A. C.; Castellano E. E.; Piro O. E.; Parajón-Costa B. S.; *Polyhedron* **2005**, *24*, 49.

41. Alves Junior, S.; de Almeida, F. V.; de Sá, G. F.; de Mello Donegá, C.; *J. Lumin.* **1997,** *72***,** 478.

42. Mesquita, M. E.; Júnior, S. A.; Oliveira, F. C.; Freire, R. O.; Júnior, N. B. C.; Sá, G. F.; *Inorg. Chem. Commun.* **2002**, *5*, 292.

43. Chrysochoos, J.; *J. Chem. Phys.* **1978**, *69*, 5545.

44. Latva, M.; Takalo, H.; Mukkala, V. L.; Matachescu, C.; Rodríguez-Ubis, J. C.; Kankare, J.; *J. Lumin.* **1997**, *75*, 149.

45. Lima, P. P.; Oscar, M. L.; Alves-Jr., S.; *Quim. Nova* **2005**, *28*, 805.

Pedro Henrique Viana de Carvalho[1]
Alysson Santos Barreto[1]
Marcelo O. Rodrigues[2]
Vanessa de Menezes Prata[1]
Péricles Barreto Alves[1]
Maria Eliane de Mesquita[1]
Severino Alves Júnior[2]
Sandro Navickiene[1]

[1]Departamento de Química,
 Universidade Federal de Sergipe,
 São Cristóvão, SE, Brazil
[2]Departamento de Química
 Fundamental, Universidade
 Federal de Pernambuco, Recife,
 PE, Brazil

Original Paper

Two-dimensional coordination polymer matrix for solid-phase extraction of pesticide residues from plant *Cordia salicifolia*

The 2D coordination polymer ($_\infty$[Gd(DPA)(HDPA)]) was tested for extraction of acephate, chlorpropham, pirimicarb, bifenthrin, tetradifon, and phosalone from the medicinal plant *Cordia salicifolia*, whose extracts are commercialized in Brazil as diuretic, appetite suppressant, and weight loss products, using GC/MS, SIM. Considering that there are no Brazilian regulations concerning maximum permissible pesticide residue concentrations in medicinal herbs, recovery experiments were carried out (seven replicates), at two arbitrary fortification levels (0.5 and 1.0 mg/kg), resulting in recoveries in range of 20 to 107.7% and SDRSDs were between 5.6 and 29.1% for $_\infty$[Gd(DPA)(HDPA)] sorbent. Detection and quantification limits for herb ranged from 0.10 to 0.15 mg/kg and from 0.15 to 0.25 mg/kg, respectively, for the different pesticides studied. The developed method is linear over the range assayed, 0.5–10.0 μg/mL, with correlation coefficients ranging from 0.9975 to 0.9986 for all pesticides. Comparison between $_\infty$[Gd(DPA)(HDPA)] sorbent and conventional sorbent (neutral alumina) showed similar performance of $_\infty$[Gd(DPA)(HDPA)] polymeric sorbent for three (bifenthrin, tetradifon, and phosalone) out of six pesticides tested.

1 Introduction

Coordination polymers, also known as metal-organic frameworks (MOFs), are a relatively new class of nanostructured materials that form an important interface between materials science and synthetic chemistry [1, 2]. In recent years, these compounds have received significant attention that can also be explained by interesting structure obtained by self-assembling metal ions with multifunctional ligands and interesting applications in strategic scientific and industrial fields [3].

Currently, the most of works about coordination polymers are focused on investigations of gas sorption, separation, and storage, catalysis as promising applications of these materials [4–7]. On other hand, the exploration of coordination polymers as pre-concentrators for the SPE has been few reported [8]. Our group has been interested in these materials because they can be tailored to selective sorption profile based on hydrophobic and hydrophilic properties, shape and size of porous. The materials normally used as preconcentrators do not have high enough sorption capacity or are not selective enough for specific analytes or they cause low or incomplete desorption of the analytes [9]. Thus, the co-ordination polymers could be regarded as interesting and versatile alternative as adsorbent materials used on detection of trace of the environment pollutants [10].

Medicinal plants are widely consumed as home remedies and raw materials for the pharmaceutical industries for the production of phytopharmaceuticals [11]. The herbs are usually prepared using natural and cultivated plants collected, dried and packaged without an effective hygienic, sanitary and residual control. Therefore, it is important to know the risk that their consumption supposes to health, since in the developing countries 65% of the population depends exclusively on the medicinal plants for basic cares of health [12–14]. On the other hand, the extraction procedure is a critical step in the determination of drugs, pollutants and naturally occurring substances in medicinal herbs [15–17]. In general, the determination of these compounds including

Correspondence: Professor Sandro Navickiene, Departamento de Química, Universidade Federal de Sergipe, Av. Marechal Rondon, s/n. Jardim Rosa Elze. Cep. 49100-000. São Cristóvão/SE. Brazil
E-mail: sandnavi@ufs.br
Fax: 0055 7921056651

pesticides in medicinal herb matrix is usually accomplished using chromatographic techniques and involves preliminary steps including sampling, extraction and clean-up [18]. Matrix solid-phase dispersion (MSPD) is an extraction method that provides a good alternative to traditional extraction techniques for chromatographic analysis [19–22]. MSPD can be carried out simultaneously with sample homogenization, extraction and clean-up and it requires only a small sample size and small amounts of solvent [23, 24]. It avoids the drawbacks generally associated with liquid–liquid extraction, such as the use of large volumes of solvent, the occurrence of troublesome emulsions, and slow speed [25–29]. Thus, MSPD is an analytical technique used for extraction of analytes from semi-solid and viscous samples. The principle of this technique is based on the use of the same bonded-phase solid supports as in SPE, which also are used as grinding material for producing the disruption of sample matrix. During this procedure, the bonded-phase support acts as an abrasive, and the sample disperses over the surface of the support. The classic methods used for sample disruption such as mincing, shredding, grinding, pulverizing, and pressuring are avoided in this procedure. The MSPD technique has many applications to the processing of samples of biological origin (animal tissues, plant materials, fats, *etc.*) [30–34]. The sample is placed in a mortar containing the sample and a bonded phase material. The mixture is then crushed with a pestle. During this operation, the bonded phase and its support serve several functions including a) is an abrasive that promotes mechanical disruption of the sample structure, b) assists in sample disruption and analysis of cell membranes similar to a solvent, and c) adsorbs the analytes or other compounds of interest from the sample. After this step, the material containing the sample and the solid sorbent are transferred into a SPE column. The selection of sorbent to be mixed with the sample depends on the nature of the material to be analyzed. Principles similar to those used for the selection in standard SPE are utilized in MSPD [35]. The literature describes chromatographic methods for the determination of pesticide residues in medicinal plants using classical sorbent material such as C_{18}-bonded silica [36]. During recent years, research on new materials for extraction, purification and separation processes of organic compounds in a wide polarity range has also been proposed by the growing interest for environmental preservation and human health protection.

In view of this, the aim of this study was evaluating the performance of coordination polymer $_\infty$[Gd(DPA)(HDPA)], as a new adsorbent material for matrix solid-phase dispersion for the multiclass analysis of pesticides in medicinal plant *C. salicifolia* Cham, which is commercialized in Brazil as diuretic, appetite suppressant, and weight loss products, using GC/MS.

2 Experimental

2.1 Chemicals and solvents

HPLC grade solvents, dichloromethane, ethyl acetate, cyclohexane, and chloroform, were purchased from Mallinckrodt Baker (Paris, KY, USA). Certified standards of acephate, chlorpropham, pirimicarb, bifenthrin, tetradifon, and phosalone were purchased from Dr. Ehrenstorfer (Augsburg, Germany). All standards were at least 97.0% pure. Analytical grade anhydrous sodium sulfate was supplied from Mallinckrodt Baker. C_{18}-bonded silica (50 μm) was obtained from Phenomenex (Torrance, CA, USA) and neutral alumina (70–290 mesh, activity I) from Macherey-Nagel (Düren, Germany). The lanthanide nitrate was obtained following the procedures previously reported [37]. Pyridine-2,6-dicarboxylic acid 99%, H_2DPA, was supplied from Sigma–Aldrich (St. Louis, MO, USA).

2.2 Pesticide standard solutions

Stock standard solutions of pesticides were prepared by exactly weighing and dissolving the corresponding compounds in dichloromethane at 500 μg/mL and stored at −18°C. These standard solutions were stable for a period of at least 2 months. The working standard solutions were prepared by diluting the stock solutions in dichloromethane as required. Matrix-matched standards were prepared at the same concentrations as those of calibration solutions by adding appropriate amounts of standards to the control matrix extract.

2.3 Synthesis of $_\infty$[Gd(DPA)(HDPA)]

A mixture of pyridine-2,6-dicarboxylic acid, H_2DPA, (0.7 mmol, 0.117 g), $Gd(NO_3)_3$ $6H_2O$ (0.35 mmol, 0.070 g), and H_2O (*ca.* 4 mL) was placed in a 8 mL Teflon-lined stainless autoclave at 160°C for 72 h. The final compound was obtained in a yield of *ca.* 60% (based on Gd) after washed with water, acetone and air-dried. Analytical Calculation for the $C_{14}H_7N_2O_8Gd$ (%): C – 34.42; H −1.44; N – 5.73. Found (%): C – 35.25; H – 1.32; N – 5.65. IR (cm^{-1}): 3455 (w), 3080 (m), 1740 (s), 1635 (s), 1605 (s), 1585 (s), 1455 (m), 1402 (w), 1300 (m), 1250 (m), 1130 (m), 1080 (m), 1020 (m), 940 (w), 765 (m), 725 (s), 654 (m), 584 (m), 523 (w), 411 (s).

2.4 Solid-phase characterization

Elemental analysis was performed on a CHNS-O analyzer Flash 1112 Series EA Thermo Finnigan. FT-IR spectra were recorded on KBr pellets (spectral range 4000–400 cm^{-1}) using a Bruker IFS 66, Fig. 1. The thermoanalytical curves were obtained in duplicate with a thermoba-
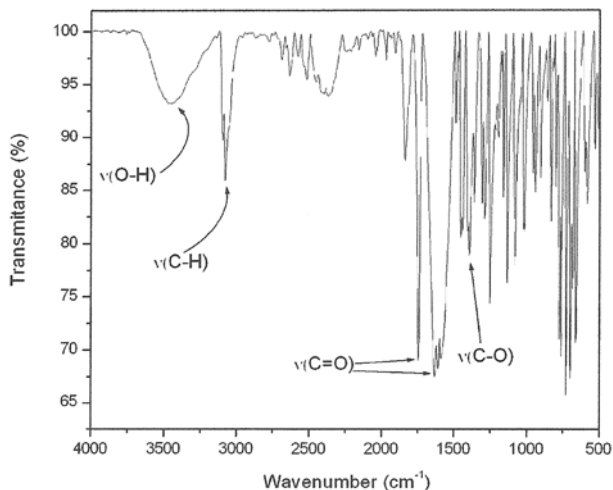
Figure 1. Infrared spectrum of ∞[Gd(DPA)(HDPA)].

lance model TGA 50 (Shimadzu, Japan) in 25–1200°C temperature range, using a platinum crucible with *ca.* 3.0 mg of sample, under dynamic nitrogen atmosphere (50 mL/min) and with a heating rate of 10°C/min, Fig. 2.

A suitable single-crystal of ∞[Gd(DPA)(HDPA)] (where H₂DPA stands for pyridine-2,6-dicarboxylic acid) was manually harvested from the crystallization vial and mounted on a glass fibre [38], which can show various coordination geometries using completely (DPA, di-2-pyridylamine) or partially (HDPA) deprotonated carboxylic groups. These ligands not only chelate to a metal ion, thus acting as a terminating ligand to prevent the formation of polymeric species, but also can form intermolecular hydrogen bonds through the noncoordinating amino groups, thus facilitating the possible formation of an extended hydrogen-bonded structure [39]. Data were collected at ambient temperature on a Nonius Kappa CCD area-detector diffractometer (Mo K$_\alpha$graphite-monochromated radiation, λ = 0.7107 Å) controlled by the Collect software package [40]. Images were processed using the software packages Denzo and Scalepack [41], and data were corrected for absorption by the empirical method implemented in SADABS. The structure was solved using the direct methods implemented in SHELXS-97 [42], which allowed the immediate location of the majority of the heavy atoms. All the remaining nonhydrogen atoms were directly located from difference Fourier maps calculated from successive full-matrix least squares refinement cycles on F^2 using SHELXL-97 [43].

2.5 GC/MS system and operating conditions

A Shimadzu system (Kyoto, Japan), consisting of a QP-5050*A* mass spectrometer equipped with a GC-17A gas chromatograph with a Shimadzu AOC 20i auto-injector and a split/splitless injector was used for the identifica-
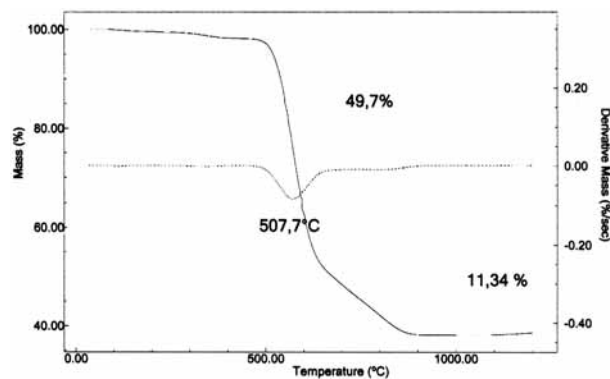
Figure 2. Thermogravimetric curve of ∞[Gd(DPA)(HDPA)].

tion and quantification of the pesticides studied. A fused-silica column DB-5MS (5% phenyl – 95% PDMS; 30 m × 0.25 mm id, 0.25 µm), supplied by J&W Scientific (Folsom, CA, USA), was employed, with helium (99.999% purity) as carrier gas at a flow-rate of 1.4 mL/min. The column temperature was programmed as follows: 60°C for 1 min, then directly to 300°C at 10°C/min and holding for 3 min. The solvent delay was 5 min. The injector port was maintained at 250°C, and 1 µL sample volumes were injected in splitless mode (0.7 min). The data were acquired and processed with a PC with Shimadzu class 5000 software. The total analysis time was 28 min and equilibration time 2 min.

The eluent from the GC column was transferred via a transfer line heated at 280°C, and fed into a 70 eV electron impact ionization source, also maintained at 280°C. The analysis was performed in the SIM mode. For the first acquisition window (5.0 to 10.0 min), the ions monitored were m/z 136, **142**, and 168 (acephate). For the second acquisition window (11.0 to 20.0 min), the ions monitored were m/z 154, **171** and 213 (chlorpropham), m/z 152, **166** and 238 (pirimicarb). For the third acquisition window (20.0 to 28.0 min), the ions monitored were m/z **165**, 181, and 322 (bifenthrin), m/z **227**, 356 and 362 (tetradifon), m/z 121, 257 and **367** (phosalone). Values of m/z in bold type correspond to the quantification ion for each analyte.

2.6 Sample preparation and fortification

Dried porangaba leaves (*C. salicifolia* Cham; Family Boraginaceae) samples used for method development were purchased in the bulk packages format from a local market located in the municipality of Aracaju, state of Sergipe, Brazil. No indication as regards the geographical origin of the plant samples was given in the labels. A representative portion of medicinal plant (100 g) was homogenized using a household blender, sieved (1–2 mm), and stored in jars away from light and moisture until used for analysis. Fortified samples were prepared by adding 500 µL of

a mixture of the standard solutions to 0.5 g of sample resulting in two final concentrations 0.5 and 1.0 mg/kg of pesticides in the sample. The fortified plant samples were left to stand for 30 min at room temperature to allow the solvent to evaporate before extraction. Seven replicates were analyzed at each fortification level. The extraction procedure was as described below.

2.7 Extraction procedure

An aliquot of dried and powdered medicinal plant (0.5 g) was placed into a glass mortar (*ca.* 50 mL) and 0.5 g of sorbent material (neutral alumina or $_\infty$[Gd(DPA)(HDPA)] polymer) was added. The medicinal plant was then gently blended into the sorbent material with a glass pestle, until a homogeneous mixture was obtained (*ca.* 1 min). The homogenized mixture was introduced into a 100×20 mm id polypropylene column, filled with 0.1 g of silanized glass wool at the base, followed by, in order, 1.0 g of anhydrous Na_2SO_4 and 0.5 g of C_{18}. A 30 mL portion of cyclohexane/dichloromethane (3:1, v/v) was added to the column and the sample was allowed to elute dropwise. Columns were placed on an 18-port vacuum manifold. The eluent was collected into a graduated conical tube and concentrated to a volume of 1 mL, using first a rotary vacuum evaporator (40°C), followed by a gentle flow of nitrogen. A 1 μL portion of the extract was then directly analyzed by GC/MS.

3 Results and discussion

3.1 Characterization of $_\infty$[Gd(DPA)(HDPA)]

The hydrothermal reaction propitiated to the isolation of a large amount of a single-crystalline phase composed by crystals exhibiting a parallelepipedic morphology. The compound containing only Gd^{3+} ion as metal center was formulated as $_\infty$[Gd(DPA)(HDPA)] on basis of single-crystal X-rays diffraction studies at ambient temperature (Table 1), TGA, and CHNS elemental. The compound $_\infty$[Gd(DPA)(HDPA)] consists of a 2-D layer structure. It is noteworthy to mention that the $_\infty$[Gd(DPA)(HDPA)] is isostructural to Ho^{3+} compound previously report by Fernandes *et al.* [44]. The thermal decomposition of $_\infty$[Gd(DPA)(HDPA)] occurs in two consecutive stages with weight losses of 49.7% and 11.3 respectively, remaining a residue of approximately 39% attributed to the formation of the stoichiometric amount of Gd_2O_3 (calculated residue 37.2%).

3.2 MSPD procedure

The type of the sorbent and the polarity of elution solvent are known to be key factors in MSPD, since they determine both the efficacy of the extraction and the

Table 1. Crystal data and structure refinement of $_\infty$[Gd(DPA)(HDPA)].

Identification code	[Gd(DPA)(HDPA)]
Empirical formula	$C_{14} H_7 N_2 O_8 Gd$
Formula weight	487.46
Temperature	293(2) K
Wavelength	0.71073 Å
Crystal system	monoclinic
Space group	$P2_1/c$
Unit cell dimensions	$a = 12.2790(4)$ Å, $\alpha = 90°$.
	$b = 8.3880(3)$ Å, $\beta = 02.411(2)°$.
	$c = 13.5380(3)$ Å, $\gamma = 90°$.
Volume	1361.78(7) $\mathring{A}^3$
Z	4
Density (calculated)	2.378 Mg/m^3
Absorption coefficient	4.924 mm^{-1}
F(000)	928
Crystal size	$0.224 \times 0.189 \times 0.18$ mm
Theta range for data collection	$2.88 - 27.49°$
Index ranges	$-15 \leq h \leq 12, -9 \leq k \leq 10,$
	$-17 \leq l \leq 17$
Reflections collected	7990
Independent reflections	8847/2841 [R(int) = 0.0284]
Completeness to theta = 25.35°	91.2%
Absorption correction	Semi-empirical from equivalents
Max and min transmission	0.2284 and 0.1936
Refinement method	Full-matrix least-squares on F2
Data/restraints/parameters	2841/0/226
Goodness-of-fit on F2	1.123
Final R indices [I > 2sigma(I)]	$R_1 = 0.0210$, $wR_2 = 0.0526$
R indices (all data)	$R_1 = 0.0215$, $wR_2 = 0.0528$
Largest diff. peak and hole	0.644 e $- 0.981$ e $\cdot$ $\mathring{A}^{-3}$

purity of the final extracts [45–51]. Therefore, in this study, a new material, $_\infty$[Gd(DPA)(HDPA)] polymer, for matrix solid-phase dispersion was synthesized, characterized, and the performance of the $_\infty$[Gd(DPA)(HDPA)] polymer as sorbent material was compared with neutral alumina, which was used as extracting phase to carry out the multiclass analysis of the pesticides (acephate, chlorpropham, pirimicarb, bifenthrin, tetradifon, and phosalone) in medicinal plant *C. salicifolia* in our previous developed and validated MSPD procedure [52]. On the other hand, considering that there are no Brazilian regulations concerning maximum permissible pesticide residue concentrations in medicinal herbs, recovery experiments were carried out, in seven replicates, at two arbitrary fortification levels (0.5 and 1.0 mg/kg) to the medicinal plant matrix. The recoveries from fortification studies of six pesticides were evaluated by GC/MS (SIM) based on external calibration using medicinal herb-matched standards. Average recoveries ranged from 62.9 to 129.9%, with RSD values of 6.3 to 26% using neutral alumina as sorbent, and 20 to 107.7%, with RSD values of 5.7 to 29.1%, using $_\infty$[Gd(DPA)(HDPA)] polymer as sorbent.
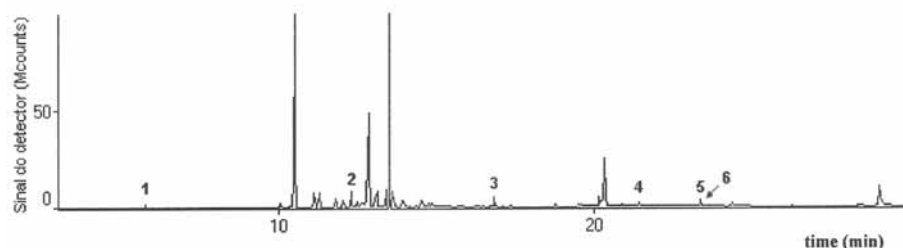
Figure 3. GC/MS (SIM mode) chromatogram of a typical porangaba (*C. salicifolia*) extract fortified at a concentration level of 0.5 µg/g, using 0.5 g of porangaba + 0.5 g of ∞[Gd(DPA)(HDPA)] polymer + 1.0 g co-sorbent and cyclohexane/dichloromethane (3:1, v/v, 30 mL). The numbered peaks are as follows: 1, acephate; 2, chlorpropham; 3, pirimicarb; 4, bifenthrin; 5, tetradifon; 6, phosalone. See Experimental for details on GC/MS system and operating conditions.

Table 2. Average% recoveries (%RSD) of fortified pesticides in medicinal plant from MSPD method with GC/MS analysis.

Pesticide	Fortification level (µg/g)	Mean recovery* (%)	RSD (%)	Mean recovery* (%)	RSD (%)
				sorbent/co-sorbent	
		alumina/C_{18}		∞[Gd(DPA)(HDPA)]/C_{18}	
acephate	0.5	85.7	19.7	30.0	20.0
	1.0	62.9	15.8	20.0	9.0
chlorpropham	0.5	115.8	10.6	31.0	9.0
	1.0	129.9	11.3	47.3	20.0
pirimicarb	0.5	117.6	12.4	47.0	5.6
	1.0	81.3	7.7	51.3	10.8
bifenthrin	0.5	94.6	26.0	107.7	23.1
	1.0	84.1	6.3	80.0	5.7
tetradifon	0.5	108.5	24.1	106.2	26.4
	1.0	82.5	11.0	95.1	29.1
phosalone	0.5	105.1	19.7	73.4	20.1
	1.0	78.5	15.9	46.0	10.6

* $n = 7$.

Considering the acceptability criteria for recovery in the range of 70–130%, acephate, chlorpropham, pirimicarb, bifenthrin, tetradifon, and phosalone presented lower to excellent recoveries for medicinal herb sample. Comparison of ∞[Gd(DPA)(HDPA)] polymer as sorbent with the commercially available neutral alumina showed ∞[Gd(DPA)(HDPA)] polymer as a similar extracting phase for three of the six pesticides under investigation. Recoveries of acephate, chlorpropham, and pirimicarb presented lower recovery values for ∞[Gd(DPA)(HDPA)] polymer in comparison to the neutral alumina solid-phase. Figure 3 shows a chromatogram of medicinal herb sample spiked with the six pesticides at concentration of 0.50 mg/kg, for which the recovery was 30–107.7%. Concentrations were calculated by comparing peak areas from extracted ion current profiles with those obtained from matrix-matched standards. Table 2 presents recoveries of the six pesticides at two concentration levels for the medicinal herb.

Robustness may be defined as the measure of the ability of an analytical method to remain unaffected by small but deliberate variations in method parameters, providing an indication of its reliability during normal usage. Robustness testing is a systematic process of varying a parameter and measuring the effect on the method by monitoring system suitability and/or the analysis of samples [53]. In relation to the method, it should be noticed that in none of the medicinal herb samples tested has the detection of the pesticides been excessively interfered with by matrix peaks. With the developed method, nearly 101 recovery tests with these six pesticides in different herb *C. salicifolia* samples were conducted. The overall recovery was found to be 61% including the studied concentration levels. Despite the number of different samples with varying origin which have been tested, the functioning of the instrument was fully adequate. The routine clean up of the insert and/or ion source box has been shown to be sufficient to maintain a tidy performance. Furthermore, considering different medicinal herbs, the comparison between the extraction efficiency of proposed MSPD procedure with that of the Yariwake *et al.* [54] demonstrates that the average recov-

ery value for 0.5 mg/kg (*n* = 7) was 106.2% for tetradifon, which was similar to that obtained by the authors in *Passiflora alata* Dryander, 101.4%. However, the concentration level of this last method was 0.3 mg/kg (*n* = 3), using neutral alumina as dispersant material.

On the other hand, pesticides are found in medicinal herbs at trace levels, mixed with other compounds of high concentrations. Due to the large number of active ingredients, trace analysis of these substances require techniques with the detection capability of greatest number of compounds possible and with the fewest number of extraction and clean-up steps [55]. Traditionally, the initial extraction of pesticide residues from medicinal herbs is performed by solvent extraction such as the European Pharmacopoeia procedures [55], which are costly, time-consuming and require larger samples and greater volumes of hazardous solvents. However, low sample throughput due to manual concentration steps and large amounts of both sample and high purity organic solvent limits the application of this method [56]. Analytical methods employing smaller amounts of sample and extracting solvent would be preferred, such as the procedure based on matrix SPE described herein, which combines extraction, concentration and sample introduction steps, consequently it has high sample throughput with minimum effort and time.

The linearity of a method is a measure of range within which detector response is directly proportional to the concentration of analyte in standard solutions or samples. Linearities for all compounds were determined using blank medicinal herb samples fortified at concentration levels ranging from 0.05 to 10.0 μg/mL. The slope and intercept values, together with their SDs, were determined using regression analyses. Linear regression coefficients for all pesticides ranged from 0.9975 to 0.9986. These results indicated the correct linearity of the calibration curves at the respective spiking levels. The limits of detection (LOD) for the pesticides studied were calculated considering the SD of the analytical noise (a value of seven times the SD of the blank) and the slope of the regression line, and ranged from 0.10 to 0.15 mg/kg. The limits of quantification (LOQ) were determined as the lowest concentration giving a response of ten times the average of the baseline noise, calculated using seven unfortified samples. The LOQ values for these compounds ranged from 0.15 to 0.25 mg/kg [57]. The repeatability of the method was performed by successive six time analyses of 5.0 μg/mL of pesticide standard solution, and presented as the RSDs, which was in the range of 1.8–3.2%.

Finally, a focus of our work has been to explore the scientific and technological feasibility of the coordination polymers application. Economical aspects have not been in the foreground, but they are clearly a consequence. Nevertheless, the time of preparation of an aliquot of 0.5 g of this polymer was 36 h at a cost of US$ 4.20.

3.3 Application of the method to real samples

The MSPD procedure developed was applied to the determination of pesticides in medicinal plant *C. salicifolia*. Four different samples of this medicinal plant, obtained from local markets in the city of Aracaju (Brazil), and originating from conventional agriculture, were analyzed using this procedure. No pesticide residues, at concentrations above the detection limit, were found in these samples.

4 Conclusions

New material ($_\infty$[Gd(DPA)(HDPA)] polymer) for matrix solid-phase dispersion was developed, characterized and tested in the multi-class analysis of pesticides in medicinal herb. Results have show that the $_\infty$[Gd(DPA)(HDPA)] polymer can be successfully applied for analysis of bifenthrin, tetradifon and phosalone in medicinal herb Cordia salicifolia. Performance of the $_\infty$[Gd(DPA)(HDPA)] polymer was lower than one observed for neutral alumina for acephate, chlorpropham, and pirimicarb. The new solid phase may be useful as a screening protocol to identify pesticides in medicinal herb by industrial pharmaceutical and official regulatory laboratories.

5 References

[1] Rao, C. N. R., Natarajan, S., Vaidhyanathan, R., *Angew. Chem. Int. Ed.* 2004, *43*, 1466–1496.

[2] Rowsell, J. L. C., Yaghi, O. M., *Microp. Mesop. Mater.* 2004, *73*, 3–14.

[3] Mueller, U., Schubert, M., Teich, F., Puetter, H., Schierle-Arndt, K., Pastré, J., *J. Mater. Chem.* 2006, *16*, 626–636.

[4] Chen, B., Ma, S., Hurtado, E. J., Lobkovsky, E. B., Zhou, H. C., *Inorg. Chem.* 2007, *46*, 8490–8492.

[5] Bastin, L., Bárcia, P. S., Hurtado, E. J., Silva, J. A. C., Rodrigues, A. E., Chen, B., *J. Phys. Chem. C* 2008, *112*, 1575–1581.

[6] Szeto, K. C., Prestipino, C., Lambert, C., Zecchina, A., Bordiga, S., Bjørgen, M., Tilset, M., Lillerud, K. P., *Chem. Mater.* 2007, *19*, 211–220.

[7] Dubbeldan, D., Galvin, C. J., Walton, K. S., Ellis, D. E., Snurr, R. Q., *J. Am. Chem. Soc.* 2008, *130*, 10884–10885.

[8] Zhuo, Y. Y., Yan, X. P., Kin, K. N., Wang, S. W., Liu, M. G., *J. Chromatogr. A* 2006, *1116*, 172–178.

[9] Masqué, N., Marcé, R. M., Borrull, F., *Trends Anal. Chem.* 1998, *17*, 384–394.

[10] Ni, Z., Jerrell, J. P., Cadwallader, K. R., Masel, R. I., *Anal. Chem.* 2007, *79*, 1290–1293.

[11] Chang, K., *Chemosphere* 2003, *52*, 1361–1371.

[12] Zuin, V. G., Vilegas, J. H. Y., *Phytotherapy Research* 2000, *14*, 73–88.

[13] Tadeo, J. L., *Analysis of Pesticides in Food and Environmental Samples*, CRC Press, p. 10–12, 2008.

[14] Menghini, L., Epifano, F., Leporini, L., Pagotti, R., Tirillini, B., *J. Med. Food* 2008, *1*, 193–194.

[15] Tang, F., Yue, Y., Hua, R., Cão, H., *J. AOAC Int*. 2006, *89*, 489 – 502.

[16] Tang, F., Yue, Y., Hua, R., Ge, S., Tang, J., *J. AOAC Int*. 2005, *88*, 720 – 728.

[17] Liang, Y. Z., Xie, P., Chang, K., *J. Chromatogr. B* 2004, *812*, 53 – 70.

[18] Lino, C. M., Guarda, L. M. C., Silveira, M. I. N., *J. AOAC Int*. 1999, *82*, 55 – 60.

[19] Wu, J., Li, L., Zou, Y., *J. AOAC Int*. 2005, *88*, 1261 – 1264.

[20] Romanik, G., Gilgenst, E., Przyjazny, A., Kaminski, M., *J. Biochem. Biophys Methods* 2007, *70*, 253 – 261.

[21] Jeong, M. L., Zahn, M., Trinh, T., Brooke, F. A., Ma, W. W., *J. AOAC Int*. 2008, *91*, 630 – 636.

[22] Zuin, V. G., Yariwake, J. H., Bicchi, C., *J. Chromatogr. A* 2003, *985*, 159 – 166.

[23] Sánchez-Brunete, C., Miguel, E., Tadeo, J. L., *Talanta* 2008, *74*, 1211 – 1217.

[24] Bogialli, S., Di Corcia, A., *J. Biochem. Biophys. Methods* 2007, *70*, 163 – 179.

[25] Santos, T. F. S., Aquino, A., Dórea, H. S., Navickiene, S., *Anal. Bioanal. Chem*. 2008, *390*, 1425 – 1430.

[26] Silva, M. G. D., Aquino, A., Dórea, H. S., Navickiene, S., *Talanta* 2008, *76*, 680 – 684.

[27] Barker, S. A., *J. Chromatogr. A* 2000, *885*, 115 – 127.

[28] Barker, S. A., *J. Chromatogr. A* 2000, *880*, 63 – 68.

[29] Barker, S. A., *J. Biochem. Biophys. Methods* 2007, *70*, 151 – 162.

[30] García de Llasera, M. P., Reyes-Reyes, M. L., *Food Chemistry* 2009, *114*, 1510 – 1516.

[31] Frenich, A. G., Bolaños, P. P., Vidal, J. L. M., *J. Chromatogr. A* 2007, *1153*, 194 – 202.

[32] Hercegová, A., Dömötörová, M., Kruzlicová, D., Matisová, E., *J. Sep. Sci.* 2006, *29*, 1102 – 1109.

[33] Abhisash, P. C., Jamil, S., Singh, N., *J. Chromatogr. A* 2007, *1176*, 43 – 47.

[34] Bliesner, D. M., *Validating Chromatographic Methods-A Practical Guide*, Wiley, New Jersey, p. 1 – 7, 2006.

[35] Poole, C. F., *J. Chromatogr. A* 2007, *1158*, 241 – 250.

[36] Moldoveanu, S. C., Daniel, V., *Sample Preparation in Chromatography*, Elsevier Science, Amsterdam, p. 394 – 396, 2002.

[37] Choppin, G. R., Bünzli, J. C. G., *Lanthanides Probes in Life, Chemical and Earth Sciences-Theory and Practice*, Elsevier, Amsterdam, p. 219, 1989.

[38] Kottke, T., Stalke, D., *J. App. Cryst*. 1993, *26*, 615 – 619.

[39] Zhang, Y., Wang, S., Enright, G. D., Breeze, S. R., *J. Am. Chem. Soc*. 1998, *120*, 9398 – 9399.

[40] Hooft, R., Collect: Data Collection Software, Delft, The Netherlands, Nonius B. V. 1998.

[41] Otwinowski, Z., Minor, W., In *Methods in Enzymology*, C. W. Carter Jr., R. M. Sweet, Eds. Academic Press: New York, 1997; Vol. 276, p. 307.

[42] Sheldrick, G. M., SADABS v.2.01, Bruker/Siemens Area Detector Absorption Correction Program 1998, Bruker AXS, Madison, Wisconsin, USA.

[43] Sheldrick, G. M., *SHELXS-97*, Program for Crystal Structure Solution, University of Göttingen 1997.

[44] Fernandes, A., Jaud, J., Dexpert-Ghys, J., Brouca-Cabarrecq, C., *Polyhedron* 2001, *20*, 2385 – 2391.

[45] Moral, A., Sicilia, M. D., Rubio, S., Pérz-Bendito, D., *Anal. Chim. Acta* 2006, *569*, 132 – 138.

[46] Tamayo, F. G., Casillas, J. L., Martin-Esteban, A., *J. Chromatogr. A* 2005, *1069*, 173 – 181.

[47] Abad, F. C., Winck, P. R., Benvenutti, E. V., Peralba, M. C. R., Caramão, E. B., Zini, C. A., *J. Sep. Sci.* 2007, *30*, 2109 – 2116.

[48] Schirmer, C., Meisel, H., *J. Chromatogr. A* 2006, *1132*, 325 – 328.

[49] Melo, L. F. C., Collins, C. H., Jardim, I. C. S., *J. Chromatogr. A* 2004, *1032*, 51 – 58.

[50] Hajšlová, J., Zrostlíková, J., *J. Chromatogr. A* 2003, *1000*, 181 – 197.

[51] Lehotay, S. J., Mastovska, K., Yun, S. J., *J. AOAC Int*. 2005, *88*, 630 – 638.

[52] Carvalho, P. H. V., Prata, V. M., Alves, P. B., Navickiene, S., *J. AOAC Int*. 2009, in press.

[53] Boyd, R. K., Basic, C., Bethem, R. A., *Trace Quantitative Analysis by Mass Spectrometry*, Wiley, Sussex, p. 533 – 535, 2008.

[54] Zuin, V. G., Yariwake, J. H., Lanças, F. M., *J. Braz. Chem. Soc.* 2003, *14*, 304 – 309.

[55] *European Pharmacopoeia*, Conseil de l'Europe: Strasbourg, p. 122, 1997.

[56] Huie, C. W., *Anal. Bioanal. Chem*. 2002, *373*, 23 – 30.

[57] The European Commission, Quality Control Procedures for Pesticide Residues Analysis, SANCO no 10232/2006, Brussels, p. 1 – 25, 2006.

Volatile Constituents and Antibacterial Activity From Seeds of *Bowdichia virgilioides* Kunt

Marcelo O. Rodrigues, Péricles B. Alves,* Paulo C. L. Nogueira, Samísia M. F. Machado and Valéria R. S. Moraes,

METABIO (Grupo de Pesquisa em Metabólitos Secundários Bioativos), Departamento de Química, Universidade Federal de Sergipe, 49100-000, São Cristovão, SE, Brazil

Adauto de S. Ribeiro,

LEEP (Laboratório de Estudos Ecológicos e Paleoambientais), Departamento de Biologia, Universidade Federal de Sergipe, 49100-000, São Cristovão, SE, Brazil

Edisleide S. Silva and José Gerson R. Feitosa,

Departamento de Morfologia, Universidade Federal de Sergipe, 49100-000, São Cristovão, SE, Brazil

Abstract

The essential oil from seeds of *Bowdichia virgilioides* Kunt (Fabaceae) growing in Brazil was obtained by hydrodistillation and analyzed by GC-FID and GC/MS. This analysis resulted in the identification of 17 components. The main constituents of the essential oil were β-elemene (6.9%), β-caryophyllene (44.1%), germacrene-D (7.9%), bicyclogermacrene (6.4%) and caryophyllene oxide (8.9%). The oil was tested for its antimicrobial activity against seven bacteria using the standard gel diffusion method.

Introduction

Bowdichia virgilioides Kunt (Fabaceae) is a tree commonly known in Brazil as "sucupira." The tallest evergreen tree in the savannas, usually between 4–10 m in height, with a legume fruit 4–7.5 cm long, 10–15 mm wide, flat, very light (0.08–0.11 g) and wind dispersed. Seed size is 5–6 mm and average weight is 0.02 g (1).

Bowdichia vigilioides seeds are used in Brazilian folk medicine to treat rheumatism, arthritis, skin diseases, blood purification, diabetes and malaria (2–6). Several phytochemical studies of this species disclosed the presence of alkaloids (4,7–9), flavonoids (3,10–12), benzofuranoids (11,13) and triterpenoids (13–15). In previous works, the essential oil from the fruits of *B. virgilioides* showed a high percentage of farnesol, geraniol and β-caryophyllene (16), while Arriaga et al. (17) reported the presence of 4-ethyl-2-methoxyphenol (11%), 2-tridecanone (54.6%) and 2-pentadecanone (9 %) as major compounds in the oil of the roots harvested from Ceará state, Brazil. The aim of this work was to analyze the chemical composition of the essential oil from seeds of *B. virgilioides* and evaluate its antibacterial activity against seven microorganisms. To the best

of our knowledge, there are no previous reports on *B. virgilioids* volatile composition from seeds and its antibacterial activity.

Experimental

Plant material: The seeds were collected from Sergipe state, Northeastern Brazil. The voucher specimen #ESA 07215 has been deposited in the Herbarium of the Department of Biology, Federal University of Sergipe, Brazil.

Isolation of the essential oil: The oil from dried seeds was obtained by hydrodistillation for 3 h using a Clevenger–type apparatus. The oil was extracted from the distillation water with Et_2O, dried over anhydrous sodium sulfate, filtered, and reduced the *ca*. 0.5 mL at room temperature under reduced pressure on a rotatory evaporator. The oil was kept at -4°C until GC analysis.

Gas chromatography: GC analysis was carried out using a Shimadzu model 17A gas chromatograph, fitted with an FID (supplied with air and hydrogen of high purity) and split inlet (split ratio 1:100). The system was equipped with a J&W Scientific DB-5MS fused silica capillary column (30 m x 0.25 mm x 0.25 μm); column temperatures were programmed from

60–200°C at 4°C/min, then raised to 280°C at 15°C/min. GC injector and detector temperatures were 250°C and 280°C, respectively; He was used as the carrier gas at a flow rate of 2 mL/min. The percentage composition of each component was determined from the area of the component divided by the total area of all components isolated under these conditions.

Gas chromatography/mass spectrometry: GC/MS analysis was performed in a Shimadzu model QP5050A system equipped with J&W Scientific DB-5MS fused silica capillary column (30 m x 0.25 mm, 0.25 μm film thickness). The oil (0.5 μL) was injected using the split injection method (split ratio 1:100). The column temperature was initially 50°C, then raised to 200°C at a rate of 4°C/min, held at 200°C for 5 min, and then heated to 280°C at 20°C/min. Helium was used as the carrier gas at a flow rate of 1.2 mL/min. Ionization potential was 70eV; scanning speed was 0.84 scan/s from m/z 40-550.

Identification procedure: The oil was analyzed by gas chromatography (GC) and gas chromatography/mass spectrometry (GC/MS). The constituents were identified by their retention indices as well as by computerized matching of the acquired mass spectra with those stored in the NIST 21 and NIST107 mass spectral library of the GC/MS data system, and other published mass spectra (18). The retention indices were obtained by co-injection of the oil sample with a C8-C19 linear hydrocarbons mixture according to Van den Dool and Kratz (19) under the same operating conditions. The percentage of the oil components (Table I) was computed from GC (FID) peak areas without correction factors.

Antibacterial bioassay: Disc diffusion method was employed for the determination of antibacterial activities of the oil (20). For the bioassays, four Gram-positive bacteria (*Bacillus subtillis* ATCC6633, *Bacillus bulgaricus* ATCC11842, *Enterococcus faecalis* ATCC4883 and *Staphylococcus aureus* ATCC29737) and three Gram-negative bacteria (*Pseudomonas aeruginosa* ATCC19424, *Salmonella enteritidis* ATCC13076 and *Escherichia coli* ATCC10536) were used. Each microorganism had been previously suspended in physiological saline solution 0.9% w/v. A suspension of the tested microorganism (0.1 mL of 108 cells/μL) was spread on the solid media plates. Six millimeter diameter wells were punched into the agar and filled with 20 μL of the oil solution at a concentration of 20 mg/mL in dimethylsulphoxide (DMSO) and distilled sterile water 1:1. Pure DMSO and standard antibiotic of streptomycin sulfate 1 mg/mL in physiological saline solution were individually used as negative and positive controls for bacteria, respectively. These plates, after staying at 4°C for 2 h, were incubated at 37°C for 24 h. The antimicrobial activity was evaluated by measuring the inhibition-zone diameter observed in millimeters. All the tests were performed in triplicate and repeated twice.

Results and Discussion

The oil isolated by hydrodistillation from the seeds of *Bowdichia vigilioides* Kunt was found to be yellow liquid at a yield of 2.2% v/w, based on dry weight. As shown in Table I, 17 components were identified in the seed oil representing 95.8 % of the oil composition. The main components of the oil were β-elemene (6.9%), β-caryophyllene (44.1%), germacrene D (7.9%), bicyclogermacrene (6.4%) and β-caryophyllene

oxide (8.9%). Thus, the results showed that the seed oil of *B. virgiloides* was characterized by the presence of large amounts of sesquiterpene hydrocarbons (82.5%) and oxygen containing sequiterpenes (13.2%).

As expected, the chemical composition of the seed oil showed both qualitative and quantitative differences when compared to other plant parts. Thus, farnesol, geraniol and β-caryophyllene predominated in the oil from fruits (16), while 4-ethyl-2-methoxyphenol, 2-tridecanone and 2-pentadecanone were major components from the root oil (17).

The results of the antibacterial activity of the seed oil of *B. virgilioides* are summarized in Table II. The oil showed activity against Gram-positive *Bacillus subtilis*, *Bacillus bulgaricus*, *Enterococcus faecalis* and *Staphylococcus aureus*. However, the oil had low activity against Gram-negative *Pseudomonas aeruginosa*, *Salmonella enteretidis* and *Escherichia coli*. Recently, Almeida et al. (21) reported the weak antimicrobial activity of the leaf oil of *B. virgilioides*. However, to our knowledge, this is the first report on the chemical composition and antibacterial activity of the seed oil of this species.

Table I. The chemical constituents of the seed oil of *Bowdichia vigilioides* Kunt

Compounds[a]	RI[b]	Peak area (%)
α-cubebene	1352	0.4
α-copaene	1378	5.8
β-cubebene	1393	3.0
β-elemene	1394	6.9
β-caryophyllene	1422	44.1
α–humulene	1456	4.6
allo-aromadendrene	1463	2.0
γ-muurolene	1478	0.3
germacrene D	1483	7.9
viridiflorene	1491	0.3
bicyclogermacrene	1498	6.4
α-muurolene	1502	0.3
germacrene A	1507	0.4
δ-cadinene	1525	0.2
spathulenol	1580	4.1
caryophyllene oxide	1585	8.9
α-cadinol	1656	0.2
Total		95.8

[a] Compounds listed in order of elution from a J&W Scientific DB-5MS; [b] Retention index.

Table II. Halos diameter (mm) of the evaluation of the seed oil of *Bowdichia vigilioides* against bacteria

| Bacteria	Diameter of inhibition (mm)	
	EO	ST
Gram-positive		
Bacillus subtilis	28.3	28.6
Bacillus bulgaricus	33.3	36.0
Enterococcus faecalis	32.5	25.0
Staphylococcus aureus	11.3	10.0
Gram-negative		
Pseudomonas aeruginosa	-	35.5
Salmonella enteritidis	-	22.0
Escherichia coli	-	18.0

EO = Essential oil from the seed of *B. virgilioids* (20 mg/mL); ST = Standard (Streptomycin sulfate – positive control).

References

1. C. Garcia-Núñez, A. Azócar and J.F. Silva, *Seed Production and Soil Seed Bank in Three Evergreen Wood Species From a Neotropical Savanna*. J. Trop. Ecol., **17**, 563-576 (2001)

2. M.P. Correia, *Dicionário das Plantas Úteis do Brasil e das Exóticas Cultivadas*. Vol. 6: 149. Ministério da Agricultura, Rio de Janeiro, Brazil (1984).

3. L.S.M. Velozo, B.P. da Silva, R.R. Bernardo and J.P. Parente, *Odoratin 7-O-β-D-Glucopyranoside From* Bowdichia virgiloides. Phytochemistry, **52**, 1473-1477 (1999).

4. J.M. Barbosa-Filho, J.R.G.S, Almeida, V.C.O. Costa, E.V.L. Da-Cunha, M.S. Silva and R. Braz-Filho, *Bowdichine, a New Diaza-Adamantane Alkaloid From* Bowdichia virgilioides. J. Asian Nat. Prod. Res. **6(1)**, 11-17 (2004).

5. E. Deharo, G. Bourdy, C. Quenevo, V. Muñoz, G. Ruiz and M. Sauvian, *A Search for Natural Bioactive Compounds in Bolívia Through a Multidisciplinary Approach. Part V. Evaluation of the Antimalarial Activity of Plants Used by the Tacana Indians*. J. Ethnopharmacol, **77**, 91-98 (2001).

6. R. Braga, *Plantas do Nordeste Especialmente do Ceará. Imprensa Oficial*. Fortaleza, Ceará, Brazil (1960).

7. R. Torrenegra, P. Bauereiss and H. Achenbach, *Homoormosanine-type Alkaloids From* Bowdichia virgiloides. Phytochemistry, **28**, 2219-2221 (1989).

8. H. Achenbach, P. Bauerreiss and R. Torrenegra, *New Highly Cyclized Quinolizidine Alkaloids From* Bowdichia-virgiloides. Arch. Pharm., **321**, 675-675 (1988).

9. G.R Torrenegra, R.S. Escarria, P. Bauereiss and H. Achenbach, *Homoormosanine, the Major Alkaloid of the Bark from* Bowdichia virgiloides. Planta Med., **49**, 276-277 (1985).

10. L.S.M. Velozo, B.P. Da Silva and J.P. Parente, *Constituents From the Roots of* Bowdichia virgilioides. Fitoterapia, **70**, 532-535 (1999).

11. D.B.F. Juck, L.C. De Resende, J.P. David, L.P. De Queiroz and J.M. David, *Two New Isoflavonoides From* Bowdichia virgilioides. Nat. Prod. Res., **20**, 27-30 (2006).

12. A.M.C. Arriaga, G.A. Gomes and R. Braz-Filho, *Constituents of* Bowdichia virgilioides. Fitoterapia, **71**, 211-212 (2000).

13. F.N. Melo, V.R. Navarro, M.S. Da Silva, E.V.L. Da-Cunha, J.M. Barbosa-Filho and R. Braz-Filho, *Bowdenol, a New 2,3-Dihydrobenzofuran Constituent From* Bowdichia virgilioides. Nat. Prod. Lett., **15**, 261-266 (2001).

14. C.P. Cordero, C.J. Gómez-González, C.J. Leon-Acosta, S.J. Morantes-Medina and F.A. Aristizabal, *Cytotoxic Activity of Five Compounds Isolated From Colombian Plants*. Fitoterapia, **75**, 225-227 (2004).

15. A.J. Calle, A.R. Umana and E. Moreno, *Isolation of Lupeol From the Bark of* Bowdichia virgilioides. HBK. Rev. Colombiana Cienc. Quim.-Farm., **4**, 93-94, (1983).

16. J. Jorge-Neto, *Pharmacognostic Study of Essential Oil of Sucupira,* Bowdichia virgilioides. Rev. Fac. Farm. Odontol. Araraquara, **4**, 203-204 (1970).

17. A.M.C. Arriaga, M.I.L. Machado, G.A. Gomes and A.A. Craveiro, *Volatile Constituents From Roots of* Bowdichia virgilioides *Kunt*. J. Essent. Oil Res., **10**, 205-206 (1998).

18. R.P. Adams, *Identification of Essential Oil Components by Gas Chromatography/Quadrupole Mass Spectroscopy*. Allured Publ. Corp., Carol Stream, IL (2001).

19. H. Van den Dool and P.D.J. Kratz, *A Generalization of the Retention Index System Including Linear Temperature Programmed Gas-Liquid Partition Chromatography*. J. Chromatogr, **11**, 463-471 (1963).

20. NCCLS, *National Committee for Clinical Laboratory Standards Performance Standards for Antimicrobial Disk and Dilution Susceptibility Tests for Bacteria Isolated from Animals; Tentative Standards*. Waine, NCCLS, Document M31-T, p. 64 (1997).

21. J.R.G.S. Almeida, R.N. Silva Filho, X.P. Nunes, C.S. Dias, F.O. Pereira and E.O. Lima, *Antimicrobial Activity of the Essential Oil of* Bowdichia virgilioides *Kunt*. Rev. Bras. Farmacogn., **16** (supl.), 638-641 (2006).
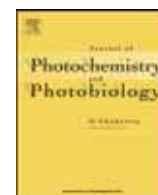
Highly luminescent di-ureasil hybrid doped with a Eu(III) complex including dipicolinate ligands

Maria E. Mesquita [a,c], S.S. Nobre [b], M. Fernandes [c], R.A.S. Ferreira [b], Sílvia C.G. Santos [a],
Marcelo O. Rodrigues [d], L.D. Carlos [b,**], V. de Zea Bermudez [c,*]

[a] Department of Chemistry, UFS, 49100-000 São Cristóvão, SE, Brazil
[b] Department of Physics, CICECO, University of Aveiro, 3810-193 Aveiro, Portugal
[c] Department of Chemistry, CQ-VR, University of Trás-os-Montes e Alto Douro, 5001-801 Vila Real, Portugal
[d] Departamento de Química Fundamental, UFPE, 50590-470 Recife, PE, Brazil

ABSTRACT

A short chain di-urea cross-linked poly(oxyethylene) (POE)/siloxane hybrid host (di-ureasil), designated as d-U(600), was doped with the $Na_3[Eu(dipic)_s] \cdot xH_2O$ (where $dipic^{2-}$ is the dipicolinate ion) complex. The resulting material is non-porous, semi-crystalline and thermally stable up to 145 °C. Because of the presence of the bulky $dipic^{2-}$ ligands, the addition of the complex to d-U(600) leads to the partial destruction of the hydrogen-bonded POE/urea aggregates of the hybrid matrix and to the formation of extra urea/urea aggregates. The incorporation of the complex into d-U(600) accounts for an increase of both the $^5D_0$ lifetime and quantum efficiency values (1.950 ± 0.007 ms and 0.50, respectively) with respect to those of the isolated complex (1.7 ms and 0.46, respectively). The addition of the complex also contributes to an enhancement of the absolute emission quantum yield value, whose maximum value (0.66 excited at 280 nm) is the highest value reported for organic–inorganic hybrids modified by lanthanide complexes.

© 2009 Elsevier B.V. All rights reserved.

1. Introduction

The lanthanide (Ln) ions possess characteristic 4f open-shell configurations, +3 being the most stable oxidation state, and exhibit a close chemical resemblance across the periodic series due to the small and regular decrease in their ionic radii. The Ln^{3+} ions are attractive from the optical standpoint, owing to the shielding of the 4f electrons from interaction with the chemical environment provided by the filled $5s^2$ and $5p^6$ sub-shells. The emission bands, that range from the ultraviolet (UV) to the near infrared (NIR) spectral regions, are *quasi* monochromatic and long-lived. Large pseudo-Stokes shifts are observed and high luminescence quantum yields may be obtained. However, because the parity and spin-forbidden 4f–4f transitions have low molar absorption coefficients that may severely limit the light output, the direct photoexcitation of Ln^{3+} ions is not very efficient.

A significant enhancement of the Ln^{3+} luminescence intensity may be achieved through the design of lanthanide complexes comprising sensitizing ligands, i.e., molecules able to absorb the excitation energy and transfer it to Ln^{3+} ions, which in turn undergo the typical radiative emitting process. This process is known as *antenna* effect [1]. A further advantage of these ligands is that they act as protecting cages, shielding the Ln^{3+} ions from deleterious quenching processes. Such complexes emit in the near-UV (Ce^{3+} and Gd^{3+}), visible (vis) (blue, Tm^{3+}; green, Tb^{3+} and Er^{3+}; yellow, Dy^{3+}; orange, Sm^{3+}; red, Eu^{3+}) and NIR (Nd^{3+}, Er^{3+}, Tm^{3+} and Yb^{3+}) spectral regions and thus are of great interest for a wide range of photonic applications [2]. In these compounds the Ln^{3+} species (hard acids) are strongly bonded to organic molecules bearing adequate donor species (hard bases), typically oxygen and/or nitrogen atoms. Calixarenes, β-diketones, cryptands, podands and heterocyclic and aromatic carboxylic acids have been extensively explored in this context. The pyridinecarboxylate (typically named picolinate (pic^-))-based molecules, which are based on the latter class of ligands, are particularly interesting owing to their chemical stability and photophysical properties [3–5]. These attractive features explain the significant number of systematic studies carried out on lanthanide dipicolinates [4–11]. Complexes formed between Eu^{3+} and pyridine-2,6-dicarboxylic acid (or dipicolinic acid (H_2dipic)) have been proposed for applications in biological systems and immunoassays [12–14].

The incorporation of lanthanide complexes into sol–gel derived organic/inorganic hybrid frameworks [15] represents a suitable strategy that has been adopted in recent years to produce materials with improved luminescence properties [16,17]. A few hybrid

---

* Corresponding author. Tel.: +351 259 350253; fax: +351 259 350480.
** Co-corresponding author. Tel.: +351 234 370946; fax: +351 234 424695.
  E-mail addresses: lcarlos@ua.pt (L.D. Carlos), vbermude@utad.pt (V. de Zea Bermudez).

materials incorporating lanthanide dipicolinate complexes have been investigated by several authors [18–20].

In the present paper we report for the first time the thermal behaviour, morphology and optical features of a hybrid sample based on a low molecular weight di-urea cross-linked poly(oxyethylene) (POE)/siloxane hybrid matrix (di-ureasil) comprising POE segments with about 8.5 oxyethylene repeat units (designated as d-U(600)) and $Na_3[Eu(dipic)_3] \cdot xH_2O$, a complex in which the Eu^{3+} coordination sphere includes dipicolinate ligands. The properties of di-ureasil structures [21,22] doped with lanthanide ions have been widely explored [23]. So far, the ligands of the few Eu^{3+}-based complexes that have been added to [24–29] or formed within [30] di-ureasil matrices belong to the classes of heterocyclic compounds [24,25,30], β-diketonates [24–29] and phosphine oxides [27].

We will use here an attractive synthesis strategy that we have explored recently in the context of our investigation of the di-ureasils [26,29]. It relies on the addition of lanthanide complexes to these POE/siloxane hybrid networks whose available cation coordinating sites – the carbonyl oxygen atoms of the urea cross-links and/or the ether oxygen atoms of the POE chains – enable *in situ* formation of new complexes devoid of water ligands and improved optical features.

2. Experimental

2.1. Materials

Europium nitrate ($Eu(NO_3)_3 \cdot 6H_2O$), pyridine-2,6-dicarboxylic acid (H_2dipic, Aldrich, 99,99%) and 3-isocyanatepropyltriethoxysilane (ICPTES, Fluka) and sodium hydroxide (NaOH, PA Pronalab) were used as received. The O,O′-bis-(2-aminopropyl) polypropylene glycol-block-polyethylene glycol-block-polypropylene glycol employed, commercially designated as Jeffamine ED-600® (Fluka, average molecular weight 600 g mol^{-1}), ethanol (CH_3CH_2OH, Merck, PA grade) and tetrahydrofuran (THF, Merck, puriss. PA grade) were stored over molecular sieves. High purity distilled water was used in all the experiments.

2.2. Synthesis

2.2.1. Synthesis of Na_3[Eu(dipic)_3]·xH_2O
The europium dipicolinate complex was prepared according to a procedure reported elsewhere [10].

2.2.2. Synthesis of the di-ureasil samples
A xerogel with a concentration of Eu:Si = 1:146 (g/g) was synthesized using a method described in detail previously [29]. The sample was obtained as a transparent, flexible monolith with an orange-like hue. In agreement with the terminology used in previous papers [22], the hybrid matrix of the material obtained has been designated as d-U(600), where d indicates di, U denotes the urea group and 600 corresponds to the average molecular weight of the starting organic precursors. The doped sample will be henceforth described by the d-U(600)@Eu notation. A non-doped sample (d-U(600)) was also obtained.

2.3. Characterization

The Fourier Transform infrared (FT-IR) spectrum of the doped di-ureasil sample was acquired at room temperature on a Unicam FT-IR spectrophotometer. The spectra were collected in the 4000–500 cm^{-1} range by averaging 120 scans at a resolution of 4 cm^{-1}. About 2 mg of each sample was mixed with potassium bromide (Merck, spectroscopic grade) finely ground and pressed into pellets. The xerogel pellet was kept at 80 °C under vacuum to minimize the levels of absorbed water.

The thermal characteristics of the sample were determined by means of differential scanning calorimetry (DSC) and thermogravimetric analysis (TGA). For the DSC experiment a disk section of the xerogel with a mass of approximately 10 mg was placed in a 30 μl aluminium can and stored in a desiccator over phosphorous pentoxide (P_2O_5) for 1 week at room temperature under vacuum. After this drying treatment the can was hermetically sealed and the thermogram was recorded using a DSC131 Setaram differential scanning calorimeter. The sample was heated at 10 °C min^{-1} from 25 to 190 °C. For the TGA experiments the xerogel was first stored in a desiccator over P_2O_5. It was subsequently transferred to an open platinum crucible and analyzed from 25 to 800 °C using a TA Instruments Q50 thermobalance at a heating rate of 10 °C min^{-1}. In both experiments the purge gas used was high purity nitrogen supplied at a constant 30 (DSC)/20 (TGA) cm^3 min^{-1} flow rate.

To evaluate the morphology of the xerogel film, scanning electronic microscopy (SEM) micrographs were obtained using a SEM/ESEM-FEI Quanta 400 scanning electron microscope at high acceleration voltage (20 kV). A small portion of the sample was cut, fixed on an aluminium stub with carbon tape and then coated with Au/Pd.

X-ray diffraction (XRD) measurements were performed at room temperature with a PANalytical X'Pert Pro equipped with a X'Celerator detector using monochromated CuK$_\alpha$ radiation (λ = 1.541 Å) over the 2θ range between 10° and 70°. The xerogel sample, analyzed as a film, was not submitted to any thermal pretreatment.

The photoluminescence features were recorded at room temperature with a modular double grating excitation spectrofluorimeter with a TRIAX 320 emission monochromator (Fluorolog-3, Jobin Yvon-Spex) coupled to a R928 Hamamatsu photomultiplier, using the front face acquisition mode. The excitation source was a 450 W Xe arc lamp. The emission spectra were corrected for detection and optical spectral response of the spectrofluorimeter and the excitation spectra were weighted for the spectral distribution of the lamp intensity using a photodiode reference detector. The lifetime measurements were acquired with the setup described for the luminescence spectra using a pulsed Xe–Hg lamp (6 μs pulse at half width and 20–30 μs tail).

The absolute emission quantum yields were measured at room temperature using a quantum yield measurement system C9920-02 from Hamamatsu with a 150 W Xe lamp coupled to a monochromator for wavelength discrimination, an integrating sphere as sample chamber and a multichannel analyzer for signal detection. Three measurements were made for each sample so that the average value is reported. The method is accurate to within 10%.

3. Results and discussion

In an attempt to elucidate the role played by the complex on the hydrogen-bonded array of d-U(600) we inspected the "amide I" region of the non-doped and doped xerogels. Classical deconvolution techniques of the 1750–1600 cm^{-1} interval [31] allowed us to resolve the "amide I" band profile of d-U(600) and d-U(600)@Eu hybrid into five and four components, respectively (Fig. 1). The spectral data indicate that the addition of an extremely small amount of $Na_3[Eu(dipic)_3] \cdot xH_2O$ to d-U(600) affects the global profile of the "amide I" band. The intensity maximum of the "amide I" envelope is shifted from approximately 1653 to 1645 cm^{-1}, a proof that the hydrogen bonds in the doped sample are globally stronger than those in the non-doped host matrix. Doping results in considerable band redistribution, meaning that the proportion of hydrogen-bonded aggregates in the material suffers marked changes. Upon
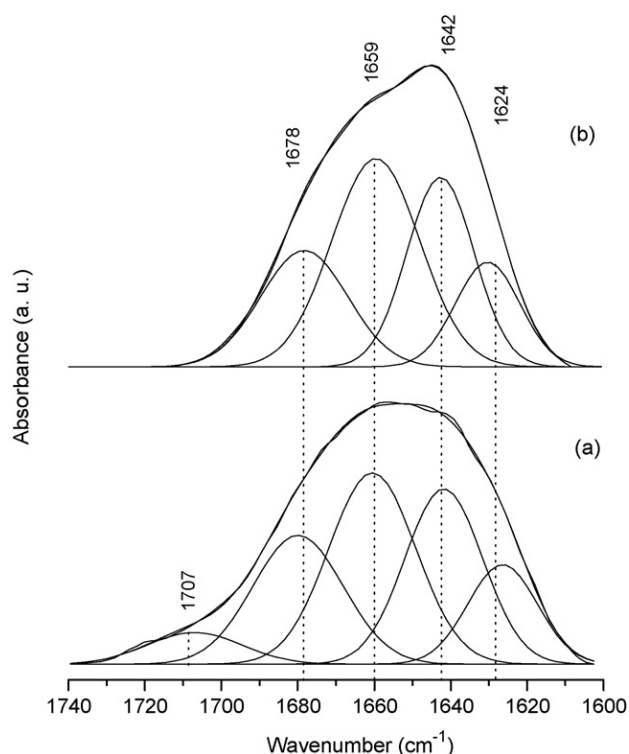
Fig. 1. Curve fitting results of the FT-IR spectra of d-U(600) (a) and d-U(600)@Eu (b).

incorporation of $Na_3[Eu(dipic)_3] \cdot xH_2O$ into the d-U(600) framework the $1707\,cm^{-1}$ band (Fig. 1(a)), attributed to the presence of weak hydrogen-bonded POE/urea aggregates [22,32–34] vanishes (Fig. 1(b)), revealing that the most disordered hydrogen-bonded aggregates of d-U(600) are completely destroyed. Concomitantly the amount of stronger aggregates increases. The absence of a band at $1750\,cm^{-1}$ band in the "amide I" region of the doped material (Fig. 1(b)), associated with urea groups free from any interaction [22,32–34], suggests that all the cross-links of the d-U(600)@Eu sample are involved in hydrogen bonding interactions, similarly to the situation observed in the non-doped matrix. Given the extremely low concentration of the complex in the doped sample examined (*cf.* Section 2.2) and considering the bulkiness of the $dipic^{2-}$ ligand, we may venture that the rupture of the hydrogen bonds observed appears to be solely a consequence of the existence of severe steric constraints [35,36]. Thus, one of the most critical points that will remain unconfirmed in the present work is the coordination of the Eu^{3+} ions to the urea carbonyl groups in the europium complex. In lanthanide complex-doped di-ureasils the coordination of the lanthanide ions to the carbonyl oxygen atoms of the urea cross-links of the hybrid matrix may be easily monitored in the "amide I" region through the detection of a new event that emerges typically around $1620\,cm^{-1}$ [24,25]. In the "amide I" region of d-U(600)@Eu this Eu^{3+} coordination-sensitive feature is not detected (Fig. 1(b)). It is very likely, however, that the concentration of Eu^{3+} is too low to yield a detectable band by FT-IR.

The XRD patterns of the d-U(600)@Eu hybrid are reproduced in Fig. 2. The diffractogram of the hybrid displays the characteristic broad, Gaussian band centred around 21°, associated with ordering within the siliceous domains [37]. In addition, several Bragg peaks are distinctly seen in this diffractogram. As these peaks do not correspond to those of the free complex (not shown), the nature of the new crystalline phase formed in the hybrid medium will remain unknown.
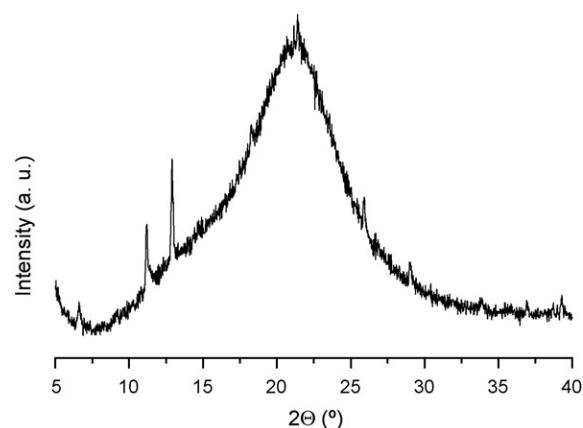
Fig. 2. XRD patterns of the $Na_3[Eu(dipic)_3] \cdot xH_2O$ complex (a) and of the d-U(600)@Eu hybrid (b).

The DSC curve of the d-U(600)@Eu hybrid material (not shown) reveals that this sample is entirely amorphous within the range of temperatures examined. On the basis of the conclusions drawn from the XRD data, we may deduce that the new crystalline phase formed within the amorphous hybrid d-U(600) structure upon addition of the complex has a melting temperature higher than the maximum temperature examined by DSC. The d-U(600)@Eu hybrid starts to decompose at about 145 °C (Fig. 3). The thermal degradation takes place in only two stages.

The SEM micrograph reproduced in Fig. 4 demonstrates that the doped hybrid sample displays a non-porous texture. The morphology of this sample is composed of a homogeneous, smooth surface of the hybrid host material in which complex-containing spherical particles with an average diameter of 1.34–0.67 µm are uniformly dispersed, as confirmed by an EDX probe. This type of morphology is similar to that reported very recently for dextrin microparticles incorporating $[Eu(dipic)_3]^{3-}$ ions [38].

The excitation spectrum of the d-U(600)@Eu was monitored within the $^5D_0 \rightarrow {}^7F_2$ transition (Fig. 5). This spectrum displays a large broad band ascribed to the overlap between the $\pi \rightarrow \pi^*$ transitions of the organic ligands [9] with the hybrid host excited states as we will discuss next. Fig. 5 also shows the typical excitation spectrum monitored within the hybrid host intrinsic emission, which is formed of a broad band between 280 and 450 nm, attributed to donor–acceptor pairs recombination occurring in the siliceous and urea-cross-linkages, respectively [37–42]. The overlap between the hybrids' broad band and the excitation spectrum monitored within the Eu^{3+} emission lines (Fig. 5) indicates the existence of hybrid-to-

Fig. 3. TGA curve of the d-U(600)@Eu hybrid.

Fig. 4. SEM image of the d-U(600)@Eu hybrid.

Fig. 6. Emission spectrum of the d-U(600)@Eu hybrid excited at 280 nm. The inset shows the emission spectra excited at (1) 280 nm, (2) 330 nm, (3) 360 nm, (4) 380 nm, and (5) 420 nm.

Eu^{3+} energy transfer. The negligible intensity of the Eu^{3+} intra-$4f^6$ lines in the excitation spectrum monitored within the Eu^{3+} emission lines (Fig. 5) points out that the Eu^{3+} sensitization process is more efficient than direct excitation into the 4f lines.
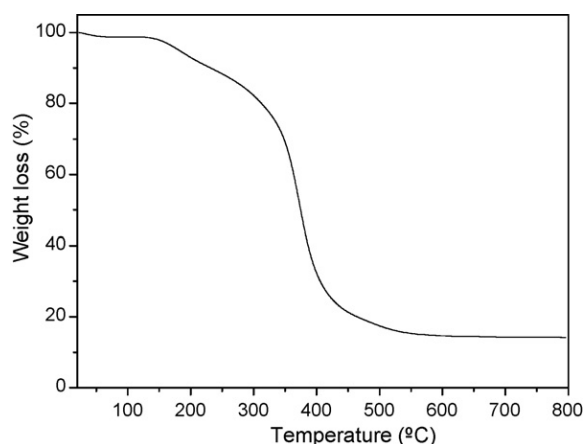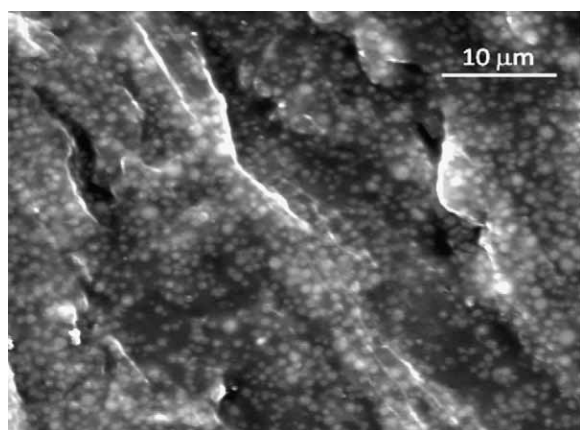
Fig. 6 displays the Eu^{3+} emission features of the d-U(600)@Eu hybrid under UV excitation. The spectrum shows a series of lines ascribed to the $^5D_0 \to {^7F_{0-4}}$ transitions and a low-relative intensity broad band whose peak position deviates to the red as the excitation wavelength increases (280–420 nm) (inset in Fig. 6). Such broad band was already detected for the non-doped d-(600) di-ureasil [37,39–42], and other analogous hybrids, such as the di-urethanesils [25,39] and the mono- [43] and di-amidosils [44]. Its origin has been ascribed to the overlap of two distinct emissions mediated by donor–acceptor pair transitions that occur within the urea, urethane or amide, respectively, cross-linkages and within the siliceous skeleton, due to the presence of oxygen related defects, $^\bullet O$—O—$Si{\equiv}(CO_2)$ [37–42].

The experimental values for the intensity parameters (Ω_2, Ω_4) for the hybrid were determined from the emission spectrum following a methodology detailed elsewhere [24,27,45]. The obtained values for Ω_2 and Ω_4 are 5.80×10^{-20} and 1.48×10^{-20} cm^2, respectively. The values obtained for Ω_2 suggest that Eu^{3+} is in a less polarisable chemical environment when compared with efficient systems including β-diketonate ligands [24,27,45,46]. The value of Ω_2 for the hybrid reflects, not only the hypersensitive behaviour of the $^5D_0 \to {^7F_2}$ transition, but also that it is in a low polarisable

chemical environment in comparison to the situation found in the complex, which displays a higher Ω_2 value (6.125×10^{-20} cm^2) [9].

The $^5D_0$ emission decay curve was monitored within the $^5D_0 \to {^7F_4}$ transition excited at 280 nm (Fig. 7). For time values below 1.00 ms the emission decay curve displays a rise time behaviour (inset in Fig. 7) followed by a single exponential function characterized by a lifetime value of 1.950 ± 0.007 ms. This value is higher than that found for the isolated complex, suggesting an effective interaction between the hybrid host and the complex. The higher value found for the hybrid material relatively to that of the isolated complex (1.7 ms) [9] may be further interpreted through the estimation of the $^5D_0$ radiative (A_r) and non-radiative (A_{nr}) transition probabilities, and the quantum efficiency (q) [$q = A_r/A_r + A_{nr}$] based on the emission spectrum and $^5D_0$ lifetime ($\tau^{-1} = A_r + A_{nr}$) [17]. The radiative contribution is calculated from the relative intensities of the $^5D_0 \to {^7F_{0-4}}$ transitions (the $^5D_0 \to {^7F_{5,6}}$ branching ratios are neglected due to their poor relative intensity with respect to that of the remaining $^5D_0 \to {^7F_{0-4}}$ lines). The $^5D_0 \to {^7F_1}$ transition does not depend on the local ligand field and thus may be used as a reference for the whole spectrum. An effective refractive index of 1.5 was used leading to $A_{01} \approx 50\,s^{-1}$, where A_{01} stands for the Einstein's coefficient of spontaneous emission between the $^5D_0$ and the $^7F_1$ Stark levels. The estimated values for A_r, A_{nr} and q are 0.256 ms^{-1},

Fig. 5. Excitation spectra of the d-U(600)@Eu hybrid monitored at (1) 460 nm and (2) 615.0 nm. The shadow region assigns the overlap between the two spectra.

Fig. 7. Emission decay curve of the d-U(600)@Eu hybrid excited at 280 nm and monitored at 615 nm. The solid line corresponds to the data best fit using a single exponential function ($R > 0.99$). The inset shows a magnification of the emission decay curve in the time interval 0.00–5.00 ms plotted in semi-log scale.

$0.256 \, ms^{-1}$ and 0.50, respectively. Comparing these values with those previously reported for the isolated complex ($A_r = 0.276 \, ms^{-1}$, $A_{nr} = 0.312 \, ms^{-1}$ and $q = 0.46$) [9] we may conclude that the complex incorporation into the d-U(600) host leads to an increase in the q value, essentially due to an increase in the A_r value.

The absolute emission quantum yield (ϕ) for the d-U(600)@Eu hybrid was measured under 280 and 370 nm excitation wavelengths being 0.66 and 0.15, respectively. Both values ar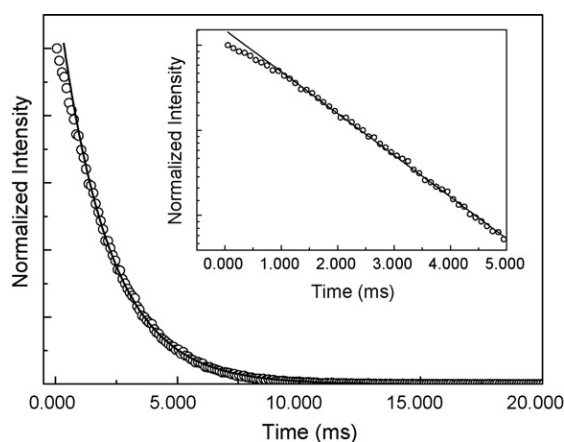e higher that the quantum yield known for the isolated complex (0.06 excited at 370 nm) [9], reinforcing that its incorporation into the hybrid network enhances the overall emission features. In particular, we should give emphasis that the increase of the measured absolute emission quantum yield values for the hybrid, when compared with the values obtained for the isolated complex, may be attributed to the effective interaction between the hybrid host and the complex [26,29] and to the contribution of the hybrids' intrinsic emission to the overall photoluminescence features (Fig. 6). Moreover, we stress the maximum quantum yield value (0.66 under 280 nm excitation wavelength) is the highest value reported for organic–inorganic hybrids modified by lanthanide complexes [17]. We should note that, although by definition $q \geq \phi$, the observation of a lower q value (0.50) relatively to the ϕ value (0.66) under the same excitation wavelength (280 nm) results from the contribution of the hybrids' intrinsic emission to the overall luminescence features.

4. Conclusion

A europium dipicolinate complex was added to the short chain d-U(600) di-ureasil POE/siloxane hybrid structure prepared by the sol–gel method. The addition of the $Na_3[Eu(dipic)_3] \cdot xH_2O$ complex to d-U(600) has major consequences in terms of hydrogen bonding interactions, leading to a significant breakdown of the most disordered hydrogen-bonded aggregates of d-U(600) and to the concomitant formation of stronger aggregates. This effect was associated with the bulkiness of the ligands. The hybrid sample is thermally stable up to $145\,^{\circ}C$ and has a non-porous texture, being composed of a homogeneous, smooth surface of the hybrid host material and $1.34–0.67\,\mu m$-diameter spherical particles of complex. In spite of the low complex concentration, a crystalline phase of unknown nature is formed in the doped xerogel. Upon incorporation of $Na_3[Eu(dipic)_3] \cdot xH_2O$ into the di-ureasil matrix, an increase of both the $^5D_0$ lifetime and quantum efficiency values (1.950 ± 0.007 ms and 0.50, respectively) with respect to those of the isolated complex (1.7 ms and 0.46, respectively) results. The complex incorporation also contributes to enhance the absolute emission quantum yield value, whose maximum value (0.66 excited at 280 nm) is the highest value reported so far for lanthanide-containing organic–inorganic hybrids. This quantum yield enhancement can be attributed to the effective interaction occurring between the hybrid host and the complex and to the contribution of the hybrids' intrinsic emission to the overall photoluminescence features.

Acknowledgements

References

[1] J.M. Lehn, Angew. Chem. Int. Ed. 29 (1990) 1304.
[2] J.-C. Bünzli, C. Piguet, Chem. Soc. Rev. 34 (2005) 1048.
[3] C. Qin, X.L. Wang, E.B. Wang, Z.M. Su, Inorg. Chem. 44 (2005) 7122.
[4] J.B. Lamture, Z. Hong Zhou, A. Suresh Kumar, T.G. Wensel, Inorg. Chem. 34 (1995) 864.
[5] M.E. de Mesquita, S.A. Júnior, F.C. Oliveira, R.O. Freire, N.B.C. Júnior, G.F. De Sá, Inorg. Chem. Commun. 5 (2002) 292.
[6] A. Fernandes, J. Jaud, J. Dexpert-Ghys, C. Brouca-Cabarrecq, Polyhedron 20 (2001) 2385.
[7] A.-L. Gassner, C. Duhot, J.-C.G. Bünzli, A.-S. Chauvin, Inorg. Chem. 47 (2008) 7802.
[8] M.O. Rodrigues, N.B. da Costa Júnior, C.A. de Simone, A.A.S. Araújo, A.M. Brito-Silva, F.A. Almeida Paz, M.E. de Mesquita, S.A. Júnior, R.O. Freire, J. Phys. Chem. B 112 (2008) 4204.
[9] P.P. Lima, O.L. Malta, S. Alves Júnior, Quim. Nova 28 (2005) 805.
[10] N. Tancrez, C. Feuvrie, I. Ledoux, J.Z. Yss, L. Toupet, H. Le Bozec, O. Maury, J. Am. Chem. Soc. 127 (2005) 13474.
[11] C. Reinhard, H.U. Guldel, Inorg. Chem. 41 (2002) 1048.
[12] A. D'Aléo, A. Picot, A. Beeby, J.A. Gareth Williams, B. Le Guennic, C. Andraud, O. Maury, Inorg. Chem. 47 (2008) 10258.
[13] M.L. Cable, J.P. Kirby, K. Sorasaenee, H.B. Gray, A. Ponce, J. Am. Chem. Soc. 129 (2007) 1474.
[14] A. D'Aléo, G. Pompidor, B. Elena, J. Vicat, P.L. Baldeck, L. Toupet, R. Kahn, C. Andraud, O. Maury, Chem. Phys. Chem. 8 (2007) 2125.
[15] P. Gomez-Romero, C. Sanchez, Functional Hybrid Materials, Wiley Interscience, New York, 2003.
[16] L.D. Carlos, R.A. Sá Ferreira, V. de Zea Bermudez, in: G. Kickelbick (Ed.), Hybrid Materials—Synthesis, Characterization and Applications, Wiley–VCH Verlag GmbH & Co. KGaA, Weinheim, 2007, Cp. 9.
[17] L.D. Carlos, R.A. Sá Ferreira, V. de Zea Bermudez, S.J.L. Ribeiro, Adv. Mater. 21 (2009) 509.
[18] A.C. Franville, D. Zambon, R. Mahiou, Y. Troin, Chem. Mater. 12 (2000) 428.
[19] K. Driesen, R. Van Deun, C. Gorller-Walrand, K. Binnemans, Chem. Mater. 16 (2004) 1531.
[20] K. Lunstroot, K. Driesen, P. Nockemann, K. Van Hecke, L. Van Meervelt, C. Gorller-Walrand, K. Binnemans, S. Bellayer, L. Viau, J. Le Bideau, A. Vioux, Dalton Trans. (2009) 298.
[21] M. Armand, C. Poinsignon, J.-Y. Sanchez, V. de Zea Bermudez, US Patent 5,283,310 (1993).
[22] V. de Zea Bermudez, L.D. Carlos, L. Alcácer, Chem. Mater. 11 (1999) 569.
[23] R.A. Sá Ferreira, L.D. Carlos, V. de Zea Bermudez, in: H.S. Nalwa (Ed.), Encyclopedia of Nanoscience and Nanotechnology, American Scientific Publishers, North Lewis Way, CA, USA, 2004, Cp. 4.
[24] P.P. Lima, R.A. Sá Ferreira, R.O. Freire, F.A. Paz, L. Fu, L.S. Alves Júnior, L.D. Carlos, O.L. Malta, Chem. Phys. Chem. 7 (2006) 735.
[25] L. Fu, R.A. Sá Ferreira, N.J.O. Silva, A.J. Fernandes, P. Ribeiro-Claro, I.S. Gonçalves, V. de Zea Bermudez, L.D. Carlos, J. Mater. Chem. 15 (2005) 3117.
[26] C. Molina, K. Dahmouche, Y. Messadeq, S.J.L. Ribeiro, M.A.P. Silva, V. de Zea Bermudez, L.D. Carlos, J. Lumin. 93 (2003) 104.
[27] P.P. Lima, S.A. Junior, O.L. Malta, L.D. Carlos, R.A. Sá Ferreira, R. Pavithran, M.L.P. Reddy, Eur. J. Inorg. Chem. 19 (2006) 3923.
[28] P.P. Lima, R.A.S. Ferreira, S.A. Júnior, O.L. Malta, L.D. Carlos, J. Photochem. Photobiol. A 201 (2009) 214.
[29] M. Fernandes, V. de Zea Bermudez, R.A. Sá Ferreira, L.D. Carlos, N.V. Martins, J. Lumin. 128/2 (2007) 205.
[30] L. Fu, R.A. Sá Ferreira, S.S. Nobre, L.D. Carlos, J. Rocha, J. Lumin. 122–123 (2006) 265.
[31] PeakFit®, Jandel Scientific, Peak separation and analysis software for Windows, San Rafael, CA, 1995.
[32] V. de Zea Bermudez, R.A. Sá Ferreira, L.D. Carlos, C. Molina, K. Dahmouche, S.J.L. Ribeiro, J. Phys. Chem. B 105 (2001) 3378.
[33] S.C. Nunes, V. de Zea Bermudez, D. Ostrovskii, L.D. Carlos, J. Mol. Struct. 702 (2004) 39.
[34] L. Fu, R.A. Sá Ferreira, M. Fernandes, S.C. Nunes, V. de Zea Bermudez, G. Hungerford, L.D. Carlos, Opt. Mater. 30 (2008) 1058.
[35] M. Fernandes, V. de Zea Bermudez, R.A. Sá Ferreira, L.D. Carlos, A. Charas, J. Morgado, M.M. Silva, M.J. Smith, Chem. Mater. 19 (2007) 3892.
[36] M. Fernandes, S.S. Nobre, M.C. Gonçalves, A. Charas, J. Morgado, R.A.S. Ferreira, L.D. Carlos, V. de Zea Bermudez, J. Mater. Chem. 19 (2009) 733.
[37] L.D. Carlos, V. de Zea Bermudez, R.A. Sá Ferreira, L. Marques, M. Assunção, Chem. Mater. 11 (3) (1999) 581.
[38] P.P. Luz, A.M. Pires, O.A. Serra, J. Fluoresc. 18 (2008) 695.
[39] L.S. Fu, R.A.S. Ferreira, N.J.O. Silva, L.D. Carlos, V. de Zea Bermudez, J. Rocha, Chem. Mater. 16 (2004) 1507.
[40] L.D. Carlos, R.A.S. Ferreira, R.N. Pereira, M. Assunção, V. de Zea Bermudez, J. Phys. Chem. B 108 (2004) 14924.
[41] S.S. Nobre, P.P. Lima, L. Mafra, R.A. Sá Ferreira, R.O. Freire, L. Fu, U. Pischel, V. de Zea Bermudez, O.L. Malta, L.D. Carlos, J. Phys. Chem. C 111 (2007) 3275.
[42] L.D. Carlos, R.A.S. Ferreira, V. de Zea Bermudez, S.J.L. Ribeiro, Adv. Funct. Mater. 11 (2001) 111.
[43] L.D. Carlos, V. de Zea Bermudez, V.S. Amaral, S.C. Nunes, N.J.O. Silva, R.A.S. Ferreira, J. Rocha, C.V. Santilli, D. Ostrovskii, Adv. Mater. 19 (2007) 341.
[44] S.C. Nunes, V.D.Z. Bermudez, J. Cybinska, R.A.S. Ferreira, J. Legendziewicz, L.D. Carlos, M.M. Silva, M.J. Smith, D. Ostrovskii, J. Rocha, J. Mater. Chem. 15 (2005) 3876.
[45] L.D. Carlos, Y. Messaddeq, H.F. Brito, R.A.S. Ferreira, V. de Zea Bermudez, S.J.L. Ribeiro, Adv. Mater. 12 (2000) 594.
[46] O.L. Malta, H.F. Brito, J.F. Menezes, F.R.G. Silva, S. Alves Jr., S.F. Farias Jr., A.V.M. de Andrade, J. Lumin. 75 (1997) 255.

Theoretical and Experimental Studies of the Photoluminescent Properties of the Coordination Polymer [Eu(DPA)(HDPA)(H₂O)₂]·4H₂O

Marcelo O. Rodrigues,*,† Nivan B. da Costa Júnior,‡ Carlos A. de Simone,§
Adriano A. S. Araújo,‡ A. M. Brito-Silva,∥ Filipe A. Almeida Paz,⊥ Maria E. de Mesquita,‡
Severino A. Júnior,*,† and Ricardo O. Freire*,‡

Departamento de Química Fundamental, UFPE, 50590-470, Recife - PE, Brazil, Departamento de Química, UFS, 49100-000, São Cristóvão - SE, Brazil, Departamento de Química, UFAL, 57072-970, Maceió - AL, Brazil, Pós-Graduação em Ciência de Materiais, UFPE, 50590-470, Recife - PE, Brazil, Departamento de Química, CICECO, Universidade de Aveiro, 3810-193, Aveiro, Portugal

Received: June 28, 2007; In Final Form: December 4, 2007

We report on the hydrothermal synthesis of the [Eu(DPA)(HDPA)(H₂O)₂]·4H₂O lanthanide-organic framework (where H₂DPA stands for pyridine-2,6-dicarboxylic acid), its full structural characterization including single-crystal X-ray diffraction and vibrational spectroscopy studies, plus detailed investigations on the experimental and predicted (using the Sparkle/PM3 model) photophysical luminescent properties. We demonstrate that the Sparkle/PM3 model arises as a valid and efficient alternative to the simulation and prediction of the photoluminescent properties of lanthanide-organic frameworks when compared with methods traditionally used. Crystallographic investigations showed that the material is composed of neutral one-dimensional coordination polymers $_\infty^1$[Eu(DPA)(HDPA)(H₂O)₂] which are interconnected via a series of hydrogen bonding interactions involving the water molecules (both coordinated and located in the interstitial spaces of the structure). In particular, connections between bilayer arrangements of $_\infty^1$[Eu(DPA)(HDPA)(H₂O)₂] are assured by a centrosymmetric hexameric water cluster. The presence of this large number of O−H oscillators intensifies the vibronic coupling with water molecules and, as a consequence, increases the number of nonradiative decay pathways controlling the relaxation process, ultimately considerably reducing the quantum efficiency ($\eta = 12.7\%$). The intensity parameters (Ω_2, Ω_4, and Ω_6) were first calculated by using both the X-ray and the Sparkle/PM3 structures and were then used to calculate the rates of energy transfer (W_{ET}) and back-transfer (W_{BT}). Intensity parameters were used to predict the radiative decay rate. The calculated quantum yield obtained from the X-ray and Sparkle/PM3 structures (both of about 12.5%) are in good agreement with the experimental value (12.0 ± 5%). These results clearly attest for the efficacy of the theoretical models employed in all calculations and create open new interesting possibilities for the design in silico of novel and highly efficient lanthanide-organic frameworks.

Introduction

The use of lanthanide ions in the construction of coordination polymers, also known as metal−organic frameworks (MOFs), has recently received much attention,[1−3] since the intrinsic magnetic and photoluminescence (PL) properties of these materials render them as potential candidates for the development of functional devices.[4−6] In particular, these framework-based materials can efficiently be used in light conversion molecular devices (LCMD),[7] in which light is absorbed by the coordinated ligands and then transferred to the emitting metal ion, ultimately increasing the overall PL properties.[8] Europium-based systems are of particular interest because they usually have long lifetimes and quantum efficiencies.[9] In addition, the Eu³⁺ (4f−4f) transitions are particularly sensitive to the coordination modes of the organic ligands and, therefore, can be efficiently used to infer structural features of individual coordination environments.[10] These photophysical characteristics have been extensively explored in materials science, in particular, in the development of luminescent probes in biomedical assay,[11] organic light-emitting diodes (OLEDs),[12] and sensors.[13]

A great diversity of organic ligands have been strategically developed and used on the synthesis of new europium complexes, among which the pyridinecarboxylate-based molecules are of particular interest due to their chemical stability and photophysical properties.[14−15] For example, pyridine 2,6-dicarboxylic acid (H₂DPA) has been widely employed on the preparation of complexes with Eu³⁺ cations which find applications in biological systems and immunoassays.[16−17] Moreover, H₂DPA also plays a decisive role on the construction of coordination polymers since it can establish bridges between metals centers and adopt several coordination modes.[18] It is important to emphasize that, even though a number of reports on the synthesis of MOFs with Eu³⁺ and H₂DPA residues are available in the literature, a detailed study of the PL properties of these compounds is, to date, nonexistent.[19−20]

In silico methods are nowadays particularly efficient addressing interesting chemical problems associated with structure prediction and anticipation of photophysical properties.[21] For

* Corresponding authors. E-mail: mzohio@hotmail.com (M.O.R.), salvesjr@ufpe.br (S.A.J.), and rfreire@ufs.br (R.O.F.).
† Departmento de Química Fundamental, UFPE.
‡ UFS.
§ UFAL.
∥ Pós-Graduação em Ciência de Materiais, UFPE.
⊥ CICECO.

[Eu(DPA)(HDPA)(H₂O)₂]·4H₂O

J. Phys. Chem. B, Vol. 112, No. 14, 2008 **4205**

example, quantum chemical methods are able to calculate the ground state geometry of lanthanide centers, and first principles methods using effective core potentials (ECPs) have proven their effectiveness in lanthanide chemistry.[22−24] Nevertheless, these methodologies are computationally very demanding and, thus, inappropriate for expanded systems such as MOFs. Sparkle/ AM1 algorithms[25] are instead based on a sophisticated parametrization scheme for semiempirical calculations, allowing the prediction of coordination geometries whose accuracy is comparable to those obtained from ab initio/ECP calculations but at much smaller expense of computational power.[25−26] The Sparkle/AM1 model has been successfully applied to the prediction of the ground state geometries of lanthanide complexes, the corresponding ligand field parameters,[27−29] plus a number of other spectroscopic properties such as electronic spectrum, singlet and triplet energy positions,[30−32] and intensity parameters.[33−35] By using the two latter series of calculated parameters, we have recently built up rate equations involving energy transfer mechanisms which allowed the determination of PL efficiencies and quantum yields,[36,37] and, in a more recent study, we have reported the design of a highly photoluminescent europium complex simply based on theoretical studies.[37]

In this paper, we report a detailed (theoretical and experimental) photophysical study of the properties of the one-dimensional coordination polymer, [Eu(DPA)(HDPA)(H₂O)₂]· 4H₂O, recently described very briefly by Harrowfield and collaborators.[38] Spectroscopic properties such as intensity parameters Ω_λ ($\lambda = 2, 4$ and 6), rates of energy transfer (W_{ET}) and back-transfer (W_{BT}), branching ratios (β_{OJ}), radiative (A_{rad}) and nonradiative (A_{nrad}) decay rates, quantum efficiency (η), and quantum yield (q) of this material were theoretically predicted using the Sparkle/PM3 geometry and data derived from single-crystal X-ray diffraction investigations. We decided to use the Sparkle/PM3 parametrization[25] model since it has a better quantum chemical description of the coordinated ligands, which ultimately is reflected in the overall quality of the predicted PL properties.

Experimental Details

Synthesis of Eu(DPA)(HDPA)(H₂O)₂]·4H₂O. A mixture of pyridine-2,6-dicarboxylic acid, H₂DPA, (0.8 mmol, 0.134 g), Eu₂O₃ (0.070 g, 0.2 mmol), and H₂O (ca. 4 mL) was placed in a 8 mL Teflon-lined stainless autoclave at 180 °C for 72 h. The final compound (0.123 g) was obtained in a yield of ca. 60% (based on Eu) after being washed with water and acetone and being air-dried. Anal. calcd for C₁₄H₁₄N₂O₁₄Eu (%): C, 28.68; H, 2.41; N, 4.78. Found (%): C, 27.38; H, 2.52; N, 4.90. IR (cm⁻¹): 3565−3065 (s), 1613 (s), 1566 (s), 1450 (s), 1395 (s), 1377 (s), 1284 (m), 1191 (w), 1076 (m), 1016 (w), 916 (w), 700 (m), 591 (w), 506 (w), 408 (w). The IR spectra (coordination polymer and H₂DPA ligand) are presented in Supporting Information (Figure S3).

General Instrumentation. Elemental analysis was performed on a CHNS−O analyzer Flash 1112 Series EA Thermo Finnigam. FT-IR spectra were recorded on KBr pellets (spectral range 4000 to 400 cm⁻¹) using a BRUKER IFS 66.

Photoluminescence spectra at room temperature and 77 K were obtained using a ISS PC1 spectrofluorometer. The excitation device was equipped with a 300 W xenon lamp and a holographic grating. Emission spectra were collected with a 25 cm monochromator (resolution of 0.1 nm) connected to a photomultiplier. The excitation and emission slit width were fixed at 1.0 mm, with all used monochromators having 1200 grooves/mm. The experimental quantum yield (q) was deter-

mined by employing the method developed by Bril et al.,[39] for which the q value for a give sample can be calculated by a direct comparison with standard phosphors whose q values were previously determined by absolute measurements. q can thus be determined by:

$$q = \left(\frac{1 - r_{ST}}{1 - r_x}\right)\left(\frac{\Delta\Phi_x}{\Delta\Phi_{ST}}\right)q_{ST} \qquad (1)$$

where r_{ST} and r_x correspond to the amount of exciting radiation reflected by the standard and the sample, respectively, and q_{ST} is the quantum yield of the standard phosphor. The terms $\Delta\Phi_x$ and $\Delta\Phi_{ST}$ correspond to the respective integrate photon flux (photon·s⁻¹) for the sample and standard phosphors. As standard phosphor we used sodium salicylate (Merck PA), whose q_{ST} is 55% at room temperature as reported by Malta and co-workers.[40]

Differential scanning calorimetry (DSC) data was recorded in a DSC 50 cell (Shimadzu) in the 25−400 °C temperature range, under dynamic nitrogen atmosphere (50 mL·min⁻¹), and by using an aluminum crucible with ∼2.0 mg of the sample and a heating rate of 10 °C·min⁻¹. The DSC cell was calibrated with indium (mp 156.6 °C; ΔH_{fus} = 28.54 J·g⁻¹). The thermoanalytical curves were obtained in duplicate with a thermobalance model TGA 50 (Shimadzu) in 25−1200 °C temperature range, using a platinum crucible with approximately 3.0 mg of sample, under dynamic nitrogen atmosphere (50 mL·min⁻¹) and with a heating rate of 10 °C·min⁻¹.

Single-Crystal X-ray Diffraction. A detailed description of the crystallographic characterization of the compound is presented in Supporting Information.

Theoretical Studies

Geometry Optimization and Transition Energies. The Sparkle/PM3[25] model, implemented in the Mopac2007 software package,[41] was used to calculate the ground state geometry of the [Eu(DPA)(HDPA)(H₂O)₂]·4H₂O compound. MOPAC keywords: PRECISE, GNORM= 0.25, SCFCRT = 1.D-10 (to increase the SCF convergence criterion) and XYZ (for Cartesian coordinates).

The X-ray and Sparkle/PM3 optimized geometries were used to calculate the singlet and triplet excited states using configuration interaction single (CIS) based on the intermediate neglect of differential overlap/spectroscopic (INDO/S) method[42−43] implemented in the ZINDO program.[44]

Judd-Ofelt Intensity Parameters Calculation. The experimental intensity parameters, Ω_λ, for [Eu(DPA)(HDPA)(H₂O)₂]· 4H₂O were determined from:

$$\Omega_\lambda = \frac{4e^2\omega^3 A_{0J}}{3\hbar\chi\langle^7F\|U^\lambda\|^5D_0\rangle^2} \qquad (2)$$

where A_{0J} are the coefficient of spontaneous emission for the $^5D_0 \rightarrow {}^7F_J$ transition, χ is the Lorentz local-field correction term given by $\chi = n(n^2 + 2)^2/9$, n is the refractive index of the medium (in this case $n = 1.5$), and $|\langle^5D_0\|U^{(\lambda)}\|^7F_J\rangle|^2$ are the square reduced matrix element whose values are 0.0032, 0.0023, and 0.0002 for $\lambda = 2, 4$, and 6, respectively.[45,46] The transition $^5D_0 \rightarrow {}^7F_6$ is not observed experimentally thus the experimental Ω_6 parameter cannot be estimated.

The coordinative interaction between a lanthanide cation and a ligand L can be described by the Judd-Ofelt theory,[47−48] after which the intensity parameters Ω_λ ($\lambda = 2, 4$, and 6) are defined by:

4206 *J. Phys. Chem. B, Vol. 112, No. 14, 2008*

Rodrigues et al.

$$\Omega_\lambda = (2\lambda + 1) \sum_{t,p} \frac{|B_{\lambda tp}|^2}{(2t + 1)} \tag{3}$$

with

$$B_{\lambda tp} = \frac{2}{\Delta E} \langle r^{t+1} \rangle \theta(t, p) \gamma t_p - \left[\frac{(\lambda + 1)(2\lambda + 3)}{2\lambda + 1} \right] \langle r^t \rangle (1 - \sigma_\lambda) \langle f \| C^{(\lambda)} \| f \rangle \Gamma_p^t \delta_{t,\lambda+1} \tag{4}$$

Details on the parameters of eqs 3 and 4 are widely discussed in the literature.[49−52]

The values of charge factors (*g*) and the polarizability of the ligand L (α) (Table 2) used for the calculation of γ_p^t and Γ_p^t, respectively, were adjusted using a nonlinear minimization of an eight-dimension response surface. The generate simulating annealing (GSA) method was employed in order to find one of its local minima, which ideally should be the global one and be chemically feasible. During the minimization stage, both the Sparkle/PM3 and the single-crystal X-ray diffraction geometries were used. The response function, F_{resp}, was thus defined as:

$$F_{resp} = \sum_{i=1}^{2} |\Omega_2^{Calc} - \Omega_2^{Exp}| + |\Omega_4^{Calc} - \Omega_4^{Exp}| \tag{5}$$

where *i* runs over the Sparkle/PM3 and crystallographic geometries, Ω_2^{Calc} and Ω_4^{Calc} correspond to the intensity parameters calculated for each structure, and Ω_2^{Exp} and Ω_4^{Exp} to the intensity parameters obtained from the collected emission spectra. As stated above, the Ω_6 parameter was not considered in the minimization procedure because it is not observed experimentally. All values were found to be in the range of those physically acceptable.

Energy Transfer Rates. The theoretical procedure adopted to describe the energy transfer processes between the ligands and the lanthanide ion was developed by Malta and collaborators.[53−54] According to their model, the energy transfer rates, W_{ET}, can be inferred from the sum of two terms:

$$W_{ET} = W_{ET}^{mm} + W_{ET}^{em} \tag{6}$$

where W_{ET}^{mm} corresponds to the energy transfer rate obtained from the multipolar mechanism, and given by:

$$W_{ET}^{mm} = \frac{2\pi}{\hbar} \frac{e^2 S_L}{(2J + 1)G} F \sum_\lambda \gamma_\lambda \langle \alpha' J' \| U^{(\lambda)} \| \alpha J \rangle^2 + \frac{2\pi}{\hbar} \frac{e^2 S_L}{(2J + 1)G R_L^6} F \sum_\lambda \Omega_\lambda^{e.d.} \langle \alpha' J' \| U^{(\lambda)} \| \alpha J \rangle^2 \tag{7}$$

where *G* is the degeneracy of the ligand initial state and α specifies a given 4f spectroscopic term, *J* is the total angular momentum quantum number of the lanthanide ion. The R_L parameter (eq 7) has been calculated by:

$$R_L = \frac{\sum_i c_i^2 R_{L,i}}{\sum_i c_i^2} \tag{8}$$

with c_i being the molecular orbital coefficient of the atom *i* contributing to the ligand state (triplet or singlet) involved in the energy transfer, and $R_{L,i}$ corresponding to the distance from atom *i* to the Eu^{3+} ion.

The second term of the eq 6, W_{ET}^{em}, corresponds to the energy transfer rate obtained from the exchange mechanism. This term is calculated by:

$$W_{ET}^{em} = \frac{8\pi}{3\hbar} \frac{e^2 (1 - \sigma_0)^2}{(2J + 1)R_L^4} \times F \langle \alpha' J' \| S \| \alpha J \rangle^2 \sum_m \left| \langle \phi | \sum_k \mu_Z(k) s_m(k) | \phi' \rangle \right|^2 \tag{9}$$

where *S* is the total spin operator of the lanthanide ion, μ_Z is the z component of the electric dipole operator and s_m (*m* = 0, ±1 is a spherical component of the spin operator (both for the ligand electrons), and σ_0 is a distance-dependent screening factor.[51]

The quantities *F* and γ_λ are given by:

$$F = \frac{1}{\hbar \gamma_L} \sqrt{\frac{\ln 2}{\pi}} \exp\left[-\left(\frac{\Delta}{\hbar \gamma_L} \right)^2 \ln 2 \right] \tag{10}$$

where γ_L is the ligand state bandwidth-at-half-maximum, and Δ is the transition energy difference between the donor and acceptor involved in the transfer process.

$$\gamma_\lambda = (\lambda + 1) \frac{\langle r^\lambda \rangle^2}{(R_L^{\lambda+2})^2} \langle 3 \| C^{(\lambda)} \| 3 \rangle^2 (1 - \sigma_\lambda)^2 \tag{11}$$

The $\langle r^\lambda \rangle$ quantity is the expected radial value of r^λ for 4f electrons (eq 11), $\langle 3 \| C^{(\lambda)} \| 3 \rangle$ is a reduced matrix element of the Racah tensor operator $C^{(\lambda)}$,[45,55] and the σ_λ are screening factors due to the 5s and 5p filled sub-shells of the lanthanide ion.

Branching Ratios and Radiative Decay Rate. The fluorescence branching ratio, β_{0J}, consisting of the relative contribution of each $^5D_0 \rightarrow {}^7F_J$ transition to the emission spectrum, can be quantified as the ratio of the area of each band to the sum of areas of the all bands in the experimental emission spectrum. This quantity can be estimated using the Judd-Ofelt theory:[45]

$$\beta_{0,J} = \frac{A_{0,J}}{A_{Rad}} \tag{12}$$

where $A_{0,J}$ is the spontaneous emission of the each band and A_{rad} is the experimental radiative decay rates.

The $^5D_0 \rightarrow {}^7F_1$ transition can be considered as reference because it is independent of the chemical environmental, and therefore it is used in the calculus of the A_{0J} (where *J* = 2 and 4) and other intensity parameters. The spontaneous emission coefficient A_{01} is determined from emission spectra and can be estimated according to:[52]

$$A_{01} = 0.31 \times 10^{-11} \times \eta^3 \times (\sigma_1)^3 \tag{13}$$

The experimental radiative rate of the spontaneous emission, A_{rad}, can be determined by summing of the all spontaneous contributions. For this purpose, each spontaneous emission coefficient A_{02} and A_{04} is obtained from:[56]

$$A_{0J} = A_{01} \sum_J S_{0J} \times \sigma_1 / S_{01} \times \sigma_J \tag{14}$$

where S_{01} and S_{0J} are the integrated intensities of the $^5D_0 \rightarrow {}^7F_1$ and $^5D_0 \rightarrow {}^7F_J$ (*J* = 2 and 4) transitions, and σ_{01} and σ_{0J} are their barycentered energies, respectively.

[Eu(DPA)(HDPA)(H₂O)₂]·4H₂O

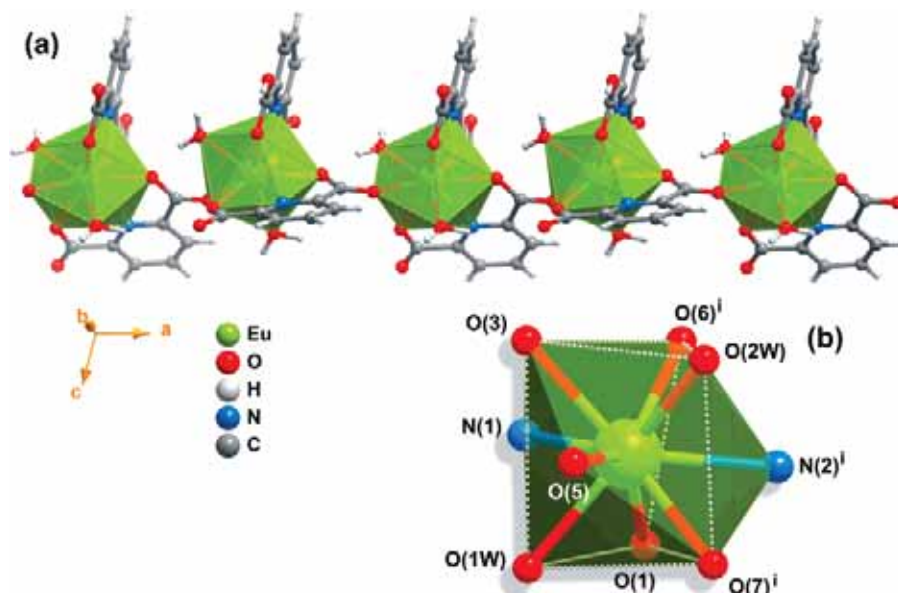*J. Phys. Chem. B, Vol. 112, No. 14, 2008* **4207**

Figure 1. (a) Perspective view of the 1D $_\infty^1$[Eu(DPA)(HDPA)(H₂O)₂] coordination polymer running along the [100] direction of the unit cell. (b) Schematic representation of the distorted tricapped trigonal prismatic coordination environment of the crystallographically independent Eu³⁺ center. Symmetry transformation used to generate equivalent atoms: (i) $^1/_2 + x$, $^1/_2 - y$, z.

TABLE 1: Spherical Atomic Coordinates for the Single-Crystal X-ray and Sparkle/PM3 (Inside the Parentheses) {EuN₂O₇} Coordination Polyhedron, Unsigned Deviation Obtained for the Lanthanide-Coordinated-Atom Distances, Charge Factors (g) and the Polarizability (α) of the Coordinated Atom

atom	R (Å)	θ (degree)	φ (degree)	unsigned deviation	g^a	α^a
Eu	0.000 (0.000)	0.000 (0.000)	0.000 (0.000)	**0.000**		
O	2.459 (2.459)	9.000 (19.153)	99.879 (129.115)	**0.000**	0.74	2.42
O	2.509 (2.486)	119.852 (139.906)	223.790 (226.316)	**0.023**	0.74	2.42
N	2.563 (2.486)	60.326 (79.589)	204.908 (228.174)	**0.077**	2.08	0.01
O	2.507 (2.461)	87.463 (91.071)	142.119 (146.336)	**0.046**	0.74	2.42
O	2.436 (2.470)	146.482 (127.018)	333.225 (344.470)	**0.034**	0.74	2.42
N	2.564 (2.582)	147.440 (133.418)	120.821 (97.443)	**0.018**	2.08	0.01
O	2.439 (2.469)	75.275 (61.155)	359.611 (358.940)	**0.030**	2.00	6.49
O	2.434 (2.475)	86.136 (59.874)	70.491 (72.742)	**0.041**	1.59	0.23
O	2.399 (2.465)	76.870 (109.035)	285.642 (306.221)	**0.066**	1.59	0.23

^{a} Obtained using a nonlinear minimization technique.

TABLE 2: Theoretical Intensity Parameters Ω_2, Ω_4, Ω_6, Radiative (A_{rad}) and Nonradiative (A_{nrad}) Decay Rates, Quantum Efficiency (η) and Quantum Yield (q) Values Derived from the Single-Crystal X-ray Diffraction and Optimized Sparkle/PM3 Models Where Related Experimental Data, Including the Lifetime (τ) of the Eu³⁺ Center, Were Obtained at Ambient Temperature for the As-Synthesized [Eu(DPA)(HDPA)(H₂O)₂]·4H₂O Material

	Ω_2 (10^{-20}cm²)	Ω_4 (10^{-20}cm²)	Ω_6 (10^{-20}cm²)	A_{rad} (s⁻¹)	A_{nrad} (s⁻¹)	τ (ms)	η (%)	q (%)
experimental data	4.32	1.51		211.84	1454.80	0.6	12.7	12.0
X-ray structure	4.31	2.18	6.53	217.10	1449.54		13.0	12.5
Sparkle/PM3 structure	4.32	1.52	12.10	211.74	1454.90		12.7	12.5

The lifetime (τ) of the excited state $^5D_0$ was determined from single-exponential fittings of decay curves and is consistent with the presence of a single crystallographically independent Eu³⁺ center (see crystallographic details). The experimental set up used for these lifetime measurements comprises a Nd:YAG (third harmonic) coherent laser with $\lambda = 355$ nm used as the excitation source (frequency of 5 Hz and pulse width of 7 ns), a Tektronix TDS a 1012 oscilloscope and a fast detector ET 2000. The experimental arrangement used for lifetime measurements is presented in Figure S4 of Supporting Information.

The experimental nonradiative rate A_{nrad} is determined from:

$$\tau^{-1} = A_{rad} + A_{nrad} \quad (15)$$

The theoretical fluorescence branching ratio is similar to the spontaneous emission probability (A) of the transition and can be obtained from the Einstein coefficient to express the rate of

relaxation from an excited state $^5D_0$ to a final state ^7F_J, with $J = 0-6$. The spontaneous emission probability taking into account both the magnetic dipole mechanisms and the forced electric dipole is then given by:

$$A(^5D_0 - ^7F_J) = \frac{64\pi^4\nu^3}{3h(2J+1)}\left[\frac{n(n^2+2)^2}{9}S_{ed} + n^3 \cdot S_{md}\right] \quad (16)$$

where ν is the energy gap between the $^5D_0$ and ^7F_J states (in cm⁻¹), h is Planck's constant, $2J + 1$ is the degeneracy of the initial state, and n is the refractive index of the medium. S_{ed} and S_{md} are the electric and magnetic dipole strengths, respectively. S_{ed} is given by:

$$S_{ed} = e^2 \cdot \sum_{\lambda=2,4,6} \Omega_\lambda |\langle^5D_0||U^{(\lambda)}||^7F_J\rangle|^2 \quad (17)$$

The $^5D_0 \rightarrow {}^7F_J$ transitions ($J = 0$, 3, and 5) are forbidden in the magnetic and induced electric dipole schemes, that is, their

Figure 2. Optimized molecular structure of $_\infty^1$[Eu(DPA)(HDPA)-(H$_2$O)$_2$] obtained from the Sparkle/PM3 model.

strengths are taken as zero. The $^5D_0 \rightarrow {}^7F_1$ is the only transition which does not have electric dipole contribution and can be theoretically determined: $S_{md} = 9.6 \times 10^{-42}$ esu$^2 \cdot$cm^2.[58]

Therefore, the theoretical radiative decay rate (A_{rad}) of eq 15 is ultimately calculated as the sum of all individual spontaneous emission coefficient for the $^5D_0 \rightarrow {}^7F_{0,1,2,4}$ transitions:

$$A_{rad} = \sum_{J=1}^{6} A(^5D_0 - {}^7F_J) \qquad (18)$$

The emission quantum efficiency η can be expressed as

$$\eta = \frac{A_{rad}}{A_{rad} + A_{nrad}} \qquad (19)$$

The numerical solution of the rate equations describing the kinetics of the 4f–4f luminescence was carried out according to the model developed by Malta and collaborators, [55] thus yielding the time dependence of the energy level populations, which reach the steady-state regime after 10^{-6}–10^{-5} s. These steady-state populations were further used to calculate the emission quantum yield given by:

$$q = \frac{A_T \eta_2}{\phi \eta_1} \qquad (20)$$

where the sub-indices 1 and 2 indicate the ground state and the emitting level of the complex, A_T corresponds to the sum of the coefficients of spontaneous emission for the $^5D_0 \rightarrow {}^7F_{0,1,2,4}$ transitions and ϕ is the pumping rate.

Results and Discussion

Crystal Structure and Sparkle/PM3 Geometry Prediction. The structure of [Eu(DPA)(HDPA)(H$_2$O)$_2$]·4H$_2$O contains a single crystallographically independent Eu^{3+} cation bound to two H$_{2-x}$DPA^{x-} residues (where $x = 1, 2$) which exhibit slightly distinct coordination fashions (Figure 1a), even though both the mono-deprotonated, HDPA$^-$, and the fully deprotonated, DPA^{2-}, residues are anti,anti-chelated to the lanthanide; one carboxylate group from the latter residue further establishes a syn-bridge with a symmetry-related Eu^{3+} cation, imposing a Eu$\cdots$Eu^i separation of 6.497[1] Å [symmetry transformation: (i) 1/2 + x, 1/2 − y, z]. This leads to the formation of a neutral one-dimensional coordination polymer, $_\infty^1$[Eu(DPA)(HDPA)(H$_2$O)$_2$] (Figure 1a), running parallel to the [100] direction of the unit cell. The coordination sphere of Eu^{3+} also comprises two water molecules and can be best described as a distorted tricapped trigonal prism, {EuN$_2$O$_7$} (Figure 1b), with local C_{2v} symmetry

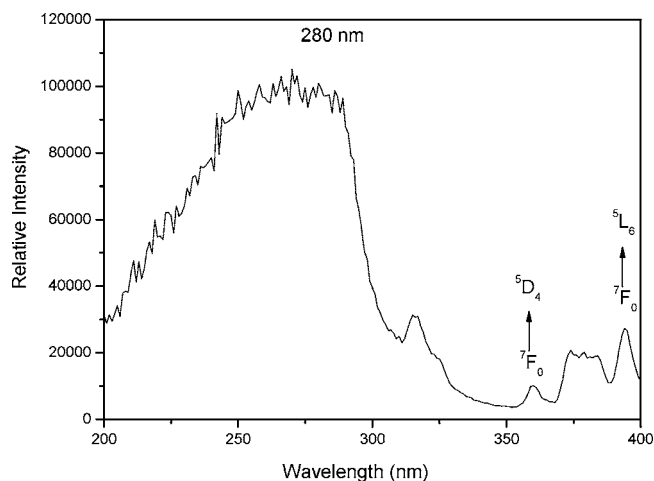**Figure 3.** Excitation spectra of [Eu(DPA)(HDPA)(H$_2$O)$_2$]·4H$_2$O recorded at 300 K by monitoring emission of Eu^{3+} at 615 nm.
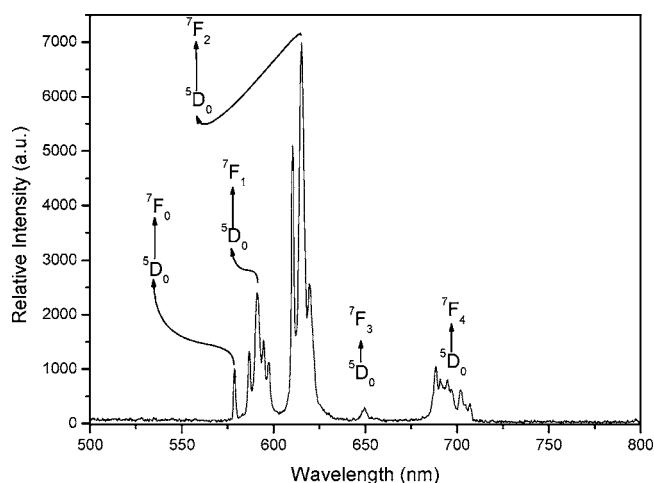
Figure 4. Emission spectrum of [Eu(DPA)(HDPA)(H$_2$O)$_2$]·4H$_2$O recorded at 77K and upon excitation at 280 nm.

which deviates from the typical D_3 reported for similar compounds.[59] The registered Eu−O bond lengths were found in the 2.394(2)−2.508(2) Å range, and the two Eu−N are identical and of 2.564(2) Å. These values are well within the expected ranges found for similar compounds in which Eu^{3+} coordinated to H$_2$DPA residues,[38,60−64] while the Eu−O bond lengths are usually in the 2.40−2.51 Å range (median of 2.45 Å), the Eu−N distances are instead in the 2.49−2.57 Å range (median of 2.54 Å).

Spherical atomic coordinates for the crystallographic and Sparkle/PM3 {EuN$_2$O$_7$} coordination polyhedra are summarized in Table 1, with the optimized geometry obtained from the Sparkle/PM3 model being represented in Figure 2. It is important to emphasize that the Sparkle/PM3 model agrees well with the data derived from the crystallographic studies, with the minimized Eu$\cdots$Eu internuclear distance across the chain being of 6.694 Å, and the Eu−O and Eu−N distances found in the 2.459−2.486 Å and 2.582−2.584 Å ranges, respectively. This good agreement between the two structural models is further supported by an unsigned average error of only 0.037 Å (Table 1).

Thermal Analysis. In Figure S5 of Supporting Information, there are presented the TG/DTG curves recorded in dynamic nitrogen atmosphere. The thermal decomposition of [Eu(DPA)-(HDPA)(H$_2$O)$_2$]·4H$_2$O develops in three consecutive stages. The average of first weight loss of approximately 15.3% occurs in the 40−190 °C temperature range and is attributed to the release

TABLE 3: Calculated Values of Intramolecular Energy Transfer and Back-Transfer Rates in [Eu(DPA)(HDPA)(H$_2$O)$_2$·4H$_2$O] Polymer

	singlet →^{5}D$_4$		triplet → ^{5}D$_1$		triplet → ^{5}D$_0$	
	$W_{ET1}{}^a$ (s^{-1})	$W_{BT1}{}^b$ (s^{-1})	$W_{ET2}{}^a$ (s^{-1})	$W_{BT2}{}^b$ (s^{-1})	$W_{ET3}{}^a$ (s^{-1})	$W_{BT3}{}^b$ (s^{-1})
X-ray structure	2.13×10^4	0.00	2.39×10^7	4.72	8.98×10^6	3.85×10^{-4}
Sparkle/PM3 structure	1.88×10^4	1.92×10^{-13}	1.13×10^8	2.93×10^2	4.82×10^7	2.70×10^{-2}

^{a} W_{ET}, transfer rate. ^{b} W_{BT}, back-transfer rate.

of uncoordinated water molecules housed in the channels (calculated value for five water molecules of *ca.* 15.2%). Decomposition of the dehydrated phase proceeds with two further weight losses to give a residue (*ca.* 32.4%) attributed to the formation of the stoichiometric amount of Eu$_2$O$_3$ (calculated residue of *ca.* 29.8%). DSC measurements agree well with the thermogravimetric behavior, with a deep and broad endothermic peak being registered in the 58−99 °C temperature range. Noteworthy is the fact that DSC further shows that no other phase transition is registered up to approximately 400 °C at which time thermal decomposition of the organic component starts to settle in. This is a clear indication that the dehydrated material is indeed stable up to this temperature.

Photophysical Properties. The excitation spectra of [Eu-(DPA)(HDPA)(H$_2$O)$_2$]·4H$_2$O was registered in the 200−400 nm range by monitoring the emission of Eu^{3+} at 615 nm, and it is showed in Figure 3. The [Eu(DPA)(HDPA)(H$_2$O)$_2$]·4H$_2$O excitation exhibits a broad band between 200 and 310 nm (λ_{max} = 280 nm) from $\pi \rightarrow \pi^*$ electronic transition of the ligand. The peaks observed in the 310−400 nm range result from the f−f transitions of the Eu^{3+} ion, and they are very weak in comparison to the ligand absorption. It is clearly indicate that a typical antenna effect involving the organic ligand is the most probable photophysical pathway responsible for the luminescence of the sample.

Figure 4 shows the emission spectra recorded in the 500−720 nm range, displaying the typical narrow bands corresponding to the centered Eu^{3+} ^{5}D$_0 \rightarrow ^7$F$_J$ transitions, with the main emission centered at approximately 615 nm and corresponding to the ^{5}D$_0 \rightarrow ^7$F$_2$ transition. The relative intensities and splitting of the emissions bands are particularly influenced by symmetry of the first coordination sphere.

The emission spectrum has a single peak at approximately 578 nm attributed to the ^{5}D$_0 \rightarrow ^7$F$_0$ transition, which remains unaltered once the temperature is lowered to 77 K. This clearly indicates the presence of a single Eu^{3+} center, which in good agreement with the crystallographic and Sparkle/PM3 models (see section dedicated to crystal description). Selection rules for the electric dipole transition indicate that the ^{5}D$_0 \rightarrow ^7$F$_0$ is only observed if the point symmetry of Eu^{3+} is either C$_{nv}$, C$_n$ or C$_s$,[67] again in accord with the structural models presented above. The ^{5}D$_0 \rightarrow ^7$F$_1$ transition, which is ruled by a magnetic dipole mechanism and being largely independent of the ligand field effects, exhibits four well-defined Stark components, thus supporting the presence of a low site symmetry for Eu^{3+}.[68] The presence of a fourth emission line on the ^{5}D$_0 \rightarrow ^7$F$_1$ transition can be attributed to electron/phonon coupling, caused by non-coordinated water molecules, delocalized from equilibrium position after the decreasing temperature.[10] Moreover, the ^{5}D$_0 \rightarrow ^7$F$_2$/^{5}D$_0 \rightarrow ^7$F$_1$ ratio for [Eu(DPA)(HDPA)(H$_2$O)$_2$]·4H$_2$O is of approximately 2.8, which is considerably higher than 0.67 typical of europium center exhibiting centrosymmetric.[69] The emission spectrum, at 300 K, of the coordination polymer is presented in Supporting Information (Figure S6).

Table 2 summarizes the theoretical (derived from the expression depicted in Experimental Section) and experimental values

for the intensity parameters (Ω_2, Ω_4, and Ω_6 radiative and nonradiative rates of spontaneous emission (A_{rad} and A_{nrad}, respectively), quantum efficiency (η) and yield (q), and experimental lifetime (τ) for [Eu(DPA)(HDPA)(H$_2$O)$_2$]·4H$_2$O. The short lifetime of 0.6 ms can be directly associated to the nonradiative decay channels controlling the relaxation process (see Table 2) and arising from the vibronic coupling with the water molecules present in the structure. Indeed, it is well-known that O−H oscillators are the most effective quenchers of the Eu^{3+} excited state, both in solution and in the solid state.[71,72] This quenching effect is particularly important in the solid state, with even uncoordinated water molecules can contribute to the overall effect. For example, the single uncoordinated water molecule in compound [Eu(oda)$_3$]·H$_2$O (oda = oxidiacetate), located at 5.05 Å from the optical center, has an astonishing rate of contribution to the overall quenching of 260 s^{-1}.[73] Since in [Eu(DPA)(HDPA)(H$_2$O)$_2$]·4H$_2$O two of the four crystallographically independent water molecules of crystallization have an effective distance to the lanthanide center smaller than 5.0 Å, it is thus feasible to assume that the same effect can also occur in the material in study. Therefore, the water clusters have a dual structural function: while on the one hand they stabilize the supramolecular framework of [Eu(DPA)(HDPA)(H$_2$O)$_2$]·4H$_2$O, on the other they also constitute a nonradiative channel. Indeed, this later function provides a plausible explanation for the observed short lifetime and experimental radiative rate (A_{rad} = 211.84 s^{-1}), the high value for experimental nonradiative rate (A_{nrad} = 1454.83 s^{-1}) and the low experimental quantum efficiency (η = 12.7%). These results are also consistent with the theoretical considerations proposed by Föster and Dexter,[74,75] which predict that the probability of energy transference scales to $1/R^6$, where R is the distance between the donor and the acceptor (the water cluster in this case).

The theoretical intensity parameters Ω_λ (λ = 2, 4, and 6) calculated using the Sparkle/PM3 and crystallographic models are summarized in Table 2. The theoretical values are in excellent agreement with those obtained experimentally. It is worth mentioning that the values for Ω_2 are relatively small when compared with those of Eu-β-diketonates.[76] This is a clear indication of a reduced degree of covalence involving the metal−ligand coordination bond and also of a slightly polarizable chemical environment for the lanthanide center.[77−79]

The ligand-to-metal energy transfer may occur through either the singlet or triplet ligand states. The energies of the triplet and singlet states calculated for the crystallographic structure using the INDO/CIS method are 22 313.7 cm^{-1} and 37 126.6 cm^{-1}, respectively. The same physical quantities obtained using the Sparkle/PM3 structure are 21 774.3 cm^{-1} and 35 812.3 cm^{-1}, respectively. As clearly depicted in Figure 5, the singlet state of the $_\infty$^{1}[Eu(DPA)(HDPA)(H$_2$O)$_2$] coordination polymer does not have appropriate resonance conditions with the europium trivalent ion. Thus, we decided to consider the singlet → ^{5}D$_4$ channel in all our calculations. The parameters needed to calculate the energy transfer rates and emission quantum yield have been obtained from the Sparkle/PM3 and X-ray structures and from spectroscopic calculations.
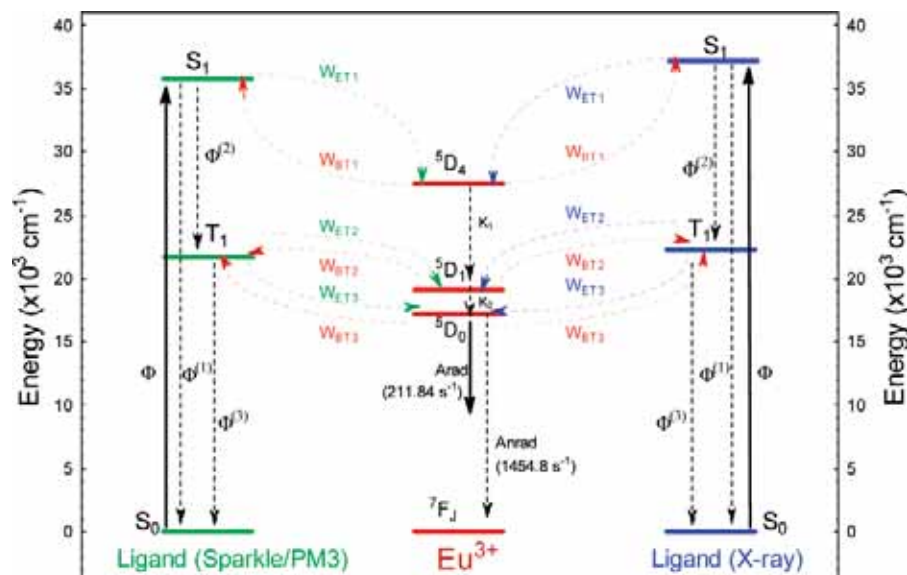
Figure 5. Energy level diagram for [Eu(DPA)(HDPA)(H$_2$O)$_2$]·4H$_2$O showing the most probable channels for the intramolecular energy transfer process.
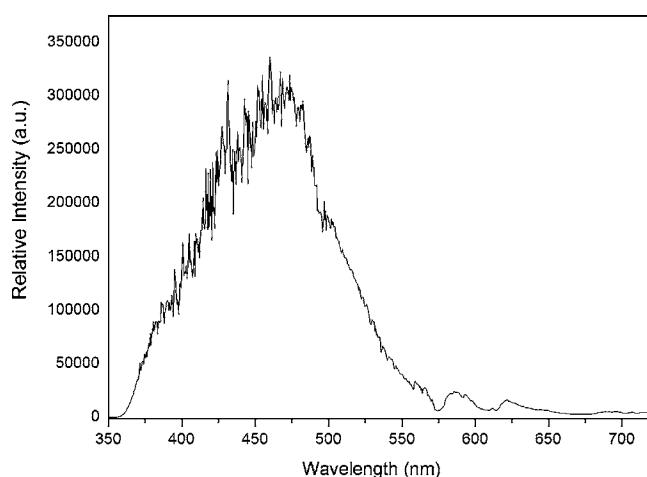

Figure 6. Emission spectrum of [Gd(DPA)(HDPA)(H$_2$O)$_2$]·4H$_2$O recorded at 77K and upon excitation at 280 nm.

Figure 7. Data comparison for emission spectra of [Eu(DPA)(HDPA)-(H$_2$O)$_2$]·4H$_2$O, expressed by branching ratios β_{OJ}.

The triplet state of the ligand was determined from the phosphorescence spectrum at 77 K from Gd compound. Since Gd^{3+} has no energy levels below 32 000 cm^{-1}, it cannot accept energy from the ligand triplet state. The triplet state energy was estimated from shortest-wavelength phosphorescence band, which was assumed as being 0−0 transition.[80] The Figure 6 shows the low-temperature phosphorescence spectrum of the Gd compound obtained in the range 370−720 nm when excited at 340 nm. As can be observed from Figure 6, the triplet state is centered at 460 nm (21 740 cm^{-1}), whose the theoretical values are in good agreement.

The energy transfer rates are larger for those levels dominated by the exchange mechanism, $^5D_0$ and $^5D_1$, than for those dominated by the dipole−dipole. Typical values of the remaining transfer rates were assumed to be identical to those found for coordination compounds, namely, $\Phi = 10^4$, $\Phi^{(1)} = 10^6$, $\Phi^{(2)} = 10^8$, and $\Phi^{(3)} = 10^5$ s^{-1}.[54] The energy transfer rates from the ligand triplet state (T1) to the $^5D_1$ and $^5D_0$ levels and energy transfer rates from the singlet state (S1) to the $^5D_4$ level are summarized in Table 3. Clearly, the values of the energy transfer rate indicate it is predominant from the triplet state of the ligand to the $^5D_1$ and $^5D_0$ levels of the Eu^{3+} ion.

The comparison between branching ratio, β_{OJ}, values for the $^5D_0 \rightarrow {}^7F_J$ transitions obtained from experimental spectrum
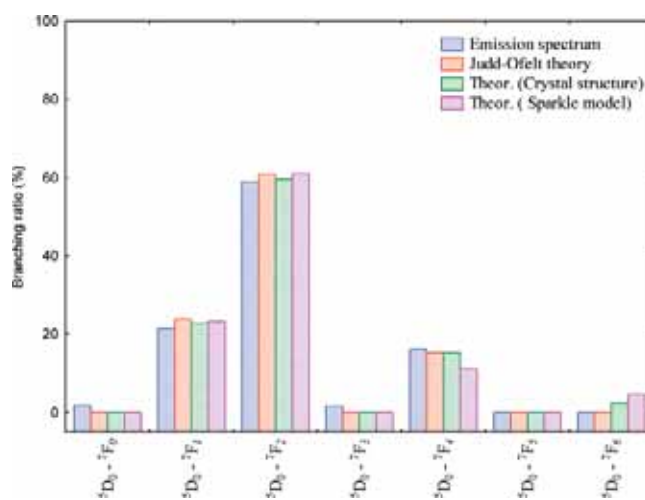
emission, with those estimated from the Judd-Ofelt theory and also those theoretically calculated the from crystallographic and simulated Sparkle/PM3 models is represented in Figure 7. As expected, the theoretical values are in very good agreement with those obtained experimentally.

The lifetime value (τ) of the $^5D_0$ level, the radiative (A_{rad}) and nonradiative (A_{nrad}) rates used in the quantum yield calculations, plus the theoretical quantum yields (derived from the Sparkle/PM3 and crystallographic structural models) are all given in Table 2. Notably, all values for the latter physical property are in perfect agreement with each other.

Conclusions

We have successfully reacted H$_2$DPA with Eu^{3+} under typical hydrothermal conditions to produce a photoluminescent material, [Eu(DPA)(HDPA)(H$_2$O)$_2$]·4H$_2$O, whose crystal structure was elucidated by single-crystal X-ray crystallography and showed to be composed by one-dimensional $_\infty^1$[Eu(DPA)(HDPA)-(H$_2$O)$_2$] coordination polymers, mutually interacting via an extensive hydrogen-bonding network composed of water clusters. The optimized molecular geometry for this material was obtained by employing the Sparkle/PM3 model, and shows a

[Eu(DPA)(HDPA)(H$_2$O)$_2$]·4H$_2$O

J. Phys. Chem. B, Vol. 112, No. 14, 2008 **4211**

very good agreement with crystallographic structure, thus rendering this in silico approach as a new and more efficient alternative over the traditional concepts used in the investigation of coordination polymers containing lanthanides ions.

The intensity parameters acquired experimentally (from emission spectra) are in excellent agreement with those calculated from both crystallographic and Sparkle/PM3 structures. The values of Ω_2 denote low covalent nature of the metal–ligand bonds thus showing that chemical environment around the Eu^{3+} metallic center is slightly polarizable. This observation was further confirmed by using the intensity ratio $^5D_0 \rightarrow {}^7F_2$/ $^5D_0 \rightarrow {}^7F_1$. Values for the intermolecular energy transfer rate indicate that the energy transfer is predominant from the triplet state of the ligand to the $^5D_1$ and $^5D_0$ levels of the Eu^{3+} ion. The small values calculated for the quantum efficiency, lifetime and quantum yield can be directly associated with nonradiative decay channels controlling the relaxation process of $^5D_0$ level, namely, the presence of water clusters which provide a structurally important source of O–H oscillators.

The calculated quantum yields obtained from the crystallographic and Sparkle/PM3 structural models (both of about 12.5%) are in good agreement with the experimental value (12.0 ± 5%). These results, associated with the excellent predictions of the intensity parameters, radiative rate, and quantum efficiencies certify the efficacy of the theoretical models used in all calculations and open new and interesting possibilities for the design in silico of highly efficient lanthanide–organic frameworks.

Supporting Information Available: Discussions about the crystallographic characterization of the compound. Additional drawings showing the TG/DTG curves; experimental setup used to measure the lifetimes of [Eu(DPA)(HDPA)(H$_2$O)$_2$]·4H$_2$O; a comparison between the FT-IR spectra of [Eu(DPA)(HDPA)-(H$_2$O)$_2$]·4H$_2$O and H$_2$DPA and emission spectra of [Eu(DPA)-(HDPA)(H$_2$O)$_2$]·4H$_2$O recorded at 300 K. This material is available free of charge via the Internet at http://pubs.acs.org.

References and Notes

(1) Bettencourt-Dias, A. *Inorg. Chem.* **2005**, *44*, 2734–2741.

(2) Mueller, U.; Schubert, M.; Teich, F.; Puetter, H.; Schierle-Arndt, K.; Pastré, J. *J. Mater. Chem.* **2006**, *16* (7), 626–636.

(3) Grant, A. B.; Marc, A. K.; Robin, D. R. *J. Alloys Comp.* **2002**, *344*, 123–127.

(4) Pan, L.; Huang, X.; Li, J.; Wu, Y.; Zeng. N. *Angew. Chem., Int. Ed.* **2000**, *39*, 527–530.

(5) Hifumi, H.; Yamaoka, S.; Tanimoto, A.; Citterio, D.; Suzuki, K. *J. Am. Chem. Soc.* **2006**, *128*, 15090–15091.

(6) Viswanathan, S.; Bettencourt-Dias, A. *Inorg. Chem.* **2006**, *45*, 10138–10146.

(7) Parvithran, R.; Kumar, N. S. S.; Biju, S.; Reddy, M. L. P.; Junior, S. A.; Freire, R. O. *Inorg. Chem.* **2006**, *45*, 2184–2192.

(8) Alpha, B.; Ballardinni, R.; Balzani, V.; Lehn, J. M.; Perathoner, S.; Sabbatini, N. *Angew. Chem., Int. Ed.* **1987**, *26*, 1266–1267.

(9) Shi, Q.; Zhang, S.; Wang, Q.; Ma, H.; Yang, G.; Sun, W. S. *J. Mol. Struct.* **2007**, *837*, 185–189.

(10) Choppin, G. R.; Bünzli, J. C. G. *Lanthanides Probes in Life Chemical and Earth Sciences Theory and Practice;* Elsevier: Amsterdam, 1989.

(11) Richardson, F. S. *Chem. Rev.* **1982**, *82*, 541–552.

(12) Kido, J.; Okamoto, Y. *Chem. Rev.* **2002**, *102*, 2357–2368.

(13) Zhao, B.; Chen, X. Y.; Cheng, P.; Liao, D. Z.; Yan, S. P.; Jiang, Z. H. *J. Am. Chem. Soc.* **2004**, *126*, 15394–15395.

(14) Wang, F. Q.; Zheng, X. J.; Wan, Y. H.; Sun, C. Y.; Wang, Z. S.; Wang, K. Z.; Jin, L. P. *Inorg. Chem.* **2007**, *46*, 2956–2958.

(15) Qin, C.; Wang, X. L.; Wang, E. B.; Su, Z. M. *Inorg. Chem.* **2005**, *44*, 7122–7129.

(16) Meskers, S. C. J.; Ubbink, M.; Canters, G. W.; Dekkers, H. P. J. M. *J. Phys. Chem.* **1996**, *100*, 17957–17969.

(17) Liu, M.; Zhao, L.; Lin, J. M. *J. Phys. Chem. A* **2006**, *110*, 7509–7514.

(18) Zhao, B.; Yi, L.; Dai, Y.; Chen, X. Y.; Cheng, P.; Liao, D. Z.; Yan, S. P.; Jiang, Z. H. *Inorg. Chem.* **2005**, *44*, 911–920.

(19) Fernades, A.; Jaud, J.; Dexpert-Ghys, J.; Brouca-Cabarrec, C. *Polyhedron* **2001**, *20*, 2385–2391.

(20) Brayshaw, P. A.; Hall, A. K.; Harrison, W. T. A.; Harrowfield, J. M.; Pearce, D.; Shand, T. M.; Skelton, B. W.; Whitaker, C. R.; White, A. H. *J. Eur. Inorg. Chem.* **2005**, 1127–1141.

(21) Mellot-Draznieks, C.; Férey, G. *Prog. Solid State Chem.* **2005**, *33*, 187–197.

(22) Dolg, M.; Stoll, H.; Savin, A.; Preuss, H. *Theor. Chim. Acta* **1989**, *75*, 173–194.

(23) Cundari, T. R.; Stevens, W. *J. Chem. Phys.* **1993**, *98*, 5555–5565.

(24) Dolg, M. *In Modern Methods and Algorithms of Quantum Chemistry*; Grotendorst, J., ed.; John von Neumann Institute for Computing, Jülich, NIC series, 2000, *1*, 479.

(25) Freire, R. O.; Rocha, G. B.; Simas, A. M. *Inorg. Chem.* **2005**, *44*, 3299–3310.

(26) Freire, R. O.; Rocha, G. B.; Simas, A. M. *J. Mol. Model.* **2006**, *12*, 373–389.

(27) Freire, R. O.; Rocha, G. B.; Albuquerque, R. Q.; Simas, A. M. *J. Lumin.* **2005**, *111*, 81–87.

(28) Albuquerque, R. Q.; Freire, R. O.; Malta, O. L. *J. Phys. Chem. A* **2005**, *109*, 4607–4610.

(29) Beltrão, M. A.; Santos, M. L.; de Mesquita, M. E.; Barreto, L. S.; Júnior, N. B. C.; Freire, R. O.; dos Santos, M. A. C. *J. Lumin.* **2006**, *116*, 132–138.

(30) da Costa, N. B.; Freire, R. O.; dos Santos, M. A. C.; de Mesquita, M. E. *J. Mol. Struct. (Theochem)* **2001**, *545*, 131–135.

(31) de Mesquita, M. E.; Junior, S. A.; Oliveira, F. C.; Freire, R. O.; Júnior, N. B. C.;de Sá, G. F. *Inorg. Chem. Commun.* **2002**, *5*, 292–295.

(32) Mesquita, M. E.; Junior, S. A.; Júnior, N. B. C.; Freire, R. O.; Silva, F. R. G.; Sá, G. F. *J. Solid State Chem.* **2003**, *171*, 183–188.

(33) de Mesquita, M. E.; Gonçalves e Silva, F. R.; Albuquerque, R. Q.; Freire, R. O.; da Conceição, E. C.; da Silva, J. E. C.; Júnior, N. B. C.; de Sá, G. F. *J. Alloys Comput.* **2004**, *366*, 124–131.

(34) Mesquita, M. E.; Junior, S. A.; Silva, F. R. G.; Couto, M. A. S.; Freire, R. O.; Júnior, N. B. C.; Sá, G. F. *J. Alloys Comput.* **2004**, *374*, 320–324.

(35) Pavithran, R.; Reddy, M. L. P.; Alves, S., Jr; Freire, R. O.; Rocha, G. B.; Lima, P. P. *Eur. J. Inorg. Chem.* **2005**, *20*, 4129–4127.

(36) Freire, R. O.; Silva, F. R. G.; Rodrigues, M. O.; Mesquita, M. E.; Júnior, N. B. C. *J. Mol. Model.* **2005**, *12*, 16–23.

(37) Freire, R. O.; Albuquerque, R. Q.; Júnior, S. A.; Rocha, G. B.; Mesquita, M. E. *Chem. Phys. Lett.* **2005**, *405*, 123–126.

(38) Brayshaw, P. A.; Hall, A. K.; Harrison, W. T. A.; Harrowfield, J. M.; Pearce, D.; Shand, T. M.; Skelton, B. W.; Whitaker, C. R.; White, A. H. *Eur. J. Inorg. Chem.* **2005**, 1127–1141.

(39) Bril, A.; De Jager-Veenis, A. W. *J. Res. Nat. Bureau Stand.* **1976**, *80A*, 401–407.

(40) Malta, O. L.; Brito, H. F.; Menezes, J. F. S.; Gonçalves e Silva, F. R.; de Mello, Donegá, C.; Alves, Jr. S. *Chem. Phys. Lett.* **1998**, *282*, 233–238.

(41) Stewart, J. J. P. *MOPAC2007*, Version 7.058; Stewart Computational Chemistry: Colorado Springs, CO, 2007.

(42) Ridley, J. E.; Zerner, M. C. *Theor. Chim. Acta* **1976**, *42*, 223–236.

(43) Zerner, M. C.; Loew, G. H.; Kirchner, R. F.; Mueller-Westerhoff, U. T. *J. Am. Chem. Soc.* **1980**, *102*, 589–599.

(44) Zerner, M. C. *ZINDO manual*, QTP, University of Florida: Gainesville, FL 32611, 1990.

(45) Judd, B. R. *Operator Techniques in Atomic Spectroscopy*, 2nd ed. McGraw-Hill Book Company: New York, 1998.

(46) Guan, J.; Chen, B.; Sun, Y.; Liang, H.; Zhang, Q. *J. Non-Cryst. Solids* **2005**, *351*, 849–855.

(47) Judd, B. R. *Phys. Rev.* **1962**, *127*, 750–761.

(48) Ofelt, G. S. *J. Chem. Phys.* **1962**, *37*, 511–520.

(49) Malta, O. L.; Ribeiro, S. J. L.; Faucher, M.; Porcher, P. *J. Phys. Chem. Solids* **1991**, *52*, 587–593.

(50) Malta, O. L.; Couto dos Santos, M. A.; Thompson, L. C.; Ito, N. K. *J. Lumin.* **1996**, *69*, 77–84.

(51) Malta, O. L.; Brito, H. F.; Meneses, J. F. S.; e Silva, F. R. G.; Alves, S., Jr.; Farias, F. S., Jr.; de Andrade, A. V. M. *J. Lumin.* **1997**, *75*, 255–268.

4212 *J. Phys. Chem. B, Vol. 112, No. 14, 2008*

Rodrigues et al.

(52) de Sá, G. F.; Malta, O. L.; de Mello Donegá, C.; Simas, A. M.; Longo, R. L.; Santa-Cruz, P. A.; da Silva, E. F., Jr. *Coord. Chem. Rev.* **2000**, *196*, 165−195.

(53) Malta, O. L.; e Silva, F. R. G. *Spectrochim. Acta Part A* **1998**, *54*, 1593−1599.

(54) Malta, O. L.; e Silva, F. R. G.; Longo, R. *Chem. Phys. Lett.* **1999**, *307*, 518−526.

(55) Carnall, W. T.; Crosswhite, H.; Crosswhite, H. M. *Energy Structure and Transition Probabilities of the Trivalent Lanthanides in LaF3*; Argonne National Laboratory Report; unnumbered, 1977.

(56) Araujo, A. A. S.; Brito, H. F.; Malta, O. L.; Matos, J. R.; Teotônio, E. E. S.; Storpirtis, S.; Izumi, C. M. S. *J. Ionrg. Biochem.* **2002**, *88*, 87−93.

(57) Van Deun, R.; Binnemans, K.; Görrler-Walrand, C.; Adam, J. L. *J. Phys. Condens. Matter* **1998**, *10*, 7231−7241.

(58) Weber, M. J.; Varitimos, T. E.; Matsinger, B. H. *Phys. Rev. B* **1973**, *8*, 47−53.

(59) Brayshaw, P. A.; Bünzli, J. C. G.; Froidevaux, P.; Harrowfield, J. M.; Kim, Y.; Sobolev, A. N. *Inorg. Chem.* **1995**, *34*, 2068−2076.

(60) Zhao, B.; Chen, X. Y.; Cheng, P.; Liao, D. Z.; Yan, S. P.; Jiang, Z. H. *J. Am. Chem. Soc.* **2004**, *126*, 15394−15395.

(61) Renaud, F.; Piguet, C.; Bernardinelli, G.; Bunzli, J. C. G.; Hopfgartner, G. *Chem.-Eur. J.* **1997**, *3*, 1660−1667.

(62) Brayshaw, P. A.; Harrowfield, J. M.; Sobolev, A. N. *Acta Cryst. C* **1995**, *51*, 1799−1802.

(63) Brayshaw, P. A.; Bunzli, J. C. G.; Froidevaux, P.; Harrowfield, J. M.; Kim, Y.; Sobolev, A. N. *Inorg. Chem.* **1995**, *34*, 2068−2076.

(64) Zhou, D. J.; Huang, C. H.; Wang, K. Z.; Xu, G. X. *Polyhedron* **1994**, *13*, 987−991.

(65) Bernstein, J.; Davis, R. E.; Shimoni, L.; Chang, N. L. *Angew. Chem., Int. Edit. Engl.* **1995**, *34*, 1555−1573.

(66) Doedens, R. J.; Yohannes, E.; Khan, M. I. *Chem. Commun.* **2002**, *1*, 62−63.

(67) Binnemans, K.; Van Herck, K.; Göller-Walard, C. *Chem. Phys. Lett.* **1997**, *266*, 297−302.

(68) Bejan, C. C. C.; Rocha, G. B.; Albuquerque, R. Q.; Demnitz, F. W. J.; de Sá, G. F.; Júnior, S. A. *J. Lumin.* **2005**, *113*, 79−88.

(69) Klink, S. I.; Graves, L.; Reinhoudt, D. N.; van Veggel, F. C. J. M.; Werts, M. H. V.; Geurts, F. A. J.; Hofstraat, J. W. *J. Phys. Chem. A* **2000**, *104*, 5457−5468.

(70) Georgge, M. R.; Golden, C. A.; Grossel, M. C.; Curry, R. J. *Inorg. Chem.* **2004**, *43*, 6887−6889.

(71) Tedeschi, C.; Azéma, J.; Gornitzka, H.; Tisnès, P.; Picard, C. *J. Chem. Soc., Dalton Trans.* **2003**, *9*, 1738−1745.

(72) An, Y.; Berry, M. T.; van Veggel, F. C. J. M. *J. Phys. Chem. A* **2000**, *104*, 11243−11247.

(73) May, P. S.; Richardson, F. S. *Chem. Phys. Lett.* **1991**, *179*, 277−281.

(74) Förster, T. *Discuss. Faraday Soc.* **1959**, *27*, 7−17.

(75) Dexter, D. L. *J. Chem. Phys.* **1953**, *21*, 836−850.

(76) Lima, P. P.; Sá, F. R. A.; Freire, R. O.; Paz, F. A. A.; Fu, L.; Júnior, S. A.; Carlos, L. D.; Malta, O. L. *Chem. Phys. Chem.* **2006**, *7*, 735−746.

(77) Mesquita, M. E.; de Sá, G. F.; Malta, O. L. *J. Alloys Comput.* **1998**, *275*, 844−847.

(78) Driesen, K.; Fourier, S.; Göller-Walrand, C.; Binnemans, K. *Phys. Chem. Chem. Phys.* **2003**, *5*, 198−202.

(79) Santos, E. R.; Santos, M. A. C.; Freire, R. O.; Júnior, S. A.; Barreto, L. S.; Mesquita, M. E. *Chem. Phys. Lett.* **2006**, *418*, 337−341.

(80) Chandler, B. D.; Cramb, D. T.; Shimidzu, G. K. H. *J. Am. Chem. Soc.* **2006**, *128*, 10403−10412.

Theoretical and Experimental Studies of the Photoluminescent Properties of the Coordination Polymer [Eu(DPA)(HDPA)(H₂O)₂]·4H₂O.

Supporting Information

Marcelo O. Rodrigues[1]*, Nivan B. Costa Júnior[2], Carlos A. de Simone[3], Adriano A. S. Araújo[2], A. M. Brito-Silva[4], Filipe A. Almeida Paz[5], Maria E. de Mesquita[2]; Severino A. Júnior[1]*and Ricardo O. Freire[2]*

[1] Departamento de Química Fundamental, UFPE, 50590-470, Recife - PE, Brazil.
[2] Departamento de Química, UFS, 49100-000, São Cristóvão - SE, Brazil.
[3] Departamento de Química, UFAL, 57072-970, Maceió – AL, Brazil
[4] Pós-Graduação em Ciência de Materiais, UFPE, 50590-470, Recife - PE, Brazil
[5] Departamento de Química, CICECO, Universidade de Aveiro, 3810-193, Aveiro, Portugal..

Author email address: mzohio@hotmail.com (Marcelo O. Rodrigues);
salvesjr@ufpe.br (Severino Alves Júnior)
rfreire@ufs.br (Ricardo O. Freire)

Single-Crystal X-ray Diffraction (crystallographic characterization of the compound)

A suitable single-crystal of [Eu(DPA)(HDPA)(H$_2$O)$_2$]·4H$_2$O (where H$_2$DPA stands for pyridine-2,6-dicarboxylic acid) was manually harvested from the crystallization vial and mounted on a glass fibre.[1] Data were collected at ambient temperature on a Nonius Kappa charge-coupled device (CCD) area-detector diffractometer (Mo K$_\alpha$ graphite-monochromated radiation, λ = 0.7107 Å) controlled by the Collect software package.[1] Images were processed using the software packages Denzo and Scalepack,[3] and data were corrected for absorption by the empirical method implemented in SADABS.[4] The structure was solved using the direct methods implemented in SHELXS-97,[5] which allowed the immediate location of the majority of the heavy atoms. All the remaining non-hydrogen atoms were directly located from difference Fourier maps calculated from successive full-matrix least squares refinement cycles on F^2 using SHELXL-97.[6] All non-hydrogen atoms were successfully refined using anisotropic displacement parameters.

Hydrogen atoms associated with all water molecules (both coordinated and housed within the channels present in the structure) were directly located from difference Fourier maps, and included in the final structural model with the O–H and H···H distances restrained to 0.95(1) Å and 1.55(1) Å, respectively (in order to ensure a chemically reasonable geometry for these molecules), and using a riding model with an isotropic displacement parameter fixed at *1.5* times U_{eq} of the atom to which they are attached. Even though an approximate position for the hydrogen atom of the protonated carboxylic acid group of HDPA$^-$ could also be determined from determined from difference Fourier maps, the atomic parameters for this atom were instead restrained to produce the final structural model by using the *HFIX 147* instruction in SHELXL. Hydrogen atoms attached to carbon were located at their idealized positions by employing the *HFIX 43* instructions in SHELXL, and included in subsequent refinement cycles in riding-motion approximation with isotropic thermal displacements parameters (U_{iso}) fixed at 1.2 times U_{eq} of the carbon atom to which they are attached.

The last difference Fourier map synthesis showed the highest peak (1.291 eÅ^{-3}) and deepest hole (-1.838 eÅ^{-3}) located at 0.91 Å and 0.81 Å, respectively, from Eu.

Information concerning crystallographic data collection and structure refinement details is summarized in Table S1. Hydrogen bonding geometric details is given in Table S2.

Table S1 - Crystal and Structure Refinement Data for [Eu(DPA)(HDPA)(H$_2$O)$_2$]·4H$_2$O.

Formula	C$_{14}$H$_{19}$EuN$_2$O$_{14}$
Formula weight	591.27
Crystal system	Monoclinic
Space group	$P2_1/a$
a/Å	12.8310(2)
b/Å	11.2170(4)
c/Å	13.9930(4)
α/º	90
β/º	102.474(2)
γ/º	90
Volume/Å^3	1966.41(9)
Z	4
D_c/g cm^{-3}	1.997
μ(Mo-Kα)/mm^{-1}	3.268
Crystal size/mm	0.21×0.16×0.11
θ range	2.67 to 27.49
Index ranges	$-16 \leq h \leq 16$
	$-14 \leq k \leq 13$
	$-14 \leq l \leq 18$
Reflections collected	14940
Independent reflections	4467 (R_{int} = 0.0432)
Completeness to θ = 27.49º	98.8%
Final R indices [I>2σ(I)]^{a,b}	R1 = 0.0271
	wR2 = 0.0707
Final R indices (all data)^{a,b}	R1 = 0.0293
	wR2 = 0.0723
Weighting scheme^c	m = 0.0366
	n = 2.4610
Largest diff. peak and hole	1.291 and -1.838 eÅ^{-3}

$$^a R1 = \sum \left\| F_o \right| - \left| F_c \right\| / \sum \left| F_o \right|; \quad ^b wR2 = \sqrt{\sum \left[w \left(F_o^2 - F_c^2 \right)^2 \right] / \sum \left[w \left(F_o^2 \right)^2 \right]}$$

$$^c w = 1/\left[\sigma^2 \left(F_o^2 \right) + \left(mP \right)^2 + nP \right] \text{ where } P = \left(F_o^2 + 2F_c^2 \right)/3$$

The hydrothermal reaction between Eu$_2$O$_3$ and pyridine-2,6-dicarboxylic acid (H$_2$DPA) led to the isolation of a large amount of a single-crystalline phase composed by crystals exhibiting a parallelepipedic morphology, whose structure was ultimately unveiled from single-crystal X-ray diffraction studies at ambient temperature and formulated as [Eu(DPA)(HDPA)(H$_2$O)$_2$]·4H$_2$O (Table 1).

Table S2 - Hydrogen bonding geometry (distances in Å and angles in degrees) for [Eu(DPA)(HDPA)(H$_2$O)$_2$]·4H$_2$O.[a]

D–H···A	d(D···A)	<(DHA)
O(2)–H(2)···O(3W)	2.478(4)	175(1)
O(1W)–H(1A)···O(4)[i]	2.733(3)	167(4)
O(1W)–H(1B)···O(6)	2.718(3)	155(3)
O(2W)–H(2A)···O(5W)[ii]	2.723(3)	161(3)
O(2W)–H(2B)···O(6W)	2.744(3)	165(3)
O(3W)–H(3A)···O(4)[iii]	2.641(4)	174(5)
O(3W)–H(3B)···O(4W)[iii]	2.799(5)	143(4)
O(4W)–H(3B)···O(3)	2.950(4)	157(5)
O(5W)–H(3B)···O(8)[iv]	2.686(3)	172(4)
O(5W)–H(3B)···O(6W)[v]	2.903(4)	147(3)
O(6W)–H(3B)···O(7)[vi]	2.916(3)	162(3)
O(6W)–H(3B)···O(8)[vii]	2.893(3)	175(4)

[a] Symmetry transformations used to generate equivalent atoms: (i) ½-x, -½+y, 1-z; (ii) ½-x, ½+y, 2-z; (iii) x, -1+y, z; (iv) ½+x, ½-y, z; (v) -½+x, ½-y, z; (vi) 1+x, y, z; (vii) ½-x, -½+y, 2-z.

It is noteworthy to mention that a previous report of this material has been recently published by Harrowfield and collaborators[7] during their investigations of novel materials to be used as precursors for the isolation of lanthanide/transition metals mixed oxides. Since in that paper the structural features of this material were not described in the context of the Crystal Engineering of MOFs, we have redetermined its crystal structure and summarize in the following paragraphs the most relevant aspects which are of considerable importance for the theoretical studies performed and here described. A search in the literature and in the Cambridge Structural Database (CSD, Version 5.28, November 2006)[8]-[9] also reveals that H$_2$DPA has been widely employed in the isolation of multi-dimensional MOF materials[10]-[23].

The supramolecular structure of [Eu(DPA)(HDPA)(H$_2$O)$_2$]·4H$_2$O is essentially mediated by the extensive hydrogen bonding network involving the various types of water molecules present in the structure. The coordinated water molecule O(1W) acts as a bifurcated donor promoting, on the one hand, structural cohesion of the $_\infty^1$[Eu(DPA)(HDPA)(H$_2$O)$_2$] coordination polymer via the O(1W)–H(1B)···O6 interaction with a neighboring coordinated PDA^{2-} residue and, on the other, it establishes a hydrogen bonding bridge with an adjacent polymer by donating the H(1A) hydrogen to the HPDA$^-$ (Figure S1a and Table S2 for details on the hydrogen bonding geometry). These recursive supramolecular interactions along the

[100] direction of the unit cell lead to the formation of a bilayer arrangement of $_\infty^1[Eu(DPA)(HDPA)(H_2O)_2]$ coordination polymers as depicted in Figure S1b.

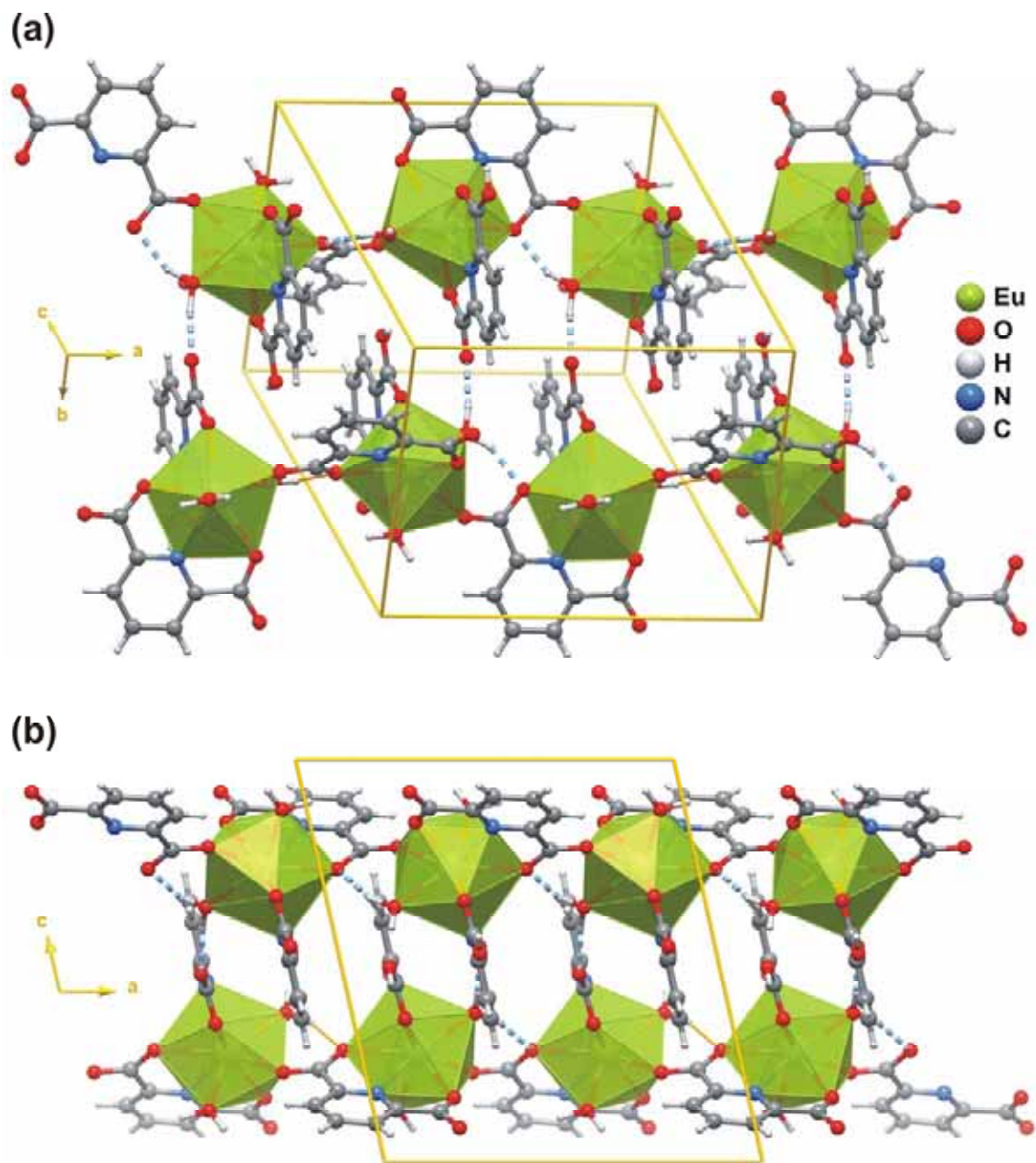**Figure S1 – (a)** Schematic representation of the hydrogen bonding interactions establishing physical links between neighboring $_\infty^1[Eu(DPA)(HDPA)(H_2O)_2]$ coordination polymers and which lead to **(b)** bilayers placed in the *ab* crystallographic plane. Hydrogen bonds are represented as ligh-blue dashed lines.

Another interesting structural feature of the compound in study resides in the fact that supramolecular connections along the [001] crystallographic direction between adjacent bilayers of polymers are remarkably assured by a typical centrosymmetric hexameric water cluster involving the coordinated water molecule O(2W) plus another two solvent molecules housed within the interlayer space [O(5W) and O(6W)] (see Figure S2 and Table S2 for details on the hydrogen bonding geometry of each individual interaction). This cluster, characterized by a graph set motif of $R_2^6(12)$, exhibits a chair-like configuration with a very much identical to that commonly found in a number of compounds reported in the literature and also in I_h ice.
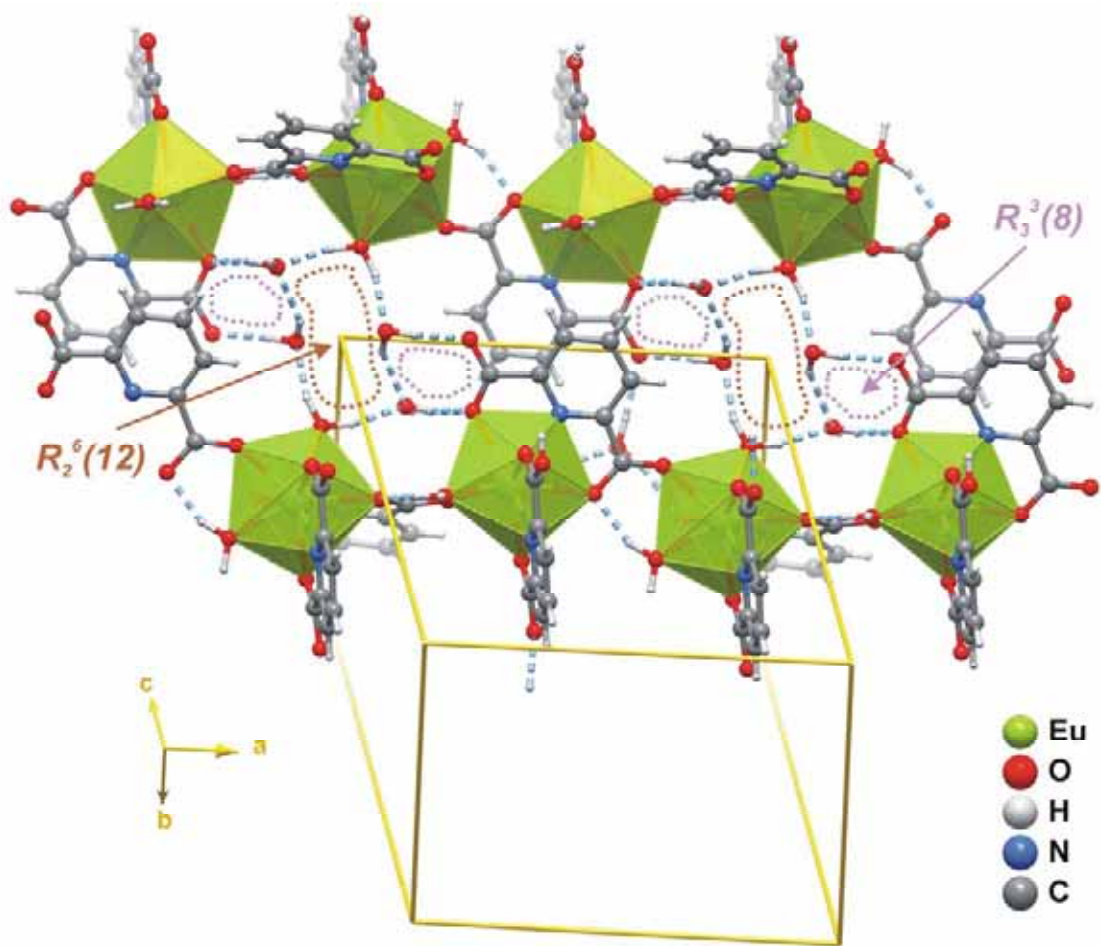
Figure S2 –Schematic representation of the centrosymmetric hexameric water clusters [composed by the O(2W) coordinated water molecule plus O(5W) and O(6W) located in the interlayer space] interconnecting neighboring $_\infty^1$[Eu(DPA)(HDPA)(H$_2$O)$_2$] coordination polymers via a recursive $R_2^6(12)$ decorated by two identical $R_3^3(8)$ graph set motifs. Hydrogen bonds are represented as ligh-blue dashed lines. For geometrical details on the hydrogen bonds see Table S2.
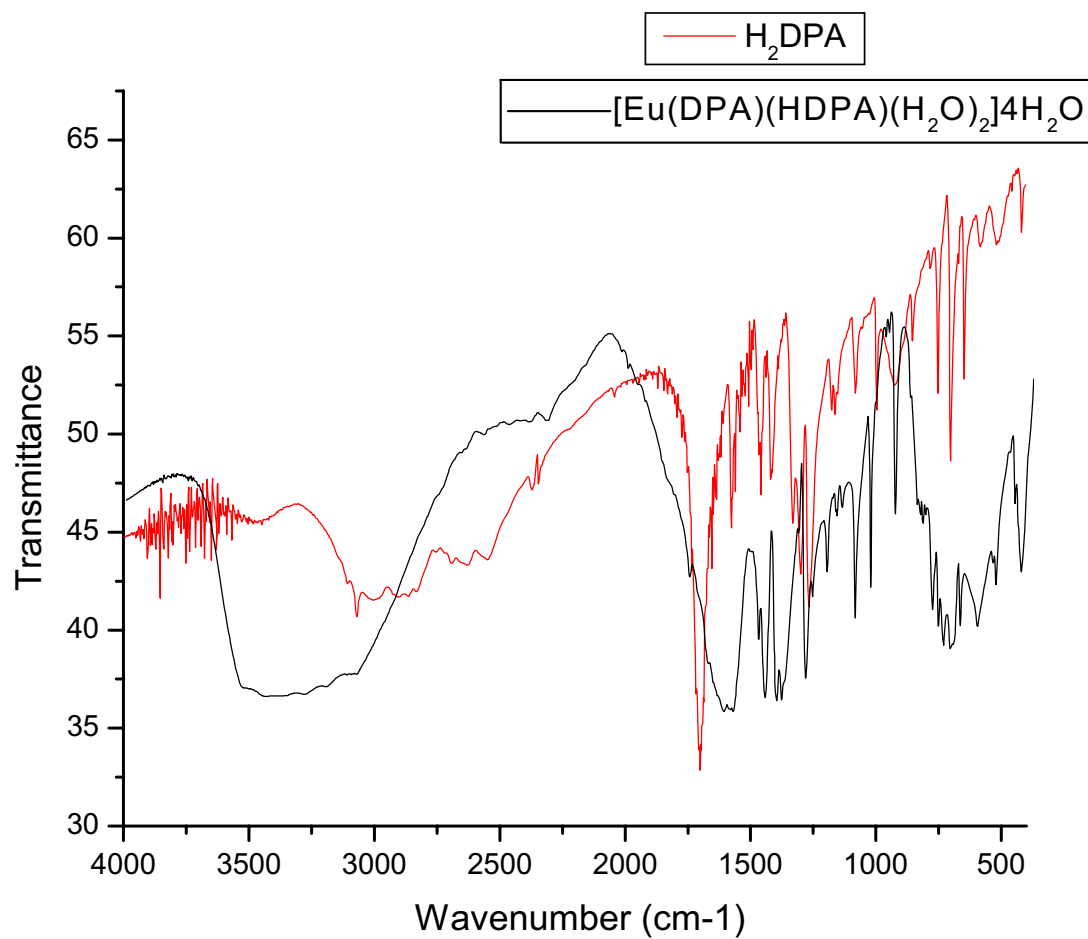
Figure S3: Comparison of the FTIR spectrums between the compounds [Eu(DPA)(HDPA)(H$_2$O)$_2$].4H$_2$O and H$_2$DPA at 300K.
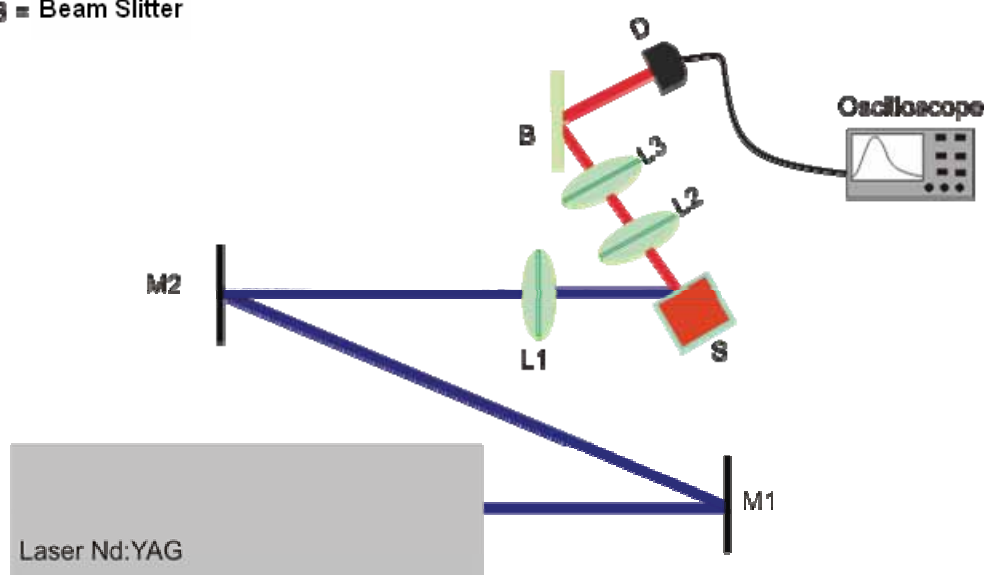
Figure S4. The experimental arrangement used to lifetime measurement of [Eu(DPA)(HDPA)($H_2O)_2$]. $4H_2O$ complex.
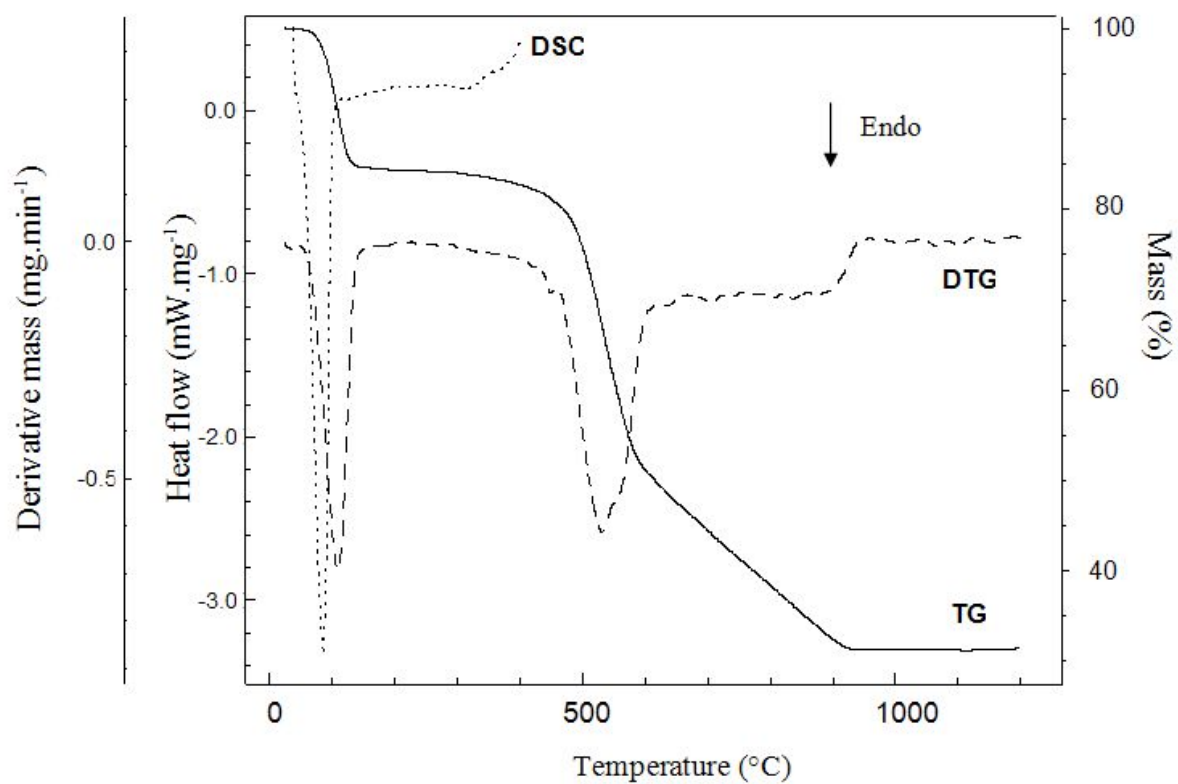
Figure S5: TG/DTG curves recorded in dynamic nitrogen atmosphere (50 ml.min^{-1}), and heating rate 10°C.min^{-1}

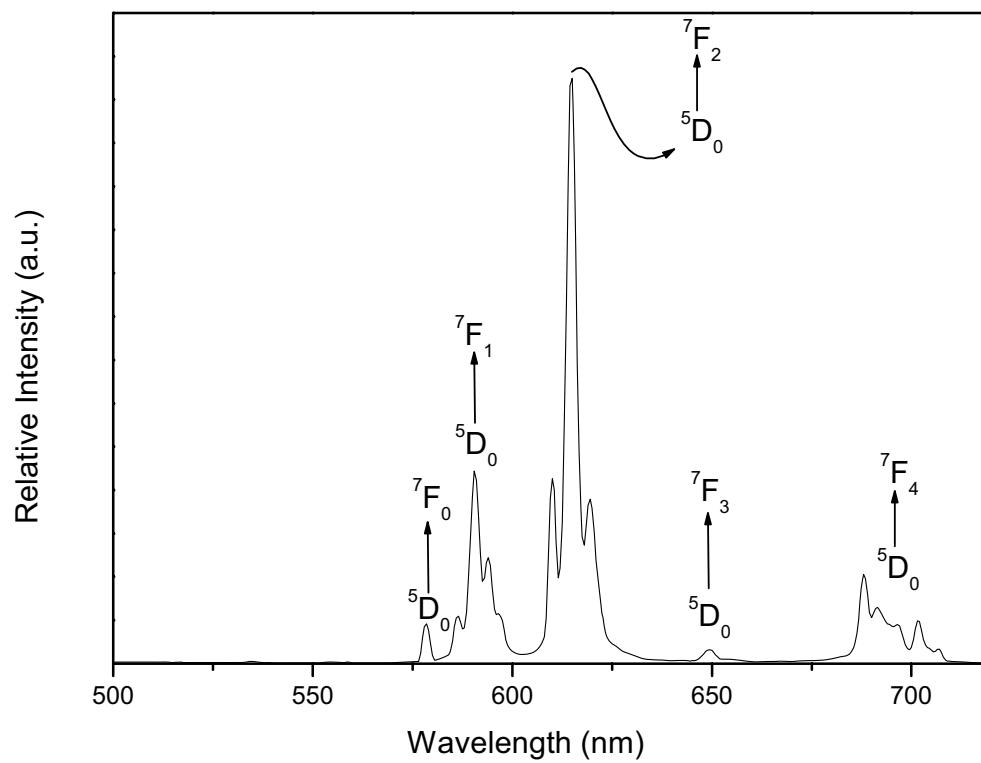**Figure S6-** Emission spectra of [Eu(DPA)(HDPA)(H$_2$O)$_2$]·4H$_2$O recorded at 300 K by monitoring excitation of ligand at 280 nm.

References

(1)   Kottke, T.; Stalke, D. *J. App. Cryst.* **1993**, *26*, 615-619.

(2)   Hooft, R. *Collect: Data Collection Software, Delft, The Netherlands, Nonius B. V.* **1998**.

(3)   Otwinowski, Z.; Minor, W., In *Methods in Enzymology*, Carter Jr., C. W.; Sweet, R. M., Eds. Academic Press: New York, **1997**; Vol. 276, p 307.

(4)   Sheldrick, G. M. *SADABS v.2.01, Bruker/Siemens Area Detector Absorption Correction Program* **1998**, *Bruker AXS, Madison, Wisconsin, USA*.

(5)   Sheldrick, G. M. *SHELXS-97, Program for Crystal Structure Solution, University of Göttingen* **1997**.

(6)   Sheldrick, G. M. *SHELXL-97, Program for Crystal Structure Refinement, University of Göttingen* **1997**.

(7)   Brayshaw, P. A.; Hall, A. K.; Harrison, W. T. A.; Harrowfield, J. M.; Pearce, D.; Shand, T. M.; Skelton, B. W.; Whitaker, C. R.; White, A. H. *Eur. J. Inorg. Chem.* **2005**, 1127-1141.

(8)   Allen, F. H. *Acta Cryst. B* **2002**, *58*, 380-388.

(9)   Allen, F. H.; Motherwell, W. D. S. *Acta Cryst. B* **2002**, *58*, 407-422.

(10)   Ramezanipour, F.; Aghabozorg, H.; Shokrollahi, A.; Shamsipur, M.; Stoeckli-Evans, H.; Soleimannejad, J.; Sheshmani, S. *J. Mol. Struct.* **2005**, *779*, 77-86.

(11)   Prasad, T. K.; Rajasekharan, M. V. *Inorg. Chem. Commun.* **2005**, *8*, 1116-1119.

(12)   Prasad, T. K.; Sailaja, S.; Rajasekharan, M. V. *Polyhedron* **2005**, *24*, 1487-1496.

(13)   Liu, S. H.; Li, Y. Z.; Meng, Q. J. *Acta Cryst. E* **2005**, *61*, M1111-M1113.

(14)   Zhao, B.; Yi, L.; Dai, Y.; Chen, X. Y.; Cheng, P.; Liao, D. Z.; Yan, S. P.; Jiang, Z. H. *Inorg. Chem.* **2005**, *44*, 911-920.

(15)   Ghosh, S. K.; Bharadwaj, P. K. *Inorg. Chem.* **2004**, *43*, 2293-2298.

(16)   Duan, L. Y.; Li, Y. G.; Liu, F. C.; Wang, E. B.; Wang, X. L.; Hu, C. W.; Xu, L. *J. Mol. Struct.* **2004**, *689*, 269-274.

(17)   Ghosh, S. K.; Bharadwaj, P. K. *Inorg. Chem.* **2003**, *42*, 8250-8254.

(18)   Brouca-Cabarrecq, C.; Fernandes, A.; Jaud, J.; Costes, J. P. *Inorg. Chim. Acta* **2002**, *332*, 54-60.

(19)   Sailaja, S.; Rajasekharan, M. V. *Acta Cryst. E* **2001**, *57*, M341-M343.

(20)   Fernandes, A.; Jaud, J.; Dexpert-Ghys, J.; Brouca-Cabarrecq, C. *Polyhedron* **2001**, *20*, 2385-2391.

(21)   Rzaczynska, Z.; Brzyska, W.; Mrozek, R.; Ozga, W.; Glowiak, T. *J. Coord. Chem.*
       1998, *43*, 321-334.

(22)   Swarnabala, G.; Rajasekharan, M. V. *Inorg. Chem.* **1998**, *37*, 1483-1485.

(23)   Starynowicz, P. *Acta Cryst. C* **1992**, *48*, 1428-1430.

High Photoluminescent Metal-Organic Frameworks as Optical Markers for the Identification of Gunshot Residues.

Ingrid Távora Weber[1], Adenaule James Geber de Melo[1,2], Marcella Auxiliadora de Melo Lucena[1], Marcelo Oliveira Rodrigues[1], Severino Alves Junior[1]

.

[1]Departamento de Química Fundamental, Universidade Federal de Pernambuco, Av. Prof. Luiz Freire, S/N, Cidade Universitária, 50740-540 Recife, PE, Brazil.

[2]Instituto de Criminalística, Centro de Perícias Forenses de Alagoas, Rua do Sol, 290, Centro, Maceió, AL, Brazil

ABSTRACT Gunshot residue (GSR) are solid particles produced after a firearm is discharged, and its detection is important evidence in forensic investigations. Currently, SEM-EDS is the standard technique adopted for the analysis and identification of GSR, however this methodology is inefficient for lead-free ammunition. Herein, we report the inclusion of high photoluminescent Metal-Organic Frameworks in ammunition to allow for the visual detection of GSR. The tests indicated that marked GSR is easily visible in proportions above 5.0 wt%. One gram of marker suffices to tag one hundred .38mm bullets or sixty-two .40mm bullets.

Gunshot residue (GSR) consists of solid particles produced when a firearm is discharged, and its detection provides very important evidence in forensic investigations.[1] GSR is used to estimate the distance at which a bullet is shot, recognize bullet holes, and provide important information to pinpoint suspects, deny or confirm an alibi, differentiate between homicide and suicide, etc.[2] This is possible because some of the discharged residue remains on the gun and is also normally deposited on the perpetrator's hands, clothes, hair and body.[3]

Since the early 20th century, several methodologies have been proposed to identify GSR. Initially, colorimetric methods were employed to identify barium, lead and nitrites through chemical reactions with sodium rhodizonate and *para*-sulfanilic acid (Griess reagent).[4] Although these methods involve fairly simple procedures, their results cannot be considered conclusive since they produce a high percentage of false-negatives due to their low sensitivity and high instability of the chemical species (nitrites). Moreover, colorimetric methods do not indicate whether the analytes originate from environmental or occupational contamination or from a weapon discharge.[5]

The 1960s and 70s saw the introduction of Neutron Activation Analysis (NAA) and Flameless Atomic Absorption Spectroscopy (FAAS), which served to determine barium and lead antimony, respectively. Although these methodologies allow for the determination of small amounts of metallic elements, the problem of identifying the origin of particles remains. Moreover, both these techniques require very specific instrumentation, and their results may be compromised by organic molecules.[6] The introduction of Scanning Electron Microscopy coupled to Energy Dispersive Spectroscopy (SEM-EDS) provided more reliable criteria for the identification of GSR. When a shot is fired, the residue is subjected to extreme conditions of pressure and temperature, causing the particles to assume a spheroidal shape.[7] The morphology and peculiar chemical composition of the residue enables one to distinguish between GSR and residue of environmental or occupational origin.[8] Therefore, SEM-EDS was adopted as a standard procedure for the analysis and identification of GSR.[9] Spheroidal particles consisting of both lead-antimony-barium and antimony-barium are undoubtedly considered GSR and all other combinations of characteristic metals should be assumed to be indicative of GSR.[10]

Recently, a new type of lead-free ammunition was introduced on the market. The SEM-EDS methodology is ineffective for this *clean* or *environmental* type of ammunition because it is impossible to identify the characteristic metals. Martiny *et al.* stated that the absence of a specific chemical taggant makes it very difficult to identify lead-free GSR particles, since none of the detected elements can be considered unique or characteristic of firearm handling for purposes of identification.[11]

The above described scenario justifies the need for the development of a low-cost, fast and powerful method for identifying GSR. In this perspective, our group recently proposed the inclusion of high photoluminescent markers in ammunition to allow for the visual detection of GSR.[12] It should be noted that this practical approach simplifies investigative routines considerably, enabling the identification of GSR directly at a crime scene using only an ultraviolet lamp. In addition, these markers are composed of a unique chemical composition not commonly found in the environment or in occupational tasks.

The materials proposed in this work are based on a class of crystalline materials that in the last 15 years has attracted wide attention of scientific community. Metal-Organic Frameworks (MOFs), also known as Coordination Polymers, are promising for development of the markers due to high thermal and chemical stability.[13] In terms of optical properties Lanthanide–Organic Framework (LOFs) have great potential to be efficiently used as highly photoluminescent markers, since these compounds may act as Light-Conversion Molecular Devices (LCMDs).[14]

To the best of our knowledge, only two studies have dealt with luminescent recognition of GSR. These works report the detection of lead and antimony emissions (at 385 and 660 nm, respectively) at cryogenic temperatures under Xe lamp excitation.[15] However, these methodologies are evidently unsuitable for lead-free ammunition.

The makers described in this work are based in two isostructural 2D MOFs previously reported,[16] $_\infty$[Ln(DPA)(HDPA)], where H$_2$DPA is pyridine 2,6-dicarboxylic acid and Ln= Eu^{3+} and Tb^{3+}ions. It is important to note that Eu^{3+} and Tb^{3+} materials were designed as *R-Marker and G-Marker* respectively. Crystallographic structure, powder patterns and final Rietveld plot for the materials are disposal in the Supporting Information.

Figure 1 shows the *R-Marker and G-Marker* as prepared and after shooting on the target surface, on the firearms and on the shooter's hand after firing, all subjected to irradiation under an UV lamp.
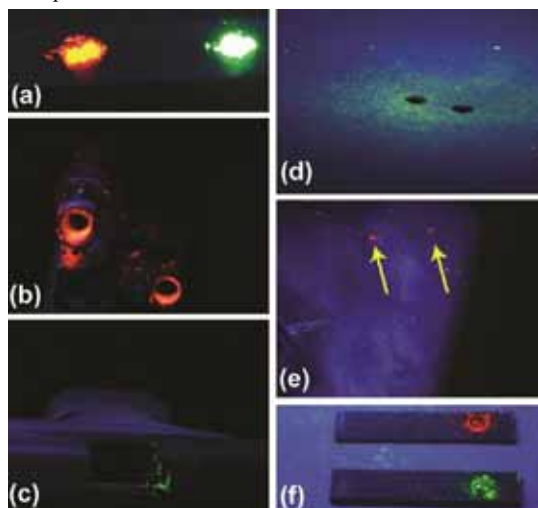

Figure 1. Images of the *R-* and *G-Markers* under Uv lamp exposition. (a): *R-Marker* and *G-Marker* as-prepared; (b) *R-Marker* on .38 gun after shot. (c): *G-Marker* on the .40 gun pistol after shot; (d) *G-Marker* on the target surface; (e) *R-Marker* on the shooter's hand (*R-Marker* residues are indicated by yellow arrows); (f) Lead-free ammunition primers' residues containing *R* and *G-Markers*

The materials are highly photoluminescent and their optical properties remain unaltered after a bullet is fired. The marked GSR was identified visually on the shooter's hand and clothes, on the gun and on the target surface, as depicted in Figure 1. The samples collected from the target surface remained luminescent for more than 30 months, even when stored in a damp environment. These results clearly attest to the efficacy and simplicity of the method, confirming the significant characteristics of the markers, i.e., (i) thermal stability — resistance to the high firing temperatures; (ii) chemical inertia — nonreactive with gunpowder, primer or the metallic parts of a gun, (iii) high luminescence; and (iv) long-term stability – remaining luminescent after long periods of time.

The tests indicated that marked GSR is easily visible in proportions above 5.0 wt%. At lower concentrations of markers, GSR particles are difficult to identify visually, but the methodology proposed here is not compromised and homogenization should allow this value to be reduced.

The emission spectra of *R-Marker* and *G-Marker* acquired at room temperature by respective excitations at maxima absorption of the organic matrices, 291 and 294 nm, display the typical red and green emissions associated with Eu^{3+} $^5D_0{\rightarrow}^7F_J$ and Tb^{3+} $^5D_4{\rightarrow}^7F_J$ transitions. After the shots, the characteristic transitions of Eu^{3+} and Tb^{3+} ions were found to be similar to those of the pure markers, suggesting that the markers' structures had not undergone any significant change. It should be noted that Eu^{3+} transitions, in particular, are affected by the chemical environment of the first coordination sphere.[17] Therefore, the relative intensity and splitting of the respective transitions serve to confirm the robustness of the markers, since they resist the extreme conditions that prevail when the bullet is fired.
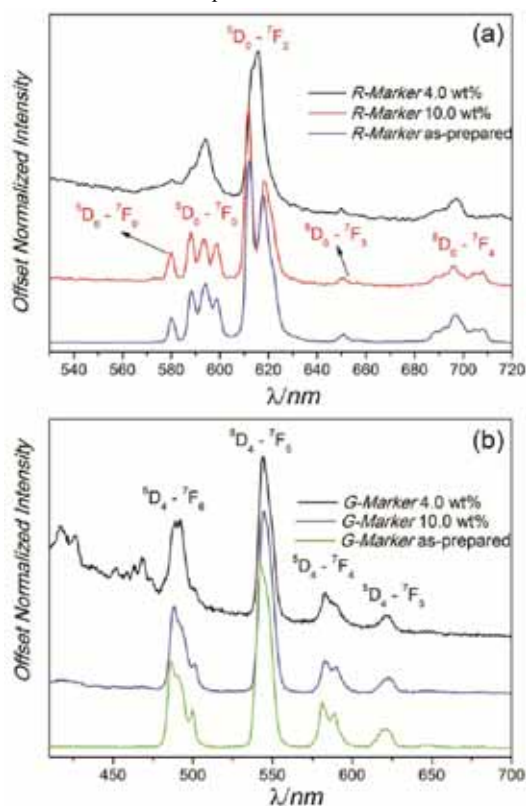

Figure 2. Emission spectra of the Markers as-prepared and marker-tagged primer after discharging. (a):*R-Marker*; (b) *G-Marker*.

FTIR spectra of the pure *G-Marker*, the pure ignited primer and the ignited primer containing 10.0 wt% of *G-Marker* are shown in Figure 3. The FTIR spectrum of ignited primer containing *G-Marker,* shown in Figure 3 (c), corresponds to ignited primer plus pure *G-Marker* spectra. It and can be demonstrated by subtracting the FTIR spectrum of the primer containing 10.0 wt% of *G-Marker* from that one of pure primer and recovering the spectrum of pure marker. Moreover, as the figure indicates, the primer spectrum showed no major change, suggesting the absence of a chemical interaction between the primer and the marker. Therefore, the hypothesis of chemical

inertness of the markers is proved, since the marker's and the primer's structure are unaltered.
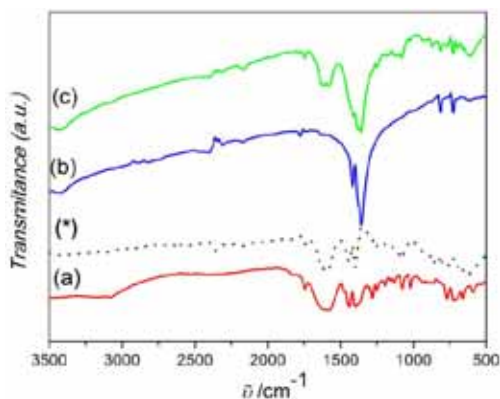

Figure 3. Infrared spectra of (a) G-Marker, (b) pure ignited primer, and (c) ignited primer containing 10wt% of G-Marker. (*) The dotted line represents the subtraction of lines (c) and (b), highlighting the marker IR absorption feature.

The SEM image (Figure 4) indicates that some of the conventional marked GSR has a spheroidal morphology which is typical of residue from conventional ammunition. In addition, the EDS image confirms the presence of Pb, Sb and Ba in the composition. Particles of markers, indicated by arrows, showed a morphology similar to that of the pure material. These results demonstrate that the SEM-EDS methodology can be used to confirm the results presented by visual and spectroscopic observations. In the case of lead-free ammunition, the rare earth ions in markers can be undoubtedly used as a chemical tag to recognize GSR. Allied to minor changes in the composition of these markers, SEM-EDS may be regarded as a versatile alternative for identifying the ammunition manufacturer and/or weapon caliber, and to distinguish between civilian, military, and law enforcement ammunition.
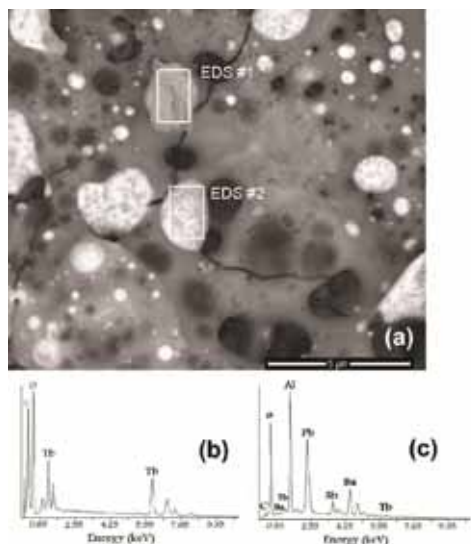

Figure 4. SEM images of marked GSR deposited on the target and EDS spectra of *G-Marker* particle (EDS #1) and traditional GSR particle (EDS #2).

The markers developed in this study are inexpensive (ranging from US$ 2.00 to 5.00 per gram in laboratory conditions). One gram of marker suffices to tag one hundred .38mm bullets or sixty-two .40mm bullets.

Supporting Information Available: Experimental procedures, crystallographic structure, X-ray powder patterns with final Rietiveld fits, and handguns, shooter body parts, primers and targets images under UV irradiation are included in the supporting information. This material is available free of charge via internet at http://pubs.acs.org.

REFERENCES

(1) Basu, S. *J Forensic Sci* **1982**, *27*, 72-91; Dalby, O.; Butler, D.; Birkett, J. W. *J. Forensic Sci.* **2010**, *55*, 924-943.

(2) Rendle, D. F. *Chem. Soc. Rev.* **2005**, *34*, 1021-1030.

(3) LaGoo, L.; Schaeffer, L. S.; Szymanski, D. W.; Smith, R. W. *J. Forensic Sci.* **2010**, *55*, 624-632; Rijnders, M. R.; Stamouli, A.; Bolck, A. *J. Forensic Sci.* **2010**, *55*, 616-623; Zeichner, A. *Anal. Bioanal. Chem.* **2003**, *376*, 1178-1191.

(4) Romolo, F. S.; Margot, P. *Forensic Sci. Int.* **2001**, *119*, 195-211.

(5) Garofano, L.; Capra, M.; Ferrari, F.; Bizzaro, G. P.; Di Tullio, D.; Dell'Olio, M.; Ghitti, A. *Forensic Sci. Int.* **1999**, *103*, 1-21.

(6) dos Reis, E. L. T.; Sarkis, J. E. S.; Rodrigues, C.; Negrini Neto, O.; Vieg, S. *Quim. Nova* **2004**, *27*, 409-413.

(7) Di Maio, V. J. M. In *Gunshot Wounds: Practical Aspects of Firearms, Ballistics, and Forensic Techniques*; Second Edition ed.; CRC Press LLC: New York, 1999.

(8) Wright, D. M.; Trimpe, M. A. *Forensic Sci. Commun.* **2006**, *8*.

(9) ASTM Standart E1588-10e1, *Standard Guide for Gunshot Residue Analysis by Scanning Electron Microscopy/ Energy Dispersive X-ray Spectrometry*, 2008, DOI: 10.1520/E1588-10E01 www.astm.org.

(10) White, R. S.; Owens, A. D. *J. Forensic Sci* **1987**, *32*, 1595-1603.

(11) Martiny, A.; Campos, A. P. C.; Sader, M. S.; Pinto, M. A. L. *Forensic Sci. Int.* **2008**, *177*, E9-E17.

(12) Weber, I. T.; Melo, A. J. G.; Alves Júnior , S.; Lucena, M. A. M.; Rodrigues, M. O. *BR Patent WO/2010/105326,* 2010.

(13) Eddaoudi, M.; Li, H.; Yaghi, O. M. *J. Am. Chem Soc.* **2000**, *122*, 1391-1397.

(14) Rodrigues, M. O.; Paz, F. A.; Freire, R. O.; de Sa, G. F.; Galembeck, A.; Montenegro, M. C.; Araujo, A. N.; Alves, S. *J. Phys. Chem. B* **2009**, *113*, 12181-12188.

(15) Jones, P. F.; Nesbitt, R. S. *J. Forensic Sci* **1975**, *20*, 231-242; Nesbitt, R. S.; Wessel, J. E.; Wolten, G. M.; Jones, P. F. *J. Forensic Sci.* **1977**, *22*, 288-303.

(16) Fernandes, A.; Jaud, J.; Dexpert-Ghys, J.; Brouca-Cabarrecq, C. *Polyhedron* **2001**, *20*, 2385-2391; Rodrigues, M. O.; Brito-Silva, A. M.; Alves, S.; De Simone, C. A.; Araujo, A. A. S.; de Carvalho, P. H. V.; Santos, S. C. G.; Aragao, K. A. S.; Freire, R. O.; Mesquita, M. E. *Quim. Nova* **2009**, *32*, 286-291.

(17) Bunzli, J. C. G.; Piguet, C. *Chem. Soc. Rev.* **2005**, *34*, 1048-1077.
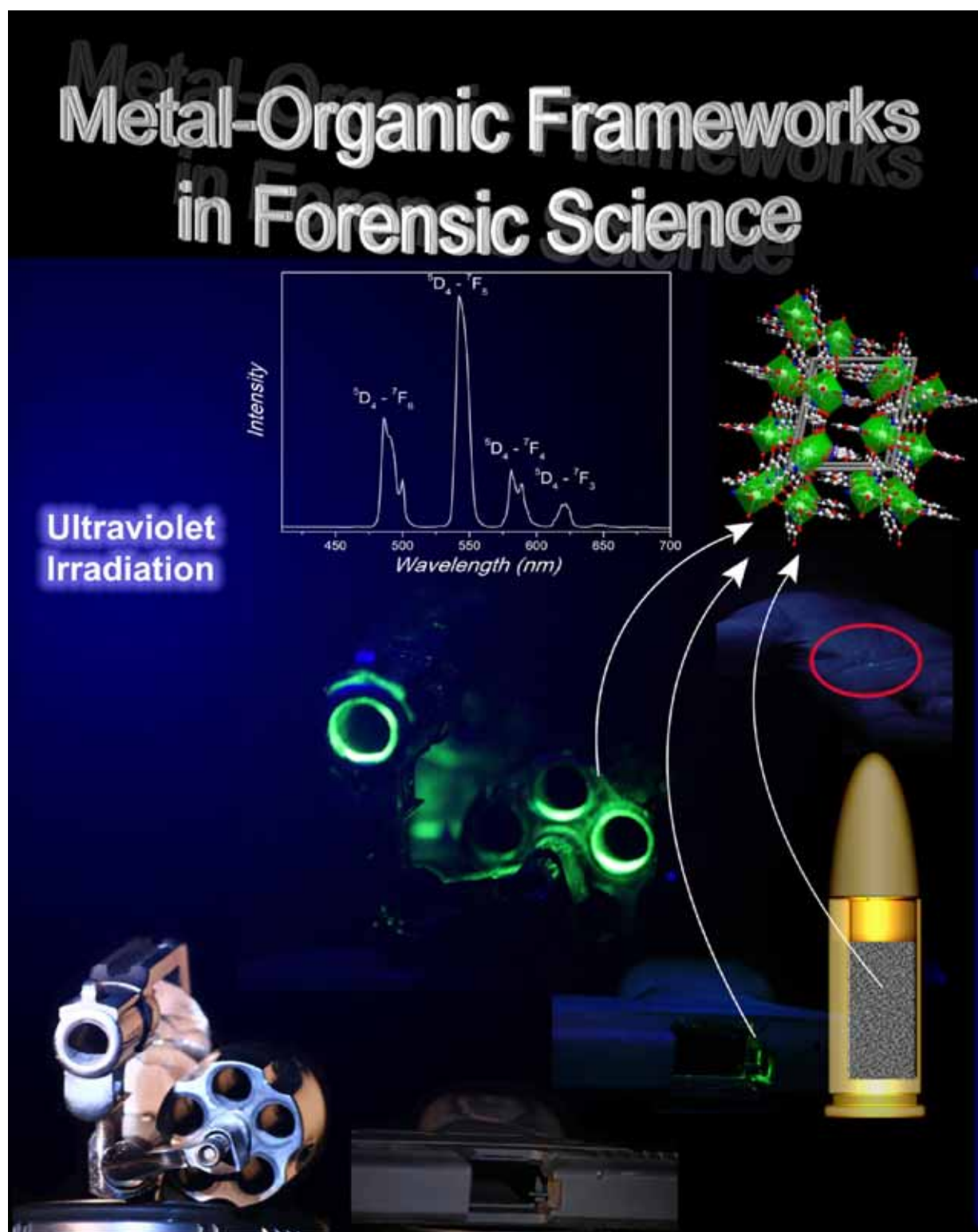
TOC Graphic

High Photoluminescent Metal-Organic Frameworks as Optical Markers for the Identification of Gunshot Residues.

Electronic Supporting Information

Ingrid Távora Weber[1], Adenaule James Geber de Melo[1,2], Marcella Auxiliadora de Melo Lucena[1], Marcelo Oliveira Rodrigues[1], Severino Alves Junior[1]

[1]Departamento de Química Fundamental, Universidade Federal de Pernambuco, Av. Prof. Luiz Freire, S/N, Cidade Universitária, 50740-540 Recife, PE, Brazil.

[2]Instituto de Criminalística, Centro de Perícias Forenses de Alagoas, Rua do Sol, 290, Centro, Maceió, AL, Brazil

Corresponding author footnote: Profº Drª Ingrid Távora Weber (ingrid@ufpe.br) Departamento de Química Fundamental, UFPE, 50670-901, Recife, PE, Brazil. Tel. +55 81 2126-7475; Fax: +55 81 2126-8442.

Experimental Procedure

R-Marker and *G-Marker* were prepared via Microwave-Assisted Hydrothermal Synthesis. A mixture of pyridine-2,6-dicarboxylic acid, H_2DPA, (0.7 mmol), $Ln(NO_3)_3.6.H_2O$, 0.35 mmol, (Ln = Eu^{3+} and Tb^{3+}) and H_2O (*ca.* 5 mL), in a 10 mL IntelliVent reactor were placed inside a CEM Focused Microwave™ Synthesis System Discover S-Class equipment. Reactions took place at 160ºC during 10 minutes, under constant magnetic stirring. The final materials were obtained in a yield of *ca.* 90% after washed with water, acetone and air-dried. The powder synchrotron X-rays diffraction patterns were acquired at temperature ambient (300K) in a 2θ range of 5-48º and using a Huber diffractometer in high resolution mode (low intensity, E=10keV) in multi-proposed powder station D10A-XRD2 beam line of Brazilian Synchrotron Light Laboratory (LNLS). Conventional.38mm SPL (CBC) and lead-free (CleanRange® CBC) .40mm S&W caliber bullets were disassembled to separate their components. Markers were added to conventional gunpowder in a ratio of 1 to 10wt% and the bullets were reassembled. For safety reasons, homogenization procedures were not performed. The bullets were then fired at distances of 10 and 40 cm from the target at an indoor shooting range. The marked GSR was collected from the target surface, the shooter's hands and the guns. The markers were also added directly to the primer of conventional and lead-free ammunition in a ratio of 1 to 10.0 wt%. GSR particles from primers were obtained by manually discharging the primer by mechanical impact onto a sample holder (black metal support). All the marked GSR was analyzed by visual observation under UV irradiation and characterized by infrared spectroscopy (FTIR Bruker model IF66), photoluminescence spectroscopy (Jobin Yvon Ramanor U1000, model H-10) and scanning electron microscopy (SEM FEI Quanta 200F).
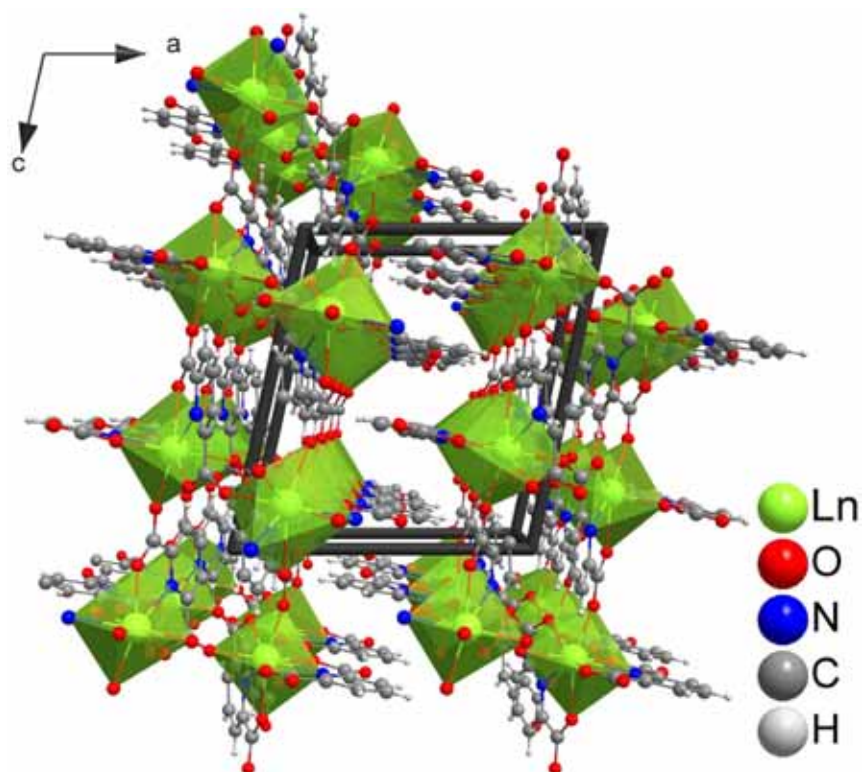
Figure S1 – Crystallographic structure of *R* and *G-Markers*. Ln= Eu^{3+} and Tb^{3+}.

The Rietveld refinement[1] for R and *G-Marker* were performed with the software GSAS/EXPGUI,[2] using as starting premise the atomic coordinates of the structural model previously reported.[3] The preferential orientation was corrected using spherical harmonic model (sixth order) proposed by Jarvinen,[4] the peak profile was adjusted by Thompson-Cox-Hastings function[5] modified by Young and Desai (pV-TCHZ),[6] surface roughness correction was refined by Pitschke function[7] and background was fitted by an eighth-degree shifted Chebyshev polynomial function. In the final runs, the following parameters were refined: scale factor, background and absorption coefficients, spherical harmonic, unit-cell parameters and pV-TCHZ correction for asymmetric parameters.
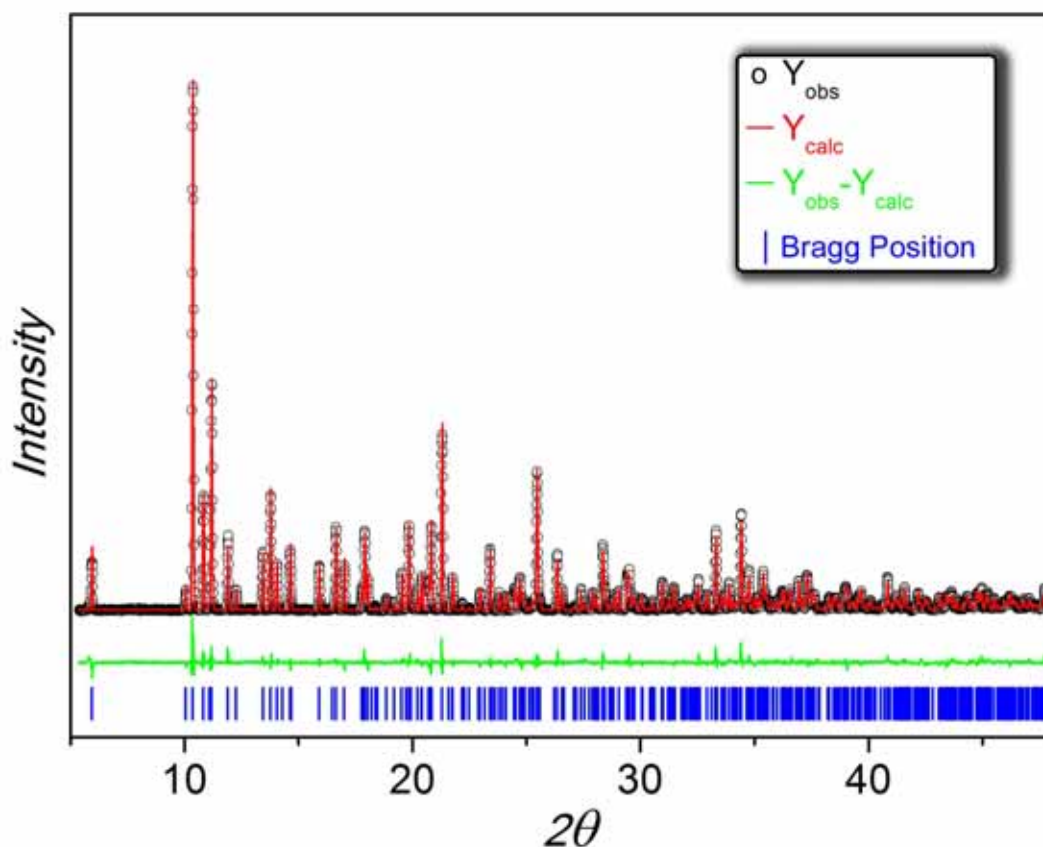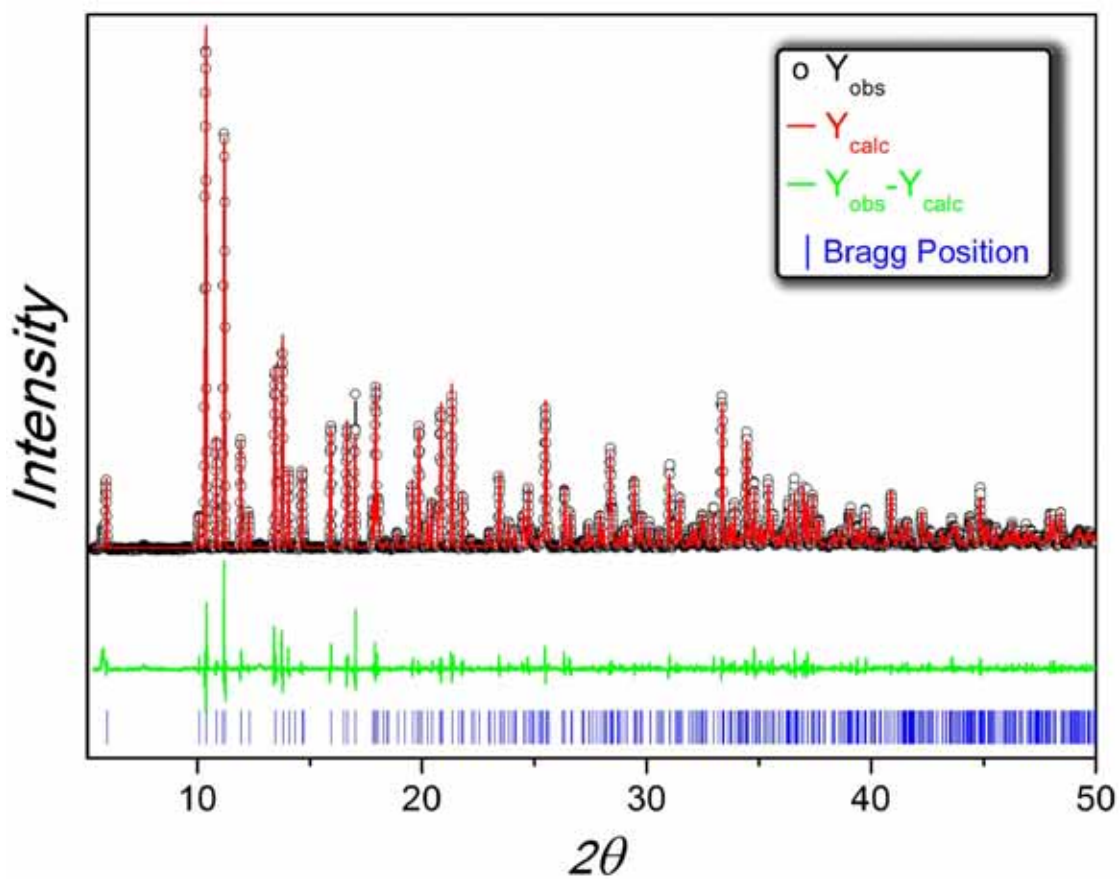
Figure S1 – Final Rietveld refinement of *R-Marker*. Observed data points are indicated as black circles, the best-fit profile (upper trace) and the difference pattern (lower trace) are drawn as solid red and gree lines, respectively. Blue vertical bars indicate the angular positions of the allowed Bragg reflections. Reliability Factors for refinement: R_p: 4.32; R_{wp}: 6.06; χ^2: 8.58; R_F^2: 9.43.

Figure S2 – Final Rietveld refinement of *G-Marker*. Observed data points are indicated as black circles, the best-fit profile (upper trace) and the difference pattern (lower trace) are drawn as solid red and green lines, respectively. Blue vertical bars indicate the angular positions of the allowed Bragg reflections. Reliability Factors for refinement: R_{p}: 4.35; R_{wp}: 6.47; χ^2: 10.43; R_{F}^2: 3.69.
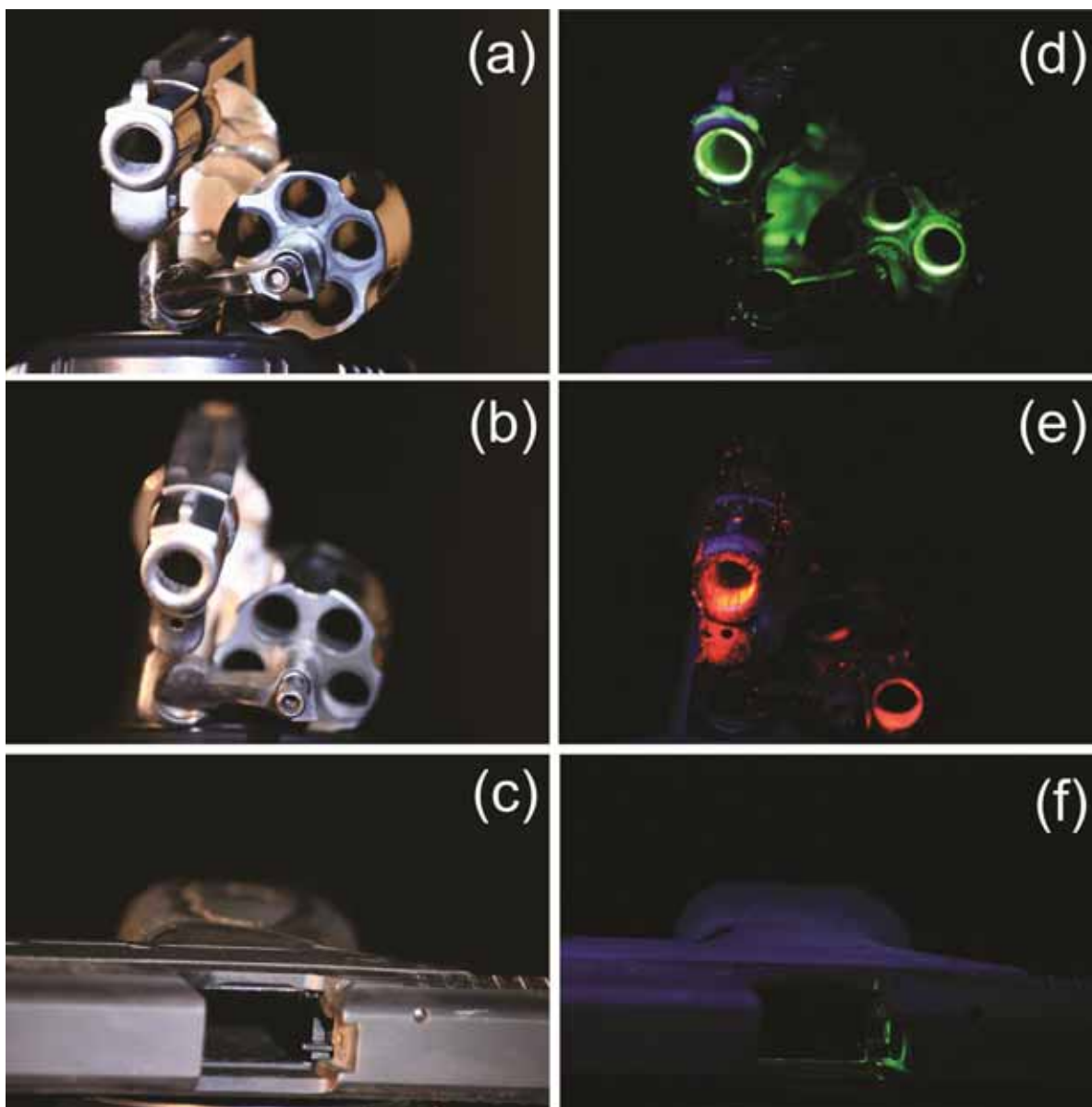
Figure S3 – Handguns and pistol after shot discharge of ammunitions containing *R* and *G-Markers*. (a), (b) and (c): no UV light irradiation; (d), (e) and (f): under UV light irradiation.
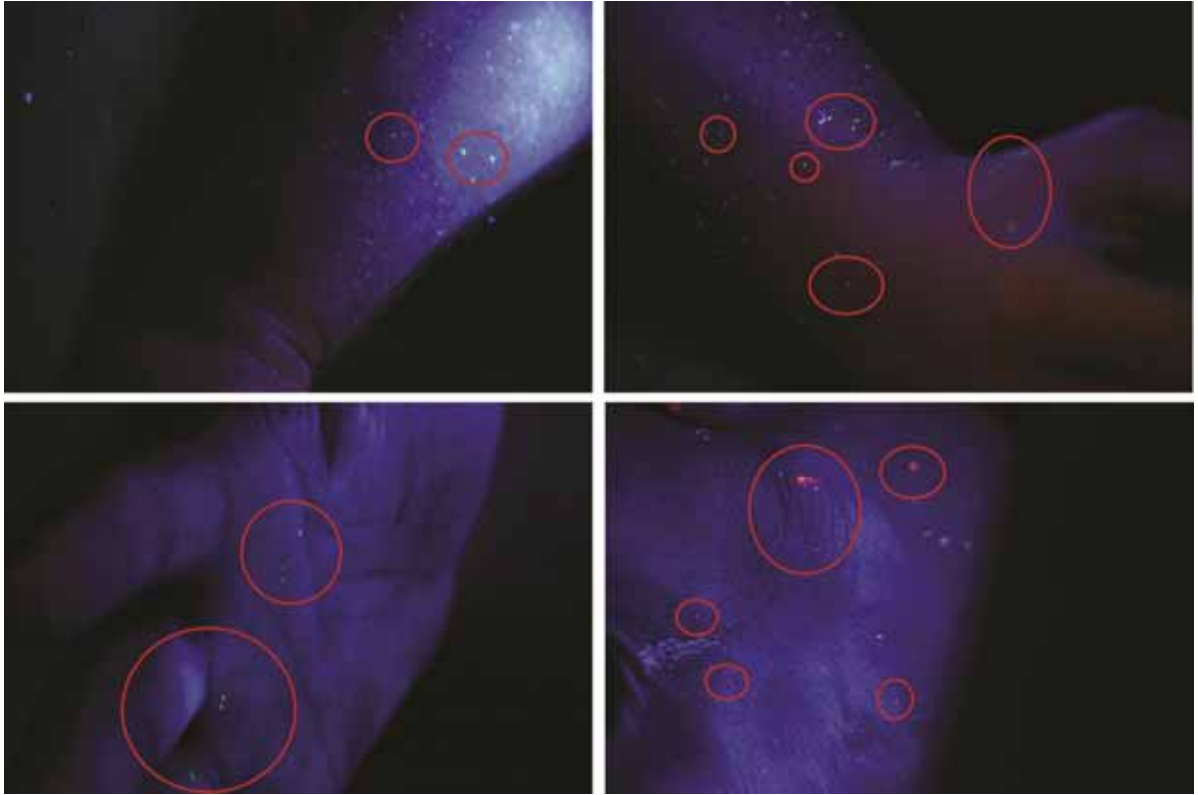
Figure S4 – *R* and *G-Marker* GSRs deposited over hands and arms of the shooter (red circles facilitate the observation of GSR). The visual identification was performed at dark-room after body parts of the shooter to be exposed to UV light irradiation.
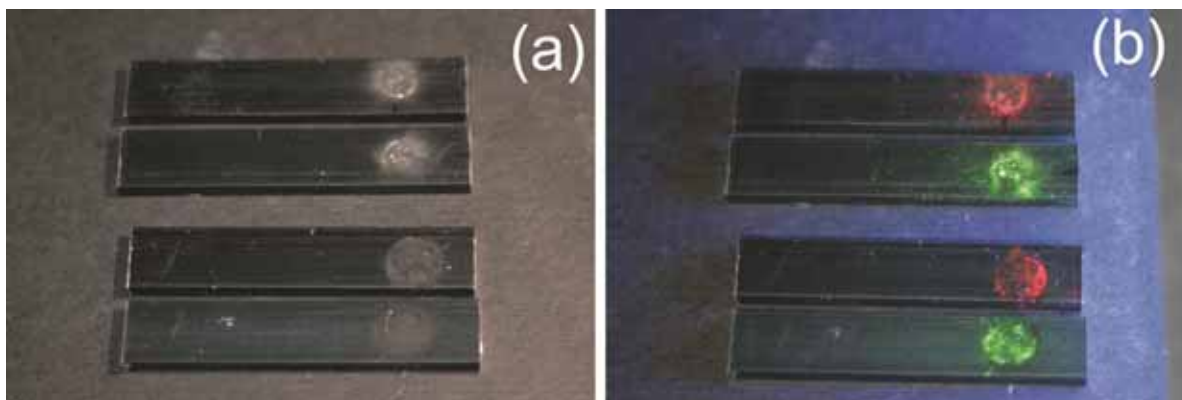
Figure S5 – R and G-Marker containing GSR from conventional (upper) and lead-free (lower) primers . (a) no UV irradiation (b) under UV lamp irradiation.
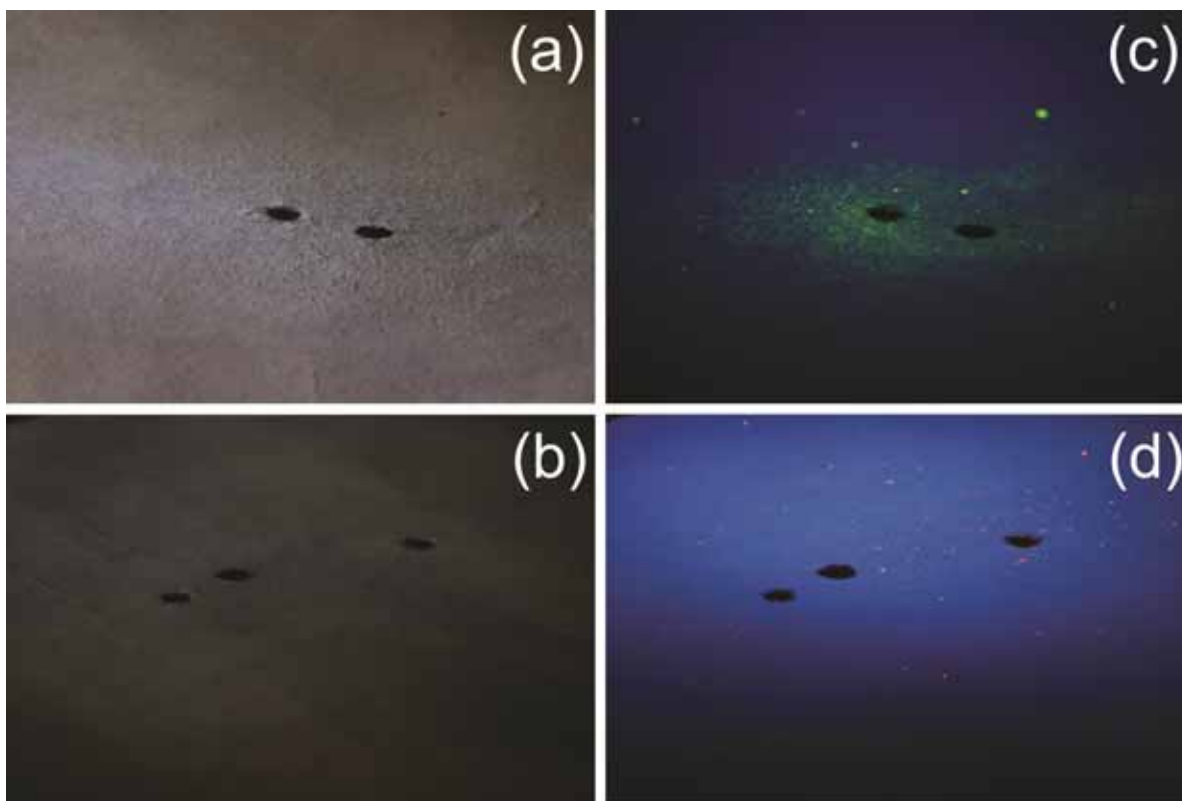

Figure S6 – R and G-Marker containing GSR deposited on the targets. (a) no UV irradiation (b) under UV lamp irradiation.

(1)   Rietveld, H. M. *J. Appl. Cryst.* **1969**, *2*, 65-71.

(2)   Larson, A. C., Von Dreele, R.B. *General Structure Analysis System (GSAS)*, Los Alamos ational Laboratory, 2004;   Toby, B. H. *J. Appl. Cryst.* **2001**, *34*, 210-213.

(3)   Fernandes, A.; Jaud, J.; Dexpert-Ghys, J.; Brouca-Cabarrecq, C. *Polyhedron* **2001**, *20*, 2385-2391.

(4)   Jarvinen, M. *J. Appl. Cryst.* **1993**, *26*, 525-531.

(5)   Thompson, P.; Cox, D. E.; Hastings, J. B. *J. Appl. Cryst.***1987**, *20*, 79-83.

(6)   Young, R. A.; Desai, P. In *Archiwun Nauki o Materialach* **1989**; Vol. 10, p 71-90.

(7)   Sidey, V. *J. Appl. Cryst.* **2004**, *37*, 1013-1014.

WIPO

Search International and National Patent Collections

| Search | Browse | Translate | Options | News | Help |

Home　IP Services　PATENTSCOPE　Database Search

1. (WO2010105326) PROCESSES FOR PRODUCING LUMINESCENT AMMUNITION AND DETECTING GUNSHOT RESIDUES

PCT Biblio. Data　　Description　　Claims　　National Phase　　Notices　　Documents

Latest bibliographic data on file with the International Bureau

Pub. No.:	WO/2010/105326	**International Application No.:**	PCT/BR2010/000105
Publication Date:	23.09.2010	**International Filing Date:**	16.03.2010

IPC: *C06B 23/00* (2006.01), *C06C 7/00* (2006.01), *C09K 11/07* (2006.01), *F42B 5/16* (2006.01)

Applicants: UNIVERSIDADE FEDERAL DE PERNAMBUCO [BR/BR]; Av. Professor Moraes Rego, 1235 Cidade Universitãria CEP:50670-901- Recife - Pernambuco (BR)

Inventors:
WEBER, Ingrid Távora; (BR).
JUNIOR, Severino Alves; (BR).
MELO, Adenaule James Geber de; (BR).
RODRIGUES, Marcelo Oliveira; (BR).
LUCENA, Marcella Auxiliadora de Melo; (BR)

Priority Data: PI0901063-7　16.03.2009　BR

Title
(EN) PROCESSES FOR PRODUCING LUMINESCENT AMMUNITION AND DETECTING GUNSHOT RESIDUES
(FR) PROCÉDÉ D'OBTENTION D'UNE MUNITION LUMINESCENTE ET PROCÉDÉ DE DÉTECTION DE RÉSIDUS DE TIR
(PT) PROCESSO DE OBTENÇÃO DE MUNIÇÃO LUMINESCENTE E PROCESSO DE DETECÇÃO DE RESÍDUOS DE TIRO

Abstract:
(EN) The present invention relates to the production of luminescent ammunition and detection of gunshot residues and the associated manufacturing process. It uses the incorporation of luminescent markers in the primer or propellant (gunpowder) of any kind of firearms ammunition of any caliber. This makes it possible both to mark ammunition and to detect gunshot residues using the luminescence emitted, including residues left by lead-free ammunition. The process is based on the luminescent properties of the markers added, thereby overcoming some of the limitations of the analytical techniques currently in use.
(FR) La présente invention concerne l'obtention d'une munition luminescente et la détection de résidus de tir (GSR, de l'anglais *Gunshot Residues*) ainsi qu'un procédé de fabrication associé. L'invention se fonde sur l'incorporation de marqueurs luminescents dans l'amorce et/ou l'agent propulsif (poudre) de munitions pour armes à feu de n'importe quel type ou calibre, ce qui permet tant le marquage des munitions que la détection de résidus de tirs au moyen de la luminescence émise, y compris lorsqu'il s'agit de munitions sans plomb. Le procédé se fonde sur les propriétés luminescentes inhérentes aux marqueurs incorporés, ce qui permet de pallier les limitations associées aux techniques analytiques actuelles.
(PT) A presente invenção trata da obtenção de munição luminescente e de detecção de resíduos de tiro - GSR (do inglês Gunshot Residues) e seu processo de fabricação. Baseia-se na inserção de marcadores luminescentes à massa iniciadora e/ou carga de projeção (pólvora) de munições para armas de fogo de qualquer natureza ou calibre, o que possibilita tanto a marcação de munições, quanto a detecção de resíduos de tiros por meio da luminescência emitida, inclusive de munições livres de chumbo. O processo baseia-se nas propriedades luminescentes inerentes aos marcadores adicionados, superando as limitações apresentadas nas técnicas analíticas usadas na atualidade.

Designated States: AE, AG, AL, AM, AO, AT, AU, AZ, BA, BB, BG, BH, BR, BW, BY, BZ, CA, CH, CL, CN, CO, CR, CU, CZ, DE, DK, DM, DO, DZ, EC, EE, EG, ES, FI, GB, GD, GE, GH, GM, GT, HN, HR, HU, ID, IL, IN, IS, JP, KE, KG, KM, KN, KP, KR, KZ, LA, LC, LK, LR, LS, LT, LU, LY, MA, MD, ME, MG, MK, MN, MW, MX, MY, MZ, NA, NG, NI, NO, NZ, OM, PE, PG, PH, PL, PT, RO, RS, RU, SC, SD, SE, SG, SK, SL, SM, ST, SV, SY, TH, TJ, TM, TN, TR, TT, TZ, UA, UG, US, UZ, VC, VN, ZA, ZM, ZW.
African Regional Intellectual Property Org. (ARIPO) (BW, GH, GM, KE, LS, MW, MZ, NA, SD, SL, SZ, TZ, UG, ZM, ZW)
Eurasian Patent Organization (EAPO) (AM, AZ, BY, KG, KZ, MD, RU, TJ, TM)
European Patent Office (EPO) (AT, BE, BG, CH, CY, CZ, DE, DK, EE, ES, FI, FR, GB, GR, HR, HU, IE, IS, IT, LT, LU, LV, MC, MK, MT, NL, NO, PL, PT, RO, SE, SI, SK, SM, TR)
African Intellectual Property Organization (OAPI) (BF, BJ, CF, CG, CI, CM, GA, GN, GQ, GW, ML, MR, NE, SN, TD, TG).

Publication Language:	Portuguese (PT)
Filing Language:	Portuguese (PT)